

NASA/TP-1999-209683



F-16XL-2 Supersonic Laminar Flow Control Flight Test Experiment

*Scott G. Anders and Michael C. Fischer
Langley Research Center, Hampton, Virginia*

December 1999

The NASA STI Program Office . . . in Profile

Since its founding, NASA has been dedicated to the advancement of aeronautics and space science. The NASA Scientific and Technical Information (STI) Program Office plays a key part in helping NASA maintain this important role.

The NASA STI Program Office is operated by Langley Research Center, the lead center for NASA's scientific and technical information. The NASA STI Program Office provides access to the NASA STI Database, the largest collection of aeronautical and space science STI in the world. The Program Office is also NASA's institutional mechanism for disseminating the results of its research and development activities. These results are published by NASA in the NASA STI Report Series, which includes the following report types:

- TECHNICAL PUBLICATION. Reports of completed research or a major significant phase of research that present the results of NASA programs and include extensive data or theoretical analysis. Includes compilations of significant scientific and technical data and information deemed to be of continuing reference value. NASA counterpart of peer-reviewed formal professional papers, but having less stringent limitations on manuscript length and extent of graphic presentations.
- TECHNICAL MEMORANDUM. Scientific and technical findings that are preliminary or of specialized interest, e.g., quick release reports, working papers, and bibliographies that contain minimal annotation. Does not contain extensive analysis.
- CONTRACTOR REPORT. Scientific and technical findings by NASA-sponsored contractors and grantees.
- CONFERENCE PUBLICATION. Collected papers from scientific and technical conferences, symposia, seminars, or other meetings sponsored or co-sponsored by NASA.
- SPECIAL PUBLICATION. Scientific, technical, or historical information from NASA programs, projects, and missions, often concerned with subjects having substantial public interest.
- TECHNICAL TRANSLATION. English-language translations of foreign scientific and technical material pertinent to NASA's mission.

Specialized services that complement the STI Program Office's diverse offerings include creating custom thesauri, building customized databases, organizing and publishing research results . . . even providing videos.

For more information about the NASA STI Program Office, see the following:

- Access the NASA STI Program Home Page at <http://www.sti.nasa.gov>
- Email your question via the Internet to help@sti.nasa.gov
- Fax your question to the NASA STI Help Desk at (301) 621-0134
- Telephone the NASA STI Help Desk at (301) 621-0390
- Write to:
NASA STI Help Desk
NASA Center for AeroSpace Information
7121 Standard Drive
Hanover, MD 21076-1320

NASA/TP-1999-209683



F-16XL-2 Supersonic Laminar Flow Control Flight Test Experiment

*Scott G. Anders and Michael C. Fischer
Langley Research Center, Hampton, Virginia*

National Aeronautics and
Space Administration

Langley Research Center
Hampton, Virginia 23681-2199

December 1999

Acknowledgments

Many individuals devoted a significant amount of their time to this experiment, and it would be impractical to list the names of all those who contributed to its success. However, special gratitude is expressed to these individuals, their companies, and the reviewers of this manuscript: Jeffrey S. Lavell, the Program Manager of the F-16XL-2 SLFC Flight Test Experiment; Naval K. Agarwal, Stan J. Miley, Chandra S. Vemuru, and Jeffrey K. Viken (LaRC Contractors); Marta R. Bohn-Meyer and Carol A. Reukauf (DFRC Program Managers); Lisa J. Bjarke (DFRC Principal Engineer); Laurie A. Marshall; Mark Collard (Operations Engineer), and Dana Purifoy (Primary Pilot); Pradip G. Parikh (BCAG program Manager) and Paul M. Vijgen (BCAG); Bala K. Bharadvaj (MDC Program Manager) and Arthur G. Powell (MDC); Earl R. Beeman II (Rockwell Program Manager); Venikit Iyer (HTC).

The authors wish to thank the following people from LaRC for reviewing this manuscript: James R. Elliot, Jr., Robert M. Hall, Ronald D. Joslin, Latunia G. Pack, and Susan J. Rickard.

The use of trademarks or names of manufacturers in this report is for accurate reporting and does not constitute an official endorsement, either expressed or implied, of such products or manufacturers by the National Aeronautics and Space Administration.

Available from:

NASA Center for AeroSpace Information (CASI)
7121 Standard Drive
Hanover, MD 21076-1320
(301) 621-0390

National Technical Information Service (NTIS)
5285 Port Royal Road
Springfield, VA 22161-2171
(703) 605-6000

Contents

List of Tables	v
List of Figures	vii
Abstract	1
1. Introduction	1
2. Nomenclature	3
3. Research Aircraft	5
3.1. Aircraft Configuration	5
3.2. F-16XL-2 Specific Flow-Field Features	5
3.2.1. Inlet-Shock System and Shock Fences	6
3.2.2. Canopy-Closure Shock	6
4. Supporting Research Flight and Wind Tunnel Tests	6
4.1. Passive-Glove Tests	6
4.2. Supersonic Low-Disturbance Quiet Tunnel Flow Physics Research	7
4.3. Transonic and Supersonic Wind Tunnel Tests	7
5. Design and Fabrication of Suction Panel and System Hardware	9
5.1. Design Criteria, Requirements, and Specifications	9
5.1.1. Aerodynamic Contour Tolerance	9
5.1.2. Surface Imperfections	9
5.1.3. Porosity	10
5.1.4. Suction Discontinuities	10
5.2. Aerodynamic Design	10
5.3. Structural and Suction System Design	12
5.4. Turbulence Diverter and Suction Patch	13
5.5. Suction-Panel Quality and Assurance Measurements	14
5.5.1. Surface Contour	14
5.5.2. Surface Waviness	14
5.5.3. Steps and Gaps	15
5.5.4. Skin Porosity	15
5.5.5. Suction Region Leak Tests	16
6. F-16XL-2 Aircraft Modification	16
7. Instrumentation	17
7.1. Pressure Taps	17
7.2. Thermocouples	18
7.3. Transition-Detection Methods	18
7.3.1. Microphones	19
7.3.2. Hot Films	19
7.4. Flow-Control Assembly	20
8. Flight-Test Objectives and Strategy	21
8.1. Test Aircraft Flight Acceptance Phase Objectives	21
8.2. Experimental Hardware Flight Acceptance Phase Objectives	21
8.3. Demonstration Phase Objectives	21

8.4. F-16XL-2 Research Phase Objectives	21
8.5. Flight-Test Point Strategy	22
9. Test Point Database	22
10. Data Analysis Tools	23
11. Results	23
11.1. Initial Flights	24
11.2. Inboard Laminar Attachment Line	24
11.3. Upper Surface Laminar Flow	26
11.4. Flight Conditions Suitable for Achievement of Laminar Flow	26
11.5. Canopy-Joint Shock Impact on Upper Surface Pressures	26
11.6. Comparison of Measured and Euler Design Pressure Distribution	27
11.7. Suction-Hole-Induced Premature Transition	28
11.8. Suction Distributions	30
11.9. Effect of Outflow on Laminar Flow	31
11.10. Suction-Panel Surface Temperature Distributions	33
11.11. Inboard Turbulent Region	34
11.12. Maximum Laminar Flow	35
11.13. Code Calibration Results	36
11.13.1. Representative Test Cases	36
11.13.2. Summary of All <i>N</i> -Factor Results	38
11.14. Supersonic Laminar Flow Control Benefits Study	39
12. Concluding Remarks	40
References	42
Appendix A—Suction-Panel Microphones	45
Appendix B—Hot-Film Locations	51
Appendix C—Database Information and Security	58
Appendix D—Flight Log	60
Appendix E—Data Repeatability and Accuracy	72
Appendix F—Flow Characteristics With Fences 1 and 2 and With No Fence	74
Tables	131
Figures	144

List of Tables

Table D1. Informal Flight Record of Major Events	60
Table 1. Individual Patch Perforated Hole Spacing	131
Table 2. Leakage From Each Region to External Surroundings.	132
Table 3. Total Internal and External Leakage From Each Region	133
Table 4. Leading-Edge External Pressure Taps	134
Table 5. Mass Flow per Suction Region and Totals	135
Table 6. Code Calibration Results From BCAG, MDC, and HTC.	136
Table 7. Comparison of <i>N</i> -Factor Calculations Between BCAG, MDC, and HTC	142
Table 8. Comparison of eMalik3d and PSE <i>N</i> -Factor Calculations	143

List of Figures

Figure A1. Planform view showing microphone (M) locations on F-16XL-2 SLFC glove.....	48
Figure A2. Kulite microphone model XCS-093-5 with M -type screen	48
Figure A3. Microphone installed against F-16XL-2 SLFC titanium skin	49
Figure A4. Two views (a and b) of microphone screen holes, as seen from above, looking through 0.015-in-diameter nominal laser drilled hole.	49
Figure A5. Microphone signal-conditioning flowchart	50
Figure B1. Hot-film layout for flights 44 to 51; 16 hot films on lower surface; 24 hot films on upper surface	52
Figure B2. Hot-film layout for flights 52 to 57.	52
Figure B3. Hot-film layout for flight 58	52
Figure B4. Hot-film layout for flight 59	53
Figure B5. Hot-film layout for flight 60	53
Figure B6. Hot-film layout for flight 61	53
Figure B7. Hot-film layout for flights 62 and 63	54
Figure B8. Hot-film layout for flight 64	54
Figure B9. Hot-film layout for flights 67 to 69.	54
Figure B10. Hot-film layout for flight 70	55
Figure B11. Hot-film layout for flights 71 to 73.	55
Figure B12. Hot-film layout for flight 74	55
Figure B13. Hot-film layout for flights 75 and 76	56
Figure B14. Hot-film layout for flight 77	56
Figure B15. Hot-film layout for flights 78 and 79	56
Figure B16. Hot-film layout for flights 80 to 82 and 85 and 86.	57
Figure B17. Hot-film layout for flights 83 and 84	57
Figure B18. Hot-film layout for flights 87 and 88	57
Figure E1. Repeatability of C_p profiles for test points taken in flight 88.	73
Figure E2. Repeatability of C_p profiles for test points taken in flights 79 and 81	73
Figure F1. The $C_{p_{\max}}$ values and attachment-line locations for different angles of attack at Mach 1.9 with fence 1; $h = 50\,000$ ft; $\beta = 0.0^\circ$	80
Figure F2. Attachment line C_p at eight BL stations for four test points at Mach 1.9 with fence 1	81
Figure F3. Measured C_p distributions for two different angles of attack at Mach 1.9 with fence 1; $h = 50\,000$ ft; $\beta = 0.0^\circ$	85
Figure F4. Isobar plots for moderate and high angles of attack at Mach 1.9 with fence 1; $h = 50\,000$ ft; $\beta = 0.0^\circ$	88
Figure F5. Isobar plots for low and moderate angles of attack at Mach 1.9 with fence 1; $h = 50\,000$ ft; $\beta = 0^\circ$	88
Figure F6. $C_{p_{\max}}$ and attachment-line location variations with angle of sideslip for Mach 1.9 with fence 1; $h = 50\,000$ ft; $\alpha = 3.6^\circ$	89

Figure F7. Measured C_p distributions for two different angles of sideslip at Mach 1.9 with fence 1; $h = 50\,000$ ft; $\alpha = 3.6^\circ$	90
Figure F8. Isobar comparison for different angles of sideslip at Mach 1.9 with fence 1; $h = 50\,000$ ft; $\alpha = 3.6^\circ$	93
Figure F9. $C_{p_{\max}}$ and attachment-line location variations with angles of attack for Mach 2 with fence 1; $h = 53\,000$ ft; $\beta = -1.5^\circ$	94
Figure F10. Measured C_p distributions for two different angles of attack at Mach 2.0 with fence 1; $h = 53\,000$ ft; $\beta = -1.5^\circ$	95
Figure F11. Isobar comparison for different angles of attack at Mach 2 with fence 1; $h = 53\,000$ ft; $\beta = -1.5^\circ$	98
Figure F12. $C_{p_{\max}}$ and attachment-line location variations with angle of sideslip for Mach 2 with fence 1; $h = 53\,000$ ft; $\alpha = 3.4^\circ$	99
Figure F13. Measured C_p distributions for two different angles of sideslip at Mach 2.0 with fence 1; $h = 53\,000$ ft; $\alpha = 3.4^\circ$	100
Figure F14. Isobar comparison for different angles of sideslip at Mach 2 with fence 1; $h = 53\,000$ ft; $\alpha = 3.4^\circ$	103
Figure F15. $C_{p_{\max}}$ and attachment-line location variations with angle of attack for Mach 1.9 for fence 2; $h = 50\,000$ ft; $\beta = 0^\circ$	104
Figure F16. Measured C_p distributions for two different angles of attack at Mach 1.9 with fence 2; $h = 50\,000$ ft; $\beta = 0^\circ$	105
Figure F17. Isobar comparison for different angles of attack at Mach 1.9 with fence 2; $h = 50\,000$ ft; $\beta = 0.0^\circ$	108
Figure F18. $C_{p_{\max}}$ and attachment-line location variations with angle of sideslip for Mach 1.9 with fence 2; $h = 50\,000$ ft; $\alpha = 3.7^\circ$	109
Figure F19. Measured C_p distributions for two different angles of sideslip at Mach 1.9 with fence 2; $h = 50\,000$ ft; $\alpha = 3.7^\circ$	110
Figure F20. Isobar comparison for different angles of sideslip at Mach 1.9 with fence 2; $h = 50\,000$ ft; $\alpha = 3.7^\circ$	113
Figure F21. $C_{p_{\max}}$ and attachment-line location variations with angle of sideslip for Mach 2 with fence 2; $h = 50\,000$ ft; $\alpha = 3.7^\circ$	114
Figure F22. Measured C_p distributions for two different angles of sideslip at Mach 2.0 with fence 2; $h = 50\,000$ ft; $\alpha = 3.7^\circ$	115
Figure F23. Isobar comparison for different angles of sideslip at Mach 2 with fence 2; $h = 50\,000$ ft; $\alpha = 3.7^\circ$	118
Figure F24. $C_{p_{\max}}$ and attachment-line location variations with angle of attack for Mach 2 with fence 2; $h = 53\,000$ ft; $\beta = -1.5^\circ$	119
Figure F25. Measured C_p distributions for two different angles of attack at Mach 2.0 with fence 2; $h = 50\,000$ ft; $\alpha = 3.7^\circ$	120
Figure F26. Isobar comparison for different angles of attack at Mach 2 with fence 2; $h = 53\,000$ ft; $\beta = -1.5^\circ$	123
Figure F27. $C_{p_{\max}}$ and attachment-line location variations with angle of attack without shock fence at Mach 1.9; $h = 50\,000$ ft; $\beta = 0^\circ$	124
Figure F28. $C_{p_{\max}}$ and attachment-line location variation without shock fence at Mach 2.0; $h = 50\,000$ ft; $\beta = 0^\circ$	125

Figure F29. $C_{p_{max}}$ and attachment-line location variation comparison between the two fences	126
Figure F30. Measured C_p distributions for the two different fences at Mach 2	127
Figure F31. Isobar comparison for the two different shock fences	130
Figure 1. Artist’s rendition of Technology Concept Aircraft (conceptual HSCT)	144
Figure 2. F-16XL-1 in-flight with test article mounted on left wing	144
Figure 3. Front in-flight view of modified F-16XL-2.	145
Figure 4. Comparison of F-16XL-2 and HSCT planforms.	146
Figure 5. F-16XL-2 baseline aircraft	146
Figure 6. Modified airplane planform features.	147
Figure 7. Front view of modified F-16XL-2.	148
Figure 8. Upper surface isobars showing flow-field features (generated by BCAG).	149
Figure 9. F-16XL-2 specific flow-field features.	149
Figure 10. Passive glove mounted on right wing of F-16XL-2	150
Figure 11. Shock fence evaluation on right wing during passive-glove tests.	151
Figure 12. Pressure distributions with and without 10-in. fence on leading-edge passive glove	152
Figure 13. F-16XL-2 1/15-scale model in the Langley Unitary Plan Wind Tunnel.	153
Figure 14. Instrumentation locations on F-16XL-2 1/15-scale model	153
Figure 15. Langley Unitary Plan Wind Tunnel data showing effect of shock fence and comparison with CFD	154
Figure 16. Details of shock fence configurations	155
Figure 17. Surface waviness design tolerances.	155
Figure 18. F-16XL-2 operating envelope	156
Figure 19. Design pressure distributions (generated by BCAG)	156
Figure 20. CFD solutions of upper surface isobars for α at and below design point (generated by BCAG)	157
Figure 21. CFD solutions of upper surface isobars for Mach numbers at and below design point (generated by BCAG)	159
Figure 22. Boundary layer disturbance growth rates for upper suction level (generated by BCAG).	160
Figure 23. Coefficient of suction C_q design range envelope for $M = 1.9$; $\alpha = 3.3^\circ$	161
Figure 24. Suction panel structure layout; 13 regions in leading edge	162
Figure 25. Suction panel leading-edge detail of flute partitions and beginning of upper surface	163
Figure 26. Suction panel upper surface detail showing stringers and flow blockers	163
Figure 27. Suction panel inner skin detail showing passageways for removal of air through lower skin into collector ducts.	164
Figure 28. Details of inboard leading-edge structure	164
Figure 29. Suction panel and support structure arrangement	165
Figure 30. Details of supporting structure	165
Figure 31. Suction panel and support structure arrangement	166
Figure 32. Inboard apex structural concept.	166
Figure 33. Suction system flow concept.	167

Figure 34. Suction system layout	167
Figure 35. Location of patches on suction panel perforated titanium skin	168
Figure 36. Details of turbulence diverter and suction patch	169
Figure 37. Minimum and maximum design suction at suction patch	170
Figure 38. Measurement grid for Computer Aided Theodelite (CAT) contour verification	170
Figure 39. Normal and streamwise paths used for surface waviness measurements	171
Figure 40. Normal path panel surface waviness measurements	172
Figure 41. Streamwise (BL) path surface waviness measurements	173
Figure 42. Measurements of splice joint gap width	174
Figure 43. Normalized porosity for each suction region.	175
Figure 44. Suction panel in cradle in preparation for fit to wing	176
Figure 45. Installed pads and hooks on F-16XL-2 wing.	176
Figure 46. Panel fit check to wing.	177
Figure 47. View of underside of suction panel	177
Figure 48. Flow assemblies, ducts, and plenum	178
Figure 49. Installed suction panel undergoing contour verification	178
Figure 50. Details of installed turbocompressor	179
Figure 51. Modified F-16XL-2 in flight	180
Figure 52. Fences 1 and 2 installed on F-16XL-2.	181
Figure 53. Suction panel internal pressure tap locations.	182
Figure 54. External pressure tap locations on left wing	182
Figure 55. External pressure tap locations in leading-edge region at BL 35	183
Figure 56. External pressure tap locations in leading-edge region at BL 70 and internal thermocouple locations in leading-edge region at BL 70.5.	183
Figure 57. Leading-edge external pressure tap installation.	184
Figure 58. Upper surface pressure tap and thermocouple installation	184
Figure 59. Cross section of upper surface pressure tap.	185
Figure 60. Cross section of stringer cutout for upper surface thermocouple installation	185
Figure 61. Cross section of upper surface thermocouple pair installation	186
Figure 62. Thermocouple locations on suction panel	186
Figure 63. Different hot-film locations used for transition detection	187
Figure 64. Splice-joint hot films installed on suction panel	187
Figure 65. Examples of laminar to turbulent hot-film signals	188
Figure 66. Typical flow control assembly (1 of 20)	188
Figure 67. Kurz thermal mass-flow sensor	189
Figure 68. Kurz thermal mass-flow sensor in duct	189
Figure 69. Flow chart of analysis procedure steps	190
Figure 70. Attachment-line suction coefficient distributions for several test points and the effect on laminar flow	191

Figure 71. Euler derived streamline traces over leading edge (BCAG)	192
Figure 72. Initial achievement of laminar flow on upper surface.	193
Figure 73. F-16XL-2 canopy joint location	194
Figure 74. Cross-section view of canopy joint	194
Figure 75. Rooftop pressure distribution showing canopy-joint shock	195
Figure 76. Canopy-joint shock impingement on suction panel	195
Figure 77. Canopy joint and fairing	196
Figure 78. Waterfall plot of C_p profiles for no fairing and final fairing.	197
Figure 79. Contours of constant C_p for no fairing and final fairing	197
Figure 80. Waterfall plot of C_p profiles for original data and data modified to eliminate pressure perturbation	198
Figure 81. Contours of constant C_p for no fairing and in absense of pressure disturbance	198
Figure 82. CFD design comparison with experimetal data for BL 50 and BL 60 for design conditions (CFD solution from BCAG).	199
Figure 83. CFD design comparison with experimental data at $\alpha = 3.75^\circ$ for BL 50 and BL 60 (CFD solution from BCAG)	202
Figure 84. Comparison of experimental isobar patterns with CFD isobar pattern (CFD solution from BCAG)	205
Figure 85. CFD design comparison with experimetal data at best laminar flow conditions for BL 50 and BL 60 (CFD solution from BCAG).	206
Figure 86. Comparison of experimental isobar patterns for extensive laminar flow with CFD isobar pattern (CFD solution from BCAG).	209
Figure 87. Maximum R_k levels used in design	210
Figure 88. R_k limit behavior across span	210
Figure 89. Perforation pattern in attachment-line region	211
Figure 90. Attachment-line $R_{\theta, C_q=0}$ values calculated from flight data (generated by BCAG).	211
Figure 91. Attachment-line characteristics for fences 1 and 2	212
Figure 92. C_q profiles for test points 88.12c1 (C_q maximum except in flute 1) and 88.11g1 (C_q minimum except in flute 1) overlayed on design operating range envelope	213
Figure 93. C_q profiles for test point 49.11p1 and upper limit of design C_q envelope.	214
Figure 94. C_q profiles for test point 77.a4g1 (extended laminar flow achieved) and design operating range envelope.	215
Figure 95. Comparison of calculated versus measured mass-flow rates	216
Figure 96. Outflow areas for test point 57.a3e5	217
Figure 97. Outflow areas for test point 63.a15g	218
Figure 98. Outflow areas for test point 70.o4i1	219
Figure 99. Outflow areas for test point 83.a2c1	220
Figure 100. Temperature measurements on panel for test point 77.a4g1	221
Figure 101. Hot-film results from selected test points showing definition of inboard turbulent region	222
Figure 102. Hot-film and trip locations used in flights 83 and 84 to investigate turbulence spreading	222
Figure 103. Wing cross section at spanwise station 62.9	223

Figure 104. Pressure and suction coefficient at BL 62.5 for test point 84.10c1	223
Figure 105. Typical turbulence spreading results from flight 84.10c1	224
Figure 106. Effect of C_q reduction on lateral spreading of turbulence	225
Figure 107. Comparison of F-16XL-2 lateral turbulence spreading with previously reported data.	226
Figure 108. Disturbance path traces shown are for $M = 2.02$; $\alpha = 3.7^\circ$; $\beta = -1.4^\circ$; (84.10c1).	226
Figure 109. Maximum extent of laminar flow achieved.	227
Figure 110. Fit of C_p data for test point 77.a4g1 (generated by HTC)	228
Figure 111. C_p contours for test point 77.a4g1 (generated by HTC)	229
Figure 112. Cross-flow Reynolds number contours for test point 77.a4g1 (generated by HTC)	230
Figure 113. N -factor calculations for films R17HF1a and R18HF1a for test point 77.a4g1 (generated by HTC)	231
Figure 114. N -factor traces on glove for test point 77.a4g1 (generated by HTC)	232
Figure 115. N -factor contours for test point 77.a4g1 (generated by HTC).	233
Figure 116. Fit of C_p data for test point 80.a3k1 (generated by HTC)	234
Figure 117. C_p contours for test point 80.a3k1 (generated by HTC)	235
Figure 118. Cross-flow Reynolds number contours for test point 80.a3k1 (generated by HTC)	236
Figure 119. Edge and surface streamlines for test point 80.a3k1 (generated by HTC)	237
Figure 120. N -factor calculations for test point 80.a3k1 (generated by HTC)	238
Figure 121. PSE results for test point 80.a3k1 (generated by HTC).	239
Figure 122. Cross-flow Reynolds number contours for test point 88.a2d1 (generated by HTC)	240
Figure 123. N -factor contours for test point 88.a2d1 (generated by HTC).	241
Figure 124. Cross-flow Reynolds number contours for test point 88.a4i1 (generated by HTC)	242
Figure 125. N -factor contours for test point 88.a4i1 (generated by HTC)	243
Figure 126. Estimate of maximum laminar flow on F-16XL-2 glove based on N -factor calculations (generated by HTC)	244
Figure 127. Summary of code calibration results for each flight	245
Figure 128. Code calibration results from MDC and BCAG	246
Figure 129. Maximum N -factors found for Splice Joint Hot Films (SJHF)	247
Figure 130. Laminarized area for SLFC benefits study	248
Figure 131. Results of SLFC benefits study	248

Abstract

The F-16XL-2 Supersonic Laminar Flow Control Flight Test Experiment was part of the NASA High-Speed Research Program. The goal of the experiment was to demonstrate extensive laminar flow, to validate computational fluid dynamics (CFD) codes and design methodology, and to establish laminar flow control design criteria. Topics include the flight test hardware and design, airplane modification, the pressure and suction distributions achieved, the laminar flow achieved, and the data analysis and code correlation.

1. Introduction

The National Aeronautics and Space Administration (NASA) initiated a multiyear research program in 1990 to develop technologies for the High-Speed Civil Transport (HSCT). The HSCT will carry 300 passengers at a cruise speed of more than twice the speed of sound (ref. 1). An illustration of a Technology Concept Aircraft (TCA) which embodies key features of the envisioned HSCT under study by Boeing Commercial Airplane Group (BCAG) and McDonnell Douglas Corporation (MDC) is presented in figure 1. The HSCT will traverse the Atlantic or Pacific in less than half the time of subsonic jets with a planned ticket price less than 20 percent above comparable subsonic travel prices. Projections call for a market of over 500 HSCT's, which translates to about 140 000 critical skill new jobs and a \$500 billion positive balance of trade for the United States; thus, the economic stakes are very high (ref. 1).

A key technology that could have a large net aerodynamic performance benefit for the HSCT is supersonic laminar flow control (SLFC). Industry studies (ref. 2) have shown that application of laminar flow control (LFC) to a HSCT offers a reduction in takeoff gross weight, mission fuel burn, aircraft skin temperatures, emissions (smaller engines with less fuel burn), and sonic boom. The risk associated with incorporating SLFC on the HSCT is high because there is a limited SLFC database, and the supersonic application may offer additional challenges, compared to the subsonic case.

A recent overview of LFC technology is presented in reference 3. There were only a small number of supersonic laminar flow flight test experiments prior to this flight program. In the 1950's, a natural laminar flow (NLF) experiment was performed on the outer

half of an F-104 wing. The wing was made smooth by applying a thin layer of fiberglass epoxy. Laminar flow was detected on the upper and lower surfaces at Mach numbers of 1.2 and 2.0 (ref. 4). No pressure data were measured, so stability code calibration using the measured transition locations could not be performed. Another NLF flight test was performed in the mid 1980's on an F-15 wing which had a glove installed over the existing wing to smooth out irregularities over a 4- ft wide span back to 30 percent chord (ref. 5). The wing sweep was 45° and the Mach number varied from 0.7 to 1.8. The transition data were correlated with stability code calculations as noted in reference 5. Another NLF flight test on an F-106 wing and vertical tail (ref. 5) about the same time was not successful in producing consistent laminar flow. Turbulence contamination of the leading-edge attachment line and strong cross flow near the leading edge were suspected to be present in this test (refs. 3 and 5).

Prior to the NASA-Industry F-16XL-2 SLFC experiment, Rockwell International and NASA performed a cooperative SLFC flight experiment in the late 1980's on the F-16XL-1 (refs. 6, 7, and 8). The suction test article was configured as a glove that fit over a segment of the existing left wing. Foam and fiberglass fairings that blended the test article into the basic wing (fig. 2) were also included. The suction surface was laser-perforated titanium, and the test area extended to about 25-percent chord nominally (about 7 ft streamwise). The span of the suction test article was 3.4 ft. Pressure orifices were installed on the fairings but not on the active suction panel. The design point flight condition was Mach 1.6, $\alpha = 2.0^\circ$, and 44 000 ft. The leading-edge radius was 0.25 in., measured normal to the 70° swept wing. At the design point, Navier-Stokes solutions predicted that R_θ would vary from 130 inboard to 150 outboard with design suction levels applied (ref. 6). The R_θ 's were never

calculated from the flight results because pressures were not measured on the suction glove. Laminarization of the attachment line was easily achieved, and laminar flow existed on the upper surface near the end of the suction panel at some span locations (refs. 7 and 8). However, laminar flow was achieved at slightly lower α and M , and at slightly higher altitude than the design point conditions. Stability code calculations and N -factor correlations using the measured transition data were not possible because there were not enough pressure measurements on the test article and there was insufficient fidelity in the suction-flow measurements. The flight experiment on the F-16XL-1 was successful in demonstrating the initial feasibility of achieving SLFC on highly swept wings and provided the confidence to move forward with a more aggressive experiment.

Consequently, in 1990 a SLFC technology development effort was initiated as part of the NASA High-Speed Research (HSR) program to provide the technology base for determination of the feasibility of SLFC for the HSCT. NASA structured the program to ensure a coordinated NASA-industry team involvement. Industry participation is crucial to ensure that practical, relevant SLFC technology is developed and validated and to ensure rapid transfer of technology application. The program contained a mix of NASA in-house and contracted tasks, including computational fluid dynamics (CFD) code development and validation, ground testing in supersonic low-disturbance facilities, and flight testing to accomplish the program objectives.

The main focus of the SLFC program was the flight demonstration of extensive LFC on the F-16XL-2 highly swept wing at supersonic speeds. The flight experiment was to address aerodynamic feasibility and the enhancement of design methods. The objectives of the flight test were

- To achieve 50- to 60-percent wing chord laminar flow on a highly swept wing at supersonic speeds
- To validate CFD codes and design methodology for supersonic laminar flow wings
- To establish initial LFC suction system design criteria to allow industry to more accurately determine benefits and integrate the concept into the HSCT

The modified test airplane used to pursue these objectives is shown in figure 3. The large, dark area on the left wing is a suction-panel glove that has been fitted over the existing wing. The area surrounding the suction panel, the passive fairing, provides a smooth contour transition from the panel to the existing airplane surface.

This experiment included a broad range of supporting efforts, including precursor flight tests, wind tunnel tests, piloted simulations, computational aerodynamics, hardware design, tooling, fabrication, software application and development, modification of the test airplane, and execution of the flight tests. These tasks were carried out by a NASA-Industry team consisting of

- NASA
 - Langley Research Center
 - Dryden Flight Research Center
- Industry
 - Boeing Commercial Airplane Group
 - McDonnell Douglas Corporation
 - Rockwell International

All parties contributed technical support and data analysis. LaRC provided the overall technical management and the wind tunnel test data. Industry's contributions included the design and fabrication of the test hardware. Dryden Flight Research Center was responsible for the installation and operation of all flight hardware and for flight testing. The team arrangement facilitated SLFC technology development and ensured a rapid transfer of technology to industry.

This paper focuses on the results of the F-16XL-2 SLFC flight test experiment and covers the entire experiment. Much of the material presented here originated from informal internal documents or reports available only to participants. This report first briefly refers to the supporting research flights and wind tunnel tests and then describes the design and fabrication of the suction panel and hardware. Next, the

instrumentation, flight test plan, database, and analysis tools are presented. Finally, the results are presented and followed by a discussion and concluding remarks.

2. Nomenclature

a	surface wave amplitude, in.	N -factor	measure of boundary-layer disturbance growth
C_p	coefficient of pressure	p	surface pressure, psi or psf
$C_{p_{\max}}$	maximum C_p value	p_i	internal pressure, psi or psf
ΔC_p	differential C_p across skin (C_p inside suction panel minus C_p outside suction panel)	R_c	Reynolds number based on mean aerodynamic chord
ΔC_{p_r}	C_p repeatability	R_{CF}	cross-flow Reynolds number
C_q	coefficient of suction	R_k	suction hole roughness Reynolds number
$C_{q_{\text{ave}}}$	average value of C_q for a region	R/ft	unit Reynolds number per ft
c	chord, ft	R_θ	Reynolds number based on momentum thickness at attachment line
diam.	diameter	$R_{\theta, C_q=0}$	R_θ at zero suction on attachment line
f	frequency, Hz, cycles/sec	R_x	Reynolds number based on chordwise distance
F-16XL-1	F-16XL airplane 1	s	surface distance along chord direction, in.
F-16XL-2	F-16XL airplane 2	s_h	perforated hole spacing, in.
g_w	allowable surface tolerance gap, in.	s_i	surface distance along inboard edge of panel, in.
h	altitude, ft	s_n	surface distance normal to leading edge, in.
h_s	allowable surface tolerance step height, in.	s_p	surface distance along span, in.
L	laminar	Δs	incremental s distance, in.
LT	laminar with “turbulent” spikes	ss	supersonic
L/D	lift-to-drag ratio	T	turbulent
M	Mach number	t	temperature
$N_{f=0}$	stationary cross-flow disturbance growth	TL	turbulent with “laminar” spikes
N_{\max}	maximum disturbance growth	TR	transitional
		x	chordwise distance, in.

α	angle of attack, deg	LaRC	Langley Research Center
β	angle of sideslip, deg	LERD	limited exclusive rights data
λ	wavelength, in.	LFC	laminar flow control
Λ	wing sweep, deg	MDC	McDonnell Douglas Corporation
Acronyms:		NLF	natural laminar flow
ARC	Ames Research Center	OD	outside diameter
BCAG	Boeing Commercial Airplane Group	PCM	pulse code modulated
BL	buttock line, in. from airplane centerline	RTB	return to base
CAT	computer-aided theodelite	SLFC	supersonic laminar flow control
CBW	constant bandwidth, Hz	TC	turbocompressor
CF	cross flow	TCA	Technology Concept Aircraft
CFD	computational fluid dynamics	TS	Tollmien-Schlichting
DES	Data Encryption Standard	CFD code acronyms:	
DFRC	Dryden Flight Research Center	BL3D	3-dimensional boundary layer code
ESP	electronically scanned pressure sensor	CDISC	constrained direct iterative surface curvature code
FDAS	Flight Data Access System	CFL3D	3-dimensional Reynolds-averaged thin-layer Navier-Stokes code
FIPS	Federal Information Processing Standards	eMalik3d	3-dimensional linear stability code
FM	frequency modulation	FT2SA	flight-to-stability analysis data reduction program developed by MDC
FS	fuselage station, in. along fuselage direction	PSE	parabolized stability equations (code)
HF	hot film	TLNS3D	3-dimensional time-dependent thin-layer Navier Stokes code
HLFC	hybrid laminar flow control	Prefixes for hot-film identification:	
HSCT	High-Speed Civil Transport	AFTHF	aft hot film
HSR	High-Speed Research	APHF	apex hot film
HTC	High Technology Corporation		
ID	identification		

CCHF	code calibration hot film
IBHF	inboard hot film
LEHF	leading-edge hot film
LSHF	lower surface hot film
OBHF	outboard hot film
RFHF	rooftop hot film
R__HF	rooftop hot film (a region number follows the R)
SJHF	splice joint hot film
TRHF	trip hot film

3. Research Aircraft

The F-16XL-2 was chosen for supersonic laminar flow control (SLFC) testing because it has a highly swept cranked wing planform that closely resembles the High-Speed Civil Transport (HSCT) configurations proposed by industry (fig. 4). The inboard section of the wing is swept 70° , while the outboard section is swept 50° . The obvious difference in size between the F-16XL-2 and the proposed HSCT configuration raises questions regarding Reynolds number effects that are beyond the scope of this experiment. The F-16XL-2 (see photograph in fig. 5) was a prototype multirole fighter airplane produced by General Dynamics (now Lockheed Martin Corporation) for United States Air Force evaluation in the early 1980's (ref. 9). In addition to the planform similarity and the availability of the airplane, this airplane is an attractive SLFC test bed because it is capable of sustaining speeds up to Mach 2 at altitudes up to 55 000 ft. The F-16XL-2 has a two-seat cockpit and a General Electric F110-GE-129 engine rated at 29 000 lb of thrust. This higher performance engine requires a large normal shock inlet, which is also found on regular F-16's with the same F110-GE-129 engine. Two F-16XL's were built, and both are on loan from the United States Air Force to NASA. The second aircraft, the F-16XL-1 used in the NASA/Rockwell flight experiment (fig. 2), has a single place cockpit and a Pratt and Whitney 100-PW-100 engine rated at 23 830 lb of thrust. The F-16XL-1 inlet is smaller than

the one used on the F-16XL-2. Both vehicles have the same overall dimensions, a length of 54.2 ft, a wing-span of 34.3 ft, and a height, at vertical tail, of 17.7 ft. The double delta cranked-arrow wing has approximately twice the wing area of the standard F-16 and is constructed of graphite polyimide composite skins with an aluminum substructure.

3.1. Aircraft Configuration

The modified F-16XL-2 test aircraft is shown in figure 3. The right side leading-edge passive glove (refs. 7, 10, and 11) was installed and tested before the left side as a precursor test that included the verification of the leading-edge region design. The suction test panel and related suction system components were installed over the left wing and in portions of the fuselage. This installation included instrumentation, power supplies, signal conditioning units, cables, wiring, suction ducting and plenum, suction control valves and flowmeters, a turbocompressor, an apex extension, and passive fairings. A schematic of the modified airplane planform, with major features labeled, is shown in figure 6. The perforated titanium suction panel was positioned near the center of the 70° swept left wing. The suction panel was 17 ft long along the leading edge and extended back to 60-percent chord. A frontal ground view of the modified airplane shown in figure 7 clearly shows the asymmetry of the configuration.

3.2. F-16XL-2 Specific Flow-Field Features

Designers knew in advance that the presence of certain F-16XL-2 specific flow-field disturbances could alter the pressure distribution on the suction panel and affect the ability to achieve extensive spanwise and chordwise laminar flow. A BCAG Euler solution showing the isobar contours on the upper surface of the modified wing is given in figure 8. The three major sources of concern were the canopy windshield shock, the canopy-closure shock, and the engine inlet-shock system (not apparent in fig. 8). The canopy windshield shock intersected the leading edge in the area of buttock line (BL) 30 to 35. The test article began at BL 41.5; therefore, the windshield shock could not reach the panel and adversely affect the potential for achieving laminar flow. The engine inlet-shock system and the canopy-closure shock are discussed in subsections 3.2.1 and 3.2.2.

These disturbances are related directly to the F-16XL-2 test aircraft and therefore are not issues for a HSCT designed to take advantage of LFC. The HSCT would have to be designed to ensure that features on the fuselage, such as windows, are smoothly blended to avoid generation of shocks across the wing. The engine inlets on the proposed HSCT are behind the potential laminarized area so that shocks originating from the inlets would not influence achievement of laminar flow.

3.2.1. Inlet-Shock System and Shock Fences

The engine inlet-shock system was a concern which arose in the early preliminary design. Figure 9 shows a schematic of the inlet-shock system along with the disturbances from the canopy on the upper surface. The inlet-shock system propagates across the lower surface of the wing, and in crossing the leading edge near midspan, disturbs the pressure distribution and alters the attachment-line flow. This flow disturbance could cause premature transition of the laminar attachment line and adversely affect the extent of laminar flow achievable on the upper surface outboard of the shock crossing. BCAG, responsible for the aerodynamic design of the suction panel and fairings, suggested that the inlet shock could be blocked by the installation of a shock fence on the lower surface. Figure 9 schematically illustrates a shock fence installed on the lower surface. Numerous CFD iterations and results from supporting flight and wind tunnel tests guided the design of a baseline and backup shock fence.

3.2.2. Canopy-Closure Shock

Due to the three-dimensional geometry of the canopy, the flow over the canopy expands as the canopy profile extends into the fuselage contour. At the end of the expansion, a “closure” shock results, as shown in figures 8 and 9. This shock traverses across the wings and therefore was a factor in the design of the suction panel because the shock likely would cause a loss of laminar flow. The panel was designed so that only the rear of the suction panel is intersected by the shock, at about 50 to 55 percent chord at midspan. In addition, the suction in this area was tailored to contend with this disturbance by providing a separate suction region and elevated suction level capabilities.

4. Supporting Research Flight and Wind Tunnel Tests

The SLFC program consisted of several supporting elements: experiments in low-disturbance level supersonic tunnels, testing of a 1/15 scale wind tunnel model of the modified configuration, and precursor flight tests of the F-16XL-2 aircraft. The goal of these program elements was to reduce risk, add value to the final experiment design, and satisfy safety of flight concerns inherent to the highly asymmetric test configuration.

4.1. Passive-Glove Tests

The leading-edge passive glove (no suction) on the right wing shown in figure 10 was designed to provide attachment-line stability criteria for leading-edge flows that are characteristic of the leading-edge radius and shape expected to be used on the large suction experiment. Five rows of flush pressure orifices in the foam-fiberglass glove measured the C_p profiles. Surface hot films were used to determine transition location along the leading edge. Data were also collected to address other concerns related to the final design. These concerns included measurement of the canopy-closure shock location on the upper surface, evaluation of the effectiveness of a preliminary shock-fence design suggested by BCAG, and evaluation of several leading-edge turbulence diverters.

To determine in-flight the position of the canopy-closure shock, two rows of pressure belts were installed on the F-16XL-2 upper wing surface in the vicinity of the shock location predicted by the Euler results. The measured shock location was about 5 percent chord forward of the predicted value (ref. 10), thereby raising the confidence that the canopy-closure shock would not limit achievement of extensive laminar flow.

To assess the effectiveness of a preliminary shock fence in blocking the inlet-shock system, a 10-in. high fence with a 60° swept leading edge was fabricated and installed on the right wing at BL 45. The fence was secured to the lower surface by using existing missile attachment points. The fence and its relationship to the engine inlet, inlet diverter, and the passive glove is shown in figures 11(a) and 11(b). The inlet diverter is a wedge-shaped structure that prevents the

fuselage boundary layer from entering the engine inlet (fig. 11(a)). Five rows of flush static pressure orifices positioned on the passive-glove leading-edge upper and lower surfaces were used to evaluate the shock-fence effectiveness in the leading-edge region. On the remaining part of the lower surface, pressure belts measured the location of the shock system and determined the effectiveness of the shock fence. This shock fence reduced the strength of the inlet-shock system pressure disturbances (ref. 10) but did not entirely eliminate its influence. An Euler code CFL3D with a detailed grid model of the F-16XL-2 (assuming a flow-through inlet condition) was modified with the shock-fence geometry and compared to the flight data. Figure 12 shows that there is very good comparison between flight data and CFD with the fence on and off. This prediction capability instilled confidence that an improved fence could be designed with CFD for the large suction glove. CFD analysis of various shock-fence configurations was used to design a baseline fence (fence 1) which, based on the model used, was effective.

To achieve laminar flow on the upper or lower surface of any wing, it is first essential to establish a laminar attachment-line boundary layer flow. Establishing this flow requires careful design in order to prevent turbulence from the fuselage boundary layer from traveling along the wing leading edge and contaminating the entire wing (refs. 12 through 14). The R_θ is a key parameter for characterizing the state of the attachment-line flow and for determining whether the attachment line will be laminar or turbulent (refs. 12 through 14). For a wing with moderate-to-high sweep and large leading-edge radius (R_θ increases with leading-edge radius), fuselage turbulence will contaminate the leading edge and spread over the entire wing. For values of R_θ below about 90 to 100 in subsonic flow, turbulent eddies decay along the leading edge, and turbulence is swept rearward over the wing (refs. 12 through 15). For larger R_θ , a passive or active (suction patch) concept is required to remove the oncoming turbulent attachment-line boundary layer and to establish a new laminar boundary layer. Once a new laminar boundary layer is established on a smooth leading edge, the allowable R_θ (~240) is much higher (refs. 12 through 14). For $R_\theta > 240$, small amplitude disturbances amplify. The sharp leading-edge “S” shape blend found inboard on the basic F-16XL-2 wing-fuselage juncture region (fig. 10), which was retained for the passive glove,

served as a natural turbulence diverter. For the SLFC suction-panel experiment, the large-radius leading edge was extended at a constant 70° leading-edge sweep into the fuselage (fig. 3), which is more representative of a HSCT wing. This modification required that a method of removing the turbulence along the leading edge be included in the final configuration. Several passive turbulence diverters were designed and tested. The best performing concept was a stream-wise slot which was selected and used for the present experiment.

4.2. Supersonic Low-Disturbance Quiet Tunnel Flow Physics Research

Research experiments were conducted in low-disturbance quiet supersonic tunnels (refs. 3 and 16) at LaRC and ARC. These experiments on swept cylinders and highly swept wing bodies concentrated on improved understanding of leading-edge flow physics and calibration of LFC design tools. Stability calculations for the flow over the swept wing bodies were performed, and correlations with measured transition locations were conducted. Both suction and nonsuction models were evaluated. These results added to the database for LFC prediction methodology, even though the results were not available in time to influence the design of the F-16XL-2 suction panel. Discussion of these experiments can be found in references 3 and 16.

4.3. Transonic and Supersonic Wind Tunnel Tests

The modified planform of the F-16XL-2 raised safety of flight concerns due to possible excessive pitchup and directional control characteristics resulting from the asymmetric configuration. If the aircraft control surfaces could not trim out these asymmetric forces and moments, severe restrictions would have to be placed on the operational envelope, jeopardizing the program objectives. LaRC conducted transonic tests in the Langley 8-Foot Transonic Pressure Tunnel and supersonic wind tunnel tests in the Langley Unitary Plan Wind Tunnel with a 1/15 scale F-16XL-2 model to obtain the required force and moment data. A photograph of the model, with the modified wing and fence in place, is shown installed in the Langley Unitary Tunnel in figure 13. The Lockheed Martin Corporation lent NASA the unmodified baseline model.

Both the gloved and baseline wing were tested for the purpose of comparing the stability and control of the two configurations.

The objectives of the tests were

- To determine stability and control characteristics of the modified aircraft
- To obtain force and moment coefficients to allow DFRC to upgrade an existing simulator model
- To verify design codes with measured surface pressures
- To determine effectiveness of the baseline shock fence in minimizing the effect of the inlet-diverter shock on leading-edge pressures

The model and instrumentation are schematically represented in figure 14. Provisions were made for installing the scaled flight-test baseline fence at BL 65, which was the span station planned in the flight tests. This fence, referred to as fence 1, was 20 in. high full scale—double the height of the fence evaluated in the supporting flight tests described earlier (fig. 11). The fence leading-edge sweep was 60° in both cases. An Euler solution predicted this fence would provide adequate blockage. Note that the model inlet did not simulate flight condition mass flows. Measured surface pressures at the design condition of $M = 1.9$ and $\alpha = 3.3^\circ$, with and without the fence, are presented in figure 15. The CFD prediction for the fence-installed condition is shown for comparison. At the inboard measuring station, there is good agreement with the Euler solution up to the canopy-closure shock. The fence had no measurable influence on these pressures except perhaps at the first leading-edge orifice. The leading-edge pressures outboard of the fence were overexpanded, resulting in a pressure peak. With the fence installed, the leading-edge pressure peak was evident but less severe (fig. 15). The comparison of the Euler results at the outboard station showed poor agreement in the leading-edge region but improved further rearward. The inability of the Euler code and the wind tunnel experiment to model the inlet mass flow may have contributed significantly to the disagreement in the leading-edge pressure profile. The Euler code assumed that all the oncoming mass of airflow passed through the inlet. The wind tunnel model inlet blocked an unknown volume of air and

resulted in a standoff shock in front of the inlet. Another contributing factor could have been the precision of the model geometry in the leading edge and, in general, the wing contour. The preliminary fence that was flight tested with the passive glove and the corresponding Euler prediction were in reasonable correlation (fig. 12), yet the Langley Unitary Plan Wind Tunnel data indicated that the larger fence was not as effective. The inability of the fence to adequately block the shock in the Langley Unitary Plan Wind Tunnel tests led to a revised design (fence 2) before flight testing began. Fence 2 was to be used as a backup if required. A comparison of fence 1 and fence 2 geometry is shown in figure 16. Fence 1 had a round leading edge and was swept 60° , but fence 2 was sharp, with only a 10° sweep. Fence 2 provided more blockage, as is evident in figure 16. Each fence had to be analyzed by DFRC for imposed load, stability and control, and handling quality concerns. It is doubtful that a fence larger than fence 2 could have been used. It is generally agreed that the shock from the inlet face rather than the diverter is the dominant source of the pressure disturbance. The strength of the inlet shock is dependent on engine mass-flow requirements at each flight condition; for example, shock strength depends on altitude, Mach number, and free-stream temperature. The inlet shock was not modeled during the design of the shock fences. A CFD code with the capability to include inlet mass-flow modeling was beyond the scope of the project and would have required details on engine performance, inlet spillage, and flow specifications not available in the design process time period.

The canopy-closure shock location measured in the wind tunnel test, which can be seen at the inboard measuring station (fig. 15), occurs considerably sooner (about 11 percent chord difference) than predicted by CFD. This result was in slight disagreement with flight data taken with the passive glove, which showed that the measured shock recovery position occurred about 5 percent chord further upstream than CFD prediction on the baseline unmodified F-16XL-2 wing (ref. 10). The viscous effects of flight and the wind tunnel would be expected to result in an earlier shock position, as compared to an Euler inviscid solution. The fidelity of the wind tunnel model overall geometry compared to the actual F-16XL-2 was not known, and geometry deviations in the upper surface and particularly the canopy shape could be partly responsible for the different results between

wind tunnel and flight. It was shown in the Langley Unitary Plan Tunnel that using small nose-right side-slip (negative β), would delay the canopy-closure shock position without altering the basic C_p shape. Thus, introduction of small negative β to move the canopy-closure shock rearward remained an option for flight if the shock prevented achieving extensive laminar flow.

DFRC used the incremental aerodynamic coefficients between the baseline F-16XL-2 and the modified configuration derived from the transonic and supersonic wind tunnel data to refine an existing F-16XL-2 simulator model. DFRC test pilots assigned to the flight test program performed piloted simulations of the modified aircraft to evaluate the handling qualities, safety, and performance of the configuration. The improved F-16XL-2 simulator model with asymmetric characteristics indicated there would be no significant adverse effect on handling qualities. The flight characteristics of the modified F-16XL-2 compared well with the simulator predictions.

5. Design and Fabrication of Suction Panel and System Hardware

5.1. Design Criteria, Requirements, and Specifications

Achievement of a successful laminar flow experiment required careful attention to the specification and control of the final hardware product, especially the outer test surface. The existing database for waviness, steps, gaps, and roughness developed and used in subsonic laminar flow experiments was used in this experiment in the absence of a supersonic flow database. Previous high subsonic laminar flow flight tests had transonic-supersonic flow over the wing upper surface where laminar flow was achieved, showing that the existing criteria were valid for locally supersonic flow. References 3 and 17 provide a review of laminar flow smoothness, waviness, steps and gaps, and other criteria compiled from previous experiments. Where possible, more stringent criteria were exercised in this experiment.

5.1.1. Aerodynamic Contour Tolerance

To ensure achievement of the design surface pressures on the final finished part, the tolerances on the

suction panel contour shape were ± 0.020 -in. deviation from design in the leading-edge region, back to $s_n = 4$ in. For the aft portion of the suction panel, after $s_n = 4$ in., the tolerances were relaxed to ± 0.050 in. These tolerances were derived from Euler calculations wherein the panel contour was perturbed by these levels and no change in calculated C_p was observed.

5.1.2. Surface Imperfections

To obtain laminar flow, surface tolerances must meet specifications for waves, steps, gaps, and roughness heights. The specifications successfully used for previous LFC flight tests are discussed in references 3 and 17. The correlations dictate maximum allowable surface wavelengths and heights, steps and gaps, and three-dimensional roughness values based on flight and wind tunnel databases. The criteria are based on high subsonic flows and have been used successfully in high subsonic and recent supersonic (refs. 5, 7, 8, and 10) flight experiments.

Surface waviness. Multiple surface waves with crests parallel to the span cannot exceed 0.007-in. total amplitude for a wavelength of 12 in., as shown in figure 17. The curve in figure 17 was calculated by using an expression for wave amplitude from reference 17 and the conditions for this experiment, as noted in the figure. For wavelengths of 2 in., the allowable total amplitude is 0.003 in. As noted in the figure, the allowable wave amplitude is triple these values for a single wave. Chordwise waves are less restrictive, with double the permissible amplitudes shown in figure 17.

Steps and gaps. Criteria for two-dimensional surface discontinuities are inversely proportional to the unit Reynolds number and are as follows:

- Step height, h_s

Forward facing: $h_s \leq 1800/R/ft$

Aft-facing: $h_s \leq 1/2$ of forward facing step height

- Gap width, g_w

For flow across: $g_w \leq 15\,000/R/ft$

For flow parallel to: $g_w \leq 1/7$ of gap width for flow across gap

Aft-facing steps are more restrictive than forward-facing steps, and flow along a gap should be avoided where possible. The accepted values for steps and gaps used in this experiment during fabrication and assembly were conservative in comparison to those calculated from the expressions presented above. The forward-facing step height limit was set at 0.003 in. (0.010 in. is given by the previous expression for h_s) and the aft-facing step height limit was set at 0.001 in. (0.005 in. is given by the previous expression for h_s). The gap-width limit (flow across) was set at 0.025 in. (0.080 in. is given by the previous expression for g_w). The design point unit Reynolds number of 2.25×10^6 was used for these calculations.

Three-dimensional roughness elements were avoided by the nature of the panel design. The perforated titanium skin was formed in two continuous sheets joined at one seam, eliminating the need for rivets or other sources of roughness. Insect residue was the only source of three-dimensional roughness, and the occasional insect impact was measured and documented as standard procedure. Reference 17 presents allowable values for roughness elements.

5.1.3. Porosity

The porosity of the suction surface depends on the diameter of the holes and their relative spacing. The nominal diameter of the laser-drilled holes was 0.0025 in. for the entire panel. Therefore, the porosity was varied by changing the spacing only. The porosity goal for the perforated skin was to have a mean porosity in each suction region within ± 5 percent of the design level (see section 5.2 for design C_q levels).

5.1.4. Suction Discontinuities

Suction discontinuities are unavoidable due to structural supports, compartment boundaries, and instrumentation in the test panel. Nonsuction areas will result wherever structures are bonded to the perforated skin. These regions of discontinuous suction are unfavorable from the point of boundary layer stability and therefore were made as small as practical. The leading-edge region is the most critical with respect to discontinuities in suction because cross-flow distur-

bances are growing at high rates in this area. For this area, the design specification was to block a width of no more than 0.2 in. (including an adhesive blockage of about 0.05 to 0.10 in.). For pressure taps, the allowable blockage area was specified to be no more than 0.06 in. in diameter, including adhesive. Nonsuction areas on the upper surface, where stingers existed underneath the titanium skin, were allowed to be much larger. The width of the stringers was specified to be less than or equal to 0.6 in., including adhesive. Boundary layer stability calculations were used to aid in the definition of the allowable discontinuities. Structural details can be found in section 5.3.

5.2. Aerodynamic Design

The glove contour and suction distribution were designed to provide a favorable environment for obtaining a robust SLFC database. The operating envelope of the unmodified F-16XL-2 is shown in figure 18. The operating envelope was bounded by flutter limits (which had to be verified for the modified configuration in the initial flights), structural dynamic pressure limits, and engine thrust-aircraft drag performance limits. A design point of $M = 1.9$ and 50 000 ft was selected as feasible for the modified F-16XL-2. A slightly higher M and altitude may be achievable, depending on the drag and engine performance of the modified configuration. The R/ft at the design condition was 2.25×10^6 , but the R/ft was dependent on the local temperature at altitude for a given flight.

Because the suction panel was designed as a glove to fit over the F-16XL-2 wing, clearance constraints to allow for suction ducting, installation hardware, instrumentation, and access produced additional design contour challenges. The foam and fiberglass passive glove area surrounding the suction panel was necessary to blend the test panel contour smoothly into the basic wing shape and was an integral part of the overall designed contour. The design pressure distribution is shown as surface isobar and pressure coefficient profiles in figure 19. BCAG designed the SLFC suction panel and fairing geometry by using a Constrained Direct Iterative Surface Curvature (CDISC) inverse design method developed by LaRC (ref. 18), coupled with a three-dimensional thin-layer Navier Stokes (TLNS3D) flow solver (ref. 19). As shown in figure 19, C_p profiles were designed with a steep leading-edge acceleration to the rooftop, followed by a

gradual favorable pressure gradient back to the canopy-closure shock location. The steep acceleration allows rapid progression through the cross-flow region. A region of gradual favorable pressure gradient is known to be stabilizing to Tollmien-Schlichting (TS) disturbances (ref. 3). The individual streamwise pressure distributions collapsed to a common level across the span. A very critical aspect of the C_p design was the absence of spanwise gradients, and therefore nearly unswept isobars existed on the upper surface of the suction panel at the design α , as shown in figure 19.

Extensive off-design calculations were performed by BCAG to determine the sensitivity of the suction panel C_p to α and Mach number variations. The effect of α at $M = 1.9$ on the isobar pattern is illustrated in figure 20 for two angles of attack below and two above the design α of 3.3° . As α is decreased below the design value, the isobars increase in sweep outboard, and the acceleration of the leading-edge flow to the upper surface is slowed. This increase in sweep produces undesirable cross-flow disturbance growth on the upper surface. Above the design α of 3.3° , the flow acceleration in the leading-edge region is steeper, resulting in an overexpansion of the leading-edge pressures. Also, a reverse isobar sweep, which increases cross-flow (CF) growth, is evident on the upper surface.

The influence of off-design Mach number on the design pressure distribution is illustrated in figure 21. Calculations were made only for Mach numbers below the design point at $M = 1.8$ and $M = 1.7$. The isobars for $M = 1.8$ and $M = 1.7$, at the design α of 3.3° , show reverse inboard sweeping of the isobars and peaks in the leading-edge pressures, as compared to the design point of $M = 1.9$. This result is similar to the effect of higher than design α (fig. 20). The lower Mach numbers also result in the canopy-closure shock occurring at earlier chord locations on the rear of the suction panel.

The design pressure distribution is conducive to obtaining laminar flow but not sufficient in itself for extensive laminar flow on a highly swept wing. Suction is also required to maintain laminar flow on the test article. The design suction distribution (C_q) was targeted to provide a flexible range of suction levels on the panel. The design was based on an N -factor

range of 4 to 12, as derived from linear boundary layer stability theory calculations performed by BCAG using the eMalik3d code (Malik, M.R.: eMalik3d: *An e^N Code for Three-Dimensional Flow Over Finite-Swept Wings*, High Technology Report No. HTC-9502, April 1995). The criteria for establishing the upper or maximum and lower or minimum levels of suction were based on flight and wind tunnel transition data which had been correlated with stability analysis. Results presented in references 5, 20, and 21 provided confidence that the N -factors selected were conservative, based on existing experience. The supersonic attachment line results from references 6 through 8 and the unpublished findings from the passive glove-supporting flight tests provided guidance for selection of the R_θ 's as shown in the following description:

Maximum suction

- Highest rationally required from boundary layer stability standpoint (ensure laminar flow based on previous experience)
- $R_\theta = 140$ on attachment line
- Envelope method (CF and TS disturbances)

N -factor = 6 for nonstationary TS waves

N -factor = 4 for stationary CF waves (frequency = zero)

Minimum suction

- Lowest for which laminar flow is possible with no outflow (natural venting)
- $R_\theta = 200$ on attachment line
- Constant wavelength method

N -factor = 10 for stationary CF waves

N -factor = 12 for nonstationary TS waves

Calculations of N -factors at four BL stations on the suction panel for the stationary ($f = 0$) and nonstationary (up to 6 kHz) disturbance waves (to determine the upper level suction) are shown in figure 22.

As indicated, the disturbance growth for the stationary waves is contained well below an N -factor of 4, while the nonstationary disturbances do not grow beyond an N -factor of 6. Similar calculations were performed to assure that the minimum suction resulted in growth rates to the levels specified.

The design point C_q upper and lower range values are presented in figure 23 for 6 BL stations across the suction panel. A cross section of the suction panel is also shown for clarification. The high levels of suction are confined to the three leading-edge flutes, 1 through 3, while the upper surface, or rooftop, has a low threshold level. The upper suction level in flute 1 is driven by the suction flow needed to lower R_θ on the attachment line to 140 (i.e., to ensure a laminar attachment line). Flutes 2 and 3, the suction ramp in the C_q plot, provide the suction flow needed to control leading-edge cross flow. The relatively constant threshold level of suction on the rooftop is required to control TS wave growth.

5.3. Structural and Suction System Design

Given the definition of the desired suction distribution for the test article, the suction system was designed to achieve this distribution as closely as possible. For instrumentation, physical size constraints in the leading-edge flutes were key in determining their number and configuration. Additional parameters that influenced aspects of the design were the pressure losses across the skin, through the collector ducts to the plenum, and in the ducting leading to the turbocompressor. The number and orientation of the individual suction regions varied during the preliminary design process, during which mass flows, pressure losses, and suction ducting sizes evolved to meet the constraints and space available. The final panel layout is presented in figure 24. The panel had 20 individually controlled suction regions: 7 on the upper surface and 13 in the leading-edge region. Flutes 1, 2, and 3 traversed the entire leading-edge length and were compartmentalized into suction regions 1 to 13 by partitions and dams. Suction region 1, the suction patch, was formed at the panel apex. The suction patch was designed to provide sufficient suction flow to relaminarize the turbulent attachment-line boundary layer in the event the passive slot turbulence diverter did not function properly (see section 5.4 for a discussion on the suction patch and turbulence diverter). The outer

surface of the panel was a 0.040-in. thick titanium skin with over 12×10^6 laser-drilled holes. The upper surface structure (see cross-section Y-Y of fig. 24) consisted of the outer titanium skin and an inner nonperforated titanium skin separated by aluminum stringers that were spaced at 1.6-in. intervals, measured normal to the leading edge. The upper surface sandwich panel was 0.6 in. thick. Limitations on the size of skins that could be laser-drilled required that the titanium skins (upper and lower) be made from two pieces, resulting in a splice joint in the test area. The spliced region resulted in a nonsuction length of 2.1 in. measured normal to the leading edge (fig. 24). The perforated suction holes in the titanium skin were nominally 0.0025 in. in diameter with spacing varying methodically from 0.010 in. to 0.055 in., depending on local suction rate requirements. The holes are tapered, with the exit diameter (on the suction side) about double the entrance diameter. The taper ensures that small particles ingested into the holes pass through and do not obstruct the flow through the hole.

Details of the leading-edge dams and partitions which form the suction regions are illustrated in figure 25 with the external titanium skin removed for clarity. Pressure orifice locations for measurement of internal region static pressures are also shown. The dams and partitions are constructed of fiberglass epoxy composite materials. The suction deadbands due to the partitions and dams were specified not to exceed 0.20 in. across to minimize the suction discontinuities. The first two stringers on the upper surface are also shown, along with flow blockers between the stringers, which define the boundaries of the individual upper surface suction regions. An enhanced view of the stringers is presented in figure 26, which illustrates the circular openings in the stringer webs that allow communication and collection of the airflow within a given region. The first stringer on the upper surface was solid in order to seal off the leading-edge section from the upper surface. The airflow collected in the upper surface regions passed through a set of holes in the lower titanium skin into their respective collector duct underneath (fig. 27). Note that there are seven sets of holes in the lower skin, one set for each of the upper surface suction regions. The entrances for the flute 3 region collector ducts (4) are also illustrated in figure 27. The inboard leading-edge region, which contained the suction patch and the beginning of the suction compartments for flutes 1, 2, and 3 had limited space due to the high sweep. The structural elements

in this apex region (fig. 28) were machined aluminum, instead of a bonded structure, to allow precise assembly.

The entire suction panel and substructure was mounted over the existing wing, resulting in a thicker gloved wing (fig. 29). An access panel on the lower surface of the leading edge allowed access to critical components in the space forward of the original F-16XL-2 front spar. The panel extended about 12 in. upstream of the original leading edge. Bonded to the lower surface of the suction panel were aluminum structural ribs that provided panel stiffness and a means for securely attaching the structure to the existing wing. Figure 30 shows the ribs (shaded for clarity) and collector channels on the suction-panel underside (the upper sandwich structure of the panel has been removed to reveal the underside details). The fastening of the suction panel to the F-16XL-2 wing was accomplished by first bonding 35 attachment pads with hooks to the F-16XL-2 wing. Each pad-hook had a complementary tongue that was located on the suction-panel ribs. The suction panel was attached to the wing by simultaneously mating all hooks and tongues at once, resulting in a precise fit. Figure 31 illustrates the shape of a typical rib and provides a cross section, which shows the suction panel, rib, and hook and pad arrangement. A close-up of the tongue, and the hook and pad arrangement is also shown. An apex region inboard of the suction panel was required to provide suction-panel structural support and to continue the cantilevered structure inward to the F-16XL-2 fuselage. This apex structure (fig. 32) consisted of an inboard suction-panel close-out rib and seven apex frames which attached directly to the F-16XL-2 fuselage structure.

The suction system beyond the suction-panel sandwich structure consisted of 20 individual collector ducts (one for each independent region), 20 individual mass-flow sensors and control valves, a common plenum, one master control valve, and a turbocompressor. The turbocompressor turbine was driven by engine bleed air, which allowed the compressor to provide the low-pressure source for the suction system. Exhaust from the compressor and turbine was dumped overboard on the right side of the aircraft, away from the suction panel. The turbocompressor was originally designed as an auxiliary power unit on the Boeing B-707 and was modified for the flow

requirements of this experiment. A planform layout of the collection and routing system is shown in figure 33. Access space was a large factor in the configuration of the collector channels. The first two and the last two collector channels were highly curved, and the remaining 16 were relatively short and straight. To minimize pressure losses and prevent generation of high internal noise levels that could feed upstream and possibly disturb laminar flow (refs. 13 and 14), flow velocities up to the turbocompressor were limited to the lowest reasonable values. Suction-flow velocities were designed to the following limits: $M \leq 0.1$ for flow in the panel collector channels; $M \leq 0.2$ at the control valves, and $M \leq 0.3$ at the compressor inlet. A schematic representation of the suction system is given in figure 34.

The suction flow through the surface in each region of the panel was set by the perforation hole spacing and by controlling the pressure in the internal suction regions. The suction-panel skin was composed of 123 patches, where a patch is defined as an area that has the same hole spacing. There were 84 patches in the leading-edge regions and 39 in the rooftop regions. The hole spacing varied from 0.010 to 0.055 in. A schematic of all suction patches is given in figure 35 with an expanded view of the leading edge. The boundaries of the suction patch, flutes 1, 2, and 3, and each suction region are denoted in figure 35 by the bold lines. Note that each suction region in flutes 1 and 2 had six patches, while in flute 3, each region had eight patches. On the upper surface, the boundary between regions 16 and 17 traversed four patches that are identified as two parts; for example, 96.1 and 96.2 (fig. 35). The hole spacing within each patch and its specific suction region affiliation is listed in table 1. The local porosity was finely tailored, within the limits of practicality, to replicate as closely as possible the design suction distribution.

5.4. Turbulence Diverter and Suction Patch

To prevent attachment-line contamination of the suction panel by the inboard turbulent boundary layer, the panel design included a turbulence diverter and a suction patch. The turbulence diverter was a narrow slot on the leading edge just inboard of the suction panel, as illustrated in figure 36. As discussed in the supporting flight research section, this slot was demonstrated effective on the leading-edge passive glove.

By removing the turbulent attachment-line boundary layer, the slot allows a new laminar attachment-line boundary layer to begin at the apex of the suction panel. The slot width, measured along the leading edge, was 0.78 in. (0.27 in. measured normal to the fuselage). The inboard streamwise edge of the suction panel, where the suction patch began, actually was the outboard slot wall of the turbulence diverter (fig. 36). Provisions were made in the design for replaceable turbulent diverter concepts in the event that laminar flow was not achievable on the attachment line with the baseline slot design. Since a laminar attachment-line flow was achievable with the baseline concept, no other designs were investigated.

The suction patch, which was the first suction region the flow encountered on the suction panel (fig. 36), was designed to relaminarize the turbulent attachment-line boundary layer if required. The suction patch was in the panel inboard region (or apex), was triangular in shape, and occupied the first 6 in. of leading-edge length. The suction requirements and dimensions of the patch were determined by BCAG based on a Direct Numerical Simulation method (ref. 22). The C_q maximum and minimum design levels for the suction patch are shown in figure 37. To relaminarize a turbulent boundary layer, high levels of suction are required. The suction patch would be used only for relaminarizing the turbulent attachment-line boundary layer in the event the baseline device, the turbulence diverter, was ineffective. The suction patch could also provide a threshold low level of suction to maintain laminar flow in the apex region.

5.5. Suction-Panel Quality and Assurance Measurements

Detailed quality and assurance measurements were performed on the finished suction panel to document the as-built article prior to flight testing and to determine any deviations from design specifications and requirements discussed previously. The measurements made included surface contour, surface waviness, steps and gaps, skin porosity, and suction region leak tests.

5.5.1. Surface Contour

The design contour specification required the panel outer contour to be within ± 0.020 in. of the

desired shape, 4 in. rearward of $s_n = 0$, measured normal to the leading edge. Aft of $s_n = 4$ in., the permissible contour deviation was ± 0.050 in. A Computer-Aided Theodelite (CAT) system was used to determine the contour of the final installed suction panel by using targets identified on a grid shown in figure 38. The grid points were clustered closer together, 2 in. by 4 in., in the leading-edge region for better resolution. Aft of $s_n = 12$, a grid of 8 in. by 8 in. was used. On the aircraft, the grid was implemented by placing targets at the grid points. The three-dimensional coordinates of these targets were then measured by the CAT system. The CAT measurements showed that contour deviations in the leading edge were within ± 0.020 in. and in the aft region were within ± 0.028 in.

5.5.2. Surface Waviness

Even though the surface contour was within the specified tolerance, some areas indicated 0.010-in. differences in the normal deviation between grid points. These differences violated the long-wave criteria. These larger deviations occurred in regions where the bonding assembly cradle (used to lay up and assemble the panel) had similar deviations from contour. These deviations were accepted since they were not excessive, and the costly alternative would have been to fabricate new tooling and a new suction-panel skin.

Smaller wavelength surface waviness was measured along the streamwise direction (along BL direction) and the normal direction to the leading edge, as shown in figure 39. The measurements were made by using a cart with a 2-in. wheelbase and a dial indicator which continually tracked along the surface (fig. 39). The allowable design criteria, described earlier for a spanwise wave with 2-in. wavelength, was established as a total wave amplitude of 0.003 in. Actual measurements made in the normal direction are shown in figure 40. Measurements were made at 10-in. intervals along the inboard edge, but only the readings at 20-in. intervals are shown here. The starting point for each measurement trace was at the panel inboard edge, proceeding to the leading edge. As a consequence, the panel splice was not evident in the measurements until $s_i = 100$. The waviness of the surface is apparent when compared to the mean, but the amplitude is small. The 0.003-in. wave amplitude criterion is attained at the splice joint in the outboard area and

produces a distorted wave signature. The splice joint structure resulted in a local flatness at the splice which produced the distinguishable wave in that area. The smaller waves along each measuring path are believed to be caused by small, within tolerance, local flat regions where the stringers are bonded to the titanium skin. A similar result was obtained from the measurements in the streamwise direction, with the splice joint area registering the greatest wave amplitudes (fig. 41). In the streamwise direction, the wave height reached 0.0035 in. at BL 90 (fig. 41), just exceeding the criteria of 0.003 in. This height was considered acceptable because the corresponding wavelength was about 20 in. (permissible wave amplitude increases with wavelength as shown in fig. 17).

5.5.3. Steps and Gaps

The gap along the splice joint was measured and found to be within the criteria of 0.025 in. except for small local regions, as noted in figure 42. The gap at the splice joint slightly exceeded the criteria over two local areas outboard, as shown. The gap could be filled later during the flight tests if laminar flow was adversely affected. The splice joint also resulted in minor steps. Typical forward facing steps were 0.0005 to 0.001 in. (design limit was 0.003 in.) and typical aft facing steps were 0.0005 in. (design limit was 0.001 in.). Residual steps were also formed due to local acid etching of the titanium skin that was done to increase the porosity where necessary. The etching process removed a small amount of metal from the surface locally, resulting in a step at the masking border. The steps were rounded by hand to avoid sharp corners. The steps were typically 0.0005 in., which was within the step criteria. Other surface imperfections were shallow scuff and scratch marks due to hot forming of the skin and they were typically 0.0005 to 0.001 in. and were not considered serious. Finally, three small dimples were detected and documented by BCAG prior to shipment to DFRC. Their depth was less than 0.001 in. and they were spread over about a 0.125-in. width. Two were next to each other at about BL 54, $s = 1.5$ in., and the third was at BL 69, $s = 1.5$ in. Experimental results did not indicate that these dimples interfered with the attainment of laminar flow.

5.5.4. Skin Porosity

As stated in section 5.1.3, the goal for suction-panel porosity was to have a mean porosity level within ± 5 percent of the design porosity. The laser drilling process, however, is not a precise technology, especially when small hole diameters are specified. Details of the process are undocumented and unavailable. The fabrication process itself may also alter the skin porosity. A method was devised to accurately map out in detail the porosity of the drilled skins, both as delivered from the laser drilling vendor and after hot forming (shaping/bending at elevated temperatures). As discussed in section 5.3, there were 20 suction regions which contained 123 patches (areas of constant hole spacing). Porosity was measured within each patch with a device known as a "sniffer." The sample size was typically 4 in. long by up to 1 in. wide. The sniffer had a rubber seal around the perimeter that contacted the skin surface. The mass-flow rate could be varied, and both the flow rate and the pressure drop across the skin were recorded for each sample. All measurements were made at atmospheric conditions. Comparisons were then made between the design pressure drop for a given flow rate and the actual pressure drop. Each sniffer sample was labeled with a relative porosity level, above or below the design target. The 1552 samples were measured on the entire suction surface. An equivalent normalized hole density parameter was defined as the ratio of the measured sample flow to the ideal sample flow at a given pressure drop.

The skins, as drilled and cleaned by the vendor, were less porous in certain areas than specified in the design. As previously discussed in section 5.1.2 on steps and gaps, an etching process (devised by engineers at BCAG) was used to open up holes and therefore increase the porosity in local areas. Areas on the skin not requiring etching were masked off, then the entire skin was emerged in an acid bath for incremental time steps. Local porosity measurements were made after each step to track the change in porosity and adjust the masking to ensure that areas were not overetched. The etching process improved the local porosity to acceptable levels according to the design specifications. Fabrication of the suction panel contributed to changes in porosity also. Skin hot forming,

local rework, pressure washing of the skin, and skin priming in preparation for bonding dams and partitions all produced porosity changes. After the suction panel was fabricated, sniffer measurements were performed again on the entire perforated skin as assembled. The measured samples did not include any blocked area from partitions, dams, flow blockers, or stringers. The data were summed up for each suction region, and the mean equivalent normalized porosity for each region was found. The result is shown in figure 43 where numbers over 1.0 indicate higher porosity than the design value, and numbers less than 1.0 represent lower porosity than the design value. Suction regions on the upper surface (regions 14 through 19) had higher porosity than design. Suction regions in the leading edge were mixed; some had lower and some had higher porosity than the design goals (fig. 43). The attachment-line flute, including the suction patch (regions 1, 2, 5, 8, and 11) were all below the design porosity levels. Over the entire panel skin, the average deviation of the mean porosity level from the design porosity is about ± 7.5 percent. Regions 1 and 7 have the greatest deviations in mean porosity, -18 percent and $+14$ percent, respectively. Although these levels were higher than the specified goal, they were deemed acceptable due to the built-in flexibility in the suction system and the inability to wait for manufacture of new skins.

To verify the flexibility of the suction system to account for the porosity deviations, BCAG incorporated the as-assembled porosity data into their three-dimensional C_q program. The results showed that the deviations had no major impact on achieving the desired suction levels. Adjustment of the flow-control valves could compensate for much of the nonideal porosity-induced changes. Also, if the high-porosity areas were later determined to cause problems, a method for locally blocking rows of holes with an acrylic lacquer was developed. Correspondingly, low porosity areas could be treated with a local etching-paste technique to open holes.

5.5.5. Suction Region Leak Tests

A criterion in the design of the suction panel was that leaks from each suction region must be smaller than 1 percent of the flow rate through the skin for that region. BCAG performed two leak tests on the assembled suction panel at atmospheric conditions.

The first test was devised to determine the leakage from each region to the external environment (outside of panel). All 20 suction regions were pressurized simultaneously to 100 psfg, and pressure indicators were installed at the sealed collector duct exits. The upper perforated surface was sealed with tape. The external leak for each is given in table 2 where the flow rate was calculated by using the BCAG C_q modeling program with 100 psf differential pressure across the skin. The percentage leak rate calculated from the two columns indicates the external leak rate is low, the highest being 0.27 percent (region 4) with some regions not registering any leak.

The second leak test was more demanding, with each suction region pressurized to 100 psfg individually while all other suction regions were left open. The leak measured in this case is the total leak to the external (outside panel) and internal (other regions) sources. The leak rates measured are shown in table 3 and, as expected, are higher than the first test results but are still acceptable. Region 3 slightly exceeded the 1-percent goal with a 1.02-percent relative total leak rate.

6. F-16XL-2 Aircraft Modification

The suction test panel and related suction system components were installed on the left wing and in portions of the fuselage. The F-16XL-2 was modified to allow installation of new instrumentation, power supplies, signal conditioning units, cables, wiring, suction ducting and plenum and panel, suction control valves and flowmeters, a suction turbocompressor, and passive foam-fiberglass contour fairings. The major areas of modification are illustrated in figure 6.

A view of the suction panel held in its protective cradle apparatus is shown in figure 44. The suction panel was shipped from BCAG to DFRC in this cradle and remained in this apparatus until ready for final installation. The F-16XL-2 graphite epoxy wing surface had 35 pads and hooks installed for attaching the suction panel to the wing. Some of these are shown in figure 45. Adhesive was used to bond the mounting pads and hooks to the wing. A "tongue" structure on the suction panel ribs fits into the hooks to secure the panel onto the wing. A preliminary installation fit check is shown in figure 46. A view under the suction panel (fig. 47) illustrates three tongues on a typical rib

for connection to the hooks on the wing surface. Also shown is a suction collector channel and two electronically scanned pressure (ESP) units. Limited space and the requirement for short orifice line lengths (10 ft maximum) to minimize pressure lag necessitated installation of numerous ESP units under the panel. Components of the flow collection, measuring, and control system are illustrated in figure 48. The view is from the inboard rear looking forward and shows three flow-control assemblies. Each of the 20 suction regions contained a flow-control assembly which consisted of a motorized flow-control valve and a mass-flow sensor (see also figs. 33 and 34).

A view of the installed suction panel undergoing the CAT measurements discussed in section 5.5.1 is illustrated in figure 49. A dense number of CAT targets grouped on strips of tape can be seen on the panel leading edge. The white spots on the panel upper surface each represent single CAT targets. Targets were also placed on the canopy and passive fairings. The suction pump was not installed at this point, as can be seen by the vacant ammunition bay behind the canopy. A detailed view of the installed suction turbocompressor is shown in figure 50. The collected suction flow from the plenum passed through the master flow-control valve into the compressor and exited in a centrifugal direction. The compressor was driven by a turbine that was powered by engine bleed air. The turbine and compressor outlets were routed overboard on the right side of the aircraft, away from the suction panel, to ensure that any flow disturbances could not adversely affect the flow over the panel. An in-flight view of the modified aircraft is presented in figure 51. The compressor and turbine overboard exhaust outlets are indicated in the figure, along with the in-flight refueling port.

Photographs of fences 1 and 2, installed on the left wing lower surface are shown in figure 52. The installation position was constrained to BL 65 because this location had available missile ordnance hard attachment points. Other attachment point locations inboard were used with experimental hardware supporting the flight test.

7. Instrumentation

The F-16XL-2 suction panel included instrumentation that would provide adequate information to

define the flow field, the suction quantities, and the boundary layer state. External pressures and temperatures were needed to calculate the external flow field, most importantly, the boundary layer. External and internal pressures and the internal temperatures were needed to determine the local mass flow through the skin. Boundary layer transition detection was needed in order to determine the extent of laminar flow and the transition location. Control of the mass flow for each region was needed as an experimental variable that would be used to vary the transition location.

7.1. Pressure Taps

Pressure was measured by using a set of ESP modules. This system was capable of recording simultaneous pressure measurements at multiple locations. Several modules were located near the suction panel, and pressure tubing was routed from them to individual pressure taps. The reference side of all the ESP modules was connected to the same reference reservoir. Several minutes after reaching altitude, a valve linking the reference tank to the ambient pressure was closed, thus keeping the reference tank from drifting. This procedure eliminated pressure lag problems between the reference tank and the ESP modules. After allowing the reference pressure side to settle, a calibration point was taken to find the output of each transducer with zero pressure differential applied at that pressure altitude and temperature. By using the calibration point, the reference pressure, and the free-stream pressure, the C_p value could be determined.

There were 72 pressure taps located inside the suction panel. Figure 53 shows the distribution of the internal pressure taps. The internal pressure taps were critical in determining the pressure drop across the perforated skin and thus the suction coefficient on the panel. Each leading-edge region had three internal pressure taps. One was located at each end of a region and one was located in the center. The upper surface internal taps were distributed within each suction region.

The left wing (suction panel and fairing) had 454 surface pressure taps which were laid out as shown in figure 54. Pressure-tap rows on the suction panel were located every 10 in., beginning at BL 50 and ending at BL 110. The leading-edge region contained the greatest concentration of taps, with a total of 113. The

density of pressure orifices in the leading edge is illustrated in figures 55 and 56 for BL 35 and 70. The BL 70 distribution is typical of all BL's on the active suction panel. Table 4 gives the streamwise distance s to each leading-edge pressure tap at each BL. The density of pressure taps was a balance between minimizing blockage of the suction surface (suction discontinuities), budget limitations, assembly complications, and obtaining a sufficient density of measurements to accurately determine the surface pressure. Figure 57 shows a typical installation of a leading-edge pressure tap. On the upper surface there were 87 pressure taps on the suction panel and another 254 on the passive fairing surrounding the suction panel. The pressure measurement on the upper surface of the suction panel was accomplished by sensing through the perforated holes in the skin. These 87 pressure taps were installed as shown in figures 58 and 59. After subtracting the thickness of the O-ring, the cavity was about 0.3 in. in diameter. For a typical upper surface hole spacing of 0.04 in., about 45 of the 0.0025-in. diameter holes were open to the cavity. This installation allowed surface pressure measurement without making any additional imperfections on the surface that might produce flow disturbances.

BCAG performed functional checks on all pressure taps before delivery to DFRC. Five of the 200 external pressure taps were found to have either an unacceptable leak or were plugged. Two of the 72 internal pressure taps were blocked and did not respond. Because there were only a few nonfunctioning taps that were spread out over the panel, the remaining functional pressure taps would still allow accurate determination of the suction panel pressures.

7.2. Thermocouples

There were 151 thermocouples internal to the suction panel that were used to measure the skin and incoming air temperature. Figures 60 and 61 present cross-sectional views that show a stringer at a thermocouple location and the installation of one thermocouple pair. The pair consisted of a stringer thermocouple, which was sandwiched between the upper skin and a stringer, and a skin thermocouple, which was welded directly to the inside surface of the skin. Due to the thermal mass of the stringers and its lack of exposure to convection currents, the sandwiched thermocouple would indicate a different temperature than the ther-

mocouple welded to the skin. Due to its direct exposure to the incoming air, the thermocouple welded to the skin was a better measurement of the air temperature in the suction region. This "pairing" arrangement also provided redundancy in the event that a thermocouple failed. In the leading edge there were four thermocouples welded to the inside surface of the skin at each of seven BL's starting with BL 50.5. The locations, given as distance from $s = 0$, for a typical BL are shown in figure 56. The distribution of thermocouple pairs on the panel is shown in figure 62. There is a row of thermocouples to complement each row of pressures, with the thermocouples offset spanwise from the pressure rows by a distance of 0.50 in. This arrangement allowed temperature measurements close to the pressure measurement locations and provided a sufficient density of temperature measurements to determine the skin temperature and suction region temperatures for the suction panel.

BCAG performed functional checks on all thermocouples before delivery to DFRC. Two of the 151 thermocouples were not operational. The loss of these two thermocouples was considered insignificant in view of the number of them installed on the suction panel and their layout.

7.3. Transition-Detection Methods

Surface hot films and subsurface microphones were chosen for transition-detection instrumentation for this experiment. Thermocouples also offered a possibility for detecting-transition, but they were not found useful for this test because of their long time constant and the short duration of the test points. The microphones had promising characteristics but were considered a new and nonflight tested method, as installed for this test. Their use as transition detectors however, is not new. A review of the literature shows that microphones have been used in many previous wind tunnel experiments and some flight experiments dating back to the use of stethoscopes in the 1950's. Of particular interest to this experiment are references 23 and 24 that describe a microphone installation used in a wind tunnel and on a sailplane. Similar to the installation used in this experiment were the miniature microphones that "listened" through a small hole. Barrett and Rickards reported that, with their technique, the different stages of transition could be differentiated. Using microphones was preferable to

other methods because microphones were nonintrusive (for the installation described here) and had quick response times. Disadvantages included coarse spacing, fixed position, and sensitivity to electronic noise in the surrounding environment. Hot films were envisioned for use in conjunction with the microphones to obtain increased spatial resolution of the transition location. Hot films also were planned as a back-up technique in case the microphones did not function as designed. Surface hot films have been used successfully many times before at DFRC for transition measurement (refs. 25 to 27). They also have quick response times but are cumbersome to install and/or move and were intrusive (tripped flow behind them). Hot films proved to be the only technique used for transition detection during this experiment.

7.3.1. Microphones

Thirty-four microphones were installed in the F-16XL-2 SLFC suction panel to provide a coarse nonintrusive indication of the transition location on the glove. Finer measurements of the transition location were planned with hot films. Signal conditioning was developed that allowed recording of the ac voltage on an onboard frequency modulation (FM) tape and also allowed real-time viewing of the RMS voltage. Early preliminary tests in a supersonic wind tunnel at LaRC, involving several different installation configurations and flush-mounted microphone data obtained during the leading-edge passive glove experiment, provided confidence in this technique.

The original instrumentation plan included installation of six microphones in the passive fairing surrounding the suction panel, and a free-stream probe that would be mounted about 4 in. above the surface at the rear of the panel. Time and resources were not available to install and test this instrumentation.

The suction-panel microphones did not perform as expected and were difficult to interpret. Wind tunnel tests at LaRC conducted before the manufacture of the panel indicated that the microphones would work. However, some controversy existed over the interpretation of the data. As a follow-on investigation, wind tunnel tests were conducted again at LaRC during the same time period as the flight testing, and the microphones performed as expected (unpublished data). High electronic noise is suspected of playing a large

role in the difficulties encountered with the microphones during the flight experiment. Appendix A provides further details on the microphones.

7.3.2. Hot Films

Over the course of the experiment, 142 different hot-film locations were used. Of these, 126 were on the upper surface and 16 were on the lower surface. The films provided a real-time indication of the boundary layer state and allowed the researcher to decide real time what the priority of a predetermined set of test points should be. The real-time indication also allowed flight-test planning for the next flight to proceed immediately after the current flight. The hot-film signals were used to define the boundary layer transition point for code calibration. The negative aspects of the hot films included their installation and removal time. Also, once installed, the hot films and their electrical leads tripped the flow downstream from them. Their installation, signal interpretation, and performance are discussed in this section.

A commercially available hot film and a LaRC manufactured hot film were used for this experiment. Both used the same electronics, which were developed at DFRC and are not described here (refs. 25 to 27). Both included an active sensing element and a temperature compensation element, and both were sanded at the leading edge to provide a smooth continuous surface up to the sensing element. The LaRC films were mounted on a low-static polyimide sheet which was bonded to the surface. These films were used only along the nonperforated edges of the panel. The LaRC films had multiple sensors close together on each sheet that could be selected by changing an electrical connection. This design allowed an easy film change after a film failed because no panels had to be removed and no taping or rebonding was required. The commercially available hot films were used for most of the hot-film installations, including hot films on the porous surface. The films and their leads were mounted on 0.002-in-thick tape that protected the perforated surface from adhesive. Hot films were installed, moved, and removed many times during the experiment to build a database containing transition location dependence on Mach number, Reynolds number, altitude, and C_q and C_p distributions. All hot-film locations that were used over the life of the program are shown in figure 63. A photograph of the

hot-film array installed at the splice joint is shown in figure 64. The hot-film locations used on a flight-to-flight basis are presented in appendix B.

The F-16XL-1 NASA-Rockwell experiment and the F-16XL-2 passive glove experiment established the criteria to distinguish between laminar and turbulent flow from the hot-film signals. The local flow state of the boundary layer relied on the recognition that the transition front passed across the sensor. Without this event, the hot-film signal for laminar flow could not be distinguished from the hot-film signal for turbulent flow. The passing of the transition front could most easily be seen as the aircraft changed α and laminar flow was achieved or lost. The hot-film signals consisted of an ac component superimposed on a dc component. As the boundary layer above the sensor makes the transition from laminar to turbulent flow (or back), the output signal goes through several stages, as depicted in figure 65. For a laminar boundary layer state (L), the dc component is at its lowest level, and the ac component remains small (in the absence of a large amount of electronic noise contamination). As bursts start forming in the boundary layer, positive turbulent spikes appear in the hot-film trace (LT). Further breakdown of the boundary layer causes the ac signal to become large and causes the dc component to shift upward (TR). As the boundary layer progresses toward fully turbulent flow, the dc component shifts to its highest level, and the ac component produces downward turbulent spikes (TL). Finally, when a full turbulent boundary layer is achieved, the dc component is at its highest level and the ac component is reduced (T). Ideally, the ac component for the turbulent case would be larger than the ac component for the laminar case. However, this was not always the case. If the laminar signal or any turbulent bursts had not been observed to this point, it would be very difficult to determine whether this signal was completely laminar or completely turbulent, based solely on the ac component.

The hot-film sensors proved to be an invaluable tool for transition detection. Sensor signals were telemetered to the ground and displayed on strip chart recorders in both the DFRC flight control room and the LaRC flight-monitoring room. The recorders provided a real-time, clear signal that could be used to make transition location-based decisions during a flight. Laminar, transitional, and turbulent data were

obtained by varying the flight condition and/or suction level so that transition moved across the fixed hot-film locations. The data from these films were used to determine the extent of laminar flow and to define the code calibration points.

7.4. Flow-Control Assembly

The flow-control assembly was located off the panel but is included in this section because of its relevancy in the control of the suction coefficient over the panel. The 20 flow-control assemblies, one for each region, were located inboard of the suction panel at the end of each collector channel, as shown earlier (figs. 33, 34, and 48). Figure 66 is a schematic of a typical flow-control assembly. Each assembly contained three static pressure taps, a thermocouple, a flow-control valve, and a mass-flow sensor. The pressure and temperature measurements were used to evaluate the performance of the suction system and as inputs to the calibration equations of each mass-flow sensor. These sensors were single point thermal convection mass-flow sensors using constant temperature anemometer circuitry (ref. 28). The sensors were selected because they best met the response time, repeatability, vibration survivability, resolution, and autoignition requirements. A detailed view of the mass-flow sensor is shown in figure 67, and figure 68 illustrates the installed configurations. There are two stings located on the probe, one is the active heated sensor, encased in a ceramic coating, and the other is the temperature compensation sensor. A custom-built facility at LaRC was assembled for the purpose of calibrating each sensor at proposed flight-test conditions. The calibration included investigations of sensitivity to valve angle, pressure, temperature, sensor orientation-clocking, sensor lead length, and incoming duct geometry. The final calibration focused on pressure and temperature variations and the use of 4 of the 20 incoming duct shapes. Care was taken to record which sensors were calibrated with which ducts and the orientation relative to the duct that was used for the calibration. Sensors 1, 2, and 7 were calibrated with the 1, 2, and 7 duct shapes. All other sensors were calibrated with duct shape 6 because it was considered typical of all other duct shapes. Ideally, each sensor duct would have been calibrated with its corresponding duct, but doing so was not practical. The design of the flow-control assembly included the ability to use the output of the mass-flow sensor to control the valve

angle. Thus, the mass flow could be held constant through changes in temperature or pressure. Control of mass flow could also be accomplished by fixing the valve angle. The system was capable of driving the valve to a specified target angle and then measuring the actual angle.

8. Flight-Test Objectives and Strategy

To accomplish the experimental objectives that were given in the Introduction, a comprehensive flight-test plan was developed that consisted of four phases. All phases are given here with their objectives. These phases were useful in guiding the direction of the experiment but were not followed in practice. Section 11 covers the actual progression of events.

8.1. Test Aircraft Flight Acceptance Phase Objectives

The goals of this phase focused on functionality checks and tests of the modified aircraft to verify and demonstrate that the aircraft was safe and could be used as a research test platform. The objectives were to accomplish

- aircraft and engine functional checks
- operational envelope (flutter) clearance
- handling qualities evaluation
- structural health monitoring
- turbocompressor checkout
- angle-of-attack calibration
- achievable repeatability of Mach number and α

8.2. Experimental Hardware Flight Acceptance Phase Objectives

The goals of this phase focused on the hardware installed on the aircraft to verify and demonstrate the performance of the various hardware components. The objectives were to

- determine altitude and α to match design C_p 's at $M = 1.9$
- determine shock fence effectiveness
- determine turbulence diverter effectiveness
- demonstrate acceptable canopy shock locations
- decide on attachment-line flute masking
- establish confidence in mass-flow sensors
- checkout instrumentation, displays, data acquisition, data retrieval
- checkout laminar flow detection instrumentation

8.3. Demonstration Phase Objectives

The goals of this phase focused on demonstrating the results. The objectives of this phase were to

- achieve 50 to 60 percent chord laminar flow at design conditions
- find maximum Reynolds number laminar flow
- achieve HLFC at demonstration point
- find maximum Reynolds number HLFC
- perform suction flow minimization (all previous cases)
- maximize the laminar run by perturbing the flight parameters

8.4. F-16XL-2 Research Phase Objectives

A research phase, or fourth phase, was to be conducted after the successful conclusion of the first three phases and was contingent on approval of additional funding. Its objectives were to

- create database for transition code calibration, achieving selected types of flow:
 - cross-flow (CF) dominated transition

- flow with cross-flow reversal
- Tollmien-Schlichting (TS) dominated transition
- both CF and TS mechanisms active to varying extent
- acquire database over range of Mach and Reynolds numbers
- find attachment-line stability limits (function of $M, R/ft, C_q$)
- establish boundary layer tripping criteria for multiple rows of holes
- establish allowable tolerances for steps, gaps, waves, roughness
- establish criteria for allowable leading-edge suction discontinuities
- investigate tripping by outflow (natural venting) and establish criteria
- investigate laminarization through shocks

8.5. Flight-Test Point Strategy

For most SLFC flights, the flight-test strategy involved (1) in-flight tanker refueling before the subsonic cruise to the starting point of the first supersonic test run; (2) conducting a supersonic test run lasting approximately 10 min and performing various stabilized test points at preplanned flight conditions of Mach, α , altitude, β , and suction distribution; (3) decelerating to subsonic conditions and repeating steps 1 and 2 two more times, for a total of three supersonic runs. Suction-valve positions were established in advance and telemetered to the aircraft from DFRC ground control during the flight. This procedure would automatically establish the desired new suction levels. Since the angles of attack of interest were typically less than aircraft trim, the pilot had to perform a “pushover” maneuver and hold stabilized conditions for approximately 10 sec. About 15 test points were obtained per run before the aircraft was required to decelerate and descend for rendezvous with the tanker. Typically, about 45 test points were completed per flight if 3 supersonic runs were conducted.

9. Test Point Database

Three types of test data were available to users that were referred to as real-time data, time-series data, and time-averaged data. The real-time data were a selected set of parameters that could be viewed during the flight as it was telemetered from the aircraft to the ground and displayed in DFRC and LaRC control rooms. After the flight, all data were stored on the DFRC Flight Data Access System (FDAS) as time-series data; for example, individual data parameter values versus time. The third data source, which was the most heavily used data, was the time-averaged data. These data were created by DFRC personnel from the time-series data stored on the FDAS system.

As noted in section 8.5, the raw data were typically collected by performing “pushovers” because the desired test point α was generally below trim α . During the approximate 10-min supersonic run, each of several predefined test conditions was held for approximately 10 sec. Test points were selected from the 10-sec intervals by applying the following criteria:

- time window—minimum of 3 sec
- Mach number held within ± 0.01
- altitude held within ± 500 ft
- angle of attack held within $\pm 0.1^\circ$
- flow-control valves fixed
- hot-film signal consistent within window

Test points meeting these criteria were added to the database. Data taken during the test point window were averaged over the time window, and the state of the boundary layer at each film was determined. These data were written to the database files and served as the common starting point for additional data analysis.

Test points added to the time-averaged database were defined by their flight number and flight-card number for reference purposes. All test point names are unique and contain the flight number first. For each test point within that flight, a four-character labeling methodology was adopted. The readers do not need to be concerned with what each letter and

number means unless they would like to refer to the original DFRC Flight Reports which contain the test point instructions. An explanation of the four-character labeling methodology can be found in appendix C along with more in-depth details pertaining to the database.

10. Data Analysis Tools

Special tools and procedures were developed in this program in advance to handle the large amount of data that was collected. A flow chart of the analysis procedure steps is shown in figure 69. Each step is discussed very briefly.

The time-averaged measurements were used to produce the necessary detailed grid that described the external flow field. Producing this grid required fitting, interpolation, or smoothing of the data, a step which admitted the most subjectivity in the code validation process. The result of this step was a grid of points over the panel surface that included temperature and pressure information.

Having generated a surface pressure and temperature distribution from the measured data, the local suction and edge velocities were calculated. The local suction coefficient, and thus mass flow, was calculated from the external and internal pressures and from the skin characteristics. MDC and BCAG wrote and used different codes to calculate C_q . However, both codes used the measured pressure drop and the skin characteristics. The MDC calculation divided the surface into a finer number of increments (10 000) than did the BCAG method. The skin characteristics used included detailed skin pressure drop data collected after the panel was fabricated. In a step independent of the C_q calculation, the edge velocities were computed by using a Surface Euler code developed by MDC. These two separate steps completed all the necessary information to enable three-dimensional boundary layer calculations using the BL3D code (ref. 29). The output from the boundary layer code was then used by a three-dimensional linear stability code (Malik, M.R.: eMalik3d: *An e^N Code for Three-Dimensional Flow Over Finite-Swept Wings*, High Technology Report No. HTC-9502, April 1995) to compute the N -factors. From the output of this code, an N -factor value could be correlated with boundary layer transition observed at a given hot-film location. A recent review of linear

stability theory can be found in reference 30. In addition to the discussion of the paper, the document cites 176 references for the reader interested in obtaining further information on linear stability theory.

11. Results

Forty-five flights were conducted during this experiment; the first flight was on October 13, 1995, and the last flight was on November 26, 1996. Early flights were devoted to resolving operational and safety-related issues. The first supersonic flight with suction on was conducted on January 24, 1996. There were 35 flights which provided supersonic data pertinent to SLFC technology (see appendix D for a log-book of key notes from each flight).

As with any high-risk technology development experiment, the F-16XL-2 SLFC Flight Experiment was not without its technical challenges. The results are initially presented in a chronological fashion, consistent with the order in which the flight testing was conducted. A discussion of safety-related, operational concerns and their resolution are reviewed, followed by the strategy pursued to establish laminar flow on the attachment line and on the upper surface. Identification of flight test conditions (M , altitude, α , β , and C_q) for achieving consistent laminar flow is detailed, along with comparison of flight-measured C_p 's with CFD. Two unexpected problems affecting laminar flow are reviewed next: a weak shock from the canopy joint and premature attachment-line suction-hole-induced disturbances. Suction levels achieved and determination of outflow regions are also presented. Temperature distributions on the suction panel are described, followed by discussion of a greater than expected inboard turbulent region and its possible causes. Test cases displaying the maximum laminar flow achieved are discussed. Finally, boundary layer transition measurements are compared with stability code calculations.

An individual flight log (appendix D) documents key findings and results, describes significant configuration changes from the previous flight, and mentions operational difficulties. The flight log is complemented by the layout of the hot-film configuration for each flight or series of flights (appendix B). A discussion of data repeatability and data accuracy is presented in appendix E.

11.1. Initial Flights

The first flight on October 13, 1995, began the Test Aircraft Flight Acceptance Phase Objectives (refer to section 8.6). Safety-of-flight problems were encountered on this flight. The design of the suction panel as a nonload-carrying glove necessitated the establishment of limits on the differential pressure which existed between the cavity under the glove and the upper surface. Initial aircraft safety verification flights, which closely monitored this differential pressure, indicated that the limits were being exceeded. The differential pressure was exceeded because of the inability to completely seal leaks from higher pressure sources to the cavity and because the load evaluation was performed at a higher α (causing low upper surface pressures) than those conditions for which calculations were performed to establish the safe differential pressure limits. Ultimately, the problem was resolved by improved sealing of high-pressure leaks, enlargement of upper surface bleed vents, a relaxation of the differential pressure safety limits locally, and operation of the aircraft at maximum loads of $2g$ rather than $3g$. Valuable time was consumed progressing through the aircraft flight acceptance phase to resolve the differential pressure issue. Other operational problems were encountered, but such problems are not unexpected in a flight-test program with a highly modified research test aircraft.

11.2. Inboard Laminar Attachment Line

To attain laminar flow on the suction panel, the attachment-line boundary layer at the panel apex had to be laminar (and must remain laminar) along the entire leading edge. The inboard region, as defined here, is the attachment-line length out to the vicinity of the shock fence (BL 65). Between the beginning of the suction panel and the shock fence (BL 41.5 to 65), the behavior of the flow was independent of whether fence 1, 2, or no fence was installed because disturbances cannot feed upstream in supersonic flow (except via the subsonic layer of the boundary layer). Outboard of BL 65, the inlet-shock system, which traversed the lower surface, produced different pressure disturbances at the point it crossed the leading edge and outboard, depending on the α , Mach number, β , altitude, and whether fence 1 or 2 was installed.

At the beginning of the suction panel, the turbulence diverter deflected the turbulent flow on the existing attachment and allowed laminar flow to begin on the test panel for a range of α (approximately 2.6° to 3.9°). Once a laminar attachment line was established on the suction panel, maintaining laminar flow required the correct level of suction. Finding the right combinations of suction levels in the attachment-line flute inboard regions (including the suction patch) was more difficult to accomplish than anticipated and remained an impediment to progress for some time. Too much suction tripped the boundary layer and too little did not stabilize the area of cross flow that started just above the attachment line (the same suction flute controlled both areas). Too little suction could also result in an attachment-line boundary layer that was more sensitive to pressure perturbations and surface roughness than it would be with more suction. Resolution of this problem required fine adjustment of the valve angles controlling the suction flow to determine the maximum and minimum suction levels permissible in each region. Flight 48 was the first flight with the suction system operational. Twelve flights (flights 48 through 59) were conducted with the original fence (fence 1) configuration to solve the inboard laminar flow problem and to achieve some limited run of laminar flow on the upper surface. Four of these flights provided no useful suction or laminar flow data.

Once it was discovered that too much suction could be detrimental to the attachment-line boundary layer, lower values were investigated. When the aircraft was operated at or near design test conditions, the attachment line was laminar in the inboard region with the suction system off. The high external pressure, coupled with the lower internal pressure in the suction compartment, produced a natural pressure differential across the surface. The natural suction (with suction system off) on the attachment line was sufficient to maintain a laminar attachment-line boundary layer. Correspondingly, with the suction system off, there was outflow in the rear upper part of the attachment-line flute (flute 1). Outflow occurred when the flute internal pressure exceeded the external pressure (which reduced over a suction region due to the flow acceleration onto the upper surface). Thus, the rearward extent of laminar flow without suction was short-lived.

The presence of a laminar attachment line without the suction system operating indicated that low levels of suction were sufficient for some α values to provide laminar flow. However, with the suction system turned on, laminar flow on the attachment line was lost for lower than expected suction levels. It was eventually concluded that this loss was due to premature suction-hole-induced transition, although it was not recognized at the time. This phenomenon was thought to be adequately accounted for in the design by using criteria successfully applied in other flight experiments. Suction-hole-induced transition is discussed in section 11.7.

Eventually the allowable range of suction level in the suction patch (region 1), in region 2, and in region 5 was determined that resulted in laminar flow out to the fence (BL 65). Figure 70 shows the suction C_q levels in flute 1 at three BL's: 42.5, 50, and 60, corresponding to regions 1, 2, and 5. The C_q 's and corresponding flow-control valve angles that allowed laminar flow are indicated in the figure. Also shown are lower surface hot films and four hot films installed at the beginning of the upper surface behind flute 3 (LEHF's 01-03) to provide confirmation of when the flow was laminar on the upper surface. Laminar flow existed on the suction patch (region 1) when its flow-control valve was set from 0° to about 13° , but higher settings produced C_q 's excessive for maintaining laminar flow. To maintain laminar flow over regions 2 and 5, the valve setting could not be beyond 16° in region 2, while valve angles up to 35° were permissible in region 5. Valve angles were used during the conduct of the experiment instead of C_q levels because they were more easily programmed into the suction-control system and the mass-flow specification option was not reliable due to the shortcomings of the mass-flow sensors (see closing paragraph of section 11.8). The C_q level allowable (excluding the suction patch) was about 13×10^{-4} at BL 50 and 60 (fig. 70). Absolute levels of suction were dependent on α , C_q , R/ft , and other factors. Note the angles of attack listed for each test point case in figure 70. Generally, it was easier to achieve laminar flow on the attachment line at lower α (about 3.4° to 3.7°), and as α approached 4° , achievement of laminar flow was inconsistent and difficult. This result was probably primarily due to the movement of the attachment line with α and a limit of the turbulence diverter effectiveness with angles of attack approaching 4° . Loss of laminar flow with

increasing α could also be partly attributed to R_θ on the attachment line increasing to a critical level with increasing α . Leading-edge C_p distributions at BL 50 and 60 became flatter or fuller with increasing α compared to outboard BL's. These flatter profiles should increase the R_θ , although calculations were not performed. In region 5, higher α cases required somewhat more suction to maintain laminar flow into the region. The suction settings in the attachment line were driven by the requirement to set suction low enough to prevent premature suction-hole-induced transition and high enough to prevent outflow in the rear part of the attachment-line flute.

The lower surface hot films generally agreed with the corresponding upper surface leading-edge films regarding flow condition. For example, hot films LSHF02 and 03 were laminar when LEHF01 was laminar (fig. 70), and when all lower surface hot films were laminar to LSHF5a, LEHF03 was usually laminar. Flutes 2 and 3 were operated with both 45° and 90° valve openings for achievement of laminar flow to the upper surface films. Interpretation of which suction regions were affecting which hot films was guided by flow streamline paths from a BCAG Euler calculation (fig. 71).

The effect of the inlet shock crossing in region 5 and possible disturbances from the fence itself produced surface pressure changes, movements in the attachment line, and thus local C_q changes that cannot be accounted for fully due to limited spanwise rows of pressure orifices. Laminar flow was not achieved past the fence region (LSHF06 was always turbulent) for fence 1 during this series of flights (through flight 59).

As observed in figure 70, the suction patch (region 1) could be operated with active suction off (a threshold level of suction from venting was still present) or with the control valve opened to about 13° . Calculations of inflow-outflow from the C_q modeling program indicated that the uppermost subregion (patch 4) of the suction patch (fig. 35) experienced outflow with the control valve set at its upper limit for laminar flow on the attachment line (about 13°). To prevent outflow, which could cause problems downstream, this subregion (patch 4) was masked over, beginning with flight 53, by using 0.002-in-thick tape. This area remained masked for the majority of the remaining flight program. The C_q values for the suction patch shown in figure 70 were with the upper

region masked. The suction-patch valve was kept closed, resulting in only a small suction level due to natural venting, for many of the baseline test points. Later flights with fence 2 used a higher level of suction for the baseline test points by opening the valve to 12.5° .

11.3. Upper Surface Laminar Flow

With the knowledge of how to maintain a laminar attachment line inboard, attention was turned to achieving a run of laminar flow on the upper surface. This objective was accomplished in flight 59, where three of the four films at the beginning of the rooftop were removed (LEHF01-03; see fig. 70) because they and their leads disturbed the flow downstream. Three new hot films were installed in region 15 (RFHF01-03), as shown in figure 72. Hot-film RFHF02 was just ahead of the skin splice joint. The hot films installed along the inboard boundary of the suction panel and the fiberglass glove access panel (shown in appendix B) were always turbulent and are not shown. These inboard films were turbulent because of a greater than anticipated inboard turbulent region which is the subject of section 11.11. The maximum extent of laminar flow measured in flight 59 was to RFHF03. The variation in suction distributions for BL 50 and 60, which supported laminar flow to RFHF03, are shown in figure 72. The attachment-line region suction levels (flute 1) were held fixed as the suction in flutes 2 and 3 and in regions 14 and 15 were varied as shown. Reducing suction below the lowest C_q shown in the figure produced turbulent flow at RFHF03.

The length of laminar run in figure 72 is about 5.5 ft, assuming transition between RFHF03 and 02. The length Reynolds number R_x is about 12.4×10^6 . After flight 59, it was concluded that improved laminar flow results with fence 1 at the design Mach number would be difficult to achieve and that improved blockage of the inlet shock was fundamental to further progress. Thus, fence 1 was removed and fence 2 installed.

11.4. Flight Conditions Suitable for Achievement of Laminar Flow

The effect of the inlet shock on the leading-edge and upper surface pressures, as well as the flow disturbances from the fences, resulted in operation of

the aircraft at test conditions slightly different from the design point of $M = 1.9$, $h = 50\,000$ ft, and $\alpha = 3.3^\circ$. A robust laminar attachment line and extensive laminar flow on the upper surface was best achieved at $M = 2.0$, $h = 52\,000$ to $53\,000$ ft, $\alpha = 3.7^\circ$ or less, and a small negative β of about -1.5° . These flow conditions were preferable, regardless of which fence was used. The increased Mach number required more inlet air ingestion, produced less inlet mass-flow spillage, and weakened the inlet shock. Also, the shock angle steepened as Mach number increased, causing the shock to impinge farther aft on both fences; this was especially important for fence 1 where the shock impinged on the swept leading-edge portion of the fence. The farther back the shock impinged on the fence, the more blockage the fence provided. Higher altitudes were beneficial because lower density air at these altitudes resulted in more inlet air volume ingestion and decreased spillage, weakening the inlet shock. Small negative β unswept the left wing, increasing $C_{p_{\max}}$ along the attachment line while raising the attachment line toward $s = 0$. These changes allowed the laminar attachment-line boundary layer to tolerate the pressure disturbances at the leading edge, which originated at the engine inlet, and continued to be laminar along the entire length of the leading edge. A significant number of flights were required to arrive at these preferred conditions. A detailed account of the behavior of the flow on the suction panel for the two fences as a function of Mach number, altitude, α , and β are presented in appendix F.

11.5. Canopy-Joint Shock Impact on Upper Surface Pressures

The examination of C_p data on the upper surface reveals the presence of a weak shock (see appendix F) which contributes to the distortion of the desired straight isobars. A search for an explanation and source of this weak disturbance led to scrutiny of the canopy joint. Figure 73 presents a schematic of the canopy-joint location and the position where a weak shock cast from this joint would traverse the suction panel. The F-16XL-2 has a two-piece canopy which is joined in the center with a metal ring that protrudes slightly. The rear portion of the canopy has a slightly reduced diameter compared to the forward section where they are joined. The joint has an upward step of approximately 0.15-in. over a 1-in. length, followed by a downward ramp of 0.45 in. over a 2-in. length

(fig. 74). The CFD grid used for flow-field calculations did not model the canopy joint because it was not recognized as a discontinuous surface and therefore a possible shock generator.

A typical isobar pattern with fence 2 installed and a C_p distribution at BL 70 for the same condition is shown in figure 75. The distortion in the isobar pattern appears to originate from the joint. This figure illustrates that although the shock was weak, as shown by looking at the BL 70 C_p distribution, the upper surface isobars were sensitive to it. To provide additional guidance about the source of the shock, upper surface C_p distributions and isobar patterns over a range of Mach number from 1.4 to 2.0 were examined. Figure 76 presents an overlay of these findings and indicates that the disturbance was a function of Mach number, providing further evidence that the canopy joint was the source. Additionally, BCAG modified the CFD grid with a simulated canopy-joint perturbation, and the resultant Euler calculation produced isobar distortions similar to the one shown in figure 75. Assuming the joint was the problem, an attempt was made to reduce the strength of the shock by the application of a gently sloping, wide fairing over the joint, as illustrated in figure 77. A fairing was fabricated with foam built up behind the joint, putty to fill in small areas, and tape in the front and around the perimeter. A sketch of the fairing cross section is presented in figure 77(a). Three views of the fairing installed for flight 85 are illustrated in figure 77(b). There was no measurable change in the surface pressures with the fairing as compared to a similar test point without the fairing, as illustrated in figure 78. The small differences shown in the C_p 's for the two test points are within the data repeatability range ($0.006 C_p$). Further, there was a row of hot films along the splice joint just behind the canopy-joint shock disturbance for the two flights with and without the fairing (see hot-film installation figures for these flights in appendix B) and the condition (laminar, transitional) of the boundary layer did not change for the same suction levels, indicating that the pressure distribution did not measurably improve or worsen with the fairing. The corresponding isobars for these two test points, which also indicate no significant difference, are shown in figure 79. The explanation for the lack of any measurable change in upper surface pressures due to the fairing has not been found. Unfortunately, limited time did not allow implementation of alternate

fairing concepts, and the fairing was removed after flight 85.

As observed in previous sections, the upper surface pressures were very sensitive to deviations in the flow field and flight conditions. To investigate this sensitivity, a forced smoothing of several upper surface data points around the canopy shock disturbance location was done for the test point 81.a10i (no fairing installed). The original and modified C_p distributions are shown in figure 80. Buttline 70 was modified the greatest but, even here, the adjustments in C_p 's made were not large. The resultant improvement in the isobars is evident in figure 81, where the slightly smoothed pressures produced isobars close to the desired (unswept) design shape. This exercise further illustrates the sensitivity of achieving the design target isobars to small deviations or variations in upper surface pressures.

11.6. Comparison of Measured and Euler Design Pressure Distribution

A comparison of the Euler predicted design point C_p profiles, with measured C_p profiles with fence 1 at selected chordwise cuts, is shown in figure 82. The extent of laminar flow was not considered in this comparison. Two test points, one on each side of the design α of 3.3° , are shown. The C_p plots for the leading-edge region are also included at each BL. On the upper surface, the CFD profile is more negative than the measured C_p at all BL's. This condition is also true in the leading-edge region except that the deviations become larger at BL 70, 80, and 90 due to the engine inlet-shock system. Recall that the CFD solution assumed no shock system was present. Also noticeable in the figure is the difference in the position of the canopy-closure shock that traversed the rear of the suction panel. The shock crossed the suction panel approximately 25 in. in front of the position indicated by the CFD solution. This disagreement was noted earlier in results from the supporting flight tests and the Langley Unitary Wind Tunnel tests. This shock did not adversely affect the experiment. The disturbance that is attributable to the canopy joint also affected the C_p distribution and is most noticeable from BL 70 outboard, as discussed in section 11.5. For the same Mach, altitude, and sideslip, the best agreement between CFD and measured C_p on the upper

surface occurs at an experimental α of about 3.7° compared to the design $\alpha = 3.3^\circ$. Figure 83 compares the CFD design C_p with the experimental C_p distribution for a representative test point flown at 3.75° . The disagreement in the leading-edge and attachment-line $C_{p_{\max}}$ is, however, more apparent for this higher flight α . Note also the overshoot in the leading-edge expansion onto the upper surface starting at BL 80 in figure 83(d), which is the effect of the inlet-shock system (fence 1 at these flight conditions was ineffective in blocking the shock).

Further comparison of CFD versus measured C_p at $M = 1.9$ is presented in the isobar plots of figure 84. The top isobar plot is the CFD solution at the design condition. As discussed in the design section, having unswept isobars was desirable on the upper surface to prevent the generation of cross flow. The second plot shows isobar contours produced from measured data at the design α (3.3°). The isobar contours are swept in the leading-edge direction. The remaining plot shows the isobar contours for $\alpha = 3.75^\circ$.

For completeness, C_p distributions obtained at two of the flight conditions most favorable to obtaining a large extent of laminar flow are shown along with the design profiles in figure 85(a) through (f). The cases shown are for the best laminar flow conditions for fence 1 and fence 2. Test point 77.a4g1 compares favorably with the design C_p profile, even though the Mach, altitude, α , and sideslip are different from the design condition. However, both flight conditions have swept and distorted isobars compared to the design, as shown in figure 86, suggesting that a higher α would have been desirable to lower cross-flow development on the upper surface. However, it was not possible to maintain laminar flow at higher angles of attack due to the lack of a robust laminar attachment line for these higher α conditions.

The design pressure distribution was not fully realized due to the upper surface flow disturbances mentioned. However, if the effects of these disturbances are factored out (as was done by example in fig. 81 for the canopy ring disturbance), one can make the case that in a global sense, the intent of unswept isobars was achieved at a slightly higher measured α , thus providing some measure of validation for the CDISC inverse design tool used to generate the design target pressure distribution. Achievement of the

design C_p distribution would have allowed the demonstration of low or no suction on the upper surface to achieve long runs of laminar flow. HLFC requires suction only in the leading edge to contain cross flow and uses tailored favorable pressure gradients over the rooftop to control Tollmien-Schlichting (TS) boundary layer disturbances. HLFC could not be demonstrated because of the distorted isobar patterns which generated additional cross flow on the upper surface.

11.7. Suction-Hole-Induced Premature Transition

One key technical challenge encountered was suction-hole-induced premature transition. When the suction system was first turned on during supersonic flight, laminar flow could not be achieved. Several flights were required to determine that the suction level in flute 1 was too high, and that by lowering and individually adjusting the five suction regions in flute 1, laminar flow could be achieved. Thus, an unexpected suction limit on the attachment line was uncovered in which the maximum suction allowed inboard was about one-half the maximum design suction level. The oversuction problem occurred only on the attachment line and was present before and after the inlet-shock system intersected the leading edge. All other suction regions on the panel could sustain laminar flow with maximum design suction or higher applied. The suction limit experienced on the attachment line was a premature suction-hole-induced tripping phenomenon where transition occurred at low values of R_k , often referred to as the Goldsmith number (refs. 31 and 32). The R_k is a measure of effective roughness caused by flow into the suction hole and is a product of the suction coefficient, the hole spacing, and the unit Reynolds number ($R_k = C_q \times s_h \times R/\text{ft}$). Goldsmith (refs. 31 and 32) studied this phenomenon for a single hole and a single row of holes in two-dimensional flows and established the criteria for critical suction levels. The disturbance flow associated with a single hole is analogous to the flow around a roughness element. The flow mechanism responsible for onset of transition was described by Goldsmith as a vortex pair structure associated with flow into each hole. The strength of the vortex and its influence on transition is related to the suction hole flow rate, hole diameter, and local boundary layer thickness. Increasing the suction rate is comparable to increasing the size of a roughness element height. At some point, the

trailing vortices from a suction hole do not dissipate but amplify and break down. LFC designers were careful not to exceed this critical suction level. Early studies with perforated suction surfaces used holes that were closely spaced laterally in a given row (refs. 31 and 32), with the idea of replacing slots with holes. The hole pattern was not square; for example, hole lateral spacing was typically 1/3 to 1/10 the streamwise value. For these cases, interaction between vortices of laterally spaced holes becomes a problem with higher suction levels.

For multiple rows of holes, hole alignment becomes an issue because the trailing vortices from each hole can be amplified by interaction with a vortex disturbance at a downstream hole, resulting in premature transition. Pfenninger (ref. 14) discussed this problem and reported that Goldsmith (ref. 31) and Head (as reported in ref. 33) experienced premature transition when holes were aligned with the flow. After experiencing premature transition due to hole alignment in flight tests, Head conducted a wind tunnel experiment to confirm that lining up holes in the local flow direction produced early transition. Gregory (ref. 33, pp. 943, 950) and Wortmann (ref. 34) reported on the influence of hole spacing and also noted hole alignment as important, recommending that holes be staggered rather than in line. More recently, Reneaux and Blanchard (ref. 35) and Lord et al. (ref. 36) reported onset of transition at high suction levels with holes aligned with the flow and the elimination of this problem by skewing the holes. Obviously, on a swept three-dimensional wing, curvature of the streamlines dictates that with or without skewing of the perforation pattern, at some locations on the wing the holes will be aligned with the streamlines for some distance. The real problem exists on the leading-edge attachment line where the highest suction levels can occur and where the streamline flow direction is along the leading edge. Skewing or offsetting the hole pattern increases the distance between holes, which helps alleviate the hole interference problem. Reneaux and Blanchard also reported that a good design practice is to space holes 10 or more diameters apart. A Navier-Stokes modeling of suction through single and multiple rows of holes (ref. 37) indicated that hole inlet shape geometric irregularities have little effect on the trailing vortices. Another observation from reference 37 was that holes inclined to the surface facing upstream (rather than normal to the sur-

face) produce stronger hole disturbances in the flow field, but holes inclined facing downstream do not.

All perforated-surface swept-wing LFC flight tests successfully conducted in the United States prior to the present experiment had the holes aligned with the local flow on the attachment line (the hole pattern was not skewed). The NASA JetStar flight test (refs. 38 through 40), the Rockwell/NASA F-16XL-1 supersonic laminar flow experiment (refs. 6 through 8) and the NASA/BCAG B-757 HLFC Experiment designed the hole size and spacing to stay below the critical Goldsmith number for a single row of holes (and had suction holes aligned with the flow). No oversuction problems due to hole alignment were encountered on the attachment line in these previous flight tests. The highest value of R_k on the attachment line experienced with laminar flow was about 5.5 on the suction patch of the B-757 HLFC experiment and about 4.3 on the Rockwell/NASA F-16XL-1 experiment.

The design of the perforated hole pattern and critical suction criteria for the present experiment followed the successful experiences from the previous flight experiments. The F-16XL-2 perforated surface had a square perforation pattern; for example, hole spacing was the same laterally and longitudinally. An R_k of 15 was used as the upper limit allowed during design of the F-16XL-2 suction panel, but the actual calculated values remained well below this number. The $R_k = 15$ value was considered conservative based on the work of Goldsmith (refs. 31 and 32). Also, unpublished data from the Jetstar LFC flight experiment indicated laminar flow was maintained to an R_k of 15 in the cross-flow region of the leading edge downstream of the attachment line. In the B-757 HLFC flight experiment, the maximum achieved R_k was 7 in the leading edge downstream of the attachment line, and the flow was laminar for this condition. The design C_q distribution for the F-16XL-2 leading-edge region (fig. 23) resulted in the highest design R_k values on the attachment line, as given in figure 87 (from a BCAG calculation). At the attachment line, a maximum R_k of about six was used for the suction patch. Outboard of the suction patch, along the attachment line, a design R_k approaching four was calculated (fig. 87), assuming maximum suction at $h = 50\,000$ ft. This R_k level was thought to be conservative. By using the lower surface hot films to monitor the condition of the attachment-line boundary layer, limits of R_k for laminar flow were

determined from the flight data and are shown in figure 88. The maximum permissible R_k for a laminar attachment line increases along the span, varying from a low of about 2.7 at BL 50 and a high of about 3.5 at BL 90.

The hole spacing along the attachment line was 0.010 in. on the 6-in. length of the suction patch and was 0.015 to 0.017 in. along the remaining leading-edge length in flute 1. A typical view of the hole pattern along the suction-panel attachment line, with simulated streamlines, is shown in figure 89. CFD analysis indicates that the streamlines at the attachment line continue downstream a considerable distance before turning towards the upper and lower surfaces (streamlines from an Euler solution were shown in fig. 71) and aggravates any potential hole alignment problem. In addition, the leading-edge flow for this flight experiment was most likely in the critical range of $R_{\theta, C_q=0}$ (R_{θ} at zero suction on the attachment line). Calculations of $R_{\theta, C_q=0}$ for this experiment were made by BCAG and are presented in figure 90. The $R_{\theta, C_q=0}$ values are considerably higher than those observed on previous flight experiments, according to BCAG. Recent unpublished subsonic wind tunnel swept-cylinder results of Poll (private communication with BCAG) attained laminar flow on the attachment line at higher $R_{\theta, C_q=0}$ and R_k values than the F-16XL-2 results. The hole pattern, however, was skewed for Poll's experiment. Thus, it is concluded that the combined effect of hole alignment with high $R_{\theta, C_q=0}$ values probably resulted in the low critical suction levels encountered on the attachment line.

The pressure disturbance caused by the inlet shock system crossing the leading edge raises the local maximum C_p , which raises the local suction coefficient C_q and R_k , and was, without doubt, a factor in the loss of laminar flow at the attachment line in this area. An example of the variation of R_k along the attachment line due to changes in $C_{p_{max}}$ and C_q is shown in figure 91 for two flights, one with fence 1 and the other with fence 2 installed. For the two cases shown, the attachment line was laminar along its entire length. The variation of R_k mirrors the variation in C_q , as illustrated in figure 91.

Because design C_q on the attachment line could not be reached, higher-than-design suction in flute 2

was required to compensate in controlling cross flow and to ensure extended runs of laminar flow. These higher suction levels in flute 2 resulted in the highest R_k locally on the panel. The maximum values reached in flute 2, which still allowed laminar flow in the rear part of the panel, varied from about 4.8 at BL 50 to 5.6 at BL 90. The calculation of R_k for flute 2 used the square pattern spacing for distance between holes, but as shown in figure 89, as the streamlines curve, the effective spacing between interfering holes increases because the holes are aligned diagonally. The R_k maximum values for laminar flow mentioned for the beginning of flute 2 above (where C_q is the highest) are thus conservatively low because the hole spacing used in the calculation of R_k is actually higher along an individual streamline. The R_k value of 5.6 at BL 90, quoted for a square pattern spacing, could be about four times higher (R_k of about 22), based on a streamline angle of about 13° at the beginning of flute 2.

11.8. Suction Distributions

The suction system was designed to provide a range of suction levels high enough to ensure the achievement of extended laminar flow and low enough to result in transition on the upper surface to obtain code calibration data. Examples of suction distributions achieved in flight, compared to the design upper and lower range, are discussed in the following paragraphs.

The maximum and minimum experimental suction levels obtained across the suction panel (BL's 50 to 100) are illustrated in figure 92 for two test points in flight 88. Attachment-line suction, controlled by flute 1, was maintained at the same level to ensure a laminar attachment line for these cases; therefore, flute 1 suction levels are unchanged for the two points. As discussed earlier, flute 1 suction was limited because of the potential for generating suction-hole-induced disturbances. For the two cases shown, all control-valve angles outside of flute 1 were set at 90° for test point 88.12c1 and at 20° for test point 88.11g1. Flute 2 was higher than design maximum when set at its maximum flow level. The suction levels in flutes 2 and 3 were typically set at their maximum values (90° valve angle), when extensive laminar flow was the goal, to compensate for the lower suction in flute 1. Suction levels on the rooftop were designed to provide a threshold level of suction without a high variation

from maximum to minimum. For the higher C_q test point case shown (88.12c1), laminar flow existed to the rear code-calibration sensors (see appendix B for flight 88 sensor locations), but the same sensors were turbulent for the lower C_q test point (88.11g1).

An example of the highest achievable suction levels in the leading edge, without regard for maintaining a laminar attachment line, is illustrated in figure 93. With valve angles for all the suction regions in flutes 1, 2, and 3 set on 90° , the C_q level in flutes 1 and 2 were consistently greater than design maximum at all spanwise locations across the suction panel. The suction level in flute 3 was at approximately the maximum design level inboard but fell slightly below design outboard starting at BL 80 (fig. 93). For this test point, the suction level on the rooftop was set less than maximum achievable. No laminar flow existed for this test point because of the high attachment-line C_q levels.

The suction distribution for a test point in flight 77, where the maximum laminar flow achieved was recorded, is shown in figure 94. Flute 1 C_q levels were set at values to support laminar flow along the entire attachment line, and all other suction regions were at their maximum level. Laminar flow was measured by the most rearward sensor at 46 percent chord; therefore, laminar flow probably could have existed beyond that location in the absence of the sensor and its leads.

Individual suction-region mass flows for the test cases discussed in figures 92 through 94 are presented in table 5, along with the design upper and lower mass-flow levels. The experimental values shown were determined from the MDC data reduction program (briefly described in the Data Analysis Tools section). The individual suction region flows reflect the C_q trends shown in figures 92 through 94. The total integrated mass-flow level for the cases in which extensive laminar flow was measured (i.e., test point 77.a4g1) was about the same as the upper limit design mass-flow level (0.2302 versus 0.2553 lbm/sec), even though the distribution per region was different. The inability to raise suction beyond a critical limit in flute 1 and maintain laminar flow was detrimental for two reasons. First, it prevented attempts at optimizing suction in the leading-edge region. Second, it may have prevented the laminar attachment line from sur-

viving the pressure disturbance from the inlet-shock system at higher α . It is possible that had more suction been permissible, the attachment line could have remained laminar at a higher α , resulting in more favorable C_p distribution on the rooftop. It is worth noting that the suction level in flute 1 was bound on both sides. The suction level was bound at an upper limit by the oversuction problem and, like other suction regions, was bound at a lower limit by outflow considerations. The upper and lower limits were not well separated, restricting the range over which suction could be varied in flute 1.

By design, the mass flow for each region could be obtained by the mass-flow sensors described in the instrumentation section or by calculating it by using the pressure drop across the skin, along with the measured skin-porosity characteristics. A comparison of the results of the two methods is shown in figure 95 for test point 77.a4g1. The difference between the two mass-flow values was not consistent from flight to flight, but the mass-flow sensor value was generally higher. In contrast, the calculated mass flows were consistent from test point to test point, and separate but similar skin pressure-drop methods by BCAG and MDC for calculating mass flow were in good agreement. The poor performance of the mass-flow sensors was partly because the sensors were single-point measurement devices (figs. 67 and 68) that were used in a highly three-dimensional flow field. Despite the considerable effort to try to account for this problem in their calibration, the sensors did not provide an accurate reading of the mass flow through the ducts. The accepted method for obtaining mass flows and suction distributions for this project was to use the measured skin-porosity characteristics and the measured pressure drop across the skin. All mass flows and C_q 's shown in this paper were determined by this method.

11.9. Effect of Outflow on Laminar Flow

Outflow is the natural venting that occurs when the internal pressure exceeds the external pressure. This venting can take place in the downstream sections of a region because of the inherent decrease in the external pressure over the surface of a region, which has nearly constant internal pressure as the flow traverses across it. The internal pressure must be at least as low as the lowest external pressure to avoid outflow. Avoiding outflow is relevant to LFC because

it could cause regions of separation and therefore transition. However, it was found that outflow could be tolerated in flute 1, and transition avoided, if the suction in flute 2 immediately downstream had a sufficiently high level to compensate. Unfortunately, there was not time to devote specific test points to investigating this topic. Most data related to outflow were collected as part of some other test point objective. Because of these limitations, there are no quantifiable results for the amount of outflow allowable or what suction level downstream of the outflow region is “sufficiently high” to prevent transition. Nevertheless, there are data showing that laminar flow existed behind regions of outflow. The tool used to verify whether outflow existed was the FT2SA program written by MDC, which, among other capabilities, included the ability to find regions of outflow. The program searched a detailed grid for locations where the internal suction region C_p was greater than the local external C_p and then output the location and the C_p difference (ΔC_p). This result could be plotted on a layout of the unfolded skin. The ΔC_p value was used instead of C_q for regions that had outflow were not valid due to the absence of skin pressure drop data for flow going in the reverse direction through the skin. It is highly unlikely that the skin characteristics documented for suction apply to flow in the reverse direction because the holes were tapered (see fig. 24). An example of a test point with outflow and the predicted outflow areas is presented in figure 96. This test condition is for Mach 1.89 with valves closed for all regions except those in flutes 2 and 3 (regions 3, 4, 6, 7, 9, 10, 12, and 13). The attachment-line flute suction region valves are closed (regions 2, 5, 8, and 11). There are outflow areas in the aft end of each region on the upper surface, as indicated by the shaded areas in the upper plot of the figure. The darkest areas indicate the largest predicted outflow. The objective of this test point was to investigate the suction requirements for obtaining a laminar attachment line. To detect the boundary layer state of the attachment line, hot-film sensors were positioned just aft of flute 3 at the end of the leading edge. The valves for the upper surface regions were left closed because laminar flow on the upper surface was not expected due to the hot-film lead wires. Even with the valves closed for the suction regions of flute 1, a natural suction occurred along the attachment line where the high leading-edge pressures exceeded the internal pressure. Outflow

occurred for this test point in the upper areas of regions 2, 5, 8, and 11. It is evident that region 2 had less outflow than other regions in flute 1 but still had outflow areas near the top and aft. The reason for the difference was an apparent leak in region 2. Integration of the mass flow over the surface of region 2, another feature of the FT2SA program, resulted in a net inflow with the region 2 valve closed. Although there was outflow, the second film indicated that the boundary layer was laminar, even though the streamline crossing it most likely went over a region of outflow. The second film shows that a laminar boundary layer will tolerate at least a small amount of outflow for cases where there is suction downstream of the outflow.

Figure 97 is for a test case at Mach 2.02 and shows considerably less outflow than the previous point. Again, hot films were placed just aft of flute 3 to detect the state of the attachment-line boundary layer. The films aft of the outflow area in region 11 indicate laminar flow. In this case, it is clear that the streamline crossing the last film must have passed over the area of outflow. For laminar flow on the upper surface, at least to the splice joint, outflow was not an issue. For $R/ft > 2.2 \times 10^6$, laminar flow was lost at the splice-joint film array before outflow areas appeared. However, for a limited number of test points at a R/ft of about 2.2×10^6 during flight 85, there were splice-joint hot films that still indicated laminar flow even though regions forward of it were very close to their outflow limit. Unfortunately, there were hardware problems with some of the pressure instrumentation, making the data for this flight questionable for code calibration use.

Because of the attachment-line hole-suction-induced transition problem, the C_q at the attachment line was forced to be below some critical value. The repercussions of this suction limit included low attachment-line C_q values which could cause outflow at the top of flute 1 and, at a minimum, reduce C_q values at the top of flute 1 where larger C_q values were desired for the control of cross flow. Several flights were made to examine solutions to this problem. The first attempt used 0.002-in-thick tape to mask the perforations from $s = 0$ down, which included the attachment line leaving only the top of flute 1 unmasked, where higher C_q values were desired and were now possible without oversuction on the

attachment line. Though earlier precursor flight testing of turbulence-diverter concepts on the right wing and results from the leading-edge passive glove test indicated it was possible to maintain a laminar attachment line with no C_q , the attachment line for this masked test case was not laminar. A hot film was placed on the attachment line 17 in. downstream from the turbulence diverter, and it confirmed no laminar flow existed. The second attempt to deal with the C_q profile in flute 1 was to mask the top of region 11 where outflow was predicted. A 0.002-in-thick mylar tape masking strip ran the entire length of region 11, starting at about 0.24 in. above $s_n = 0$ and ending at the top of the region, at about 0.64 in. The two patches sealed over were patches 67 and 77 (see fig. 35 for their location in flute 1). There were hot films far downstream of the masked area (see hot-film locations for flight 77 in appendix B). For test point 77.a4g1, laminar flow existed to hot-film R18HF1a at 46 percent chord. Thus, laminar flow survived the 0.002-in. high forward and rearward facing step and the nonsuction region in the upper part of region 11. Recall that the design specification was 0.003 in. for forward facing steps and 0.001 in. for rearward facing steps, but the specifications did not assume that the forward and rearward steps occurred together.

Laminar flow was measured far rearward in the presence of outflow also, as indicated in figure 98 for test point 70.o4i1. Calculations of outflow are evident in the upper part of region 11 because relatively low suction was applied in this region. All regions downstream were set with maximum suction achievable (valves at 90°), and laminar flow was detected at 41 percent chord. Another case, test point 83.a2c1, with confirmed laminar flow downstream of outflow, is illustrated in figure 99, where the hot-film sensors were located along the splice joint. The flight conditions for this case are similar to those in figure 98 except that the altitude is greater. The flow that crossed through the outflow area is laminar at the indicated sensor locations along the splice joint.

For the remaining flights, efforts to avoid outflow concentrated on keeping the C_q in flute 1 as high as possible without causing attachment-line over suction, a task which left little room for error.

11.10. Suction-Panel Surface Temperature Distributions

As described in the instrumentation section, temperature measurements were made on the leading edge and the upper surface with thermocouples. For the purpose of stability calculations on the upper surface, the wall temperature was defined as the averaged temperature of the thermocouple pair. However, for the purpose of C_q calculations, the flute center temperature was used because it was believed to be closer to the incoming air temperature.

The measured temperatures at each BL for test point 77.a4g1 are shown in figure 100 and represent a typical temperature distribution. The distorted distribution was due to the internal layout of the suction panel, which offered varied heat transfer conduction paths away from the panel surface. One of the largest deviations occurred at the splice joint where there was a large mass of material that provided a heat sink. The underlying ribs also caused deviations in the measured temperatures, as pointed out in the BL 90.5 cut of the figure. The measured results were as expected from thermal heat balance calculations that were performed during the design phase, which included the effects of the stringers, the splice joint, and the ribs. The temperature of the panel never quite reached an equilibrium state due to the large thermal mass and the limited time at supersonic conditions, although the temperature measured by thermocouples that were welded directly on the skin came close. The BCAG calculated adiabatic wall temperature (from BL3D) for this test condition is shown in the figure for BL 80.5. The adiabatic wall temperatures peaked at about 180°F in the leading-edge region, fell about 20°F in the first 20 in., and slowly ramped down to about 150°F by 120 in. back on the upper surface. The response time of the thermocouples was too slow to make them useful for boundary layer state (laminar-transition) determination during the 3- to 10-sec duration test points.

Earlier informal reports presenting suction panel temperature results mistakenly show an area in the middle of the panel to be hotter than expected. The leading edges at BL 90.5 and 100.5 also are shown to be cooler than expected. These temperature deviations

were the result of an error in the database that was not discovered until 7 months after the last flight. The error is awaiting final verification; therefore, the database has not been corrected.

11.11. Inboard Turbulent Region

Contrary to expectations, there was a large inboard area of turbulent flow on the suction panel. As shown in figure 101, hot-film measurements obtained over several flights indicated that there was a laminar-turbulent flow boundary defined approximately by an 8° line relative to the aircraft centerline and originating near or at the turbulence diverter location. However, aft of approximately FS 235, the boundary tracked along a line at about 11° relative to the aircraft centerline. Reference 41 states that "Observation of turbulent wedges in laminar boundary layers at supersonic speeds indicated opening angles of $\pm 7^\circ$." In addition, previous turbulence spreading data collected in reference 43 over a Mach number range was used to produce an envelope which indicated that the lateral turbulence spreading angle should be between 4.8° and 7.8° for Mach 2 flow. However, for Mach numbers close to 2, actual data points existed between 5.0° and 6.5° only. The inboard edge of the suction panel was angled outboard 5° relative to the centerline, which, by design, was to compensate for turbulence spreading. The external flow near the inboard edge of the panel turned inboard 2° , which, when combined with the 5° panel taper, allowed for 7° spreading. Thus the design appeared to be on the safe side.

In an effort to explain the larger than expected inboard turbulent region, an experiment to determine the lateral spreading angle of turbulence was performed in a rooftop section of the panel identified in figure 102. A transition trip and 10 hot films were used to measure the turbulence spreading angle during flights 83 and 84. The second array of films just forward of the splice joint (numbered 1 through 9 in fig. 102) was used to collect additional laminar flow data. The boundary layer trip used was 54 grit (nominally 0.015-in-high particles) and was 0.08 in. in diameter. This trip was bonded on a 0.002-in-thick, 0.25-in-diameter patch of tape on the panel. Boundary layer calculations, which included suction effects, indicated that the boundary layer thickness at the trip location was approximately 0.04 in. The trip was located at about $s = 14$ in. at the front edge of

region 14 where the high curvature of the streamlines had diminished. The film array was located about 20 in. downstream of the tripping element for most of the data taken. Figure 103 is a cross section of the wing at the trip location and gives the trip, film, and suction region locations. Typical C_q and C_p profiles near this cross section are shown in figure 104.

The results of the tripping experiment were evaluated by using hot-film signals and streamline traces. The streamline traces were generated from the velocity vectors which were calculated by the MDC Surface Euler code by using the experimental data at the boundary layer edge. Disturbance path traces were then generated. Two disturbance path traces that diverge from the streamlines were defined as -7.5° and $+7.5^\circ$, relative to the velocity vectors. The $+7.5^\circ$ disturbance path trace went outboard relative to the streamlines, and the -7.5° trace went inboard. Results for test point 84.10c1 are shown in figure 105, which includes the streamline trace going through the trip location, the disturbance path traces originating at the trip location, the hot-film positions, and the hot-film signals. The disturbance path traces show that hot-film 05 should be turbulent while hot-films 01 through 04 should be laminar. Even though there is no transition zone defined for the disturbance path traces, one would expect to see indications of such a zone for hot films near the line. The hot-film signals in the figure confirm that this is the case, although there appears to be slightly more activity than expected in the hot-film 04 signal. For the outboard disturbance path trace, hot-films 06 through 08 should be turbulent, 09 should be transitional, and 10 should be laminar. Looking at the hot-film signals reveals that 06 and 07 are indeed turbulent, 08 is well on its way to turbulent, but 09 and 10 are laminar, with no signs of transition yet. Both the inboard and outboard sets of films indicate that the disturbance path traces are offset in the outboard direction by about one-half the distance between films, about 0.6° , but that the spreading angle of 7.5° appears to be a good estimate. This result is typical of all test points examined and indicates that the lateral spreading of turbulence may be relative to a local streamline that is turned slightly more inboard than the one used in figure 105. Further boundary layer calculations showed that the streamline traces at the wall turned 1° to 2° farther inboard than the streamline traces at the boundary layer edge. Apparently, the lateral spreading of turbulence is occurring

relative to some local streamline trace that lies between the edge and wall streamlines. Regardless, the tripping experiment revealed that the lateral spreading angle of turbulence was between 7° and 8° relative to the local streamlines. Relative to the aircraft centerline, turbulence spread outboard at 3° due to the inboard direction of the flow in this region. This 3° spreading indicated that the 5° angle of the inboard edge of the suction panel used in the initial design should have been more than sufficient. However, this was not the case. To investigate further, the method of producing disturbance path traces from the velocity vectors was applied to the inboard and outboard regions of the panel where hot-film data were available for verification. A lateral turbulence spreading angle of $+7.5^\circ$ was used on the inboard region for a streamline originating at the beginning of the suction patch and an angle of -7.5° was used for the outboard region for a streamline originating at the outboard leading edge of the panel. The traces and films were in good agreement in the outboard region, fair for the inboard region ahead of FS 225, and very poor for the inboard region past FS 225.

Another important finding of the tripping experiment was that the lateral spreading of turbulence increased with decreasing suction level. Figure 106 presents the signal from 10 hot films for a series of test points where suction was reduced. The effect of suction can be seen clearly by looking at the hot-film 09 signal. The signal indicates laminar flow in figure 106(a) and indicates that the flow undergoes transition as suction is reduced 33 percent for the test point shown in figure 106(f). That all films were not already completely turbulent indicated that the flow progressed towards transition or turbulent as suction was reduced. For hot-films 06 through 10, it is clear that the lateral spreading widened. For hot-films 01 through 05 it is clear that turbulence spread from 01 to 03 and from 05 to 03. The turbulent spreading from 01 to 03 originated from the inboard turbulent region of the glove, which spread outboard. The turbulence spreading from 05 to 03 originated from the turbulent wedge that began at the trip and spread inboard. The turbulence spreading half-angle increased by about one film, or 1.3° , for the lowest suction case shown in figure 106(f) compared to the highest suction case shown in figure 106(a). The hot-film data for these two test points were used to compare to previous data taken by Braslow (ref. 43) and reported by Fischer (ref. 42). Following the method used in reference 43 to

present the data, a value for the percent of time that the hot-film signal indicated turbulence was found for each hot film. For the F-16XL-2, this value was determined by finding the percent of time the hot-film signal was more than halfway between its laminar and turbulent values. The value was plotted against the angle of each sensor location and is shown in figure 107 with Braslow's data and the range reported by Fischer. The angles at the 50 "percent of time turbulent" value are given in a table in the figure. The agreement between the data sets is reasonable, especially considering that the method of obtaining a spreading angle itself can cause significant disparity.

The inboard turbulent region probably was caused by two different sources. The first was due to the lateral spreading of turbulence originating at the turbulence diverter. Turbulent flow exits through the diverter slot onto the rooftop just downstream of the leading edge. It is possible that a vortex formed at this exiting turbulent jet-like flow, causing greater local turbulence spreading than predicted. The second cause of the inboard turbulent region shows up near FS 210 where boundary layer stability calculations show that a high cross-flow region existed. This high cross flow likely causes the turbulent region in this area and first appears to be the result of lateral turbulence spreading. This high cross-flow region, present because of the off design conditions and canopy-ring shock disturbances discussed earlier, persisted as the flow traveled back along the panel. The lateral spreading of turbulence found from the tripping experiment and the region of high cross flow are combined in a planform view with the available hot-film results in figure 108. The results shown in the figure are in good agreement with the boundary of the larger than expected inboard turbulent region. The consensus is that this region was unique to the design of the turbulence diverter and the flow field around the suction panel; therefore, lower turbulence spreading angles can be realized on an HSCT through aerodynamic design.

11.12. Maximum Laminar Flow

As described in previous sections, laminar flow along the entire attachment line and on the upper surface could eventually be achieved repeatably with the appropriate suction flow-control valve settings and flight conditions. The keys to accomplishing this laminar flow condition with either fence 1 or 2 was to

operate at Mach 2.0 instead of Mach 1.9, to fly at a higher altitude of about 52 000 to 53 000 ft instead of 50 000 ft, to limit the α to about 3.7° or less, and to input a small amount of negative β (about -1.5°). Also, the attachment-line region valve angles were set at levels which did not produce critical suction levels. The maximum run of laminar flow achieved is shown in figure 109. Figure 109(a) displays results for two different flight conditions with fence 2. One case (test point 70.o4i1) is at a low α (2.6°) and 50 000 ft. The other case (test point 77.a4g1) is at a higher α (3.7°) and 53 000 ft. The maximum run of laminar flow was 10.3 ft at 46 percent chord for $\alpha = 3.7^\circ$, which corresponds to $R_x = 22.7 \times 10^6$. The hot-film sensors used to identify the laminar region are shown for the $\alpha = 3.7^\circ$ case only. For other test point conditions similar to these, hot-film sensor AFTHF02 at the panel rear (see appendix B for sensor location) displayed an LT signal. For these cases, the maximum laminar flow length was obviously beyond the 46 percent chord result shown. Note that the inboard and outboard turbulent regions (fig. 108) were closing in on the laminar region, creating an increasingly narrow laminar flow path. Efforts were focused on obtaining code calibration data during the last two flights; therefore, sensors were arranged along a line as shown in the sensor positions for flights 87 and 88 (fig. B18 of appendix B). In an attempt to improve laminar flow results and obtain code calibration data in a different C_p environment, the original fence 1 was reinstalled for these last two flights. It was believed that using the successful flight conditions and attachment-line suction settings, never previously used with fence 1, would result in improved laminar flow results. In addition, the main disadvantage of fence 2 was the strong expansion fan generated at the sharp supersonic leading edge which increased cross flow on the upper surface, as discussed earlier. In flight 88, laminar flow was measured on a wide spanwise range of the rear hot-film sensors (back to 42 percent chord), demonstrating that it may have been possible to document more extensive laminar flow if these sensors were moved farther back. (However, this was the last flight.) Suction was reduced on the rooftop and in flutes 2 and 3 to move the transition front across the sensors for code calibration data (discussed in the next section). The most extensive laminar flow results from flight 88 are superimposed over the flight 77 results shown in figure 109(a) for a similar α and are shown in figure 109(b). Laminar flow exists in the same rear-

ward region for both cases: flight 77 with fence 1 and flight 88 with fence 2, with similar suction levels. Stability calculation results with values of cross flow and N -factor growth rates for these cases will be discussed in the following code calibration section.

11.13. Code Calibration Results

This experiment generated the first three-dimensional supersonic laminar flow database on detailed suction requirements and boundary layer transition. The information gathered was used as an initial validation of the design tools, including the CDISC and boundary layer stability codes. Separate analysis was performed by individuals at BCAG, MDC, and High Technology Corporation (HTC). A flow chart of the analysis procedure steps was presented earlier in figure 69 during the discussion on Data Analysis Tools. Refer to that section for a description of the procedure used to obtain N -factors from the flight data. The results of this procedure are presented here.

11.13.1. Representative Test Cases

Flights concentrating on finding the maximum extent of laminar flow possible on the panel were conducted up to flight 80. A representative code calibration test point obtained during this exercise during flight 77 is presented here. The calculations and figures presented originated from HTC reports that are not available in the open literature. Test point 77.a4g1 was flown at Mach 1.97, $\alpha = 3.70^\circ$, $\beta = -1.42^\circ$, and $h = 53\,300$ ft ($R/ft = 2.12 \times 10^6$). Flute 1 was set at a level known to support laminar flow on the attachment line at this test condition. Flutes 2 and 3 and the upper surface were set at the maximum C_q levels (valves at 90°). The average C_q on the upper surface was 0.99×10^{-4} . The objective of the test point was to investigate the extent of laminar flow possible and to use the hot-film transition information for code calibration. See figure B14 in appendix B for the hot-film locations used during this test point. Beginning with the raw pressure data, the profiles are first examined and corrected for erroneous data. These corrected data are fitted, smoothed, and interpolated to a grid suitable for input into the Surface Euler code. The C_p data and the corresponding fit for several of the BL's are shown in figure 110. The C_p contours are shown with the hot-film locations and transition measurements in

figure 111. For reasons discussed earlier, there are regions in which the C_p contours are highly swept. These regions produce areas of cross flow which destabilize the boundary layer. The resulting cross-flow Reynolds numbers, as calculated by the BL3D code are shown in figure 112. Regions of high cross flow extend far forward on the inboard half of the panel. In contrast, the outboard half of the panel has low cross-flow Reynolds numbers that extend to the end of the panel. One would expect from this plot that the outboard region would be favorable for obtaining laminar flow as far back as 50-percent chord. By using the output from the BL3D code, linear stability calculations were made which yielded the N -factors that will be shown here. (See ref. 30 for discussion on linear stability theory and N -factors.) Calculations were typically performed at several frequencies between 0 and 6 kHz to track both the stationary and the most amplified frequencies. N -factor calculations for locations near films R17HF1a and R18HF1a are shown in figure 113. From the plots, film R17HF1a had an N -factor of about 9.2 and R18HF1a had an N -factor of about 13.6. The paths of N -factor growth at four frequencies are shown in figure 114. As shown in the figure, the paths track inboard at an angle between 8° and 9° . Note that although each instability frequency originated along the same BL, they did not all cross exactly over the film location because they have different paths of maximum growth. Therefore, the N -factors from the plots in figure 113 will be slightly off, depending on local gradients. For example, the N -factors for R17HF1a and R18HF1a, found by interpolating to the exact hot-film locations, are 10.8 and 13.7, respectively. These values are above the generally accepted N -factor range for transition of 9 to 10 (refs. 20, 21, and 30). To get an N -factor correlation for a specific film location without interpolating, the calculation had to be started near the leading edge, and the instabilities at several different frequencies had to be allowed to grow until they reached the film location of interest. Each instability traveled along a different path but was typically within about 6 in. of the other when they reached 40-percent chord. Because the trajectories of the disturbances were unknown, several iterations on the starting point had to be made to get the disturbance path to cross close to the hot-film location of interest. As mentioned, interpolation can also be used to get the N -factor at an exact location of interest. N -factor calculations were made at several locations across the panel and then were combined to

produce the N -factor contour plot shown in figure 115. This plot shows that the most growth occurred between BL 65 and BL 85. The growth falls off rapidly outboard of BL 85 and then picks up again. HTC noted in an internal report that a possible reason for this increase was that there was a significant first mode TS contribution in this region. In addition, HTC estimated that the N -factors between BL 80 and 90 near the 50-percent chord line would be 12 to 13.5.

Most of the code calibration data were taken with an array of hot-film sensors placed along the splice joint of the suction panel. This array is shown in appendix B for flights 80 through 86. A representative code calibration test point obtained during flight 80 is presented here. The calculations and figures presented for this test point originated from individuals from HTC. Test point 88.a3k1 from flight 80 was flown at Mach 2.02, $\alpha = 3.71^\circ$, $\beta = -1.51^\circ$, and $h = 53\,300$ ft ($R/ft = 2.27 \times 10^6$). Flute 1 was set at a level known to support laminar flow on the attachment line at this test condition. Flutes 2 and 3 were set at the maximum C_q levels (valves at 90°). The upper surface suction regions had valve angles of 30° . The average C_q on the upper surface was 0.44×10^{-4} . The objective of the test point sequence leading up to this point was to create a code calibration point by reducing the C_q level at the same flight condition until laminar flow was lost at the splice-joint hot films. As in the previous test point, the measured C_p profiles are examined and corrected for erroneous data. The C_p data and the corresponding fit for several of the BL's are shown in figure 116. The C_p contours are shown with the hot-film locations and transition measurements in figure 117. As found in the previous test point, there are regions where the C_p contours are highly swept, which will produce areas of high cross flow. Even though the shape of the C_p profiles for this test point and test point 77.a4g1 are very close, the C_p contours differ aft of FS 300 in their sweep angle. This difference demonstrates the sensitivity of the design C_p to changes in the upper surface flow field. The cross-flow Reynolds number contour plot is shown in figure 118. To further investigate the flow on the panel for this case, boundary layer edge and surface streamlines were plotted and are shown in figure 119. The edge streamlines across the middle of the panel are angled at about 6° . The surface streamline direction is between 9° and 11° in the same area but varies considerably across the panel. Typically,

surface streamlines angled towards the fuselage more than the edge streamlines. The spreading apart and grouping of the surface streamlines indicate that there is a large change in the amount of cross flow in those areas. N -factor calculations made along paths at several locations across the panel are shown in figure 120. The paths track inboard at an angle between 4° and 5° in the middle of the panel. The most growth occurred between BL 65 and BL 85. The growth falls off rapidly outboard of BL 85; this was one of two test points where calculations were also made using a PSE (Parabolized Stability Equation) code (Malik, M.R.; Chang, C.-L.; Li, F.: The Primitive Variable Formulation of PSE: Application to 3D and Compressible Flows, Dec. 1994, High Technology Report No. HTC-9406 and Chang, Chau-Lyan: ECLIPSE: An Efficient Compressible Linear PSE Code for Swept-Wing Boundary Layers, April 1995, High Technology Report No. HTC-9503). Additional information on the PSE method can be found in reference 3, which gives a description of PSE theory and cites several references. The results for test point 80.a3k1 are presented in figure 121. The paths track inboard at about 6° in the middle of the panel. The band of low N -factors between BL 56 and BL 66 corresponds to a region of reduced cross flow and to the separation of the wall streamlines in that area. This pattern is repeated for the calculations on the outer edge and can be seen in the N -factors found when using the eMalik3d code also. The N -factors found from the PSE code are less than those found by the eMalik3d code and have about the same amount of scatter. Lower N -factor values have been found with the PSE code in the past and were not considered an unusual finding. However, it is not clear why the PSE results did not reduce the scatter.

Cross-flow Reynolds number and N -factor contour plots made by HTC for two other cases from flight 88 are shown in figures 122 through 125. Unlike the previous two test points, the original shock fence (fence 1) was installed for this last flight. The test points are close to the same flight conditions; test point 88.a2d1 was flown at Mach 2.01, $\alpha = 3.39^\circ$, $\beta = -1.51^\circ$, and $h = 53\,100$ ft ($R/ft = 2.15 \times 10^6$), and test point 88.a4i1 was flown at Mach 1.99, $\alpha = 3.38^\circ$, $\beta = -1.46^\circ$, and $h = 53\,200$ ft ($R/ft = 2.12 \times 10^6$). The major difference between the points was that the valve angles for the upper surface were set at 90° for 88.a2d1 and at 45° for 88.a4i1, resulting in an average upper surface C_q of 1.11×10^{-4} for 88.a2d1 and 0.74×10^{-4} for 88.a4i1. As expected, the N -factors

increase with reduced suction and retain the same trends. The “T” hot films outboard are due to turbulence spreading from the outboard edge of the panel. The “T” hot films inboard are due to a combination of turbulence spreading from areas forward and inboard and due to increased crossflow in that region. Figure 126 was composed by HTC, based on N -factor calculations performed on flight 88 test points. The plot shows the best estimate of the maximum extent of laminar flow and includes the experimentally determined maximum extent of laminar flow. These calculations suggest that if the hot-film sensors had been removed so that sensors and leads would not trip the flow, laminar flow would have existed to the rear of the panel (about 50 percent chord).

11.13.2. Summary of All N -Factor Results

The code calibration database consists of hot-film boundary layer transition measurements at known test conditions and suction distributions. For each test point analyzed, there is at least one hot-film- N -factor correlation. Additional test points not yet used for code calibration exist in the database. Appendix B shows the many different hot-film locations that were used. Most of the code calibration data were taken with an array of hot-film sensors placed along the splice joint of the suction panel, which was approximately 65 in. from the leading edge. This array and an additional array that was used are shown in appendix B for flights 80 through 88. The hot-film calls indicating “laminar with turbulent spikes” (LT) and transitional (TR) were compared with the N -factors computed by the stability code at the same location for the purpose of code calibration. Table 6 lists the results of all code calibration calculations. Test point, test conditions, hot-film name and its status, and the N -factor found at that location can be found in the table. Additional film calls without a corresponding N -factor are given in order to provide reference to the state of the flow near a film that does have an N -factor calculation associated with it. There are also some “L”, “TL”, and “T” hot-film calls that have N -factors listed for them. Although these are not used to calibrate the code, they are noteworthy. Brief comments about the valve setting are also presented. These data are presented graphically by flight number in figure 127. The symbols differentiate calculations performed by BCAG, MDC, and HTC and the status of the hot-film call. An additional summary plot of

N -factor results from BCAG and MDC is shown in figure 128. The X -axis is the computed N -factor for stationary, or zero frequency, cross-flow disturbances. The Y -axis is the maximum computed N -factor found by using the envelope method. Most data are bound by $11.0 < N_{\max} < 18.0$ and $7.0 < N_{f=0} < 11.5$. For all cases, the frequency range of the most amplified disturbances on the rooftop was found to be 2 kHz to 5 kHz. Reasons for the scatter include the inability to obtain a more detailed measure of the external pressure distribution due to unforeseen disturbances and the possible interaction of the cross flow and TS waves in the rooftop region, which is not accounted for in the stability calculation. Recall that, as discussed earlier, a significant amount of cross flow existed in the rooftop region due to off-design angle-of-attack and pressure disturbances crossing the test article. Aside from the large range in N -factors, the results are promising because they show that designers can use a target N -factor of 10 to 12 (by using the envelope method) for design of laminar flow wings.

Several attempts to explain the scatter in N -factors were made. Some of the scatter is the result of different approaches to handling the raw data and can be seen by looking at N -factor calculations performed by different users for the same film and test point. Table 7 lists data points where calculations were made by at least two different organizations. The numbers in boldface are typically within 1.5 of each other but are as large as 2.7 in one case. The largest part of the differences are attributed to the different fitting, smoothing, and interpolating of the raw data. The pressure tap distribution on the suction panel was designed to capture a C_p profile similar to the design profile. The density of pressure taps was considered sufficient and, as in all experiments, had some practical and financial resource restraints. The density of pressure taps could not be expected to capture unpredicted pressure gradients caused by previously unknown shocks or flow disturbances and left the end user of the data with the difficult task of representing the actual flow field with the given pressure taps. This task was feasible, but because of its subjective nature, likely contributed to the scatter found in the final results. Due to grid differences and various options available in the codes, additional contributions to the scatter are introduced during the calculation process. In a separate exercise, different methods and options within the N -factor code were investigated to see whether the scatter could be reduced or explained. This investigation included

using the fixed spanwise wave number option in the eMalik3d code (constant wavelength option). BCAG results showed that the maximum N -factor was reduced but that the scatter was actually larger. Both BCAG and MDC concluded that this method, as exercised by the eMalik3d code, was not suitable to the highly three-dimensional flow of this experiment and that the envelope method remains the recommended technique. All results presented here use this technique. Efforts to see whether there was a dependence on hot-film location also failed to explain the scatter. For example, figure 129 shows the N -factor results for the splice-joint hot films. There is not a strong pattern of results along the film array, and the scatter is no better than for figure 127, which was for all the N -factor points. Comparisons of correlation with LT hot-film signals versus correlation with TR hot-film signals did not reveal anything either (as can be seen in all the N -factor plots). Apparently, the N -factor scatter is larger than the uncertainty of the film call. In addition to the previously mentioned efforts, an attempt was made to see whether the eMalik3d method itself was partly at fault. As mentioned in the second representative test case, a linear three-dimensional compressible PSE (Parabolized Stability Equations) code was applied and compared to the eMalik3d results. This code includes nonparallel and curvature effects and has been shown previously to reduce the scatter in N -factor. However, as compared to the eMalik3d results, the results of this exercise did not produce a tighter N -factor range for the two cases investigated. For the test points examined by HTC, the eMalik3d N -factor spread was 9 to 19, and the PSE N -factor spread was 6 to 15. The results of this effort are given in table 8.

The code calibration effort contributed significantly to the development of SLFC design tools and their application. This database will continue to be useful for future development and understanding as well.

11.14. Supersonic Laminar Flow Control Benefits Study

Based on the code calibration findings which provided confidence in the design methods, an SLFC benefit study was performed by industry team members using the available TCA (Technology Concept Aircraft) wing planform configuration. The areas

assumed laminar for this study are shown in figure 130. For the high sweep, subsonic leading-edge inboard wing segment, a combination of suction in the leading edge with active cooling over the upper surface was used. A pressure distribution with a rapid acceleration in the leading edge and favorable expansion over the upper surface is required. Wall cooling in the presence of a favorable pressure distribution stabilizes the Tollmien-Schlichting disturbances present on the upper surface. Outboard, the sharp, supersonic leading-edge section does not require suction in the leading edge, and a continuous accelerating pressure distribution is employed so that natural laminar flow (without cooling) can be used. A suction zone exists behind the leading-edge flap joint for this outboard wing segment (fig. 130). Penalties associated with SLFC suction implementation were included. These included the increased weight, fuel displacement volume loss, and power requirements for both the suction system and the active cooling system. A ram air source was assumed to drive the turbocompressor. The study showed that SLFC has major positive net benefits (after accounting for SLFC penalties) for a HSCT, verifying previous study results (ref. 2). These significant benefits are illustrated in figure 131. A 6.7-percent reduction in the maximum takeoff weight could be realized, which amounts to about a 50 000-lb reduction based on a 740 643-lb maximum takeoff weight turbulent aircraft. In addition, incorporation of SLFC would produce an 11.1-percent reduction in block fuel and a 9.7-percent increase in L/D (lift-to-drag ratio). This increase in L/D represents a significant aerodynamic improvement, far exceeding any contribution from other aerodynamic improvements.

12. Concluding Remarks

The F-16XL-2 Supersonic Laminar Flow Control Flight Experiment accomplished most of the program goals and did so while staying within 2 percent of the initial estimated cost of the program. However, due to the numerous difficulties encountered that restricted the execution of many elements in the research phase, not all objectives were completely achieved. The following is a summary of major accomplishments and significant findings.

The experiment achieved extensive laminar flow at Mach = 2.0 and at altitudes up to 53 000 ft. A maximum of 46 percent chord length of laminar flow was

measured with hot-film sensors (10.5-ft length; Reynolds number = 22.7×10^6). In the absence of the hot-film sensors and leads, stability calculations confirm that laminar flow would have existed to the rear of the panel (about 50 percent chord).

The experiment generated a unique, extensive, three-dimensional supersonic boundary layer transition database. Stability analyses and code calibration results of transition data were consistent with design tool predictions, providing increased confidence in design methodology for laminar flow wings. The N -factor results show that designers can use a target N -factor of 10 to 12 for design of laminar flow wings.

Laminar flow was achieved with integrated suction levels close to the design levels, although the leading-edge suction distribution was different from the design. Suction distributions were varied, and the effects on the transition locations were recorded, but no opportunity existed to optimize-minimize suction.

Desired suction distributions were established over the suction surface and achieved maximum suction flow rates and control as designed. Thus, there was a validation of the suction system design methodology for determining perforation hole spacing, pressure drops across the surface and through the collection system, as well as the specification of the turbocompressor requirements.

By excluding the pressure disturbances from the engine inlet shock area and the canopy joint, the shape of the surface pressure distribution achieved is in good agreement with the CFD (computational fluid dynamics) design pressure distribution, thus validating the inverse design tool methodology.

Data analysis tools were developed and successfully applied to calculate suction distributions and boundary layer stability characteristics from flight data. This process involved fitting, smoothing, and interpolation routines to fit the measured pressures and temperatures with sufficient fidelity to replicate the measured trends and to be acceptable for input to CFD methods.

The experiment identified premature suction-hole-induced transition on the attachment line. This finding was significant, indicating that a perforation pattern

with holes aligned along streamlines in the leading edge caused premature transition at critical suction rates lower than anticipated. The other factor influencing premature transition at the attachment line was the presence of high $R_{\theta, C_{q=0}}$ (momentum thickness Reynolds number at zero suction) values which probably combined with the hole alignment geometry to collectively induce transition.

Laminar flow was achieved in the presence of documented surface waves, steps, gaps, and internal suction discontinuities (dams, partitions, stringers, flow blockers, internal instrumentation) in the as-manufactured suction panel. There is no evidence that transition was caused by any of these surface features or blocked suction areas; therefore, some of the existing criteria may be too conservative.

Laminarization was demonstrated through non-design upper surface pressures, including the influence of a weak shock believed to be generated by the canopy joint. Additional cross flow was present due to swept and distorted isobars, yet with relatively low suction on the upper surface, laminar flow persisted through these disturbances.

Laminar flow was achieved downstream of outflow (natural venting), with application of relatively high suction immediately aft of the outflow area. Laminar flow was also achieved downstream of a 0.002-in. high forward and rearward facing step created by a tape strip, with application of high suction aft of the tape strip. The increased suction blockage (0.40 in. normal to leading edge) created by the tape strip did not affect achievement of laminar flow.

A study of the turbulent spreading angle behind a trip was conducted and illustrated that the spreading angle is about $\pm 7.5^\circ$ relative to the local streamline. The spreading angle was shown to increase for reduced levels of suction.

The experiment demonstrated the sensitivity of trying to achieve a universal family of collapsing pressure distributions and unswept isobars on the upper surface, especially for a large gloved wing over an existing fighter aircraft. Future High-Speed Civil Transport (HSCT) aircraft designed from the beginning with supersonic laminar flow control (SLFC) requirements should be more successful in achieving

the target pressure distributions because the new design will not have to contend with pressure disturbances from existing structures that were put in place without regard to obtaining laminar flow. Future SLFC aerodynamic design methodology will have to use fully three-dimensional, validated design methods and closely spaced CFD grids in critical geometric regions that model all important flow-field effects.

The F-16XL-2 SLFC experiment was successful in demonstrating the aerodynamic feasibility of SLFC on highly swept wings at moderate Reynolds numbers. In this context, it can be viewed only as the first step. The technology level of LFC has to advance to the point where its cost savings, affordability, maintainability, and reliability can be adequately demonstrated to the airframe manufacturer and the customer, the airline industry. To achieve this level of acceptance with LFC will require a major commitment by industry and the government. A technology development effort is required to address a broad range of issues and challenges. The other significant driver is the price of aviation fuel. As long as fuel remains relatively cheap and abundant, there will be no pressing need to adapt riskier, innovative high-payoff technologies, such as LFC, which can save approximately 11 percent in mission fuel.

In the aerodynamic arena, CFD design tools and methods must be improved to ensure achievement of the desired wing pressure distribution on highly swept configurations. Configuration analyses must be performed to demonstrate that wing pressure distributions required for laminar flow do not have wave drag penalties or other negative impacts on the total aerodynamic performance. LFC design methods must also be improved to ensure increased confidence in transition prediction and suction flow requirements, which drive the sizing of the suction system components. Achievement of laminar flow on sharp, supersonic leading-edge wing segments, as found on the outboard segment of the HSCT, must be further demonstrated and refined. Optimized SLFC HSCT configurations must be developed. Maintaining a laminar attachment line in the presence of high R_{θ} requires additional study, along with further development of passive and active methods for avoiding attachment-line contamination from the fuselage. Suction-induced premature transition on the attachment line was shown to be a concern with the F-16XL-2 and should be the topic of a

research investigation to develop criteria. Variables in this study would include hole diameter, hole spacing, hole alignment or skewing, local suction levels, and unit Reynolds number effects. Research to determine concepts for minimizing the turbulence spreading angle in the wing-body juncture region should be undertaken; innovative shaping of the juncture area to accomplish this would allow more of the high chord length inboard wing to be laminarized for additional skin friction reduction benefits.

While many concepts and approaches can be evaluated and refined in selective wind tunnel and flight tests and through simulation and CFD, there will need to be a full-scale validation on a large technology demonstrator aircraft at representative flight conditions. Achievement of extensive laminar flow at large chord Reynolds numbers representative of the HSCT must be demonstrated. This vehicle could be used to demonstrate other advanced HSCT technologies (materials, structures, and propulsion) as well.

Structural concepts that allow for a perforated skin in the leading edge and other regions and internal suction ducting must be integrated into the wing structure. Advanced materials and concepts must be developed to ensure a lightweight, efficient structure which accommodates the laminar flow systems internally while meeting the surface smoothness, waviness, steps, gaps, and other manufacturing tolerance requirements. To ensure that laminar flow surface smoothness criteria are met, advanced tooling and assembly concepts need to be developed along with improved low-cost fabrication and production processes.

Concepts for suction compressors and flow control-flow management must be developed and refined to determine optimum systems. Previous systems studies explored suction units driven by engine bleed air, ram air, hydraulic, and electric sources. High-lift systems that are compatible with laminar flow requirements must be developed and integrated into the leading-edge region. A leading-edge protection system to prevent insect contamination is required, along with anti-icing and deicing systems. These systems offer challenges and opportunities for innovative systems integration.

Confidence that industry can manufacture an efficient, certifiable, reliable, safe, and cost-effective aircraft must be demonstrated. The capability must exist to accurately predict performance benefits, penalties, airplane useful life, and in-service maintenance and production costs. These are the minimum requirements to gain acceptance by the customer (the airlines).

References

1. Wilhite, Alan W.; and Shaw, Robert J.: HSCT Research Picks Up Speed. *Aerosp. America*, Aug. 1997, pp. 24–29, 41.
2. Parikh, P. G.; and Nagel, A. L.: *Application of Laminar Flow Control to Supersonic Transport Configurations*. NASA CR-181917, 1990.
3. Joslin, Ronald D.: Overview of Laminar Flow Control. NASA TP-20705, 1998.
4. McTigue, John G.; Overton, John D.; and Petty, Gilbert, Jr.: *Two Techniques for Detecting Boundary-Layer Transition in Flight at Supersonic Speeds and at Altitudes Above 20,000 Feet*. NASA TN D-18, Aug. 1959.
5. Collier, F. S., Jr.; and Johnson, J. B.: Transition Measurements and Stability Analysis. *Research in Natural Laminar Flow and Laminar-Flow Control*, Jerry N. Hefner and Frances E. Sabo, compl., NASA CP-2487, Part 3, Mar. 1987, pp. 998–1014.
6. Woan, C. J.; Gingrich, P. B.; and George, M. W.: CFD Validation of a Supersonic Laminar Flow Control Concept. AIAA-91-0188, Jan. 1991.
7. Anderson, Bianca T.; and Bohn-Meyer, Marta: *Overview of Supersonic Laminar Flow Control Research on the F-16XL Ships 1 and 2*. SAE Tech. Paper 921994, 1992.
8. Anderson, Bianca T.; Rowan, Bruce H.; and Landers, Stephen F.: *F-16XL Supersonic Laminar Flow Control Glove Initial Flight Test Results*. NASA TM-104270, 1993.
9. Talty, Patrick K.; and Caughlin, Donald J.: F-16XL Demonstrates New Capabilities in Flight Test at Edwards Air Force Base. *J. Aircr.*, vol. 25, no. 3, Mar. 1988, pp. 206–215.

10. Landers, Stephen F.; Saltzman, John A.; and Bjarke, Lisa J.: *F-16XL Wing Pressure Distributions and Shock Fence Results From Mach 1.4 to Mach 2.0*. NASA TM-97-206219, Oct. 1997.
11. Fischer, Michael C.; and Vemuru, Chandra S.: *Application of Laminar Flow Control to the High Speed Civil Transport—The NASA Supersonic Laminar Flow Control Program*. SAE Tech. Paper 912115, Sept. 1991.
12. Pfenninger, W.: Flow Phenomena at the Leading Edge of Swept Wings. *Recent Developments in Boundary Layer Research*, AGARDograph 97, May 1965.
13. Pfenninger, W.: Flow Problems of Swept Low-Drag Suction Wings of Practical Construction at High Reynolds Numbers. *Ann. New York Acad. Sci.*, vol. 154, Artic. 2, Nov. 1968, pp. 672–703.
14. Pfenninger, Werner: Laminar Flow Control Laminarization. *Special Course on Concepts for Drag Reduction*, AGARD R-654, June 1977, pp. 3-1–3-75.
15. Braslow, A. L.; Maddalon, D. V.; Bartlett, D. W.; Wagner, R. D.; and Collier, F. S., Jr.: Applied Aspects of Laminar-Flow Technology. *Progress in Astronautics and Aeronautics*, Vol. 123, AIAA, 1990, pp. 47–78.
16. Joslin, Ronald D.; Fischer, Michael C.; Parikh, Pradip; Bharadvaj, Bala; and King, Lyndell: Presented at 1997 NASA High-Speed Research Aerodynamic Performance Workshop, February 25–28, 1997, Hampton, Virginia.
17. Braslow, Albert L.; and Fischer, Michael C.: Design Considerations for Application of Laminar Flow Control Systems to Transport Aircraft. *Aircraft Drag Prediction and Reduction*. AGARD-R-723, 1985, pp. 4-1–4-27.
18. Campbell, Richard L.: Efficient Constrained Design Using Navier-Stokes Codes. AIAA-95-1808, June 1995.
19. Vatsa, V. N.; Sanetrik, M. D.; and Parlette, E. B.: Development of a Flexible and Efficient Multigrid-Based Multiblock Flow Solver. AIAA-93-0677, Jan. 1993.
20. Collier, F. S., Jr.; Bartlett, D. W.; Wagner, R. D.; Tat, V. V.; and Anderson, B. T.: Correlation of Boundary-Layer Stability Analysis With Flight Transition Data. *IUTAM Third Symposium on Laminar-Turbulent Transition*, IUTAM, Sept. 1989.
21. Hefner, Jerry N.; and Bushnell, Dennis M.: *Status of Linear Boundary-Layer Stability Theory and the e^n Method, With Emphasis on Swept-Wing Applications*. NASA TP-1645, 1980.
22. Spalart, P. R.: Direct Numerical Study of Leading-Edge Contamination. *Fluid Dynamics of Three-Dimensional Turbulent Shear Flows and Transition*. AGARD-CP-438, 1989, pp. 5-1–5-13.
23. Barrett, R. V.; and Rickards, J.: An Investigation of Acoustic Transition Detection Including Flight Measurements. *Boundary Layer Transition & Control*, RAE, 1991, pp. 9-1–9-11.
24. Rickards, J.; and Barrett, R. V.: Development of an Acoustic Transition Detector With Application to Boundary Layer Control by Suction. *First European Forum on Laminar Flow Technology*, RAS, 1992, pp. 228–236.
25. Chiles, Harry R.; and Johnson, J. Blair: *Development of a Temperature-Compensated Hot-Film Anemometer System for Boundary-Layer Transition Detection on High-Performance Aircraft*. NASA TM-86732, 1985.
26. Chiles, Harry R.: *The Design and Use of a Temperature-Compensated Hot-Film Anemometer System for Boundary-Layer Flow Transition Detection on Supersonic Aircraft*. NASA TM-100421, 1988.
27. Anderson, Bianca Trujillo; Meyer, Robert R., Jr.; and Chiles, Harry R.: *Techniques Used in the F-14 Variable-Sweep Transition Flight Experiment*. NASA TM-100444, 1988.
28. Kurz, Jerry: *Characteristics and Applications of Industrial Thermal Mass Flow Transmitters*. Inst. Soc. America, 1992, pp. 107–113.
29. Iyer, Venkit: *Three-Dimensional Boundary-Layer Program (BL3D) for Swept Subsonic or Supersonic Wings With Application to Laminar Flow Control*. NASA CR-4531, 1993.
30. Reed, Helen L.; and Saric, William S.: Linear Stability Theory Applied to Boundary Layers. *Annu. Rev. Fluid Mech.*, vol. 28, 1996, pp. 389–428.
31. Goldsmith, J.: *Experiments With Laminar Boundary Layer Suction Through Rows of Closely Spaced Circular Holes at High Reynolds Number and Low Turbulence*. Rept. No. BLC-36, Northrop Aircraft, Inc., Mar. 1954.
32. Goldsmith, J.: *Critical Laminar Suction Parameters for Suction into an Isolated Hole or a Single Row of Holes*. Rept. No. BLC-95, Northrop Aircraft, Inc., Feb. 1957.
33. Gregory, N.: Research on Suction Surfaces for Laminar Flow. *Boundary Layer and Flow Control—Its Principles and Application*, Volume 2, G. V. Lachmann, ed., Pergamon Press, 1961, pp. 924–960.
34. F. X. Wortmann, Translation from GERMAN to ENGLISH of “Der Einfluss der Absaugung durch Poren in der Wand auf die Instabilitaet laminarer Grenzschichten,” Institut fuer Aerodynamik und

- Gasdynamik der Universität Stuttgart, Abschlussbericht zum Vorhaben We 11/37, Feb. 17, 1970, 24 pages.
35. Reneaux, J.; and Blanchard, A.: *The Design and Testing of an Airfoil With Hybrid Laminar Flow Control*. ONERA TP No. 1992-22, Mar. 1992.
 36. Lord, Wesley K.; Zysman, Steven H.; Tillman, Gregory; and Johnson, Warren A.: *Laminar Flow Control Experiment on a Large-Scale Nacelle Model*. Pratt & Whitney Rept. 6420-55, Dec. 1995.
 37. MacManus, D.; and Eaton, J.: Micro-Scale Three-Dimensional Navier-Stokes Investigation Laminar Flow Control Suction Hole Configurations. AIAA-96-0544, Jan. 1996.
 38. Maddalon, Dal V.; Fisher, David F.; Jennett, Lisa A.; and Fischer, Michael C.: Simulated Airline Service Experience With Laminar-Flow Control Leading-Edge Systems. *Research in Natural Laminar Flow and Laminar-Flow Control*. Jerry N. Hefner and Frances E. Sabo, compl., NASA CP-2487, Part 1, 1987, pp. 195–218.
 39. Fisher, David F.; and Fisher, Michael C.: Development Flight Tests of Jetstar LFC Leading-Edge Flight Test Experiment. *Research in Natural Laminar Flow and Laminar-Flow Control*, Jerry N. Hefner and Frances E. Sabo, compl., NASA CP-2487, Part 1, 1987, pp. 117–140.
 40. Maddalon, D. V.; Collier, F. S., Jr.; Montoya, L. C.; and Land, C. K.: Transition Flight Experiments on a Swept Wing With Suction. AIAA-89-1893, June 1989.
 41. Groth, E. E.: Boundary Layer Suction Experiments at Supersonic Speeds. *Boundary Layer and Flow Control—Its Principles and Application*, Volume 2, Pergamon Press, 1961, pp. 1049–1076.
 42. Fischer, Michael: Spreading of a Turbulent Disturbance. *AIAA J.*, vol. 10, no. 7, July 1972, pp. 957–959.
 43. Braslow, Albert L.; Knox, Eugene C.; and Horton, Elmer A.: *Effect of Distributed Three-Dimensional Roughness and Surface Cooling on Boundary-Layer Transition and Lateral Spread of Turbulence at Supersonic Speeds*. NASA TN D-53, 1959.

Appendix A

Suction-Panel Microphones

The F-16XL-2 SLFC suction panel contained 34 microphones to provide a coarse nonintrusive indication of the transition location on the glove. Figure A1 shows the microphone locations on a plan-form view of the panel. Hot films were to provide finer measurements of the transition. Preliminary tests in a supersonic wind tunnel at LaRC and data obtained during the leading-edge passive glove experiment demonstrated this technique. However, the suction-panel microphones did not perform as expected during this flight test. Interpretation of the signals was difficult at best. To further investigate this difficulty, wind tunnel tests were conducted again at LaRC simultaneously with the flight testing. The microphones performed as expected (unpublished data). High electronic noise is suspected of playing a large role in the difficulties encountered with the microphones during the flight experiment.

Specifications

The microphones used in the F-16XL-2 SLFC experiment were manufactured by Kulite Semiconductor Products, Inc. (Model XCS-093-5). The pressure range of the transducers was 5 psid, and they were covered with a protective mesh screen. These solid state sensors use a four-arm Wheatstone bridge on a silicon diaphragm. The microphones included a temperature compensator, located 6 in. behind the microphone, which was designed for a temperature range of 140°F to 240°F. The backside of the transducer was pressurized by a vent tube which was a 0.009-in-inside-diameter tube 5.75 in. long. The low-acceleration sensitivity specifications were quoted as 0.005 percent full scale in the perpendicular direction and 0.0005 percent full scale in the transverse direction. A schematic of a microphone is shown in figure A2.

A dynamic calibration was performed at LaRC which verified that the microphones have a flat frequency response to at least 10 kHz. The microphone sensitivities, which were individually measured and recorded at LaRC, were about 20 mV/psi.

Installation

During fabrication of the suction glove at BCAG, 34 microphones were installed inside the suction-panel sandwich structure. The face of each microphone was mounted flush against the inside surface of the 0.040-in-thick titanium skin with its center aligned with a 0.015-in-diameter laser-drilled hole. Only a small portion of the microphone face was exposed through the hole. Figure A3 shows a schematic view of a microphone installed against the titanium skin. As shown in figure A4, installation deviations on the order of 0.004 in. dramatically affected the “window” between the acoustic source and the microphone diaphragm. These schematics represent typical as-installed views. Each microphone installation was unique in the amount it was off from the centerline of the hole in the suction panel. Also, because the 0.015-in-diameter holes were laser-drilled, the holes were not round, and each had a unique shape. These factors, in turn, contributed to making the output of each microphone signal unique. The 5.75-in-long vent tube, connected to the backside of the transducer, was open to the inside of the suction panel. The internal pressure of the suction panel was typically less than 0.7 psi below the external pressure, well below the 5 psid limit of the transducer. The wiring exited from the side of the panel structure and then to signal-conditioning electronics. Once the lower, nonperforated titanium skin of the suction glove sandwich structure was bonded in place, the microphones became inaccessible for troubleshooting, repair, or replacement.

Signal Conditioning

A schematic of the signal conditioning is shown in figure A5. The maximum output of the microphones was estimated by using flush-mounted microphone data obtained during the passive-glove flight experiment. The gain on the amplifier card was set based on this estimated microphone output and the voltage range available on the Constant Bandwidth (CBW) modules. The amplifier card also provided a 15-Vdc excitation voltage for the microphones that was regulated in order to help minimize the effect of possible variations in the aircraft power supply. The output signal of the amplifier card was passed onto the RMS-to-dc converter card and recorded on an onboard FM tape. The data from the FM tape were available

for postflight examination. The RMS-to-dc converter card output the RMS of the ac signal and applied a gain of 8 to use fully the voltage range of the PCM (Pulse Code Modulation) system. The offset amplifier subtracted 5 V from the signal to further meet the requirements of the PCM/telemetry system.

As stated previously, the frequency response of the microphones was shown at LaRC to be flat to at least 10 kHz. The specifications from the manufacturer indicated that the frequency response was flat to 20 kHz. The frequency response of the amplifier card was flat to 10 kHz and was down 3 dB at 35 kHz. The signal output from the amplifier card was recorded on the onboard FM tape for the frequency range 0 to 2 kHz. The signal was also read by the RMS-to-dc converter card, which calculated the RMS voltage over a 0.1-sec interval and converted the result to a dc voltage. Although only a 0- to 2-kHz bandwidth was recorded on the FM tape, the RMS value included all the energy in the 0- to 35-kHz frequency range.

Although the microphone data were collected two different ways, as shown in figure A5, the real-time RMS data were the main focus for practical use of the signal. The RMS data were displayed real time in the DFRC control room on custom made displays. The signal could be output on strip charts as well. The displays were designed to allow operators to make decisions based on transition location during the flight.

Performance

Upon completion of the suction panel, 2 of the 34 microphones were found to be nonfunctional. The output of M7503 (M75 indicates the BL where the microphone is located; 03 indicates it is the third microphone back from the leading edge) was 10 percent of its expected value, and the 0.015-in. hole for M8506 could not be located. Between flights 45 and 46, it was reported that four additional microphones were not functioning. M6508 and M6509 had open circuits, M7507 gave no response, and M8505 had a short circuit. After additional examination of the signals, it was found that M7502 was functioning on the ground but not in flight, rendering it useless. The remaining 27 microphones produced a signal for the rest of the flight program. The locations of the non-functioning microphones are identified in figure A1 by the open symbols.

Very early in the flight testing, the microphone signals were not behaving as expected. It could not be determined reliably from the real-time RMS signal whether the flow was laminar or turbulent. The magnitudes of the RMS laminar and turbulent levels were very close to one another. In addition, the behavior of some of the microphone signals was much different from others. A complicating factor, which was also the case for the hot films, was that one could not distinguish between laminar and turbulent signals until it was known what each of these looked like relative to each other for similar flight conditions. Because the microphones could not be used in real time, the usefulness of the microphones was severely affected, and they were not used for transition detection. The post-flight data were often not available until after the flight-test planning had to be completed for the next flight, greatly reducing the value of the postflight microphone data. Any transition information needed for planning of the next flight had to be collected and interpreted from real-time data. This procedure de-emphasized efforts to interpret the postflight microphone data and brought the use of hot films to the forefront earlier than planned.

Troubleshooting and investigations into why the microphones performed as they did were very limited and remained a low priority for assignment of available resources. However, several avenues of research into the problem were carried out, some of which are described here. Unfortunately, none offered definitive answers or solutions to the problem. In preparation for the use of these microphones on the F-16XL-2, a test was conducted in the Langley Low-Disturbance Mach 3.5 Supersonic Tunnel. The test used the same type of microphones, electronics, and installation configuration as in the flight test. The microphones behaved as predicted during this wind tunnel test, clearly detecting the onset of transitional flow as compared to a neighboring hot-film sensor. This finding suggests that the problems encountered in flight were directly related to the operating environment in which they were installed (vibration, electronic noise, and sound propagation through structure) and not the flow physics. A close examination was made from the flight microphones of the FM signals versus the RMS signals. This examination did not reveal any insight into interpreting the signal. The RMS signal responded correctly to what was seen in the FM time signal. Apparently, the microphone responds to the

transition process, both from laminar to transitional flow and vice versa, but it also responds to other flow and to vibrational and electronic influences. DFRC also participated in investigating the problem by modifying the signal conditioning of four microphones. The amplifier gain was doubled, and a capacitor was inserted in series with the signal path to the RMS-to-dc converter. This alteration changed the lower cutoff frequency to 85 Hz in an attempt to eliminate low-frequency contamination of the signal. Examination of the signals from the modified signal conditioning revealed that this change smoothed out the signal somewhat but did not improve the ability to interpret the signal.

The illustrations showing how the sensing “window” is different from microphone to microphone cannot completely explain the microphone performance. An additional explanation for the microphone performance is directly related to the frequency band limitations of the recorded microphone signal, which was in the 0- to 2-kHz range in which extraneous noise can be significant. These sources include sound propagating through the structure, resonance particular to each unique hole, power supply noise, and other electronic noise in the surrounding environment. Possibly, improvements could have been made by setting the recorded microphone frequency band from 5 to 10 kHz.

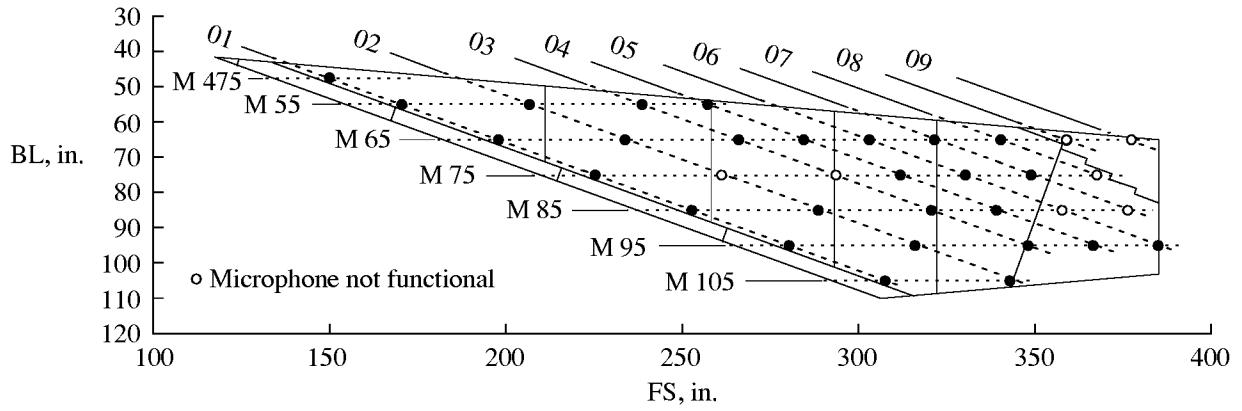


Figure A1. Planform view showing microphone (M) locations on F-16XL-2 SLFC glove.

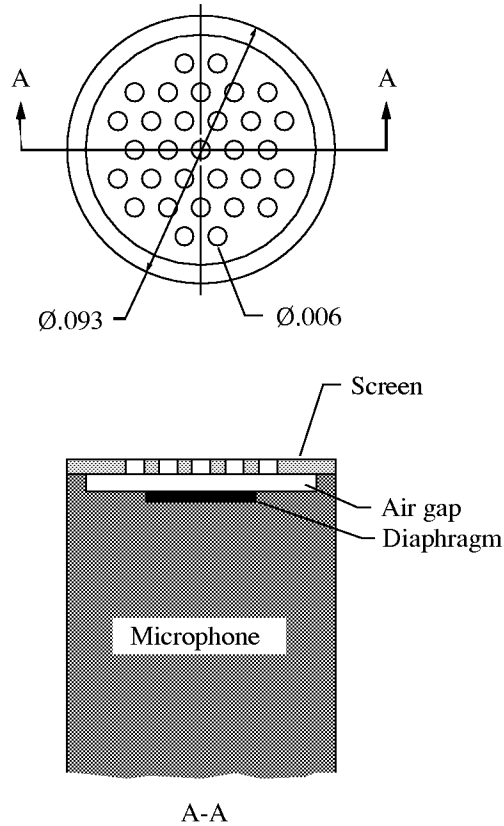


Figure A2. Kulite microphone model XCS-093-5 with M-type screen. Dimensions are in inches.

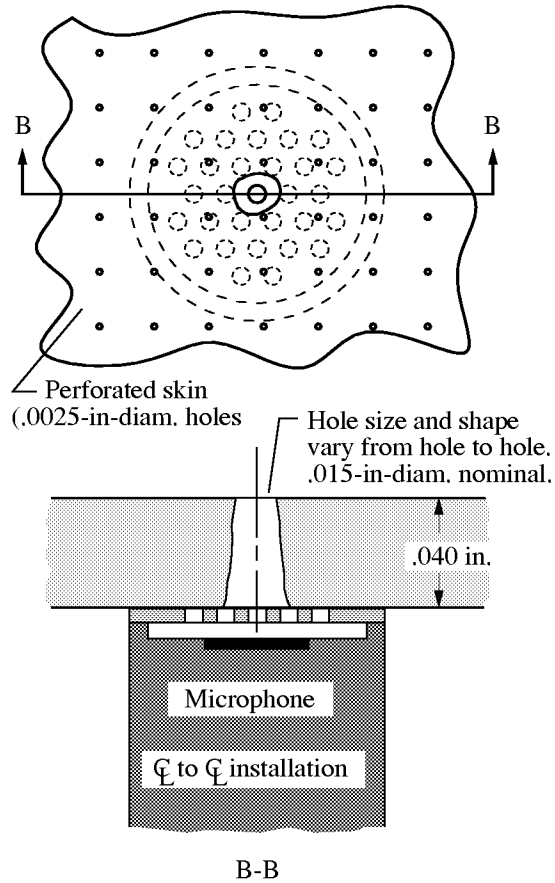


Figure A3. Microphone installed against F-16XL-2 SLFC titanium skin. Installation is centerline to centerline (C-C).

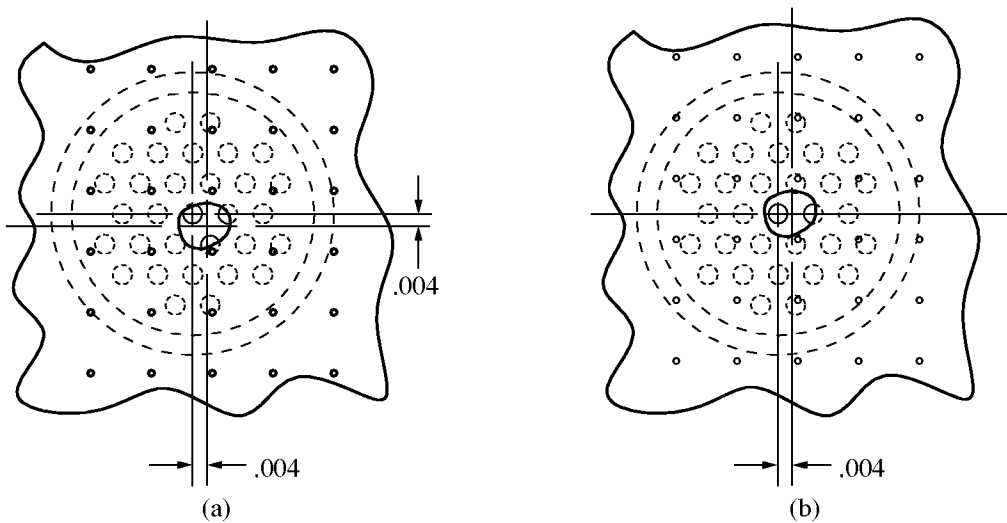


Figure A4. Two views (a and b) of microphone screen holes, as seen from above, looking through 0.015-in-diameter nominal laser drilled hole. Dimensions are in inches.

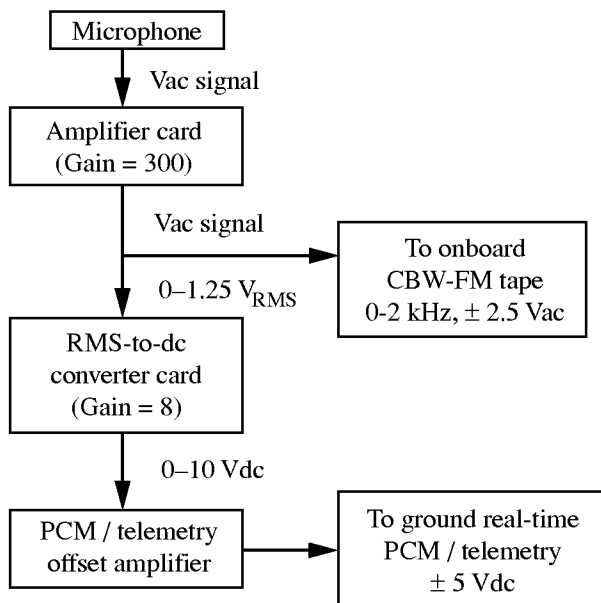


Figure A5. Microphone signal-conditioning flowchart.

Appendix B

Hot-Film Locations

The hot-film locations used during the flight test are shown in figures B1 through B18; 142 different hot-film locations were used. Of these, 126 were on the upper surface and 16 were on the lower surface. The hot films and their leads were mounted on 0.002-in-thick tape that protected the perforated surface from adhesive residue. The flow was assumed to be turbulent behind any hot film and any hot-film lead. The hot films provided a real-time indication of the boundary layer state, which allowed in-flight decisionmaking based on their output. The hot-film output was also used to define the boundary layer transition point for calibration of transition prediction methods.

Prefixes for Hot-Film Identification Numbers

AFTHF	aft hot film
APHF	apex hot film
CCHF	code calibration hot film
IBHF	inboard hot film
LSHF	lower surface hot film
LEHF	leading-edge hot film
OBHF	outboard hot film
RFHF	rooftop hot film
R_HF	rooftop hot film (a region number follows the R)
SJHF	splice joint hot film
TRHF	trip hot film

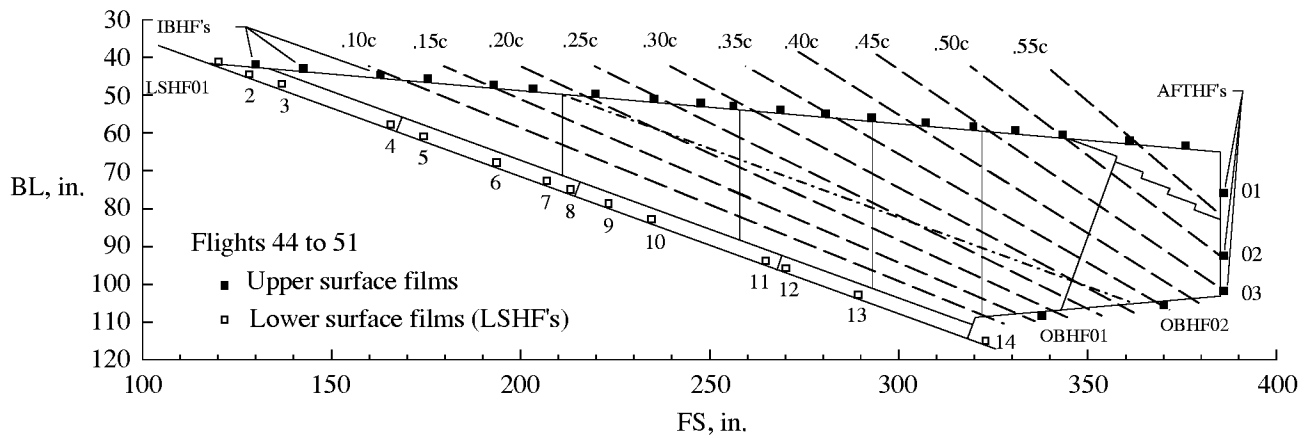


Figure B1. Hot-film layout for flights 44 to 51; 16 hot films on lower surface; 24 hot films on upper surface.

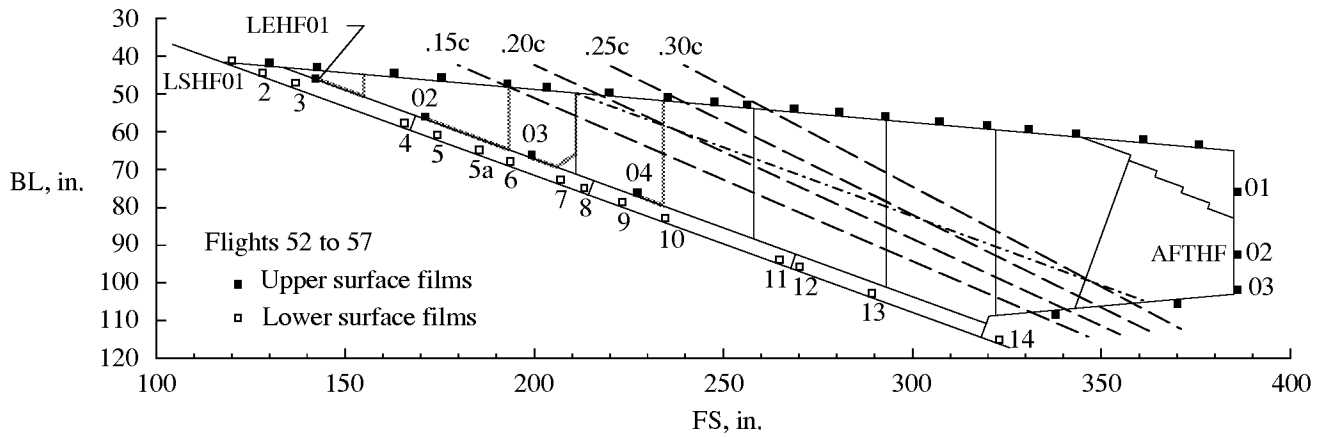


Figure B2. Hot-film layout for flights 52 to 57. Added four hot films near leading edge before flight 52. Added LSHF05a near shock fence before flight 55.

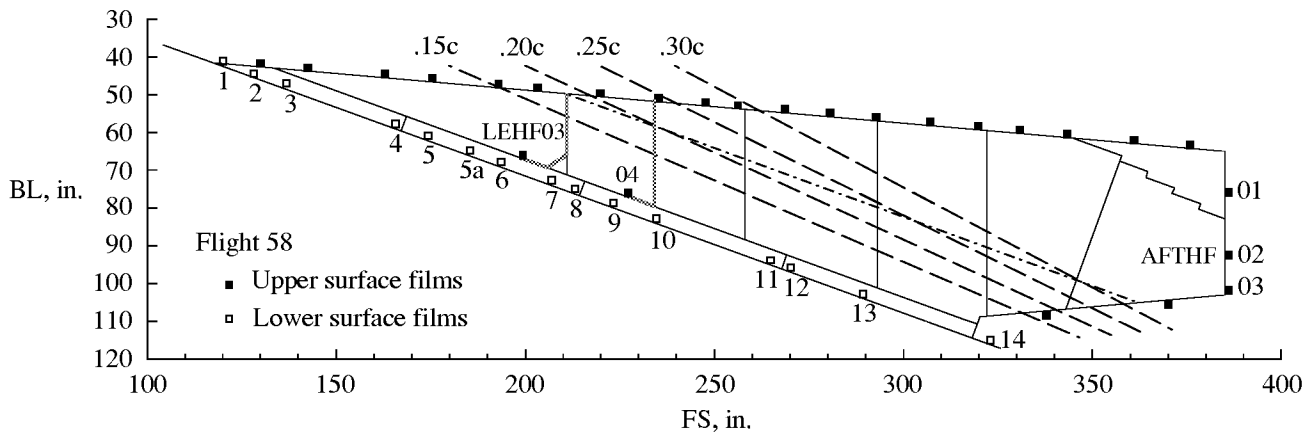


Figure B3. Hot-film layout for flight 58. Removed first two hot films near leading edge.

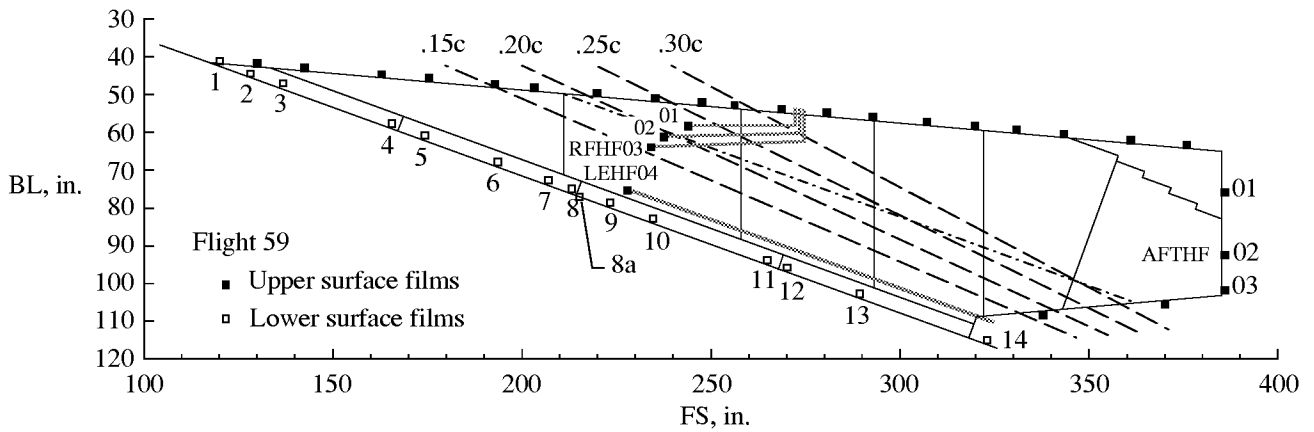


Figure B4. Hot-film layout for flight 59. Added three hot films near splice between FS 230 and FS 250 and one on attachment line at BL 76.5. Removed LSHF near shock fence, and leads for hot film near leading edge were rerouted.

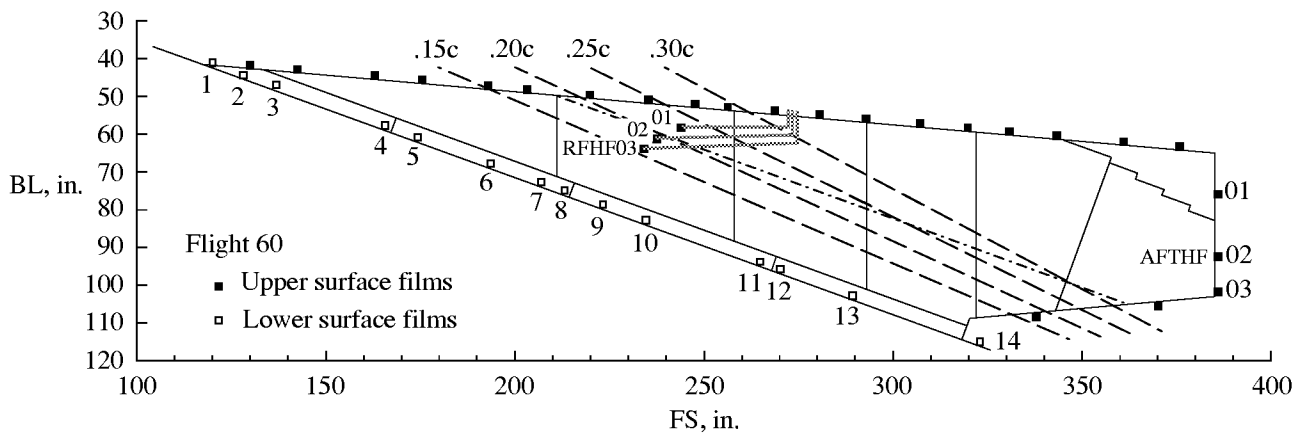


Figure B5. Hot-film layout for flight 60. Removed hot film near leading edge and hot film on attachment line.

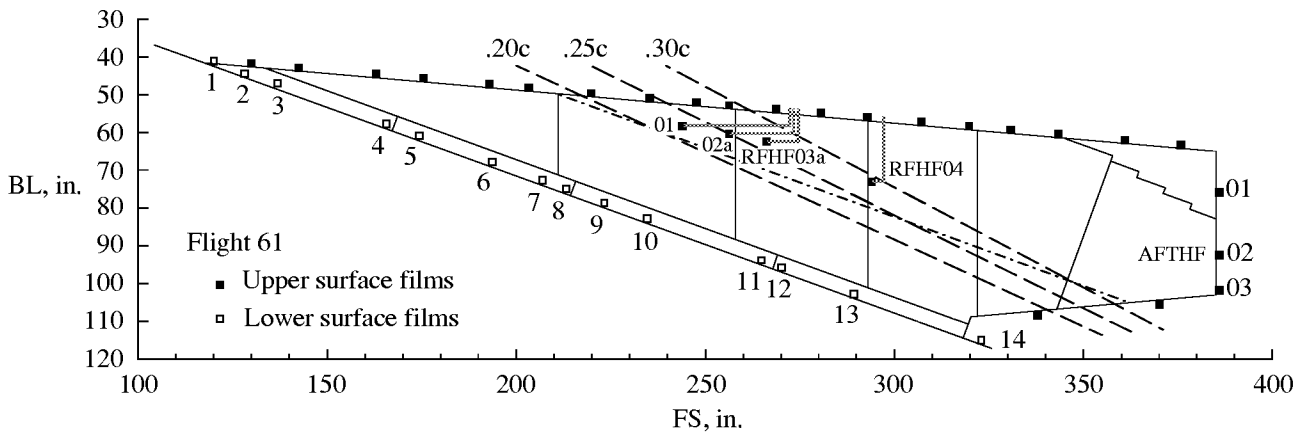


Figure B6. Hot-film layout for flight 61. Moved two hot films aft and added one hot film.

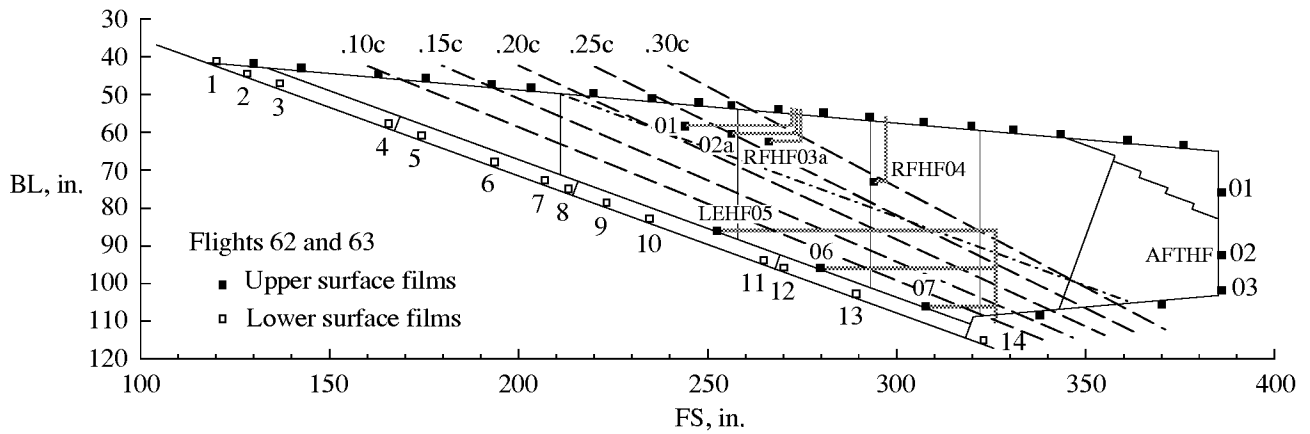


Figure B7. Hot-film layout for flights 62 and 63. Added three hot films near outboard leading edge.

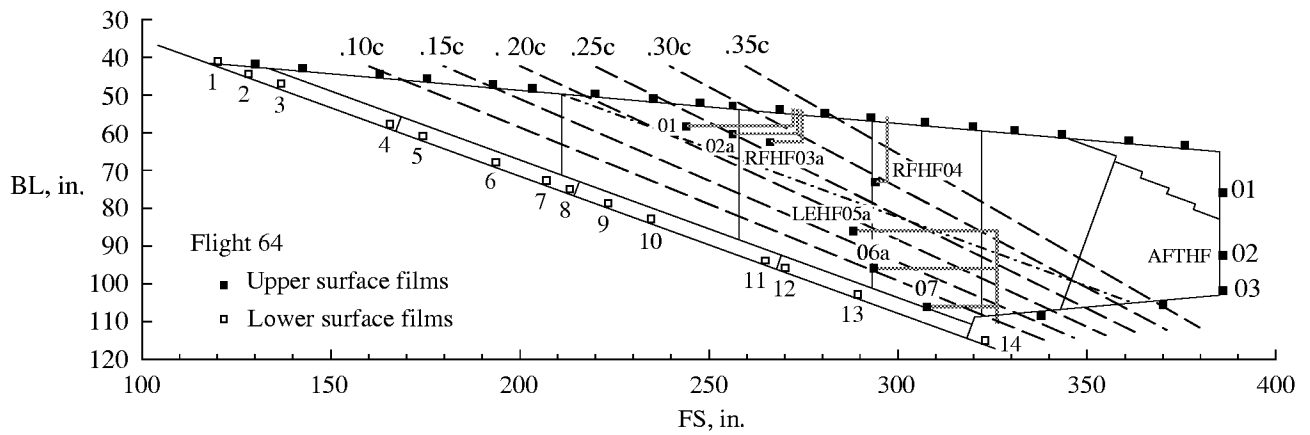


Figure B8. Hot-film layout for flight 64. Moved two outboard films.

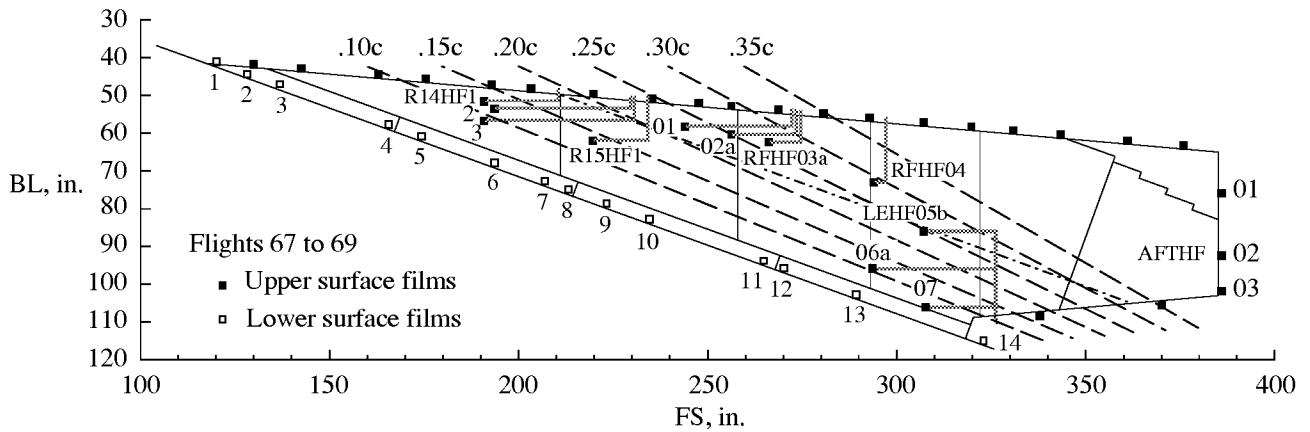


Figure B9. Hot-film layout for flights 67 to 69. Added four films between FS 190 and FS 220. Moved one outboard film.

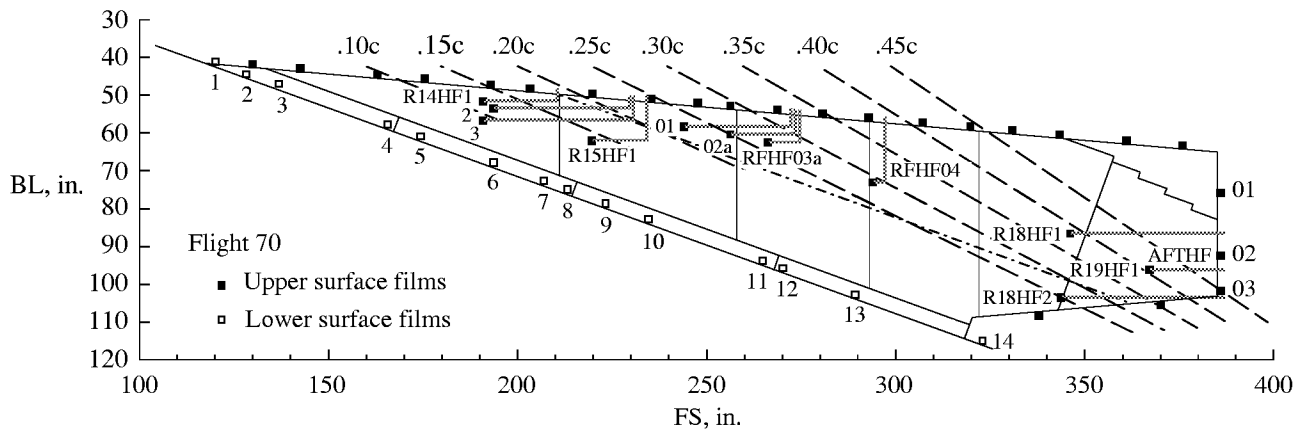


Figure B10. Hot-film layout for flight 70. Moved three outboard films on upper surface aft.

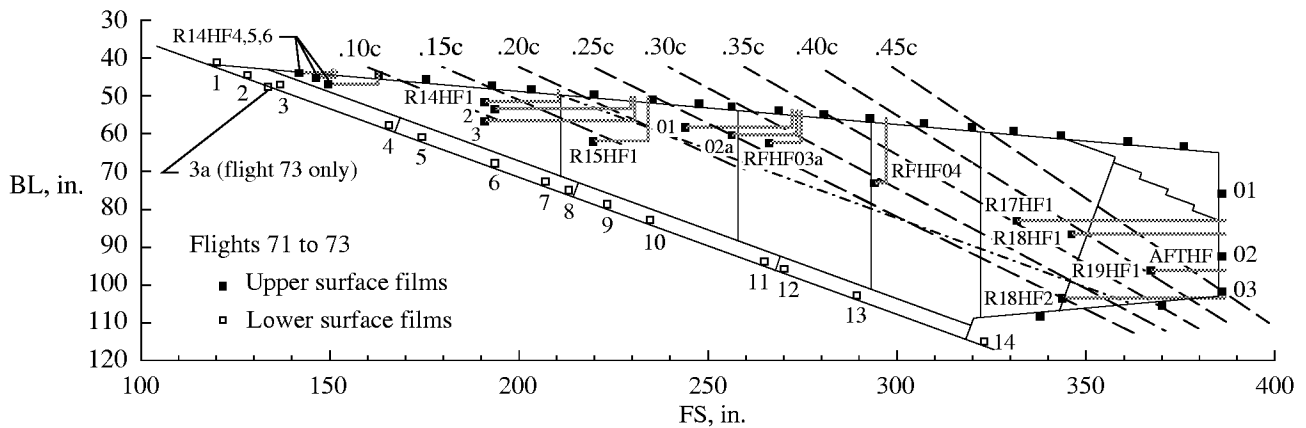


Figure B11. Hot-film layout for flights 71 to 73. Added LSHF03a for flight 73 only. Added three hot films between FS 140 and FS 150 and one hot film at FS 331.

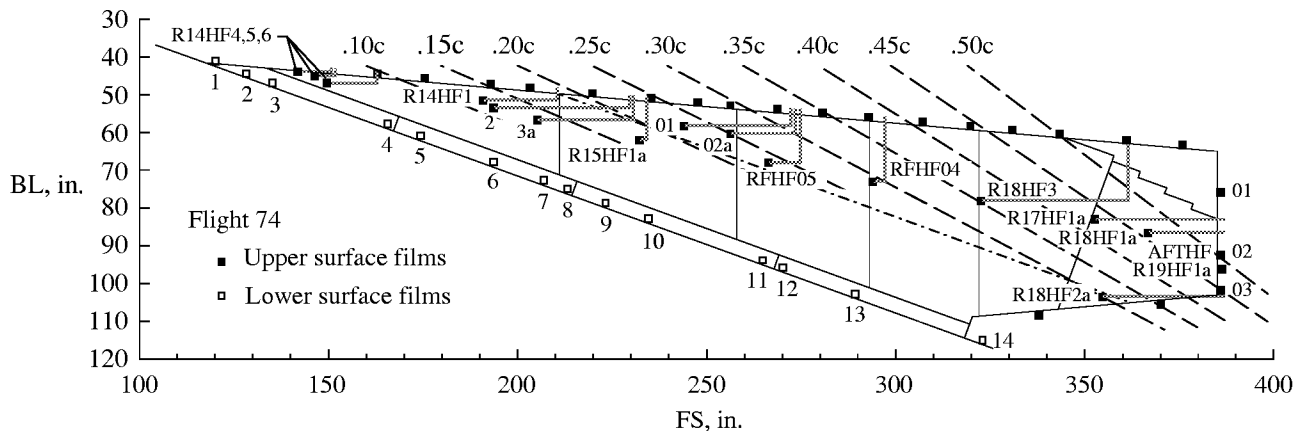


Figure B12. Hot-film layout for flight 74. Moved seven hot films and added one hot film at FS 322.

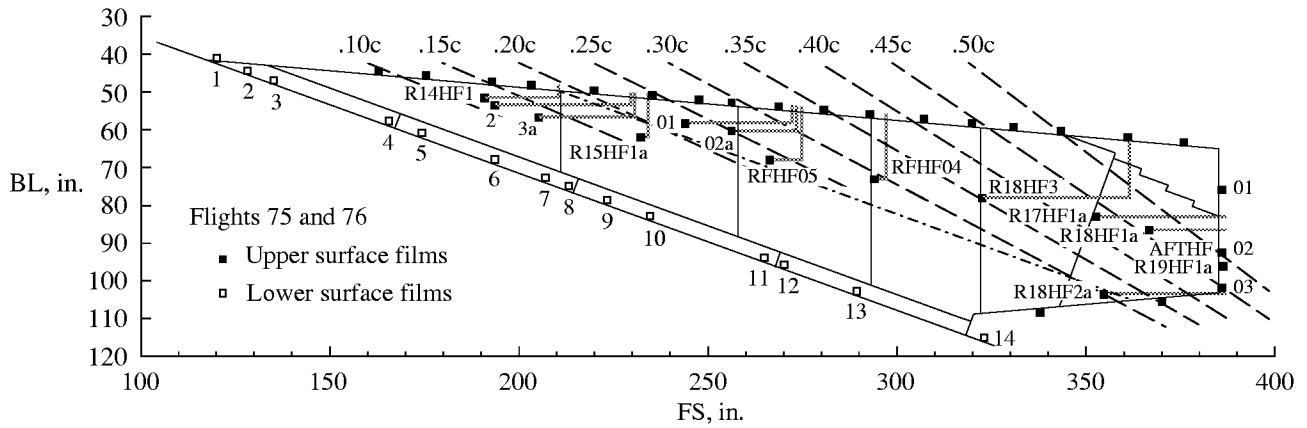


Figure B13. Hot-film layout for flights 75 and 76. Removed three hot films between FS 140 and FS 160.

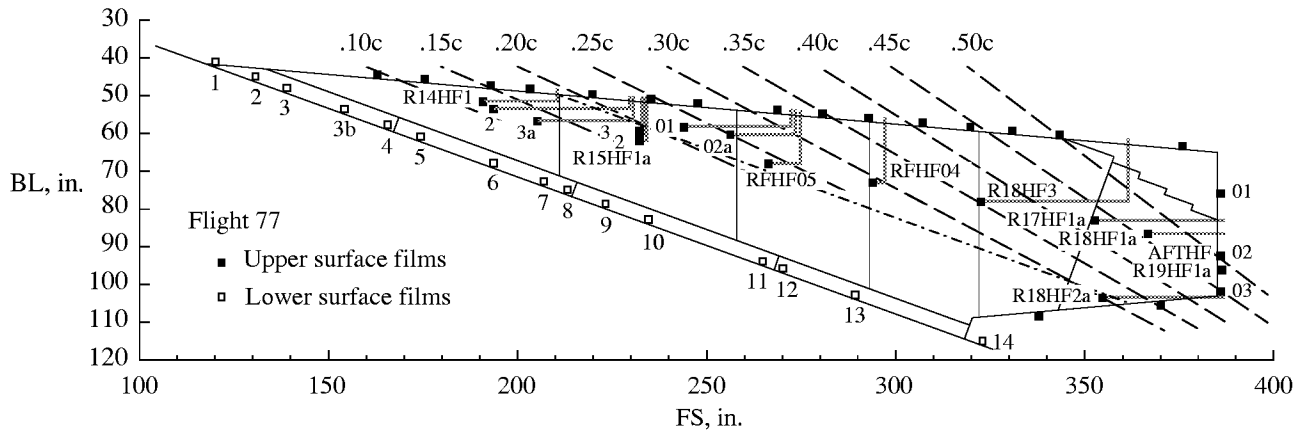


Figure B14. Hot-film layout for flight 77. Added two films at FS 232. LSHF02 and 03 moved aft slightly. Added LSHF03b.

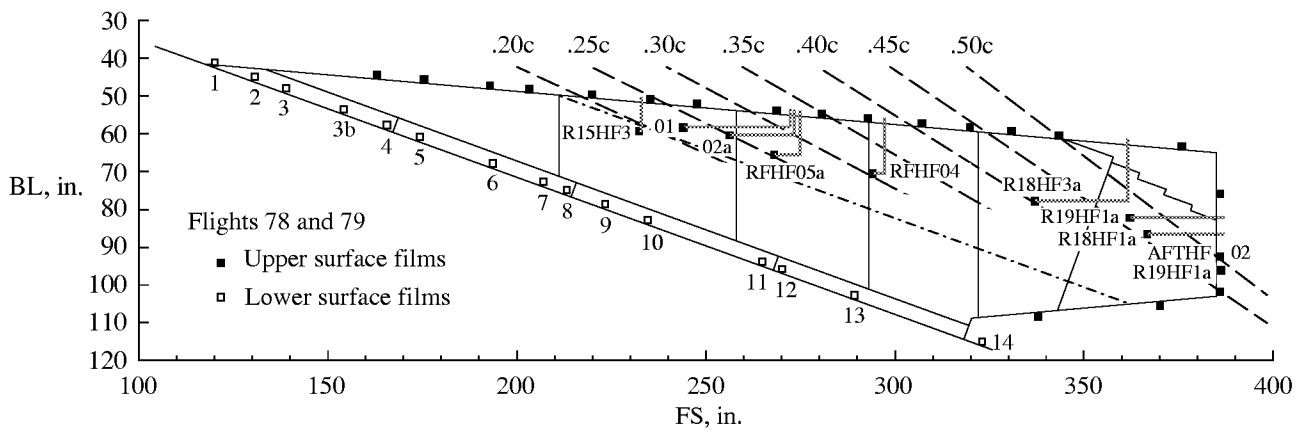


Figure B15. Hot-film layout for flights 78 and 79. Removed six films. Moved four films.

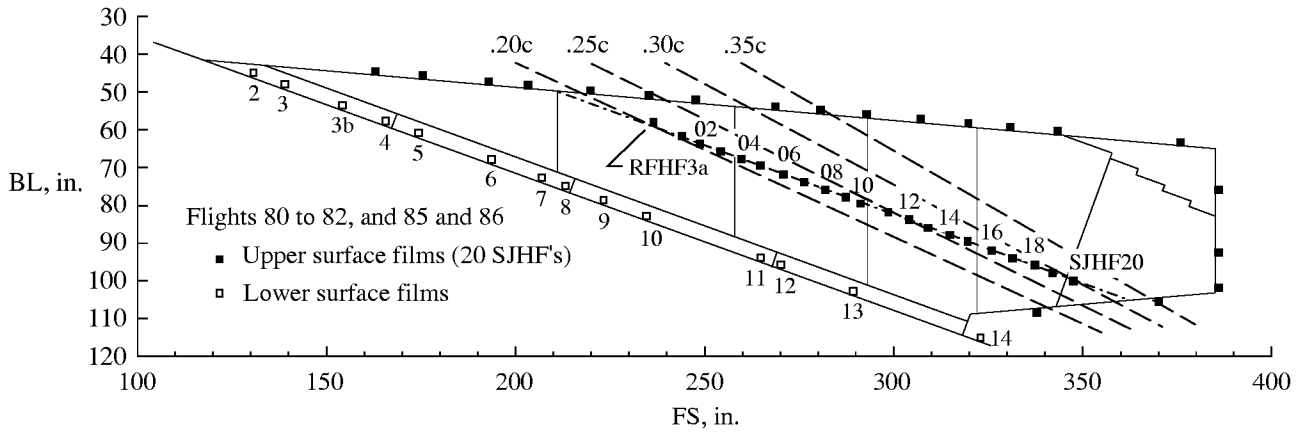


Figure B16. Hot-film layout for flights 80 to 82 and 85 and 86. Array of 21 hot films added along splice joint (RFHF3a and 20 SJHF's). Hot-film leads omitted in drawing.

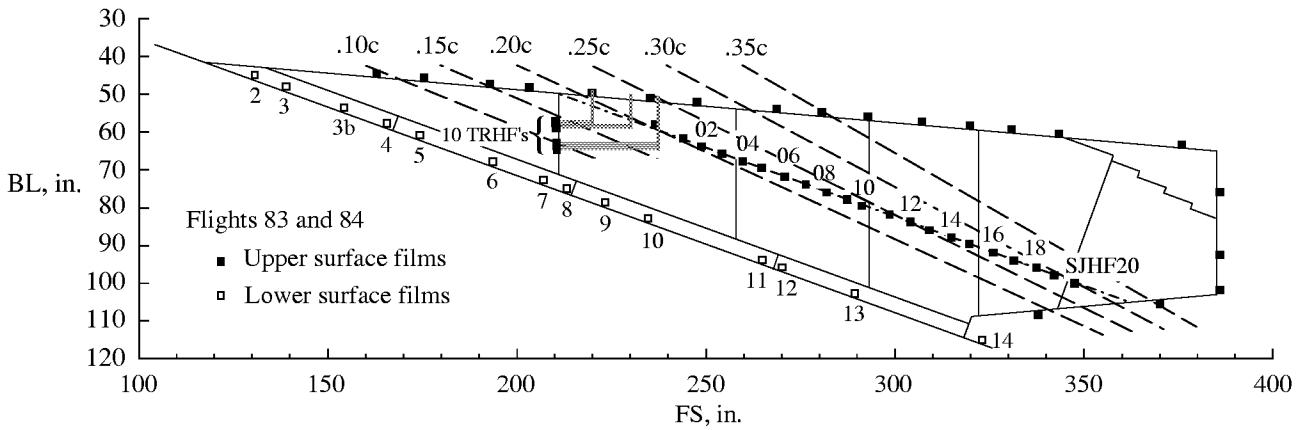


Figure B17. Hot-film layout for flights 83 and 84. Ten hot films added at FS 211. Hot-film leads omitted in drawing.

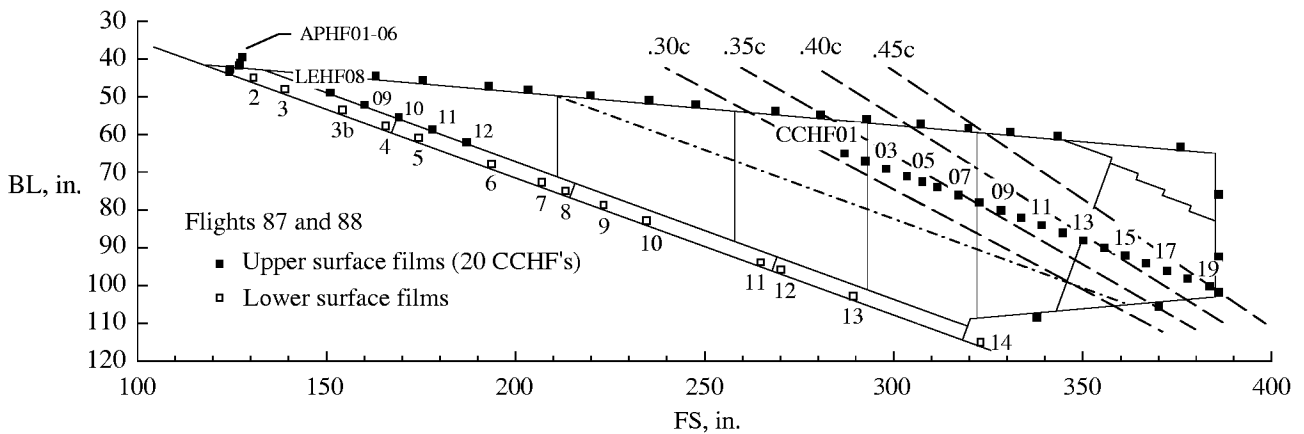


Figure B18. Hot-film layout for flights 87 and 88. All splice-joint films removed. Added six films near turbulence diverter. Added five films near leading edge. Added array of 19 hot films approximately 3 ft downstream of splice joint.

Appendix C

Database Information and Security

The large amount of data collected during this experiment was distributed to several different researchers in geographically dispersed organizations. Data were available to users by three methods: real-time data, time-series data, and time-averaged data. The real-time data were a selected set of parameters that could be viewed during the flight as it was telemetered from the aircraft to the ground, converted to engineering units, and displayed in DFRC and LaRC control rooms. The LaRC monitoring control room was much more limited in scope than the DFRC main control room but was sufficient for users to monitor key data parameters such as hot-film signals. There was also some limited access by other team members from their local sites. After the flight, all raw data were converted to engineering units, and all desired variables were calculated. These data were stored on the DFRC Flight Data Access System (FDAS). The data stored on FDAS were time-series data, for example, individual data parameter values versus time (collection rates could vary from parameter to parameter). The FDAS could be made accessible to any authorized user. The third data source, which was the most heavily used data source by a majority of the team members, was the time-averaged data. These data were created by NASA DFRC personnel from the time-series data stored on the FDAS system. The time-averaged database was a set of files containing a defined set of parameters in a specified format that was agreed upon by team members in advance of any flights. The pretest database definitions, including the file-naming conventions, allowed the development of data reduction routines without waiting for the first data to be collected. The concept of time-averaging data over a time window fit well with the way the raw data were collected. As noted earlier, the raw data were typically collected by performing “pushovers” because the desired test point α was generally below trim α . During the approximate 10-min supersonic run, each of several predefined test conditions was held for approximately 10 sec. Test points were selected from the 10-sec intervals by applying the following criteria:

- time window—minimum of 3 sec
- Mach number held within ± 0.01

- altitude held within ± 500 ft
- angle of attack held within $\pm 0.1^\circ$
- flow-control valves fixed
- hot-film signal consistent within window

Test points meeting these criteria were added to the time-averaged database. In special circumstances, when a user requested a particular time window, one or more criteria could be violated, but a note was made in the database so that the data would not be used in error. Also included in the database was a plot of the flight conditions versus time so that users could examine the time window to check for steadiness over the test point time window. Data taken during the test point window were averaged over the time window, and the state of the boundary layer at each film was determined. These data were written to the predetermined database files, made available to the team, and served as the common starting point for data analysis.

Test points added to the time-averaged database were defined by the flight number and flight-card number for reference purposes. All test point names are unique and contain the flight number first. For each test point within that flight, a four-character labeling method was adopted. The database user need not be concerned with what each letter and number means unless referring to the original DFRC flight reports that contain the test point instructions. The remainder of this paragraph explains the four-character labeling found after the flight test number. The flight test number is usually followed by an alphanumeric letter that designates which supersonic run the data were taken on (“a” for first run, “b” for second run, “c” for third run). Test instructions, which were written and reviewed at least one day in advance, were recorded on “flight cards.” These flight cards were pages of instructions for the flight crew to follow. Each page contained relevant flight condition specifications, followed by an alphabetical list of instructions. The flight-card number, or page, and the alphanumeric letter of the instruction on that card followed the supersonic run letter mentioned above. The last character usually designated the number of times that a particular flight-card instruction was performed during the same supersonic run. Due to the four-character restriction, this labeling system could not be strictly followed, but this restriction did not detract

from its usefulness. Deviations occurred occasionally for the supersonic run designation or for the number of times that an instruction was executed during a supersonic run. The following examples are provided to assist in the understanding of this labeling system:

- Example 1. 72.a2c1: Flight 72, first supersonic run, flight card 2, instruction c, first time instruction executed during this run
- Example 2. 72.b3c2: Flight 72, second supersonic run, flight card 3, instruction c, second time instruction executed during this run
- Example 3. 77.a12c: Flight 77, first supersonic run, flight card 12, instruction c, first and only time instruction executed during this run
- Example 4. 77.ex07: Flight 77, the seventh nondesignated (no flight-card instruction) data point

All sensitive information concerning this experiment was protected under a special technology control mechanism created for the High-Speed Research (HSR) Program called “Limited Exclusive Rights Data” (LERD). This control mechanism protected information from foreign interests while allowing the exchange of information within the U.S. community. The LERD status required that steps be taken to protect the data from being accessed by unauthorized parties, such as preventing interception of files as they are transferred from one computer to another or as a result of computer break-ins. This protection began at the

data source. Access to DFRC computers containing sensitive data was restricted to cleared individuals. In addition, access to the F-16XL-2 data on the DFRC FDAS was possible only from another DFRC computer and only to those with the project password. For the time-averaged database files, all data files for an entire flight were first compressed together into a single file to facilitate handling. This file was then encrypted using the Data Encryption Standard (DES) algorithm in accordance with the December 1993 Federal Information Processing Standards (FIPS) Publication 46-2 requirement. The DES is a mathematical algorithm for encrypting and decrypting files. Further details of DES can be found in the FIPS publication. DES software was made available to team members for use on several different UNIX-based systems as well as personal computer operating systems. After the file was encrypted, it was then transferred to a computer at ARC and defined to be readable only by members of a special group ID that was created for this project. This group included only those individuals that were cleared to have access to the data. Anyone in that group could copy or download the file. The file was downloaded only to areas that were protected against unauthorized access. Once the file was in its desired location, the user decrypted and uncompressed it. Knowing the format, the user could apply the data reduction routines immediately. This process satisfied the security requirements, required no new resources or product development, and was quick and simple to use. The process worked very well throughout the experiment.

Appendix D

Flight Log

Forty-five flights were conducted in the experiment, starting with flight 44 and concluding with flight 88. Eight flights were aborted for various reasons, and these often resulted in no useful SLFC data. Thirty-four of the flights were SLFC data flights. Appendix D is an informal record of the major events that transpired during each flight. No attempt was made in this appendix to list the individual test point number, flight conditions, or other detailed information.

Table D1. Informal Flight Record of Major Events

Flight number	Date	Fence	ss run	Comments
44	10/13/95	1	0	First flight, a functional check flight at subsonic conditions, experienced higher differential pressure across panel than expected. Loads and structures concerns evolved that dominated next series of flights.
45	10/25/95	1	0	Differential pressure problem continued; evaluated further in this flight. Telecons held after flight to discuss solutions.
46	11/6/95	1	0	Taped lower surface joints, possible leak sources to reduce leakage to cavity; slightly higher g 's achieved before differential pressure limit met. Debate continued on loads and safety issues due to differential pressure.
47	11/22/95	1	3	First supersonic flight almost 4 hr long. Relaxation of local differential pressures and loads permissible and restriction to $2.2g$ rather than $3g$ operation. Suction system not activated. Completed most of flutter and loads objectives. Attained C_p 's at design point and other conditions. C_p 's showed reasonable agreement with prediction for slightly higher ($.5^\circ$) flight α . Shock fence not fully effective. Laminar flow along attachment line out to LSHF04; suction existed on attachment line due to high surface pressure and low internal pressure. Turbulence diverter works over range of α up to almost 4° .
48	1/24/96	1	2	First flight with suction; tried range of suction flows. Laminar flow inboard of fence to LSHF04 without suction and with lowest suction settings; no laminar flow with higher suction. $M = 1.85$ was highest speed achieved. After third tanker refill, returned to base (RTB) due to erroneous loads measurement.
49	1/26/96	1	2	Obtained $M = 1.5, 1.7, 1.9$ data with suction. Laminar flow to lower surface hot film LSHF04 with suction system off and suction on at low level. Very sensitive to α , unit Reynolds number, suction level. Questioned whether laminar flow exists on upper surface and microphones cannot detect it.
50	2/1/96	1	0	Aborted due to gear door failure to close after takeoff.

Table D1. Continued

Flight number	Date	Fence	ss run	Comments
51	2/2/96	1	3	Suction patch valve angle was maintained at 20°. Unrecognized at the time, excessive suction in the suction patch prevented any laminar flow. Flew two $\beta = -1.6^\circ$ points, but there was no improvement in laminar flow due to tripping at suction patch.
52	2/9/96	1	3	Installed 4 hot films (LEHF01, 02, 03, 04) on upper surface at first stringer to confirm achievement of laminar flow. Adopted new flight procedure (used rest of program); flew subsonic to Colorado River; made supersonic data run heading west toward DFRC. Laminar flow detected on attachment line for suction system off case only. Suspect suction patch suction too high, triggered transition. Flew several β test points. New upper surface hot films confirm no laminar flow on upper surface.
53	2/15/96	1	1	Prior to flight, suction patch upper surface subregion corner sealed off with tape. Calculations indicate this area is outflowing for most of cases; best to tape over. Flight was terminated because turbocompressor would not come up to speed and oil temperature was high. Limited, no suction data points collected.
54	2/22/96	1	2	Problems with uplink signals prevented operation of turbocompressor; continued flight without suction system. Completed flutter clearance points. No progress in resolving lack of laminar flow.
55	2/29/96	1	3	Experienced uplink data capture problem; obtained limited data with suction at $M = 1.7$. Maintained suction patch valve at 0°; attachment line flute adjusted from 0° to 25°. Attachment line and upper surface laminar flow recorded with attachment line regions up to 20° valve angle. Confirms oversuction existed on the attachment line in previous flights. Need to evaluate at $M = 1.9$ next flight. On this flight, gap between fence and wing lower surface was sealed with tape (concern that flow disturbance could leak through gap).
56	3/1/96	1	0	Planned to obtain $M = 1.9$ data, but had to RTB because right gear door would not close.
57	3/6/96	1	2	Flew aircraft at $M = 1.9$, only one tanker refill. Obtained data on limits of attachment-line flute valve setting above which laminar flow was lost. LEHF01 and 02 showed robust laminar flow at $\alpha = 3.2^\circ$ – 4.0° with region 2 valve settings of 0°, 8°, 16°; lost laminar flow on LEHF01 and 02 for region 2 with 20° valve angle; 16° is upper limit. Used 45° and 90° valve angles in flutes 2 and 3 behind attachment line. No laminar flow observed on LEHF3 because flight 58 showed region 5 needs at least 20° for $\alpha = 3.4^\circ$ and 30° for $\alpha = 3.7^\circ$ along with region 2 needing no more than 16°. In telecon after flight decided to set region 2 at 16° and vary other attachment-line regions in next flight.

Table D1. Continued

Flight number	Date	Fence	ss run	Comments
58	3/8/96	1	2	<p>First attempt to obtain laminar flow on rooftop (region 14). Removed LEHF01 and LEHF02 because films and leads would interfere with laminar flow. Suction patch maintained at 0°; set region 2 at 16° valve setting; varied attachment-line flute (regions 5, 8, 11) over 16° to 40° range with 90° for rest of leading edge and regions 14 and 15.</p> <p>Region 5 valve setting necessary for laminar flow at LEHF03. Dependent on α:</p> <ul style="list-style-type: none"> • For $\alpha = 3.4^\circ$, need at least 20° valve angle. • For $\alpha = 3.7^\circ$, need at least 30° valve angle. <p>Successful valve angles for flute 1 regions are 16°, 35°, 35°, 35° at $\alpha = 3.4^\circ$.</p> <p>Reduced flutes 2 and 3 and rooftop regions 14° and 15° to 45° valve angle. LEHF03 inoperative in second pass; unable to determine whether upper surface laminar for these settings. Microphone signal is difficult to interpret real time, inconsistent behavior.</p> <p>Inboard perimeter hot films all turbulent, even with sideslip: inboard turbulent wedge angle probably excessive.</p>
59	3/15/96	1	2	<p>LEHF3 leads removed; LEHF4 left in place; three new hot films on upper surface (RFHF 01, 02, and 03) positioned in front of or behind joint splice (see appendix B). Pressure disturbance (perhaps from canopy joint) just at first (outboard) RFHF03. Microphones M5503 and M6502 close to inboard (RFHF01) and outboard (RFHF03) films, respectively. At $M = 1.9$, $\alpha = 3.4^\circ$, HF03 was laminar for rooftop regions 14 and 15 down to 30° valve setting, but HF02 and 03 were LT and TL at best. Laminar flow extent about 5.5 ft (assuming transition between RFHF03 and HF02). Microphone signal interpretation inconsistent from flight real time versus postflight. Best to rely on hot films. Focusing on $\alpha = 3.4^\circ$ at $M = 1.9$ because this condition results in the best laminar flow across the leading-edge span to fence location.</p>
60	3/21/96	0	1	<p>Shock fence 1 removed to obtain data without fence before fence 2 is installed. Plan called for increased (maximum) suction in all but region 2 (set at 16°) to see whether laminar flow inboard extended farther rearward. After 4 test points at $M = 1.9$, suction turbocompressor cut off during pushover due to an overspeed (first time this occurrence). Could not restart. Procedure calls for RTB. Valve 6 (for region 6) also opened slowly. Planned to come down after this flight for regular ejection seat pyro checkout; replacing suspect mass-flow sensors/valve assemblies for suction regions 6 and 20; replacing bad hot films; adding few hot films as required; fixing fairing cracks, other items. Seat egress inspection revealed two damaged explosive cord lines; had to secure replacements from Air Force.</p>

Table D1. Continued

Flight number	Date	Fence	ss run	Comments
61	4/17/96	0	3	Shock fence still removed. Four hot films on upper surface (see appendix B); RFHF01 same location; HF2a and 3a moved rearward at same BL as RFHF 2 and 3 in flight 60, HF4 new and next to M7503, which is not functional. Objectives of flight are multifold. Most test points are for $M = 1.9$, with $\alpha = 3.7^\circ$, 3.4° , and 2.8° . Few test points at $M = 1.7$ and 2.0 to track suspected canopy joint shock moving across pressure taps and hot films. Maximum suction behind attachment line to explore extended laminar flow. Suction patch suction varied to see whether laminar flow improves inboard. Suction patch valve angles of 9° and 12° worked (up to 21° tried); used 9° rest of flight. Added suction inboard did not improve run of laminar flow. Also, rooftop and leading-edge suction minimization valve settings were tried but there were consistent turbulent or TL readings on hot films. Microphone M6502 appeared to be laminar and consistent with last flight. Suspect broader turbulent wedge prohibiting laminar flow inboard.
62	4/23/96	2	1	Shock fence 2 installed. Three new outboard hot films located next to first microphones, LEHF05 (M8501), LEHF06 (M9501), and LEHF07 (M10501) to ensure we know whether laminar flow exists on upper surface leading-edge middle-outboard area. Operated at $M = 1.9$ over an α range of 3.7° to 2.2° . Results generally not good. Laminar flow existed for longest run along the lower surface (to LSHF10) and on first new hot film LEHF05 for $\alpha = 2.5^\circ$ and 2.2° only. Postflight inspection revealed insect remains in front of LSHF4 that may have produced the poor laminar flow results at higher α 's. Concern expressed that too much suction applied on attachment line. Next flight will have options for reduction in real time. Pressure data show that fence 2 has expansion off leading-edge which affects leading-edge pressures.
63	4/26/96	2	3	Reduced suction in the attachment-line flute regions 5, 8, and 11 to achieve laminar attachment line at $M = 1.9$ to area where expansion fan from fence affects leading edge. Similar results recorded in that lower α 's produced best laminar flow results. Limited test points at $M = 2.0$ resulted in improved laminar flow for same settings. Suspect engine spillage reduces at $M = 2.0$, weakening shock and making fence more effective.
64	5/1/96	2	1	Moved hot films LEHF05 and 06 to straddle pressure disturbance believed due to canopy joint. Flight control system problems caused RTB early. Flew $\alpha = 3.4^\circ$, 2.8° , 2.5° test points. Achieved robust laminar flow on LEHF05, 06, 07 for $\alpha = 2.8^\circ$ and 2.5° , no laminar flow at $\alpha = 3.4^\circ$. Flow appears to be laminar behind pressure disturbance and joint. Except for attachment line, all suction regions were at 90° valve setting. The suction patch was at 0° and 9° , with no difference noted. Attachment-line regions (flute 1) were down to 14° , 29° , 18° , 18° with laminar flow. Agreed to fly next above $h = 50\,000$ ft; lower R/ft should help laminar flow along with less engine spillage (weaker inlet shock, improved fence effectiveness).

Table D1. Continued

Flight number	Date	Fence	ss run	Comments
65	5/3/96	2	0	Hot-film RFHF05 moved rearward on joint. Planned to reach $h = 55\,000$ ft this flight. Had to RTB due to flight control system problems (leading-edge flap caution indicator). No data taken.
66	5/6/96	2	0	RTB due to flight control system problem. Leading-edge flap caution again. No data taken.
67	5/16/96	2	1	<p>Team observed gap between top of fence and bottom of wing. Concern that pressure disturbance could bleed through and affect leading edge. Gap sealed with special tape. Improved reference tank pressure system installed to eliminate reference pressure lag which caused pressure drift in previous data.</p> <p>Achieved $h = 55\,000$ ft for first time. Low free-stream temperatures necessary to reach $h = 55\,000$ ft (temperatures at altitude vary each day). No laminar conditions attempted at $55\,000$ ft. New inboard films installed to aid in determining width of inboard wedge.</p> <p>At $M = 2.0$, $50\,000$ ft saw laminar flow on rearward most hot films, RFHF04 (.29c, 7.6 ft) and RFHF05b (.25c, 5.6 ft) for $\alpha = 3.5^\circ$, 3.1° but 3.5° case not repeatable. These films very sensitive to small changes in α. ESP pressure sensors stuck in calibration mode, so specific aero test points were not acquired, although continuous data were obtained.</p> <p>Inboard hot films indicate inboard turbulent wedge angle greater than designed.</p>
68	5/17/96	2	0	RTB due to warning lights which activated when aircraft close to Colorado River (still subsonic), $h = 40\,000$ ft. No data taken. Declared emergency; landed without incident.
69	5/28/96	2	1	Flight control computer replaced for this flight; no flight control problems experienced. Achieved $M = 1.9$ at $h = 50\,000$ ft and $55\,000$ ft. Did not obtain $M = 2$ condition as planned. Entire attachment line laminar at $M = 1.9$; $h = 50\,000$ ft and $\alpha = 3.2^\circ$. Achieved laminar flow on rooftop, but RFHF04 was TL at best; T most of time; inconsistent reading. Also, the three inboard films R14HF01, 02, and 03 displayed inconsistent signals. Postflight inspection revealed two bug hits, so a turbulent wedge could have tripped these films.
70	5/31/96	2	1	Three new films on upper surface, R18HF1 (.39c), R19HF1 (.41c), R18HF2 (.25c). Achieved laminar flow on all three films, but only two for the same test point. All test points at $M = 2$ and $h = 50\,000$ ft. Achieved longest run of laminar flow to date, 8 ft 9 in., $R/f = 21.5 \times 10^6$ (R19HF1 at .41c) at $\alpha = 2.6^\circ$. Attachment line set on low suction with all other regions at 90° . Also had laminar flow all along attachment line to LSHF14 for 3.7° with $\beta = -1.4^\circ$, but upper surface not laminar. May have had outflow in outboard regions 8 and 11. Pursue outflow tripping upper surface in later flights. Advantage of $M = 2$ and small negative β apparent. Experienced flight control indicator lights again which would not reset; had to RTB after first supersonic pass.

Table D1. Continued

Flight number	Date	Fence	ss run	Comments
71	6/7/96	2	3	Planned to build on successes of last flight but conduct test points at higher α (3.7°) and vary suction in attachment line. Need higher α to improve upper surface C_p 's. One new film R17HF1 added to provide more coverage of transition front in rear. Unsuccessful in achieving laminar flow rearward at higher α 's (3.7°), with or without β . Increasing valve angles in regions 5, 8, and 11 did not result in laminar flow rearward; may have triggered R_k problem in attachment line. Retreated to backup $\alpha = 2.6^\circ$ to 3.0° . Achieved extended laminar flow at selected lower α test points, but not easily repeated. On last pass, some ESP's stuck in calibration mode so C_p data may be affected. Postflight inspection revealed insect residue may explain erratic laminar flow.
72	6/12/96	2	2	Entire first flute, including suction patch, was masked from highlight down with 1-in-wide tape. Tape end rolled down into turbulence diverter slot and smoothed over to ensure slot functioned. Objective: to determine whether suction is required on attachment line. If not, R_k tripping problem could be alleviated. Conducted a range of test points; found no laminar flow. Concern that small wrinkles of tape at turbulence diverter possibly of critical height and prevented achievement of laminar flow. Either diverter fouled by tape or attachment line needed some level of suction to stay laminar. This area reworked; made smoother for next flight.
73	6/14/96	2	1	Turbulence diverter slot improved; sharp edge exists. New hot film (LSHF3a) temporarily placed 17 in. along taped highlight from the diverter. If this film is laminar, attachment line is laminar without suction, and a range of conditions and suction levels in the other regions will be explored. No laminar flow measured for a range of conditions. Team concluded that some level of suction is needed ($R_{\theta, C_q=0}$ for our flight conditions is high). Decided to remove masking tape on flute 1 before next flight.
74	6/26/96	2	3	Moved hot film R19HF1 to rear of suction panel (9 ft 10 in., .485c), just outboard of permanent rear film AFTHF02 (10 ft 8 in., .505c). Moved other films farther rearward; added new one. Test points focus on $M = 2$; $h = 50\,000$ ft; and $\alpha = 3.7^\circ$, with small negative β . Planned to adjust/optimize suction in regions 8 and 11 and achieve extensive laminar flow at higher α where C_p 's are improved. Unable to achieve laminar flow along entire attachment line at $\alpha = 3.7^\circ$. Had repeatability problems with previous flight results and even from one supersonic pass to the next. Limited laminar flow at lower α . In postflight meeting, DFRC noted that tape seal between fence and lower surface usually was unsealed/peeled away upon landing. Team concerned tape was not sufficient to contain high-pressure disturbance, which may have leaked through gap and affected attachment line. Decided to use improved sealant for fence/wing gap for next flight.

Table D1. Continued

Flight number	Date	Fence	ss run	Comments
75	6/28/96	2	2	Team decided to seal turbulence diverter and use suction patch to relaminarize turbulent attachment-line boundary layer. Suction patch designed with sufficient C_q to relaminarize turbulent flow. Conducted series of flight test points at $\alpha = 3.7^\circ$, 3.0° , and 2.6° . Suction patch was opened over small increments up to 90° . Lower surface and upper surface films never registered laminar flow. Conclusion: probably an oversuction R_k problem reached on suction patch that prevented the attachment line from becoming laminar. Before next flight, seal was removed from diverter.
76	7/8/96	2	2	Unable to achieve laminar attachment line at $M = 2$; $h = 50\,000$ ft; $\alpha = 3.7^\circ$; $\beta = 1.5^\circ$ on numerous attempts. Flew at higher altitude, $53\,000$ ft; did achieve laminar attachment line. Lower temperature at altitude in this flight produced higher R/ft ; probably explains why $53\,000$ ft ($R/ft = 2.3 \times 10^6$) had better results than $50\,000$ ft ($R/ft = 2.6 \times 10^6$). Conducted region 8 and 11 optimization until attachment line was lost (24° valve angle first produced laminar flow, and 30° valve angle in 8 and 11 was highest allowable). Laminar flow detected rearward at $\alpha = 3.7^\circ$; $53\,000$ ft; $\beta = -1.5^\circ$, -R18HF1a (.46c) was L. Permanent seal of fence gap may have helped. For $\alpha = 2.6^\circ$, most rearward hot film, AFTHF02 was LT a few times.
77	7/12/96	2	2	Two films added on inboard upper surface to define turbulent wedge angle more precisely. Calculations made of outflow using MDA program in flute 1 for $\alpha = 3.7^\circ$ and highest valve angle allowed in regions 8 and 11 (30°). A 0.40-in-wide masking tape strip was placed on top of region 11 in suspected outflow region because outflow could trip downstream flow. With region 11 top strip masked, a valve angle of 38° was allowable while still maintaining a laminar attachment line. Without masking, valve angle limit was 30° . Achieved laminar flow at two test points on R18HF1a (.46c) for $\alpha = 3.7^\circ$ and 4.1° ; the same sensor was LT for few other cases. These LT points potential code calibration cases. Rear films AFTHF02 and R19HF1a were not laminar; suspect turbulence wedge from R18HF2a may be tripping them (removed R18HF2a for next flight). Agreed in postflight discussion to remove some inboard films, move all others back in attempt to achieve greater extent of laminar flow area inboard and rearward. Masking tape on upper part of region 11 apparently did not trip flow because laminar flow achieved rearward for some cases. Tape allowed higher suction in region 11.

Table D1. Continued

Flight number	Date	Fence	ss run	Comments
78	7/17/96	2	2	New inboard and rear film positions as noted above; fewer total films. Masking tape strip still on top of region 11. No extensive L or LT detected on rearward films. Some test points not repeatable or consistent with previous flights or expectations; i.e., could not repeat .46c laminar flow on R18HF1a from flight 77 (film was not moved). Possible that masking tape could be tripping if it rose during cruise, but postflight inspection did not show any tape release. One bug hit noted on region 2 and two on region 11 (all left minor roughness), but is not known whether they affected results. Attachment line not laminar all along the leading edge as frequently as for flight 77 at same conditions. Insect residue detected post-flight is probably the cause. Also, unit Reynolds number slightly higher in flight 78 compared to 77 ($R/ft = 2.3 \times 10^6$ versus 2.2×10^6) due to lower free-stream temperatures.
79	7/19/96	2	3	Masking tape strip on region 11 removed because of concern that it could rise and trip flow. Based on results to date, need to focus on $h = 53\,000$ ft; $M = 2$; and $\beta = -1.5^\circ$. Laminar flow results on upper surface improved over previous flight 78 and were more like flight 77. Sensor AFTHF02 (.50c) was LT for one unsteady test point at $\alpha = 3.1^\circ$. R18HF1a (.46c) was LT for numerous test points, with $\beta = -1.5^\circ$ and $\alpha = 3.7^\circ$. Apparent large number of code calibration points. Attachment line stayed laminar entire length for attachment line valve angle settings of 12° , 14° , 29° , 30° , and region 11 over a range of 24° to 40° . In postflight discussions, team concluded that priorities should now focus on achieving code calibration data, so hot films need to be reconfigured for next series of flights.
80	7/26/96	2	3	Added 20 films spaced about 2 in. in BL along (just in front of) splice joint to obtain code calibration data and to determine extent of laminar flow across span. Appendix B shows configuration. Configuration will identify turbulent wedges on both sides of test panel and 3D nature of transition front. All $M = 2$ and $h = 53\,000$ -ft data concentrated on $\alpha = 3.7^\circ$, 3.0° , and 2.6° . Reduced rooftop suction from 90° to 75° , 60° , 45° , 35° , 30° , 25° , 20° . Made three supersonic passes. On last pass, obtained test points with flutes 2 and 3 reduced. For $\alpha = 3.7^\circ$ data, repeated 3.7° baseline maximum. Ran C_q case three times and had irregular result. Best laminar flow inboard (at splice location) for two cases; all laminar flow for other. Reductions in rooftop suction produced some curious results: at 75° (regions 14 to 20), all splice joint films were laminar, then outer half not laminar at 60° , and at 35° , all splice films were laminar again. Not clear what happened. At $\alpha = 2.6^\circ$, extent of laminar flow at splice joint films continually got worse as suction was reduced. Attachment line stayed laminar throughout rooftop reduction. On third supersonic pass, ESP's stuck in calibrate position so some C_p data unusable. Obtained large number of code calibration points.

Table D1. Continued

Flight number	Date	Fence	ss run	Comments
81	8/16/96	2	3	Different engine in place for this flight and next because of maintenance/repair problem with original. Finished test points for current set of code calibration conditions with sensors at splice joint; also repeated third supersonic pass from flight 80 for which pressures were unusable. Some inconsistent results occurred again for achieving a laminar attachment line. Attachment line was laminar for $\alpha = 3.7^\circ$ and $\beta = -1.5^\circ$ for about five test points but was not for about 20 others. Suction in region 11 was being varied. Could have triggered transition for a few cases. Attachment line not laminar past LSHF10 for $\alpha > 3.75^\circ$. Occasional laminar attachment line with $\beta = 0^\circ$ and $\alpha = 3.7^\circ$. Issue raised as to whether the different engine, with probable different fuel/air mixture, required more inlet air (less spillage) to achieve the same thrust so that shock was weaker and fence more effective. In retrospect, should have capitalized on zero β laminar flow results for code calibration test points because attachment line not robust with β . Team concluded that upper surface pressures need improvement (isobars, spanwise gradients) if we are to achieve more extensive laminar flow.
82	8/28/96	2	2	Fence toed-in 1.5° in hope that flow expansion from fence leading edge is weakened and effect on upper surface pressures is improved. Test points included mostly negative $.5^\circ$ increments in β , including 0° and some positive β . Tried 3 α 's: 3.7° , 3.9° , and 4.1° . Could not achieve laminar flow past lower surface hot film LSHF10 for all combinations of α and β . Tried a range of suction levels (valve settings) in region 8 to see whether this would allow laminar flow past LSHF10, but no success (did this for two α 's). Aircraft electrical power problem caused end of flight after two passes. Suspect fence in its new alignment position is either producing a new disturbance off the leading edge or inlet shock spilling over fence is worse for new fence alignment. Isobar plots do not show any significant change in upper surface pressures, and because attachment line results were not as favorable, decided to put fence back in original position.

Table D1. Continued

Flight number	Date	Fence	ss run	Comments
83	9/13/96	2	3	Fence aligned in original position. Original engine reinstalled. Concern over need to improve upper surface pressure disturbances led to first canopy joint fairing installation for this flight. Also, 10 hot films are installed inboard to determine precise turbulent spreading angle. In setting up for first pass, pilot noticed tape flapping on fairing, apparent deterioration of fairing. Uplink failure prevented transmitting of data to set suction flow control valve positions and test point information for pilot. Did not set up for any test points on this pass; made rendezvous with tanker to refuel. Much discussion about whether to continue because of fairing condition; decided to obtain whatever pressure data we could and obtain data on turbulent wedge spreading angle, as long as pilot was comfortable with fairing condition. Turbulent wedge was not captured in 10 films; inboard 5 were turbulent and outboard 5 mixed, indicating that trip was too far inboard. For next flight, trip was moved about 5.5 in. outboard along the 70° sweep line so films would capture wedge. C_p data on effect of canopy fairing not evaluated because the true shape of fairing not known.
84	9/20/96	2	3	Fairing redone; bonding method improved. Decided not to put any fairing in front of canopy joint because it is very thin and was first to come apart in last flight. Fairing held together better, but rear region eventually lost some material because tape did not stick to foam used. Analysis of C_p and hot-film data indicated no improvement. Noted that hot-film leads from turbulent spreading angle experiment adversely affected surface pressures at one point along BL 60. Splice joint films in middle (SJHF 8-11) showed no improvement in flow status for rooftop with 35° and 30° valve angle suction (where they were TR/T in flight 80-81 and still were about that reading in flight 84), indicating that isobars in panel middle were not significantly improved with the fairing. New location of trip allowed capture of entire turbulent wedge. Obtained a laminar attachment line all the way to LSHF14 for $\alpha = 3.7^\circ$, with $\beta = 0^\circ$ and -1.5° . No laminar attachment line with $\alpha = 4.1^\circ$, except with one case at $\beta = -1.5^\circ$. Agreed to focus on $\alpha = 3.7^\circ$ and $\beta = 0^\circ$ and -1.5° for next flight; $\beta = 0^\circ$ preferred because upper surface pressures less affected. Decided to add some fairing thickness ahead of canopy joint as originally planned to laterally spread out disturbance.

Table D1. Continued

Flight number	Date	Fence	ss run	Comments
85	10/4/96	2	3	Fairing was redone with putty over foam to hold it in place. The putty sanded down to a smooth contour. Fairing in front of joint built up with layers of tape. This fairing configuration replicates original concept. Flew three passes and obtained suction reduction data. C_p data indicated no measurable change in upper surface C_p 's with this fairing compared to no fairing data (flight 81). Splice joint hot films in middle zone did not show any change either (an improvement from LT/TR/T to more laminar would be expected for the same conditions if C_p 's improved). Team expressed concern that fairing did not improve upper surface pressures, and funding existed for only a few more flights. Decided to replace fence 2 with fence 1 for next flight and fly at $M = 2$ and $h = 53\,000$ ft (never done with fence 1). Fence 1 does not have a leading-edge expansion (like fence 2) which affects upper surface pressures, and the higher M and altitude with β could make fence 1 more effective. Team also decided to remove canopy fairing because it did not measurably improve C_p 's. Retaining fairing added risk it could deteriorate during a run and contaminate data or cause safety problem.
86	10/23/96	1	3	Flew with fence 1 and canopy fairing removed. Test points were $M = 2$ and $h = 52\,000$ ft (higher ambient temperature limited achievable altitude). Attachment line stayed laminar entire length (to LSHF14) for α 's around $\alpha = 3.3^\circ$ but was intermittent laminar for $\alpha > 3.3^\circ$. LSHF's just outboard of fence showed some "trash", i.e., disturbances from fence or inlet shock traversing over fence, but attachment line apparently not affected and stayed laminar as long as the α was not more than about 3.3° . $\beta (-1.5^\circ)$ was used as usual, and isobars with fence 1 looked good. Isobars not severely swept in midspan, just at beginning of rooftop, which was a characteristic of fence 2. Problem with heater blanket for ESP no. 17 which drew an excessive current and affected some other ESP's at certain times, causing pressure drifting. C_p data from first pass were declared unusable. Decided in postflight telecons to move hot-film instrumentation from splice joint to a rearward location for code calibration at a greater length Reynolds number. Also, five hot films placed in leading-edge inboard high-cross-flow region on first stringer to obtain code calibration data. Six films placed in apex region behind suction patch and near turbulence diverter in attempt to further understand source of increased inboard turbulent spreading.
87	11/8/96	1	0	RTB due to flight control warning lights on way out to begin first run; no data taken.

Table D1. Concluded

Flight number	Date	Fence	ss run	Comments
88	11/26/96	1	3	Conducted last flight. Engine used in flights 81 and 82 reinstalled for last flight. Flew several α 's (3.7° , 3.4° , 3.2°) with and without β to find highest α where attachment line stayed laminar. Selected test point for remaining runs was $\alpha = 3.4^\circ$ and $\beta = -1.5^\circ$. Unlike flight 86, attachment line stayed solid laminar with $\alpha = 3.4^\circ$. Different engine must have had less inlet spillage and weaker inlet shock so fence was more effective. Conducted standard rooftop reduction, leading-edge reduction, and uniform reduction as far as possible in remaining time. Obtained number of code calibration test points with hot films in rear location. Difficult to bring on transition in leading edge where five new films exist; questionable number of code calibration points obtained here.

Appendix E

Data Repeatability and Accuracy

An example of the repeatability of C_p 's on the suction panel surface is illustrated in figures E1 and E2 for several test points. Figure E1 contains data from flight 88 (the last flight) and includes two data points taken in the second supersonic pass and one data point taken in the third supersonic pass. These three data points were all at $M = 2$, $\alpha = 3.4^\circ$, and $\beta = -1.4^\circ$. The repeatability is very good; the worst difference occurred in the rear portion of the panel ($\Delta C_{p_r} = 0.0035$), as shown in the figure. Comparison of test points from two other flights for $\alpha = 3.7^\circ$ (fig. E2) also shows good agreement, but the spread in C_p is higher, the greatest being 0.0073, as indicated. The repeatability of C_p involves the accuracy of the ESP pressure-sensing units and the accuracy of the flight parameters, α and β . The ESP modules were ± 5 psid range, with a calibrated accuracy of ± 25 percent of full scale, based on DFRC experience. Mach number was a calculated quantity from measured parameters. The accuracies of the air data parameters based on DFRC's flight test experience are listed below.

Mach number	± 0.005
Altitude	± 100 ft
α	$\pm 3^\circ$
β	$\pm 5^\circ$

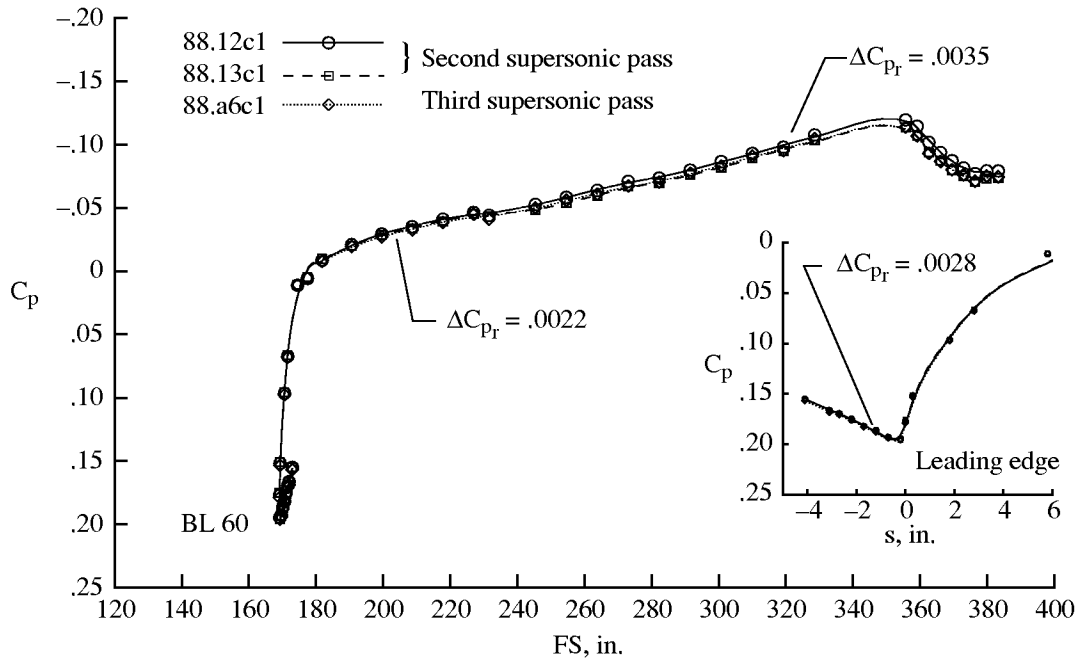


Figure E1. Repeatability of C_p profiles for test points taken in flight 88. $M = 2$; $\alpha = 3.4^\circ$, and $\beta = -1.4^\circ$.

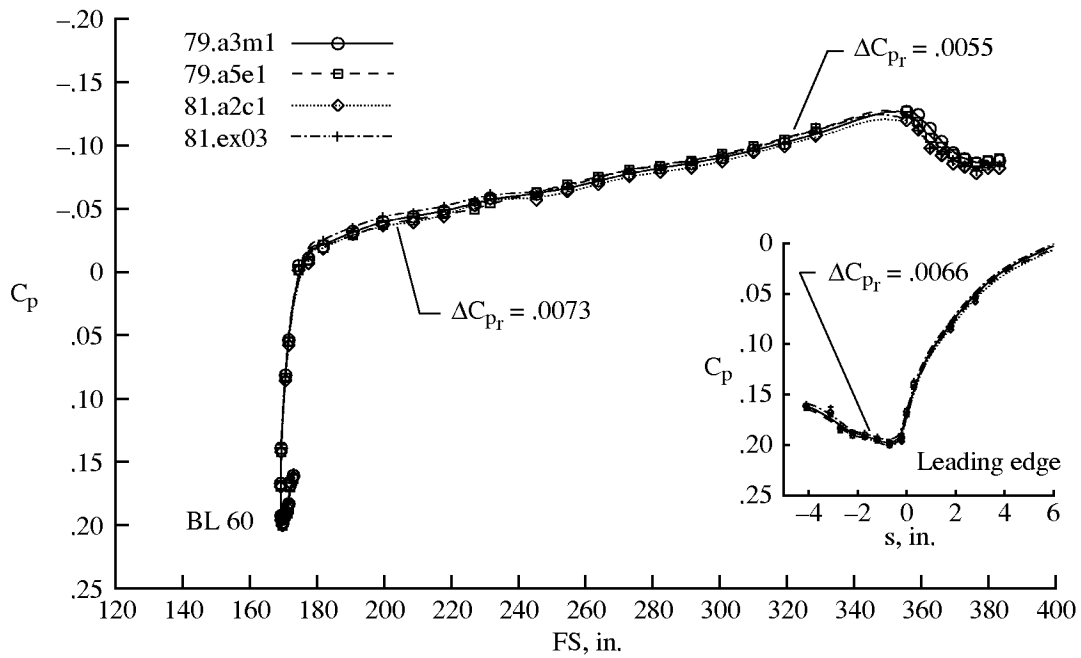


Figure E2. Repeatability of C_p profiles for test points taken in flights 79 and 81. $M = 2$; $\alpha = 3.4^\circ$; and $\beta = -1.4^\circ$.

Appendix F

Flow Characteristics With Fences 1 and 2 and With No Fence

An understanding of the interaction of the inlet-shock system with fences 1 and 2, as well as the influence of α , β , M , and altitude is essential to interpreting the data, conducting analyses, and drawing conclusions. This appendix presents the influence of these fence configurations and flight parameters on the suction panel flow field and the ability to achieve laminar flow. As defined previously, the design flight condition was $M = 1.9$, $h = 50\,000$ ft, and $\beta = 0^\circ$. Laminar flow on the attachment line was not possible beyond the fence, BL 65, for these conditions. The key to achieving more extensive laminar flow involved flying at $M = 2.0$, above 50 000 ft, and at a small negative β (-1.5°). The reasons why these off-design conditions were more favorable will be explained in the following sections. The following subsections are presented:

Section	Condition examined	Data presented from flights
F1.	Fence 1, $M = 1.9$; $h = 50\,000$ ft; $\beta = 0^\circ$, effect of α .	51, 59
F2.	Fence 1, $M = 1.9$; $h = 50\,000$ ft; $\alpha = 3.6^\circ$, effect of β .	51, 52
F3.	Fence 1, $M = 2.0$; $h = 53\,000$ ft; $\beta = -1.5^\circ$, effect of α .	88
F4.	Fence 1, $M = 2.0$; $h = 53\,000$ ft; $\alpha = 3.4^\circ$, effect of β .	88
F5.	Fence 2, $M = 1.9$; $h = 50\,000$ ft; $\beta = 0^\circ$, effect of α .	63
F6.	Fence 2, $M = 1.9$; $h = 50\,000$ ft; $\alpha = 3.7^\circ$, effect of β .	62
F7.	Fence 2, $M = 2.0$; $h = 50\,000$ ft; $\alpha = 3.7^\circ$, effect of β .	70
F8.	Fence 2, $M = 2.0$; $h = 53\,000$ ft; $\beta = -1.5^\circ$, effect of α .	76, 79, 84, 85
F9.	No fence, $M = 1.9$ and 2.0 ; $h = 50,000$ ft; $\beta = 0^\circ$, effect of α .	60
F10.	Comparison of fences 1 and 2.	85, 86

F1. Fence 1, $M = 1.9$; $h = 50\,000$ ft; $\beta = 0^\circ$, Effect of α

Figure F1 illustrates the change in the $C_{p_{\max}}$ value and the movement of the attachment-line location as a function of α for the baseline design condition with fence 1. As α increased, $C_{p_{\max}}$ increased, and the attachment line moved farther down on the lower surface away from $s = 0$. The suction level on the attachment line was essentially constant for all but the lowest α case, but because suction does not affect the measured C_p value, this was not a concern. The 4.5° case indicated a significant increase in $C_{p_{\max}}$ and downward movement of the attachment line. As discussed in section 11.2, on achieving laminar flow inboard, the attachment line was never laminar above about $\alpha = 4^\circ$. The downward movement of the attachment line with increasing α resulted in an inability to establish a laminar boundary layer at the beginning of the suction panel, probably due to the effective range of the turbulence diverter. The upper α limit of this range is about 4° . At BL 70 the $C_{p_{\max}}$ was driven

down to the lowest levels for the higher angles of attack. For the highest α , where the flow was turbulent from the apex, the attachment line moved below the perforated suction surface, past the last measuring orifice, and was therefore not defined at BL 70 in figure F1. This behavior was due to the inlet-shock system crossing the leading edge in this region (between BL 70 and BL 80). As α was increased, the attachment line was lowered into the area most strongly affected by the shock system. This movement demonstrated that fence 1 at the design condition provided limited blocking and was thus ineffective.

Examples of measured leading-edge pressures and their curve-fit that define the attachment line and $C_{p_{\max}}$ are shown for eight BL locations in figures F2(a) through (d) for all four angles of attack discussed. The curves shown were generated by free-hand. The $C_{p_{\max}}$ is defined as the maximum C_p value from the fitted curve, and the attachment-line location is defined as the distance from $s = 0$ to $C_{p_{\max}}$. This type plot is shown for this test condition only. As

noted earlier, at $\alpha = 4.5^\circ$, the attachment line at BL 70 was located below the last pressure orifice (see fig. F2(a)) and is thus not properly defined. Note that the C_p profiles at BL 50 and BL 60 tend to be flatter or fuller for the two higher α cases (figs. F2(a) and (b)), which may contribute to a higher R_θ that triggered the loss of laminar flow at these conditions.

C_p profiles on the upper surface at six BL stations are shown in figures F3(a) through (f) for two of the angles of attack. These plots also repeat the leading-edge region, except that an automated curve-fitting procedure was used to produce the curve in these plots. Differences in the leading-edge and upper surface C_p due to α variations are shown. For all BL's, a higher α produced a lower (more negative) C_p on the upper surface and a higher C_p in the leading-edge region. Looking at inboard BL's first, there are several characteristics of the individual C_p profiles worth noting. The end of the rapid expansion in the leading-edge region at BL's 50, 60, and 70 was less steep and abrupt for the lower α case. This less abrupt profile extended the cross-flow region further onto the upper surface, which was undesirable for laminar flow applications because additional suction would be required to control cross-flow disturbance growth. BL 70 also has a unique characteristic in the leading-edge region. On the lower surface leading-edge region at BL 70, the inlet-shock system crossed at about the fourth pressure tap for the 3.4° case and then moved farther downward until the attachment line was no longer defined for the 4.5° case. Looking farther outboard at BL 80, 90, and 100, the leading-edge flow on the upper surface overexpanded and resulted in a pressure peak. The lower α case showed a reduction in the size of this pressure peak, but it was still apparent. This upper surface pressure peak, generated reverse cross flow due to the alteration of the external flow field by the inlet-shock system. The attachment line moved down and caused a greater acceleration of the leading-edge flow onto the upper surface and was similar to the effect of a local increase in α .

Pressure isobar plots on the suction panel upper surface are shown in figure F4 for the same two angles of attack. This plot shows that the higher α produced isobars swept away from the leading edge. This sweeping of the isobars produced cross flow on the upper surface. The isobar plot shown in figure F5 shows the 3.4° and 2.7° cases for comparison. This plot shows that the lower α produced isobars swept

toward the leading edge and also produced cross flow but in the opposite direction compared to the $\alpha = 4.5^\circ$ case. The $\alpha = 4.5^\circ$ and 3.4° test points presented in figure F4 show the effect of the pressure peak due to the shock system crossing the leading edge, as is evident by looking at the large gradients in the isobars at the beginning of the upper surface, starting at about BL 75 and continuing outboard. Even though the 3.4° case was close to the design α of 3.3° , the isobar contours for this case deviated from the design contours. However, the general shape of the isobars were unswept over the panel, which was in agreement with the design goal. The departure from the design came from two sources, the first being the inlet-shock system effects on the flow expansion over the leading edge, and the second being the canopy joint shock incident on the upper surface (described in section 11.5).

F.2. Fence 1, $M = 1.9$; $h = 50\,000$ ft; $\alpha = 3.6^\circ$, Effect of β

The influence of β on $C_{p_{\max}}$ and attachment-line location for fence 1 is shown in figure F6. The effect of decreasing (more negative) β on $C_{p_{\max}}$ was similar to the effect of increasing α as discussed in the previous section. Both effects resulted in a higher $C_{p_{\max}}$. Decreasing β produced a higher $C_{p_{\max}}$ because negative β (nose right) resulted in a decrease in wing sweep which raised attachment-line pressures. In contrast to the $C_{p_{\max}}$ trend, the effect of decreasing β on attachment-line location is similar to the effect of decreasing α . As shown in figure F6, the attachment line moved upward with decreasing β . Later data analysis will show that small negative β was advantageous to obtaining laminar flow on the attachment line.

C_p profiles on the upper surface at six BL stations are shown in figures F7(a) through (f) for $\beta = 0^\circ$ and -3.6° . Differences in the leading edge and upper surface C_p due to β are shown. For all BL's, a more negative β produced a higher C_p on both the upper surface and the leading-edge region. At BL 50 and BL 60 a more negative β produced a less abrupt, and therefore less desirable, profile at the end of the leading-edge expansion, similar to the effect that a lower α had on the previous case. Farther outboard at BL 70, a favorable effect of negative β was evident in the leading-edge pressure comparison. The inset plot in figure F7(c) shows how the inlet-shock system, identified

by the minimum peak (up in plot) found below $s = 0$, crossed the lower surface farther aft for the negative β case (due to the unsweeping of the wing and probable asymmetric skewing of the inlet-shock system). Relative to the shock fence, the location at which the inlet-shock system impinges the fence was farther aft for the negative β case; this, in turn, meant that the fence was providing better, but still limited, blocking at the negative β condition. Recall that this fence was swept 60° , so that the farther back the shock impinged, the greater the blocking effectiveness. Farther outboard at BL's 80, 90, and 100, negative β reduced the pressure peak slightly at the beginning of the rooftop.

Pressure isobar plots on the suction-panel upper surface are shown in figure F8 for the same two angles of sideslip. Both test points show the effect of the pressure peak due to the shock system crossing the leading edge. This effect is evident by looking at the isobars at the beginning of the upper surface starting at about BL 75 and continuing outboard. As expected, the spikes in the isobar lines near the leading edge are larger for the zero β case. In general, the shape of the isobars are unswept over the panel, which is in agreement with the design goal. Departures from design were due to the inlet-shock system effects on the leading-edge flow expansion and the canopy joint shock incident on the upper surface.

F3. Fence 1, $M = 2.0$; $h = 53\,000$ ft; $\beta = -1.5^\circ$; Effect of α

The effect of α with fence 1 for conditions of both higher altitude and M and the incorporation of small negative β are shown in figure F9. These data were collected after fence 1 was reinstalled and is from flight 88, the last flight. At this point in the program, it was clear that higher altitude and Mach number, combined with the use of small negative β , were essential for best laminar flow results. The figure shows that $C_{p_{\max}}$ exhibited relatively little movement for the three angles of attack shown, but this lack of movement was not unexpected because the spread in α is only $.5^\circ$. The movement of the attachment-line location was orderly and consistent for the three cases. The most consistent achievement of laminar flow along the entire attachment line was found for the lower angles of attack (3.2° and 3.4°), where most of the laminar flow data for this last flight was obtained.

Higher altitude was beneficial for achievement of increased laminar flow for two reasons. First, unit Reynolds number was reduced with increasing altitude, and second, the engine required more ingested air volume as density decreased, which reduced inlet spillage. In turn, reduced inlet spillage weakened the shock off the face of the inlet. Higher cruise Mach number also demanded more inlet-ingested air and created less spillage, adding to the weakening of the inlet shock which struck the fence farther rearward and therefore increased the fence blocking effectiveness. The attachment line was also raised when negative β was introduced (fig. F6) which contributed to the survival of laminar flow along the leading edge.

C_p profiles on the upper surface at six BL stations are shown in figures F10(a) through (f) for $\alpha = 3.7^\circ$ and $\alpha = 3.2^\circ$. Differences in the leading edge and upper surface C_p due to α are shown. For all BL's, the higher α condition produced slightly more negative C_p 's on the upper surface and slightly higher C_p 's in the leading-edge region. As seen in the previous fence 1 cases, the lower α produced a slightly more rounded profile at the end of the leading-edge expansion at all BL's. But unlike the previous cases, there was no overexpansion at the end of the leading-edge acceleration at the outboard BL's. Also, the leading-edge pressures at BL 70 were well behaved near the attachment line. This behavior was the positive benefit of higher Mach number ($M = 2.0$ compared to $M = 1.9$), higher altitude ($h = 53\,000$ ft compared to $50\,000$ ft) and incorporation of small negative β .

Pressure isobar plots on the suction-panel upper surface are shown in figure F11 for the same two angles of attack. Both test points no longer exhibit a large spike in the isobars near the leading edge that was due to the shock system. In general, the shape of the isobars was unswept over the panel, except as noted below, and was better for the higher α test point. Departures from design were due to the remnants of the inlet-shock system and the canopy joint shock incident on the upper surface.

F4. Fence 1, $M = 2.0$; $h = 53\,000$ ft; $\alpha = 3.4^\circ$; Effect of β

Testing with fence 1 at $M = 2.0$ and higher altitudes was limited because lower Mach numbers were flown for the majority of the time that fence 1 was

installed. Also, the desired test point conditions concentrated on the use of a target β of -1.5° . However, a few cases with β at 0° were evaluated, and a comparison illustrating the effect of β is shown in figure F12. The increase in $C_{p_{\max}}$ with decreasing β was similar to that shown in figure F6 for $M = 1.9$. There was a slight shift upward of the attachment-line location with decreasing β , similar to the $M = 1.9$ case, but with a less notable change.

C_p profiles on the upper surface at six BL stations are shown in figures F13(a) through (f) for $\beta = 0^\circ$ and $\beta = -1.4^\circ$. Differences in the leading-edge and upper surface C_p due to β are shown. For all BL's, a more negative β produced a downward shift in the C_p on both the upper surface (less negative) and the leading-edge region (more positive). As seen in the previous cases with β , the negative β test point produced a slightly more rounded profile at the end of the leading-edge expansion at all BL's. But unlike the Mach 1.9 cases, there was no overexpansion at the end of the leading-edge acceleration at the outboard BL's. A significant improvement at BL 70 is realized for the attachment-line definition for this flight condition. Instead of a flat C_p distribution with an ill-defined maximum, there was a definite $C_{p_{\max}}$ and attachment-line position. The improved shape of the attachment-line C_p profiles in this region was the major benefit of using β .

Pressure isobar plots on the suction-panel upper surface are shown in figure F14 for the same two angles of sideslip. In general, the isobars are unswept over the panel, a condition which was in agreement with the design goal isobar contour shapes.

F5. Fence 2, $M = 1.9$; $h = 50\,000$ ft; $\beta = 0^\circ$; Effect of α

Fence 2 was installed and tested beginning with flight 62. The test conditions focused on the design conditions of $M = 1.9$ and 50 000 ft over a range of α . It was not apparent at this time in the flight test program that higher Mach and the use of small $-\beta$ were beneficial. The $C_{p_{\max}}$ and attachment-line locations for a range of α are shown in figure F15. The attachment-line location for fence 2 was well behaved for the test points presented. However, comparisons of the $C_{p_{\max}}$ values in figure F15 for fence 2, with the levels shown in figure F1 for fence 1 at the same flight conditions, revealed distinct differences. For fence 2,

$C_{p_{\max}}$ values at BL 70 and BL 80 were markedly reduced, while at BL 90, $C_{p_{\max}}$ reached its maximum level. These changes can be attributed to the flow field around fence 2. Unlike fence 1, fence 2 blocked the inlet-shock system from crossing between BL 70 and BL 80. However, there was an expansion from the supersonic leading edge of fence 2 itself which reduced the $C_{p_{\max}}$ at BL 70 and BL 80. In addition, the massive inlet-shock system, which was initially blocked by fence 2, eventually spilled over the 20-in-high fence and crossed the leading edge between BL 80 and BL 90. The pressure orifices at BL 90 were the first row to encounter the effects of the shock disturbance but did not encounter the peak levels. The peak levels occurred at the shock crossing which was inboard of BL 90. In essence, the effect of the inlet shock system changed from producing a $C_{p_{\max}}$ at BL 70 for fence 1 to producing a $C_{p_{\max}}$ at BL 90 for fence 2. Additionally, fence 2 introduced flow expansion effects from its supersonic leading edge that appeared at BL 70 and BL 80. The flow structure described above for fence 2 will become more apparent as other conditions of M and β are introduced in the following sections.

C_p profiles on the upper surface at six BL stations are shown in figures F16(a) through (f) for $\alpha = 2.6^\circ$ and $\alpha = 3.7^\circ$. For all BL's, a higher α produced a more negative C_p on the upper surface and a more positive C_p in the leading edge. As seen before, the lower α rounded off the corner of the C_p profiles at the end of the leading-edge expansion. Deviations from the C_p profiles from the previous fence 1 cases began at BL 70. Unlike fence 1, fence 2 blocked the inlet-shock system from crossing between BL 70 and BL 80; this can be seen in the leading-edge inset plot for BL 70, which no longer shows a pressure disturbance crossing the first few pressure taps. However, an expansion from the fence itself lowered C_p values for BL 70 and BL 80, and the spilling of the shock over the fence raised C_p at BL 90, as mentioned in the previous paragraph. Pressure isobar plots on the suction-panel upper surface are shown in figure F17 for the same test points for further comparison.

F6. Fence 2, $M = 1.9$; $h = 50\,000$ ft; $\alpha = 3.7^\circ$; Effect of β

The effect of a slight negative β for fence 2 and $M = 1.9$ at $h = 50\,000$ ft is shown in figure F18. The

behavior is very similar to the influence of β for fence 1 (fig. F6). $C_{p_{\max}}$ increased with negative β , and the attachment line moved slightly upward. The attachment-line movement outboard of BL 80 due to β was less pronounced for fence 2. The upper surface and leading-edge pressures were affected by β as shown in figures F19(a) through (f) for $\beta = 0^\circ$ and $\beta = -1.4^\circ$. Again, the behavior was very similar to the fence 1 results. For completeness, a surface isobar plot for the same two cases is presented in figure F20. The biggest C_p changes resulting from changes in β occurred at the point where the inlet-shock system crossed the leading edge after it spilled over the fence. This crossing was occurring between BL 80 and BL 90 where there are no pressure taps to record these changes.

**F7. Fence 2, $M = 2.0$; $h = 50\,000$ ft; $\alpha = 3.7^\circ$;
Effect of β**

The effect of $-\beta$ for fence 2 at Mach 2.0 and 50 000 ft on $C_{p_{\max}}$ and the attachment-line location is shown in figure F21. The behavior at Mach 2 was very similar to the data discussed previously for fence 2 at $M = 1.9$, which was also at $\alpha = 3.7^\circ$. The same trend of increasing $C_{p_{\max}}$ and upward movement of the attachment-line location with increasingly negative β was observed. It was found that $\beta = -1.4^\circ$ to -1.5° was the optimum range for achieving a laminar attachment line along the entire leading edge. This lower bound on β was due to the increase of R_k with increasingly negative β . The $C_{p_{\max}}$ increase with more negative β raised the local C_q and thus the local R_k . The R_k limit was reached on the inboard attachment line above $\beta = -1.5^\circ$, which triggered transition. In order to further show the effect of β , upper surface pressures and leading-edge region pressures are shown for $\beta = 0^\circ$ and $\beta = -3.0^\circ$ in figures F22(a) through (f). Upper surface isobars are also compared for the same test points in figure F23.

**F8. Fence 2, $M = 2.0$; $h = 53\,000$ ft; $\beta = -1.5^\circ$;
Effect of α**

This test condition was very favorable for attainment of laminar flow at angles of attack of 3.7° and below. The last series of flights with fence 2 concentrated on this condition to obtain code calibration data. Above 3.7° , the attachment line was tripped by the inlet-shock system that crossed the leading edge

inboard of BL 90. The variation of $C_{p_{\max}}$ and attachment-line location with α for this condition is shown in figure F24. $C_{p_{\max}}$ did not vary much over the range of α presented. As expected, shifting of the attachment-line location upward toward $s = 0$ occurred as α was decreased. The higher altitude of around 53 000 ft was the most successful in establishing a laminar attachment line. As mentioned earlier, higher altitude was favorable from two aspects: weakening of the engine inlet-shock system and reduction of unit Reynolds number. Though higher altitudes may have been even better, they were too difficult to achieve repeatedly from flight to flight due to free-stream temperature changes and engine performance limitations.

Upper surface pressures and leading-edge region pressure profiles are shown for two test points in figures F25(a) through (f) for $\alpha = 4.1^\circ$ and $\alpha = 3.3^\circ$. Results for the $\alpha = 4.1^\circ$ test point indicated that the higher α adversely affected the leading-edge C_p profile and attachment-line definition at BL 50. A laminar attachment line was not achievable at $\alpha = 4.1^\circ$. However, the streamwise C_p distributions at $\alpha = 4.1^\circ$ shown in figure F25 were more suitable for laminar flow on the rooftop than the lower α case. This suitability can be seen by the lack of an overpressure peak at the beginning of the rooftop and a by a well-defined attachment line. In addition, the isobars at $\alpha = 4.1^\circ$ (fig. F26) were closer to the desired unswept design condition, which minimized cross flow.

**F9. No Fence, $M = 1.9$ and 2.0 ; $h = 50\,000$ ft;
 $\beta = 0^\circ$; Effect of α**

Two flights, 60 and 61, were made with no fence installed. This configuration was flown in order to obtain a baseline data set that would help evaluate the performance of fence 1 and fence 2. Figures F27 and F28 present the variation of $C_{p_{\max}}$ and attachment-line location with α for Mach 1.9 and 2.0, respectively. Unlike any of the previous cases, the flow field with no fence at both $M = 1.9$ and $M = 2.0$ exhibited a sharp increase in $C_{p_{\max}}$ at BL 80 due to the inlet-shock system crossing in front of it. This increase illustrates that fence 1 provided some limited blocking (see fig. F1). At best, laminar flow was sustained at LSHF07, which was located on the lower surface at about BL 74. For all test points during flights 60 and 61, β ranged from $-.07^\circ$ to $.53^\circ$.

F10. Comparison of Fences 1 and 2

A direct comparison of measured surface pressures at approximately the same flight conditions for fence 1 and fence 2 illustrates the different flow field associated with each. The conditions selected were those determined at the closure of the flight testing to be the most desirable for achieving extensive laminar flow. Figure F29 shows the $C_{p_{\max}}$ and attachment-line location for both fences at $M = 2$, $\alpha = 3.6^\circ$, and $\beta = -1.5^\circ$. BL 50 and BL 60 have almost identical $C_{p_{\max}}$ and attachment-line location values, which would be expected because effects of the inlet shock did not occur inboard. As previously discussed, the $C_{p_{\max}}$ decrease at BL 70 and BL 80 for fence 2 is caused by the expansion off the leading edge of the fence. The increase at BL 90 was caused by the inlet-shock system which spilled over the fence after being displaced aft. The inlet-shock system also adversely affected the fence 1 configuration. However, the shock system crossed just aft of the BL 70 lower surface taps, which allowed the C_p to almost completely recover before reaching the BL 80 pressure taps. There is little reason not to believe that the $C_{p_{\max}}$ for the fence 1 configuration was at least as large as the $C_{p_{\max}}$ for the fence 2 configuration. The effect just was not captured as well due to the location of the leading-edge crossing of the inlet-shock system in relation to the available rows of pressure taps.

Figures F30(a) through (f) present upper surface and leading-edge C_p plots for both fences at six BL stations. The C_p distributions further illustrate the differences between shock fences 1 and 2. BL 50 and BL 60 remain unchanged (within experimental error), because they are inboard of the fence. As can be seen in the leading-edge plot for BL 70, fence 1 did not suf-

ficiently block the oncoming shock, allowing the shock to cross the first few pressure taps on the lower surface at BL 70. In contrast, fence 2 provided good blocking, and BL 70 was not adversely affected. Outboard of BL 70, fence 1's inability to block the oncoming shock system was apparent by the increased pressure at the attachment line at BL 80. As mentioned in the previous paragraph, the pressure is no doubt increased much more at the leading-edge crossing region than what is measured at BL 80. Fence 2 produced its own pressure disturbance outboard of BL 65 in the form of an expansion fan which affected the attachment-line pressure at BL 70 and BL 80 and the pressures on the upper surface between BL 70 and BL 90. The inlet-shock system, though delayed spatially, eventually spilled over fence 2 and crossed the leading edge before BL 90, as can be seen in the increased C_p at the attachment line. The effects of each fence and the inlet-shock system began to diminish at BL 100.

The upper surface isobar patterns for the fence 1 and fence 2 conditions are shown overlaid in figure F31. The effect of the expansion fan from fence 2 is apparent between BL 65 and BL 95. This expansion, which caused sweeping of the isobars, produced a flow field on the upper surface that was favorable for cross-flow disturbance growth and thus was undesirable for extensive laminar flow, especially at low suction levels. The weak shock from the canopy joint which produced the distortion in the upper surface isobar pattern also added to cross-flow generation. The upper surface flow with either fence installed thus has pressure gradients not anticipated in the design process. In spite of these disturbances, there were stream-wise regions that supported achievement of extensive laminar flow with the available suction.

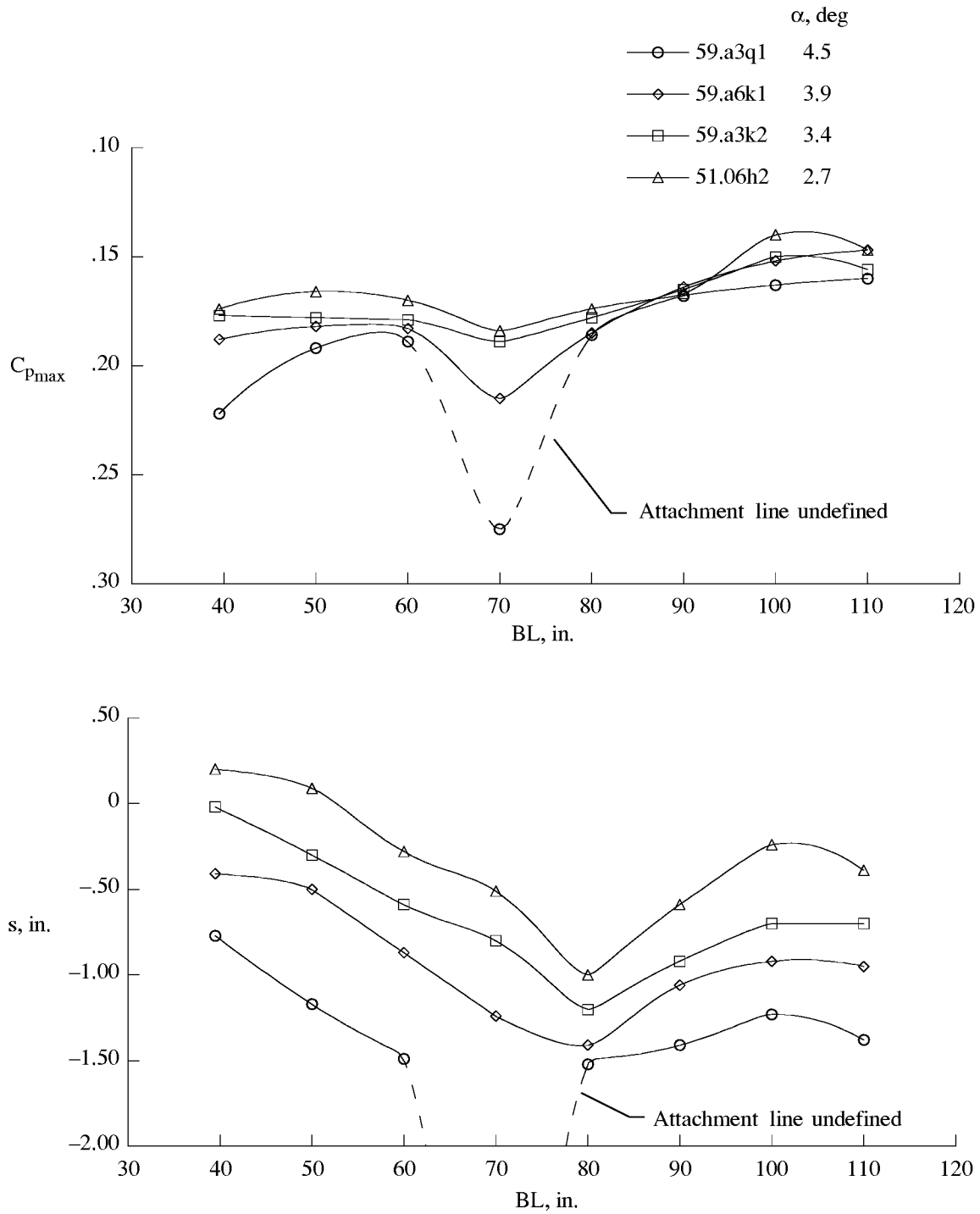
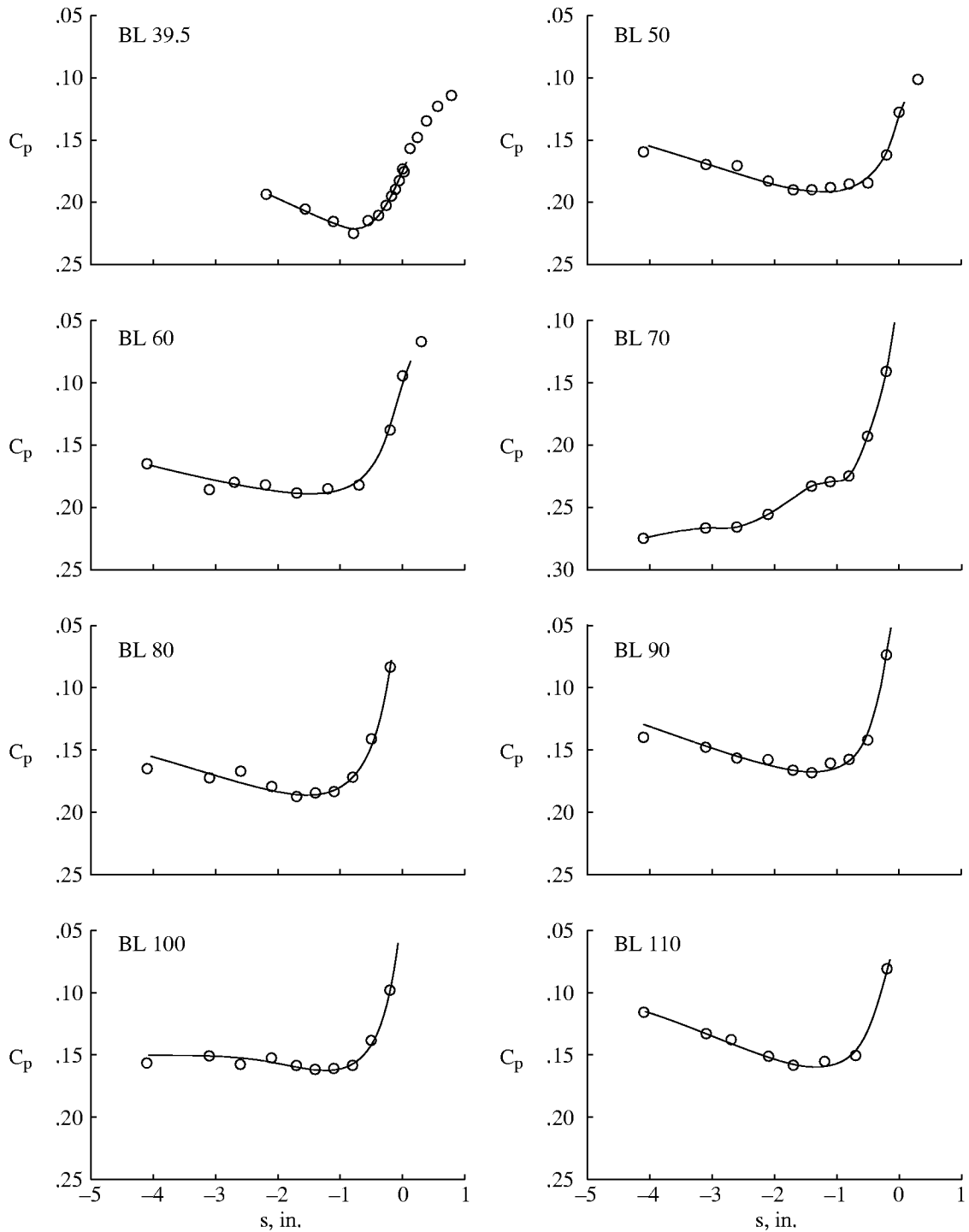
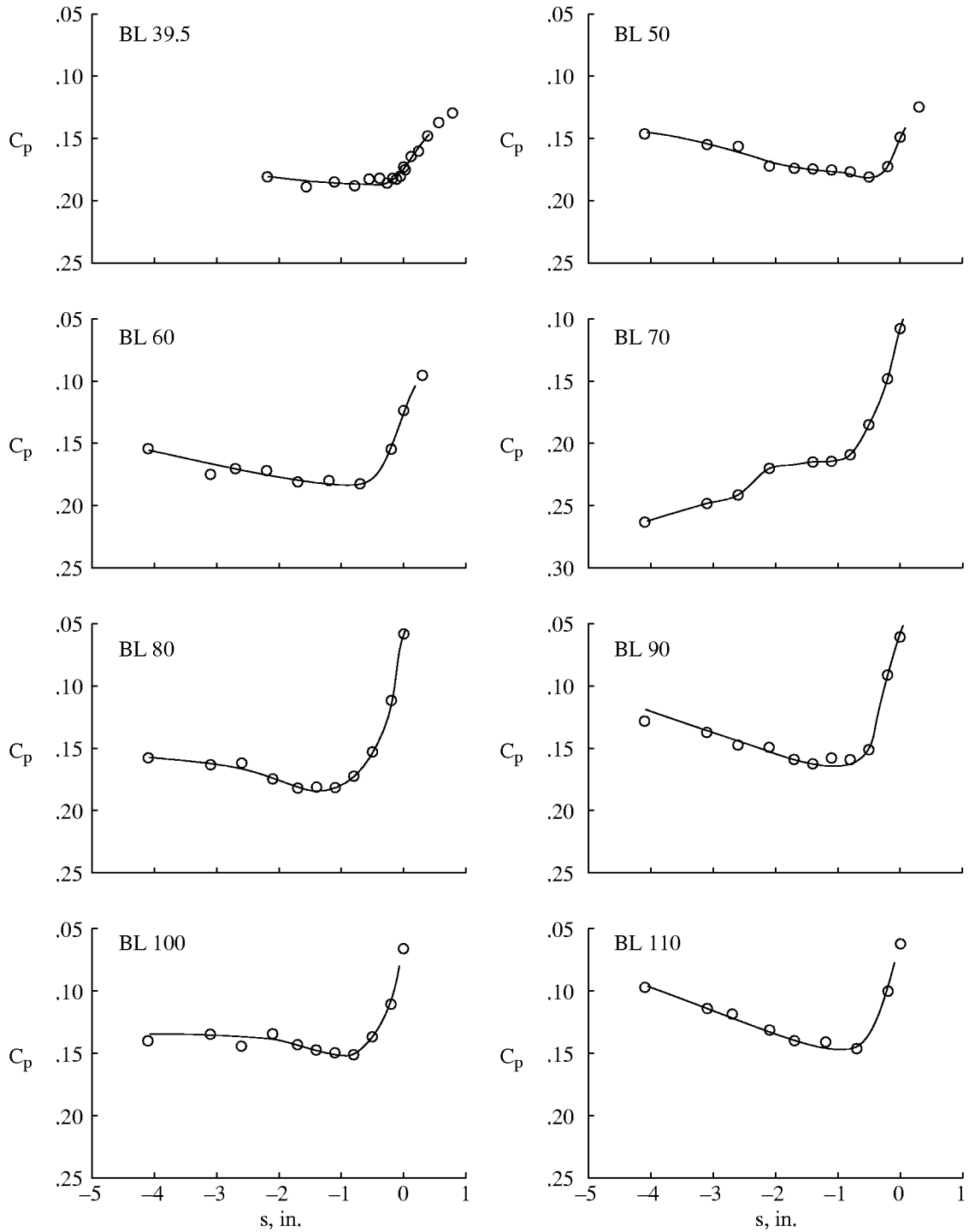


Figure F1. The $C_{p_{max}}$ values and attachment-line locations for different angles of attack at Mach 1.9 with fence 1; $h = 50\,000$ ft; $\beta = 0.0^\circ$.



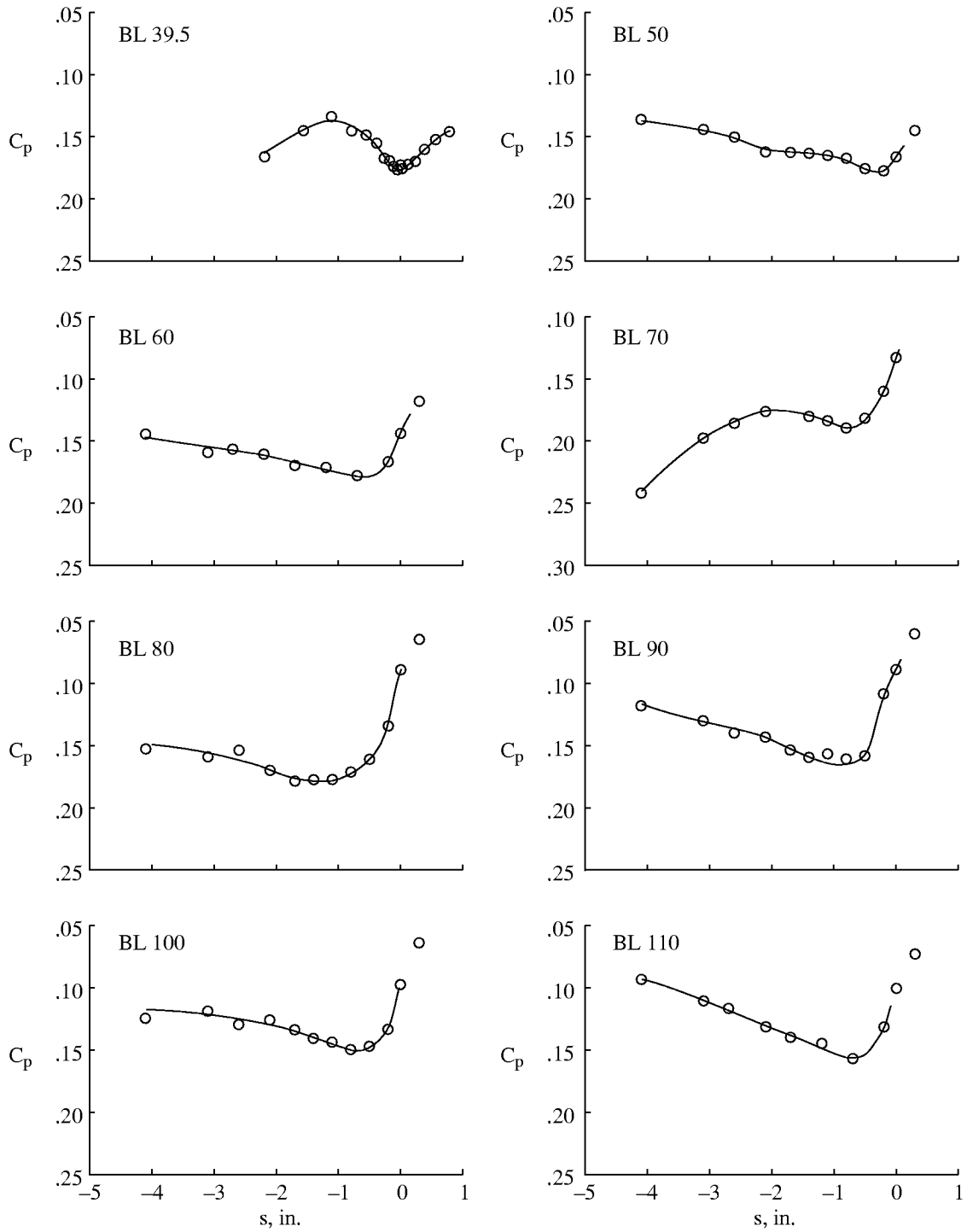
(a) Test point 59.a3q1; $\alpha = 4.5^\circ$.

Figure F2. Attachment line C_p at eight BL stations for four test points at Mach 1.9 with fence 1.



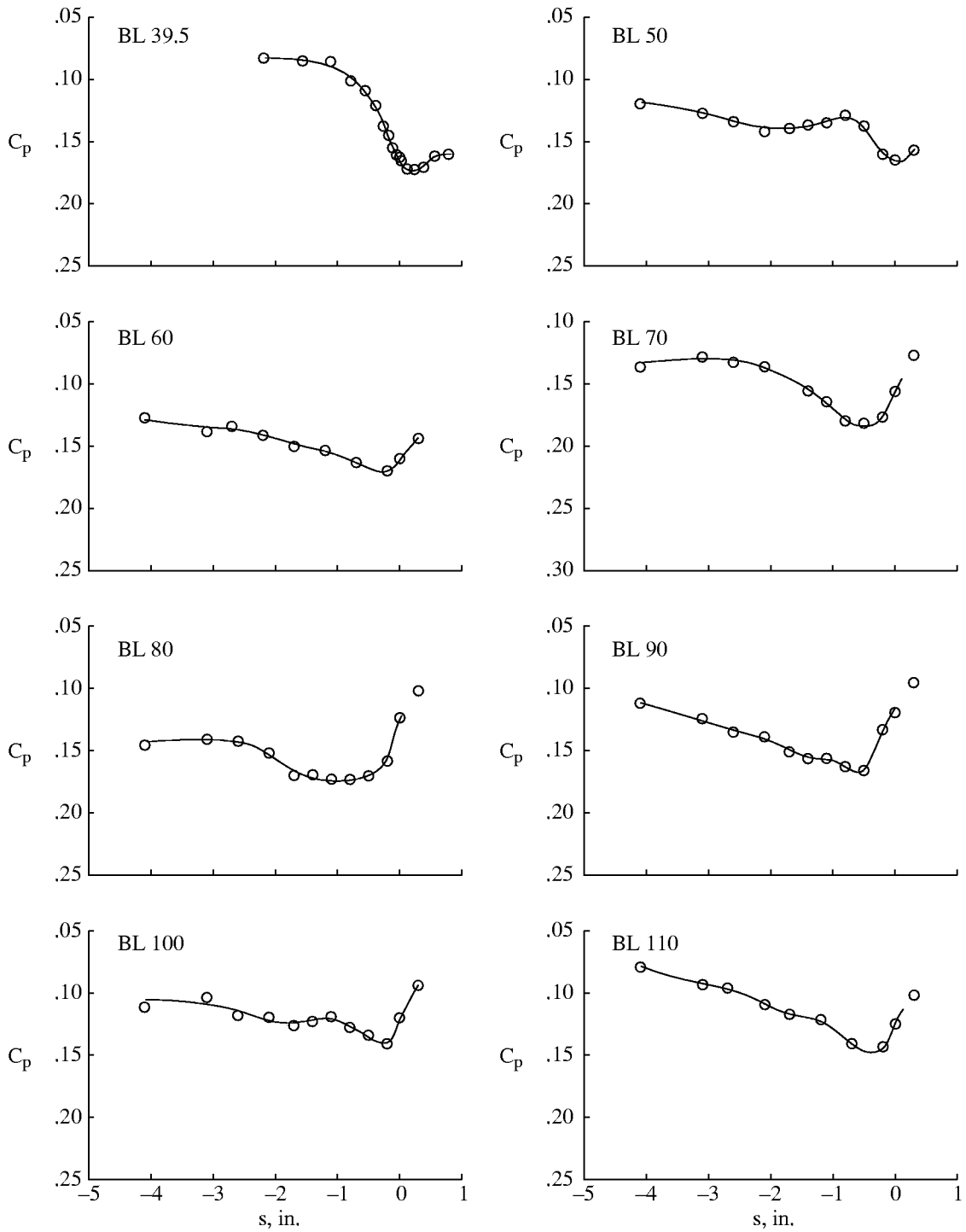
(b) Test point 59.a6k1; $\alpha = 3.9^\circ$.

Figure F2. Continued.



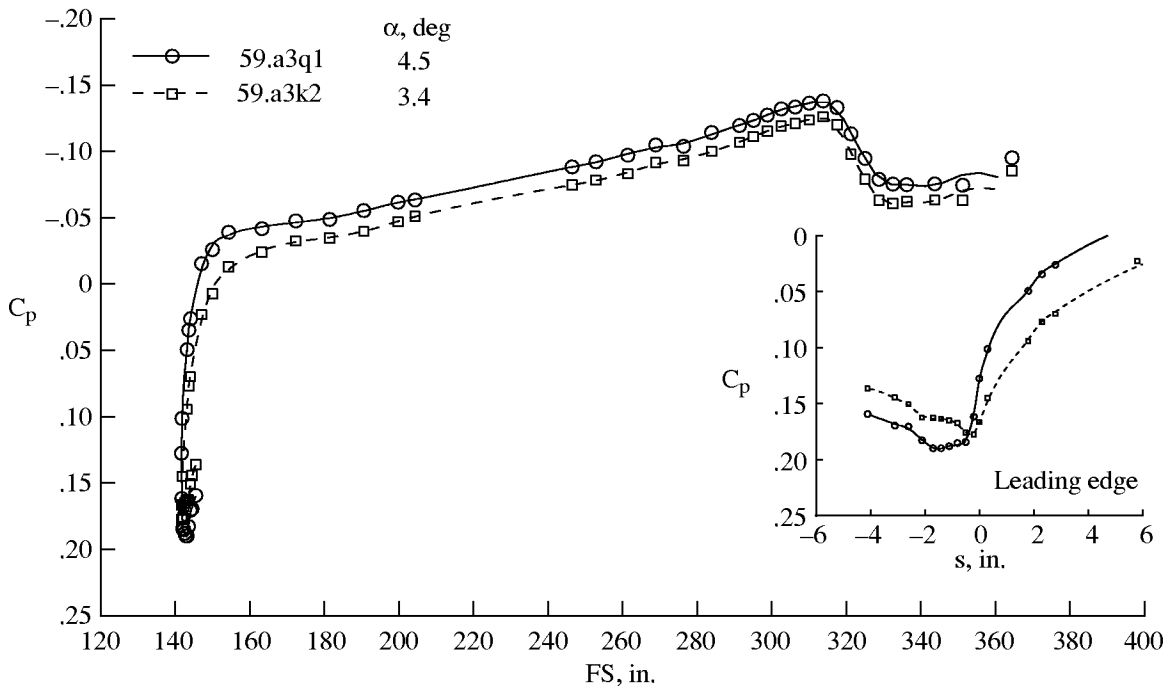
(c) Test point 59.a3k2; $\alpha = 3.4^\circ$.

Figure F2. Continued.

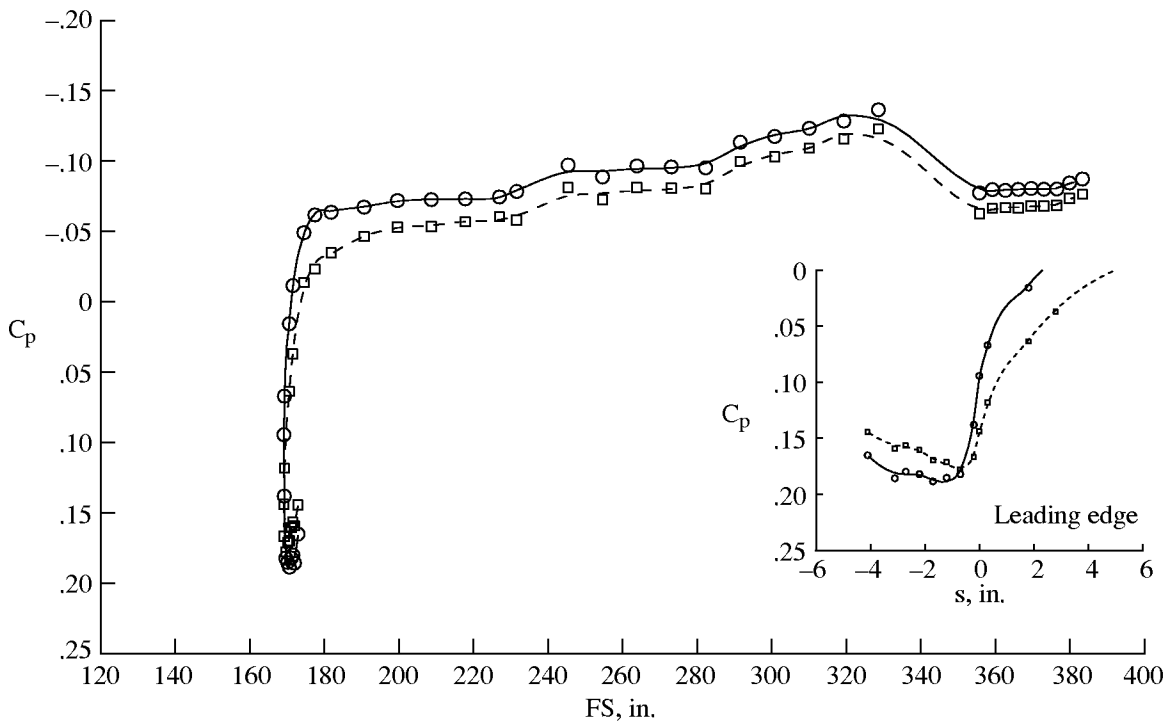


(d) Test point 51.06h2; $\alpha = 2.7^\circ$.

Figure F2. Concluded.

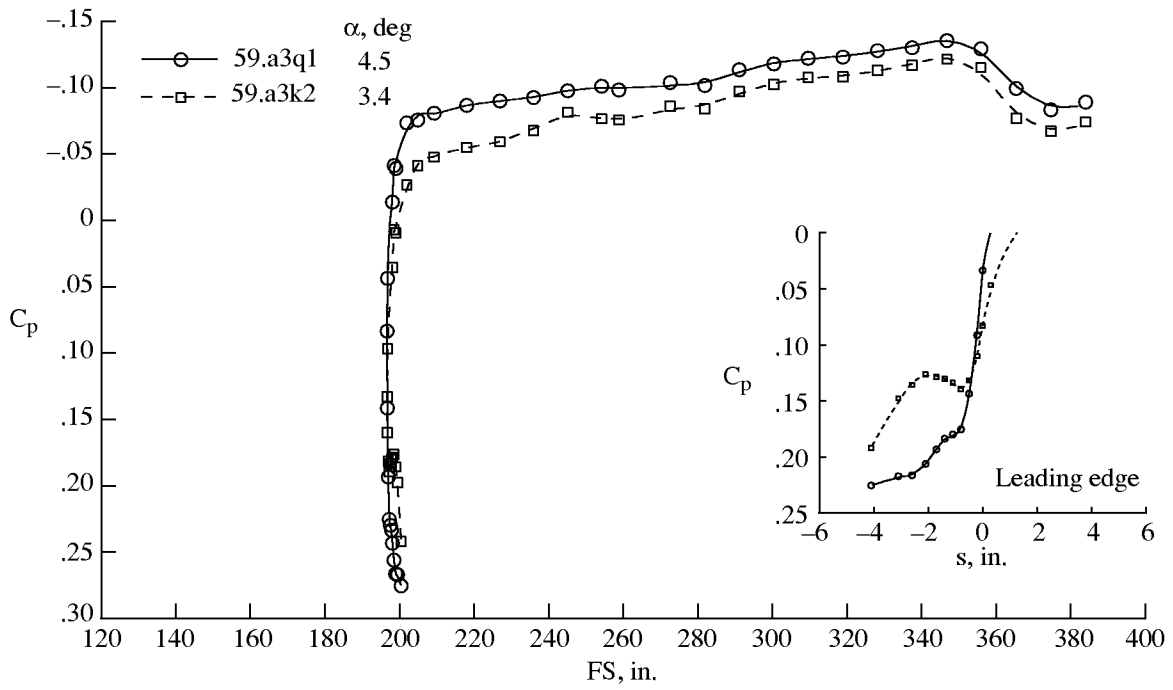


(a) BL 50.

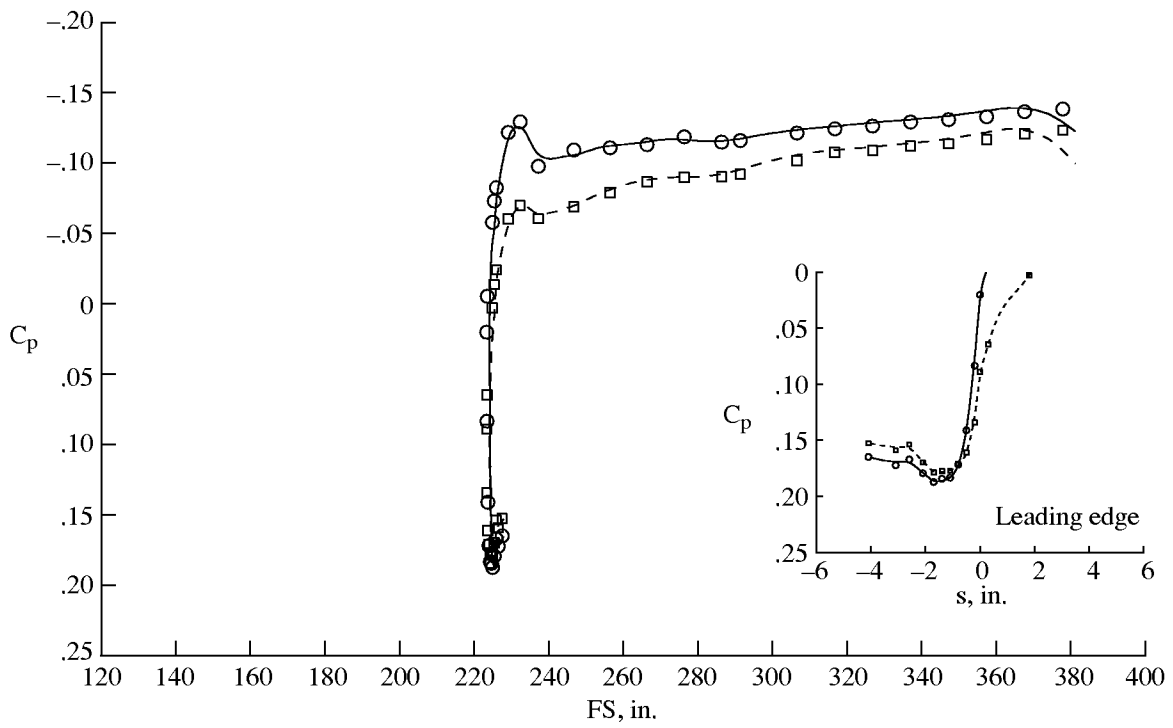


(b) BL 60.

Figure F3. Measured C_p distributions for two different angles of attack at Mach 1.9 with fence 1; $h = 50\,000$ ft; $\beta = 0.0^\circ$.

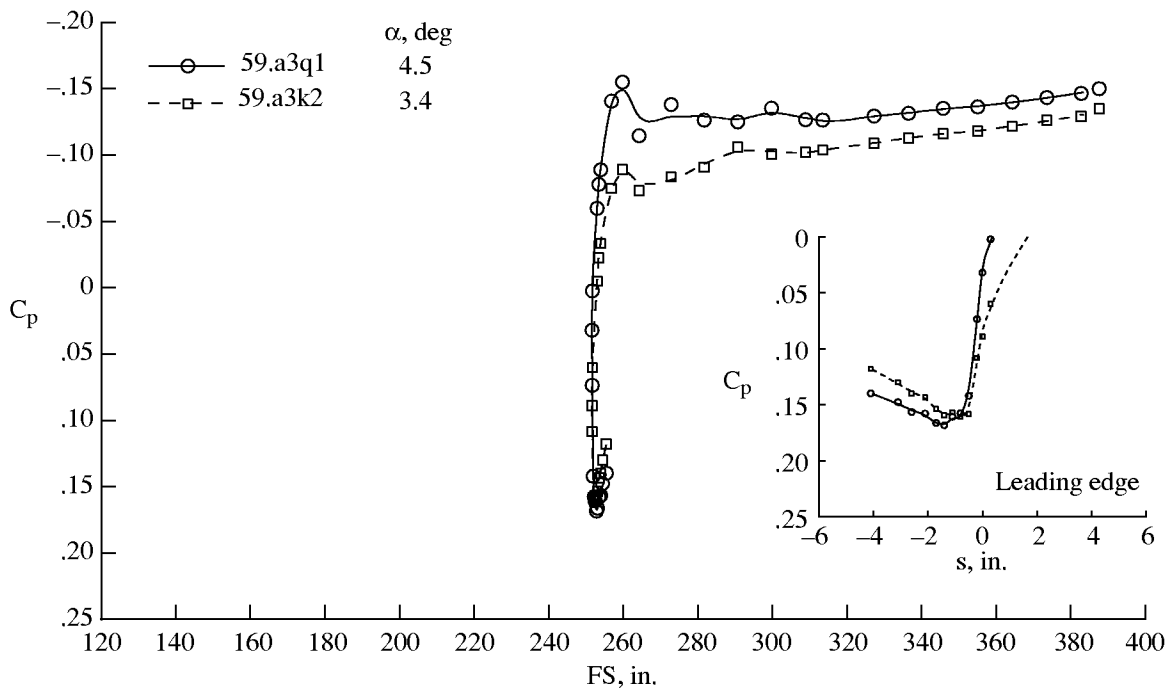


(c) BL 70.

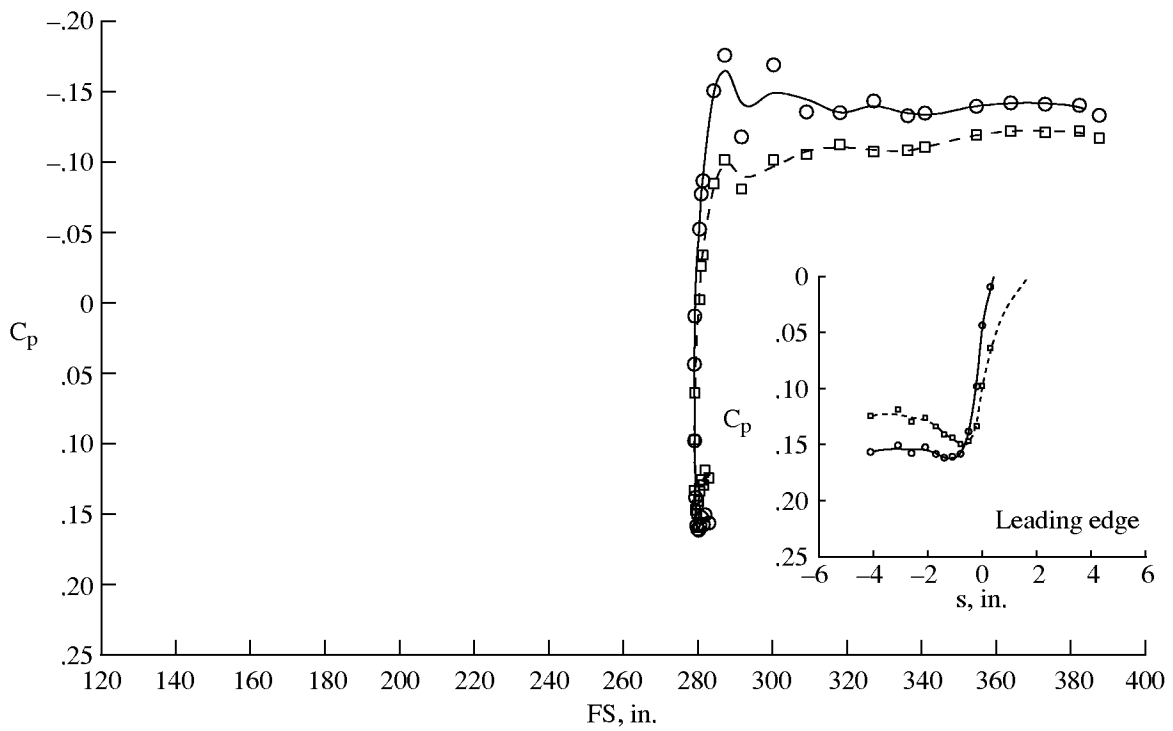


(d) BL 80.

Figure F3. Continued.



(e) BL 90.



(f) BL 100.

Figure F3. Concluded.

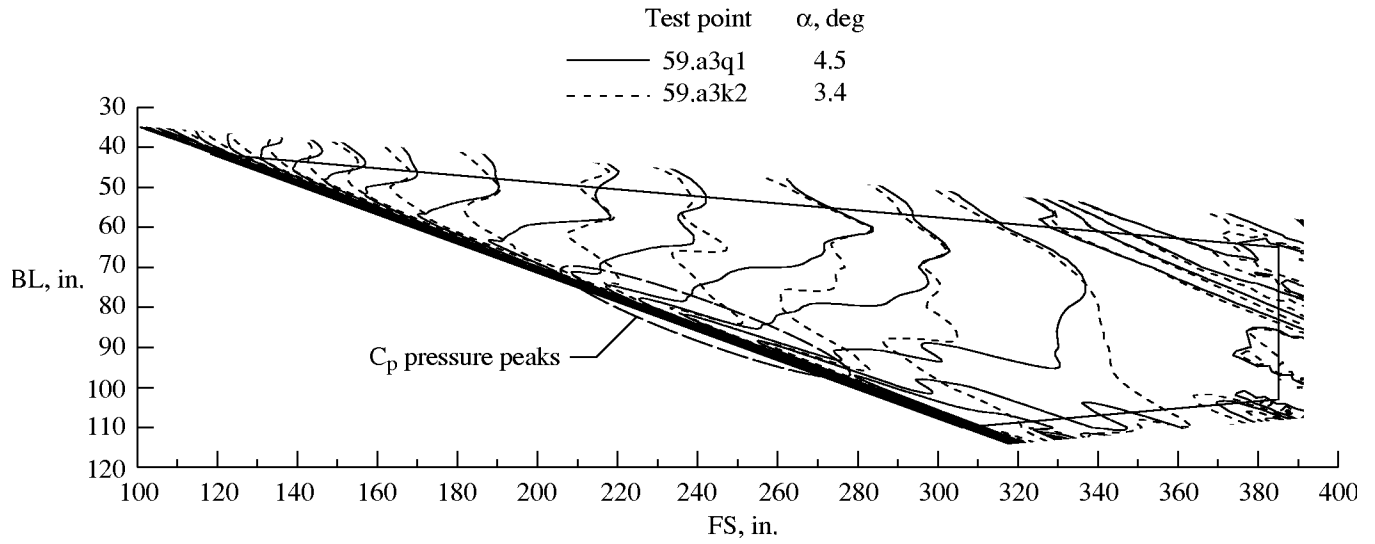


Figure F4. Isobar plots for moderate and high angles of attack at Mach 1.9 with fence 1; $h = 50\,000$ ft; $\beta = 0.0^\circ$.

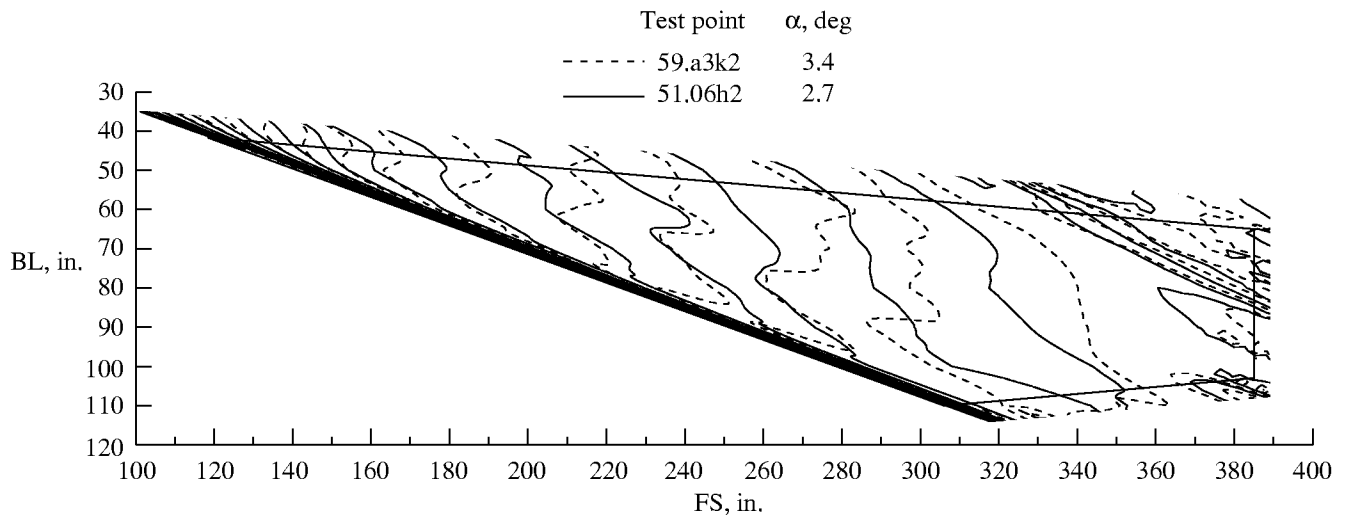


Figure F5. Isobar plots for low and moderate angles of attack at Mach 1.9 with fence 1; $h = 50\,000$ ft; $\beta = 0.0^\circ$.

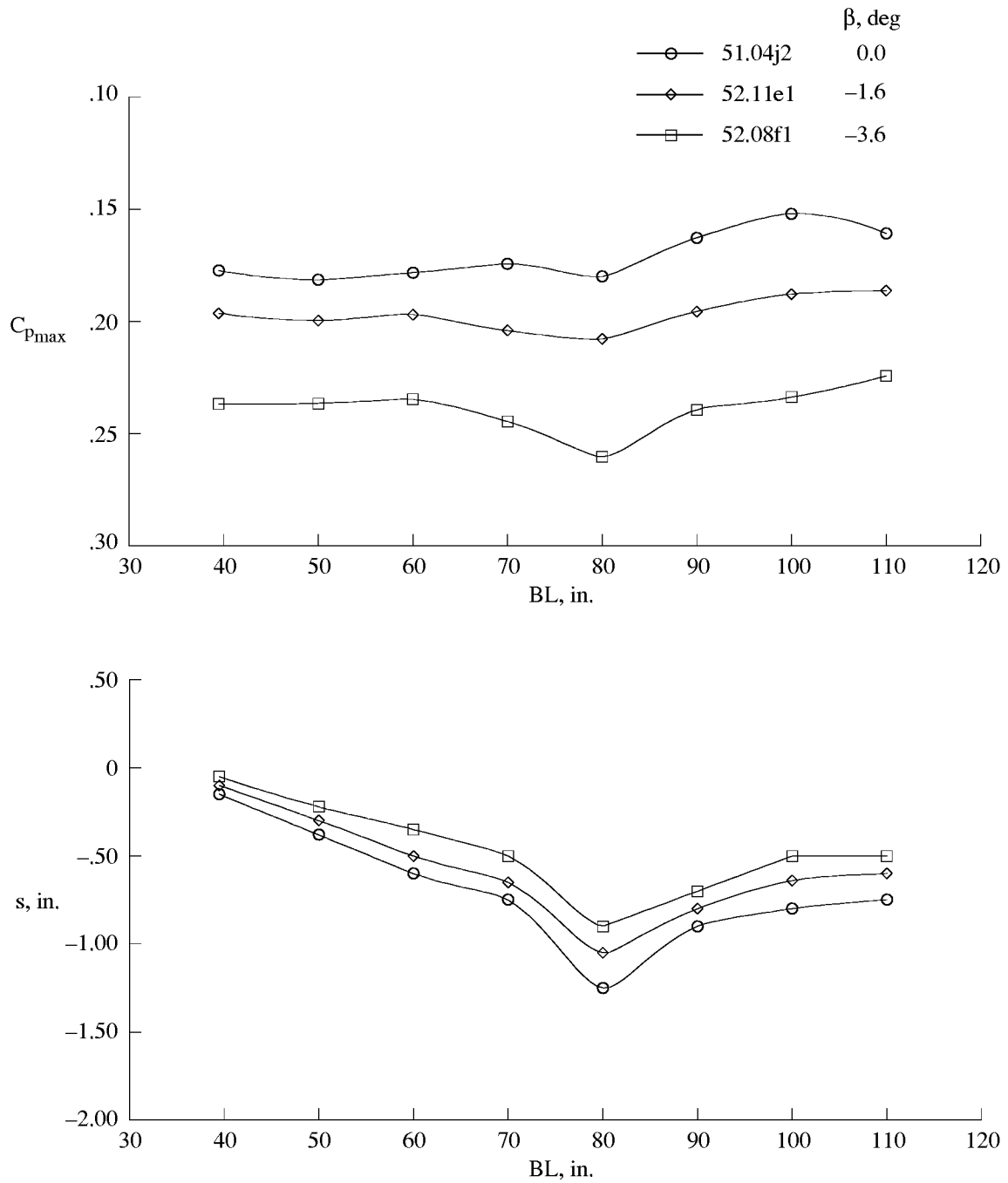
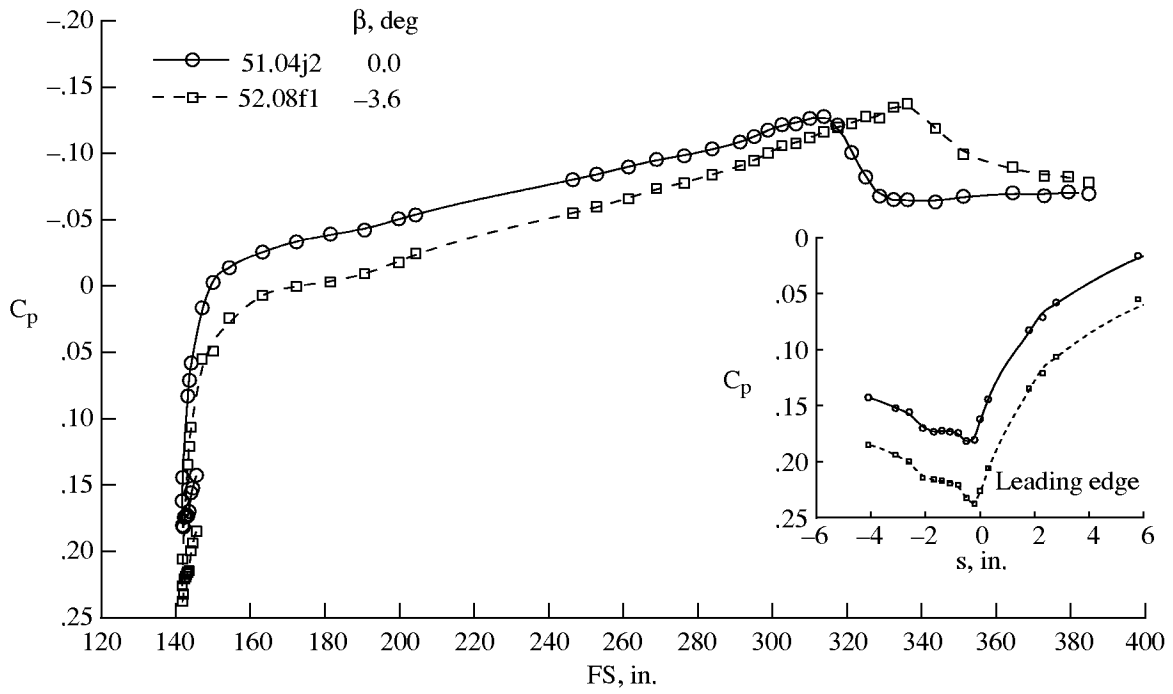
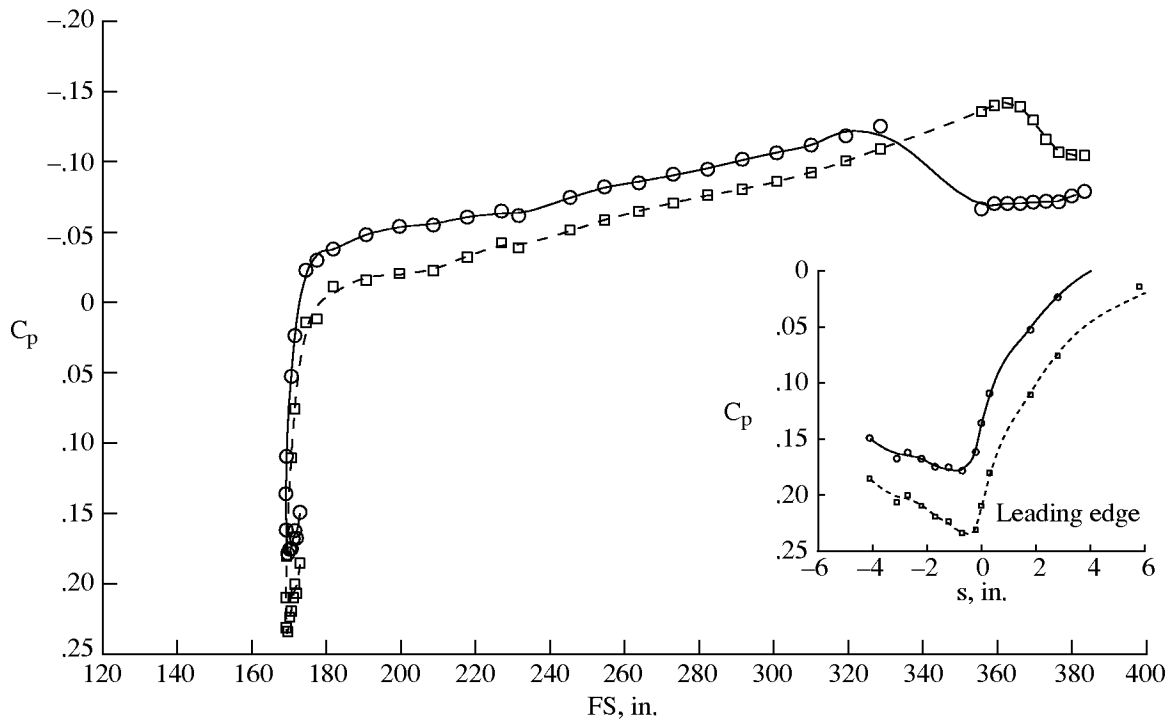


Figure F6. $C_{p_{max}}$ and attachment-line location variations with angle of sideslip for Mach 1.9 with fence 1; $h = 50\,000$ ft; $\alpha = 3.6^\circ$.

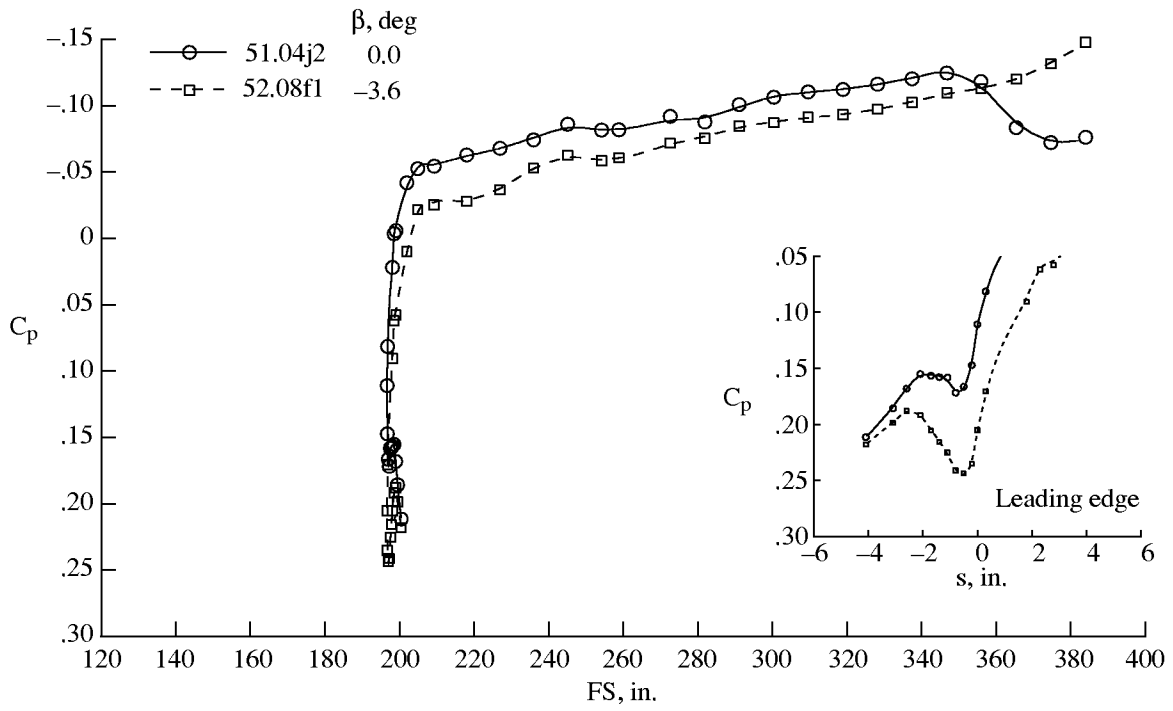


(a) BL 50.

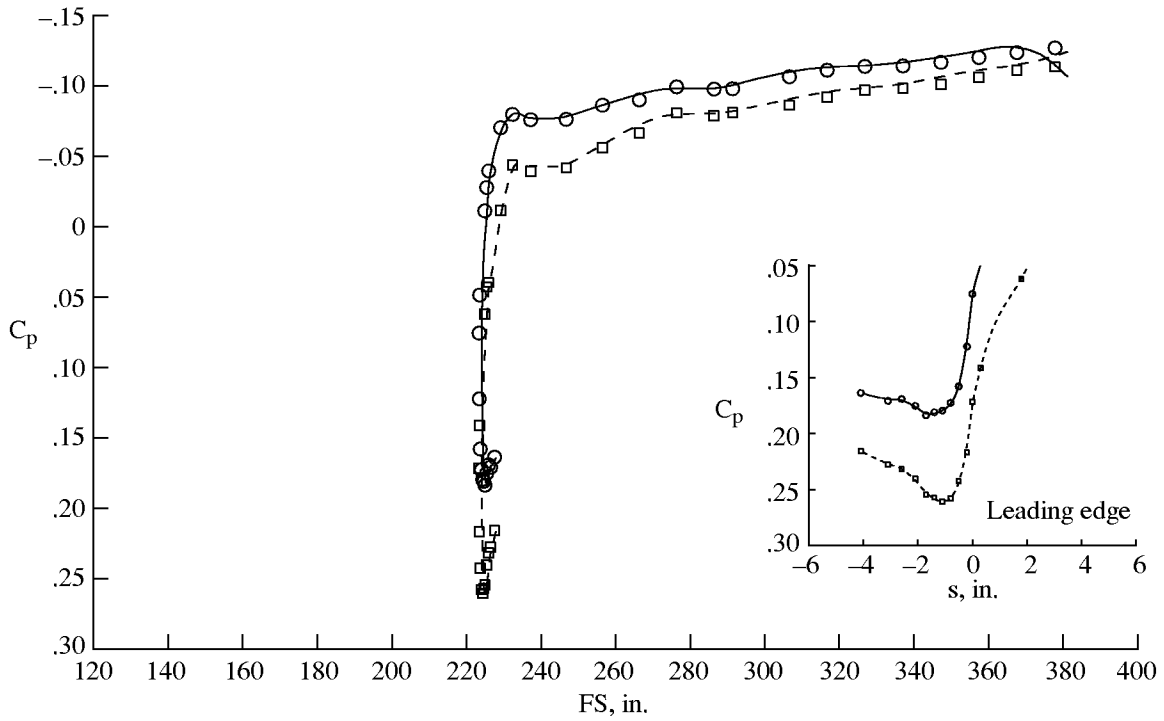


(b) BL 60.

Figure F7. Measured C_p distributions for two different angles of sideslip at Mach 1.9 with fence 1; $h = 50\,000$ ft; $\alpha = 3.6^\circ$.

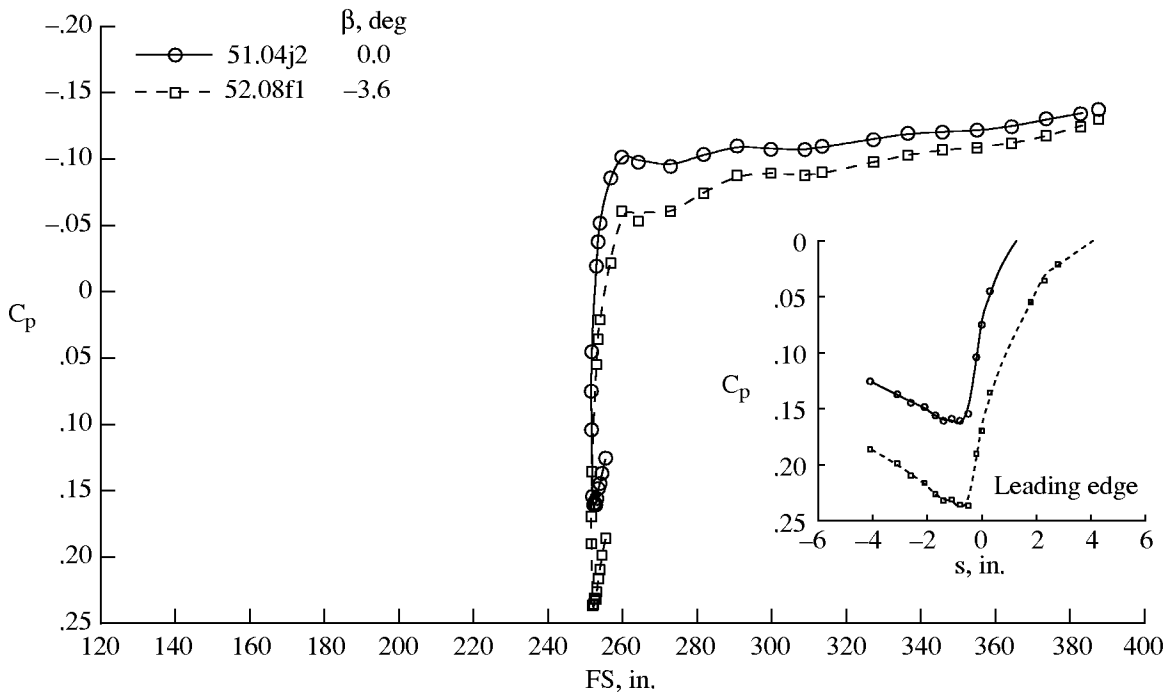


(c) BL 70.

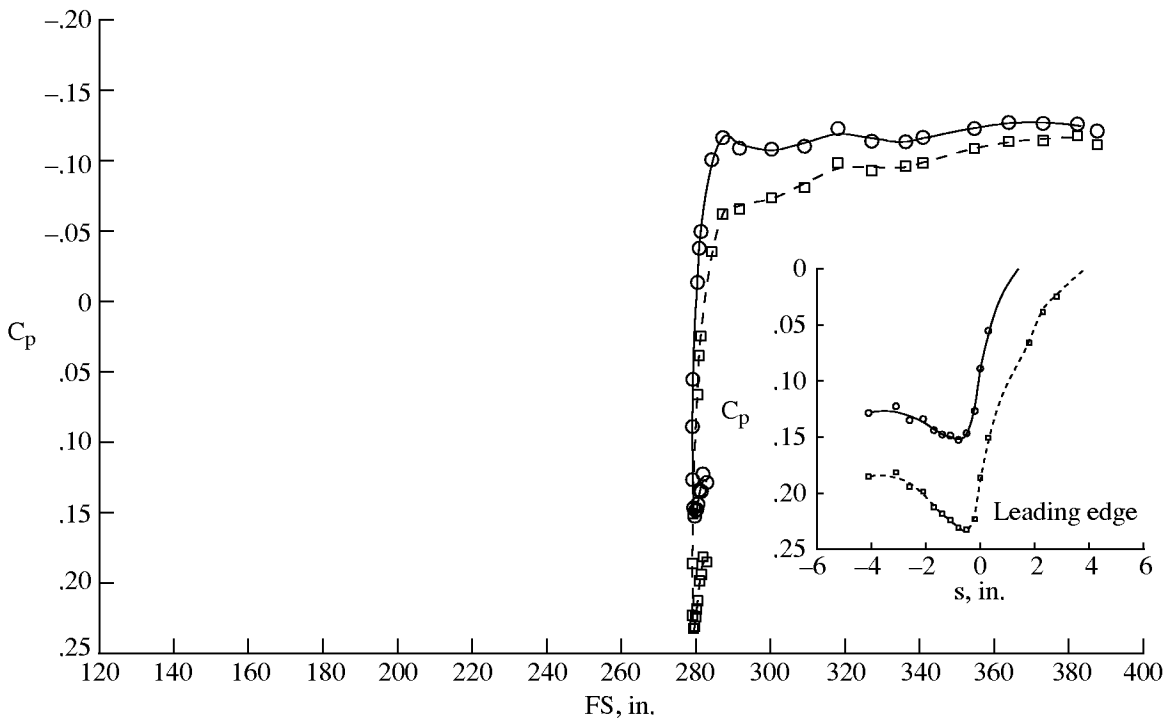


(d) BL 80.

Figure F7. Continued.



(e) BL 90.



(f) BL 100.

Figure F7. Concluded.

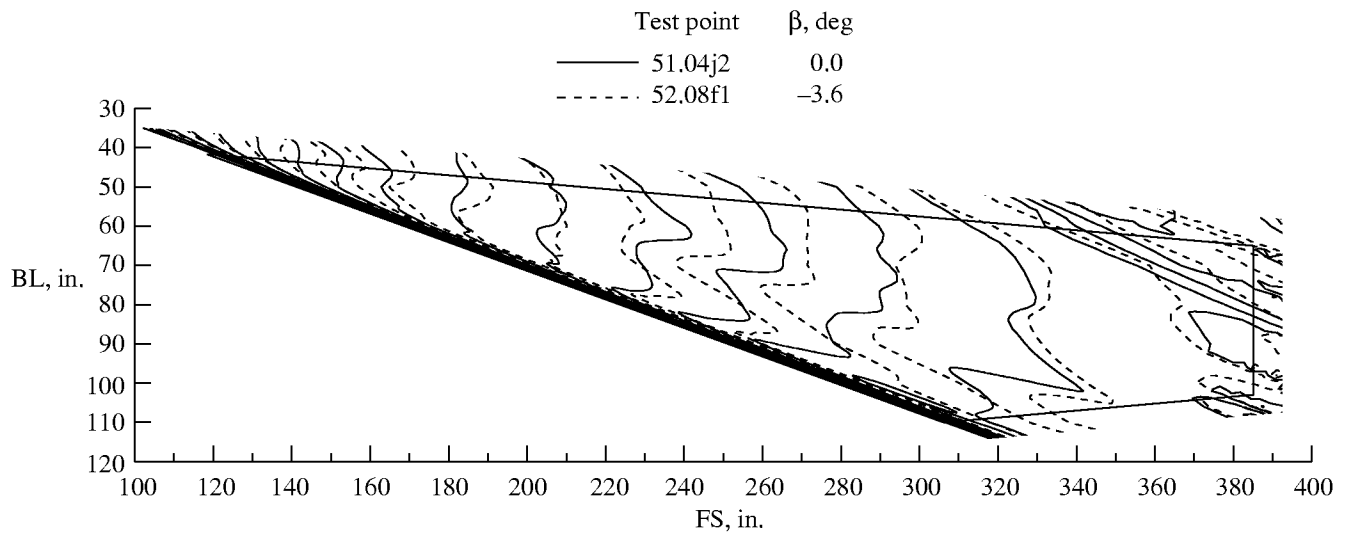


Figure F8. Isobar comparison for different angles of sideslip at Mach 1.9 with fence 1; $h = 50\,000$ ft; $\alpha = 3.6^\circ$.

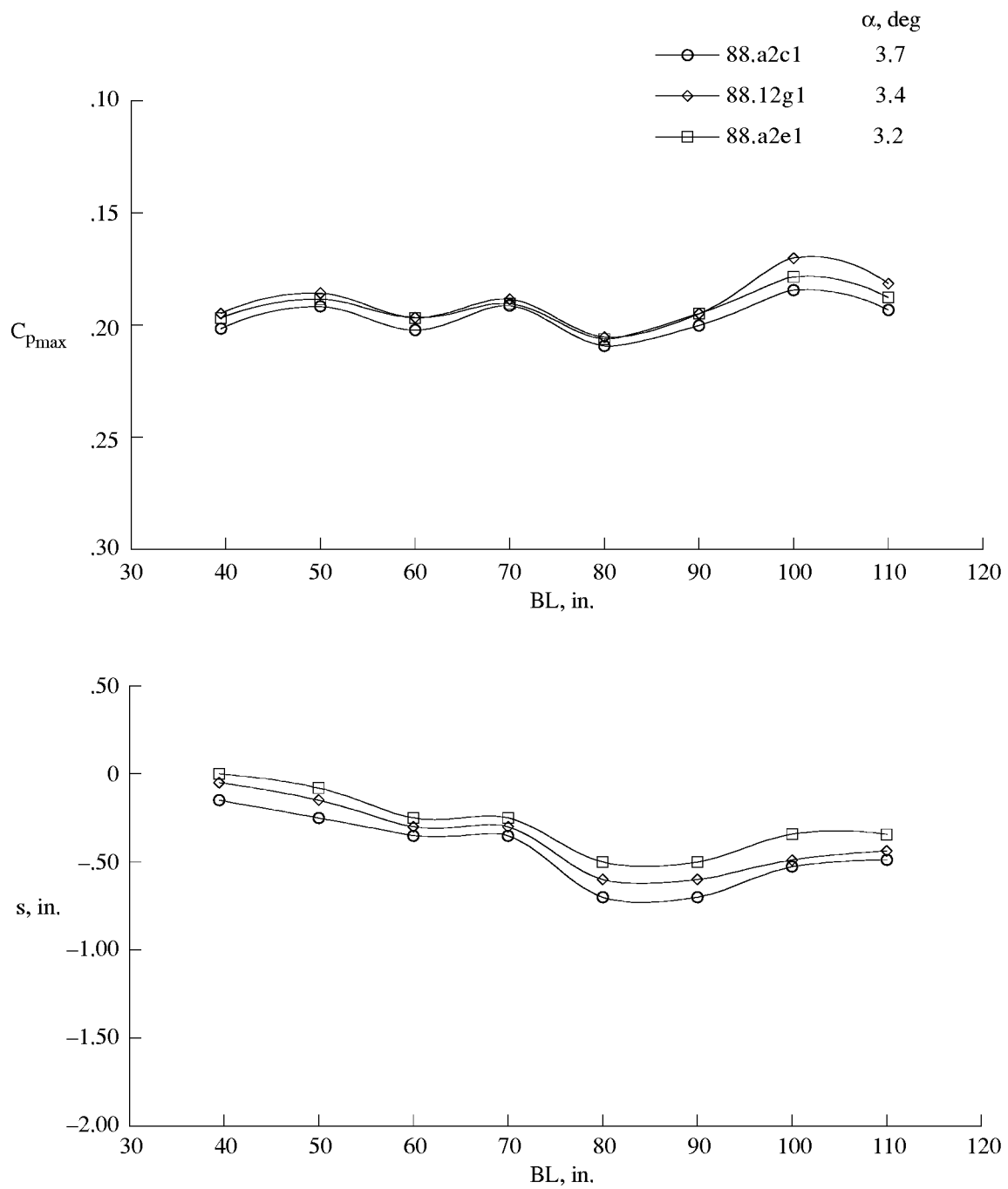
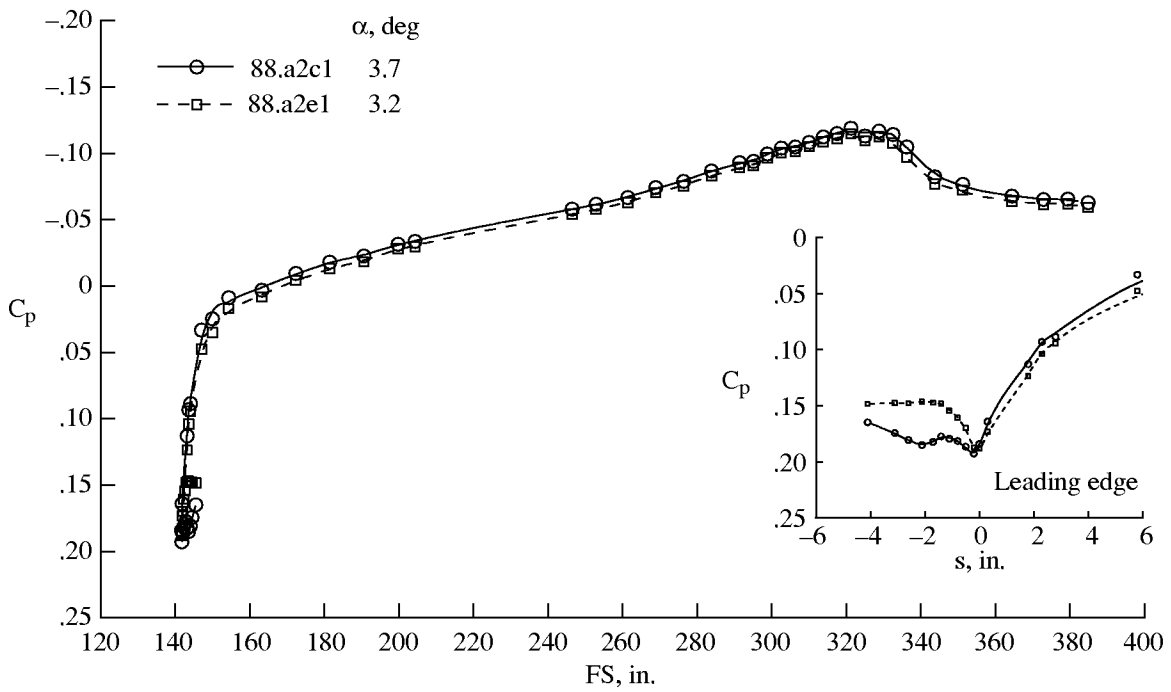
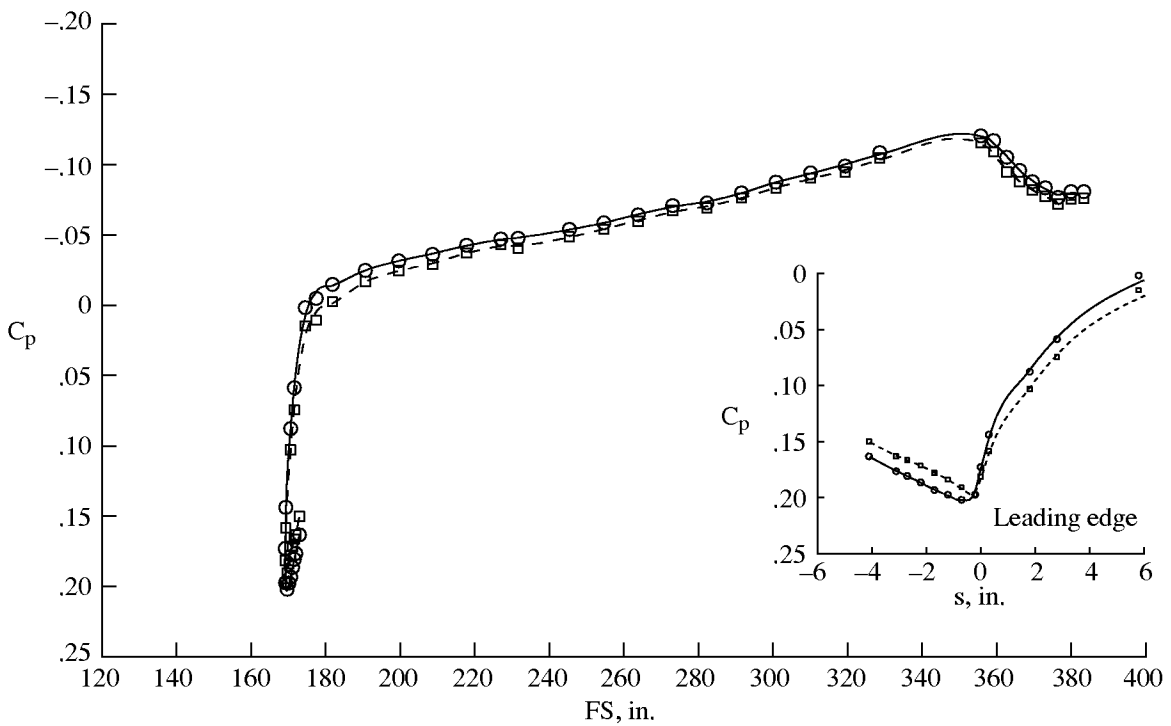


Figure F9. C_{pmax} and attachment-line location variations with angles of attack for Mach 2 with fence 1; $h = 53\ 000$ ft; $\beta = -1.5^\circ$.

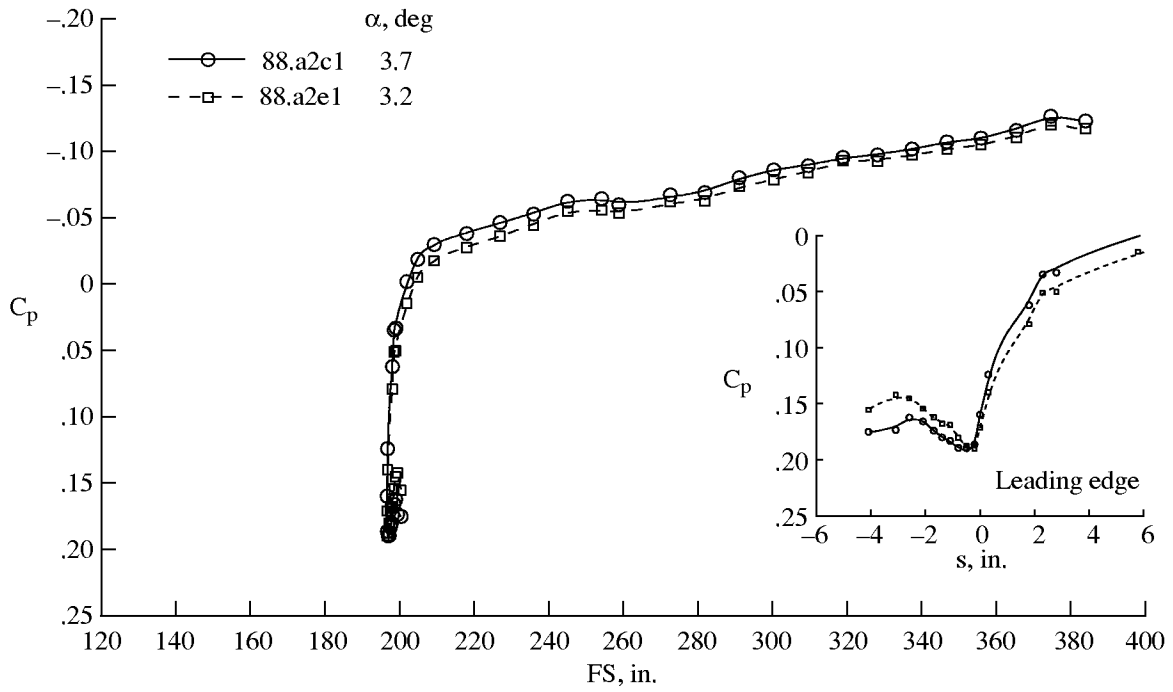


(a) BL 50.

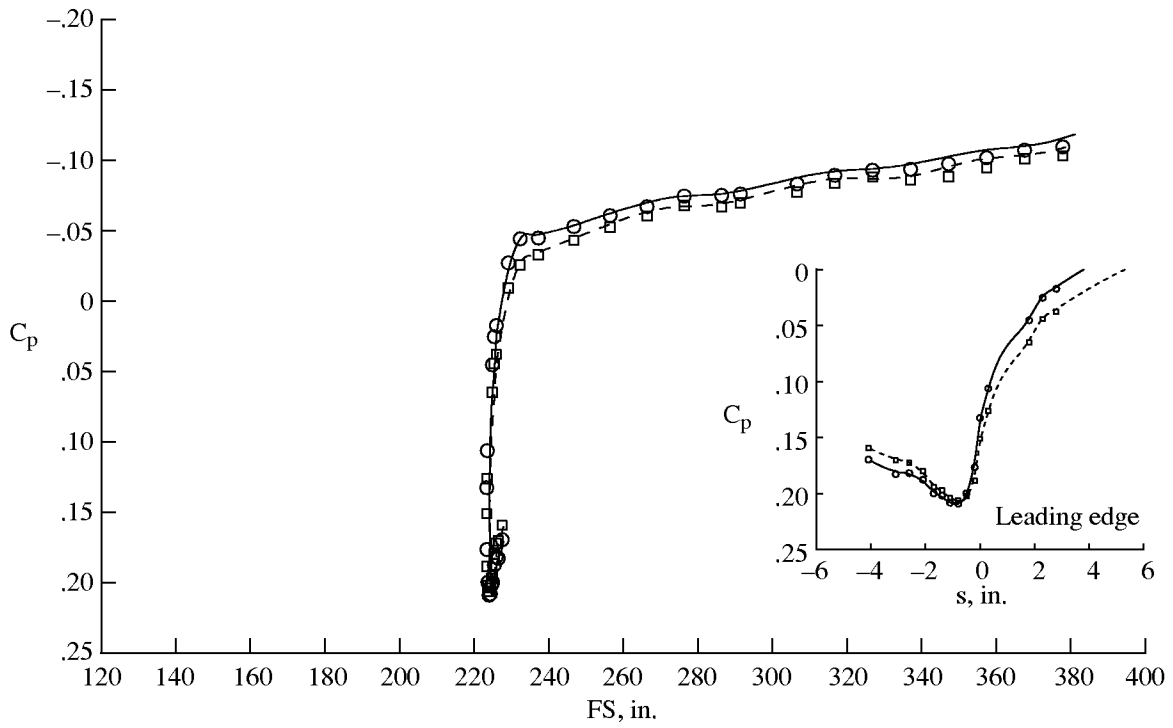


(b) BL 60.

Figure F10. Measured C_p distributions for two different angles of attack at Mach 2.0 with fence 1; $h = 53\,000$ ft; $\beta = -1.5^\circ$.

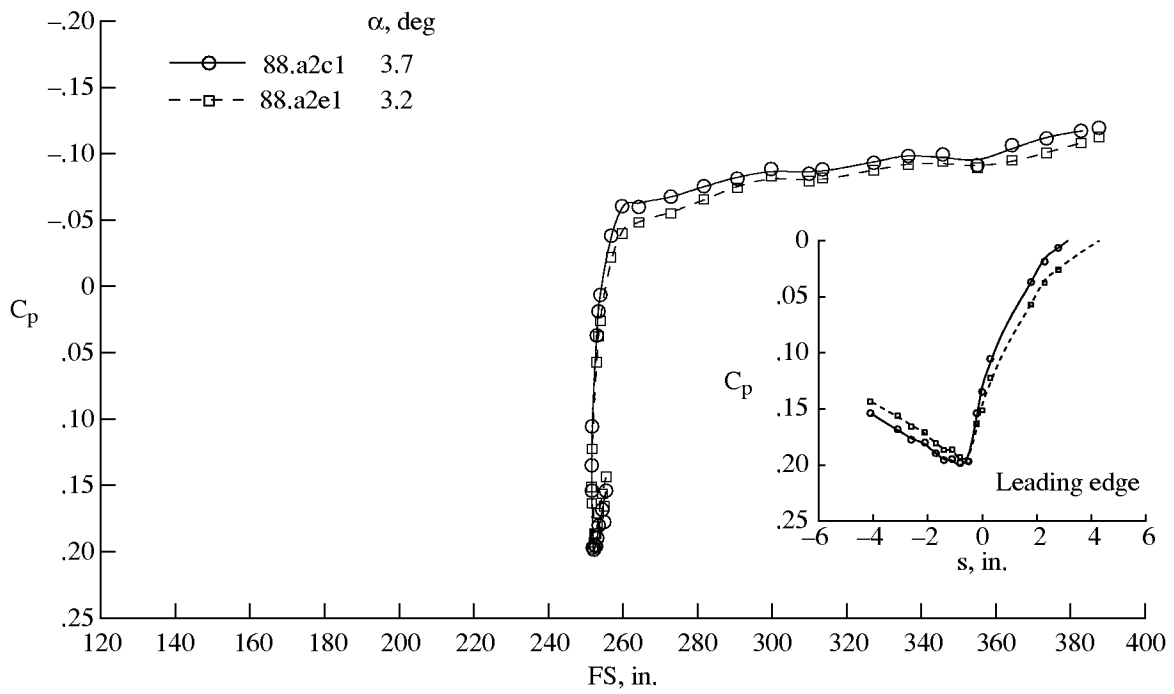


(c) BL 70.

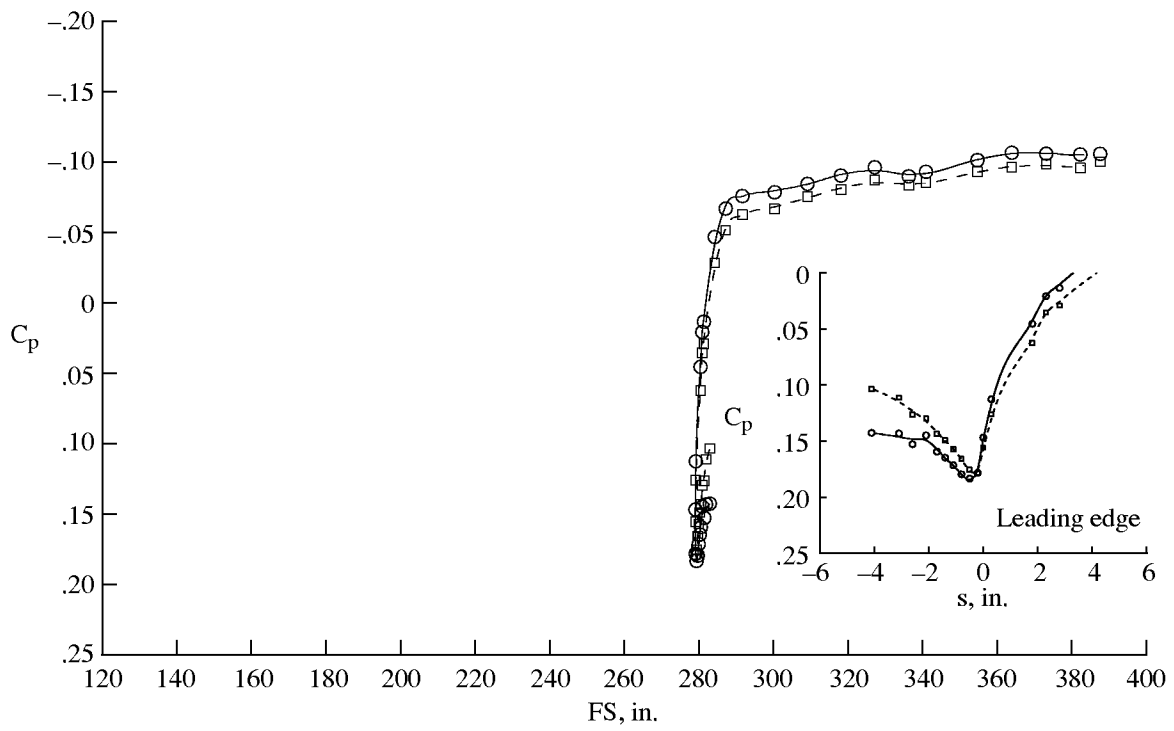


(d) BL 80.

Figure F10. Continued.



(e) BL 90.



(f) BL 100.

Figure F10. Concluded.

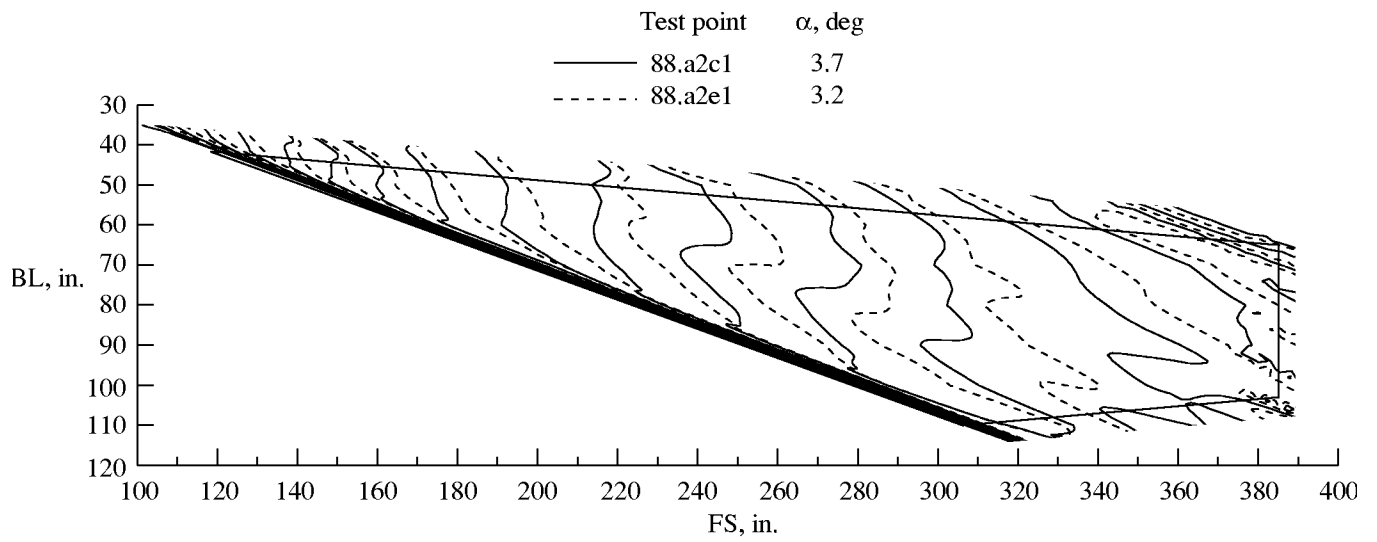


Figure F11. Isobar comparison for different angles of attack at Mach 2 with fence 1; $h = 53\,000$ ft; $\beta = -1.5^\circ$.

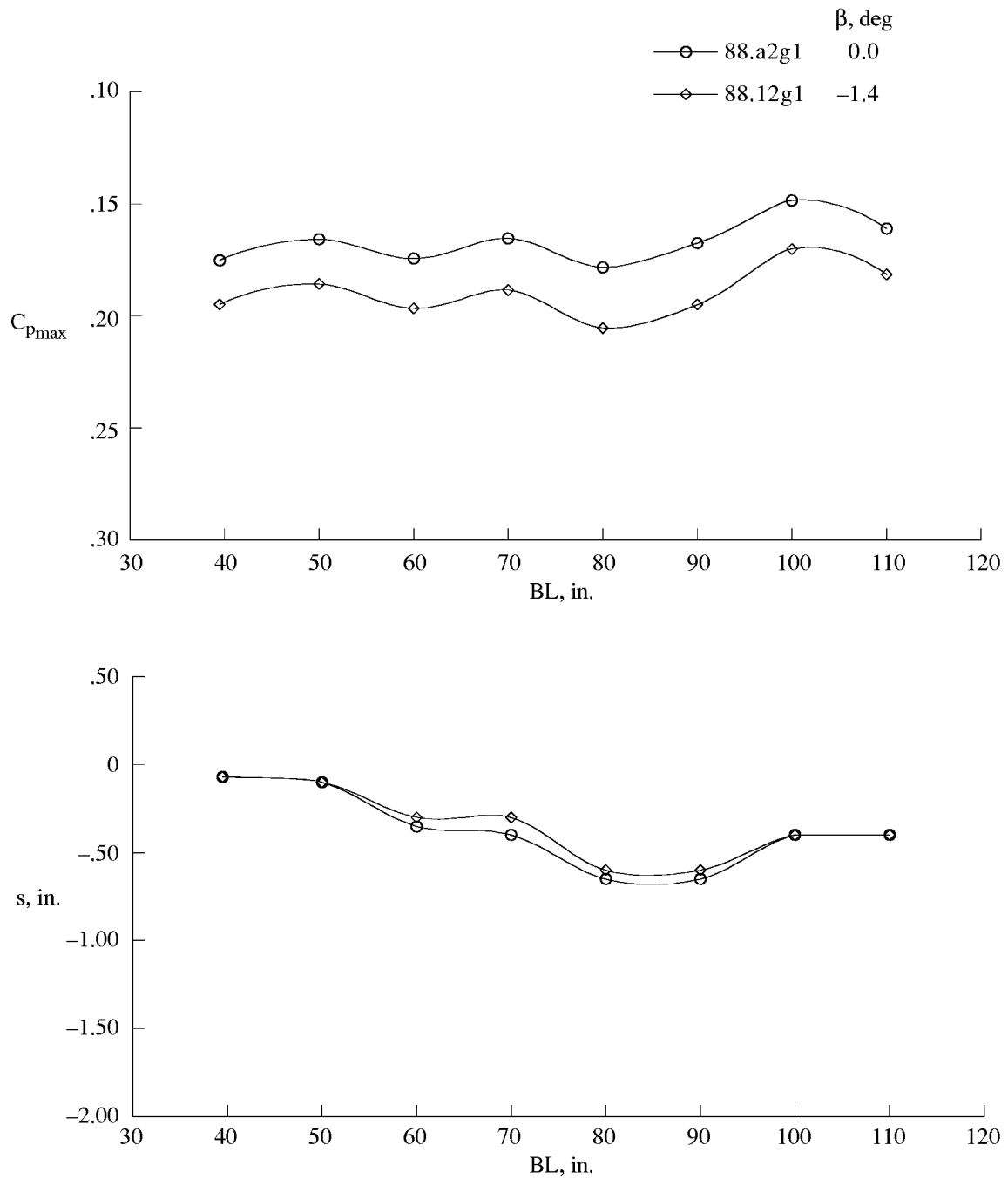
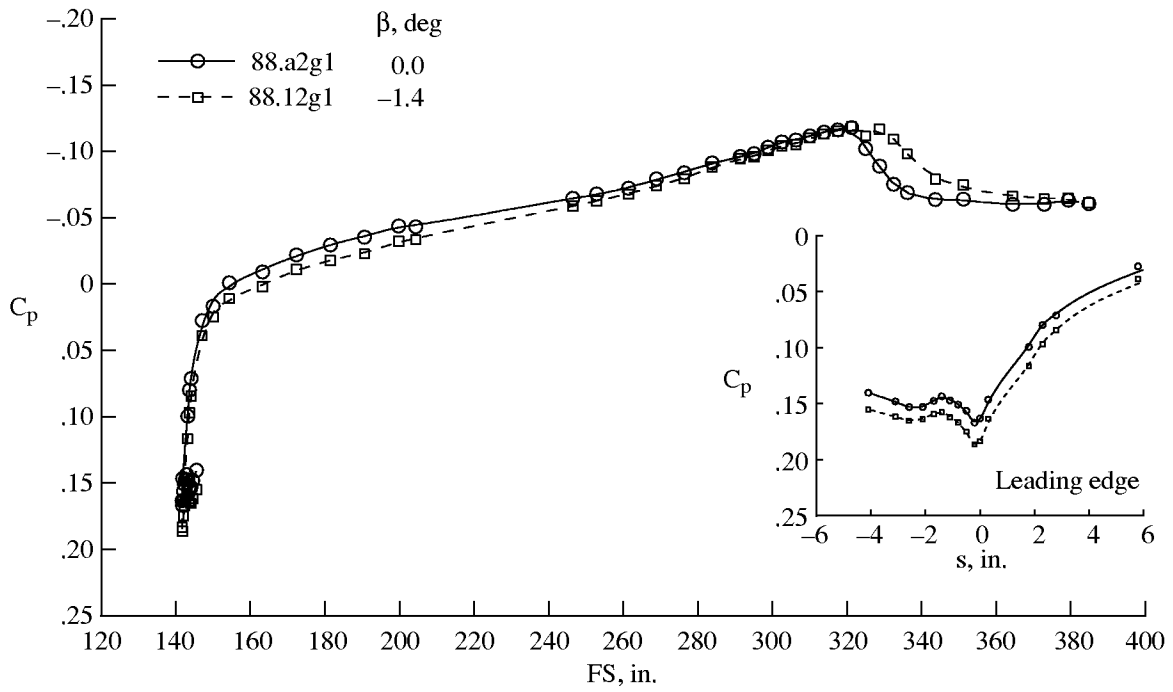
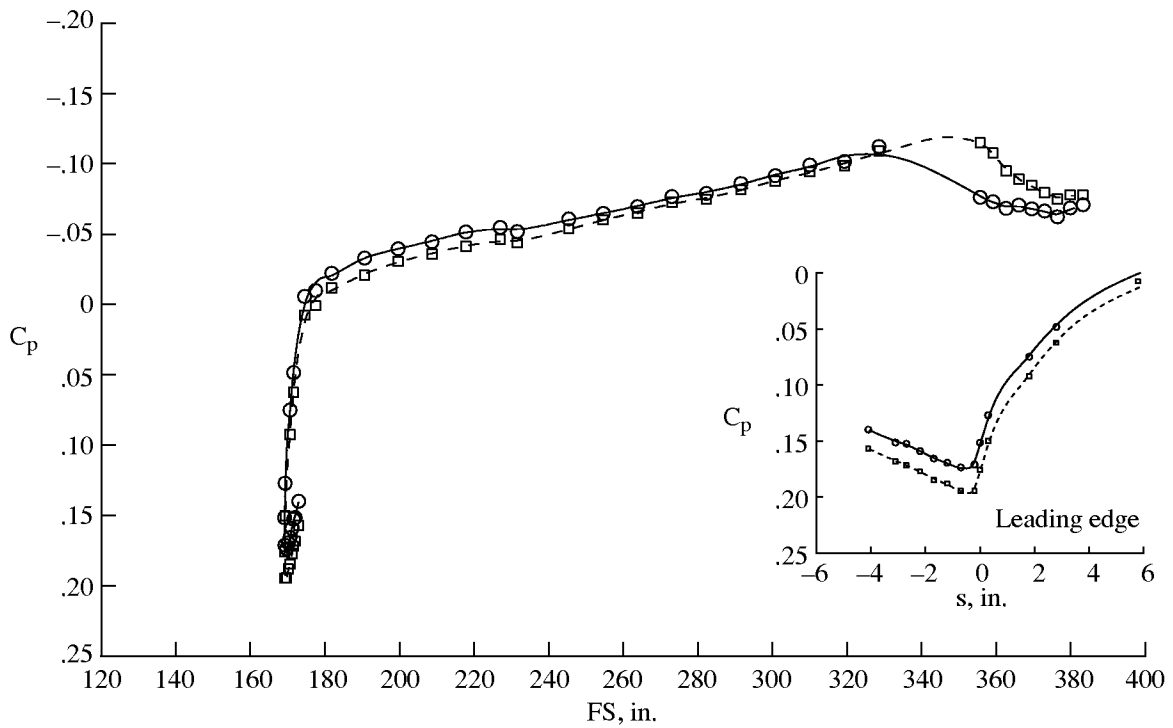


Figure F12. $C_{p_{max}}$ and attachment-line location variations with angle of sideslip for Mach 2 with fence 1; $h = 53\,000$ ft; $\alpha = 3.4^\circ$.

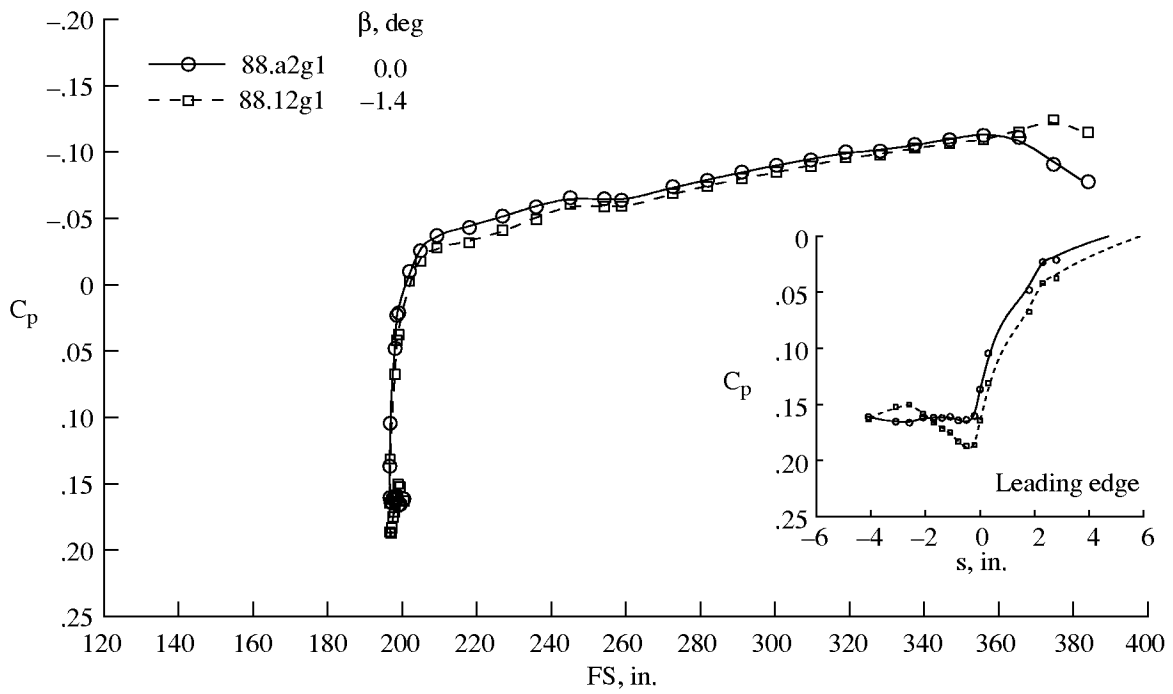


(a) BL 50.

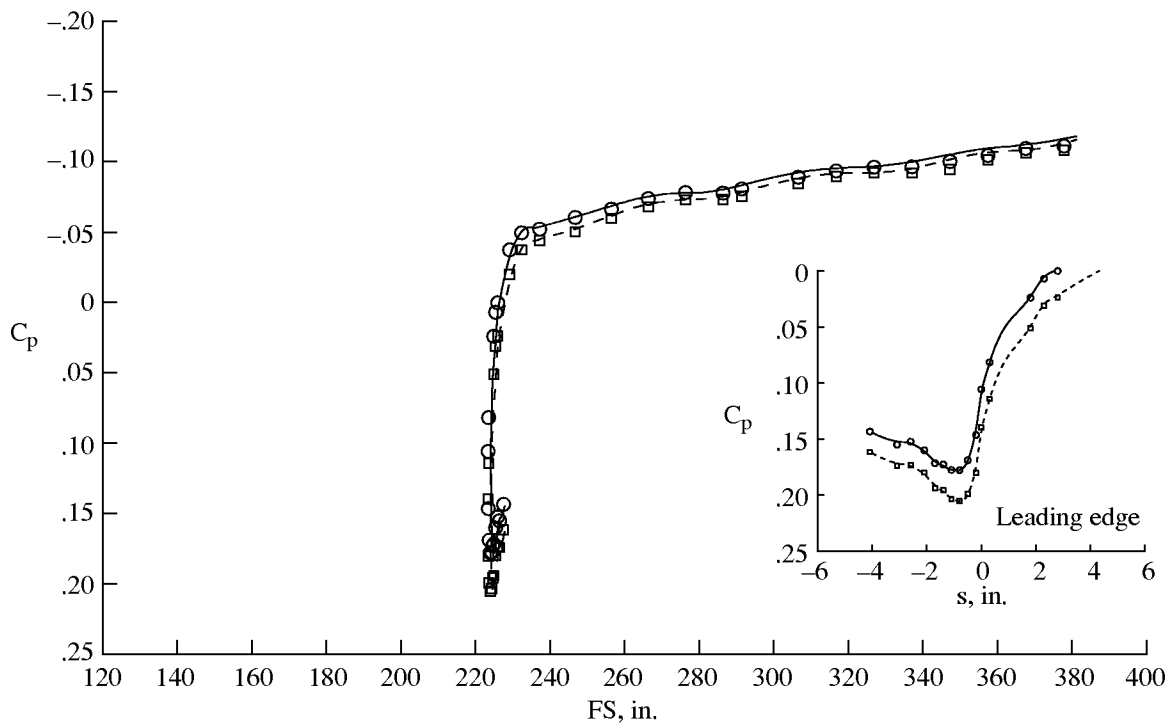


(b) BL 60.

Figure F13. Measured C_p distributions for two different angles of sideslip at Mach 2.0 with fence 1; $h = 53\,000$ ft; $\alpha = 3.4^\circ$.

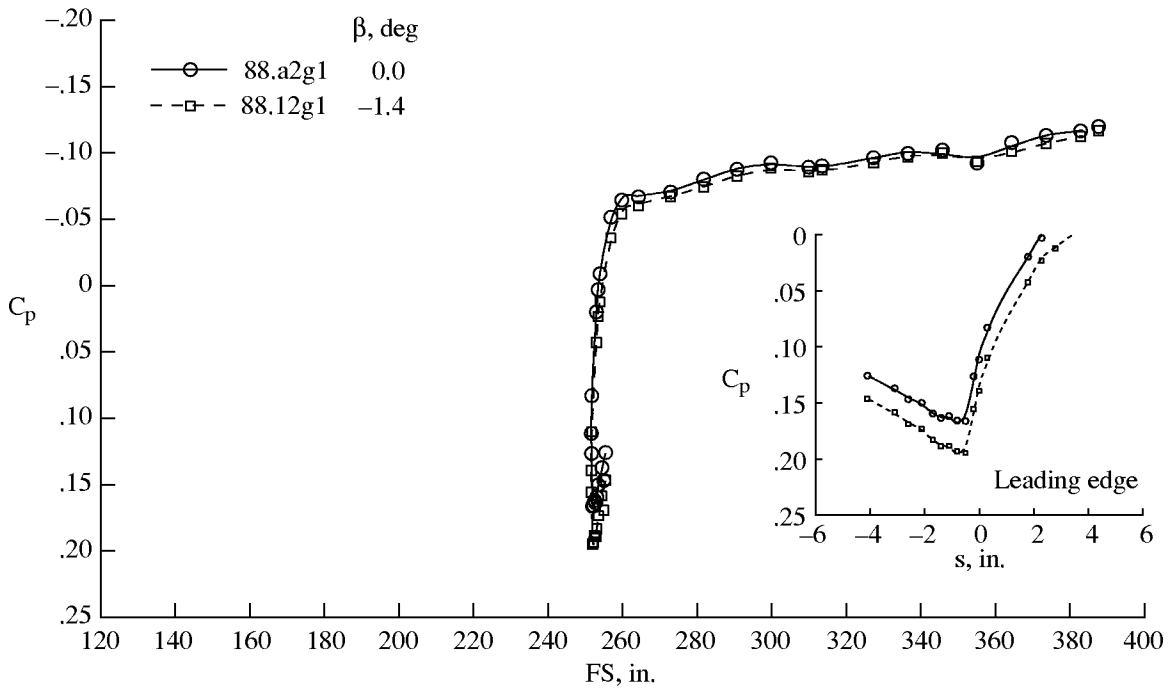


(c) BL 70.

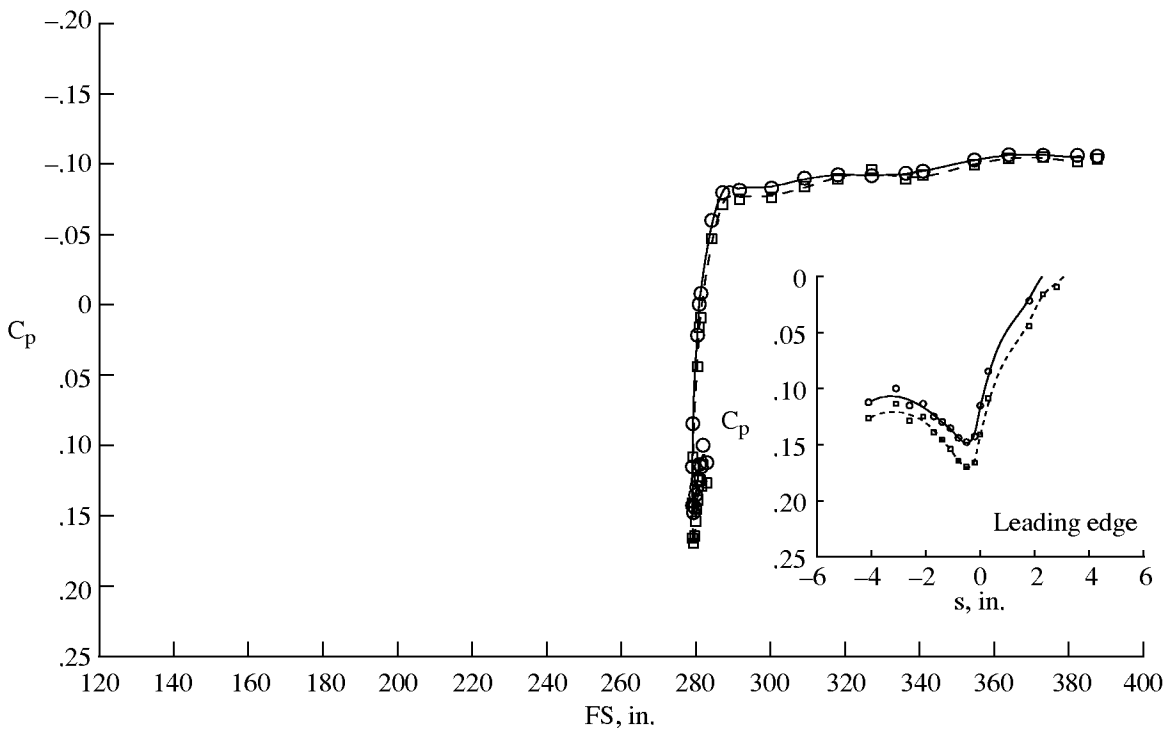


(d) BL 80.

Figure F13. Continued.



(e) BL 90.



(f) BL 100.

Figure F13. Concluded.

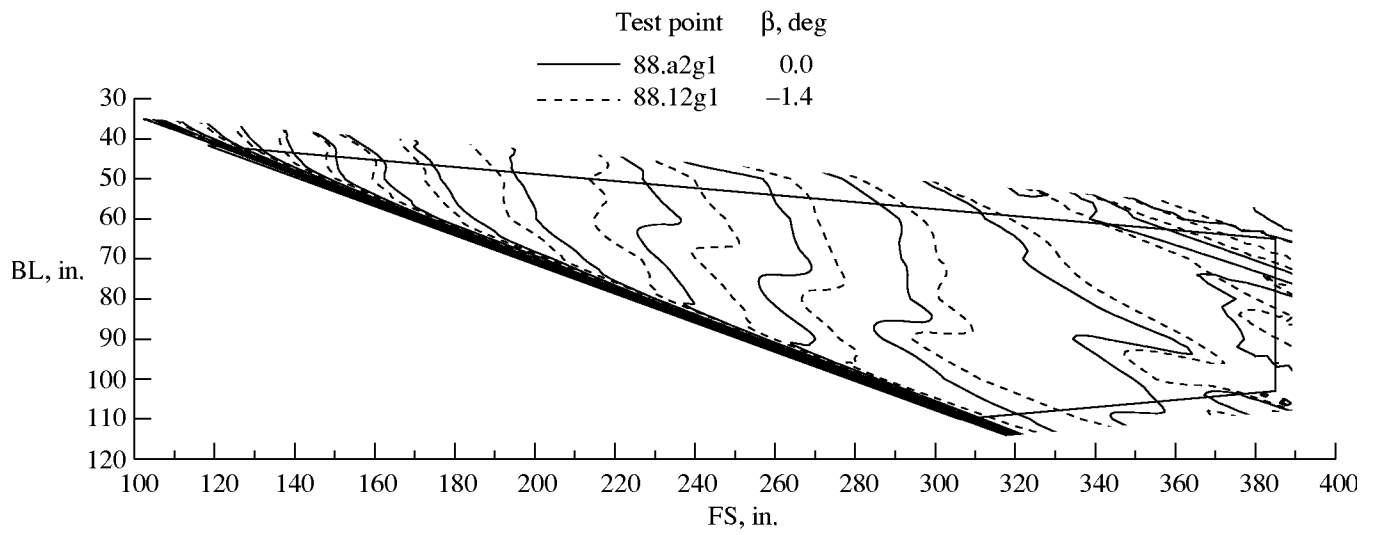


Figure F14. Isobar comparison for different angles of sideslip at Mach 2 with fence 1; $h = 53\,000$ ft; $\alpha = 3.4^\circ$.

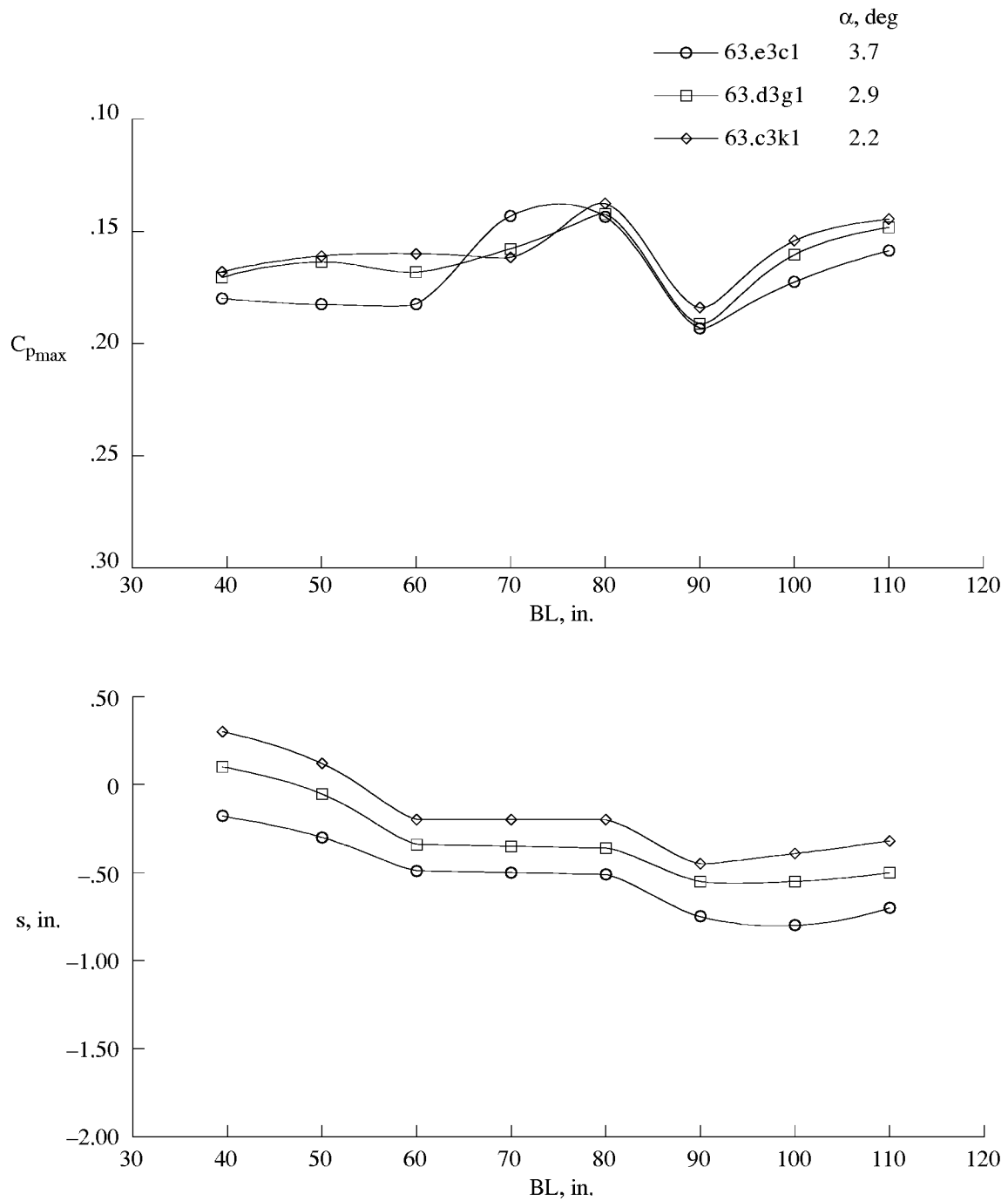
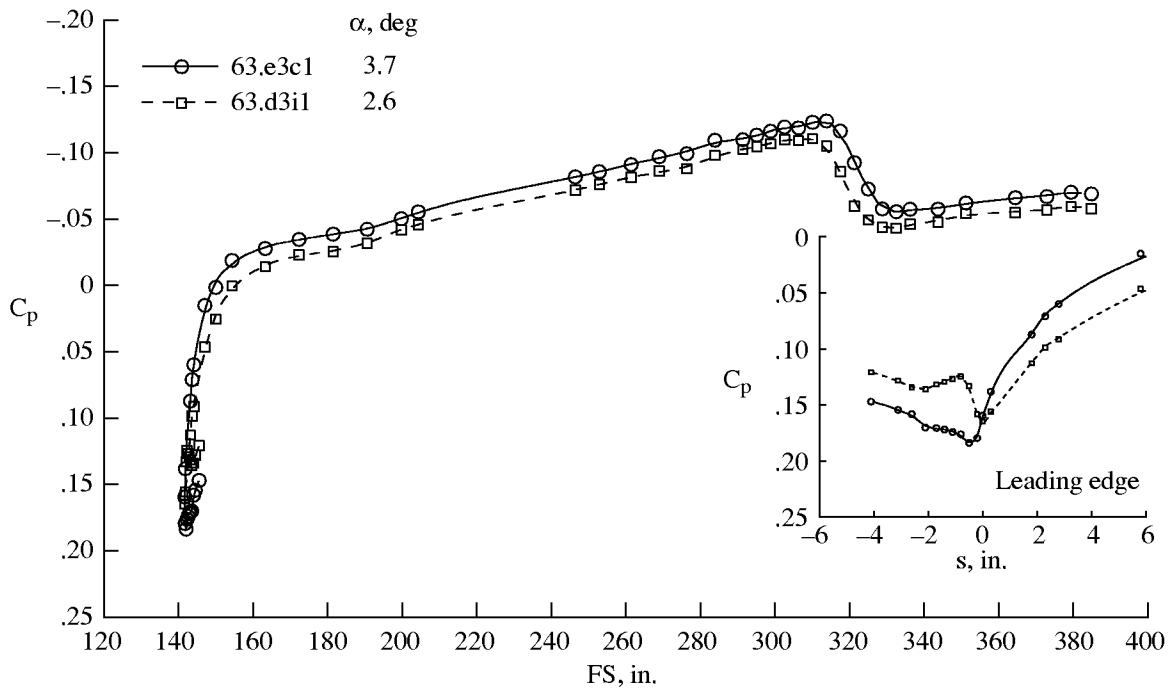
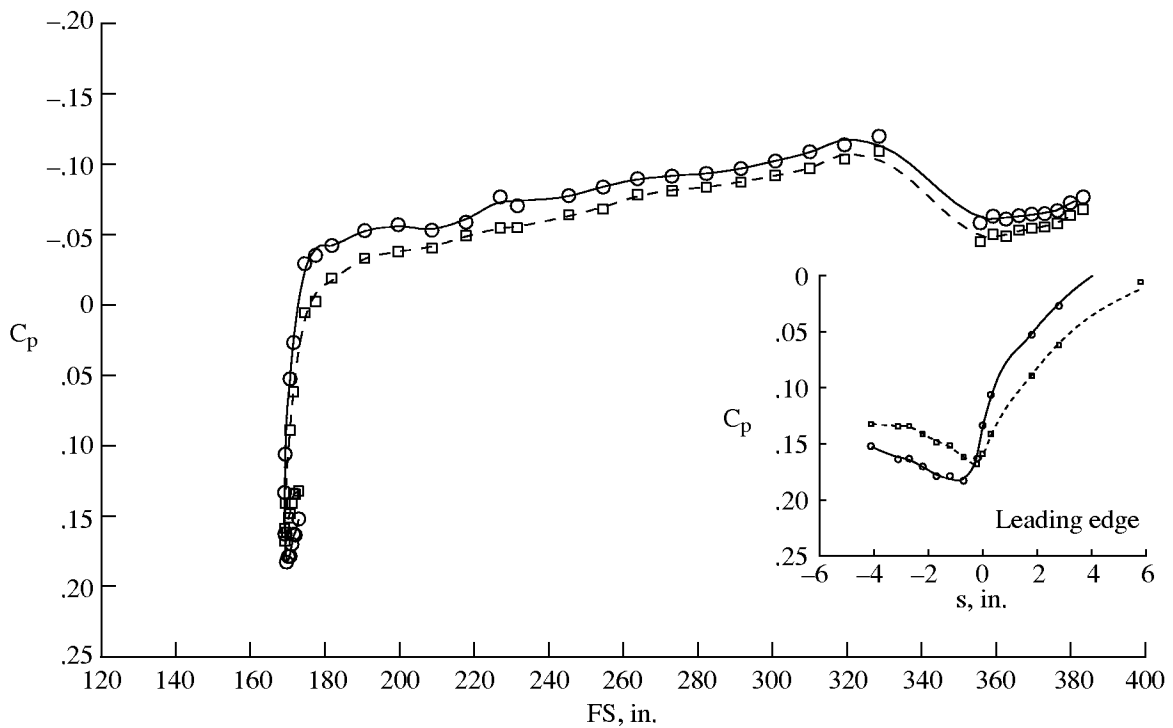


Figure F15. $C_{p_{max}}$ and attachment-line location variations with angle of attack for Mach 1.9 for fence 2; $h = 50\,000$ ft; $\beta = 0^\circ$.

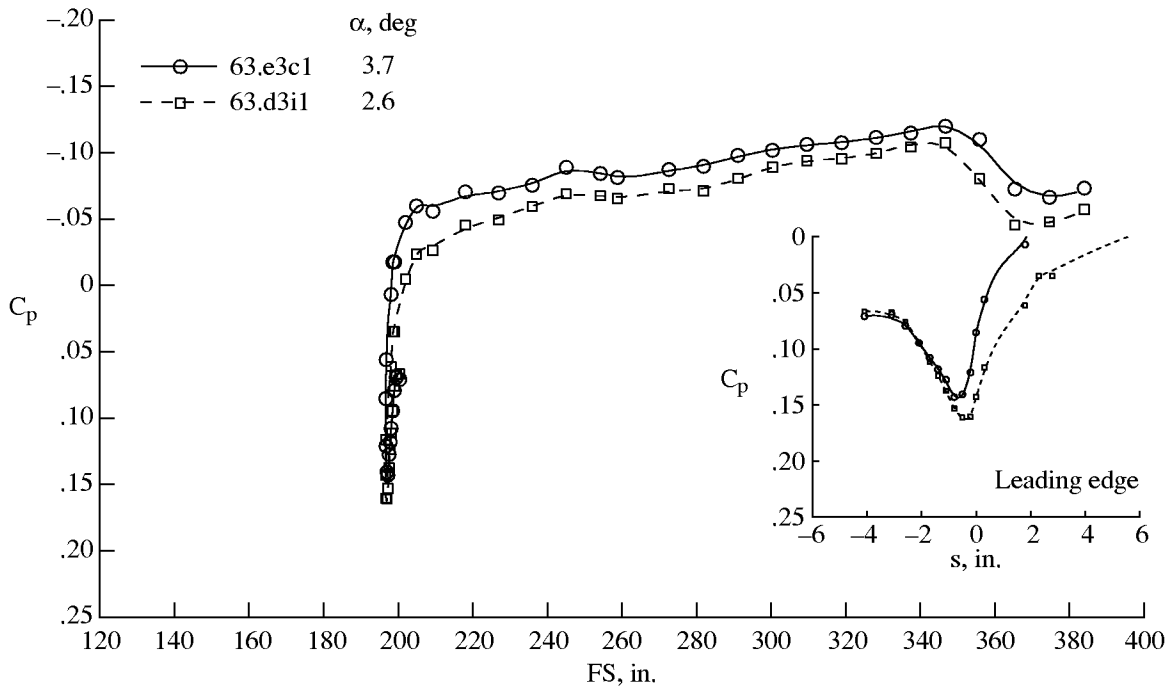


(a) BL 50.

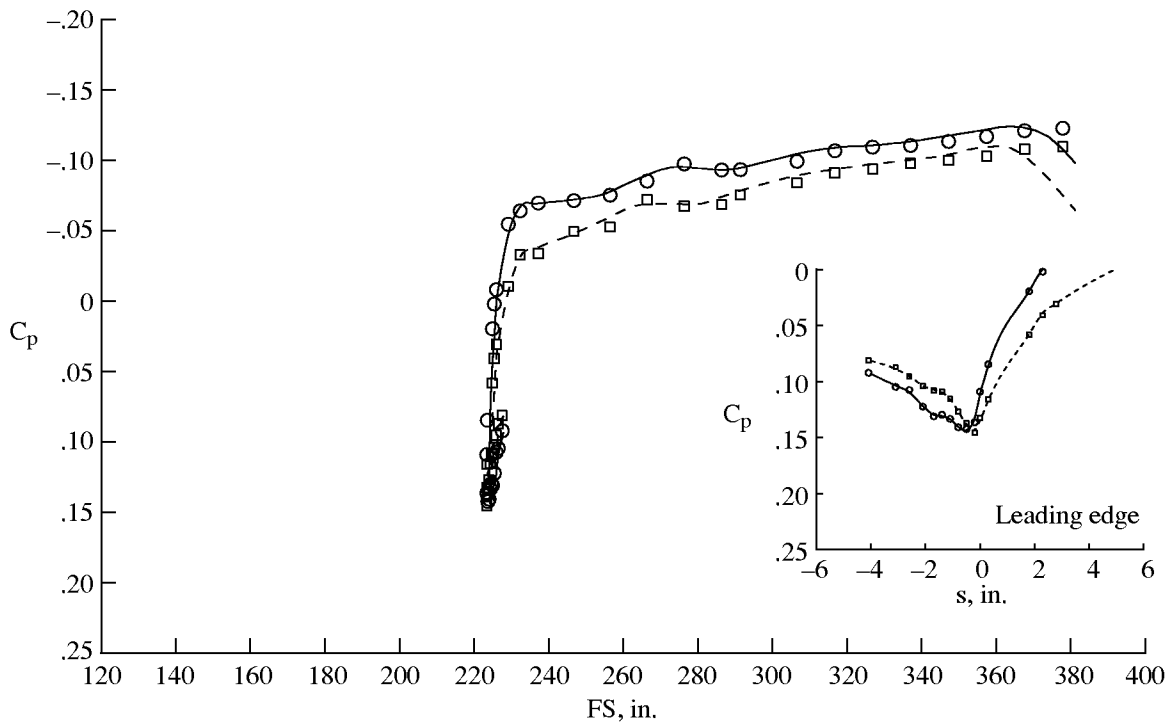


(b) BL 60.

Figure F16. Measured C_p distributions for two different angles of attack at Mach 1.9 with fence 2; $h = 50\,000$ ft; $\beta = 0^\circ$.

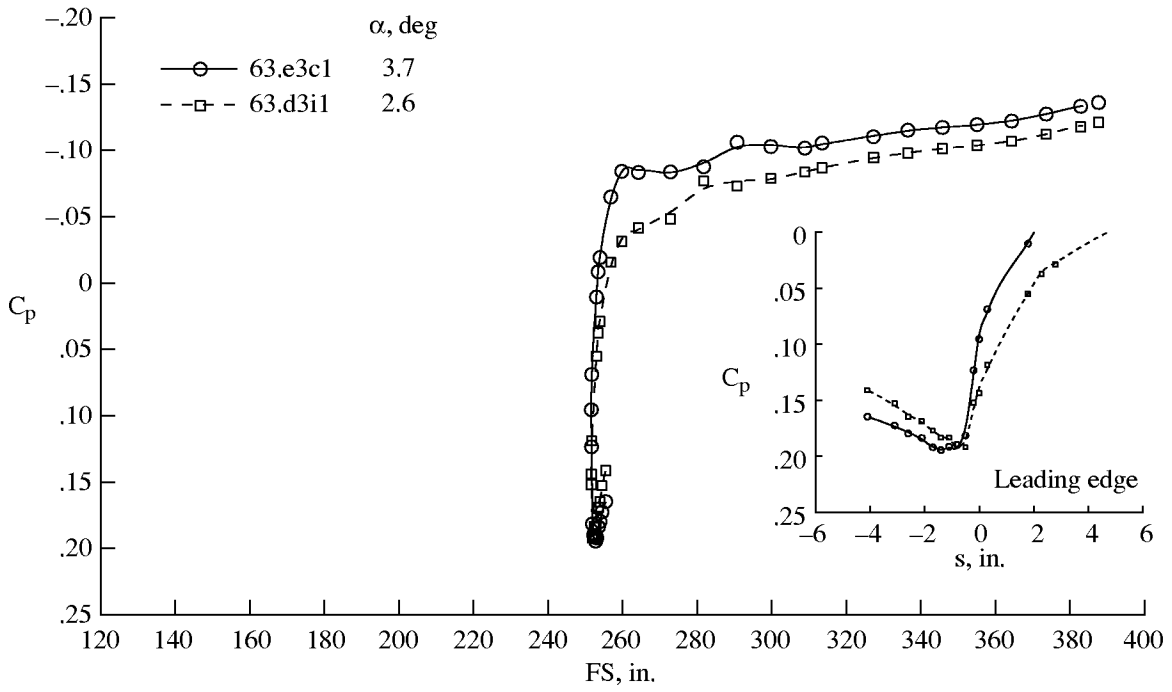


(c) BL 70.

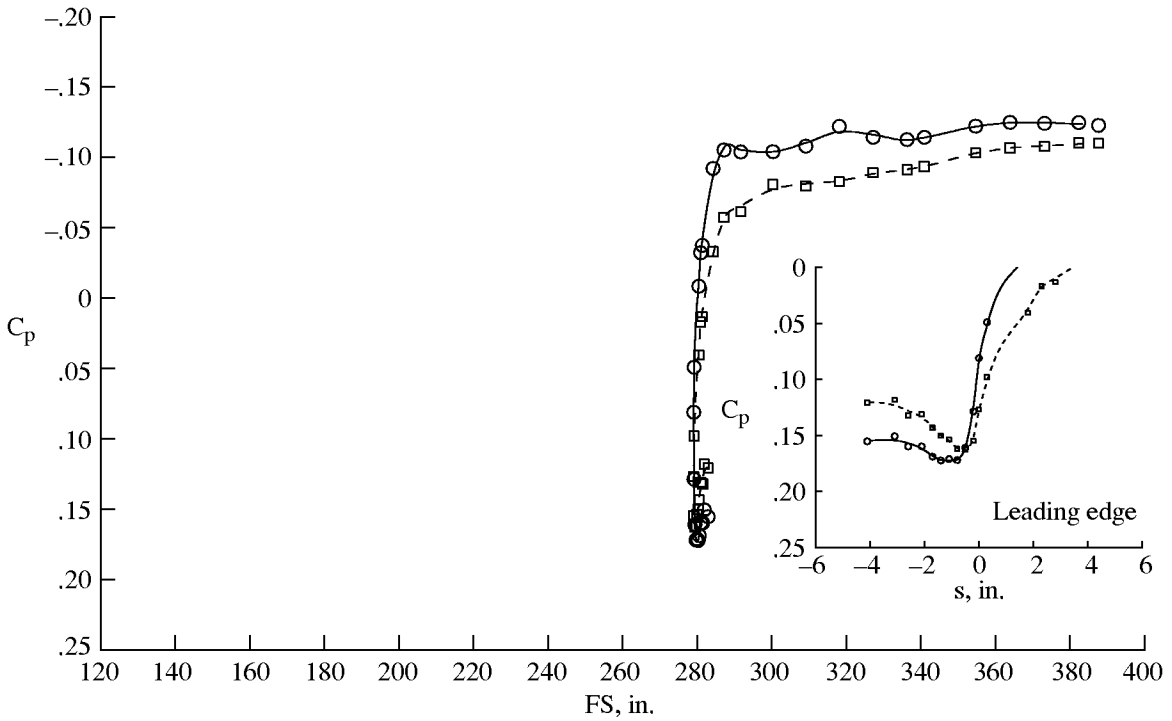


(d) BL 80.

Figure F16. Continued.



(e) BL 90.



(f) BL 100.

Figure F16. Concluded.

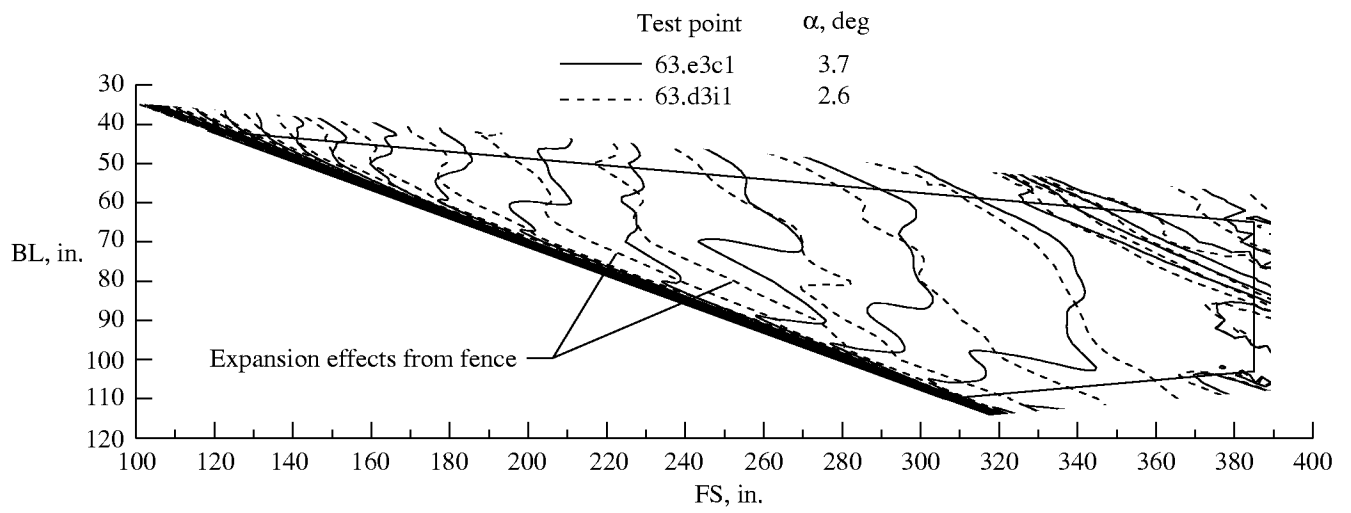


Figure F17. Isobar comparison for different angles of attack at Mach 1.9 with fence 2; $h = 50\,000$ ft; $\beta = 0.0^\circ$.

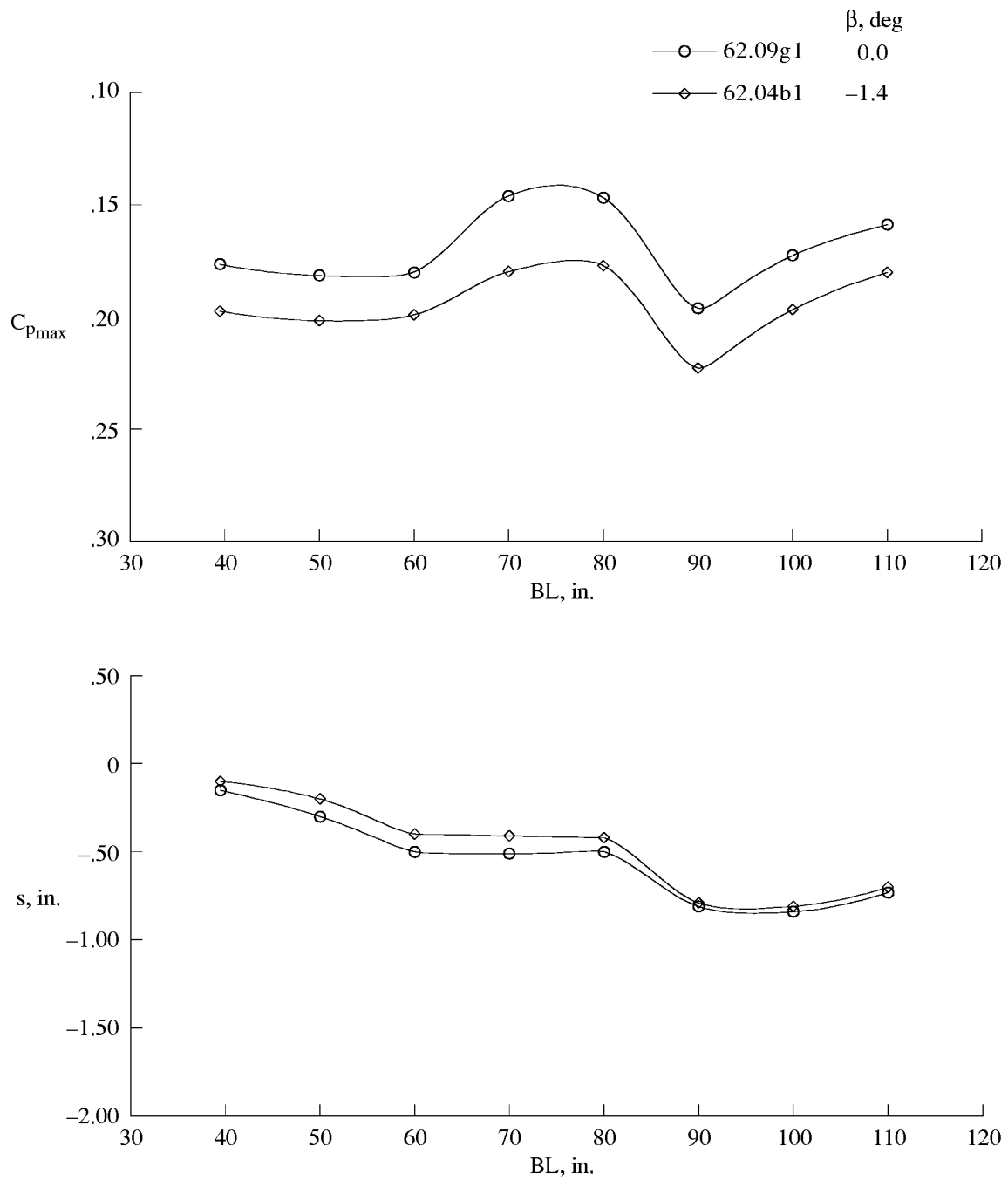
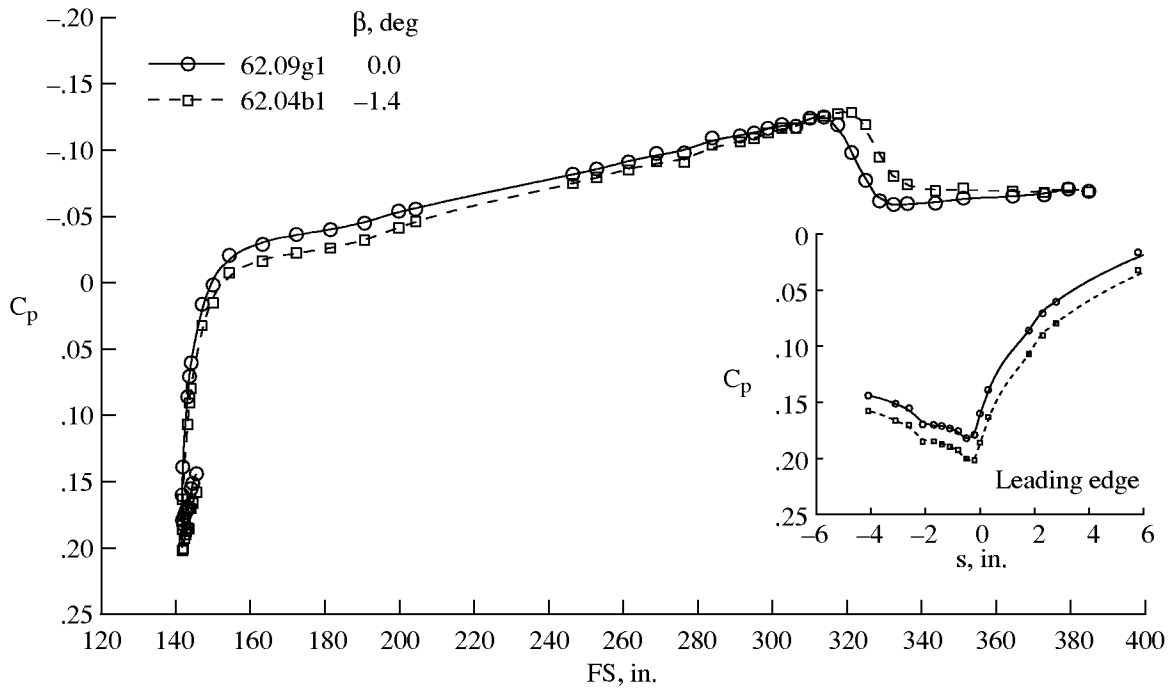
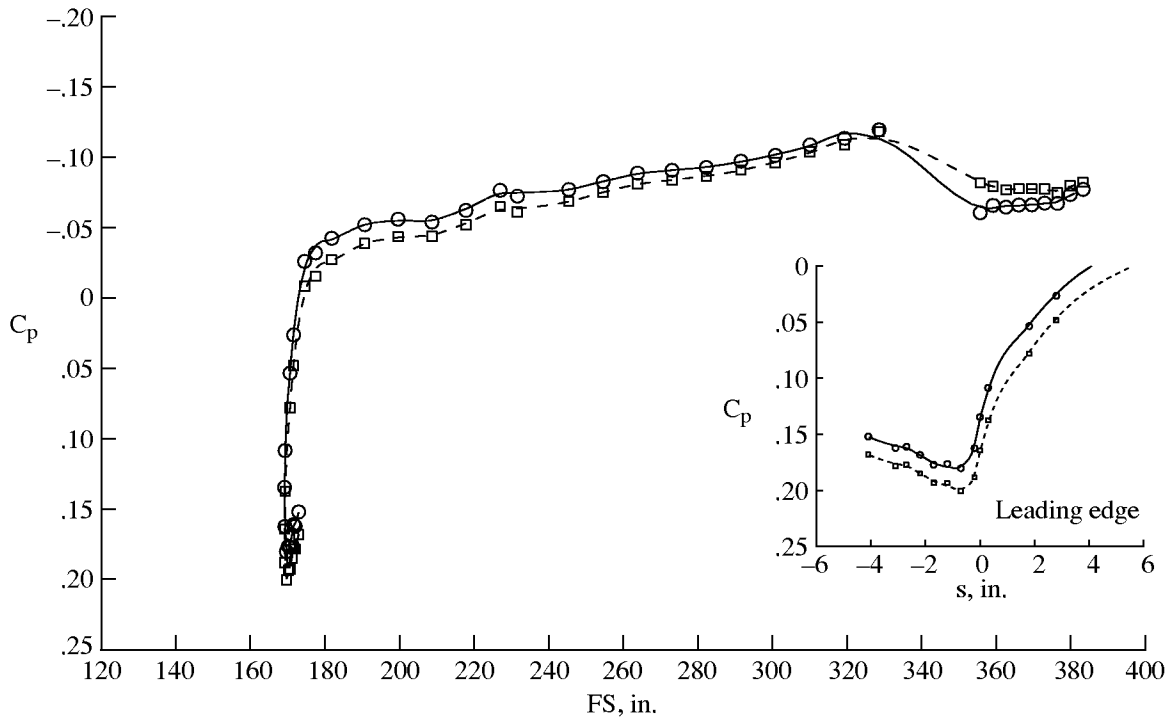


Figure F18. $C_{P_{max}}$ and attachment-line location variations with angle of sideslip for Mach 1.9 with fence 2; $h = 50\,000$ ft; $\alpha = 3.7^\circ$.

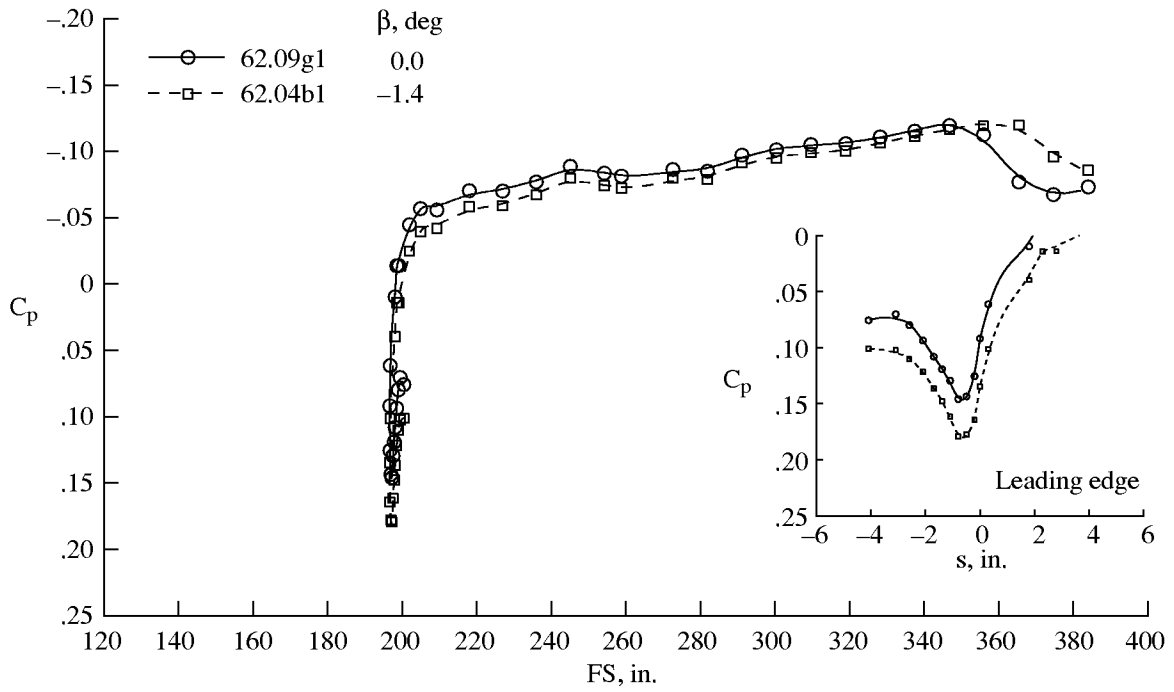


(a) BL 50.

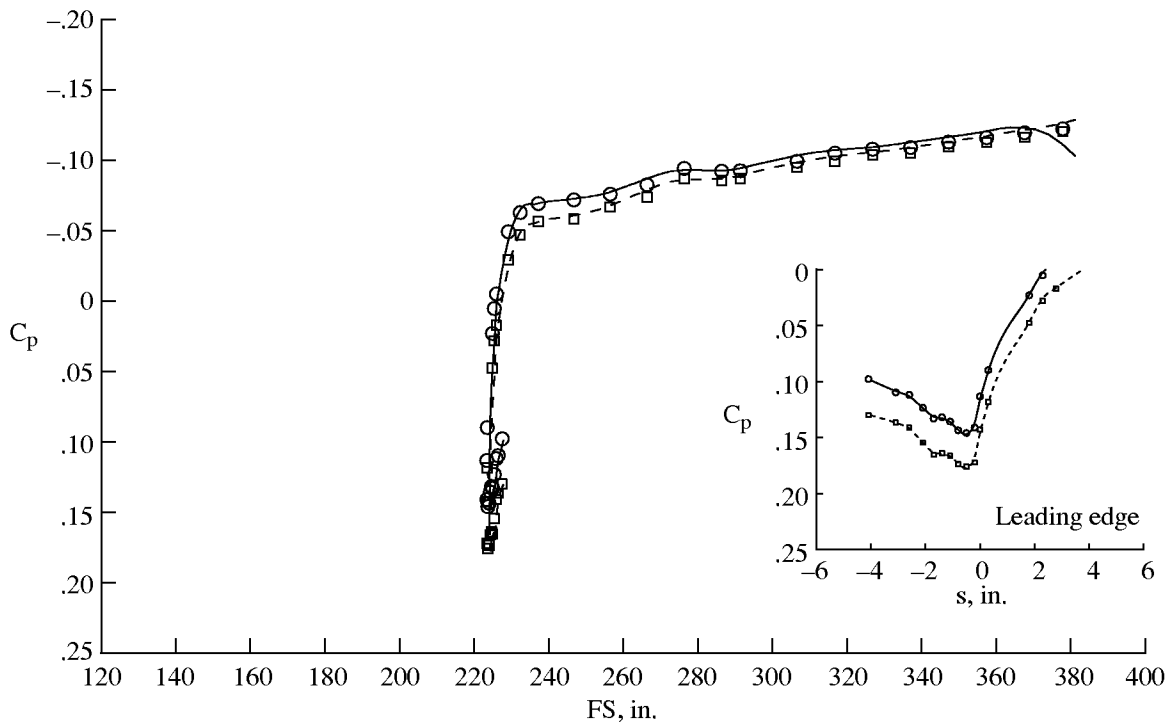


(b) BL 60.

Figure F19. Measured C_p distributions for two different angles of sideslip at Mach 1.9 with fence 2; $h = 50\,000$ ft; $\alpha = 3.7^\circ$.

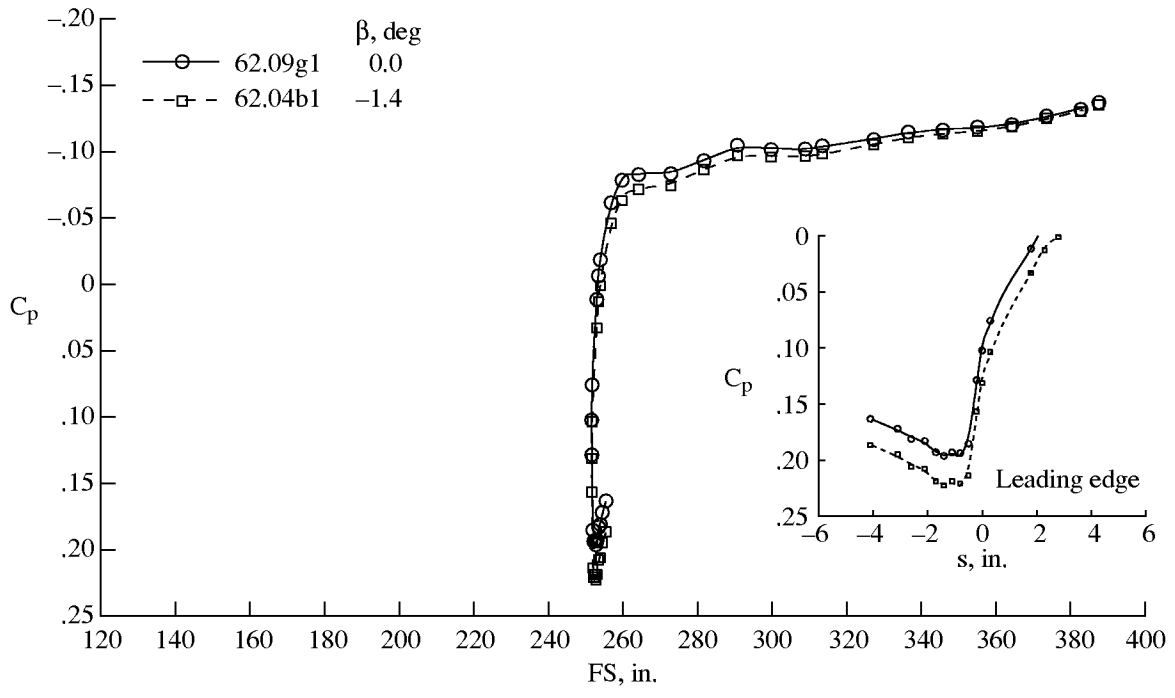


(c) BL 70.

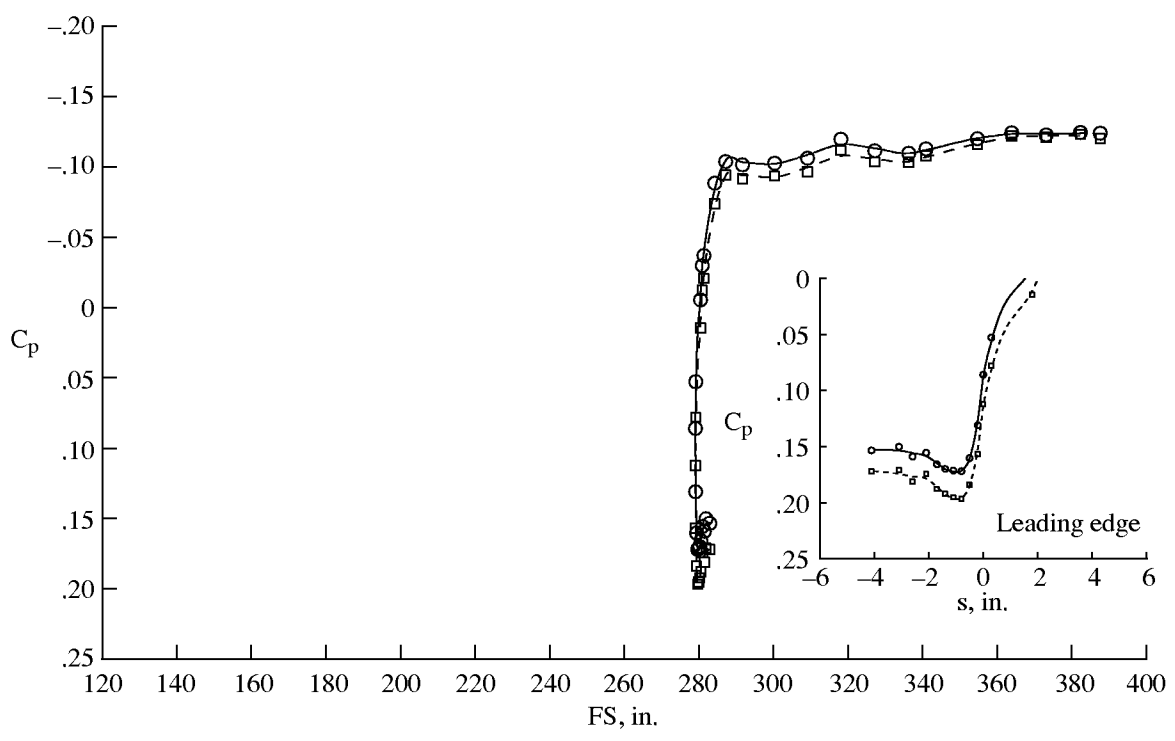


(d) BL 80.

Figure F19. Continued.



(e) BL 90.



(f) BL 100.

Figure F19. Concluded.

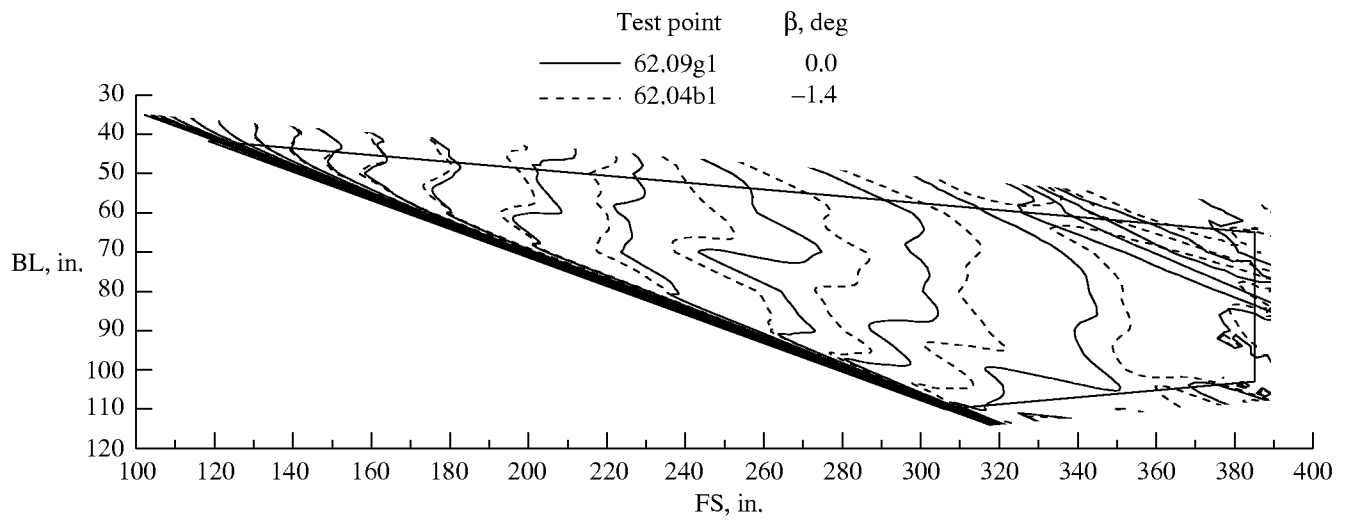


Figure F20. Isobar comparison for different angles of sideslip at Mach 1.9 with fence 2; $h = 50\,000$ ft; $\alpha = 3.7^\circ$.

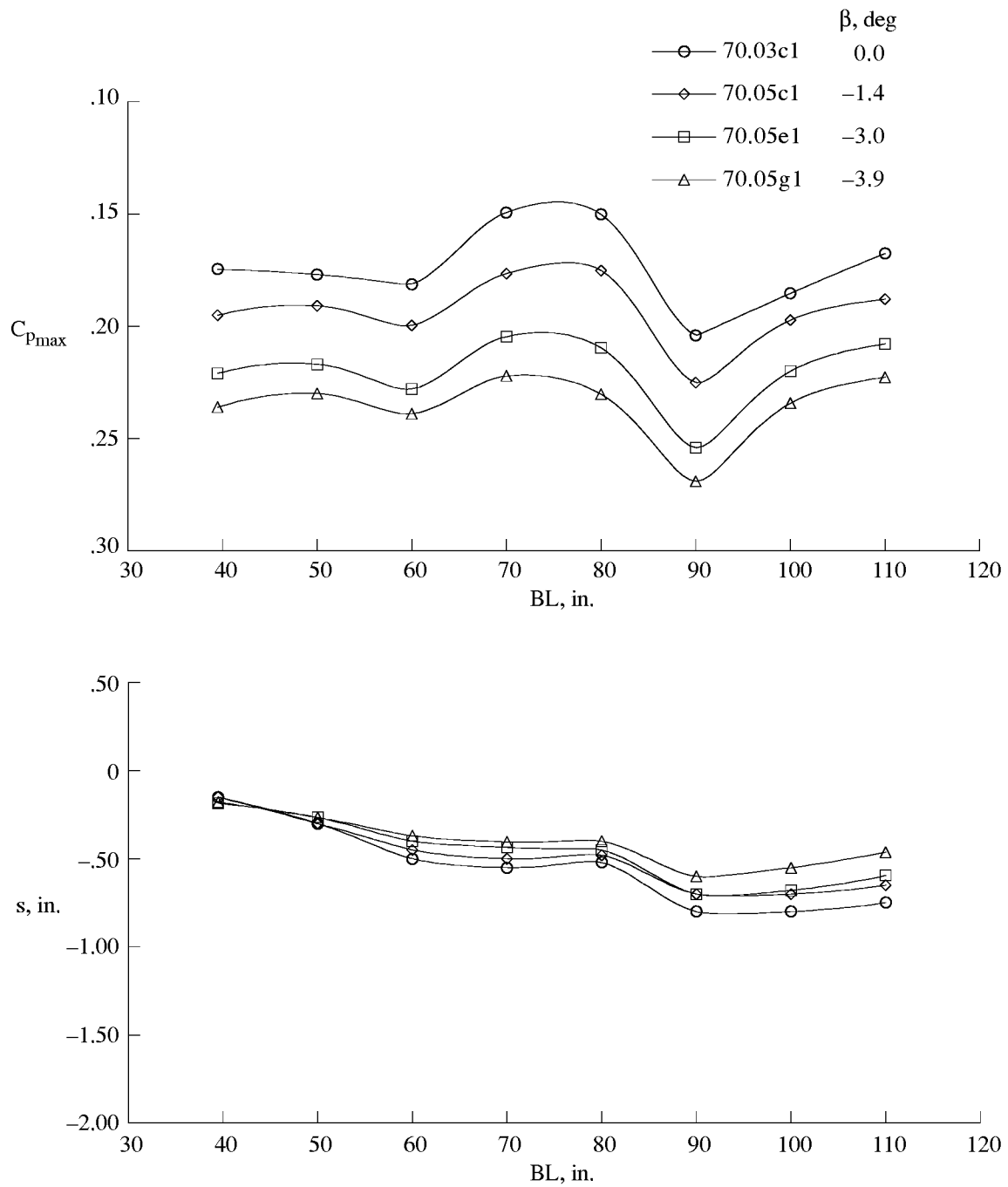
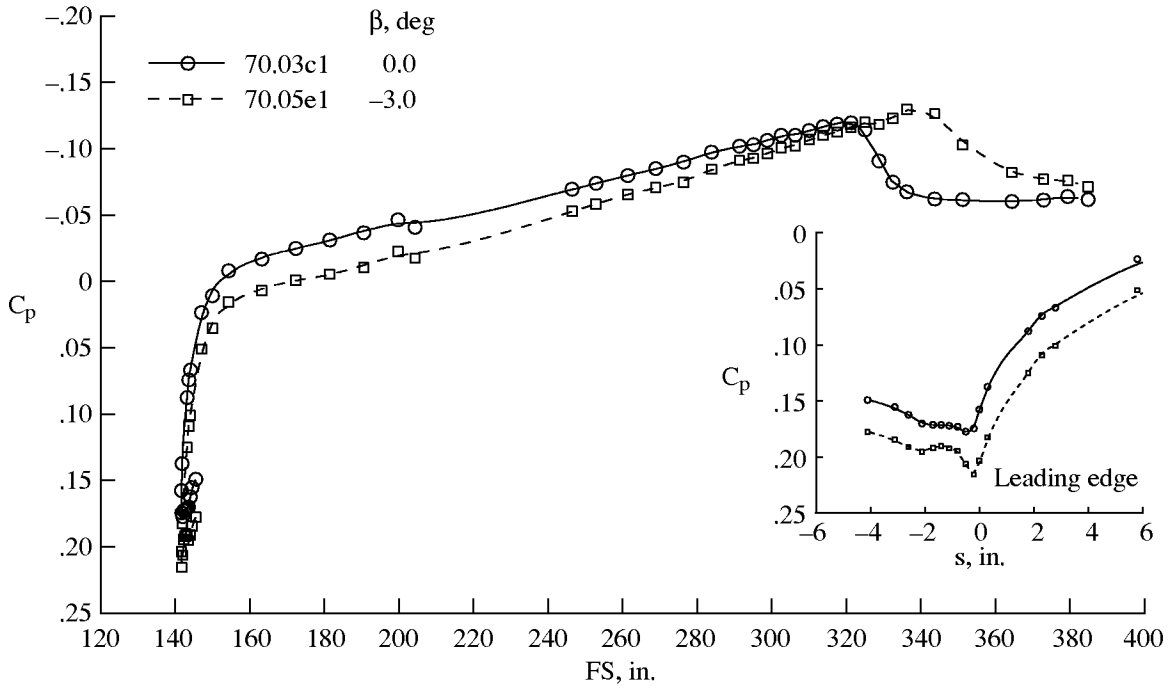
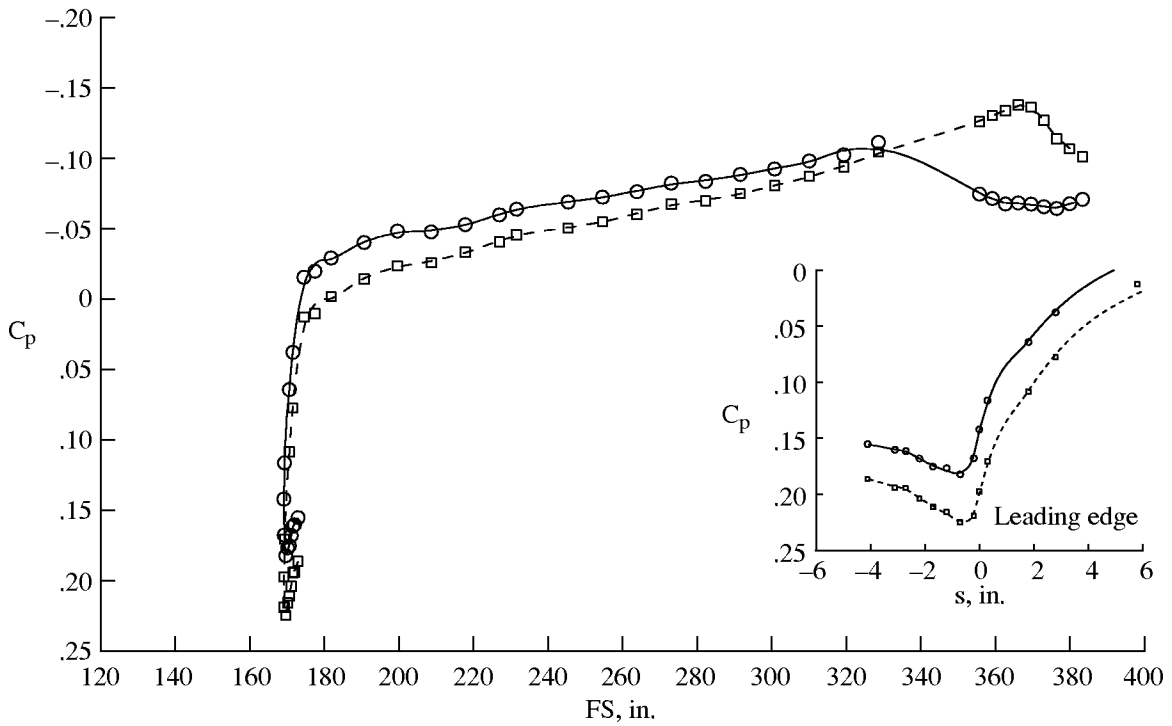


Figure F21. $C_{p_{max}}$ and attachment-line location variations with angle of sideslip for Mach 2 with fence 2; $h = 50000$ ft; $\alpha = 3.7^\circ$.

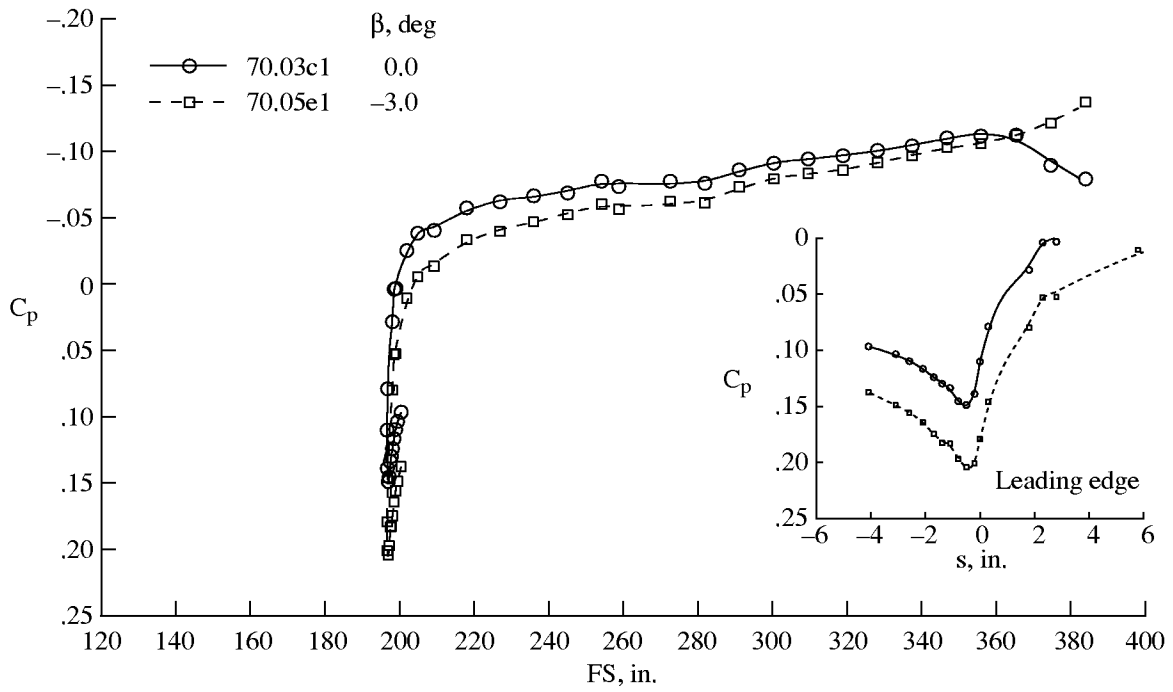


(a) BL 50.

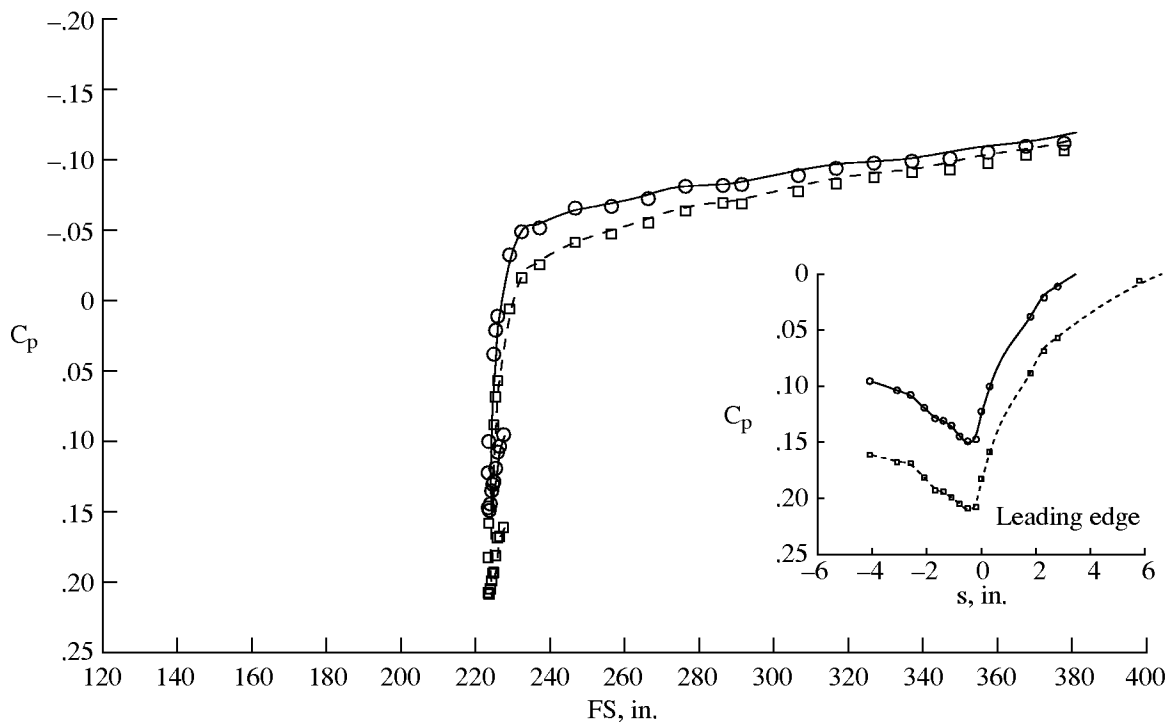


(b) BL 60.

Figure F22. Measured C_p distributions for two different angles of sideslip at Mach 2.0 with fence 2; $h = 50\,000$ ft; $\alpha = 3.7^\circ$.

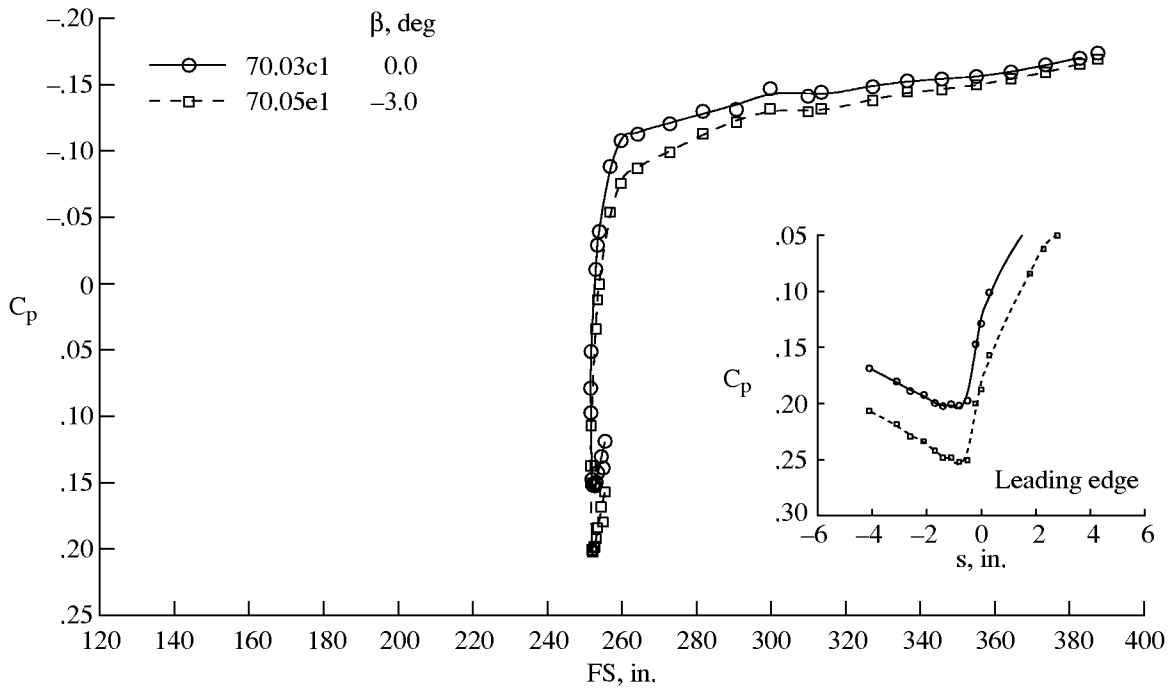


(c) BL 70.

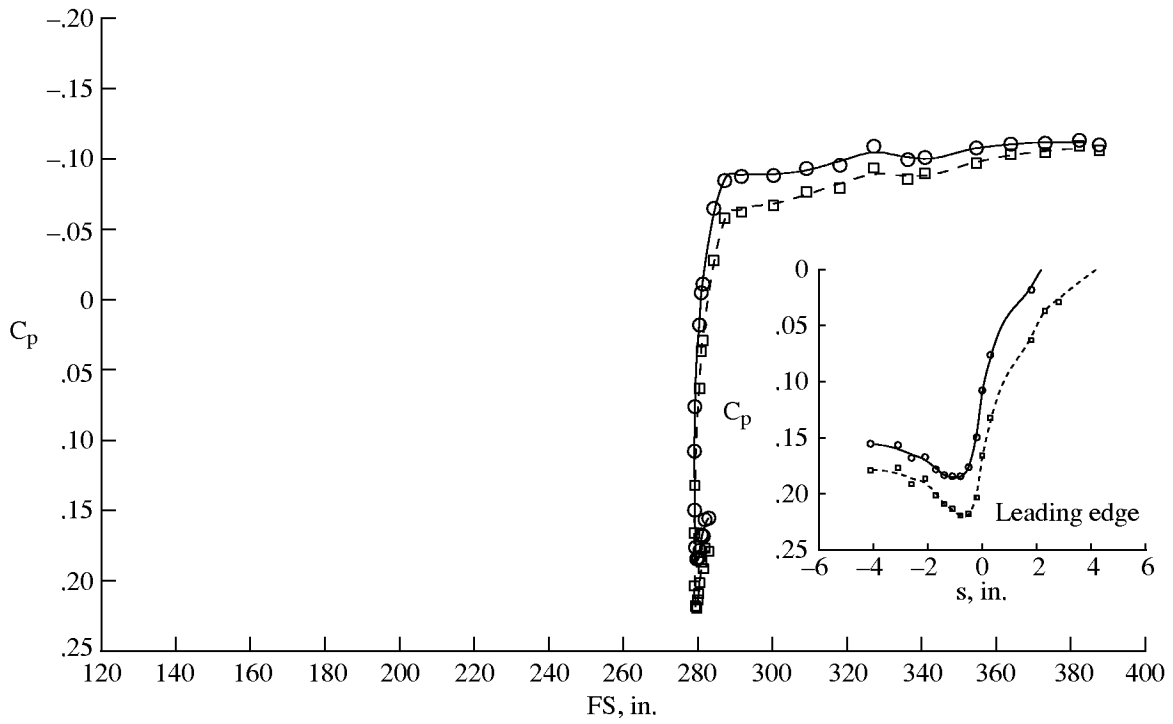


(d) BL 80.

Figure F22. Continued.



(e) BL 90.



(f) BL 100.

Figure F22. Concluded.

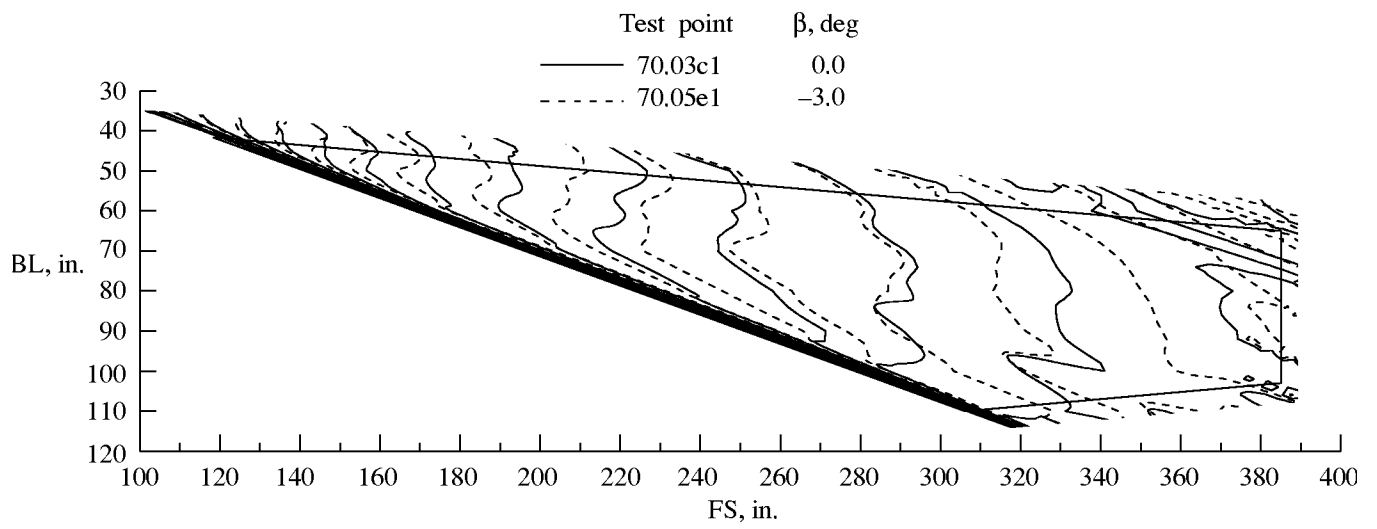


Figure F23. Isobar comparison for different angles of sideslip at Mach 2 with fence 2; $h = 50\,000$ ft; $\alpha = 3.7^\circ$.

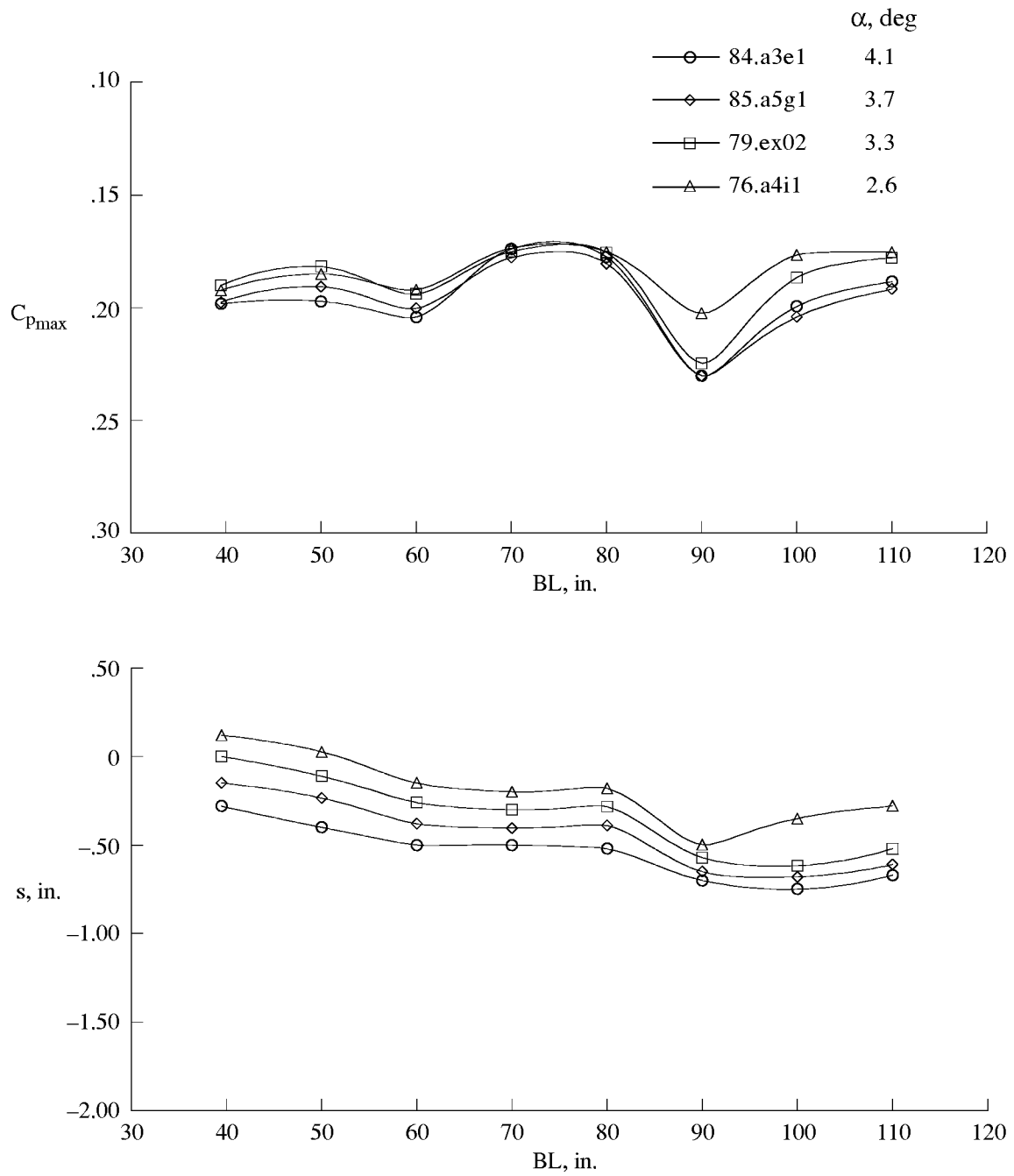
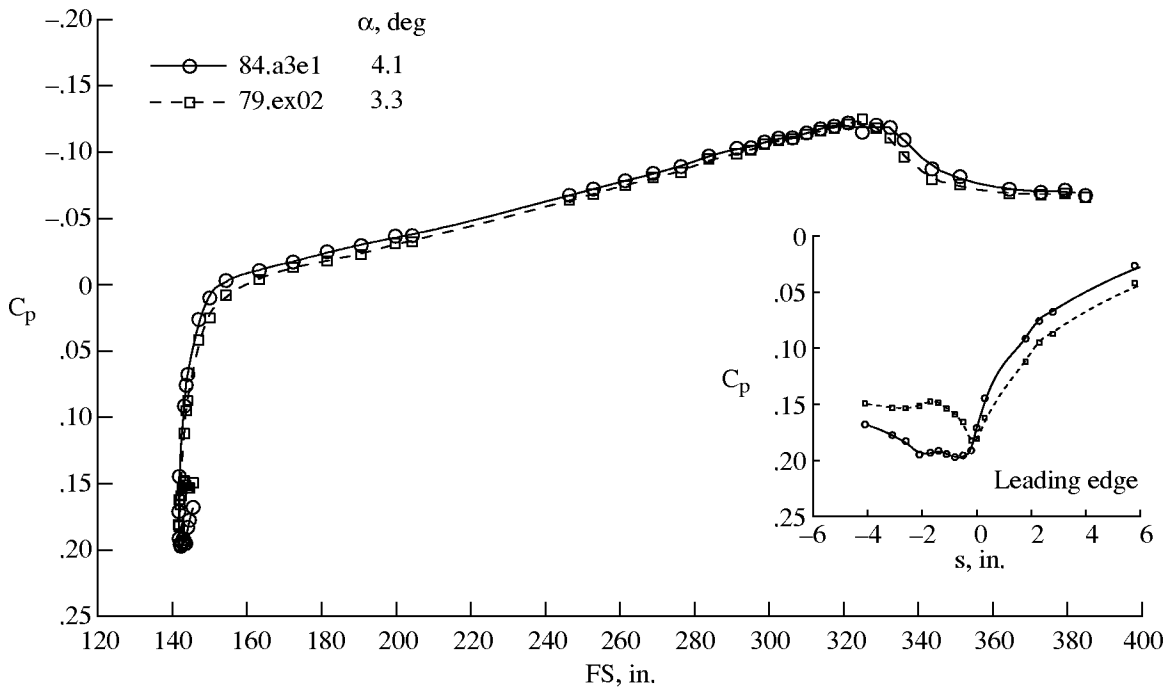
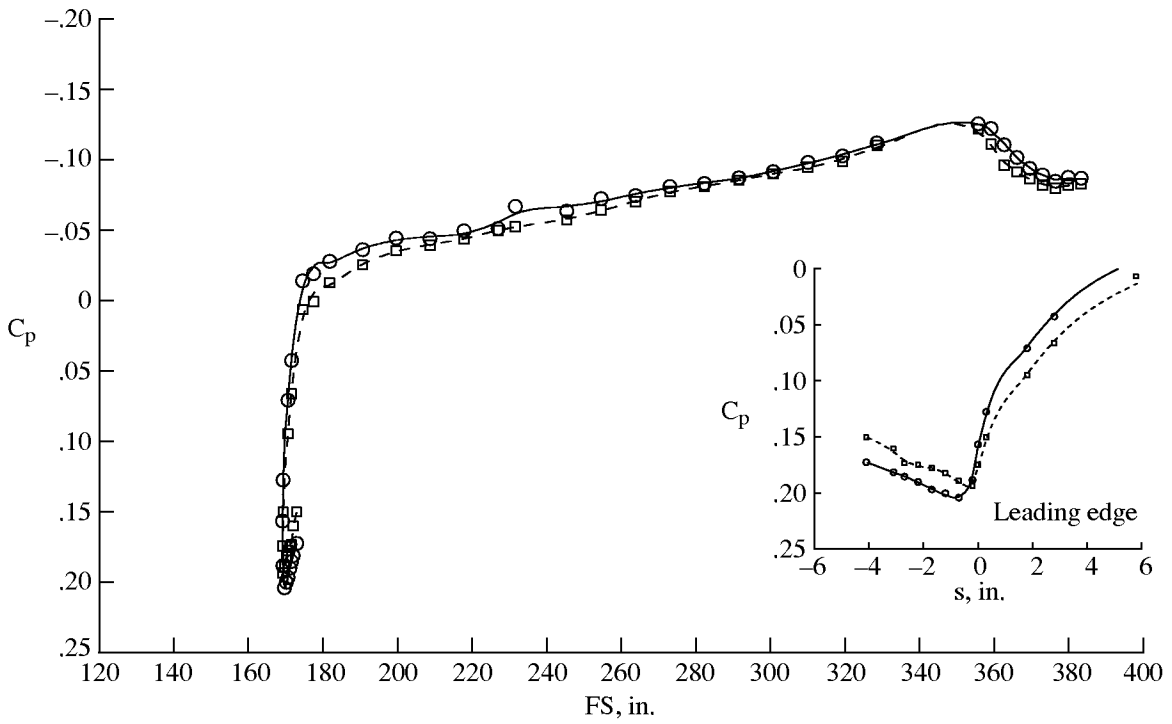


Figure F24. $C_{p_{max}}$ and attachment-line location variations with angle of attack for Mach 2 with fence 2; $h = 53\,000$ ft; $\beta = -1.5^\circ$.

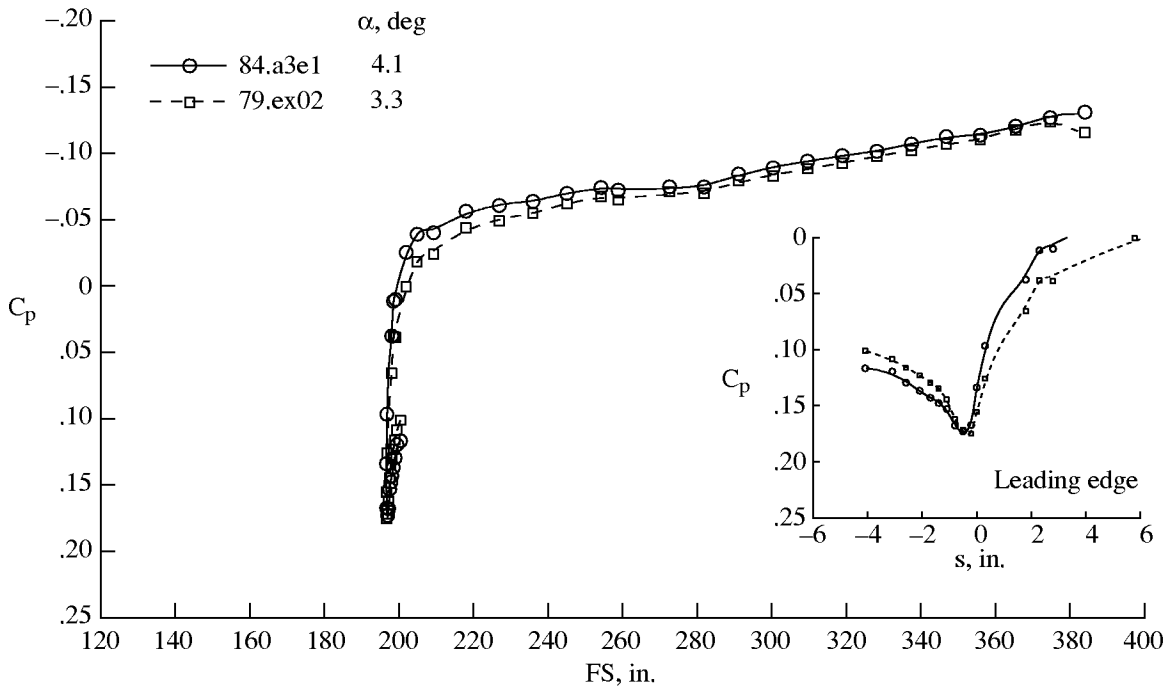


(a) BL 50.

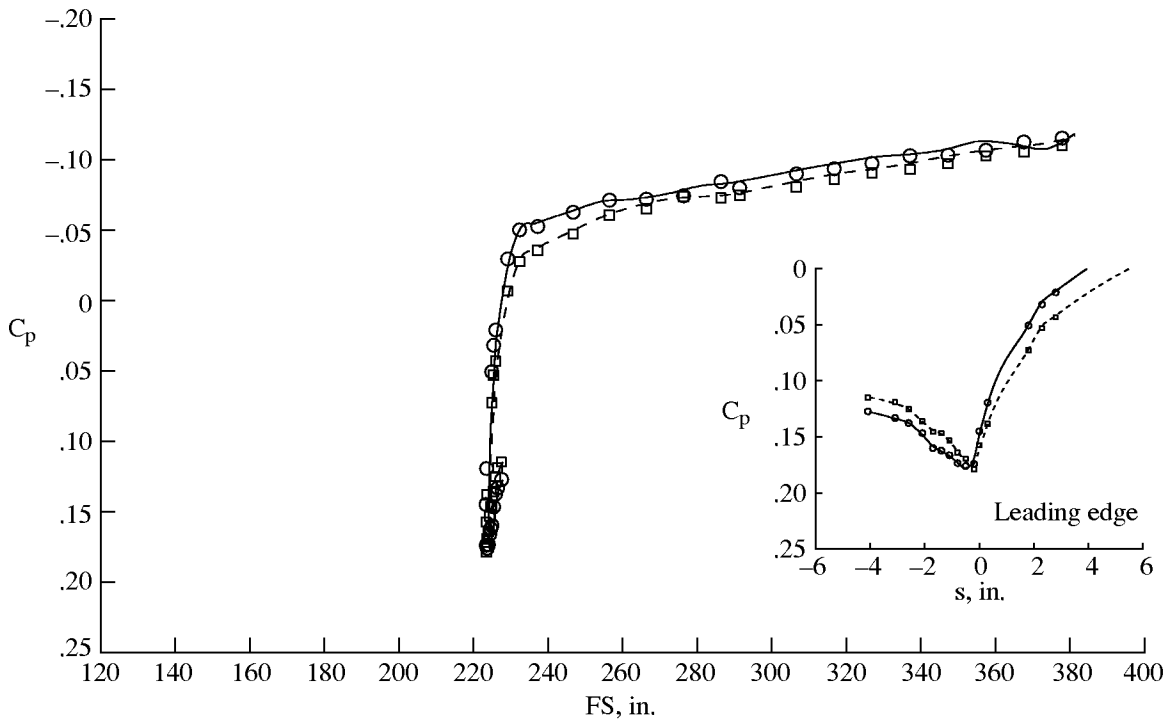


(b) BL 60.

Figure F25. Measured C_p distributions for two different angles of attack at Mach 2.0 with fence 2; $h = 50\,000$ ft; $\alpha = 3.7^\circ$.

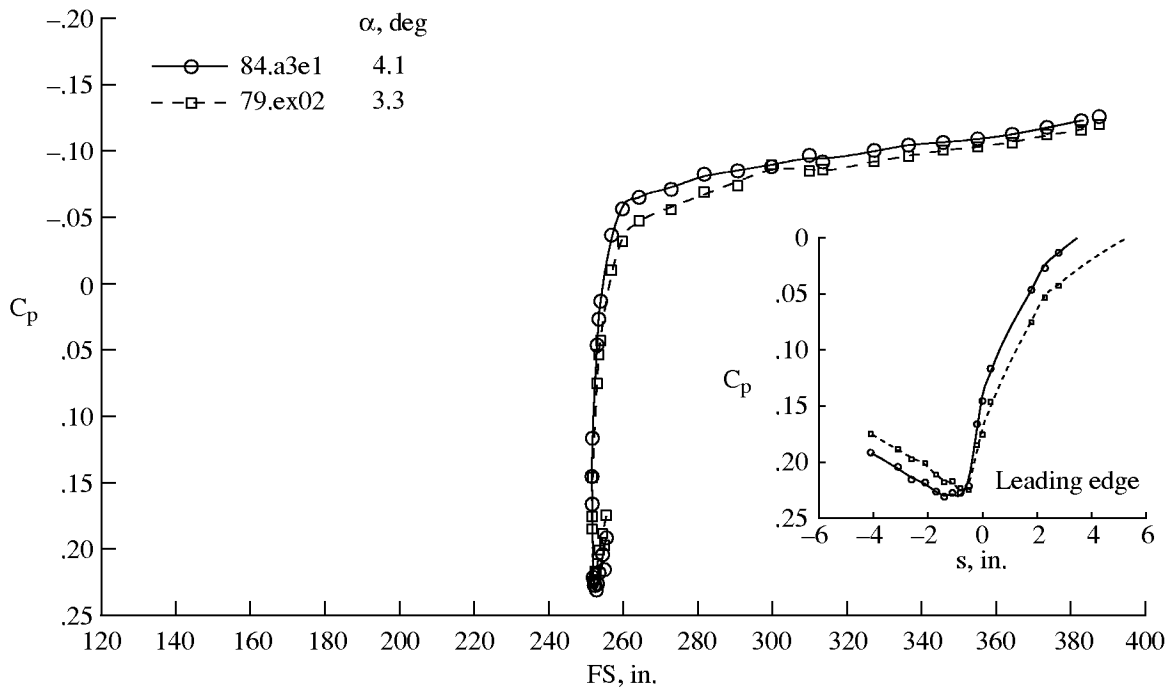


(c) BL 70.

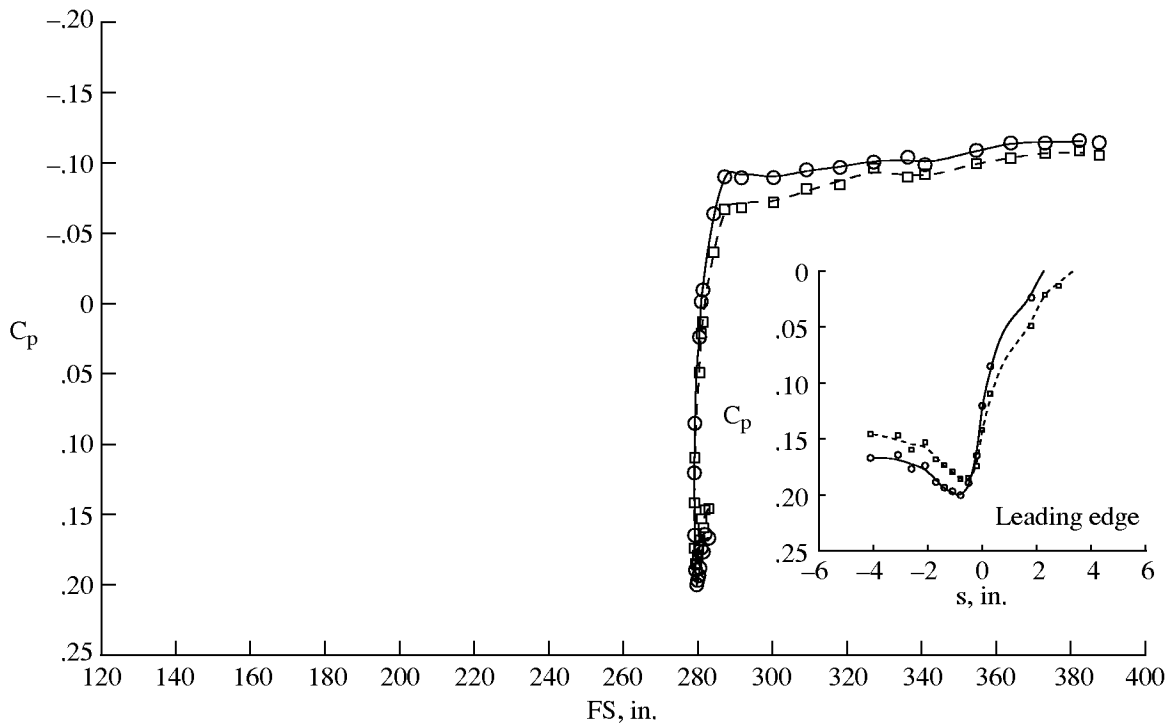


(d) BL 80.

Figure F25. Continued.



(e) BL 90.



(f) BL 100.

Figure F25. Concluded.

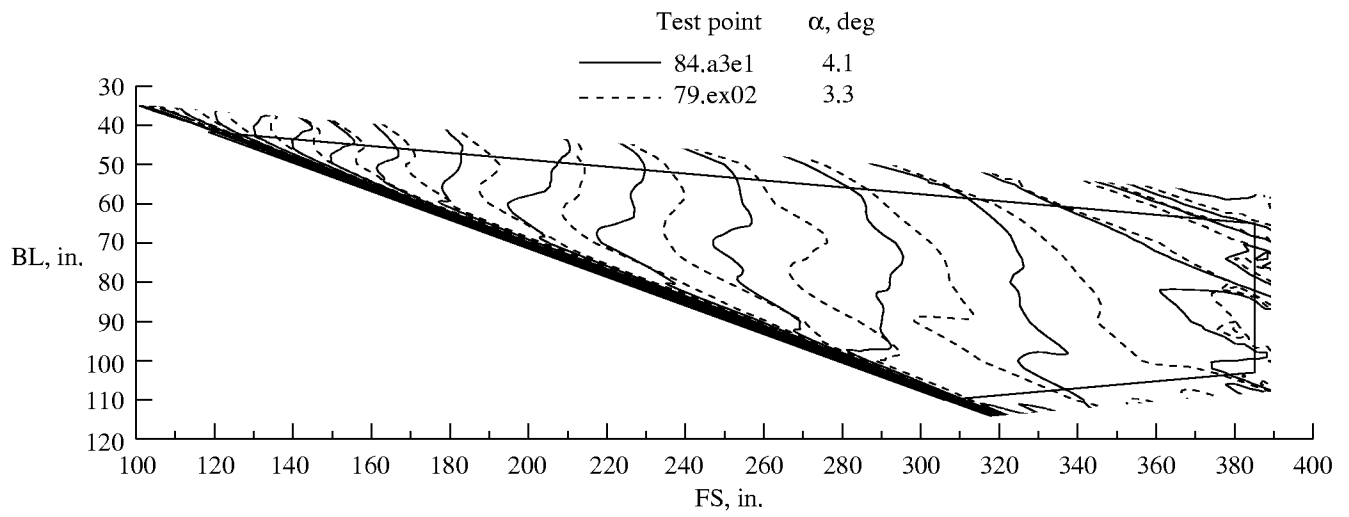


Figure F26. Isobar comparison for different angles of attack at Mach 2 with fence 2; $h = 53\,000$ ft; $\beta = -1.5^\circ$.

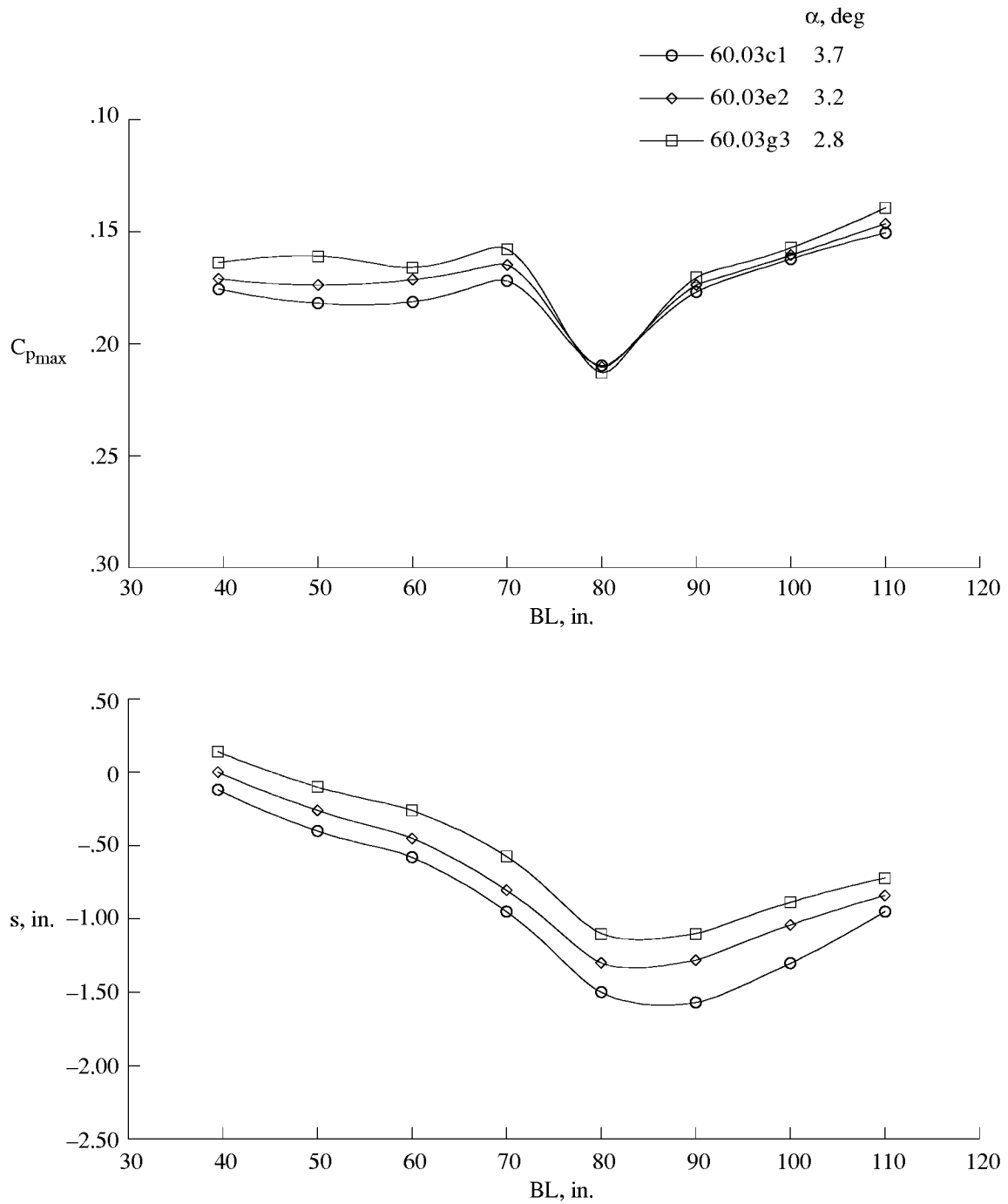


Figure F27. $C_{p_{max}}$ and attachment-line location variations with angle of attack without shock fence at Mach 1.9; $h = 50\,000$ ft; $\beta = 0^\circ$.

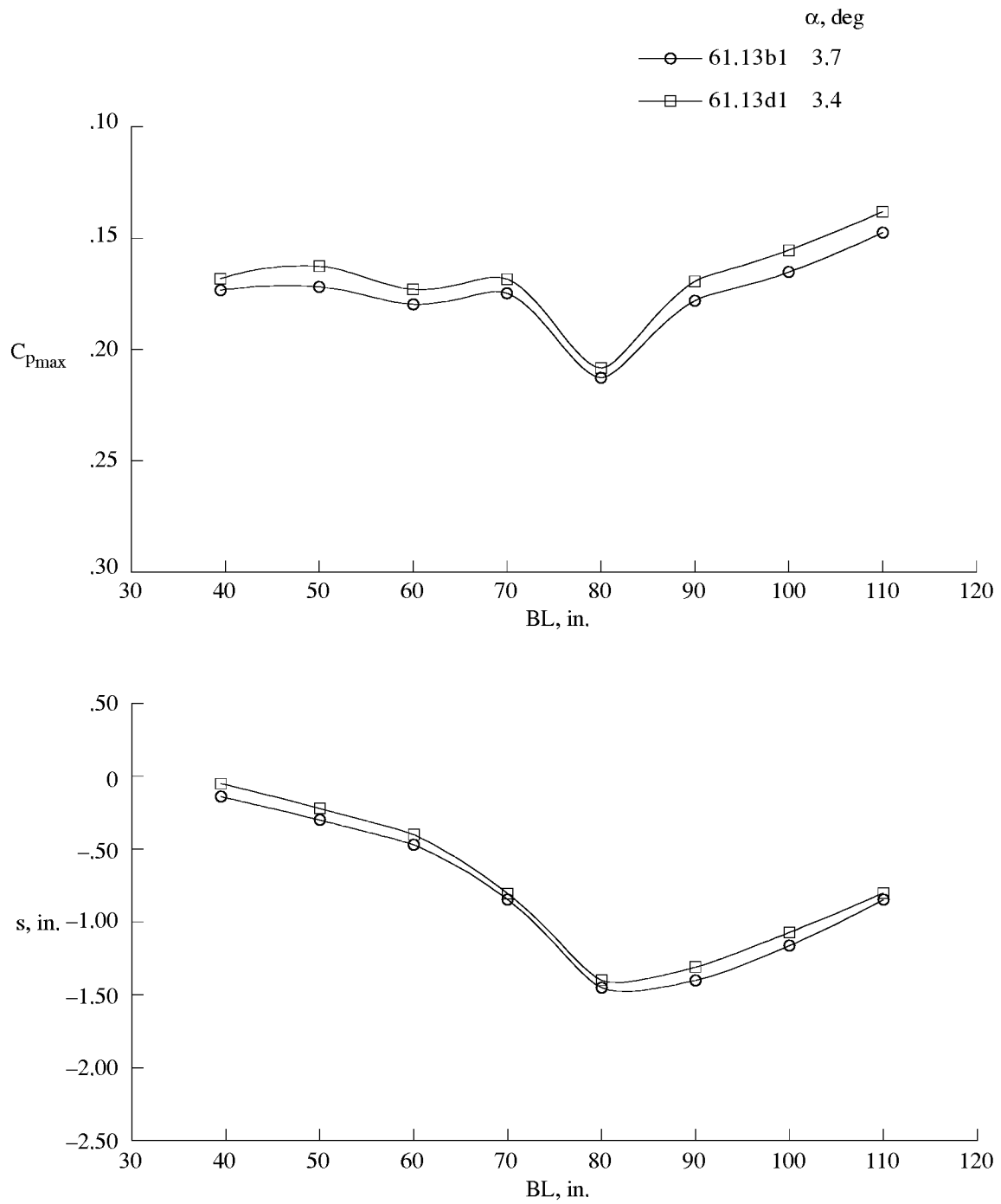


Figure F28. $C_{p_{max}}$ and attachment-line location variation without shock fence at Mach 2.0; $h = 50\,000$ ft; $\beta = 0^\circ$.

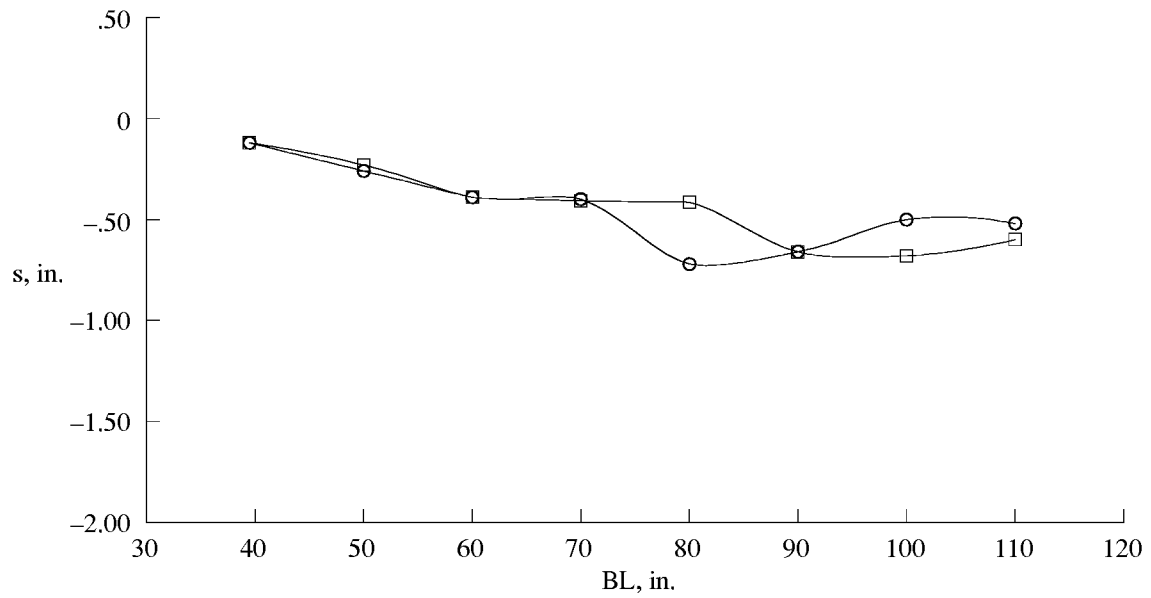
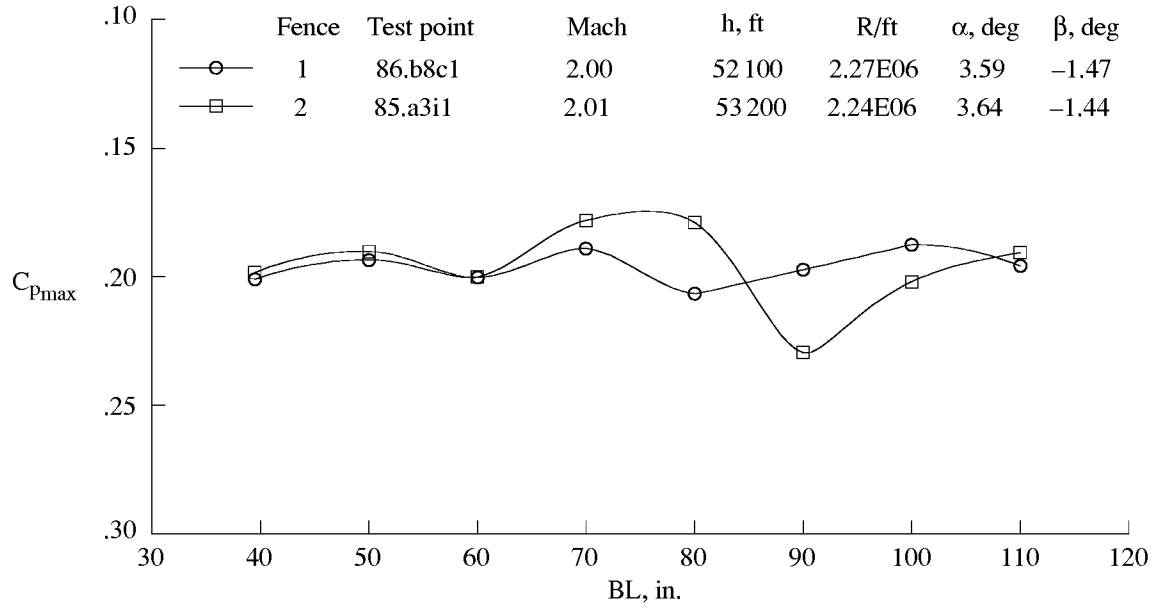
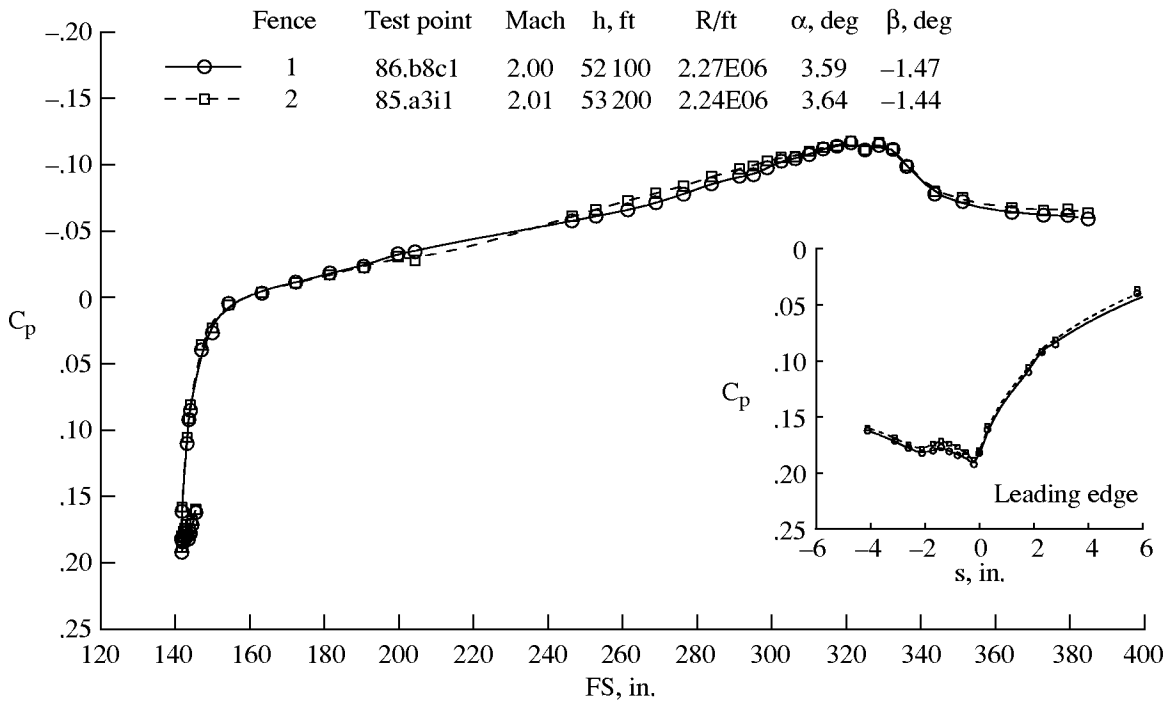
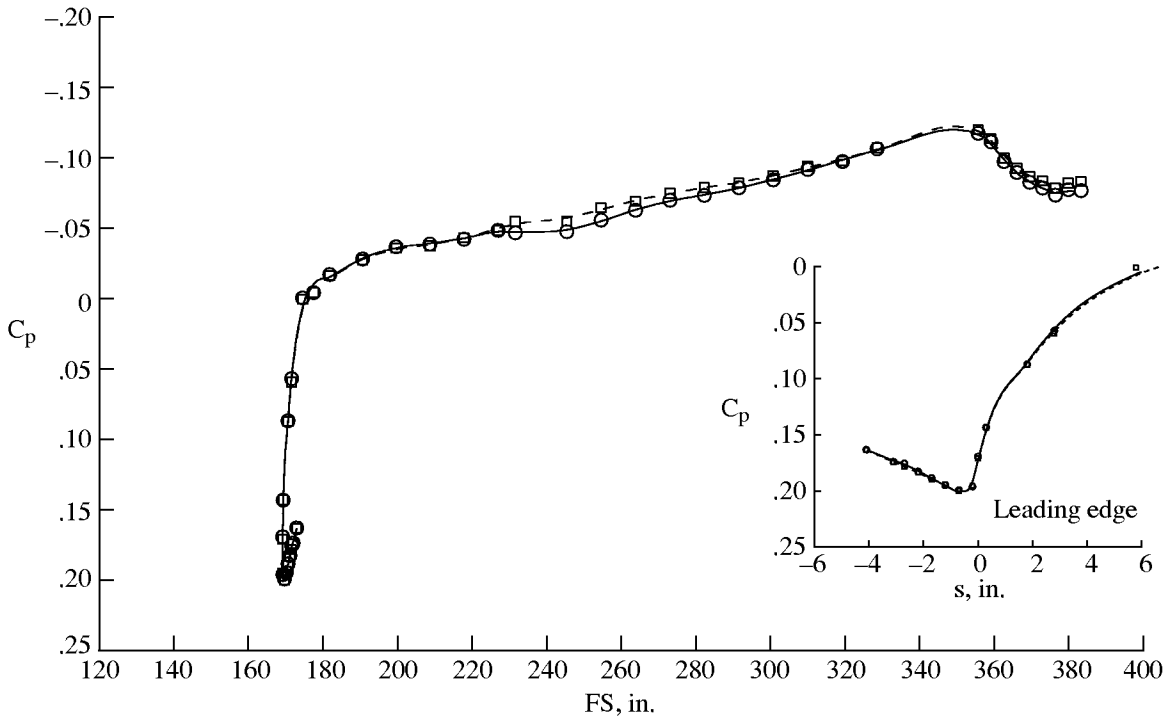


Figure F29. $C_{p_{max}}$ and attachment-line location variation comparison between the two fences.

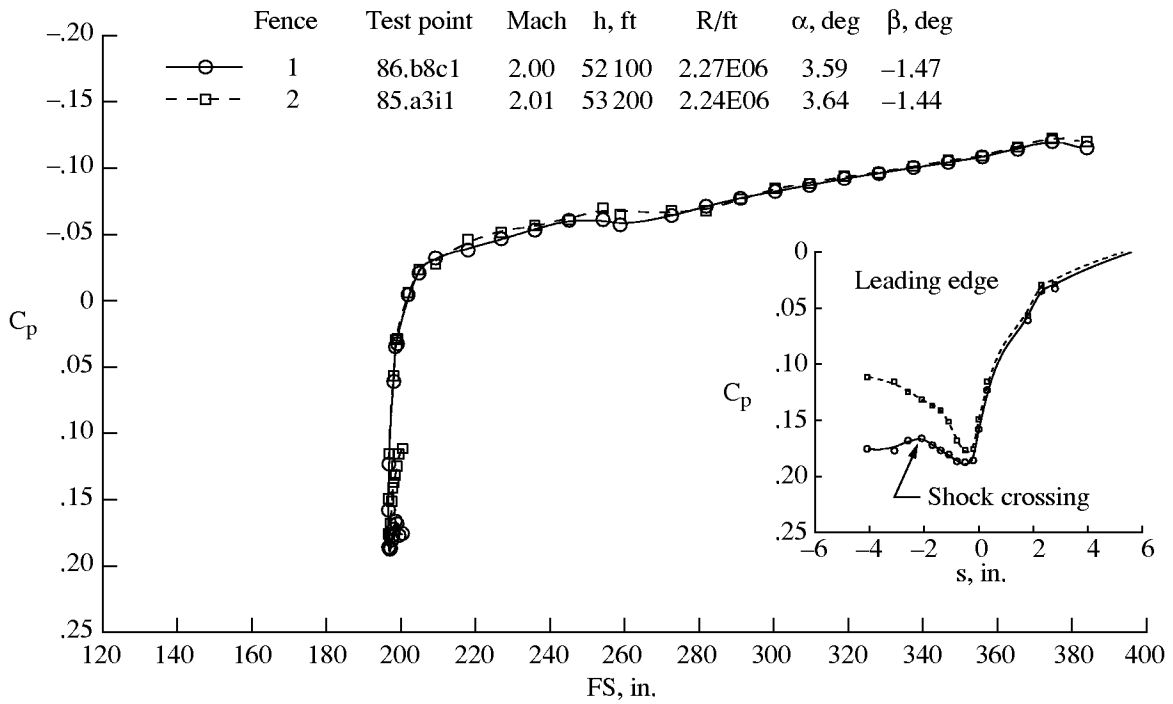


(a) BL 50.

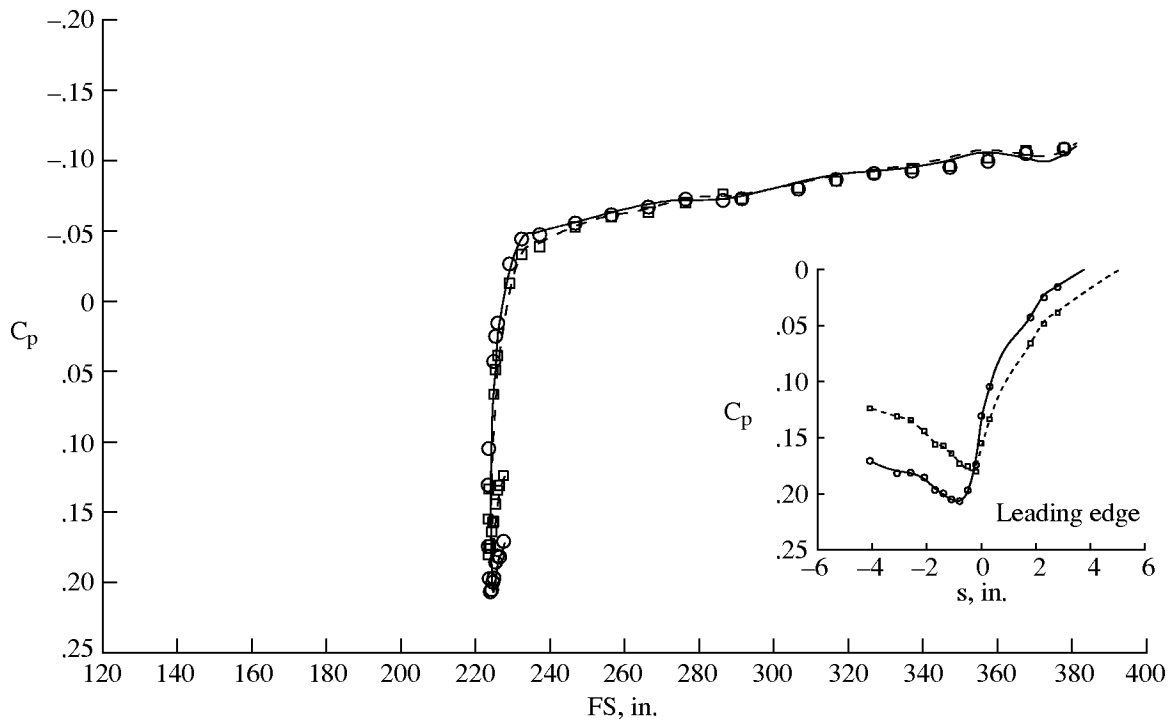


(b) BL 60.

Figure F30. Measured C_p distributions for the two different fences at Mach 2.

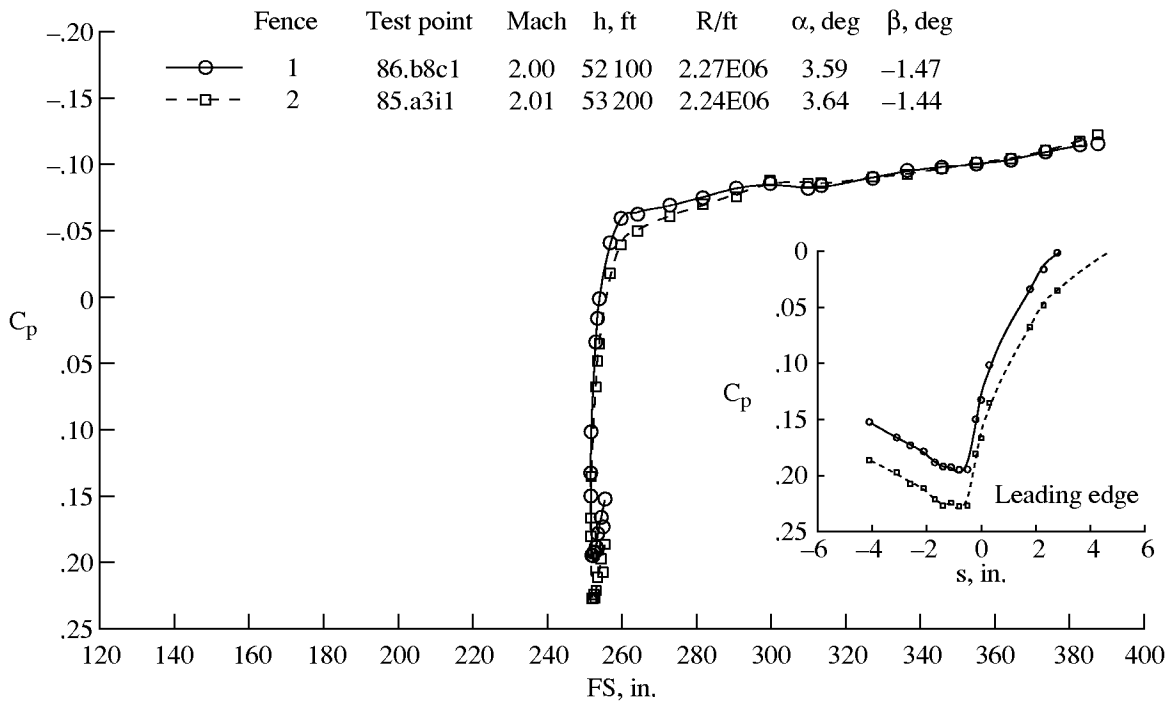


(c) BL 70.

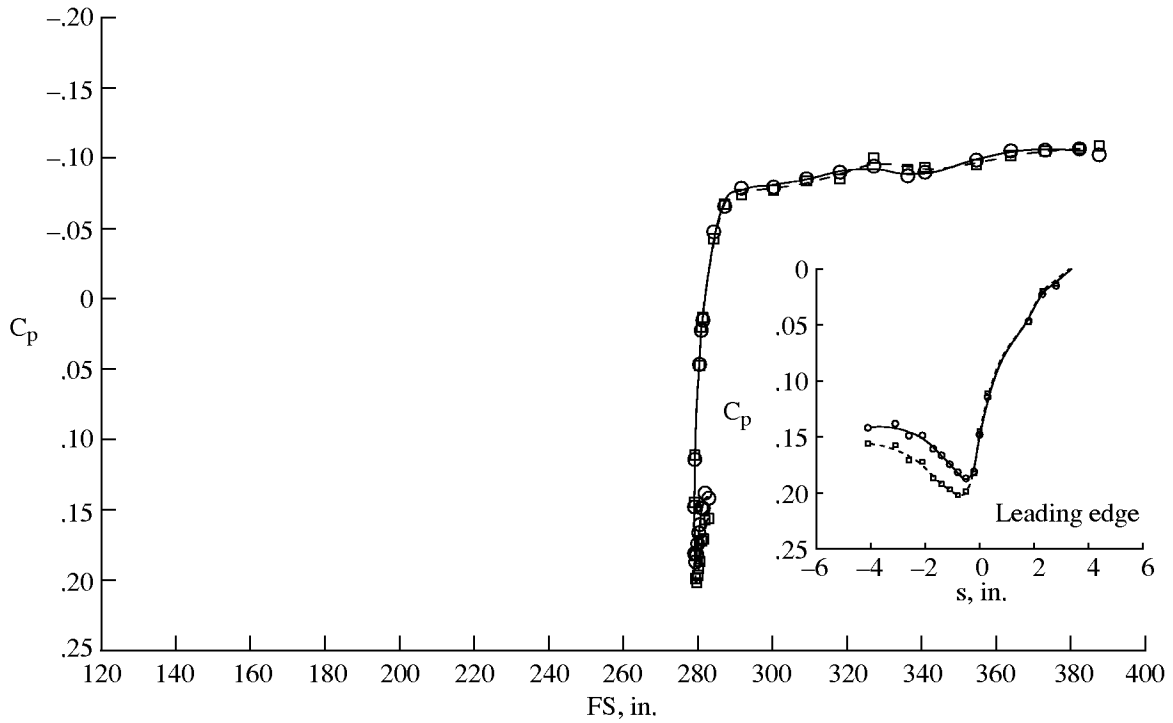


(d) BL 80.

Figure F30. Continued.



(e) BL 90.



(f) BL 100.

Figure F30. Concluded.

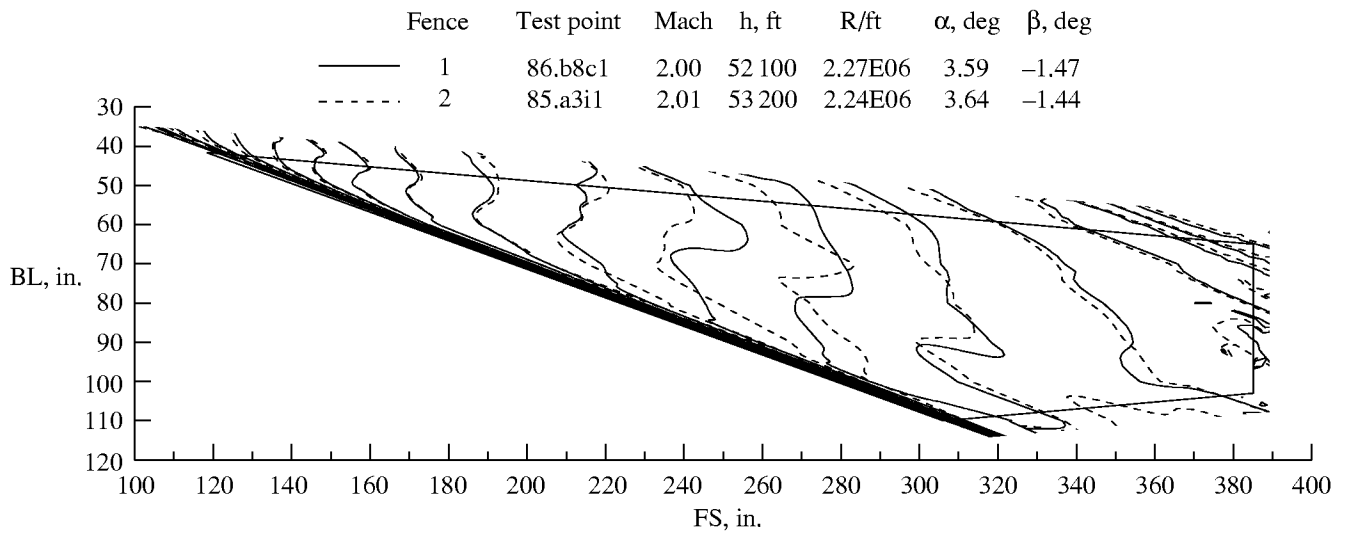


Figure F31. Isobar comparison for the two different shock fences.

Table 1. Individual Patch Perforated Hole Spacing

Patch number	Hole spacing, in.	Suction region	Patch number	Hole spacing, in.	Suction region	Patch number	Hole spacing, in.	Suction region
1	0.017	1	42	0.019	7	83	0.025	13
2	0.010	1	43	0.030	7	84	0.030	13
3	0.012	1	44	0.033	7	85	0.055	14
4	0.017	1	45	0.017	8	86	0.051	14
5	0.017	2	46	0.015	8	87	0.044	14
6	0.016	2	47	0.013	8	88	0.045	14
7	0.016	2	48	0.015	9	89	0.032	14
8	0.020	3	49	0.015	9	90	0.031	14
9	0.019	3	50	0.014	9	91	0.042	15
10	0.019	3	51	0.017	10	92	0.030	15
11	0.022	4	52	0.021	10	93	0.038	16
12	0.028	4	53	0.029	10	94	0.035	16
13	0.042	4	54	0.046	10	95	0.033	16, 17
14	0.050	4	55	0.016	8	96	0.031	16, 17
15	0.016	2	56	0.015	8	97	0.030	16, 17
16	0.016	2	57	0.013	8	98	0.025	17
17	0.016	2	58	0.015	9	99	0.024	17
18	0.017	3	59	0.014	9	100	0.025	17
19	0.018	3	60	0.014	9	101	0.035	18
20	0.019	3	61	0.015	10	102	0.033	18
21	0.020	4	62	0.018	10	103	0.034	18
22	0.025	4	63	0.024	10	104	0.032	18
23	0.030	4	64	0.040	10	105	0.030	18
24	0.040	4	65	0.015	11	106	0.030	19
25	0.017	5	66	0.014	11	107	0.042	15
26	0.017	5	67	0.012	11	108	0.030	15
27	0.016	5	68	0.012	12	109	0.035	16
28	0.019	6	69	0.013	12	110	0.038	16
29	0.018	6	70	0.013	12	111	0.030	16, 17
30	0.017	6	71	0.016	13	112	0.025	17
31	0.020	7	72	0.017	13	113	0.032	17
32	0.024	7	73	0.030	13	114	0.034	18
33	0.030	7	74	0.040	13	115	0.033	18
34	0.048	7	75	0.015	11	116	0.030	18
35	0.017	5	76	0.014	11	117	0.029	18
36	0.016	5	77	0.012	11	118	0.028	18
37	0.015	5	78	0.013	12	119	0.030	19
38	0.016	6	79	0.013	12	120	0.028	19
39	0.015	6	80	0.014	12	121	0.024	19
40	0.014	6	81	0.015	13	122	0.023	19
41	0.016	7	82	0.017	13	123	0.015	20

Table 2. Leakage From Each Region to External Surroundings

[Measuring accuracy: flow rate ± 0.04 SCFM]

Region number	Integrated skin flow rate, SCFM ^a	External leaks, SCFM ^b	Relative external leak, percent
1	58.70	0.11	0.18
2	80.50	0.11	0.13
3	93.70	0.25	0.26
4	103.40	0.28	0.27
5	95.20	0.04	0.04
6	91.70	0.04	0.04
7	127.10	0.04	0.03
8	101.40	0.07	0.07
9	118.60	0.07	0.06
10	147.30	0.00	0.00
11	150.40	0.18	0.12
12	198.20	0.11	0.05
13	225.10	0.07	0.03
14	155.10	0	0
15	315.20	0	0
16	341.3	0	0
17	477.30	0	0
18	438.40	0	0
19	387.90	0	0
20	482.80	0.49	0.1

^aCalculated from BCAG C_q modeling program with 100 psf across skin.

^bAll 20 suction regions pressurized to 100 psfg; outer surface masked with tape; pressure gauge located at each sealed collector duct.

Zeros in leak column indicate region held pressure for at least 10 min.

Table 3. Total Internal and External Leakage From Each Region

[Measuring accuracy: flow rate ± 0.04 SCFM]

Region number	Integrated skin flow rate, SCFM ^a	Total leaks, SCFM ^b	Relative total leak, percent
1	58.70	N/A	N/A
2	80.50	0.60	0.75
3	93.70	0.95	1.02
4	103.40	0.42	0.41
5	95.20	0.11	0.11
6	91.70	0.04	0.04
7	127.10	0.04	0.03
8	101.40	0.11	0.10
9	118.60	0.07	0.06
10	147.30	0.04	0.02
11	150.40	0.18	0.12
12	198.20	1.27	0.64
13	225.10	1.13	0.50
14	155.10	0.25	0.16
15	315.20	0.64	0.20
16	341.30	1.52	0.44
17	477.30	3.25	0.68
18	438.40	4.10	0.93
19	387.90	2.51	0.65
20	482.80	0.49	0.10

^aCalculated from BCAG C_q modeling program with 100 psf across skin.

^bSuction region pressurized to 100 psfg; outer surface covered with tape and other collector duct exits open.

N/A No measurement made.

Table 4. Leading-Edge External Pressure Taps^a
 [Distance in in. from $s = 0$ given for each BL]

BL									
35	39.5	50	60	70	80	90	100	110	120
○ 12		• 8.8	• 8.8	• 8.8	• 8.8	• 8.8	• 8.8	• 8.8	
○ 10									
○ 8		• 5.8	• 5.8	• 5.8	• 5.8	• 5.8	• 5.8	• 5.8	
○ 6									
○ 5		Region 4	Region 7	Region 10	Region 13				
○ 4.5									
○ 4									
○ 3.5									
○ 2.937		• 2.8	• 2.8	• 2.8	• 2.8	• 2.8	• 2.8	• 2.8	
○ 2.554	○ 2.33	• 2.3		• 2.3	• 2.3	• 2.3	• 2.3		
○ 2.21									
○ 1.899	○ 1.814	• 1.8	• 1.8	• 1.8	• 1.8	• 1.8	• 1.8	• 1.8	
○ 1.619									
○ 1.376	○ 1.396	Region 3	Region 6	Region 9	Region 12				
○ 1.14									
○ 0.935	○ 1.058								
○ 0.751	○ 0.784	Region 2	Region 5	Region 8	Region 11				
○ 0.585	○ 0.562								
○ 0.435	○ 0.383	• 0.3	• 0.3	• 0.3	• 0.3	• 0.3	• 0.3	• 0.3	○ 0.825
○ 0.300	○ 0.237								○ 0.589
○									○ 0.411
○ 0.179	○ 0.12								○ 0.283
○									○ 0.206
○ 0.069									○ 0.133
○	○ 0.024								○ 0.064
○ 0	○ 0	• 0	• 0	• 0	• 0	• 0	• 0	• 0	○ 0
○ -0.029	○ -0.053								○ -0.063
○ -0.118	○ -0.115								○ -0.13
○ -0.198	○ -0.178	• -0.2	• -0.2	• -0.2	• -0.2	• -0.2	• -0.2	• -0.2	○ -0.207
○ -0.278	○ -0.265								○ -0.3
○ -0.373	○ -0.386								○ -0.42
○ -0.487	○ -0.553	• -0.5		• -0.5	• -0.5	• -0.5	• -0.5	• -0.5	○ -0.587
○ -0.623									
○ -0.785	○ -0.787	• -0.8	• -0.7	• -0.8	• -0.8	• -0.8	• -0.8	• -0.8	○ -0.799
○ -0.979									
○ -1.209	○ -1.111	• -1.1	• -1.2	• -1.1	• -1.1	• -1.1	• -1.1		○ -1.058
○ -1.484	○ -1.562	• -1.4		• -1.4	• -1.4	• -1.4	• -1.4	• -1.4	○ -1.364
○ -1.813		• -1.7	• -1.7	• -1.7	• -1.7	• -1.7	• -1.7	• -1.7	○ -1.719
○ -2.204	○ -2.188	• -2.1	• -2.2	• -2.1	• -2.1	• -2.1	• -2.1	• -2.1	○ -2.123
○ -2.671		• -2.6	• -2.7	• -2.6	• -2.6	• -2.6	• -2.6	• -2.7	
○ -3.229		• -3.1	• -3.1	• -3.1	• -3.1	• -3.1	• -3.1	• -3.1	
		• -4.1	• -4.1	• -4.1	• -4.1	• -4.1	• -4.1	• -4.1	

^aSolid circles indicate suction panel leading-edge pressure taps (ref. 113). Open circles indicate passive fairing leading-edge pressure taps (ref. 78).

Table 5. Mass Flow per Suction Region and Totals

(a) Test Conditions

Parameter	Design	Test point			
		88.11g1	88.12c1	77.a4g1	49.11p1
Altitude, ft	50 000	53 300	53 300	53 300	50 600
Mach number	1.90	2.02	2.02	1.97	1.90
α , deg	3.3	3.3	3.4	3.7	3.7
β , deg00	-1.45	-1.43	-1.42	.06

(b) Mass Flows for Each Region

Region	Mass flow, lbm/sec for—					
	Design		Test point			
	Upper limit	Lower limit	88.11g1	88.12c1	77.a4g1	49.11p1
1	0.00480	0.00480	0.00137	0.00137	0.00147	0.00173
2	0.01590	0.00710	0.00567	0.00572	0.00748	0.02225
3	0.01020	0.00400	0.00383	0.01375	0.01255	0.01585
4	0.00910	0.00310	0.00389	0.00969	0.00880	0.01139
5	0.01730	0.00980	0.00888	0.00881	0.00866	0.02540
6	0.01230	0.00460	0.00463	0.01305	0.01182	0.01405
7	0.00910	0.00330	0.00413	0.01406	0.01246	0.01584
8	0.01730	0.00770	0.01118	0.01111	0.01124	0.02564
9	0.01390	0.00380	0.00569	0.01477	0.01494	0.01436
10	0.01100	0.00390	0.00403	0.01367	0.01341	0.01371
11	0.01700	0.00760	0.01200	0.01190	0.00490	0.02646
12	0.01500	0.00610	0.00413	0.01623	0.01524	0.01615
13	0.01330	0.00610	0.00325	0.01298	0.01202	0.01273
14	0.01000	0.00380	0.00476	0.01332	0.01237	0.00634
15	0.01480	0.00560	0.00309	0.01960	0.01836	0.00761
16	0.01590	0.00590	0.00233	0.01735	0.01639	0.00805
17	0.01610	0.00600	0.00294	0.02039	0.01865	0.00963
18	0.01530	0.00570	0.00400	0.01772	0.01605	0.01077
19	0.01230	0.00460	0.00298	0.01454	0.01300	0.00766
20	0.00470	0.01890	0.00014	0.00019	0.00034	0.00158
Totals	0.2553	0.1224	0.0929	0.2502	0.2302	0.2672

(c) Mass Flows for Suction Patch, Flutes, and Rooftop

Flute	Mass flow, lbm/sec for—					
	Design		Test point			
	Upper limit	Lower limit	88.11g1	88.12c1	77.a4g1	49.11p1
Suction patch	0.00480	0.00480	0.00137	0.00137	0.00147	0.00173
1	0.06750	0.03220	0.03773	0.03754	0.03228	0.09975
2	0.05140	0.01850	0.01828	0.05780	0.05455	0.06041
3	0.04250	0.01640	0.01530	0.05040	0.04669	0.05367
Rooftop	0.08910	0.05050	0.02024	0.10311	0.09516	0.05164
Totals	0.2553	0.1224	0.0929	0.2502	0.2302	0.2672

Table 6. Code Calibration Results From BCAG, MDC, and HTC

Flight	Test point	Mach number	h , ft	R/ft , $\times 10^6$	α , deg	β , deg	Hot film	Status	BCAG	MDC	HTC	Comments
67	ex01	2.03	50340	2.44	3.22	0.08	rfhf04	LT	13.4			Flutes 2 and 3 at 90; upper surface at 90
70	03e1	2.01	50610	2.39	3.28	0.01	rfhf04	TR		12.4		Flutes 2 and 3 at 90; upper surface at 90
70	04i1	2.02	50300	2.46	2.58	-0.07	rfhf04	T			14.3	Flutes 2 and 3 at 90; upper surface at 90
70	ex01	2.01	50810	2.42	2.92	-1.89	r14hf3 r15hf1 r18hf1 r19hf1 r18hf2 r19hf1	L L LT L L TR	12	16.4	8 8.4 11.2 13.8 11	Flutes 2 and 3 at 90; upper surface at 90
71	ex02	2.01	50550	2.50	3.47	-1.42	r18hf2 rfhf04	TR TR		14.3 12.7		Flutes 2 and 3 at 90; upper surface at 90
71	a6g1	1.98	51490	2.34	3.71	-1.42	rfhf04	LT	15			Flutes 2 and 3 at 90; upper surface at 90
76	a3e1	2.02	50510	2.57	2.63	-0.02	aft02	TR		11.8		Flutes 2 and 3 at 90; upper surface at 90
76	ex01	2.04	50840	2.53	3.61	-0.04	rfhf04	TR		17.4		Flutes 2 and 3 at 90; upper surface at 90
76	a4c1	2.03	53470	2.27	2.67	-0.16	rfhf05 aft02	TR TR		11.4 15.3		Flutes 2 and 3 at 90; upper surface at 90
76	a4i1	2.05	53400	2.30	2.62	-1.56	rfhf05	LT				Flutes 2 and 3 at 90; upper surface at 90
77	a4g1	1.97	53280	2.12	3.70	-1.42	r18hf1a rfhf05	TR L		15.8 12.2	9.5	Flutes 2 and 3 at 90; upper surface at 90
77	ex05	2.00	53340	2.19	4.11	-1.52	rfhf04 r17hf1a r18hf1a rfhf05	TR LT L L			14.8 10.8 13.7 12	Flutes 2 and 3 at 90; upper surface at 90
79	a2g1	2.02	53420	2.26	2.62	-0.12	rfhf04 rfhf05a	LT LT			15 12	Flutes 2 and 3 at 90; upper surface at 90

Table 6. Continued

Flight	Test point	Mach number	h , ft	R/ft , $\times 10^6$	α , deg	β , deg	Hot film	Status	BCAG	MDC	HTC	Comments	
79	a4g1	2.02	53440	2.25	3.67	-1.41	rfhf05a	TR			11.5	Flutes 2 and 3 at 90; upper surface at 90	
							r18hf1a	LT			6	Not included in plots	
							r15hf3a	LT	10		9		
80	b2c1	2.02	53180	2.27	3.72	-1.47	sjhf02	LT	11.5			Flutes 2 and 3 at 90; upper surface at 90	
							sjhf03	L					
							sjhf04	LT					
80	a3g1	2.01	53130	2.28	3.68	-1.47	sjhf03	LT					Flutes 2 and 3 at 90; upper surface at 45
							sjhf04	LT	15	8.7			
							sjhf05	L		12.8			
							sjhf06	L					
							sjhf07	L					
							sjhf08	LT	14.4	15.8			
							sjhf09	TR	15.2	16.1			
							sjhf10	LT	15				
							sjhf11	LT					
							sjhf13	LT					
							sjhf14	LT	12.5				
80	a3i2	2.02	53320	2.26	3.68	-1.50	sjhf15	LT				Flutes 2 and 3 at 90; upper surface at 35	
							sjhf03	LT					
							sjhf04	LT	13.4				
80	a3k1	2.02	53340	2.27	3.71	-1.51	sjhf05	LT	16.2			Flutes 2 and 3 at 90; upper surface at 30	
							sjhf06	LT	16.4				
							sjhf07	L					
							sjhf08	TL					
							sjhf01	TL					
							sjhf02	TR					
							sjhf03	TR					11.4
							sjhf04	LT	17.3				13.2
							sjhf05	LT	17.6				16.2
							sjhf06	LT	17.5				18
							sjhf07	T		16.8			17
sjhf08	T		17.2		18								
sjhf09	T		17.3										
sjhf10	T				18.7								
sjhf11	TR				17								

Table 6. Continued

Flight	Test point	Mach number	h , ft	R/ft , $\times 10^6$	α , deg	β , deg	Hot film	Status	BCAG	MDC	HTC	Comments
81	a4g1	2.02	53490	2.32	3.71	-1.52	sjhf12	L			13.2	Flutes 2 and 3 at 45; upper surface at 90
							sjhf13	L			13.7	
							sjhf14	L			10	
							sjhf15	L				
							sjhf02	TR				
							sjhf03	LT	13.1			
							sjhf04	L				
							sjhf09	L				
							sjhf10	LT	18.2			
							sjhf11	L				
sjhf13	L											
sjhf14	LT	15										
sjhf15	LT											
sjhf16	LT											
sjhf17	LT											
sjhf18	LT											
sjhf04	LT											
81	a5e1	2.04	52980	2.38	3.01	-0.07	sjhf05	LT	11.5			Flutes 2 and 3 at 60; upper surface at 60
							sjhf06	LT				
							sjhf04	LT				
81	a5g1	2.04	53300	2.32	2.96	-0.07	sjhf05	LT	13.6			Flutes 2 and 3 at 45; upper surface at 90
							sjhf06	TL				
							sjhf02	LT				
81	a6e1	2.02	53240	2.31	3.71	-1.46	sjhf03	LT	11.3			Flutes 2 and 3 at 60; upper surface at 60
							sjhf04	L				
							sjhf13	L				
81	a6g1	2.02	53260	2.32	3.67	-1.46	sjhf14	LT	13.1			Flutes 2 and 3 at 45; upper surface at 45
							sjhf15	LT	11.2			
							sjhf16	LT				
							sjhf02	TR				
							sjhf03	LT	12.6			
							sjhf04	LT			11	
							sjhf05	LT	16.3		14	
							sjhf06	L				
sjhf07	L											
sjhf08	TR			17.6								

Table 6. Continued

Flight	Test point	Mach number	h , ft	R/ft , $\times 10^6$	α , deg	β , deg	Hot film	Status	BCAG	MDC	HTC	Comments
81	a7e1	2.02	53300	2.33	3.00	-0.20	sjhf09	T	17.2			Flutes 2 and 3 at 60; upper surface at 60
							sjhf10	T				
							sjhf11	LT				
							sjhf12	LT				
							sjhf13	LT				
							sjhf14	TR				
sjhf15	TR											
sjhf16	TR											
sjhf04	LT	13										
81	a7g2	2.02	53210	2.33	3.01	-0.13	sjhf05	LT	18			Flutes 2 and 3 at 45; upper surface at 45
							sjhf06	TL				
							sjhf04	LT				
							sjhf05	LT				
							sjhf06	T				
							sjhf18	L				
sjhf19	LT											
sjhf20	LT											
sjhf02	TR	18										
81	a8c1	2.03	53510	2.28	3.65	0.06	sjhf03	LT	12.8			Flutes 2 and 3 at 90; upper surface at 90
							sjhf04	LT				
							sjhf05	LT				
							sjhf06	L				
							sjhf02	TR				
							sjhf03	LT				
sjhf04	LT											
sjhf05	L											
sjhf09	L											
sjhf10	LT											
sjhf11	LT											
sjhf13	LT											
sjhf14	LT											
sjhf15	LT											
sjhf07	L	12.8 13.8										
81	a10g	2.02	53140	2.32	3.68	-1.46	sjhf08	LT	17.6			Flutes 2 and 3 at 90; upper surface at 90
							sjhf09	TR				
							sjhf10	LT				
							sjhf08	LT				
							sjhf09	TR				
							sjhf10	LT				
sjhf08	LT											
sjhf09	TR											
sjhf10	LT	16 15.8										

Table 6. Continued

Flight	Test point	Mach number	h , ft	R/ft , $\times 10^6$	α , deg	β , deg	Hot film	Status	BCAG	MDC	HTC	Comments
81	a10i	2.02	53300	2.30	3.70	-1.47	sjhf03	TR				Flutes 2 and 3 at 90; upper surface at 35
							sjhf04	LT		11		
							sjhf05	LT		13		
							sjhf06	LT		16		
85	a3k1	2.02	53220	2.25	3.64	-1.44	sjhf07	L				Flutes 2 and 3 at 90; upper surface at 32
							sjhf08	TR		16.2		
							sjhf09	T				
							sjhf04	LT				
85	a5k1	2.02	53210	2.26	3.68	-1.46	sjhf05	LT				Flutes 2 and 3 at 45; upper surface at 45
							sjhf06	LT		12		
							sjhf07	LT		16		
							sjhf08	T		15.6		
85	a7e1	2.01	53400	2.22	3.67	-1.49	sjhf04	LT				Flutes 2 and 3 at 60; upper surface at 90
							sjhf05	LT		14.3		
							sjhf06	LT		16.2		
							sjhf07	LT		15.8		
86	b8m1	2.02	52280	2.30	3.19	-1.48	sjhf08	T				Flutes 2 and 3 at 90; upper surface at 30
							sjhf09	L		12.9		
							sjhf10	LT		13.7		
							sjhf03	TL				
86	b8m1	2.02	52280	2.30	3.19	-1.48	sjhf04	TL	15			Flutes 2 and 3 at 90; upper surface at 30
							sjhf05	TR	13.6			
							sjhf06	TR	15			
							sjhf07	LT	16.5			
							sjhf08	LT	18			
							sjhf09	LT	20			
							sjhf10	LT	19.4			
							sjhf11	LT	16			
							sjhf12	L				
							sjhf13	L				
							sjhf14	LT	16			
							sjhf15	LT	16.2			
							sjhf16	LT	14.2			
sjhf17	LT											

Table 6. Concluded

Flight	Test point	Mach number	h , ft	R/ft , $\times 10^6$	α , deg	β , deg	Hot film	Status	BCAG	MDC	HTC	Comments	
88	a2d1	2.01	53120	2.15	3.39	-1.51	cchf08	LT			8.8	Flutes 2 and 3 at 90; upper surface at 90	
							cchf09	L			10.1	cchf08 was edge of inboard turbulent region due to leading-edge films	
							cchf10	L			11	cchf17 was outboard edge of turbulent region	
							cchf11	L			10		
							cchf12	L			7.2	Same test condition as a4i1 and a5e1	
							cchf13	L			5.9		
							cchf14	I			5.1		
							cchf15	L			5.5		
							cchf16	L					
							cchf17	T					
							cchf08	TR					Flutes 2 and 3 at 90; upper surface at 45
							cchf09	LT			12.5	Same test condition as a2d1 and a5e1	
							cchf10	LT			13.2	cchf08 was edge of inboard turbulent region due to leading-edge films	
							cchf11	LT			14.9	cchf17 was outboard edge of turbulent region	
88	a5e1	2.01	53210	2.13	3.37	-1.48	cchf12	LT			9.5		
							cchf13	LT			7.5		
							cchf14	LT			8.4		
							cchf15	LT			9.8		
							cchf16	LT					
							cchf17	T					
							cchf09	TL					Flutes 2 and 3 at 90; upper surface at 30
							cchf10	TR			17	Same test condition as a2d1 and a4i1	
							cchf11	TL			16		
							cchf12	TL			20		
							cchf13	T			17.5		
							cchf14	T					
							cchf15	T					

Table 7. Comparison of N-Factor Calculations Between BCAG, MDC, and HTC

Flight	Test point	Mach number	h , ft	R/ft , $\times 10^6$	α , deg	β , deg	Hot film	Status	BCAG	MDC	HTC	Comments
70	04i1	2.02	50300	2.46	2.58	-0.07	r18hf1	LT	12		11.2	Flutes 2 and 3 at 90; upper surface at 90
77	a4g1	1.97	53280	2.12	3.70	-1.42	rffhf05	L		12.2	9.5	Flutes 2 and 3 at 90; upper surface at 90
79	a4g1	2.02	53440	2.25	3.67	-1.41	r15hf3a	LT	10		9	Flutes 2 and 3 at 90; upper surface at 90
80	a3g1	2.01	53130	2.28	3.68	-1.47	sjhf03	LT				Flutes 2 and 3 at 90; upper surface at 90
							sjhf04	LT		8.7		
							sjhf05	LT	15	12.8		
							sjhf06	L				
							sjhf07	L				
							sjhf08	LT	14.4	15.8		
							sjhf09	TR	15.2	16.1		
							sjhf10	LT	15			
							sjhf11	LT				
80	a3k1	2.02	53340	2.27	3.71	-1.51	sjhf03	TR			13.2	Flutes 2 and 3 at 90; upper surface at 30
							sjhf04	LT	17.3		16.2	
							sjhf05	LT	17.6		18	
							sjhf06	LT		16.8	17	
							sjhf07	LT	17.5	17.2	18	
							sjhf08	T		17.3		
							sjhf09	T				
							sjhf02	TR				
81	a6g1	2.02	53260	2.32	3.67	-1.46	sjhf03	LT	12.6			Flutes 2 and 3 at 45; upper surface at 45
							sjhf04	LT		11		
							sjhf05	LT	16.3	14		
							sjhf06	L				

Table 8. Comparison of eMalik3d and PSE N-Factor Calculations

Flight	Test point	Mach number	h , ft	R/ft , $\times 10^6$	α , deg	β , deg	Hot film	Status	eMalik3d			PSE HTC	Comments	
									BCAG	MDC	HTC			
79	a4g1	2.02	53440	2.25	3.67	-1.41	rffhf05a	TR			11.5 at 4 kHz	6 at 2 kHz	Flutes 2 and 3 at 90; upper surface at 90 Flutes 2 and 3 at 90; upper surface at 90	
							r18hf1a	LT			6 at 3 kHz	9 at 3 kHz		
							r15hf3a	LT	10		9 at 4 kHz	5.5 at 2 kHz		
N-factor range for 79.a4g1: 6 to 11.5 5.5 to 9														
80	a3k1	2.02	53340	2.27	3.71	-1.51	sjhff01	TL			11.4	7.7 at 3 kHz	Flutes 2 and 3 at 90; upper surface at 30 Flutes 2 and 3 at 90; upper surface at 30	
							sjhff02	TR			13.2 at 2-4 kHz	11.2 at 3 kHz		
							sjhff03	TR			16.2 at 2-4 kHz	4 kHz		
							sjhff04	LT	17.3		18 at 13 at 5 kHz	13.3 at 5 kHz		
							sjhff05	LT	17.6		17 at 13.3 at 5 kHz	13.8 at 5 kHz		
							sjhff06	LT		16.8		18 at 5 kHz		
							sjhff07	LT	17.5		17 at 17.2	15.1 at 5 kHz		
							sjhff08	T		17.3		18.7 at 17		
							sjhff09	T				2-4 kHz		
							sjhff10	T				13.2		
							sjhff11	TR				13.7		
							sjhff12	L				10		
							sjhff13	L						
							sjhff14	L						
							sjhff15	L						
N-factor range for 80.a3k1: 13.2 to 18.7 7.7 to 15.1														
N-factor range for both test points: 6 to 18.7 5.5 to 15.1														



Figure 1. Artist's rendition of Technology Concept Aircraft (conceptual HSCT).

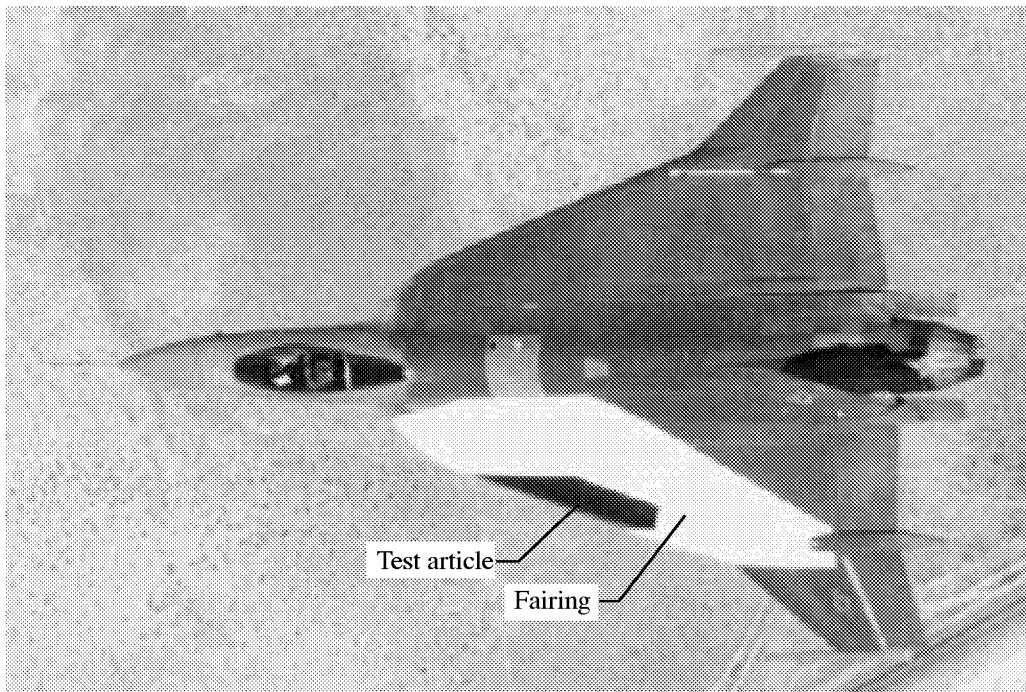


Figure 2. F-16XL-1 in-flight with test article mounted on left wing.



Figure 3. Front in-flight view of modified F-16XL-2.

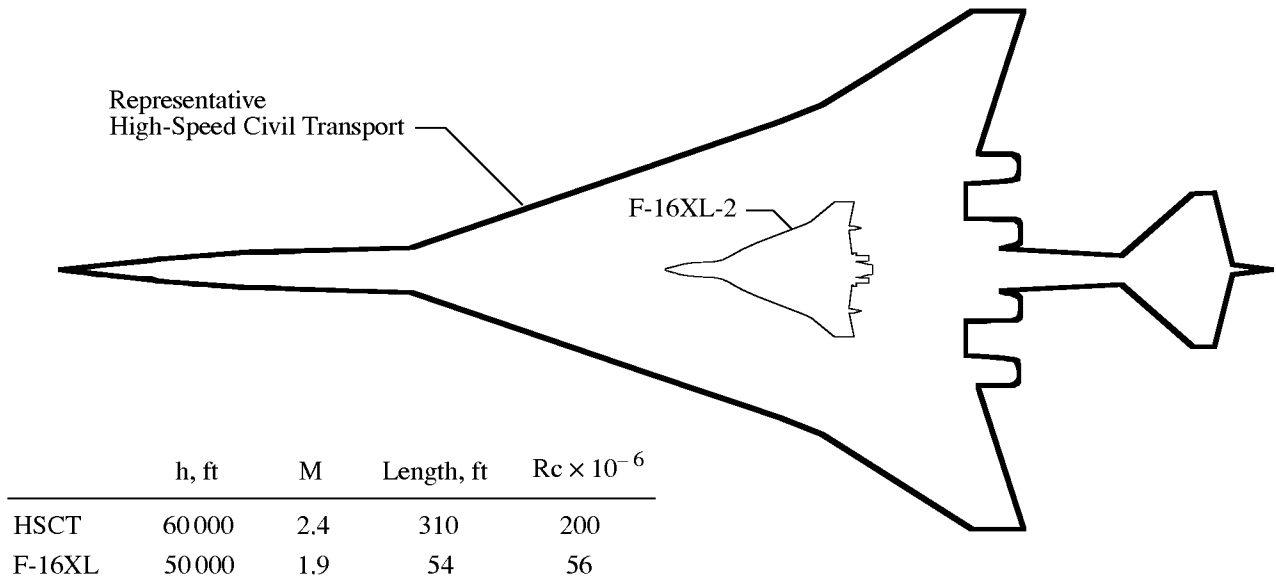


Figure 4. Comparison of F-16XL-2 and HSCT planforms.

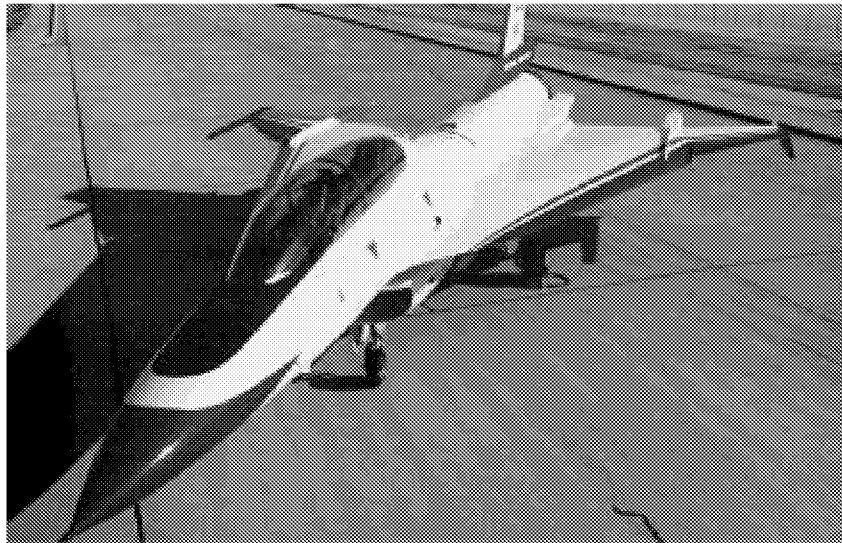


Figure 5. F-16XL-2 baseline aircraft.

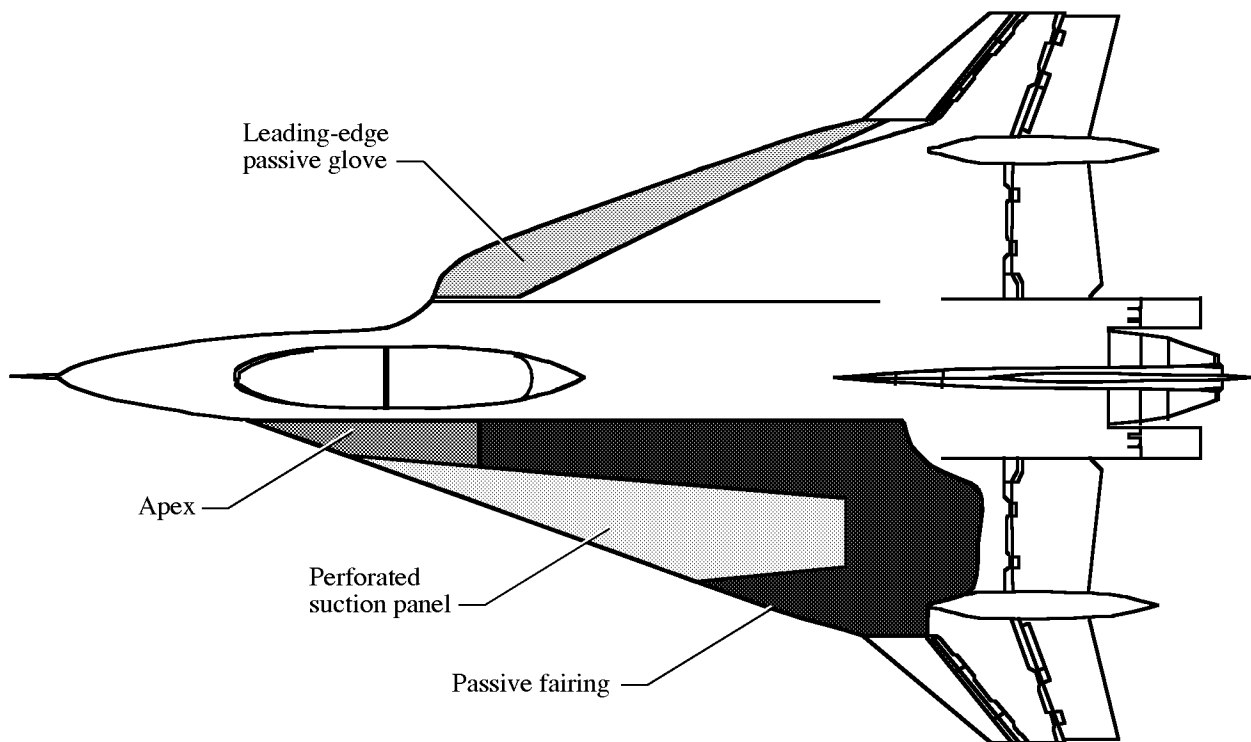


Figure 6. Modified airplane planform features.



Figure 7. Front view of modified F-16XL-2.

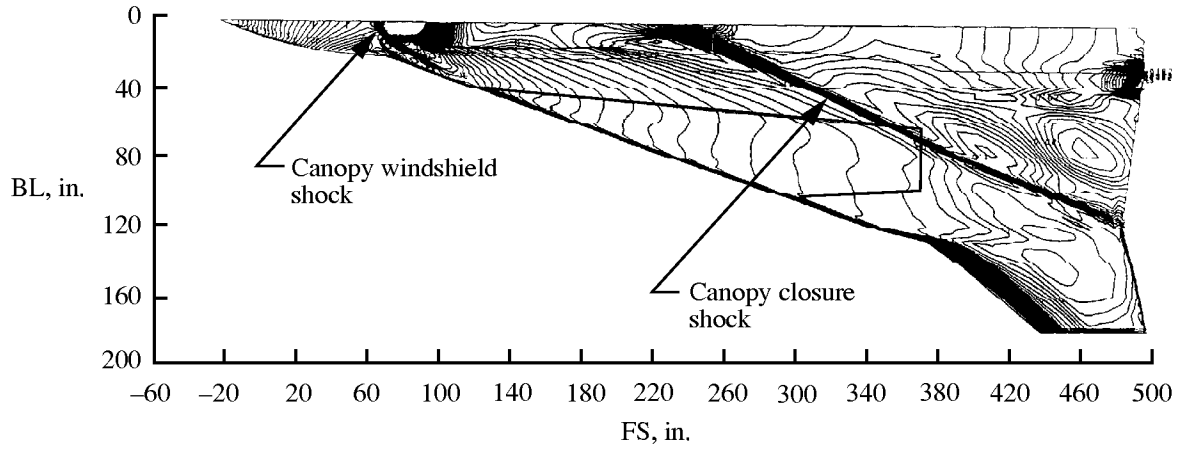


Figure 8. Upper surface isobars showing flow-field features (generated by BCAG).

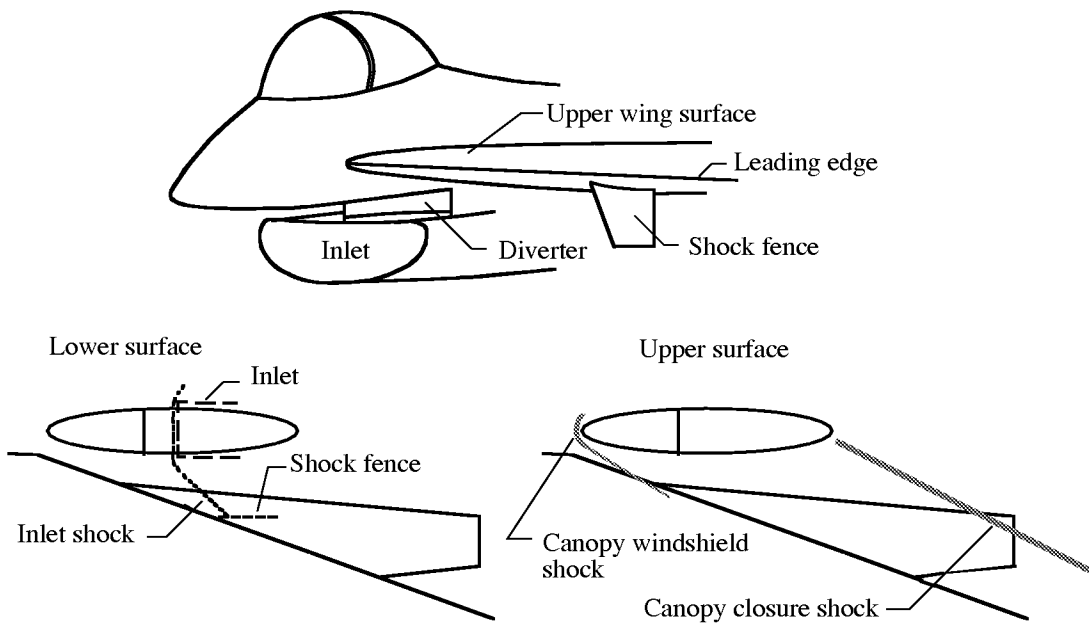


Figure 9. F-16XL-2 specific flow-field features.

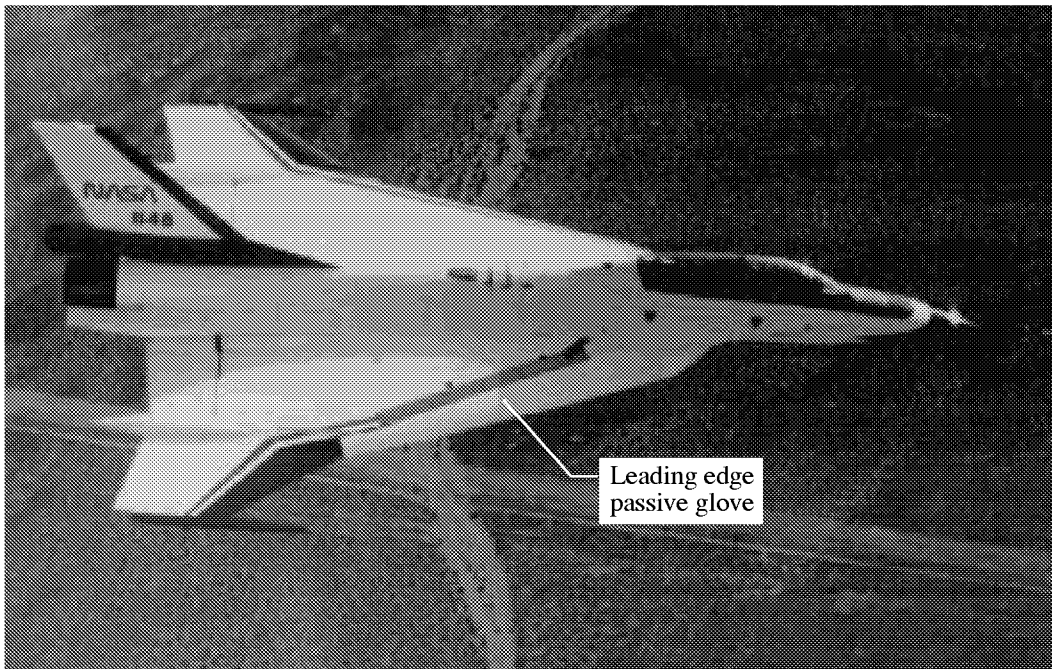
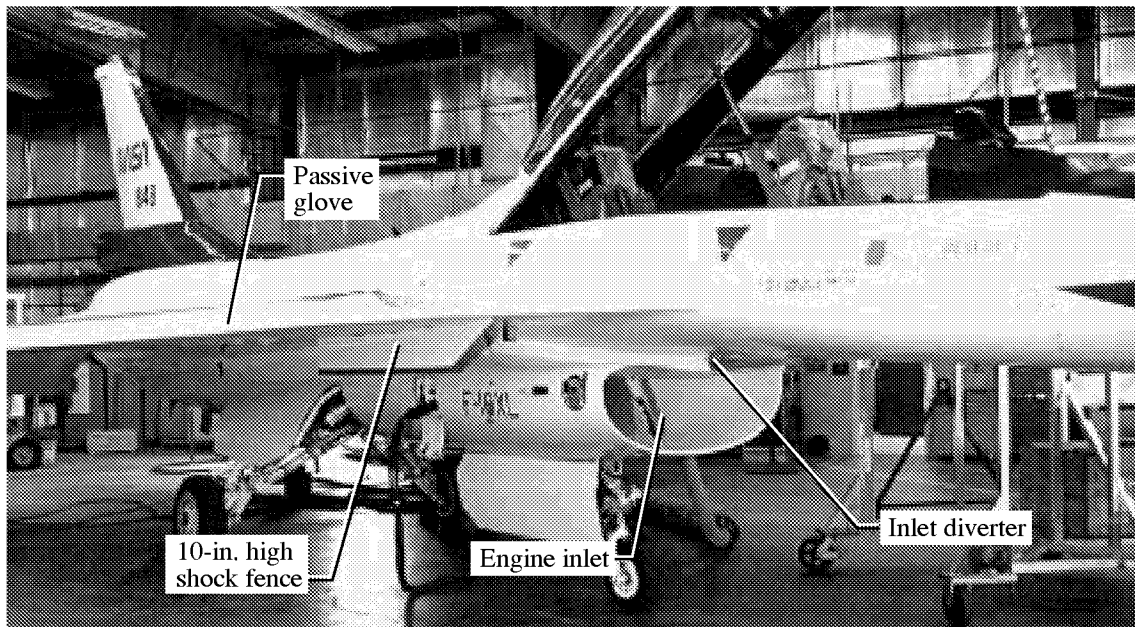
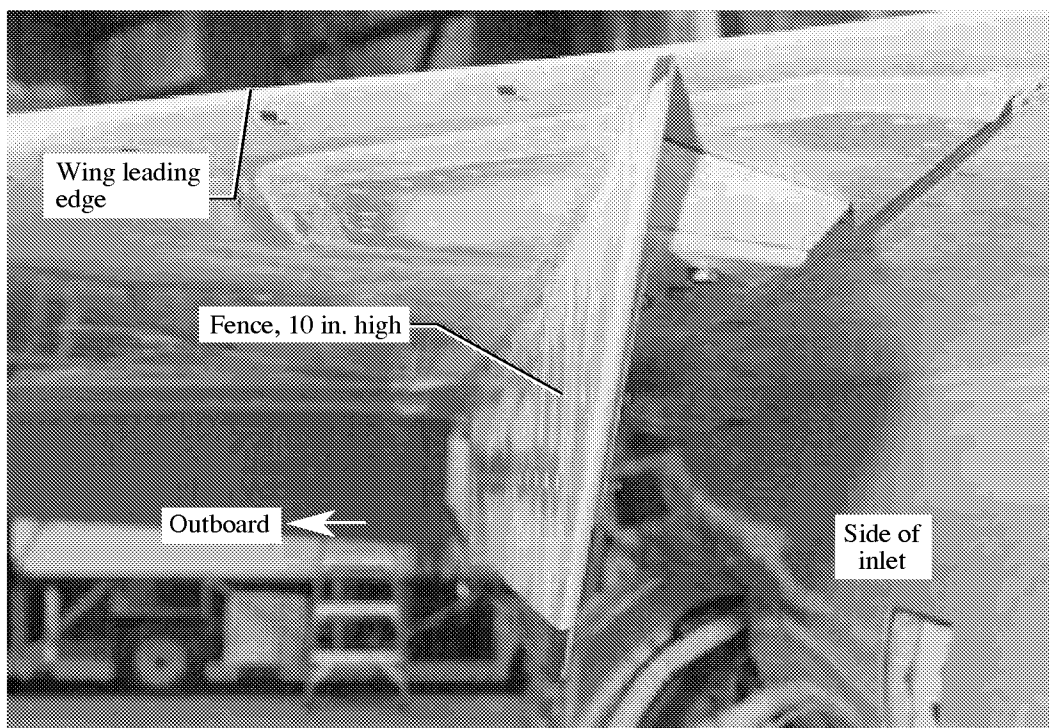


Figure 10. Passive glove mounted on right wing of F-16XL-2.



(a) Shock fence, engine inlet, and diverter details.



(b) Shock fence closeup.

Figure 11. Shock fence evaluation on right wing during passive-glove tests.

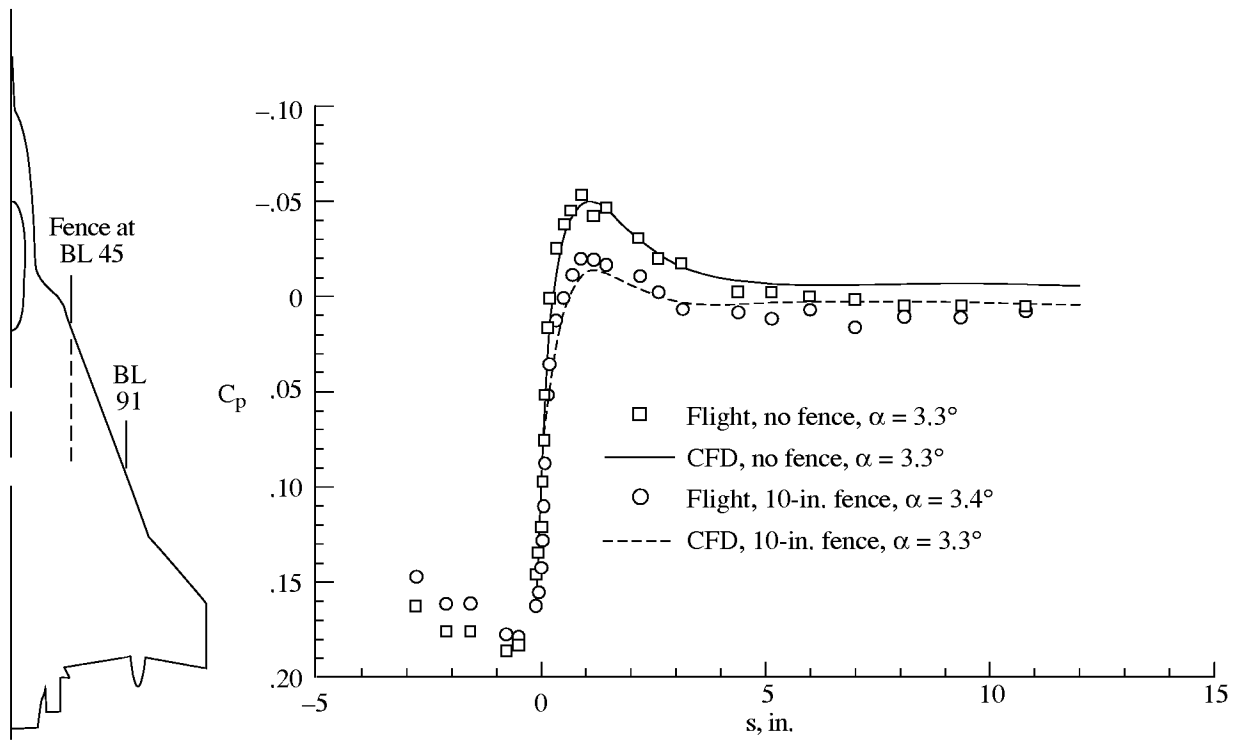


Figure 12. Pressure distributions with and without 10-in. fence on leading-edge passive glove. BL 91; $M = 1.9$; $h = 50\,000$ ft.

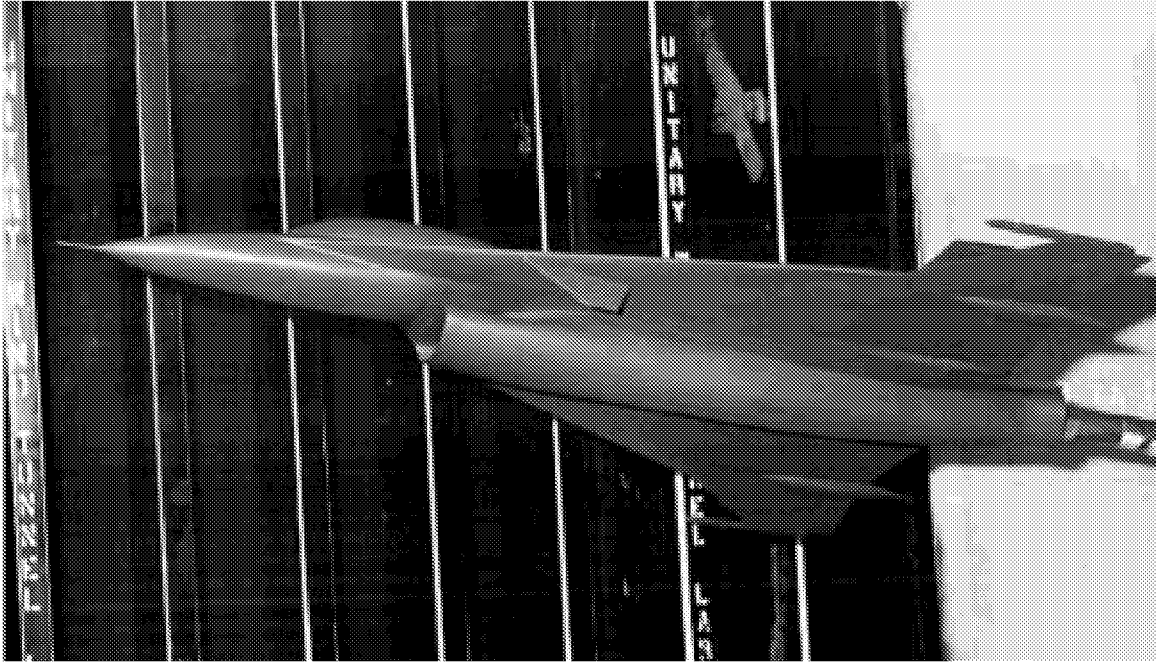


Figure 13. F-16XL-2 1/15-scale model in the Langley Unitary Plan Wind Tunnel.

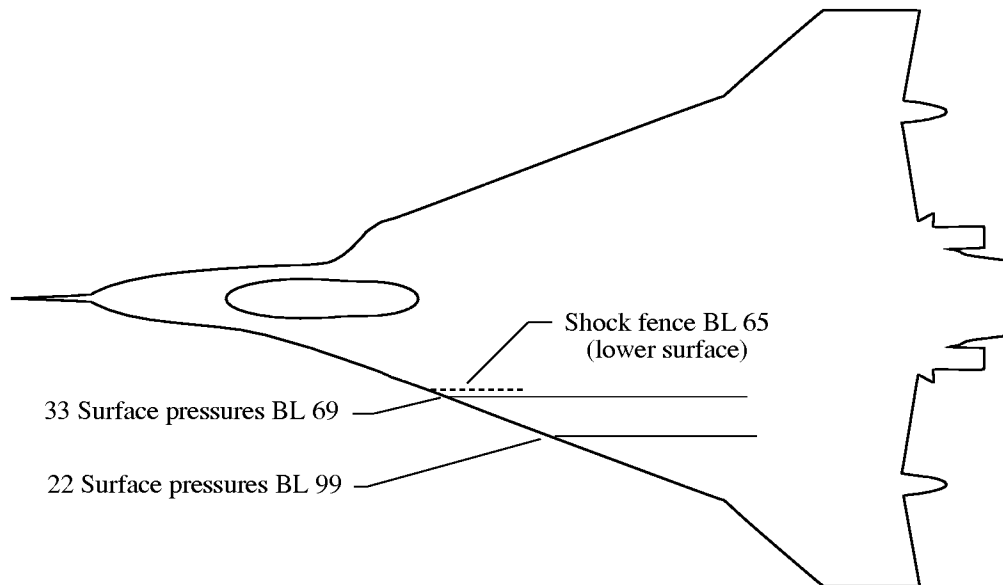


Figure 14. Instrumentation locations on F-16XL-2 1/15-scale model.

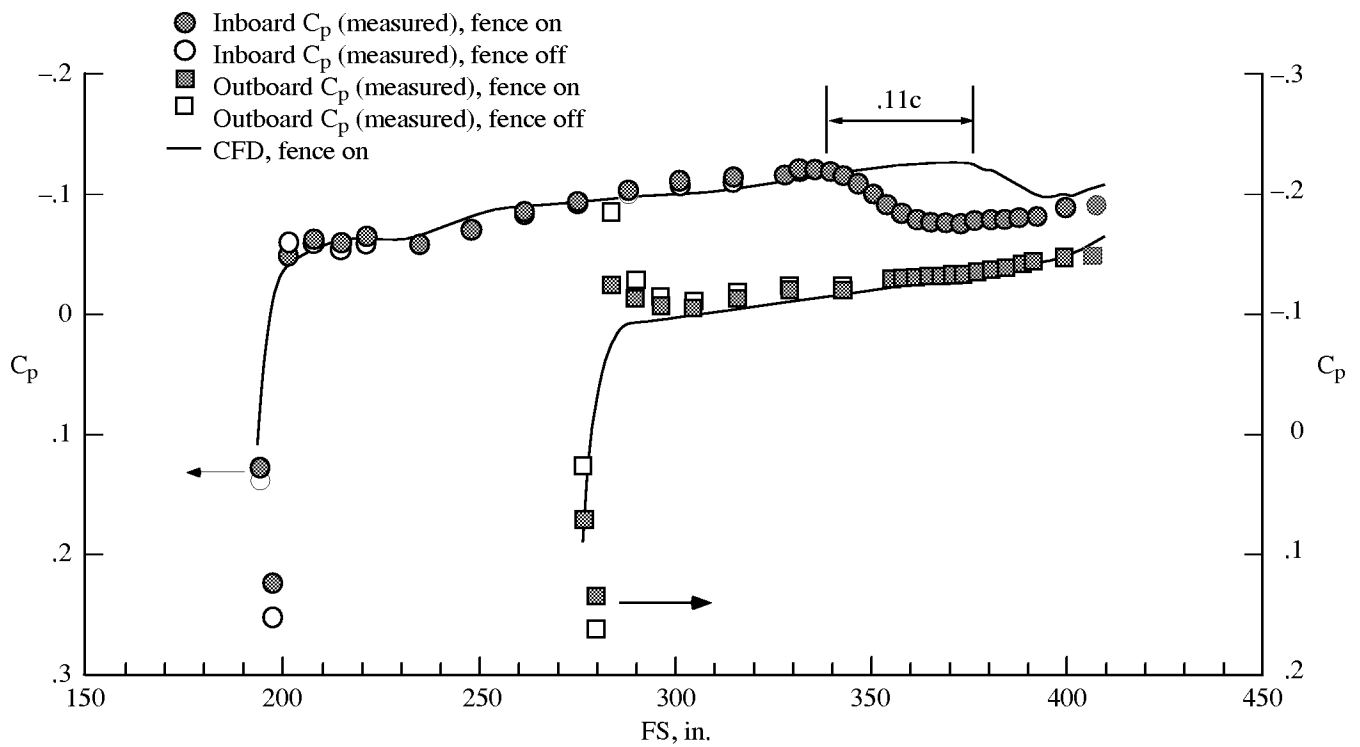


Figure 15. Langley Unitary Plan Wind Tunnel data showing effect of shock fence and comparison with CFD. $M = 1.9$; $\alpha = 3.3^\circ$; $\beta = 0^\circ$.

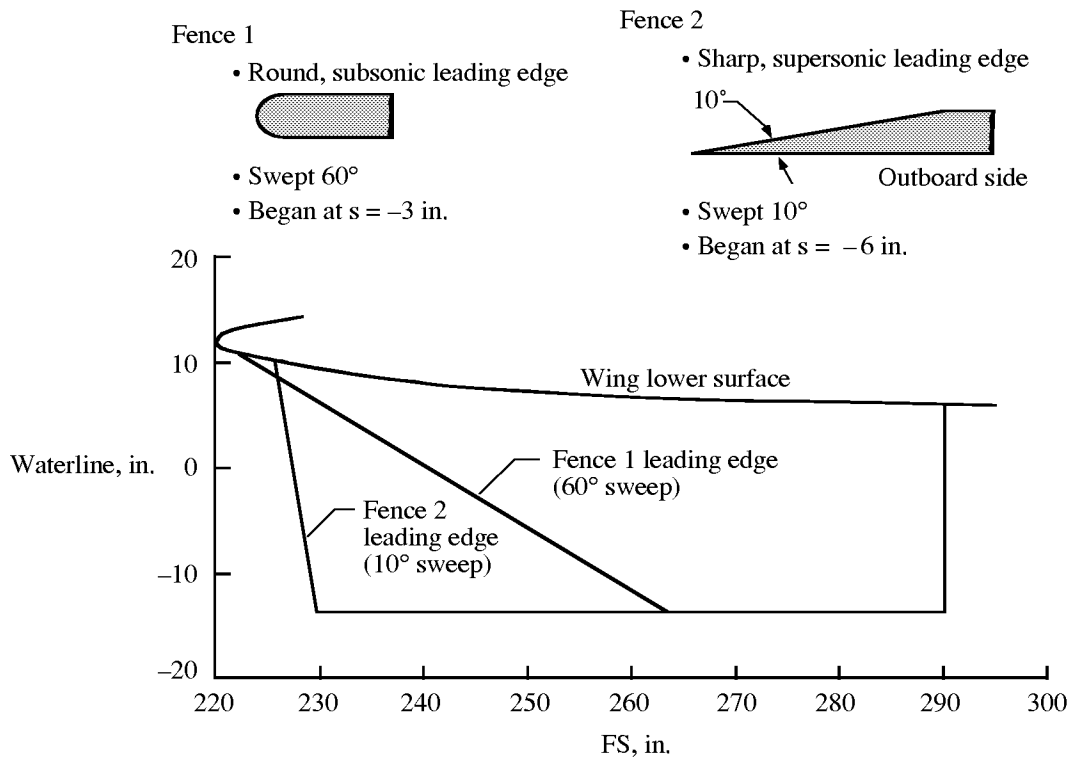


Figure 16. Details of shock fence configurations.

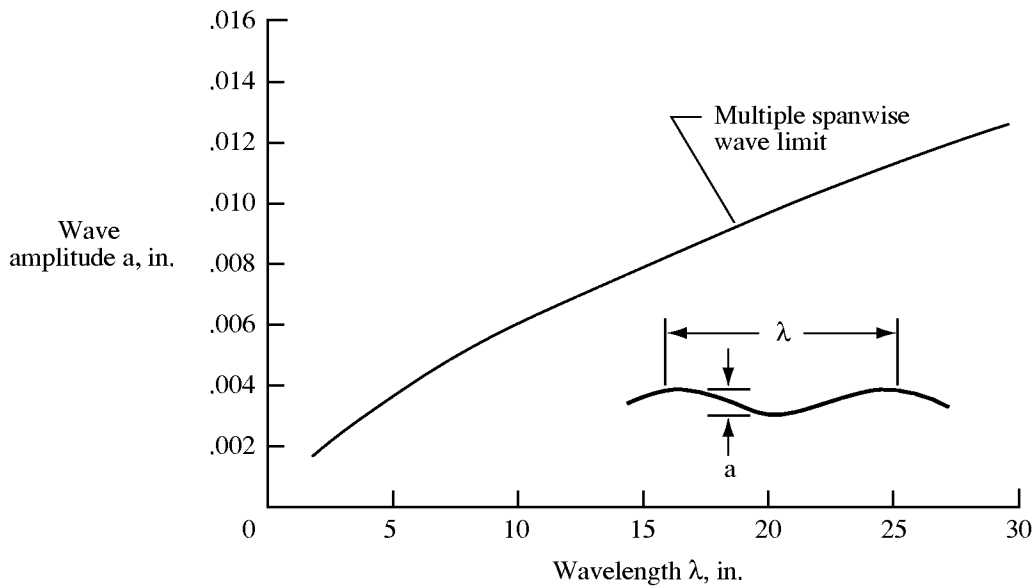


Figure 17. Surface waviness design tolerances. Special conditions: for chordwise waves, double spanwise amplitude limits; for single wave (spanwise or chordwise), triple amplitude limits. $M = 1.9$; $h = 50\,000$ ft; $R/ft = 2.25 \times 10^6$; $c = 23$ ft; $\Lambda = 70^\circ$.

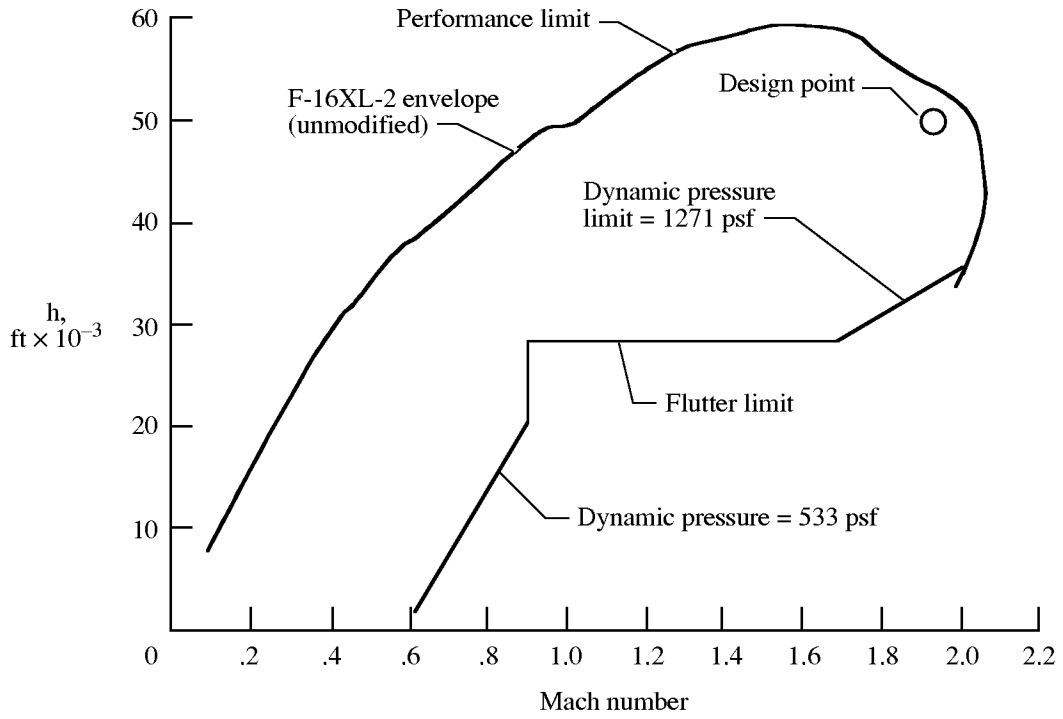


Figure 18. F-16XL-2 operating envelope.

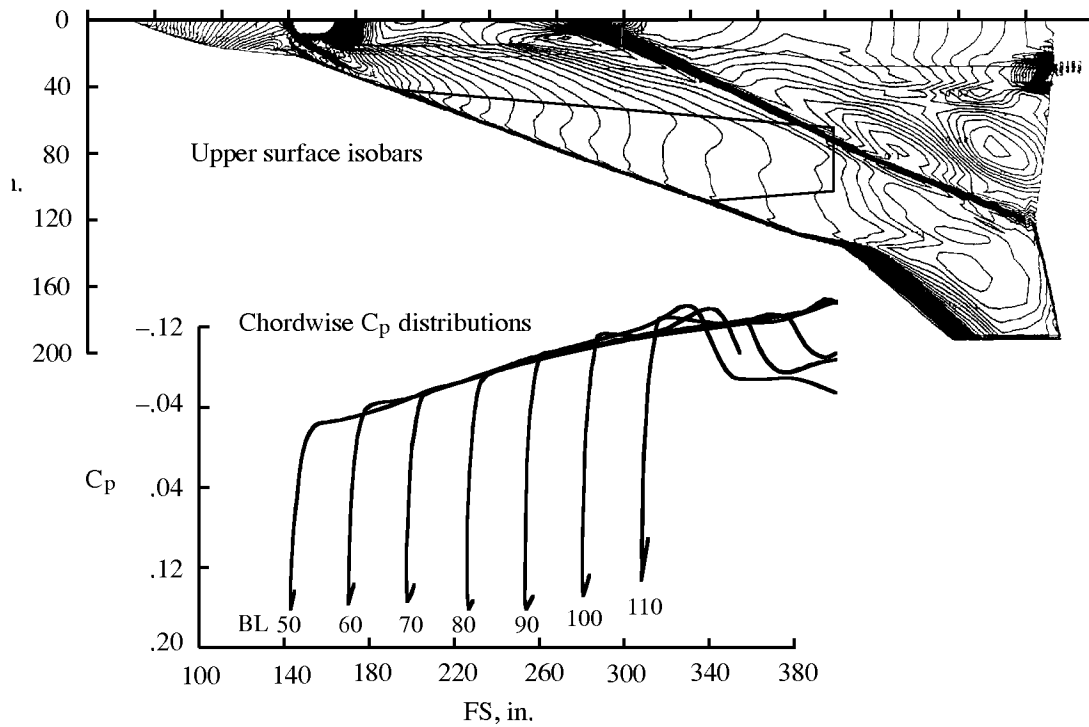
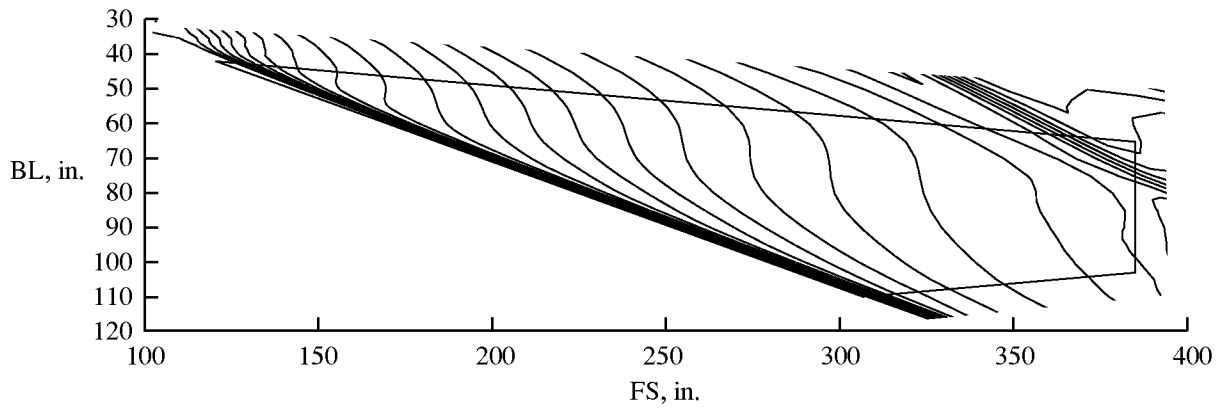
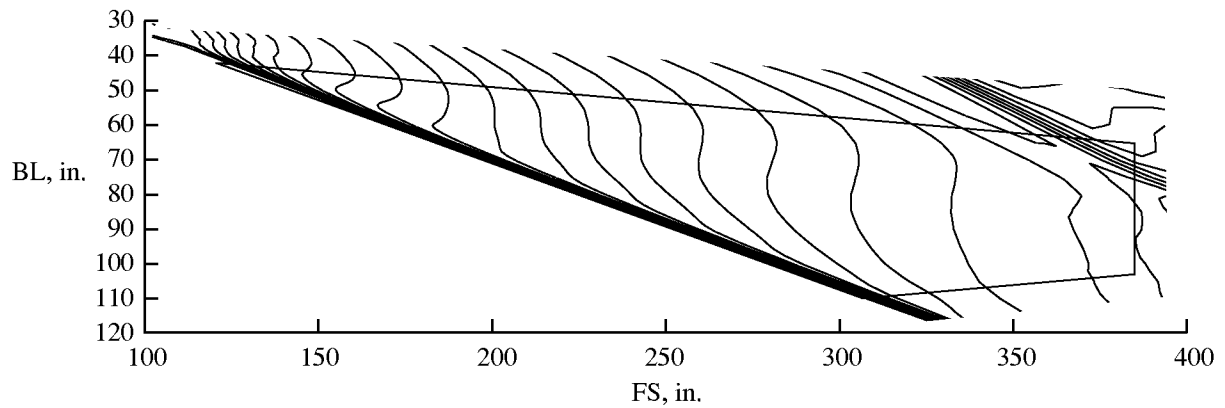


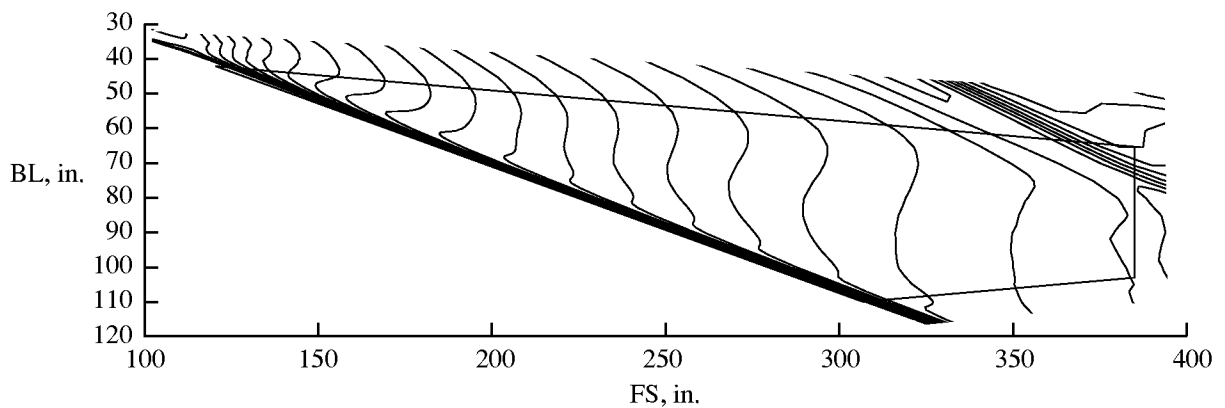
Figure 19. Design pressure distributions (generated by BCAG). $M = 1.9$; $\alpha = 3.3^\circ$.



(a) $M = 1.9$; $\alpha = 2.5^\circ$.

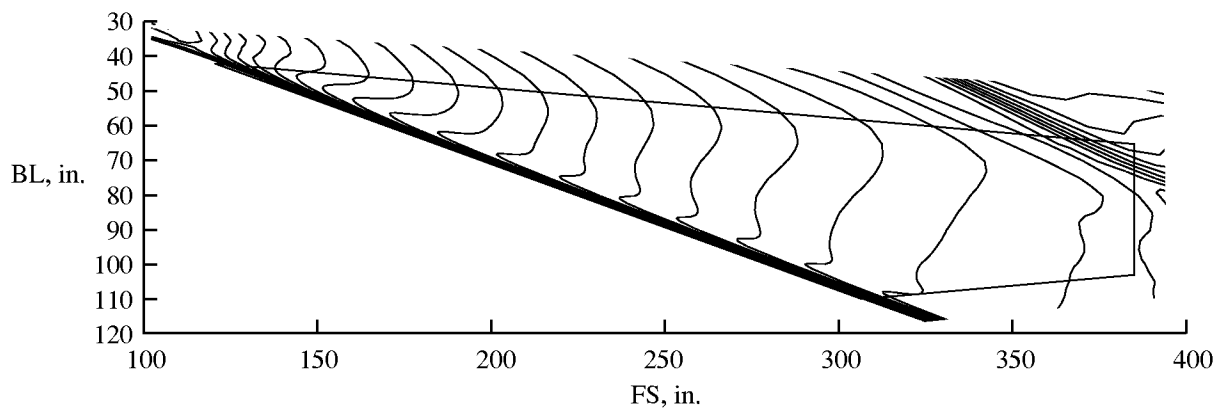


(b) $M = 1.9$; $\alpha = 3.0^\circ$.

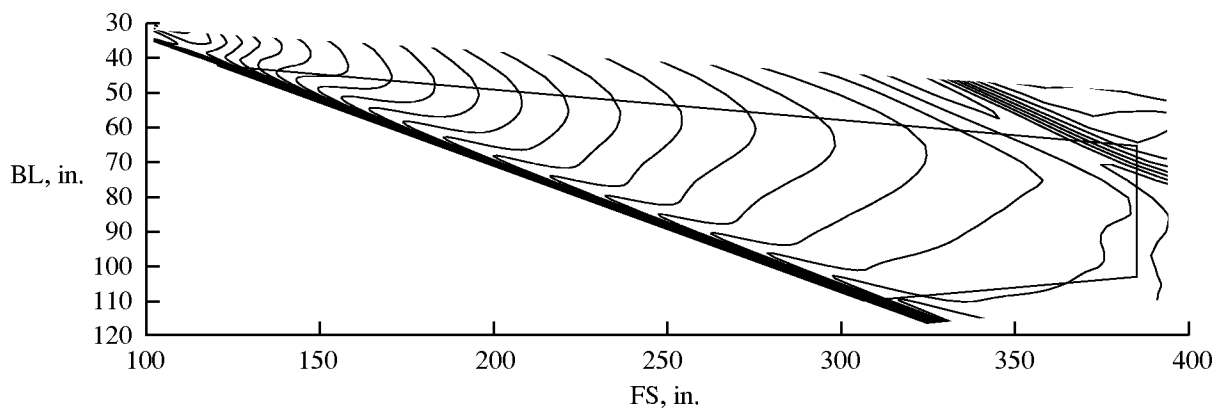


(c) $M = 1.9$; $\alpha = 3.3^\circ$.

Figure 20. CFD solutions of upper surface isobars for α at and below design point (generated by BCAG). Isobar lines are spaced $0.01C_p$.

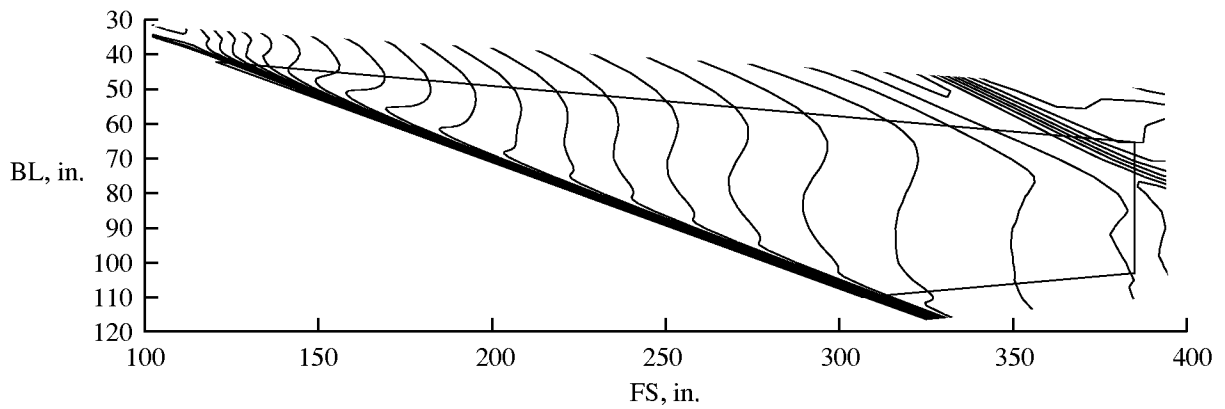


(d) $M = 1.9$; $\alpha = 3.6^\circ$.

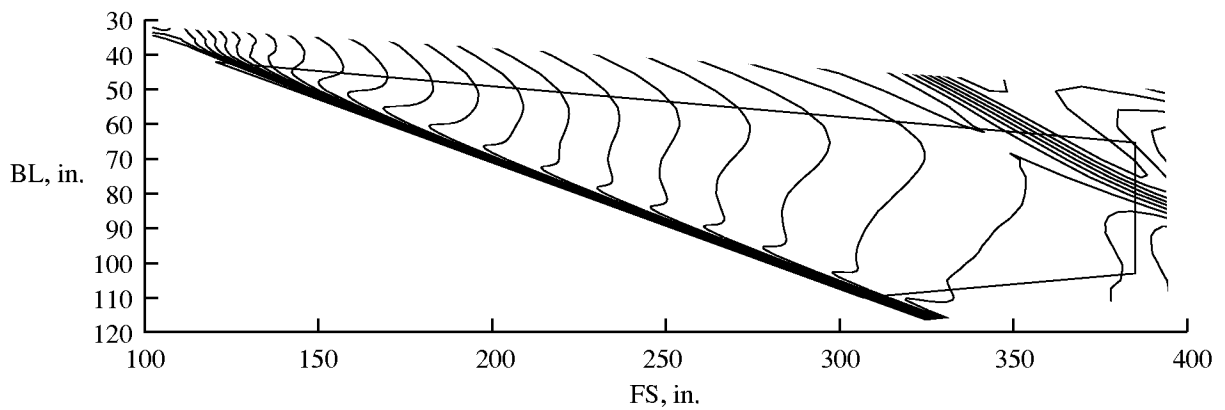


(e) $M = 1.9$; $\alpha = 4.1^\circ$.

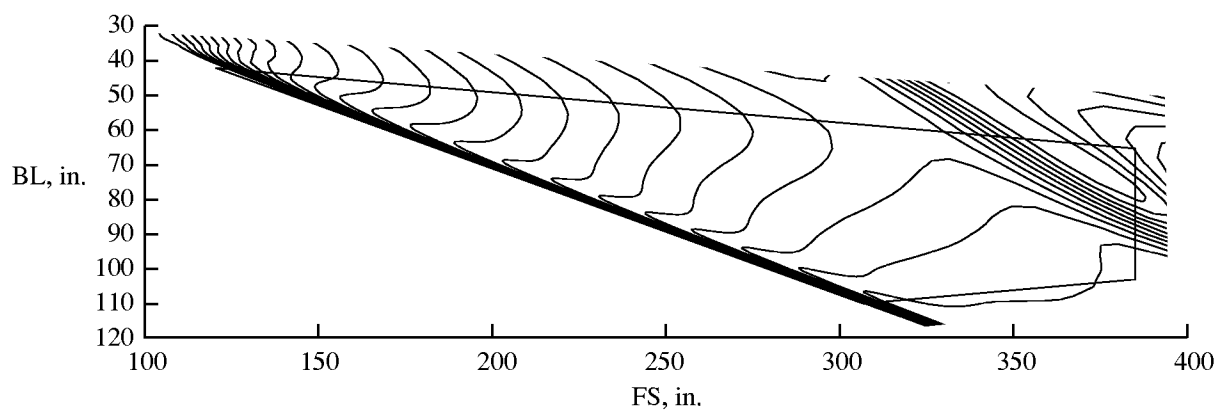
Figure 20. Concluded.



(a) $M = 1.9$; $\alpha = 3.3^\circ$.



(b) $M = 1.8$; $\alpha = 3.3^\circ$.



(c) $M = 1.7$; $\alpha = 3.3^\circ$.

Figure 21. CFD solutions of upper surface isobars for Mach numbers at and below design point (generated by BCAG). Isobar lines are spaced $0.01C_p$.

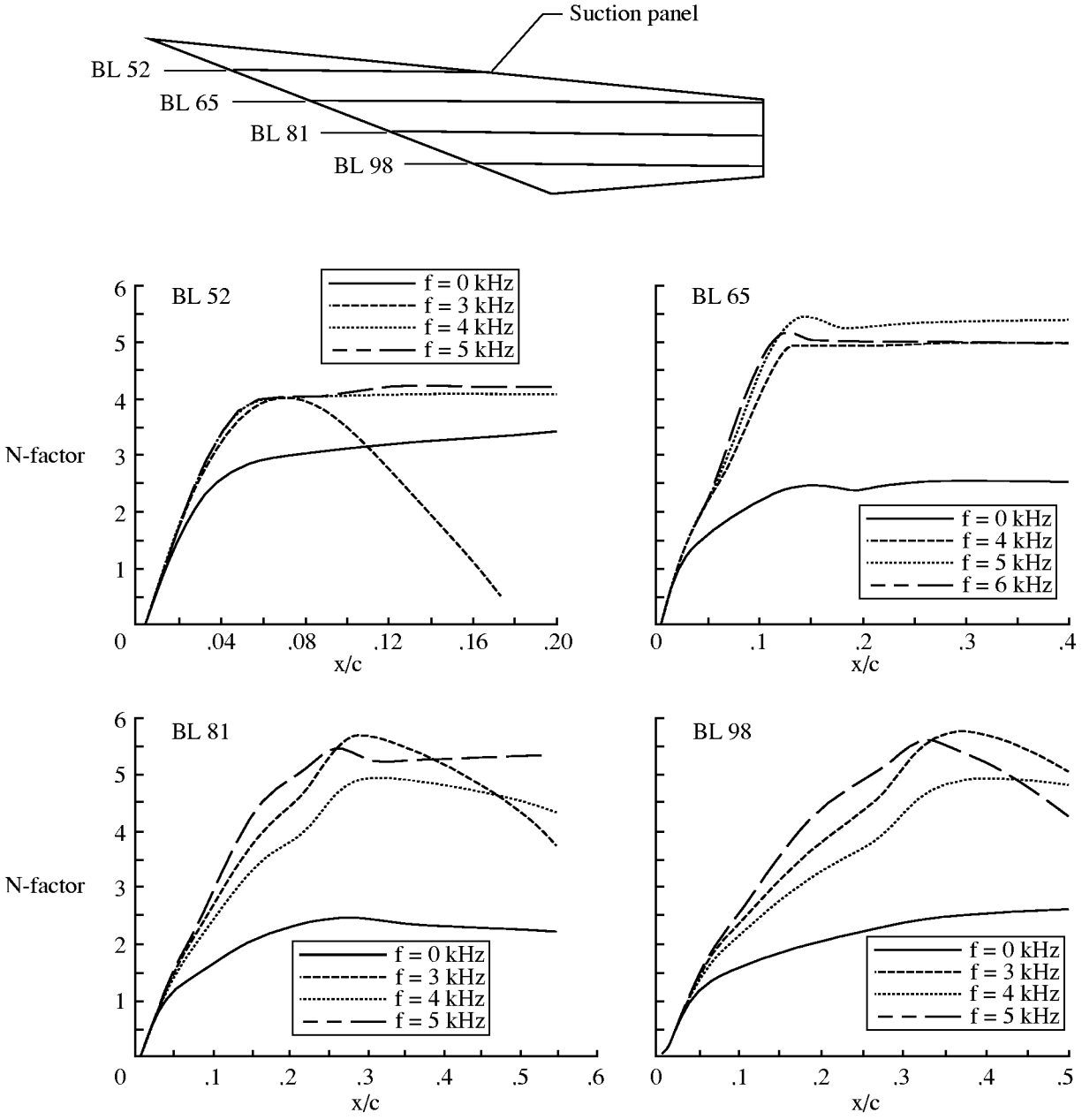


Figure 22. Boundary layer disturbance growth rates for upper suction level (generated by BCAG). $M = 1.9$; $\alpha = 3.3^\circ$; $h = 50\,000$ ft.

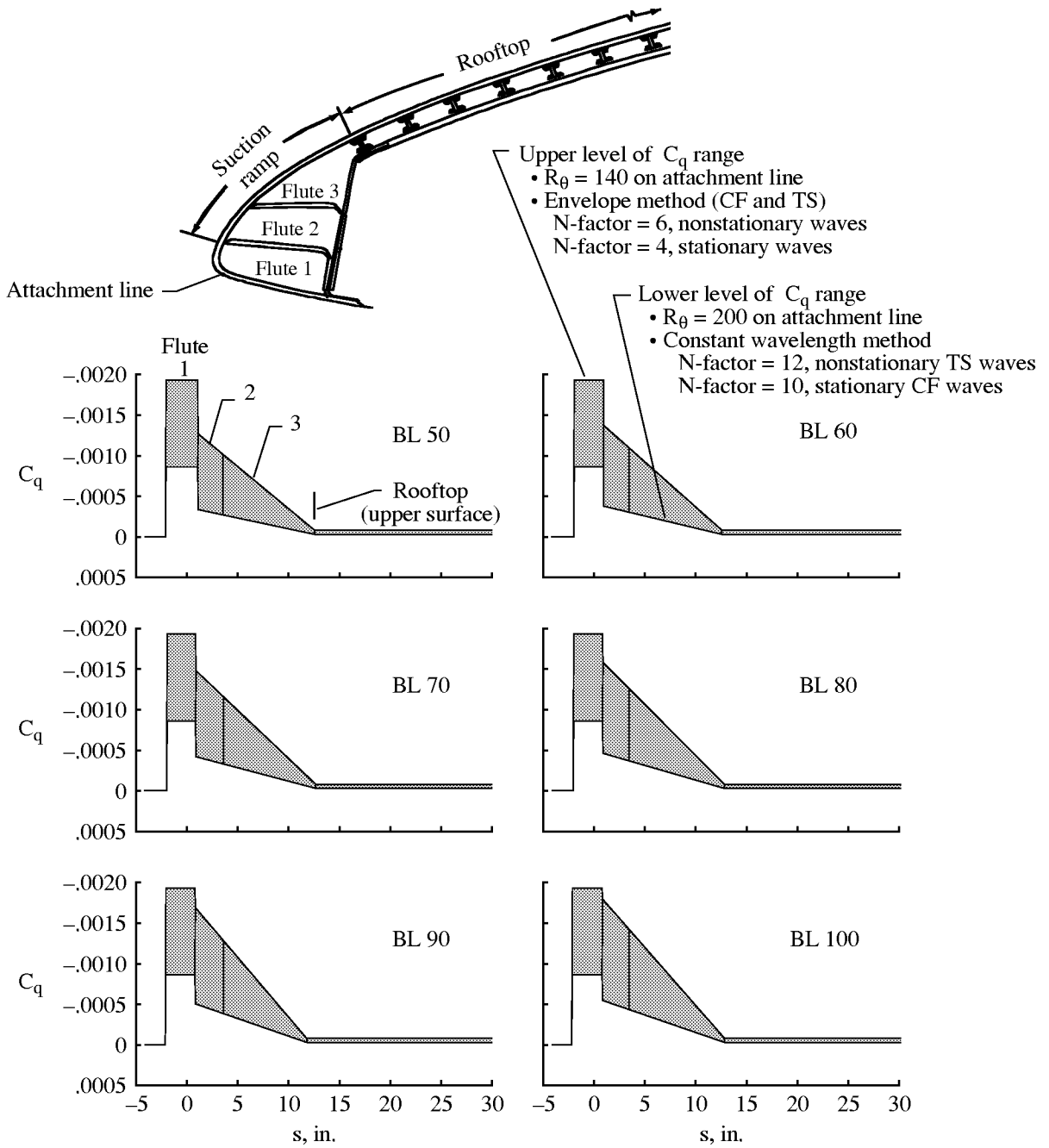


Figure 23. Coefficient of suction C_q design range envelope for $M = 1.9$; $\alpha = 3.3^\circ$. Note: Rooftop (upper surface) foreshortened for illustration.

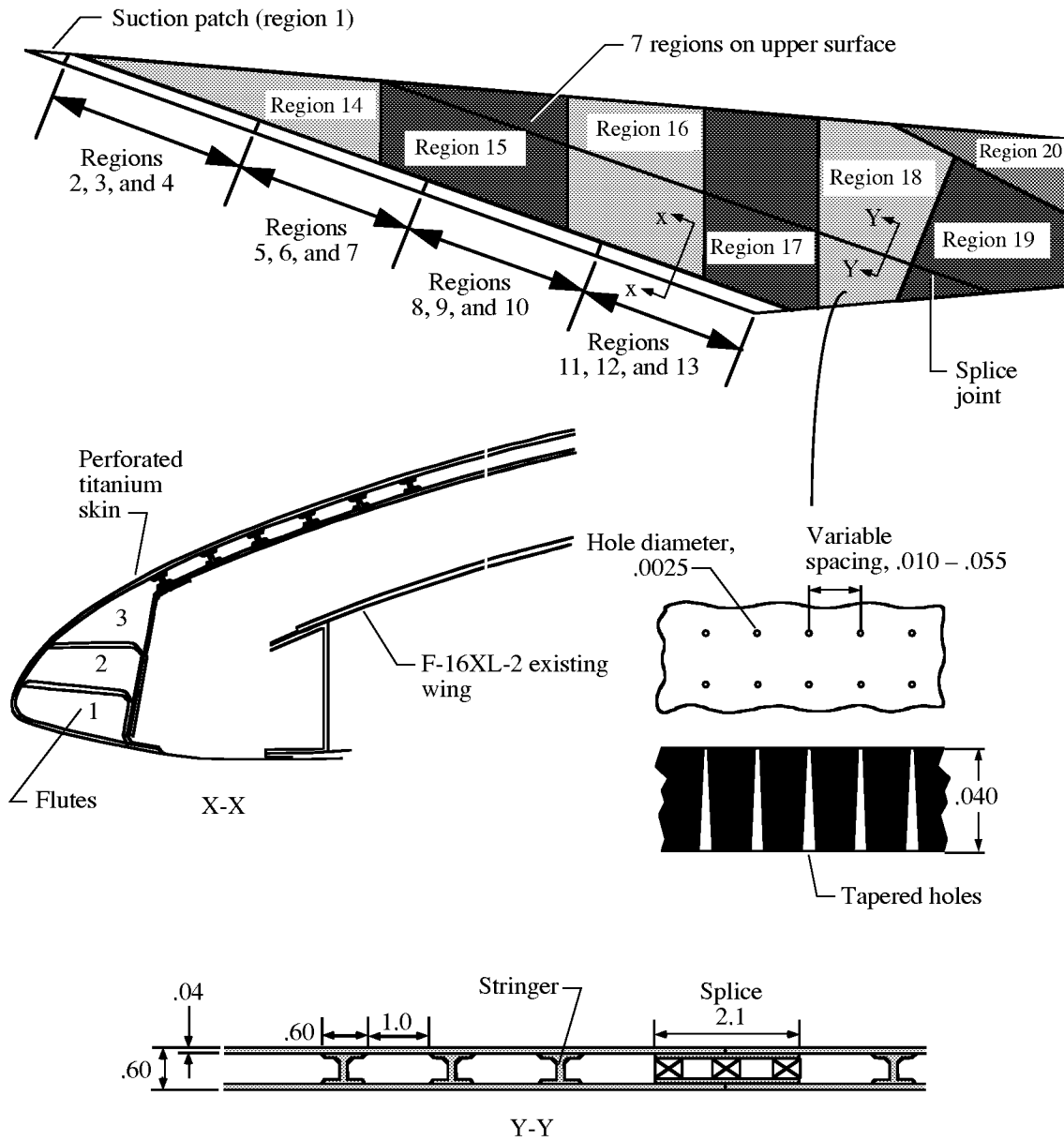


Figure 24. Suction panel structure layout; 13 regions in leading edge. All dimensions are in inches.

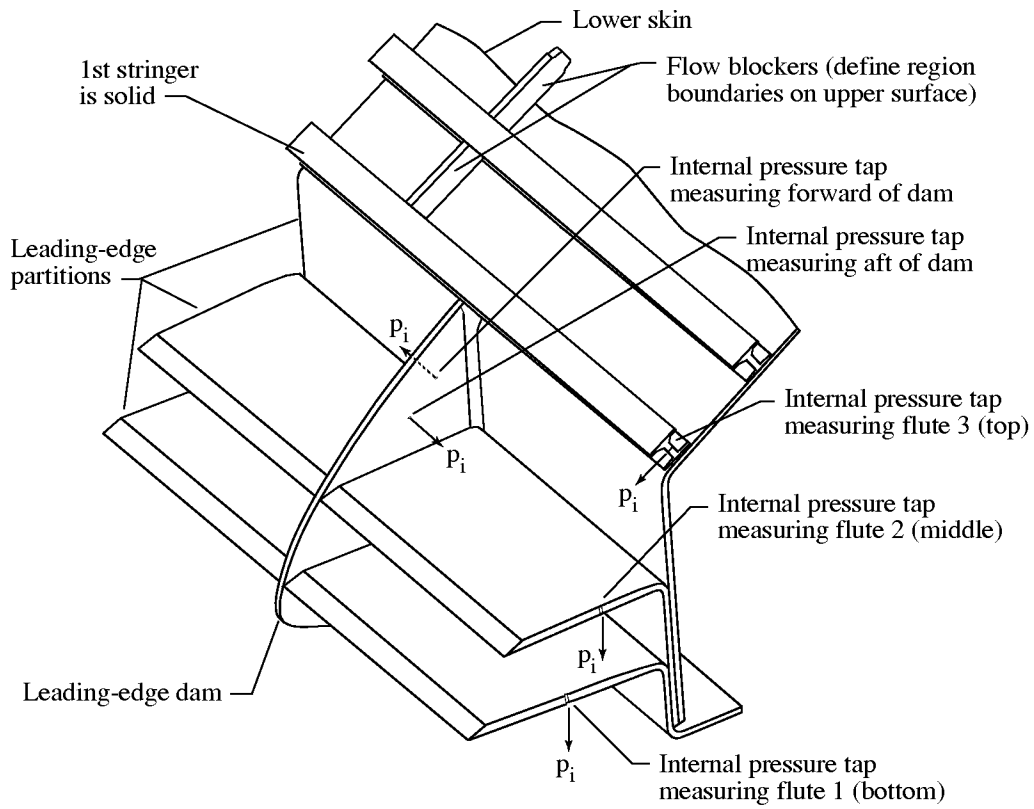


Figure 25. Suction panel leading-edge detail of flute partitions and beginning of upper surface.

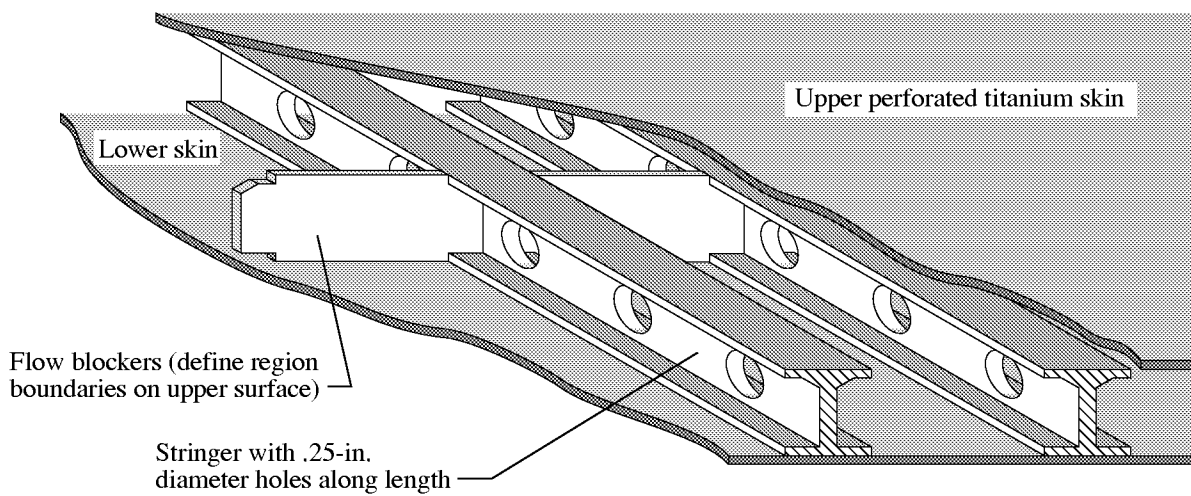


Figure 26. Suction panel upper surface detail showing stringers and flow blockers.

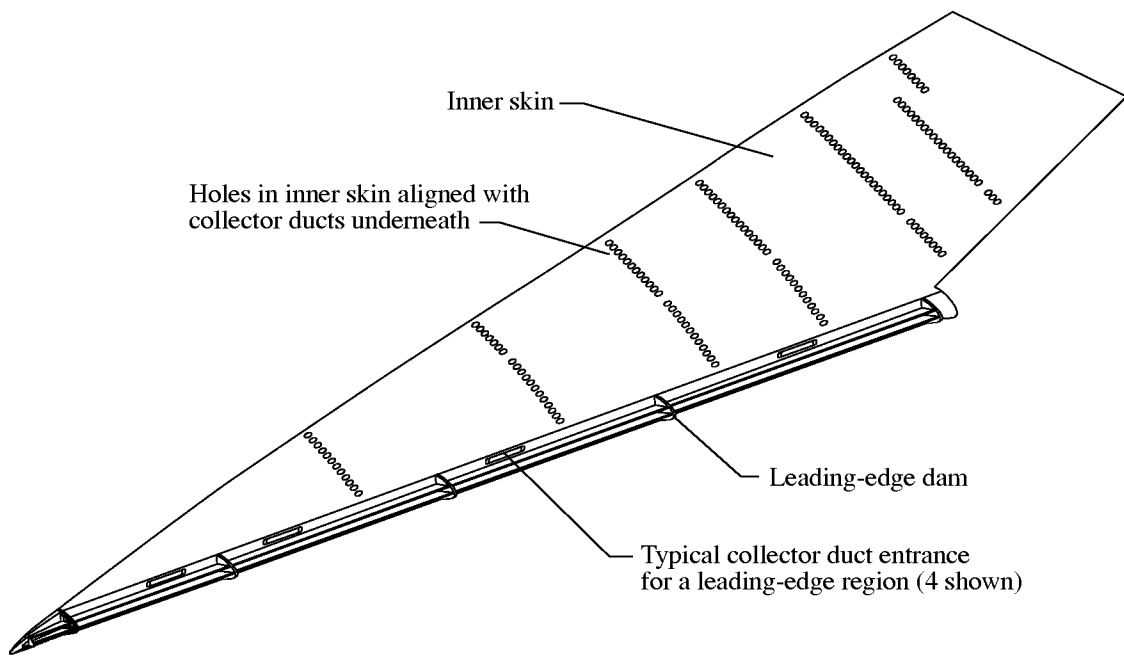


Figure 27. Suction panel inner skin detail showing passageways for removal of air through lower skin into collector ducts.

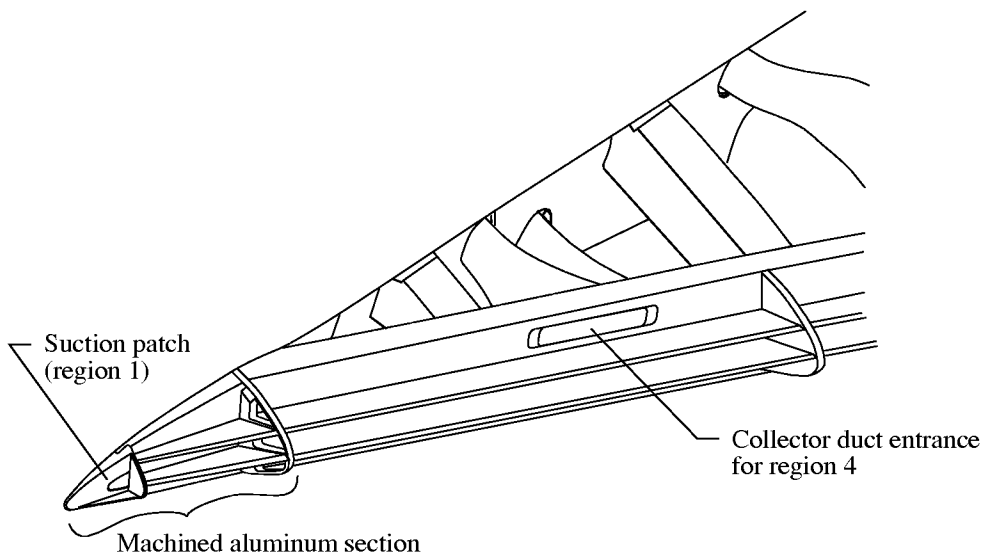


Figure 28. Details of inboard leading-edge structure.

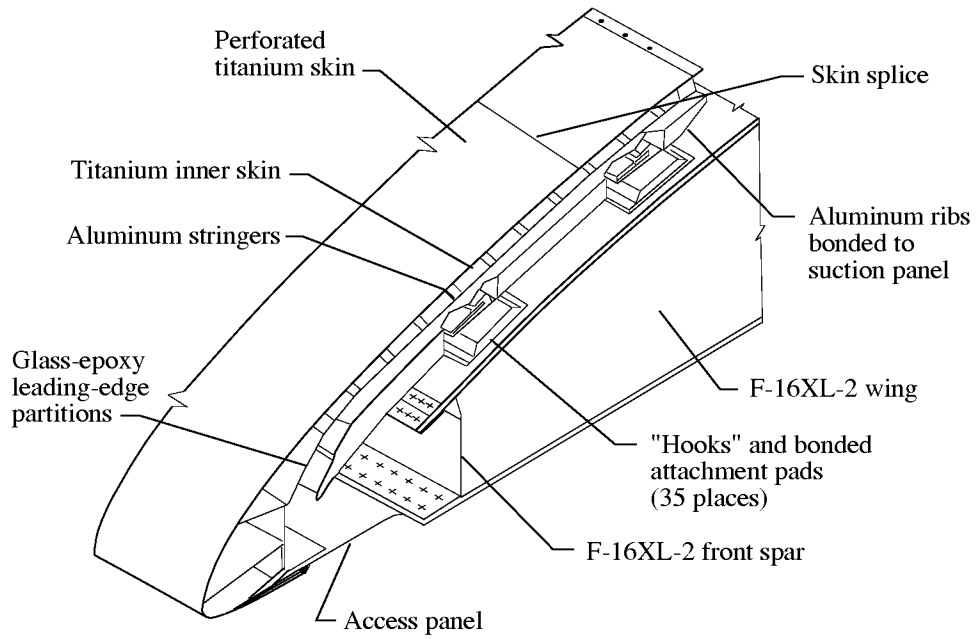


Figure 29. Suction panel and support structure arrangement.

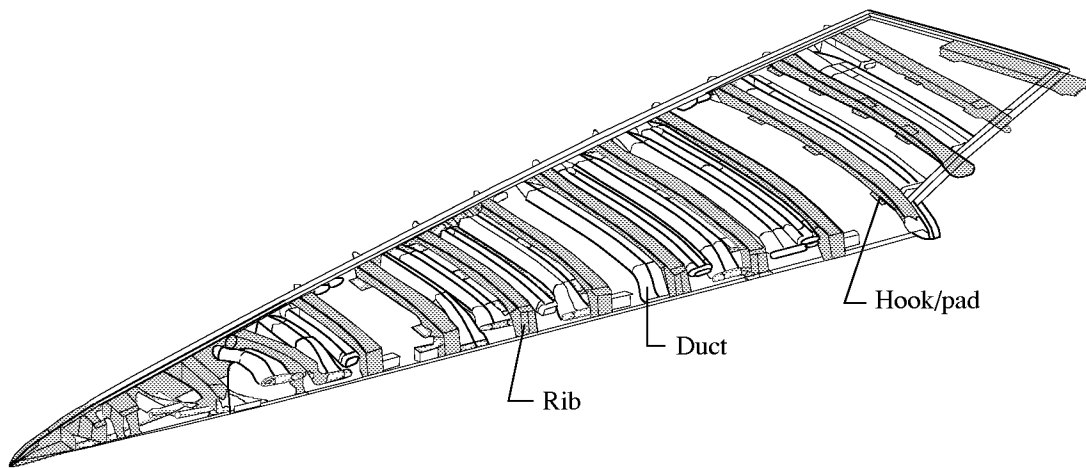


Figure 30. Details of supporting structure. Ribs are shaded. Outer skin, stringers, and inner skin have been removed.

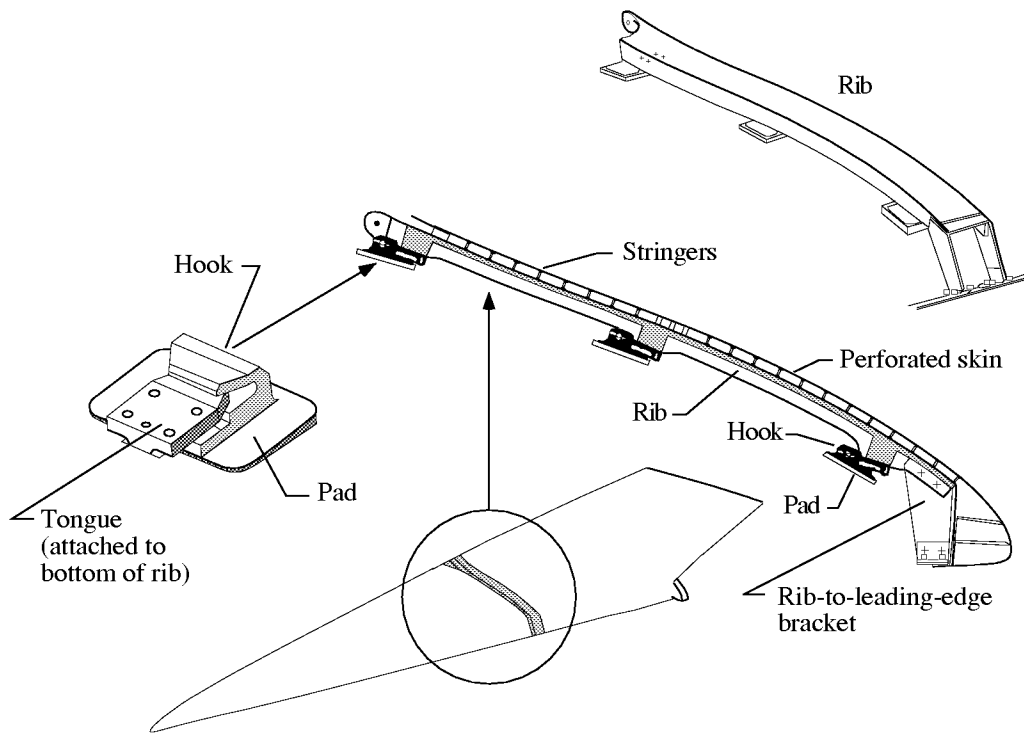


Figure 31. Suction panel and support structure arrangement.

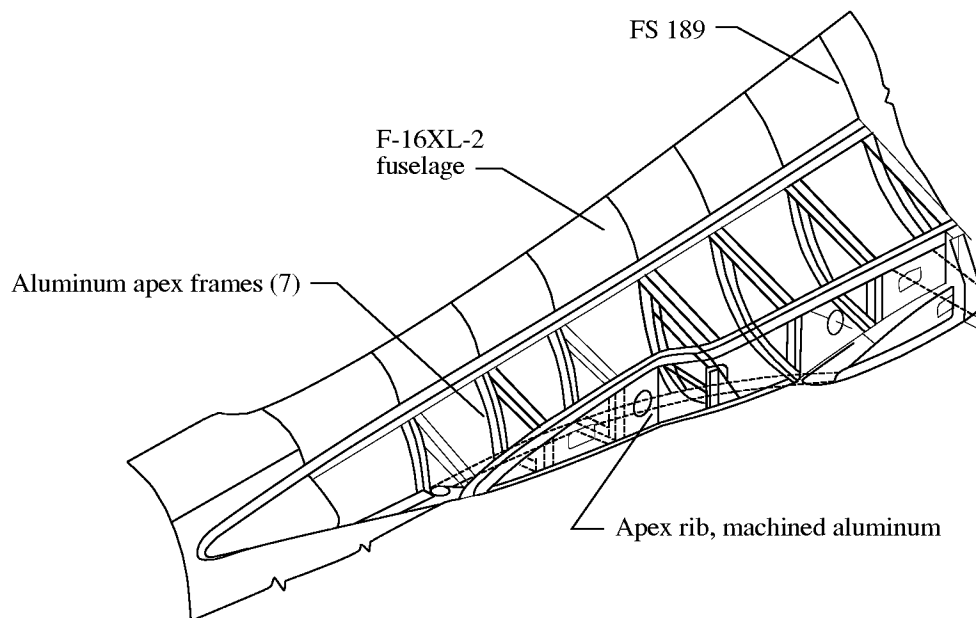


Figure 32. Inboard apex structural concept.

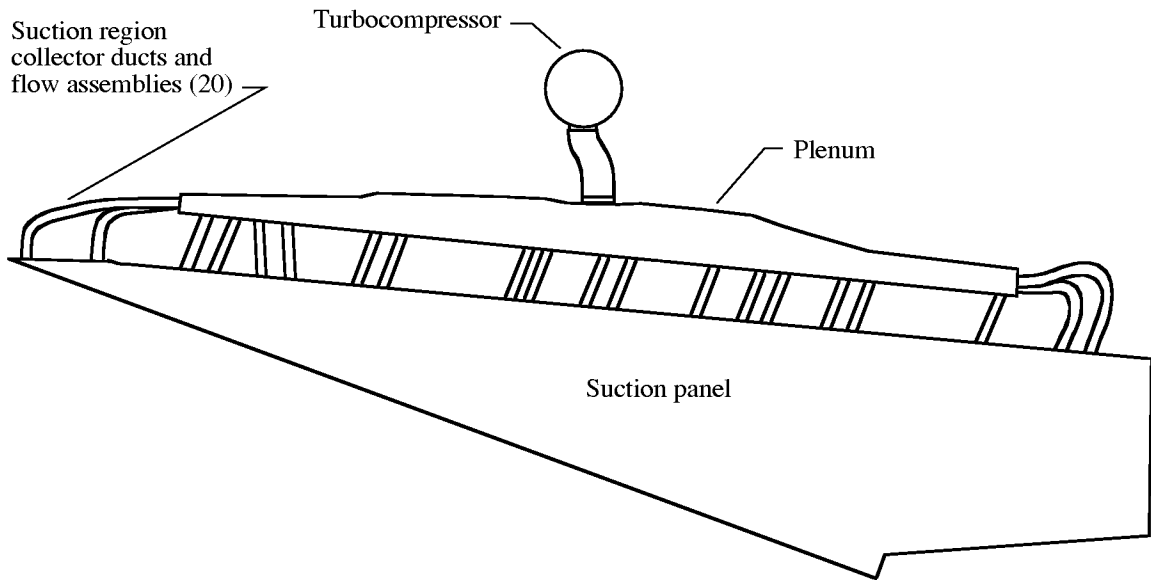


Figure 33. Suction system flow concept.

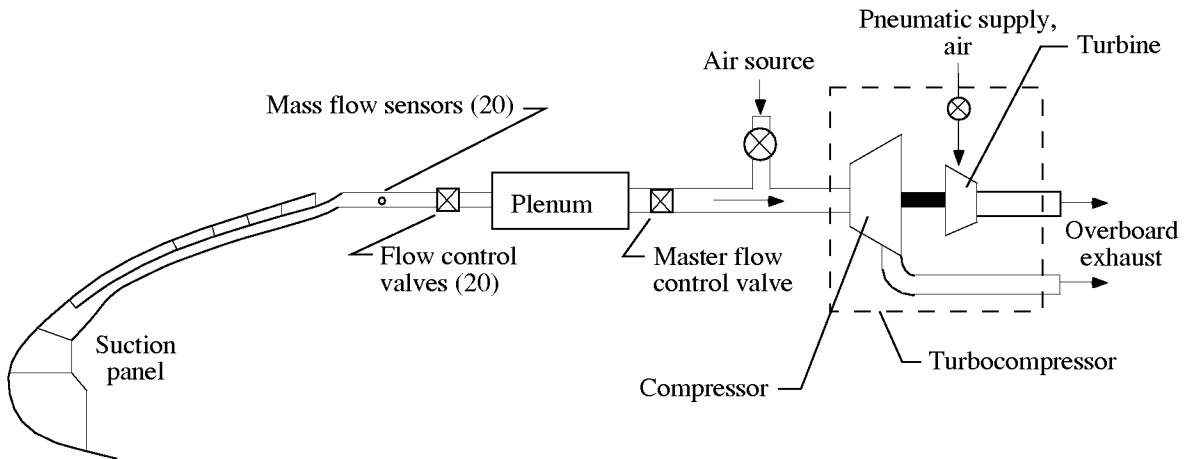


Figure 34. Suction system layout.

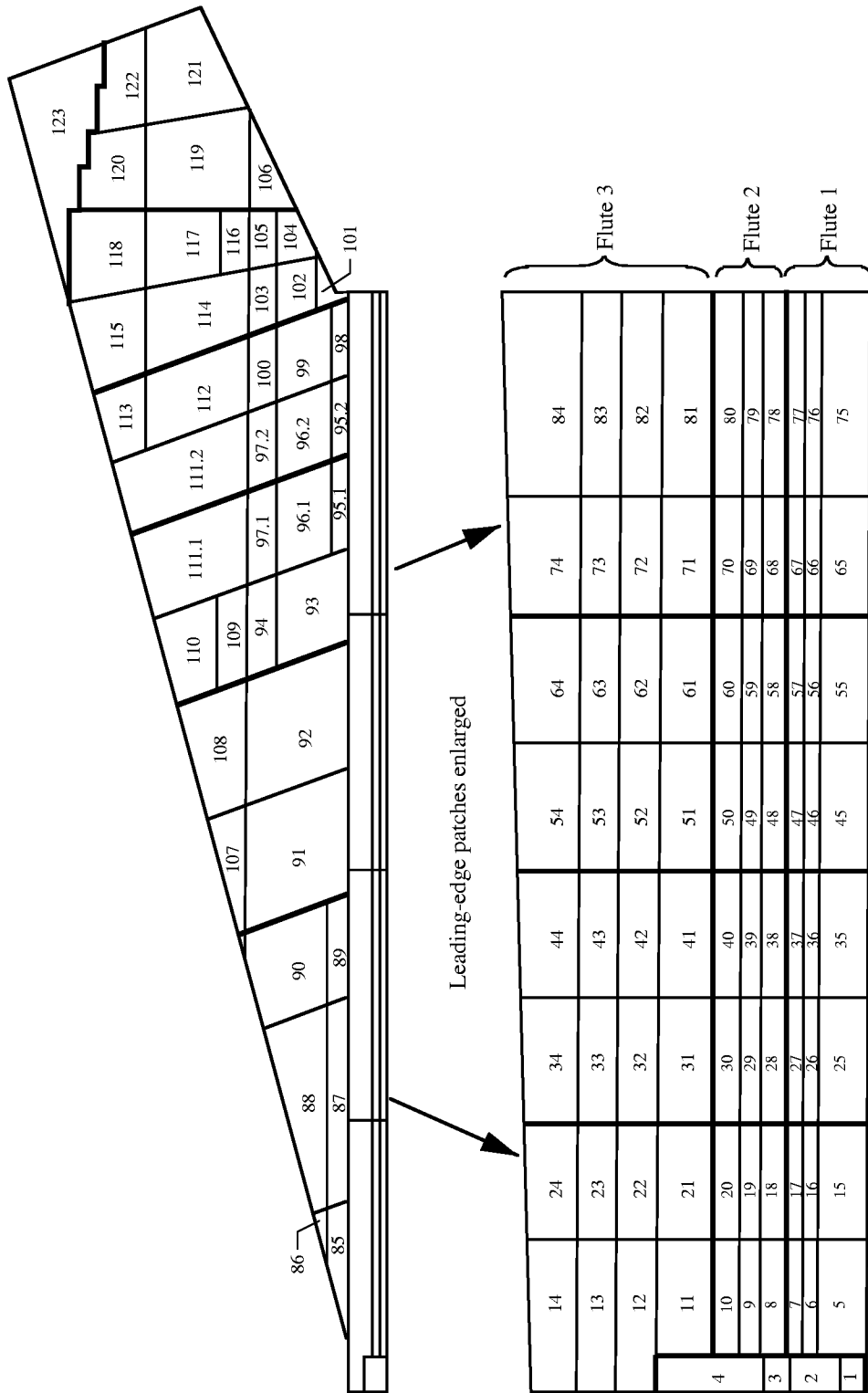
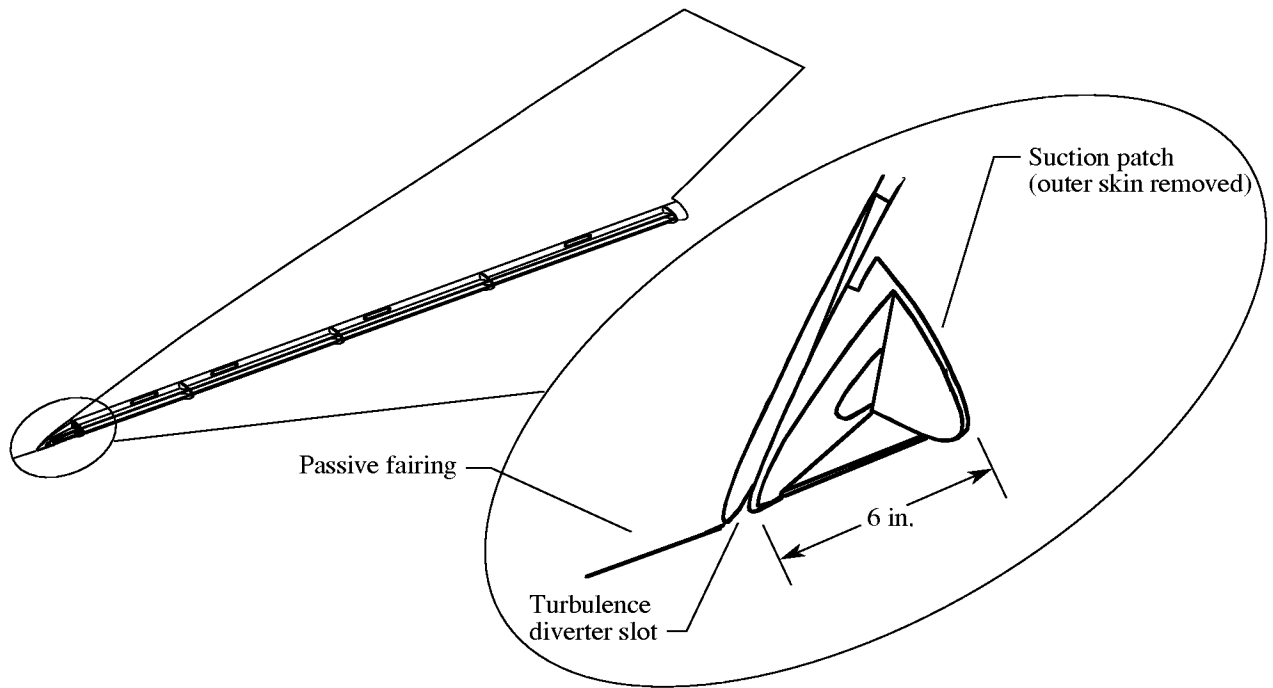
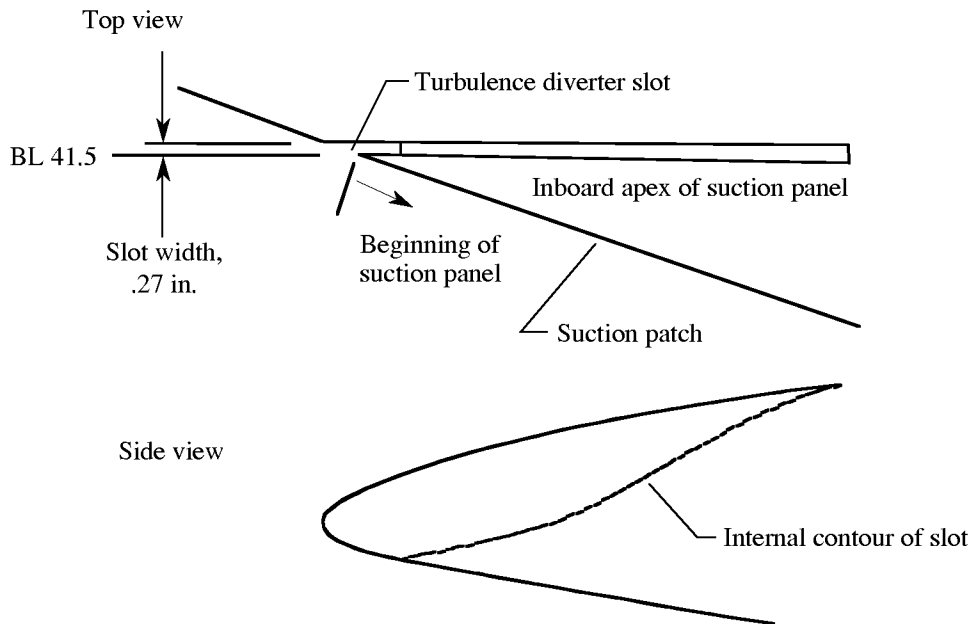


Figure 35. Location of patches on suction panel perforated titanium skin. Darker lines define 20 suction region boundaries.



(a) Isometric view of turbulene diverter slot and suction patch.



(b) Top and side views of turbulene diverter slot.

Figure 36. Details of turbulene diverter and suction patch.

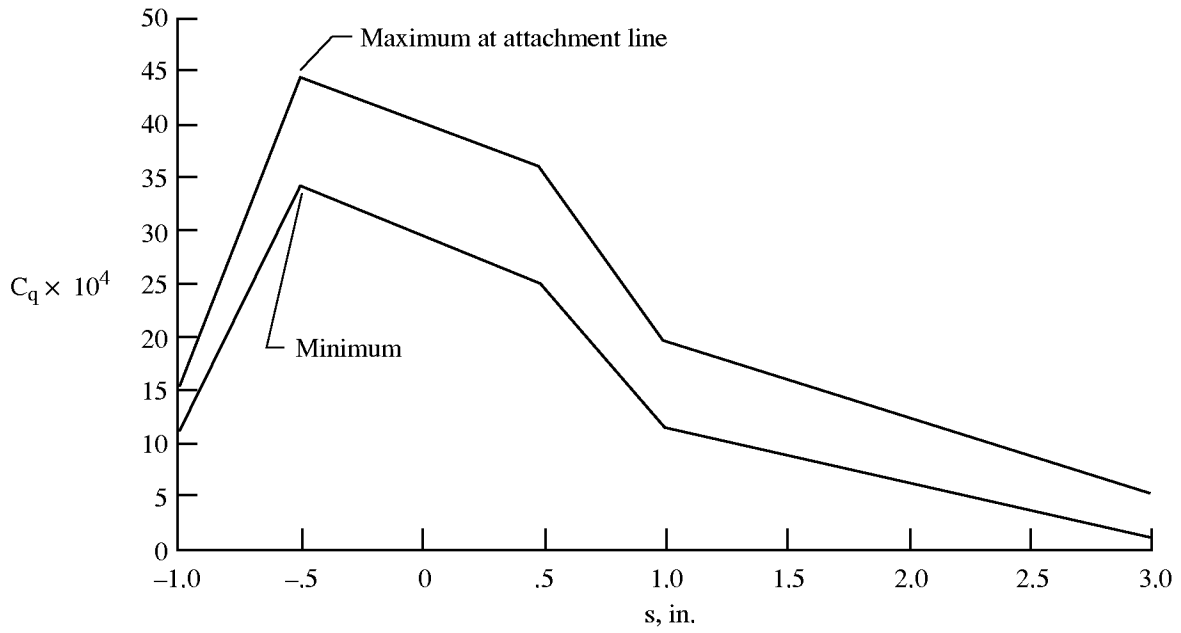


Figure 37. Minimum and maximum design C_q at suction patch. $M = 1.9$; $h = 50\,000$ ft.

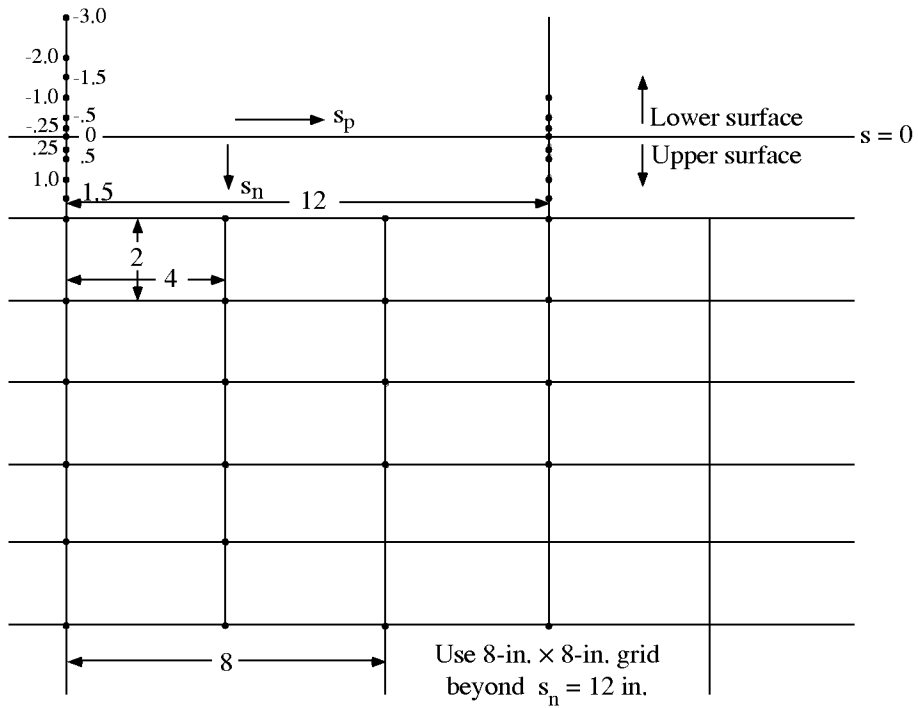


Figure 38. Measurement grid for Computer Aided Theodolite (CAT) contour verification.

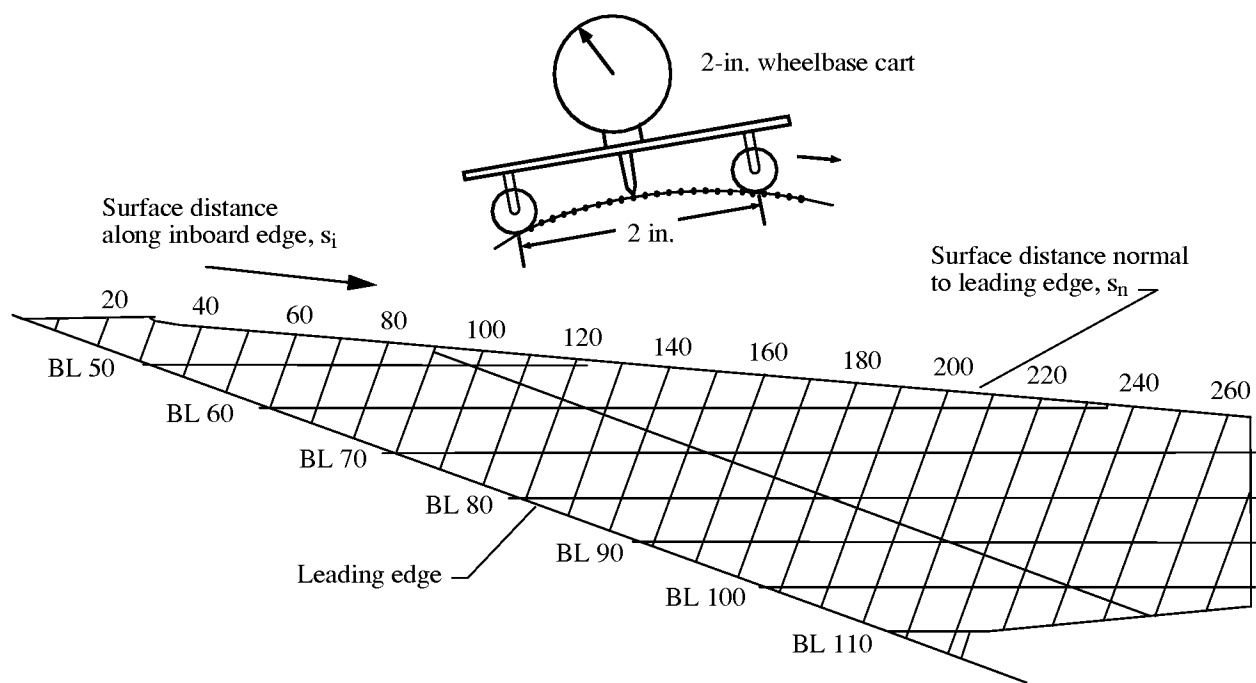


Figure 39. Normal and streamwise paths used for surface waviness measurements.

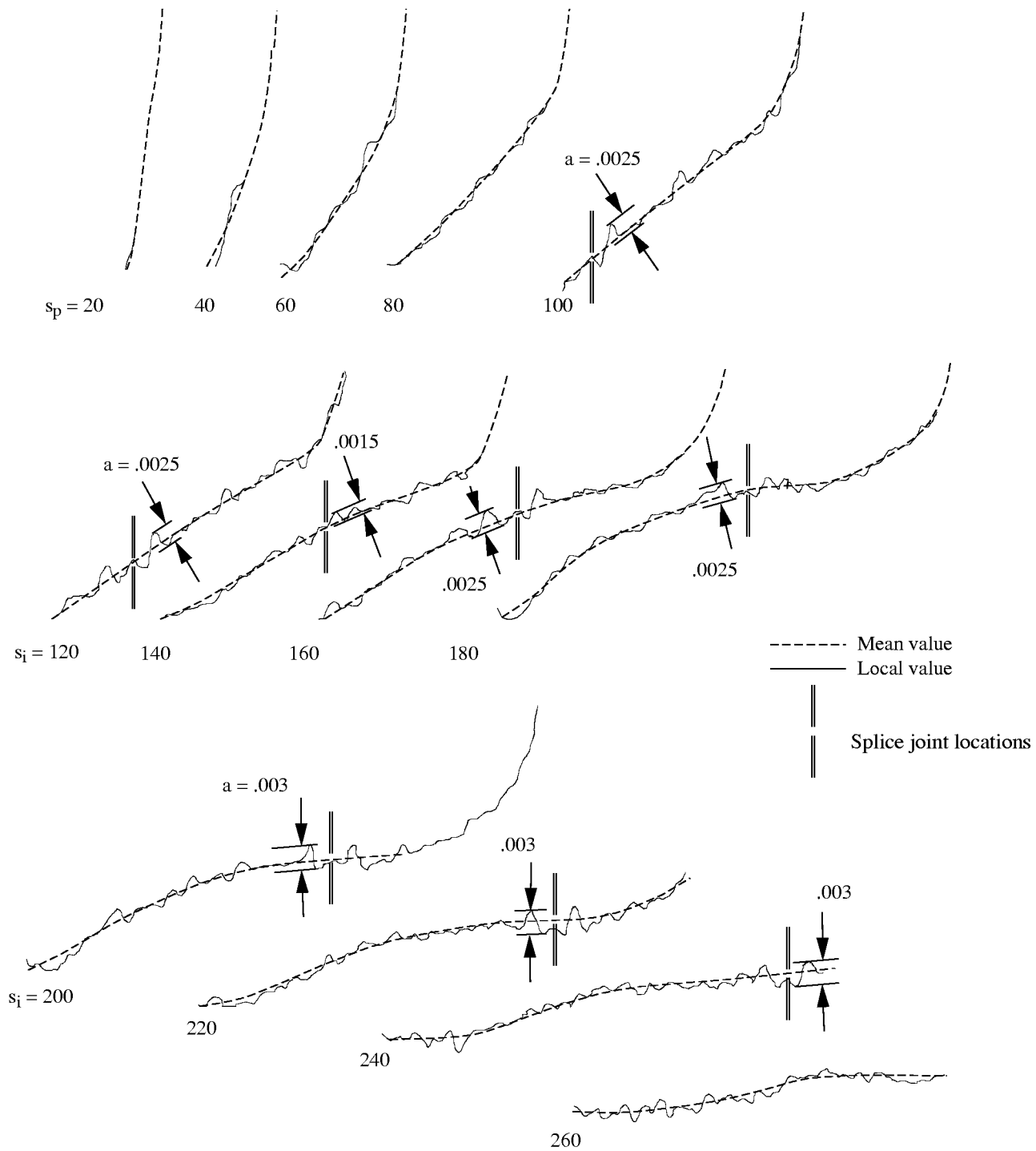


Figure 40. Normal path panel surface waviness measurements. Dimensions are in inches.

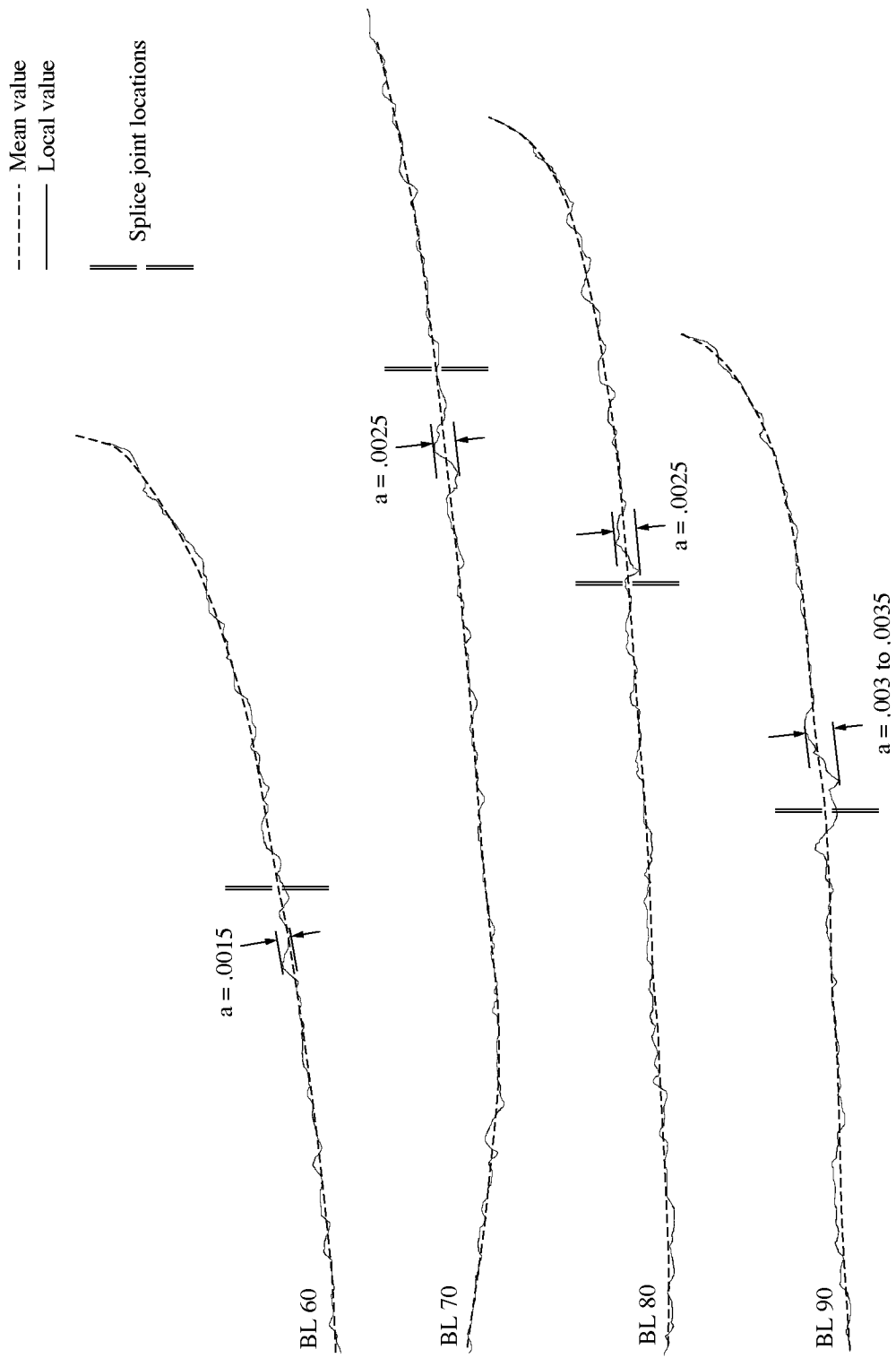


Figure 41. Streamwise (BL) path surface waviness measurements. Dimensions are in inches.

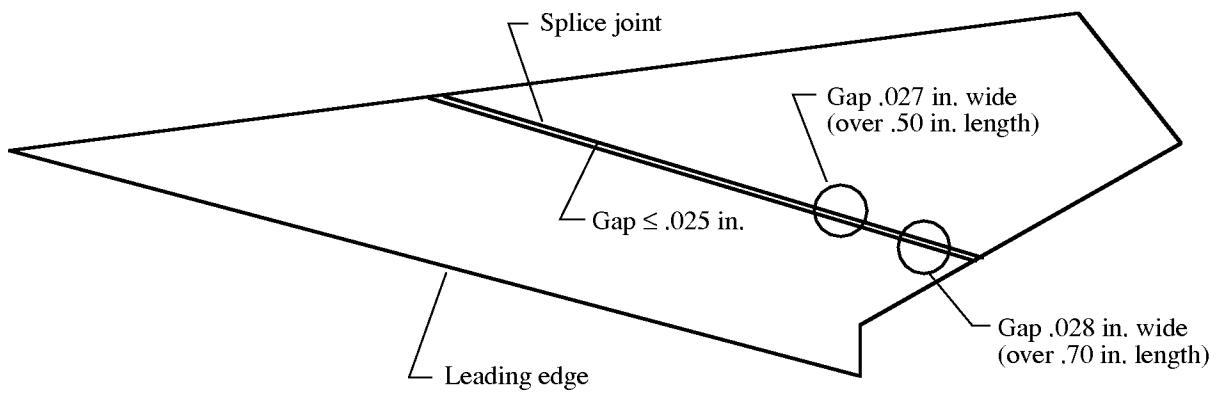


Figure 42. Measurements of splice joint gap width. Note: Panel surface is not to scale.

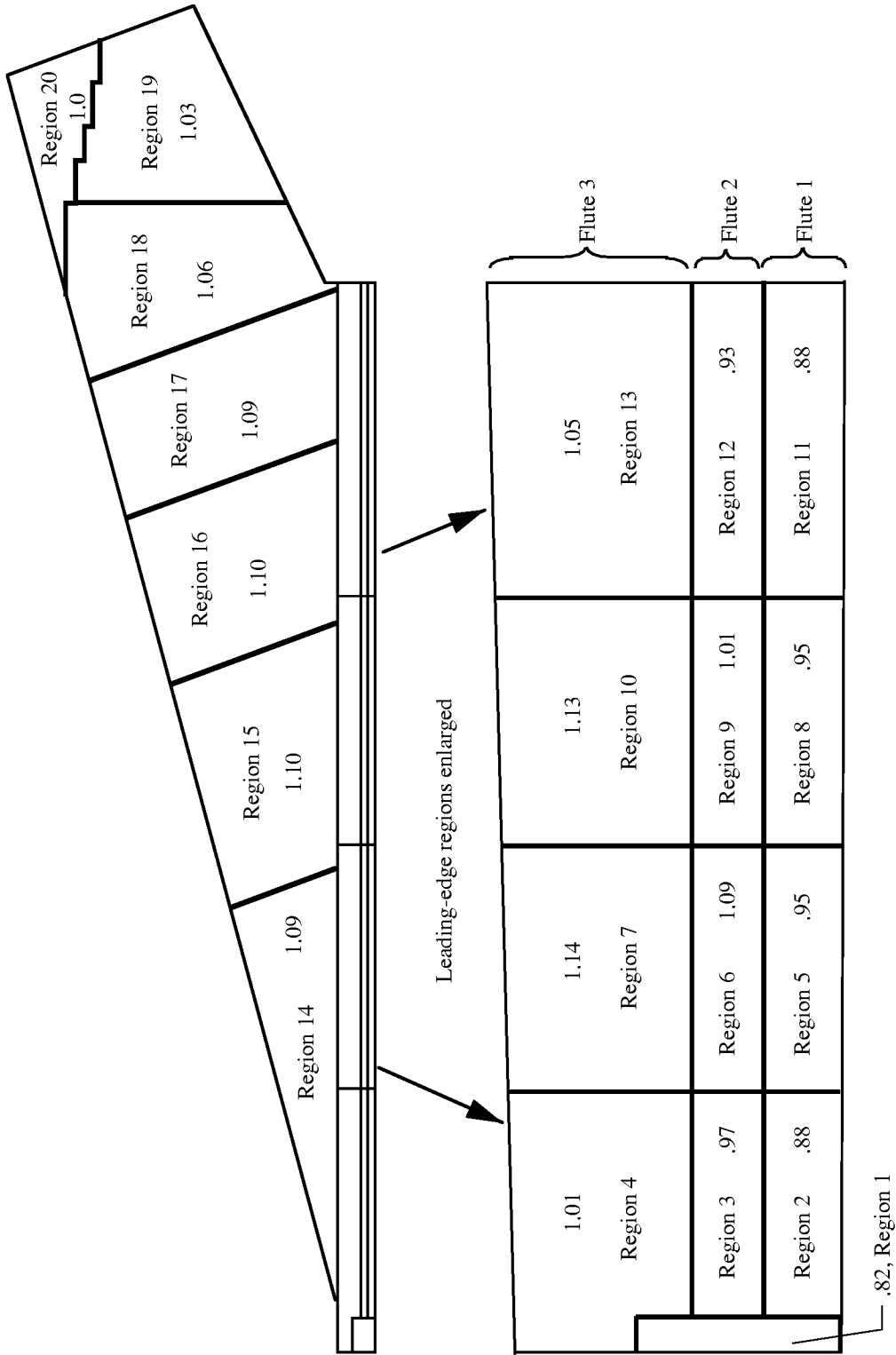


Figure 43. Normalized porosity for each suction region. Note: Numbers >1 indicate porosity above design. Numbers <1 indicate porosity below design.

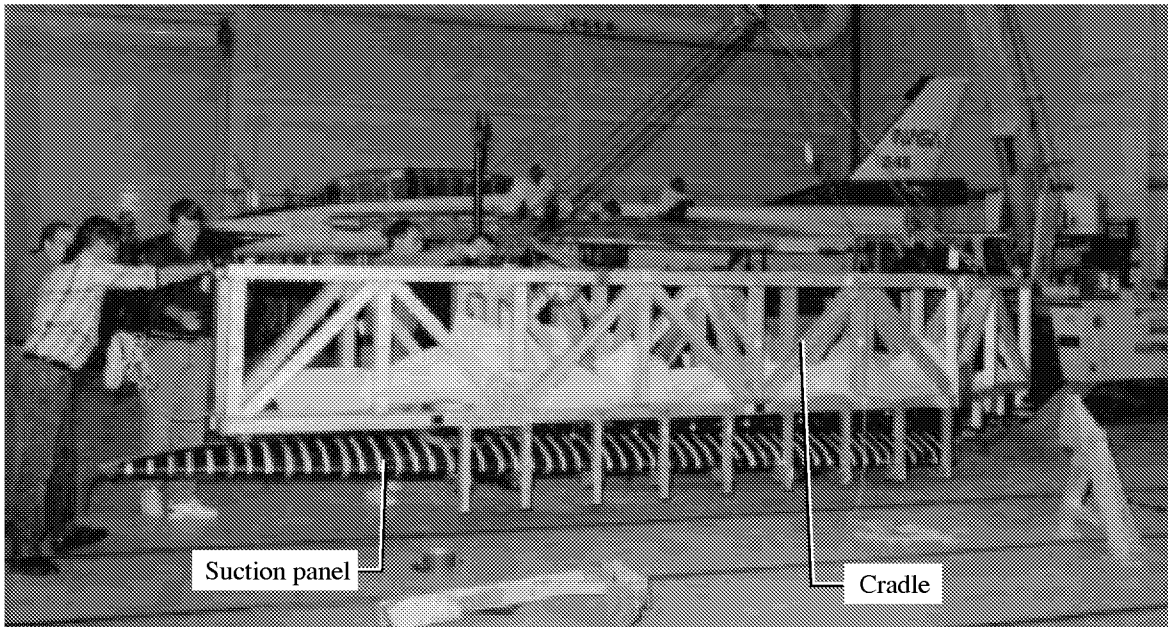


Figure 44. Suction panel in cradle in preparation for fit to wing.

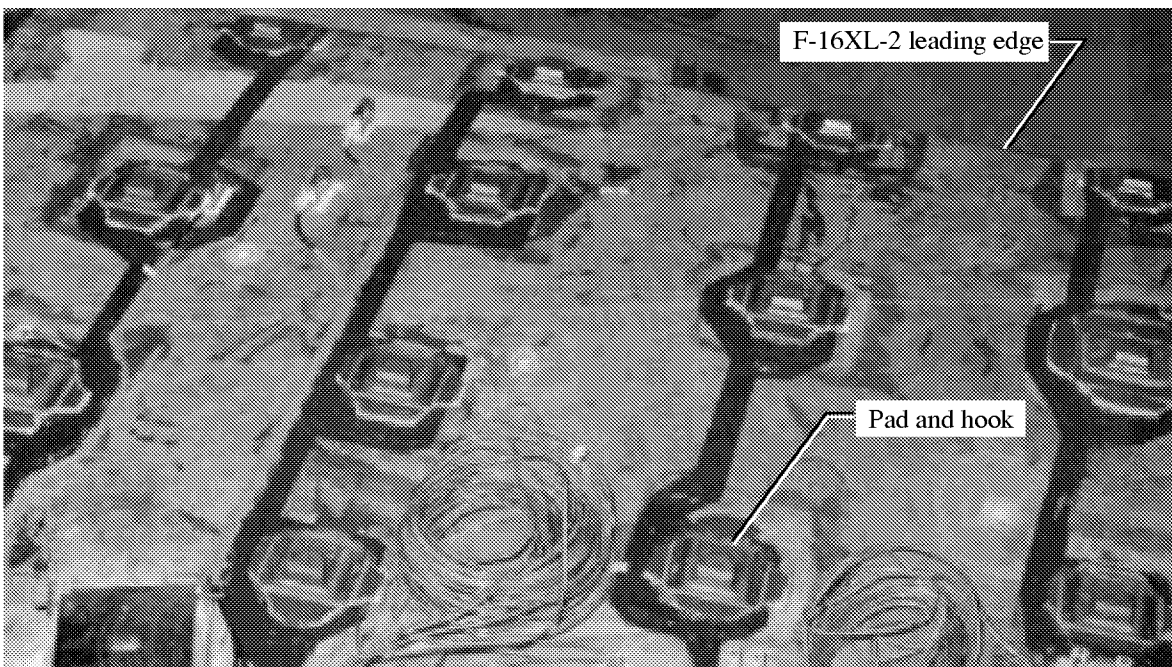


Figure 45. Installed pads and hooks on F-16XL-2 wing.

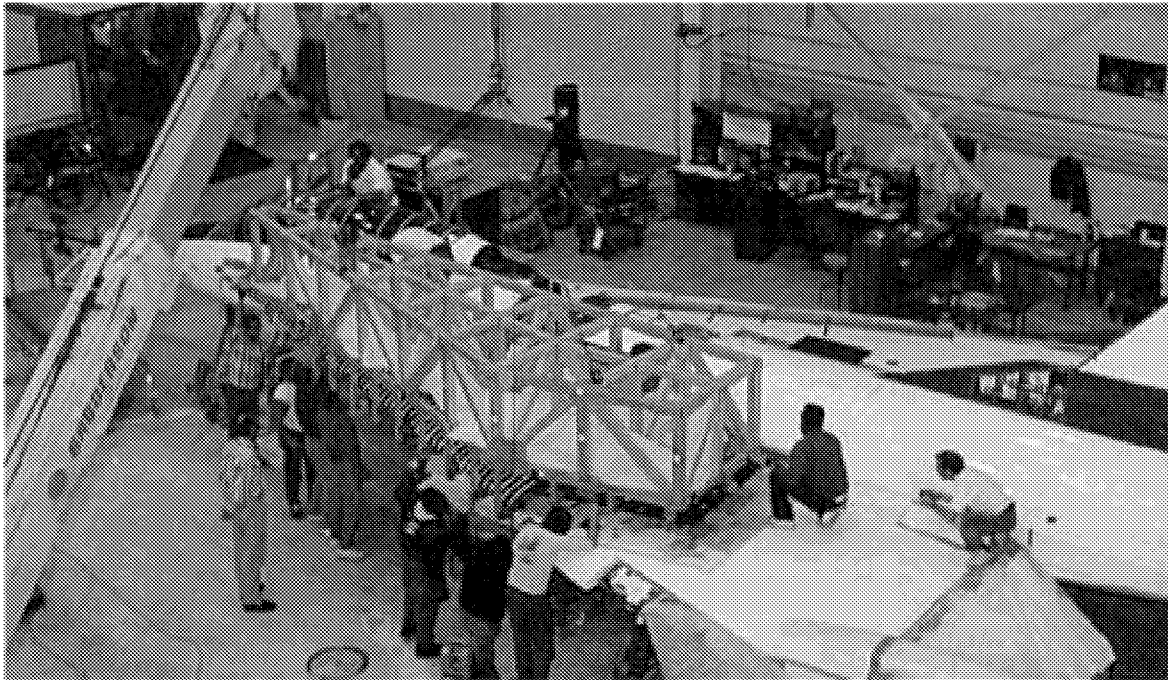


Figure 46. Panel fit check to wing.

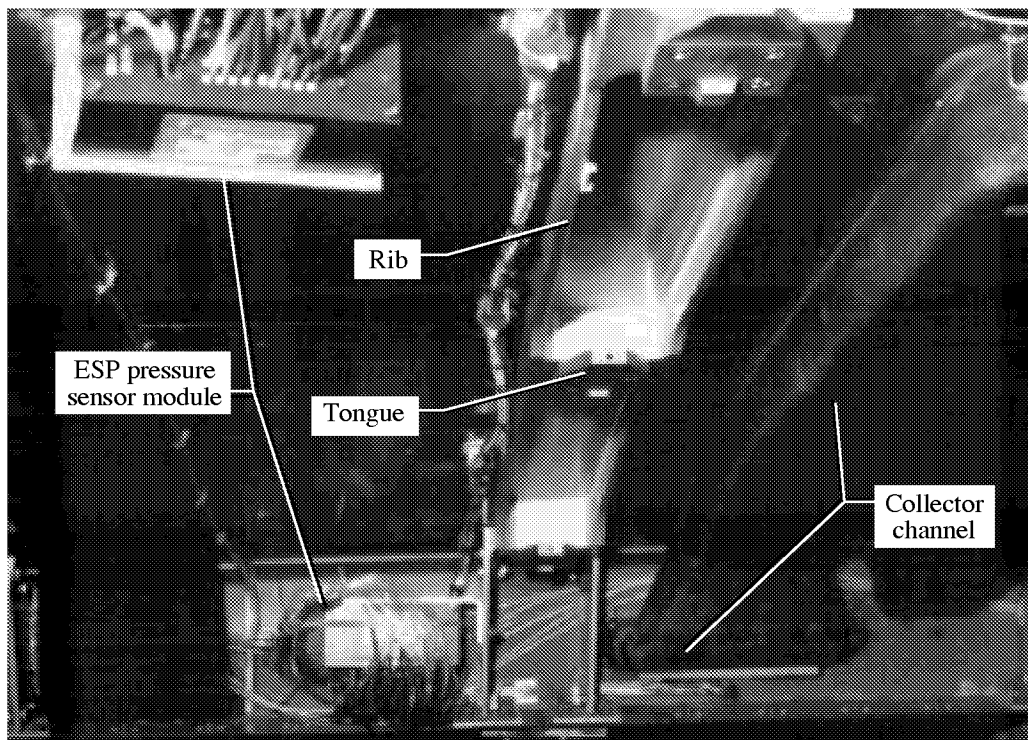


Figure 47. View of underside of suction panel.

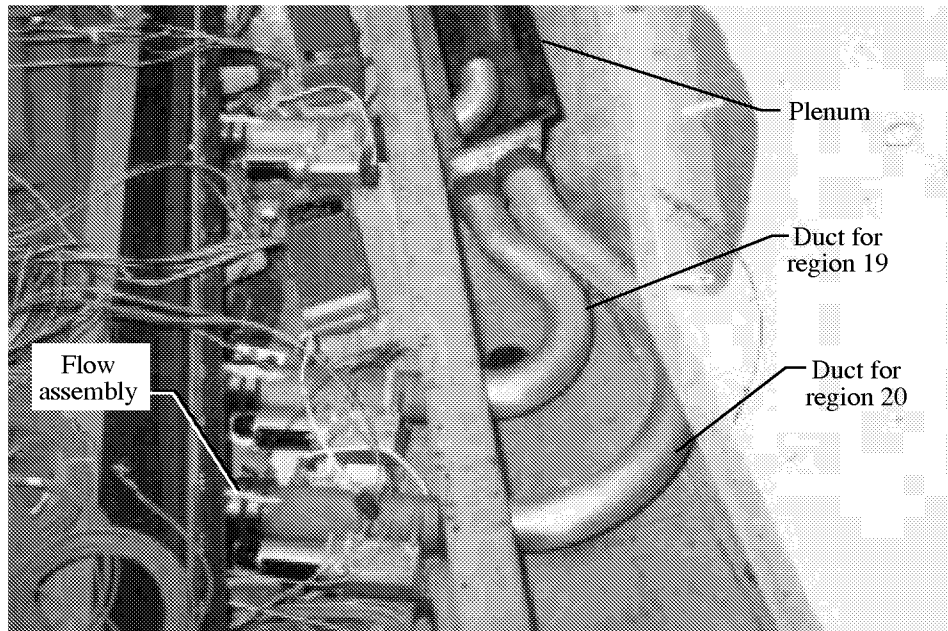


Figure 48. Flow assemblies, ducts, and plenum.

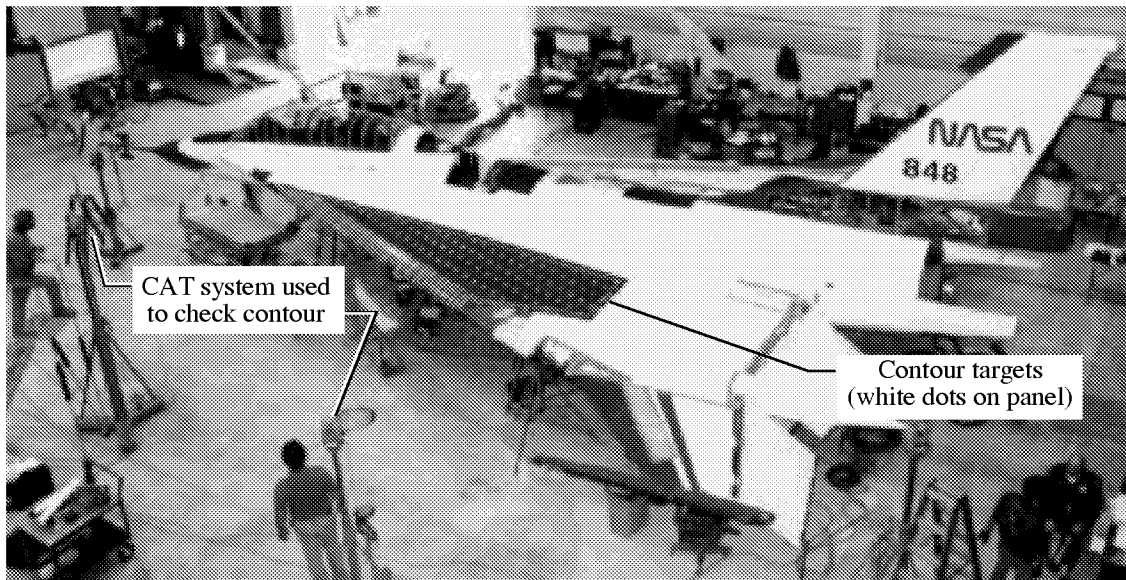


Figure 49. Installed suction panel undergoing contour verification.

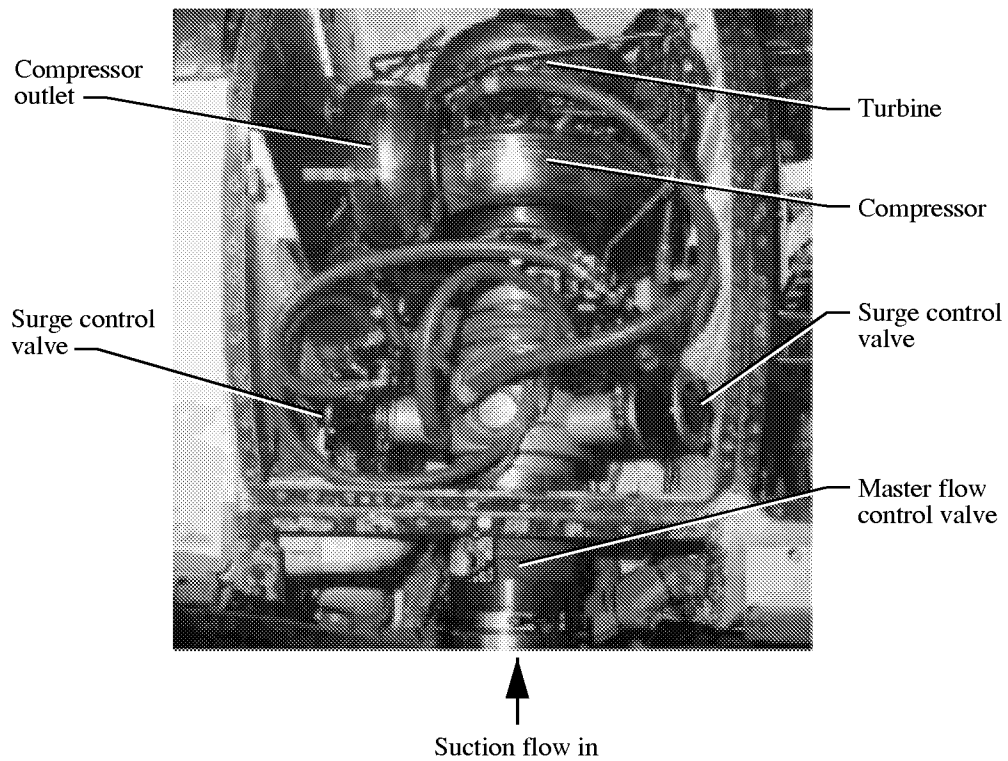


Figure 50. Details of installed turbocompressor.

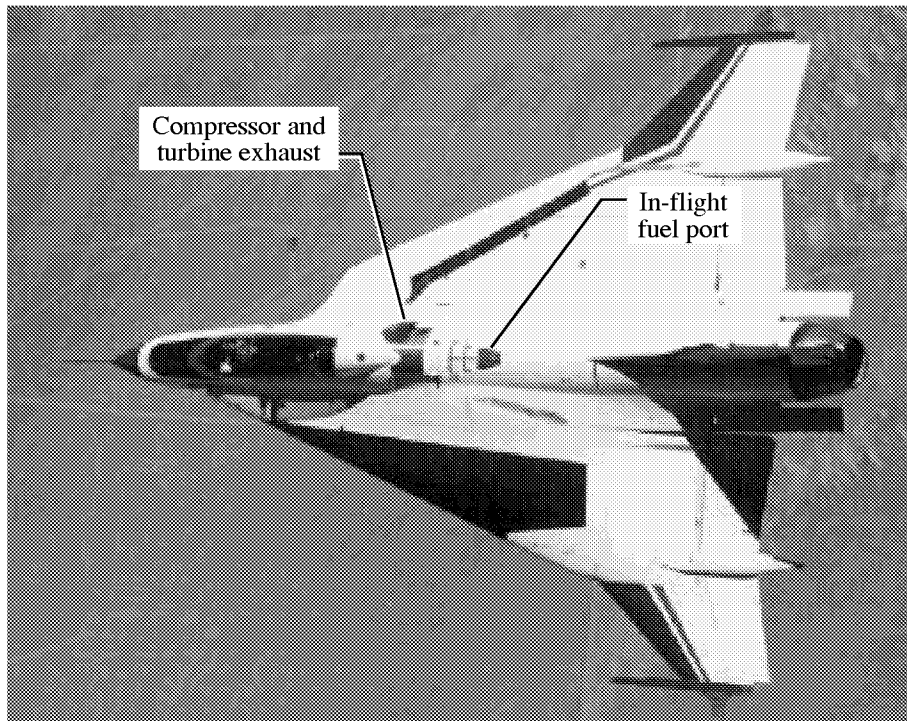


Figure 51. Modified F-16XL-2 in flight.

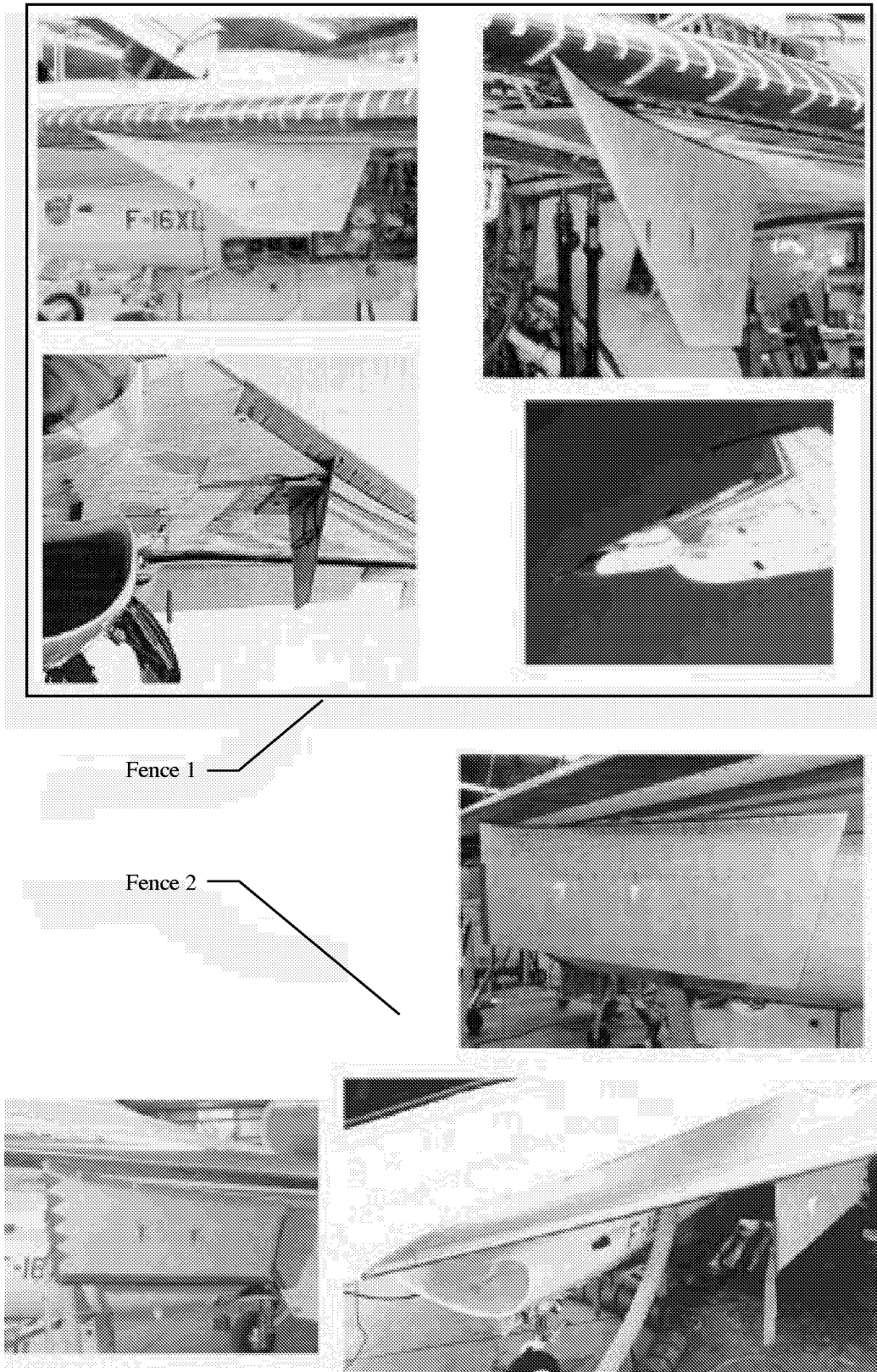


Figure 52. Fences 1 and 2 installed on F-16XL-2.

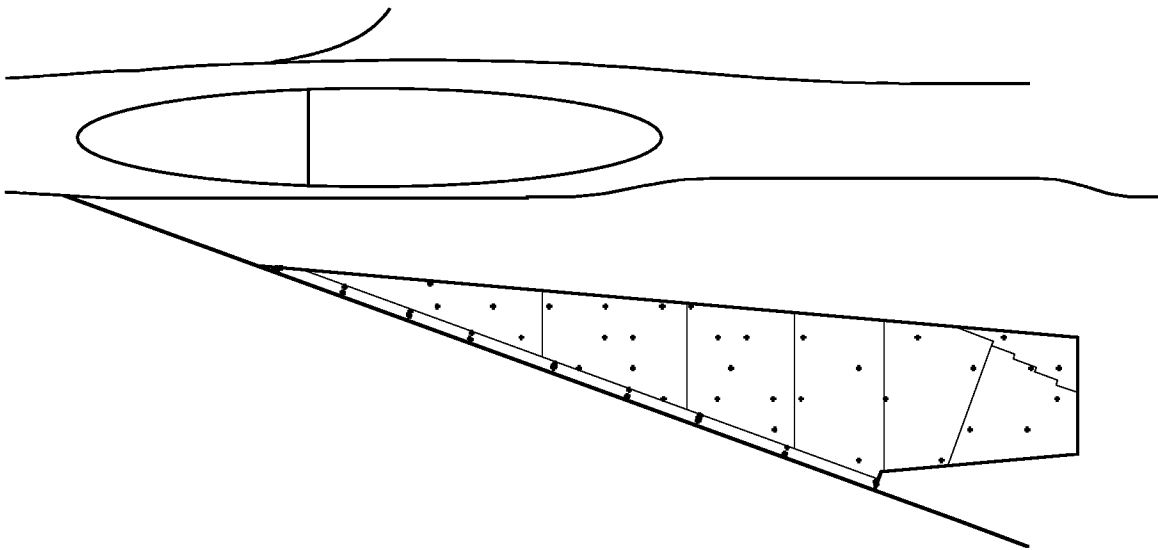


Figure 53. Suction panel internal pressure tap locations. Of 72 internal pressure taps, 39 are in leading edge (3 in each region), and 33 are distributed in upper surface region.

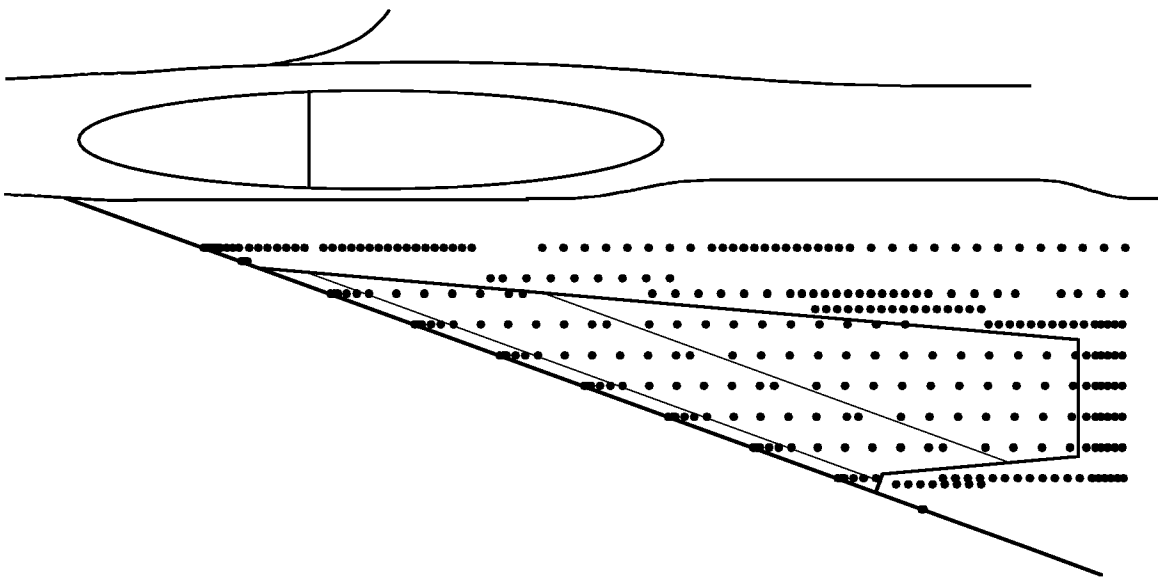


Figure 54. External pressure tap locations on left wing. Of 454 pressure taps, 200 are suction panel pressure taps (113 in leading edge), and 254 are passive fairing pressure taps.

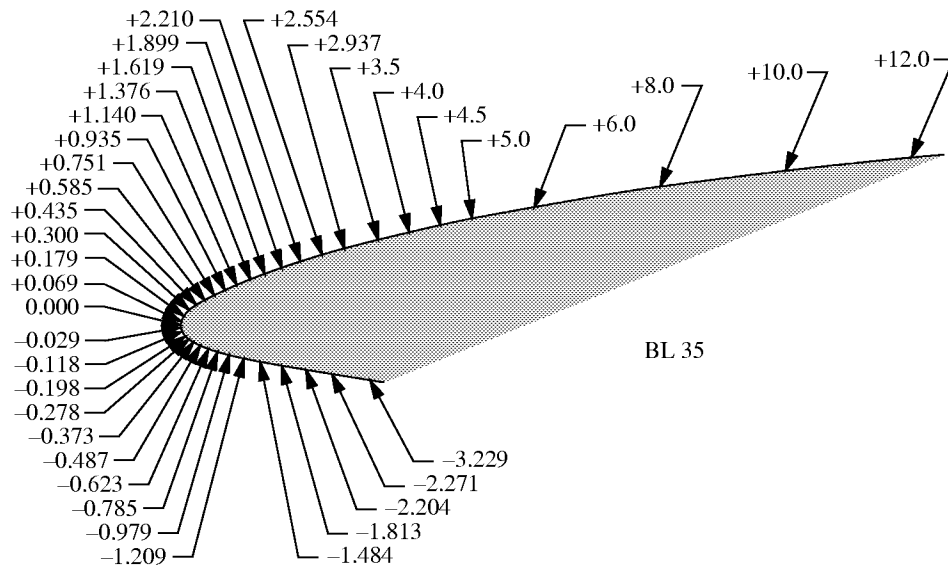


Figure 55. External pressure tap locations in leading-edge region at BL 35.

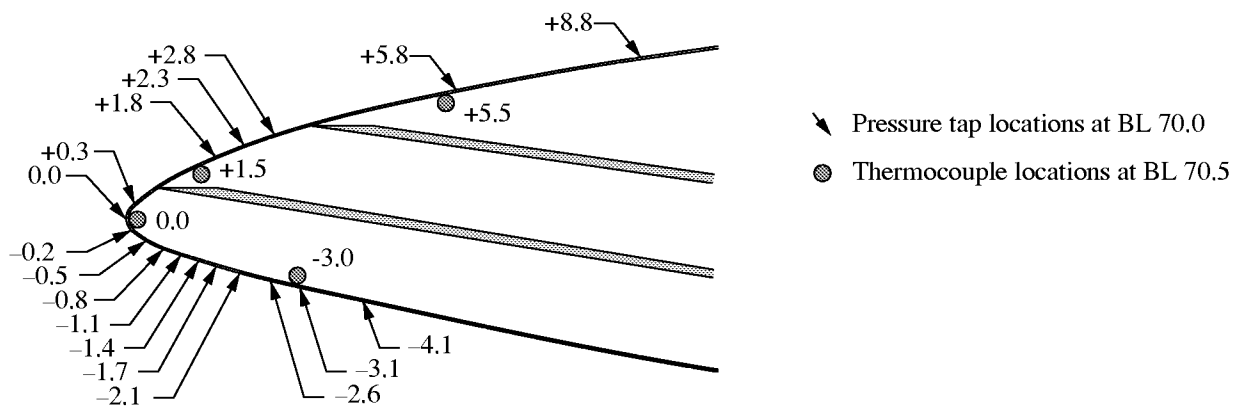


Figure 56. External pressure tap locations in leading-edge region at BL 70 and internal thermocouple locations in leading-edge region at BL 70.5.

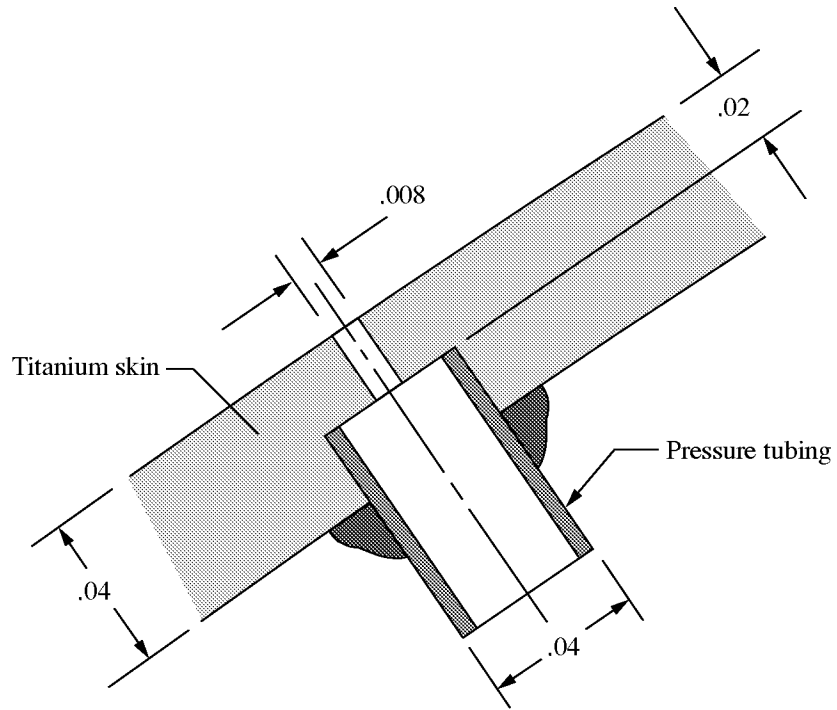


Figure 57. Leading-edge external pressure tap installation. Dimensions are in inches.

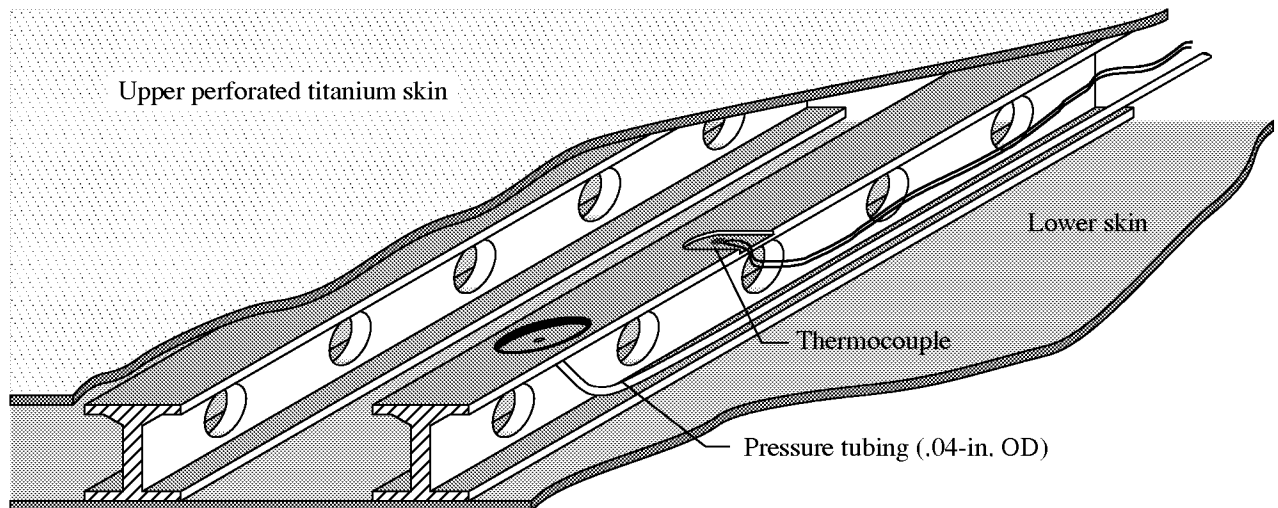


Figure 58. Upper surface pressure tap and thermocouple installation.

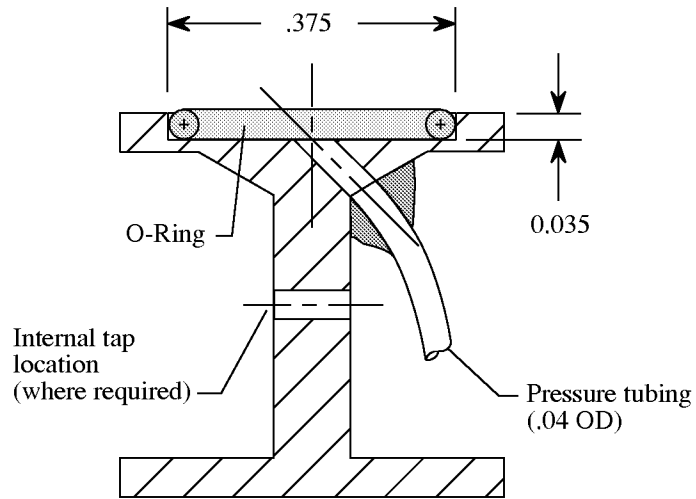


Figure 59. Cross section of upper surface pressure tap. Dimensions are in inches.

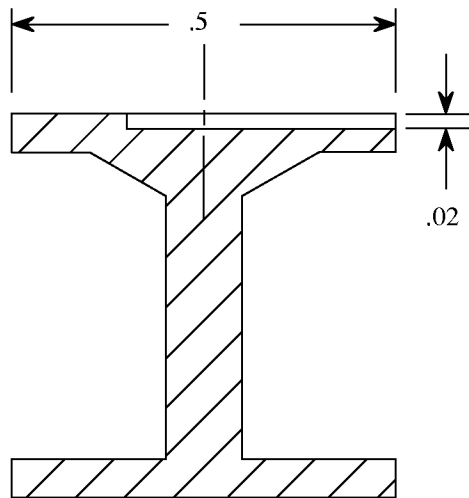


Figure 60. Cross section of stringer cutout for upper surface thermocouple installation. Dimensions are in inches.

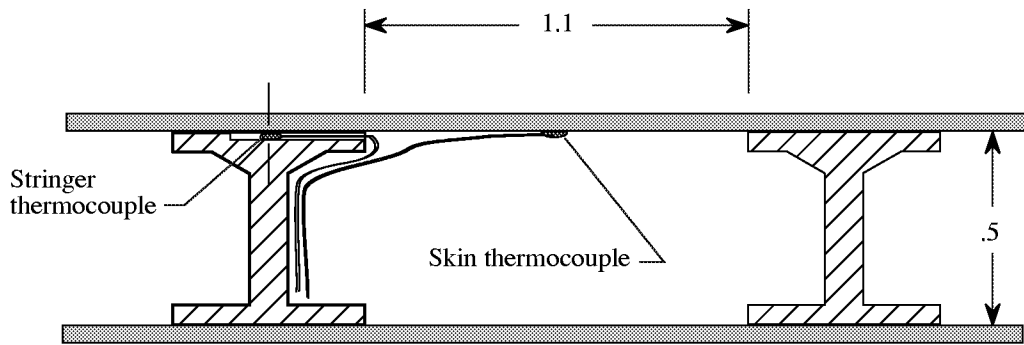


Figure 61. Cross section of upper surface thermocouple pair installation. Dimensions are in inches.

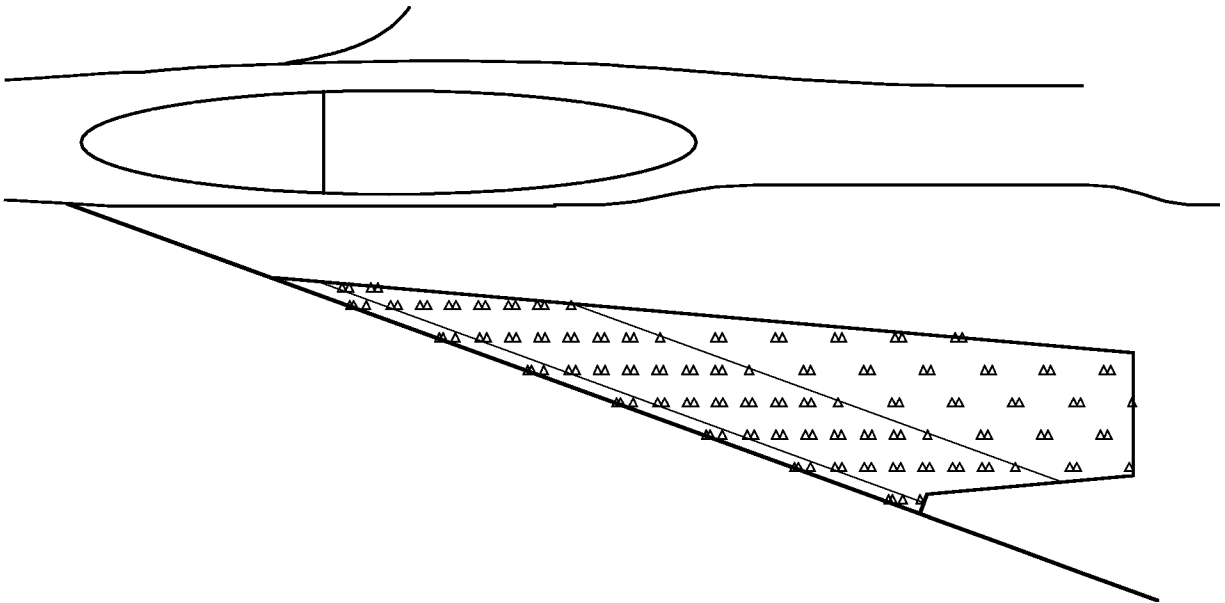


Figure 62. Thermocouple locations on suction panel. Of 151 thermocouples, 28 are in leading-edge regions (4 in each of 7 BL's), and 123 are in upper surface regions.

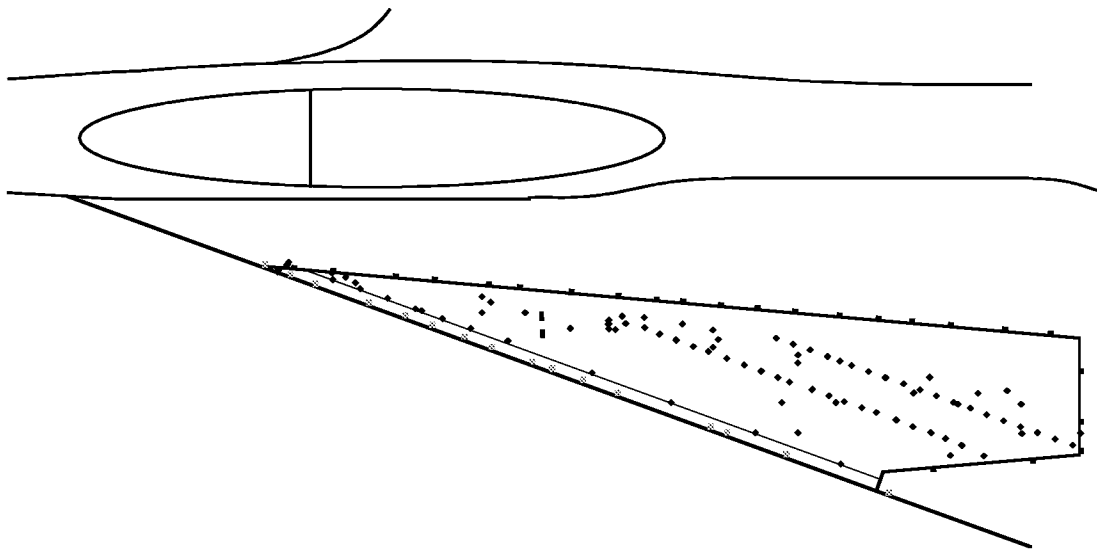


Figure 63. Different hot-film locations used for transition detection. Of 142 different film locations used, 126 are upper surface film locations, and 16 are lower surface film locations.

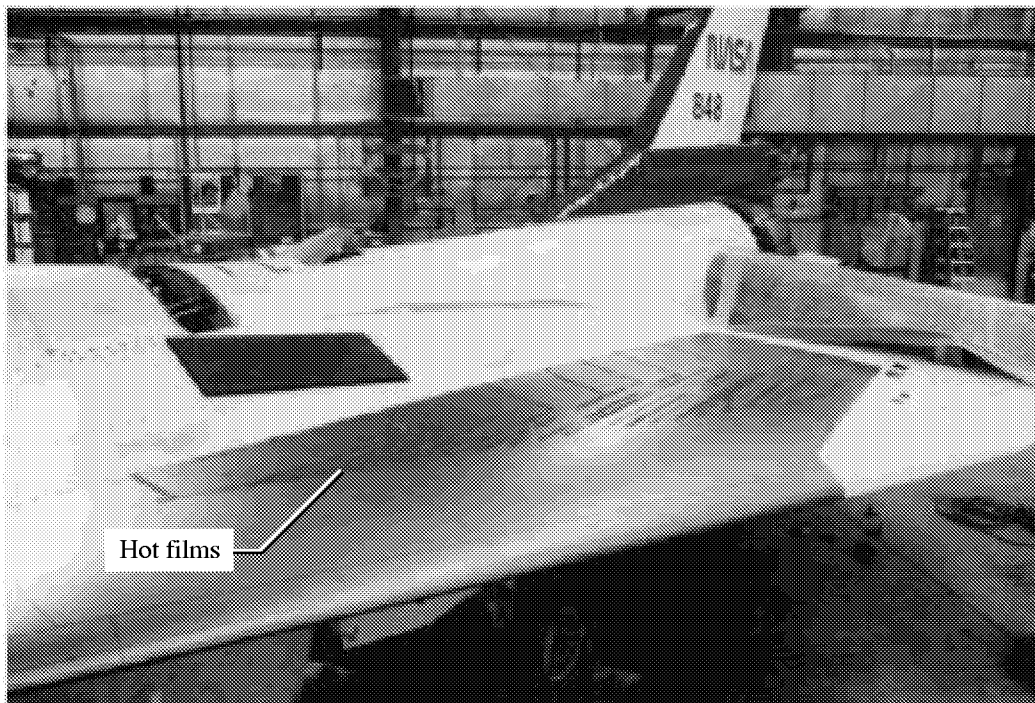


Figure 64. Splice-joint hot films installed on suction panel.

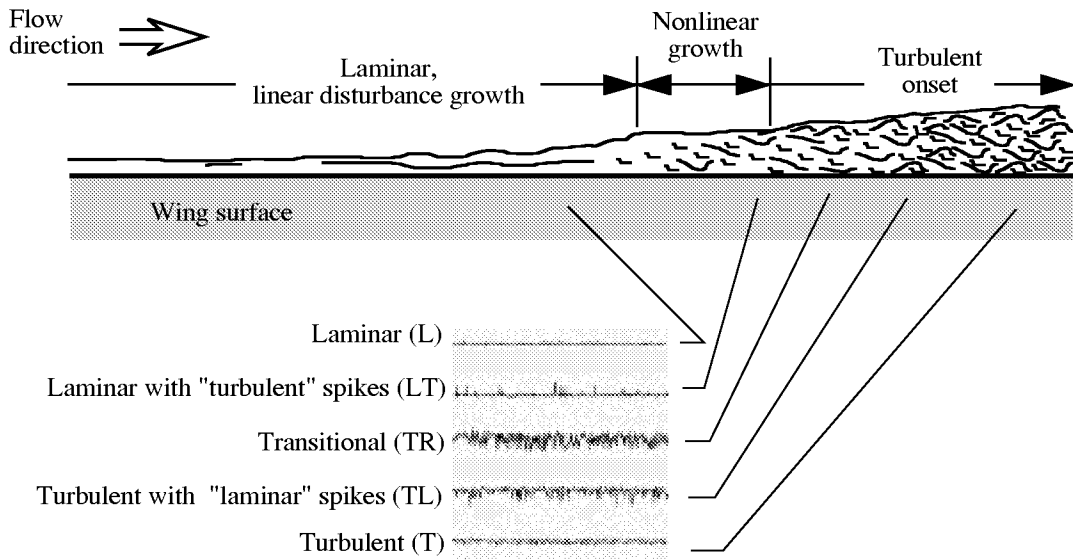


Figure 65. Examples of laminar to turbulent hot-film signals.

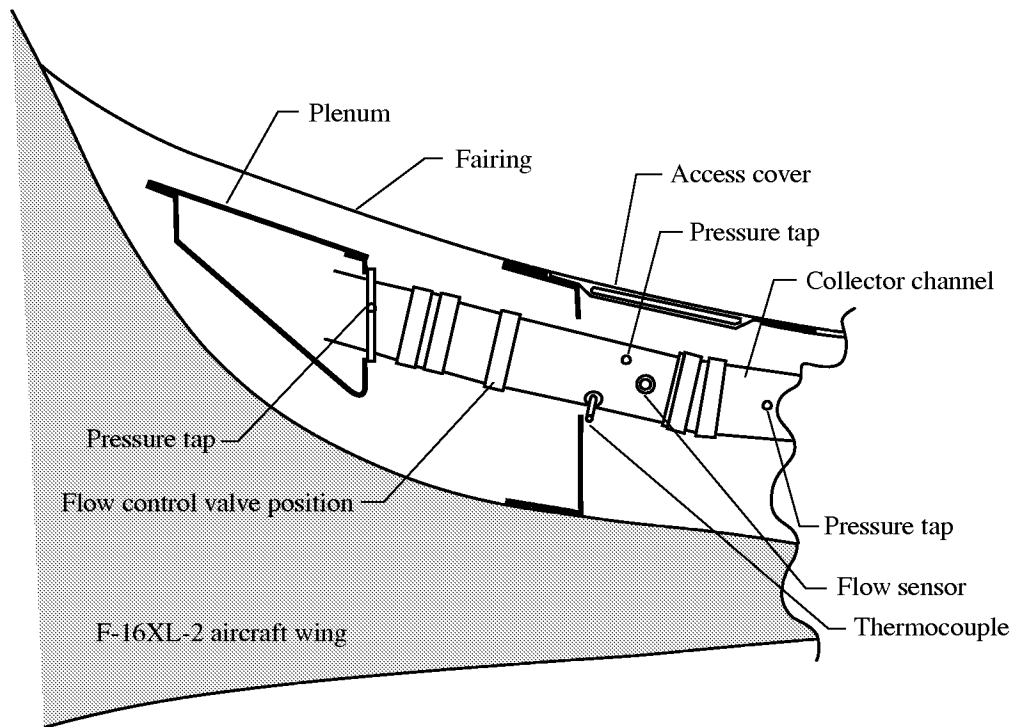


Figure 66. Typical flow control assembly (1 of 20).

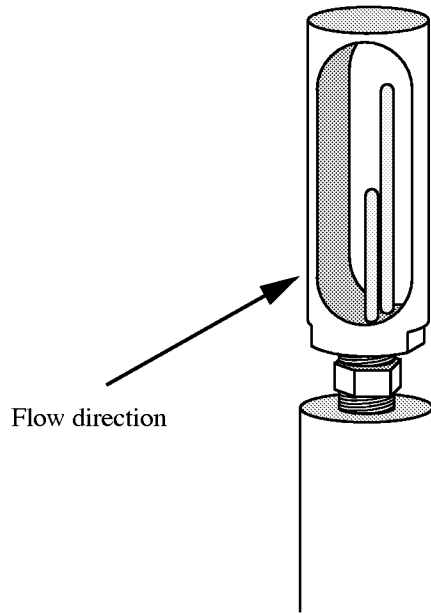


Figure 67. Kurz thermal mass-flow sensor.

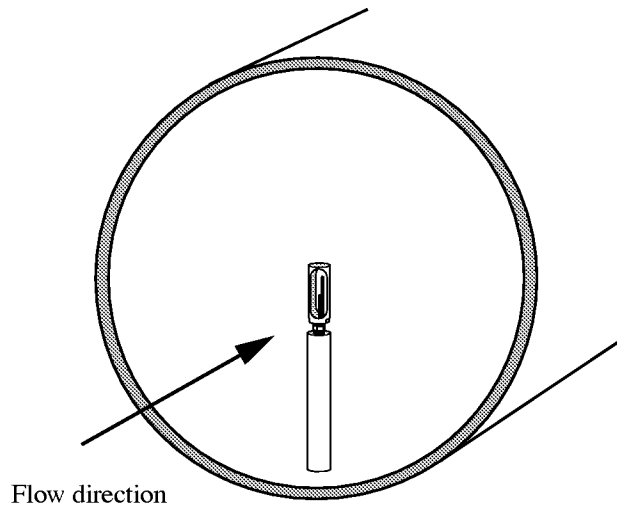


Figure 68. Kurz thermal mass-flow sensor in duct.

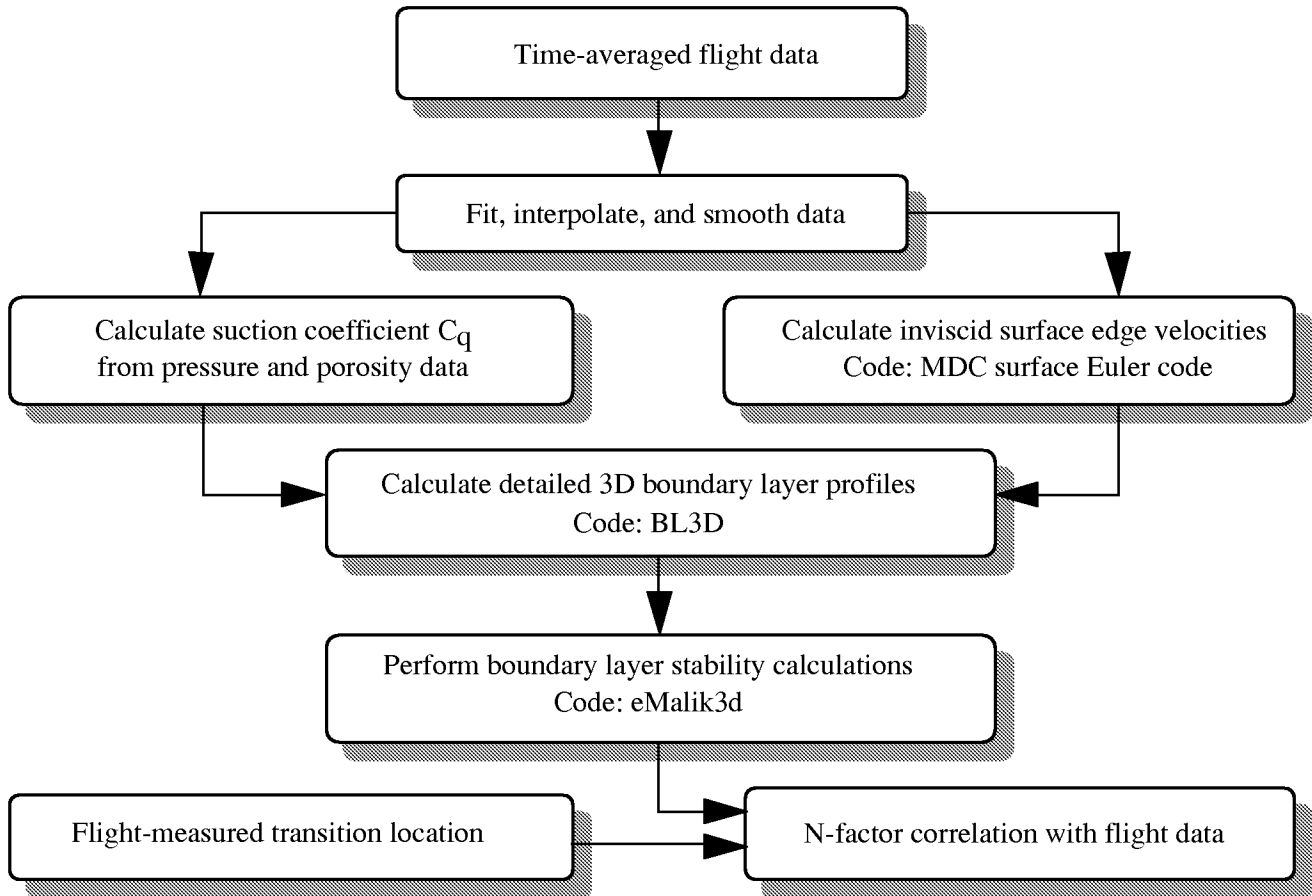


Figure 69. Flow chart of analysis procedure steps.

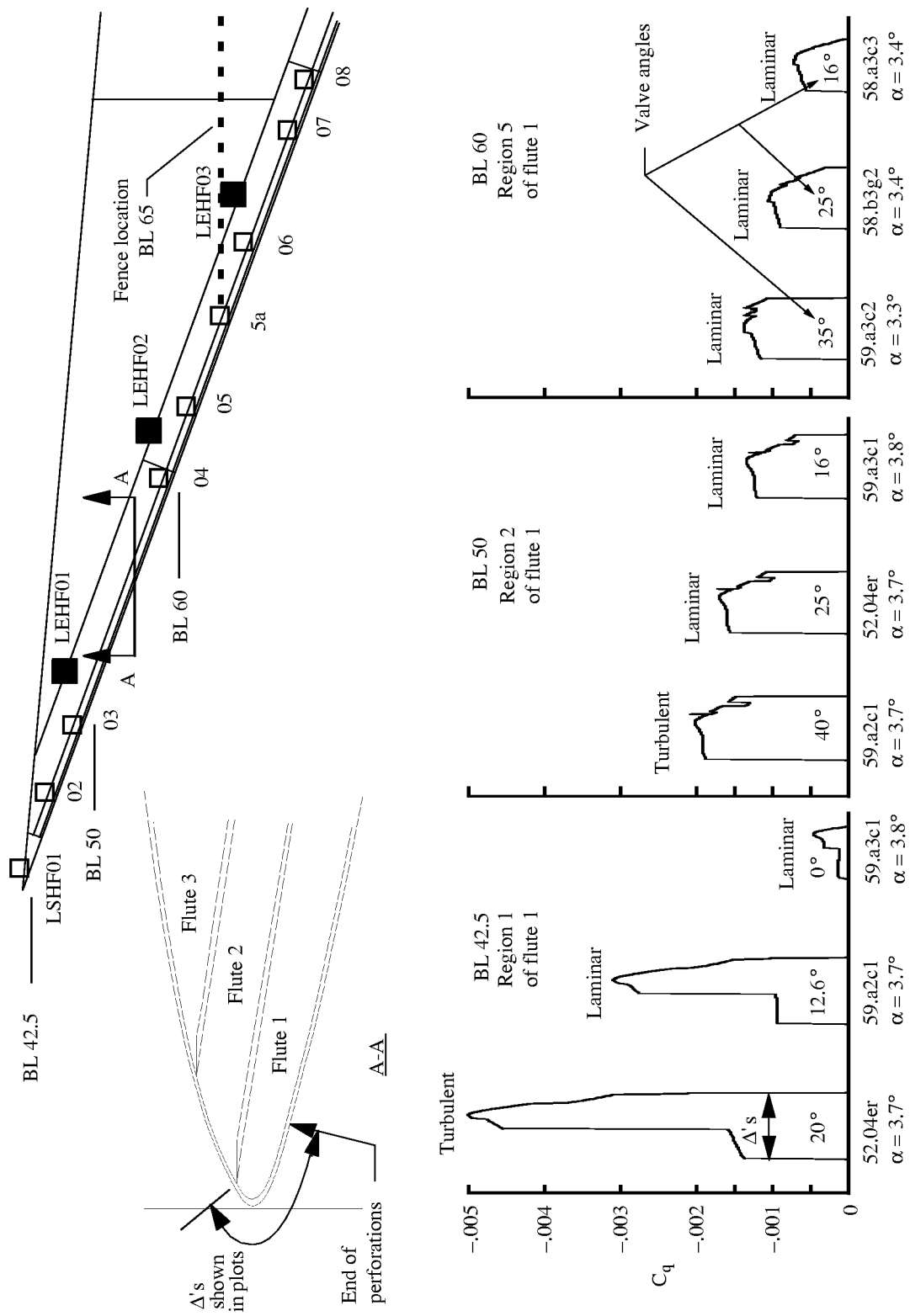


Figure 70. Attachment-line suction coefficient distributions for several test points and the effect on laminar flow. $M = 1.9$; $h = 50,000$ ft; $\beta = 0^\circ$.

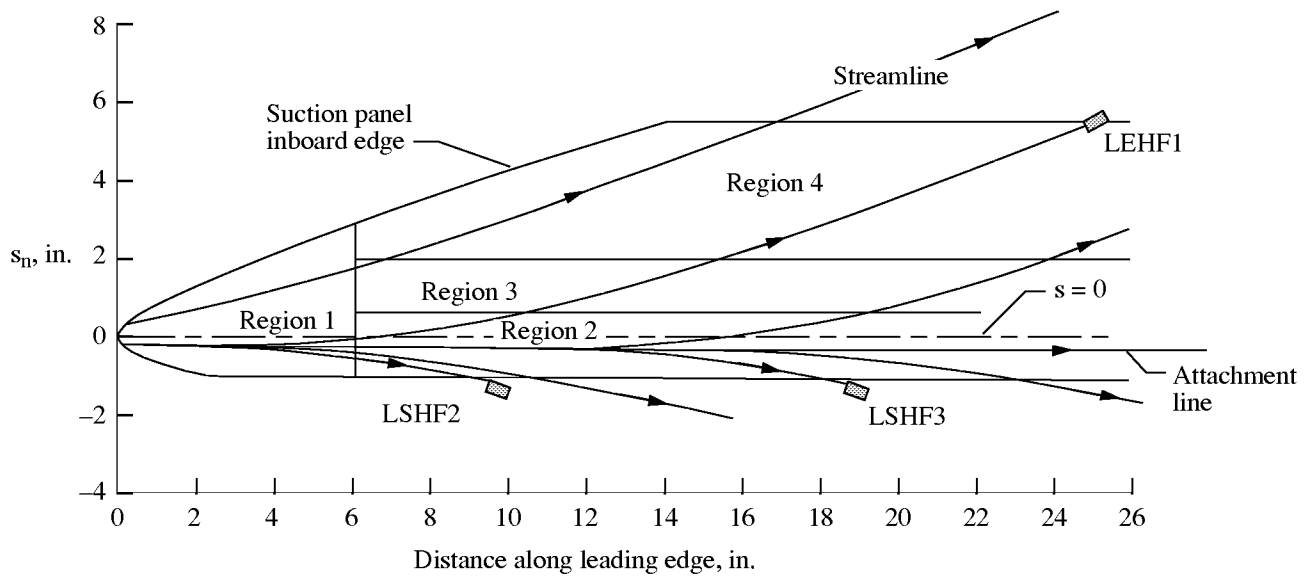


Figure 71. Euler derived streamline traces over leading edge (BCAG). $M = 1.9$; $\alpha = 3.3^\circ$.

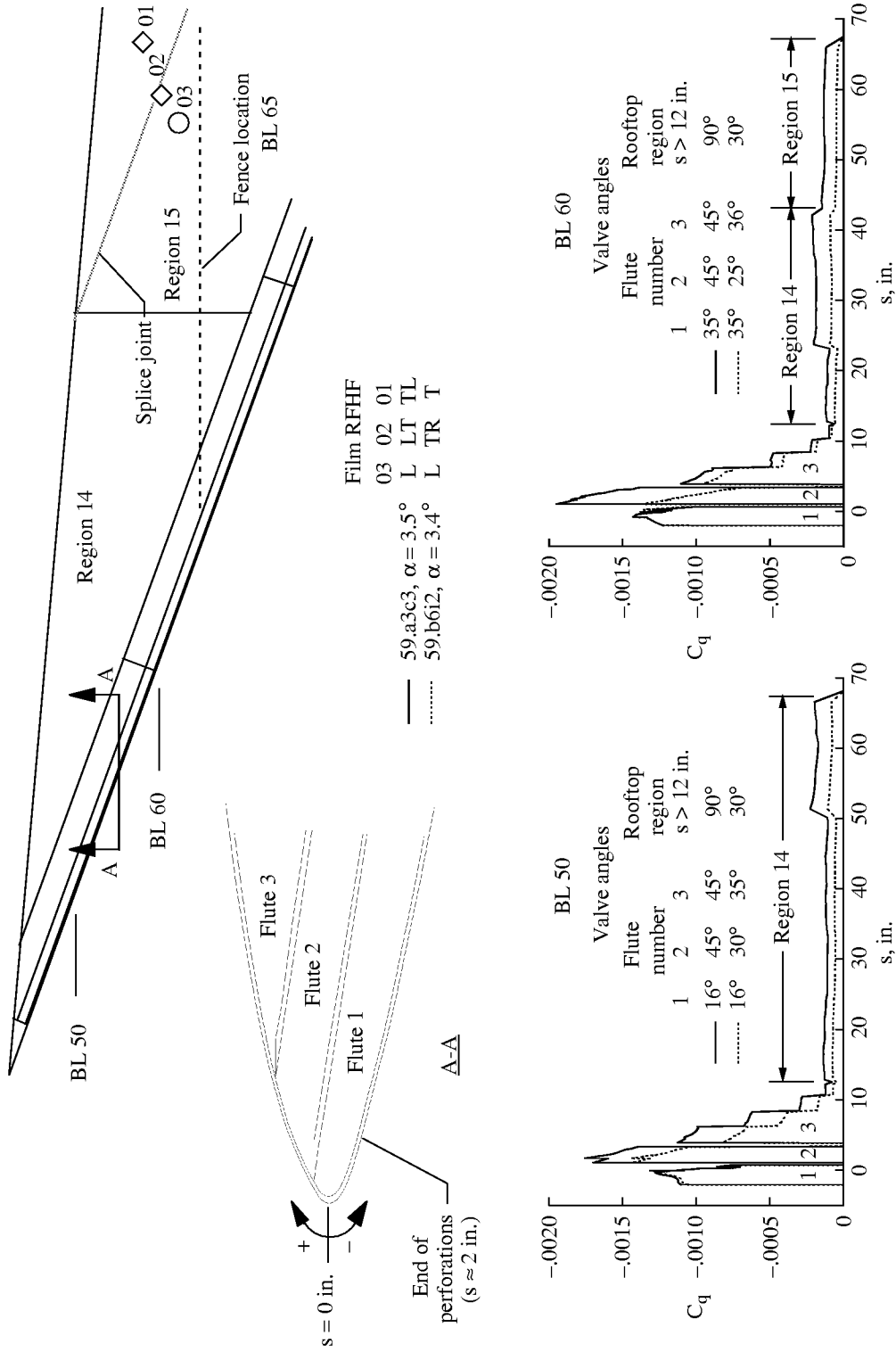


Figure 72. Initial achievement of laminar flow on upper surface. $M = 1.9$; $h = 50\,000$ ft; $\beta = 0^\circ$.

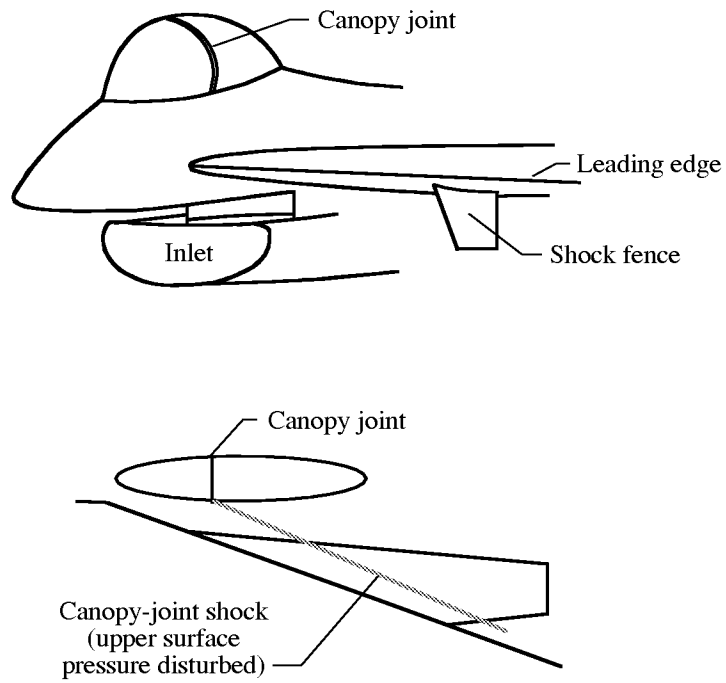


Figure 73. F-16XL-2 canopy joint location.

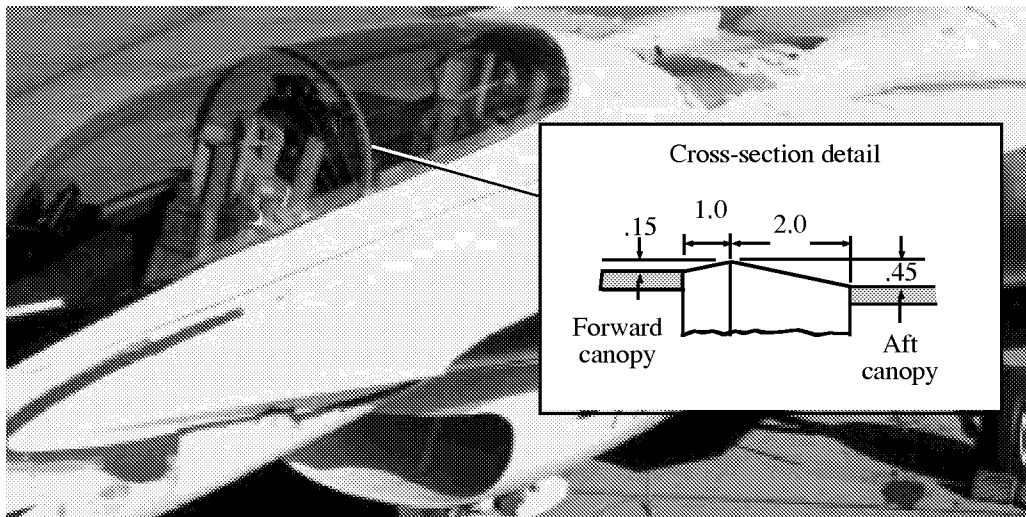


Figure 74. Cross-section view of canopy joint. Dimensions are in inches.

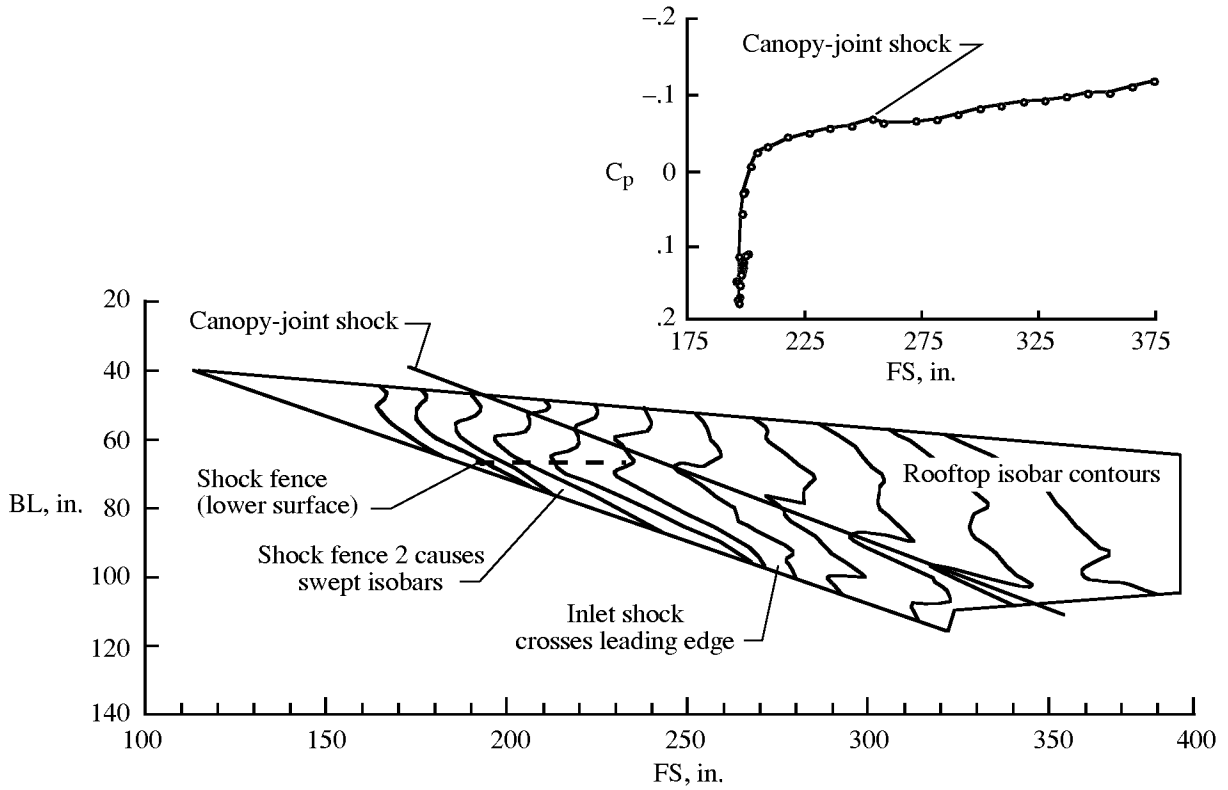


Figure 75. Rooftop pressure distribution showing canopy-joint shock. Pressure affected by canopy-joint shock and by inlet shock and fence. For BL 70; $M = 2$; $h = 53\,660$ ft; $\alpha = 3.6^\circ$.

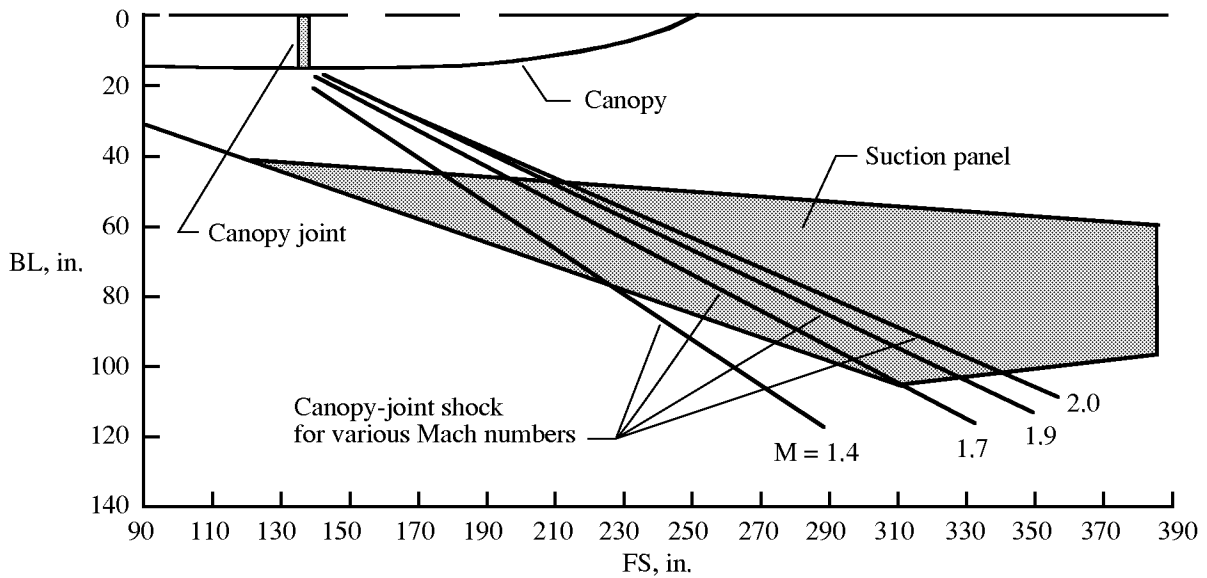
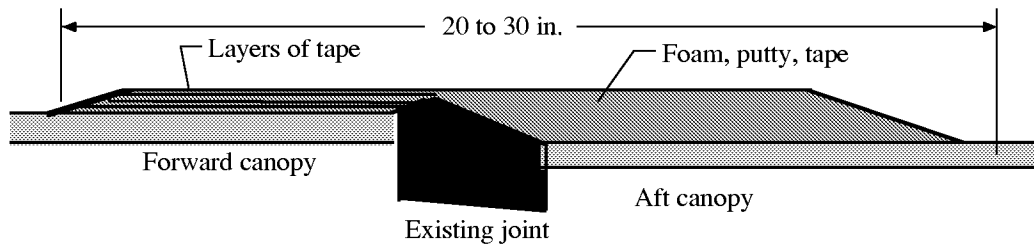
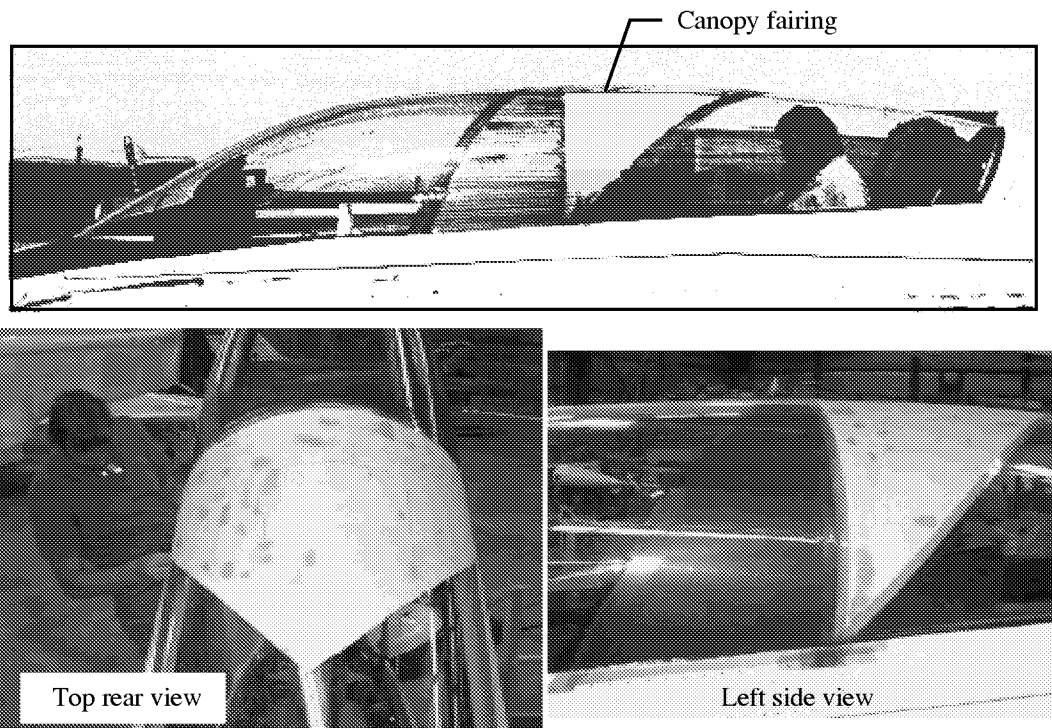


Figure 76. Canopy-joint shock impingement on suction panel.



(a) Fairing cross section.



(b) Installed canopy fairing.

Figure 77. Canopy joint and fairing.

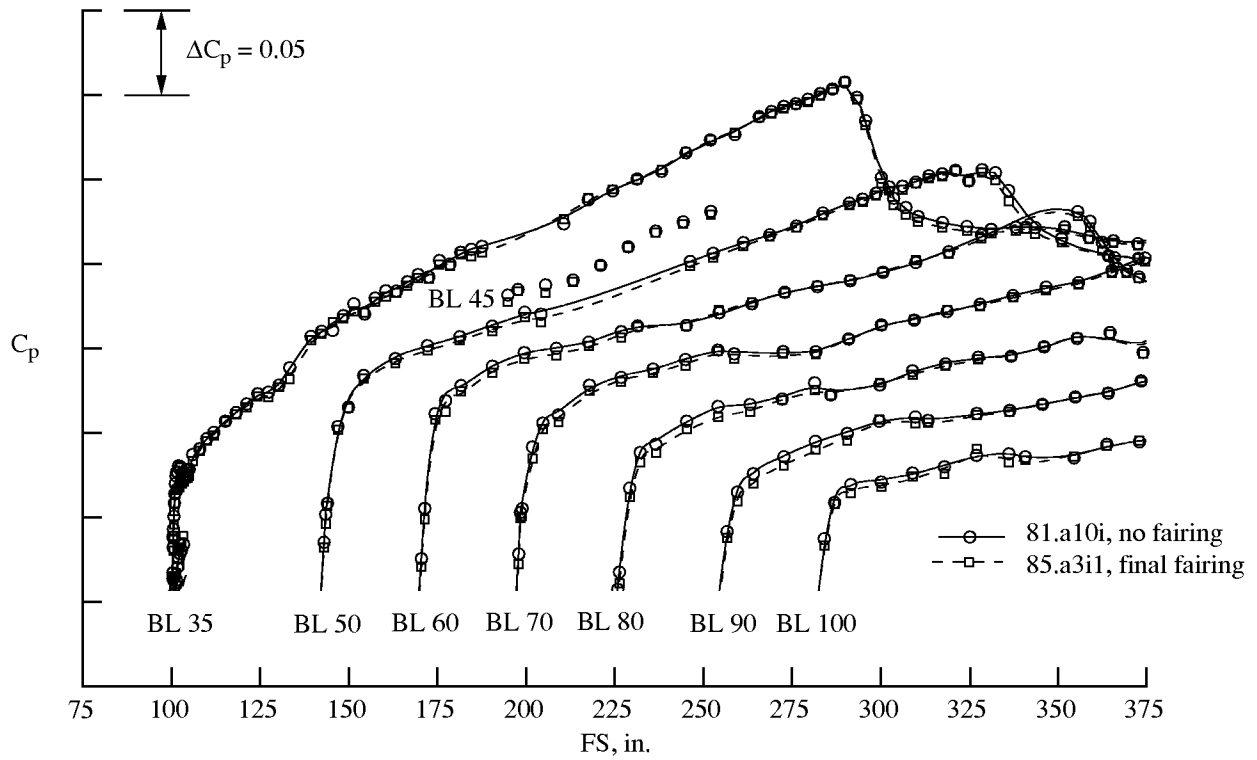


Figure 78. Waterfall plot of C_p profiles for no fairing and final fairing. For clarity, lower surface pressures are not shown, and C_p axis for each BL is offset.

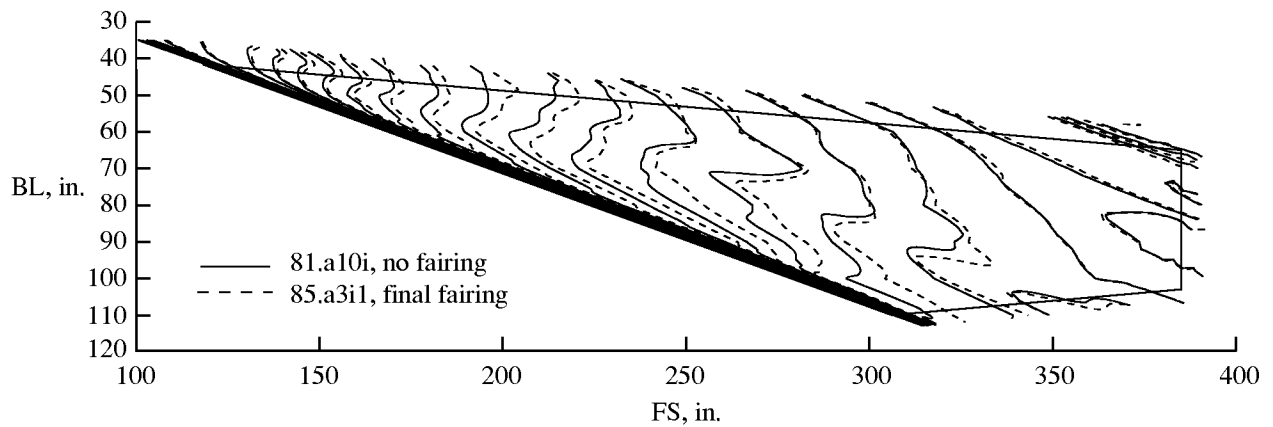


Figure 79. Contours of constant C_p for no fairing and final fairing. Isobar lines are spaced $0.01C_p$.

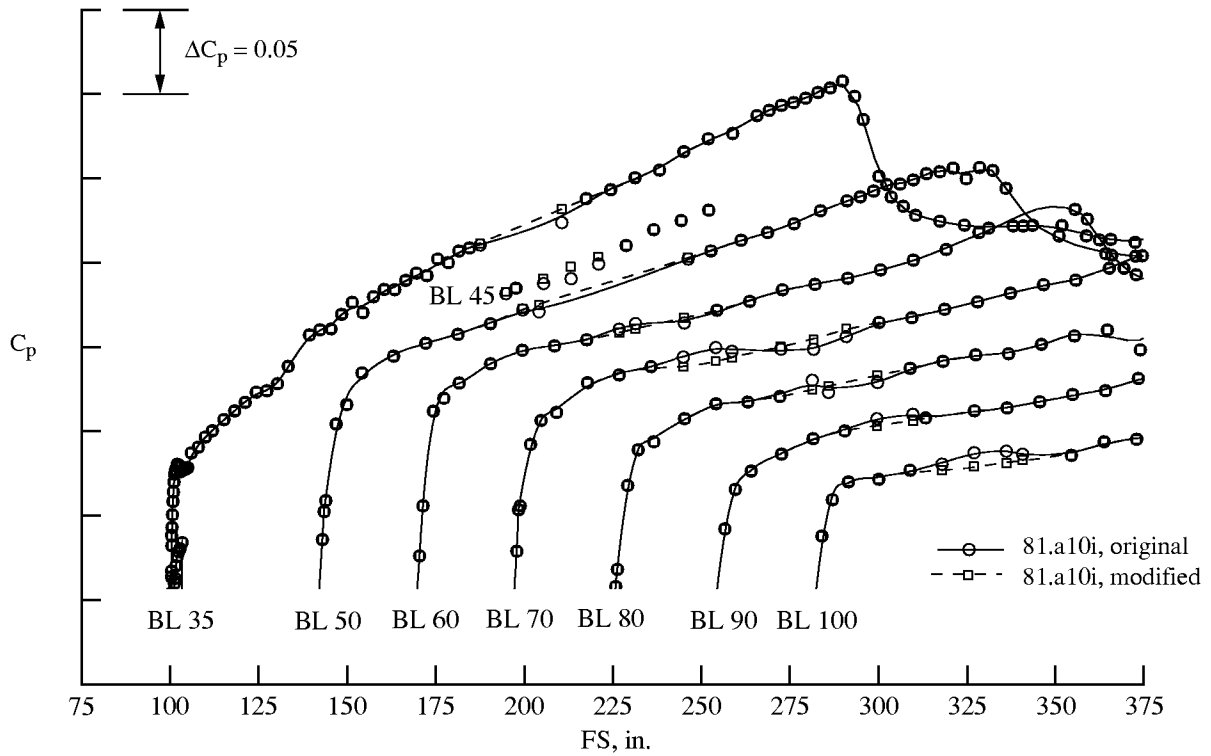


Figure 80. Waterfall plot of C_p profiles for original data and data modified to eliminate pressure perturbation. For clarity, lower surface pressures are not shown, and C_p axis for each BL is offset.

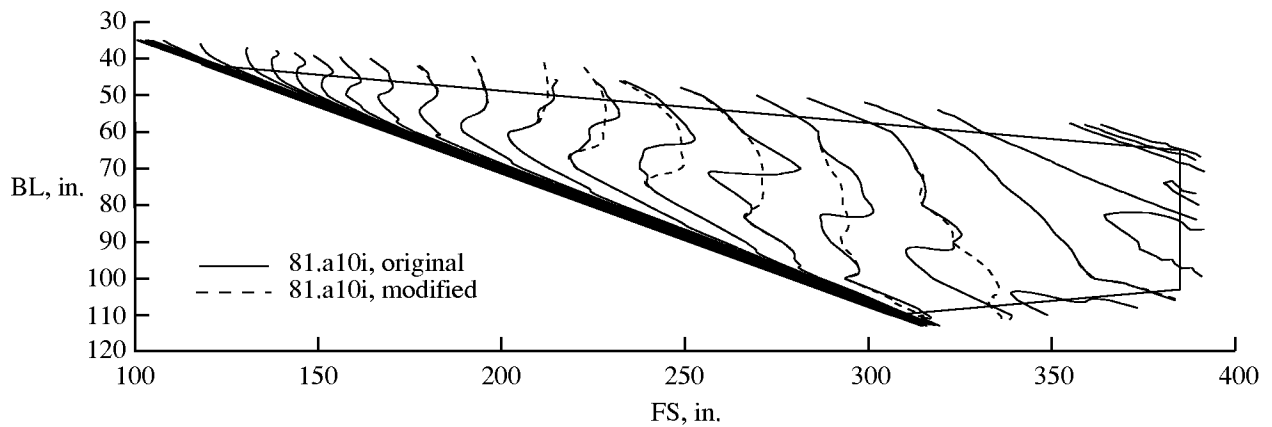
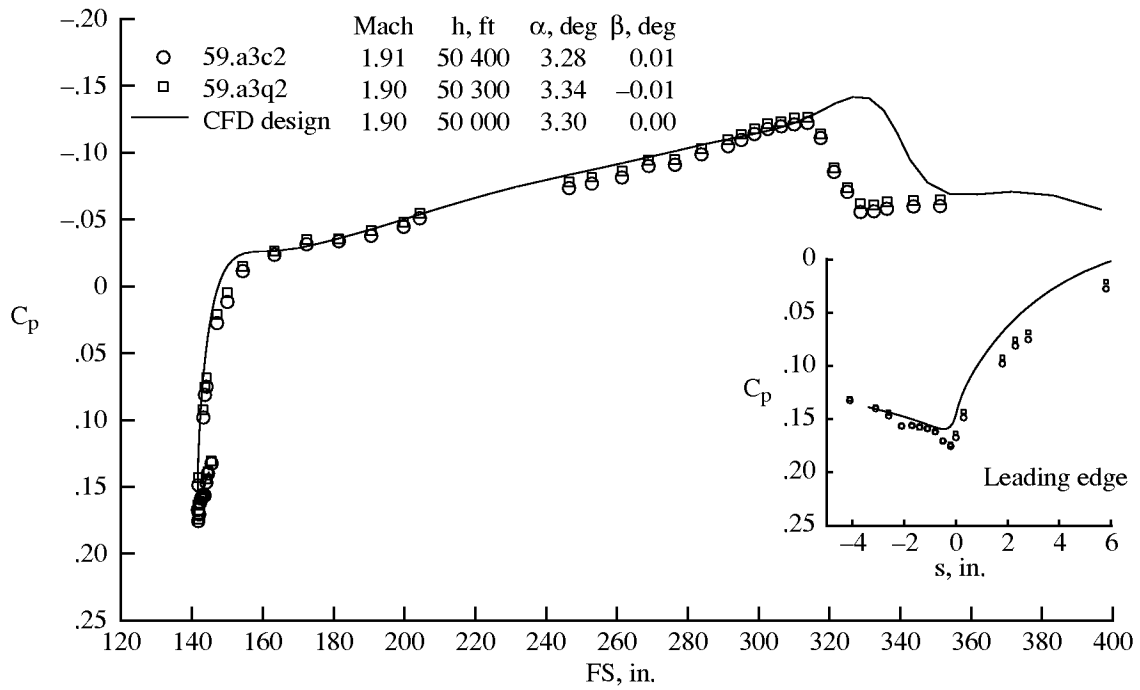
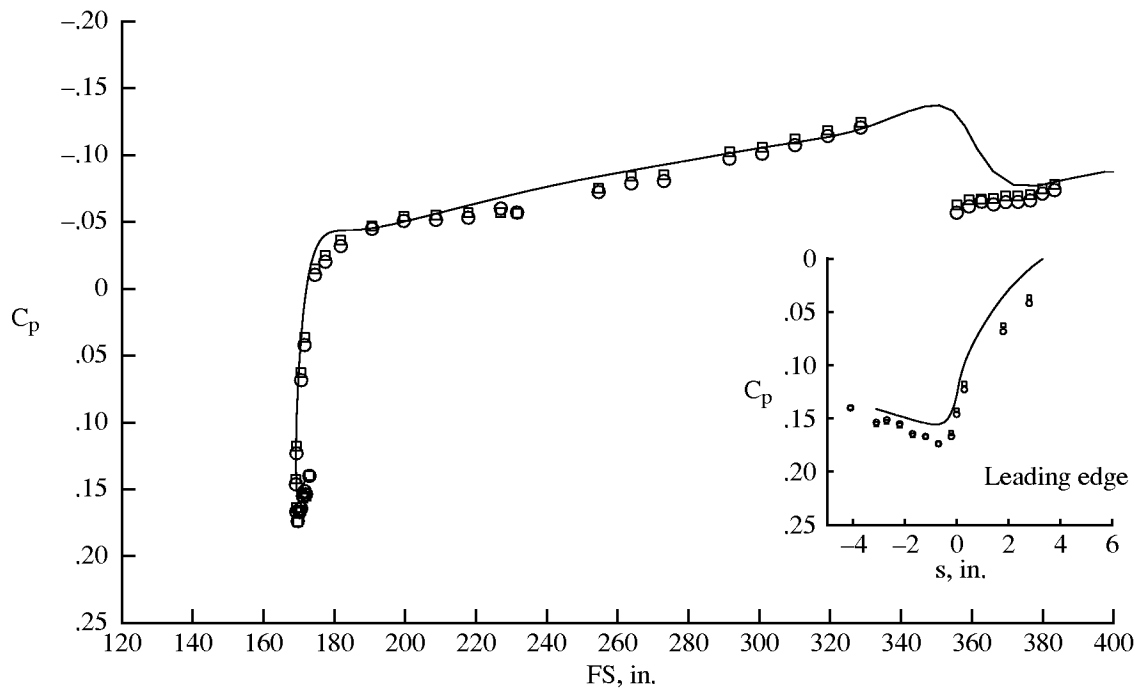


Figure 81. Contours of constant C_p for no fairing and in absence of pressure disturbance. Isobar lines are spaced $0.01 C_p$.

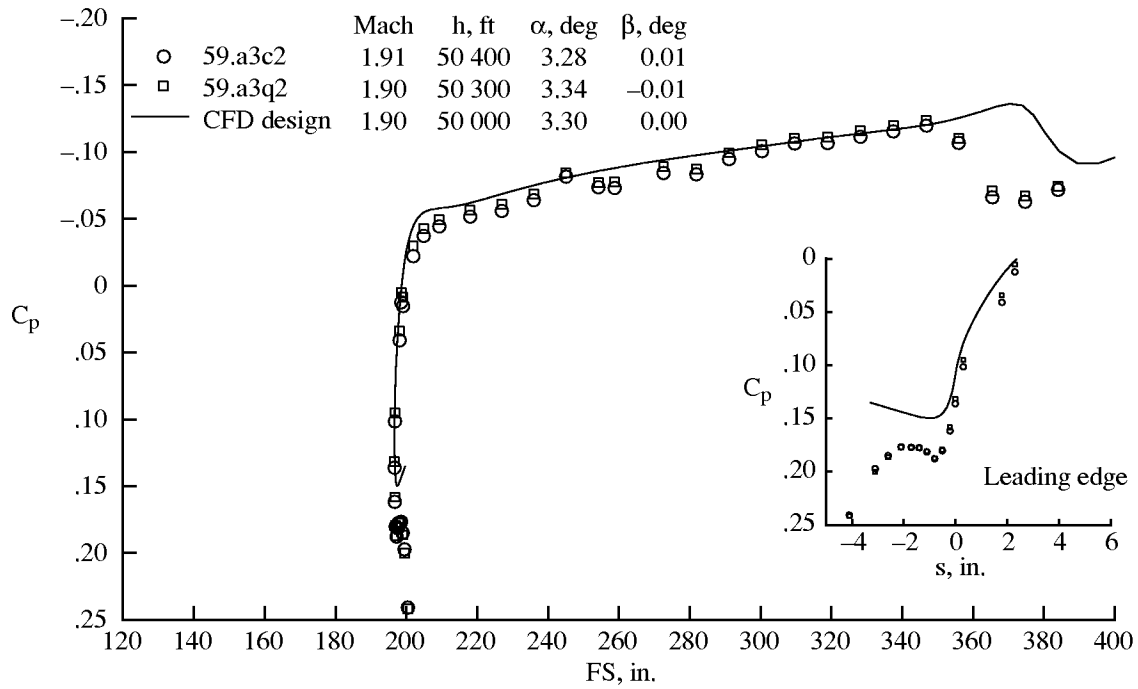


(a) BL 50.

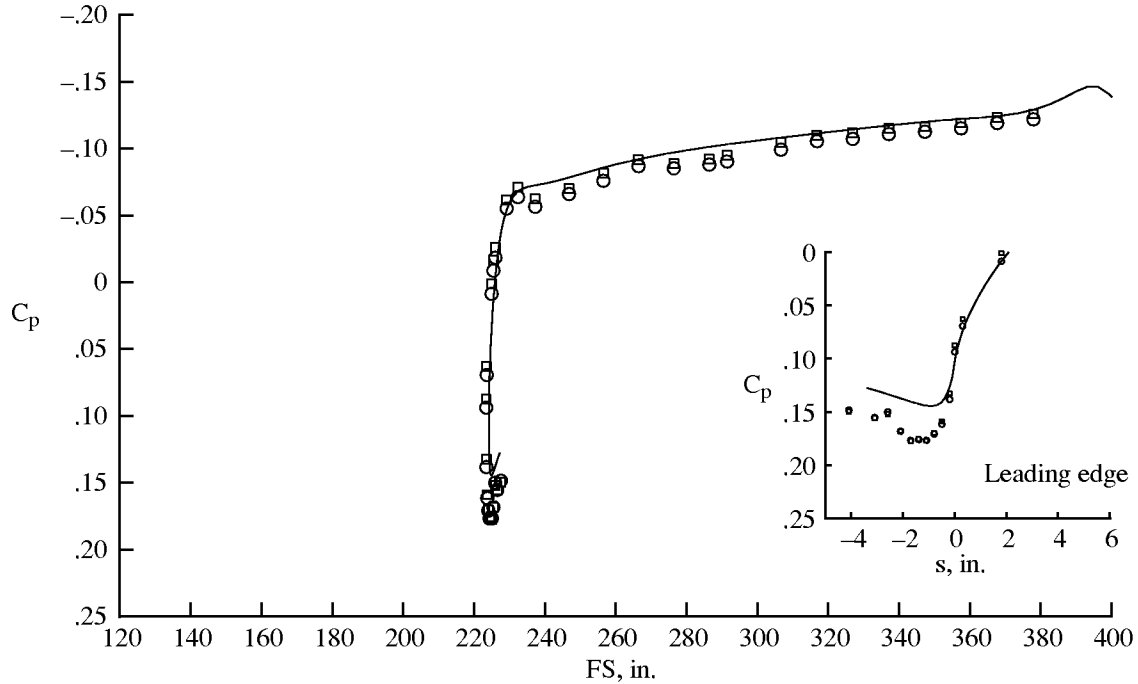


(b) BL 60.

Figure 82. CFD design comparison with experimental data for BL 50 and BL 60 for design conditions (CFD solution from BCAG).

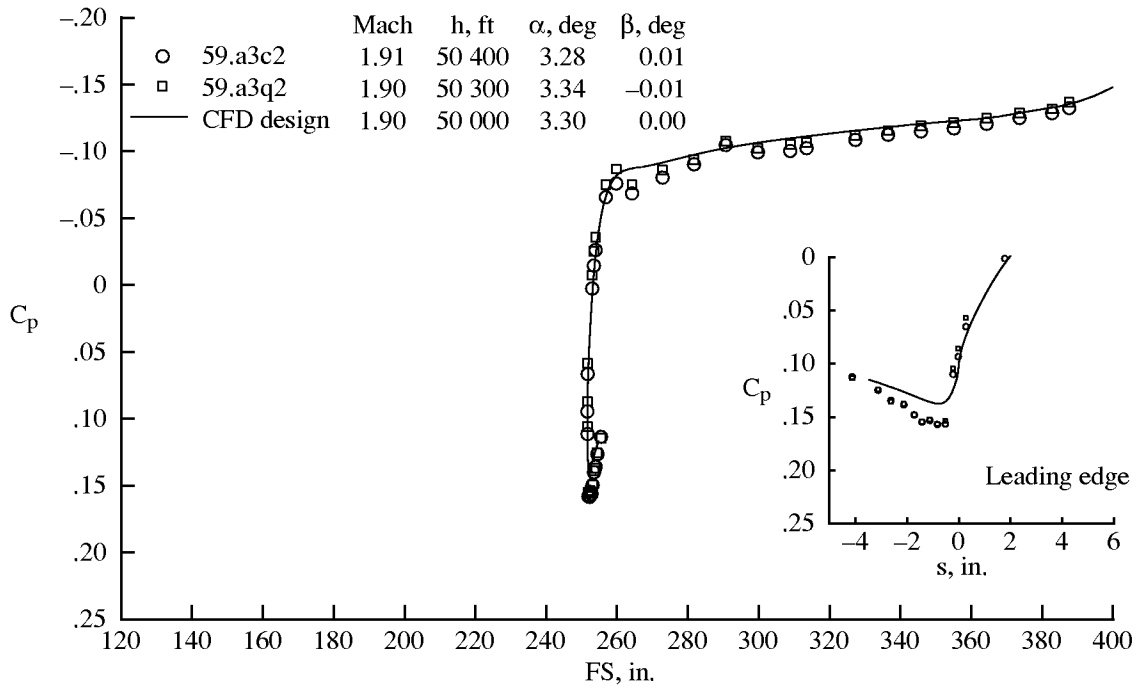


(c) BL 70.

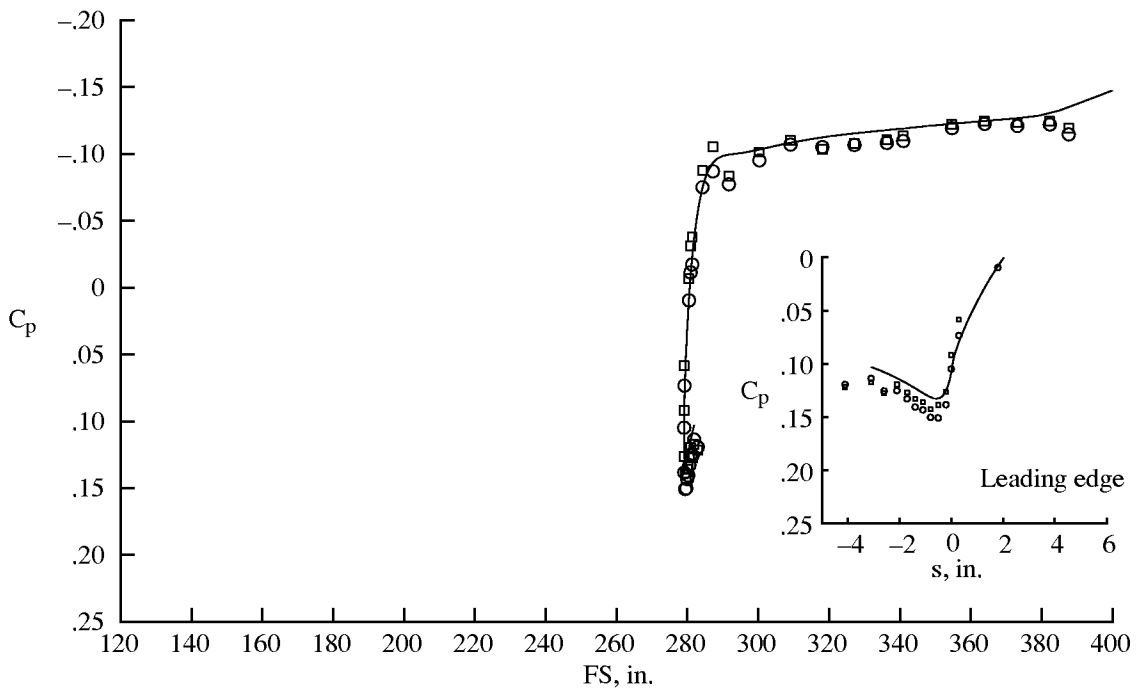


(d) BL 80.

Figure 82. Continued.

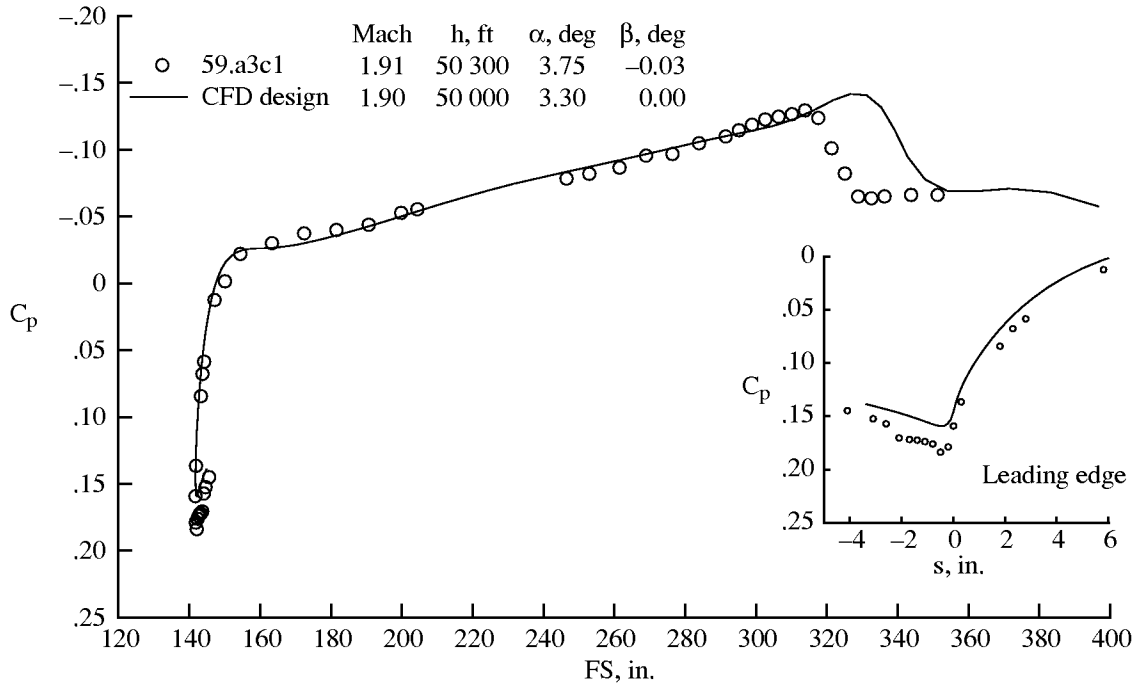


(e) BL 90.

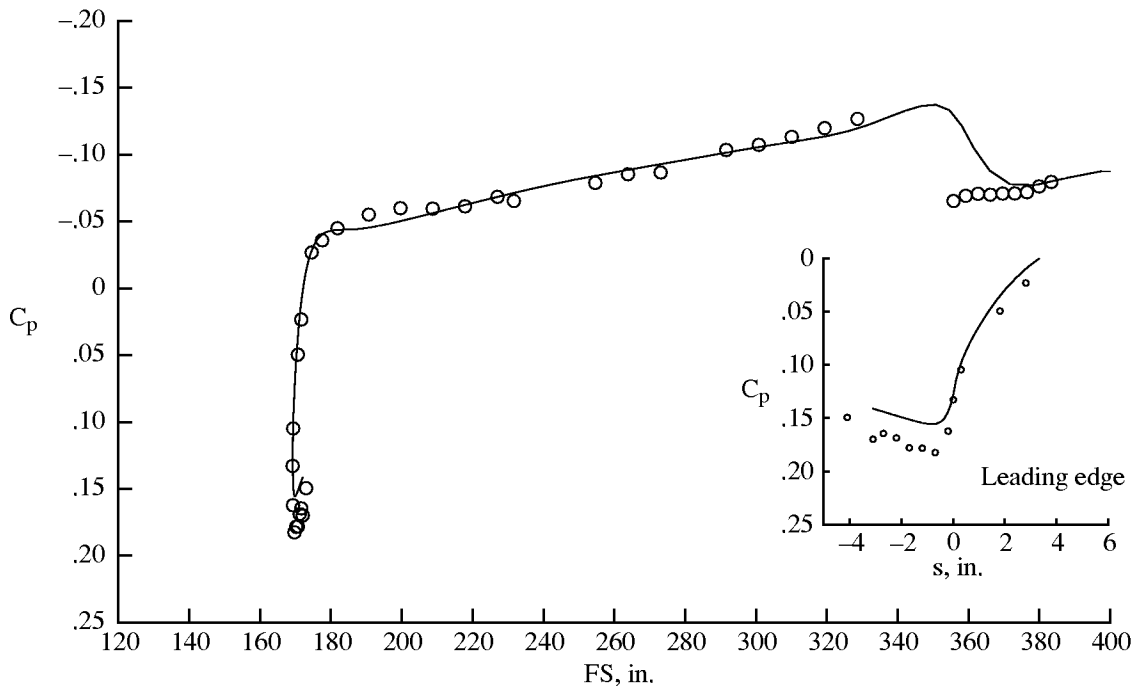


(f) BL 100.

Figure 82. Concluded.

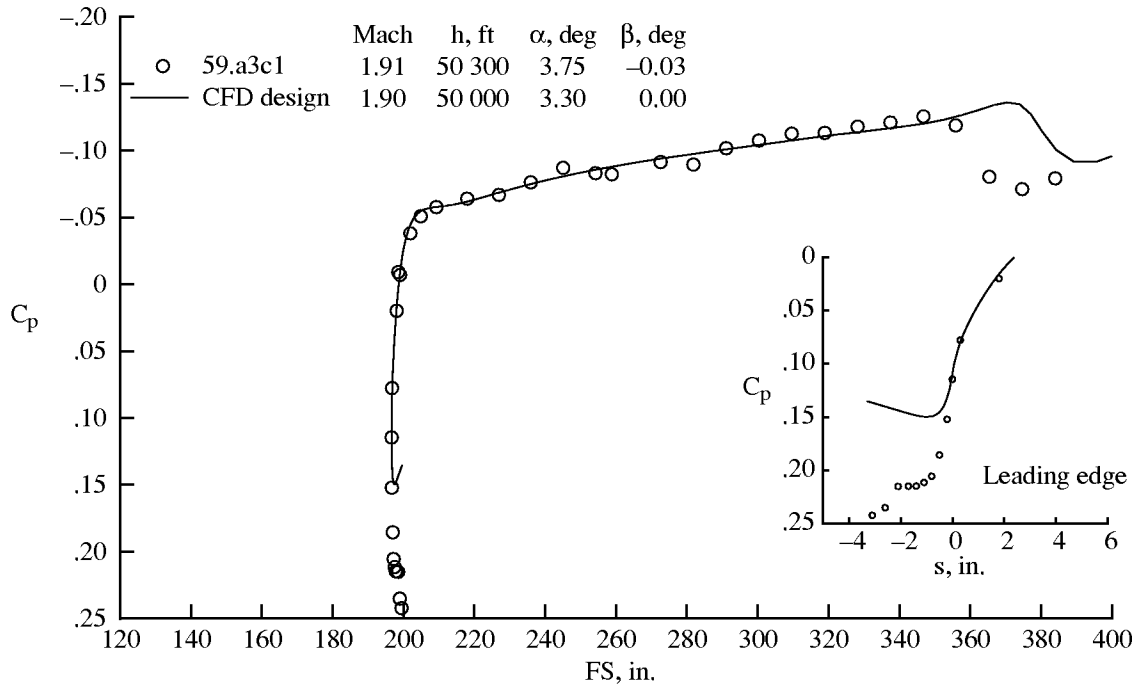


(a) BL 50.

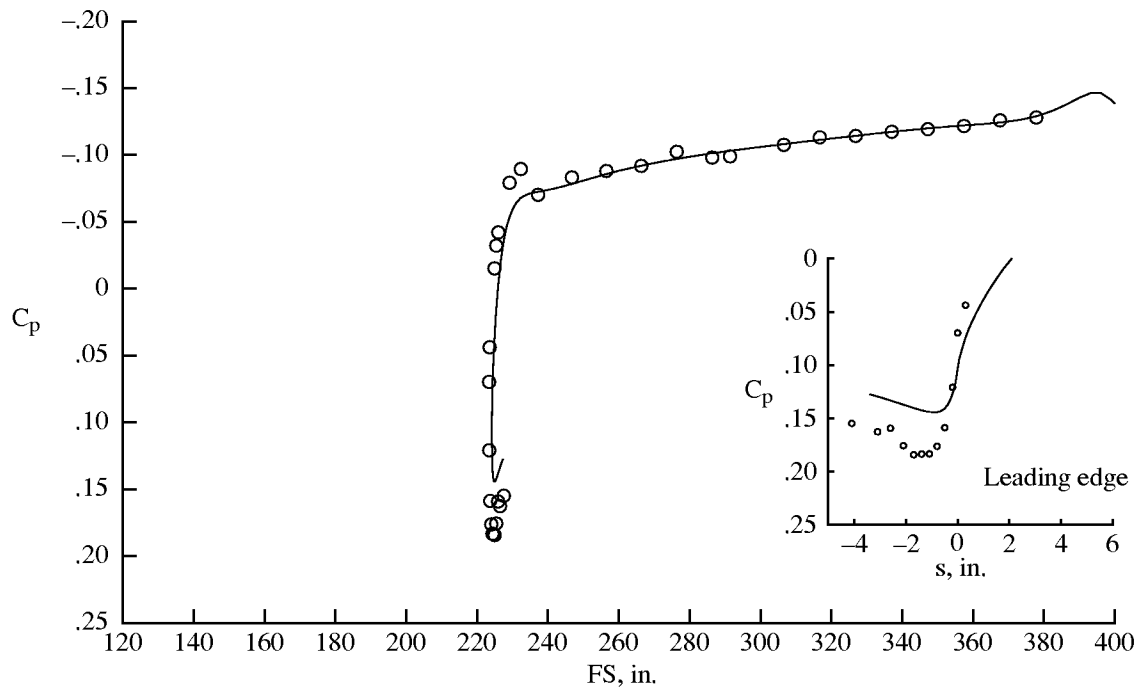


(b) BL 60.

Figure 83. CFD design comparison with experimental data at $\alpha = 3.75^\circ$ for BL 50 and BL 60 (CFD solution from BCAG).

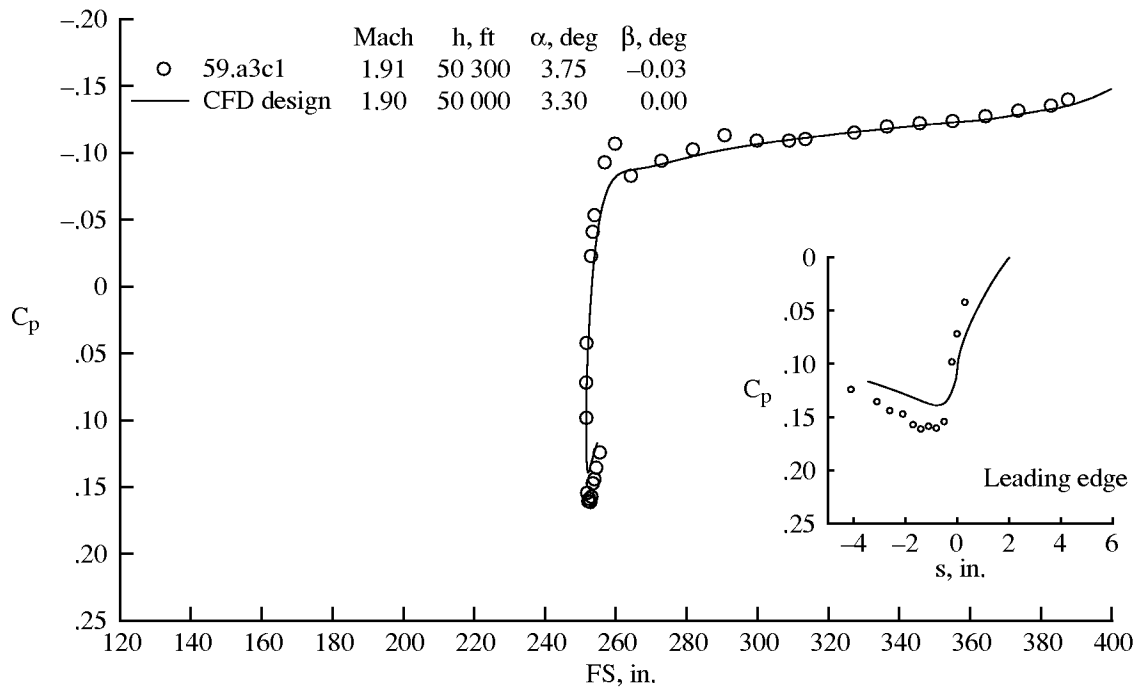


(c) BL 70.

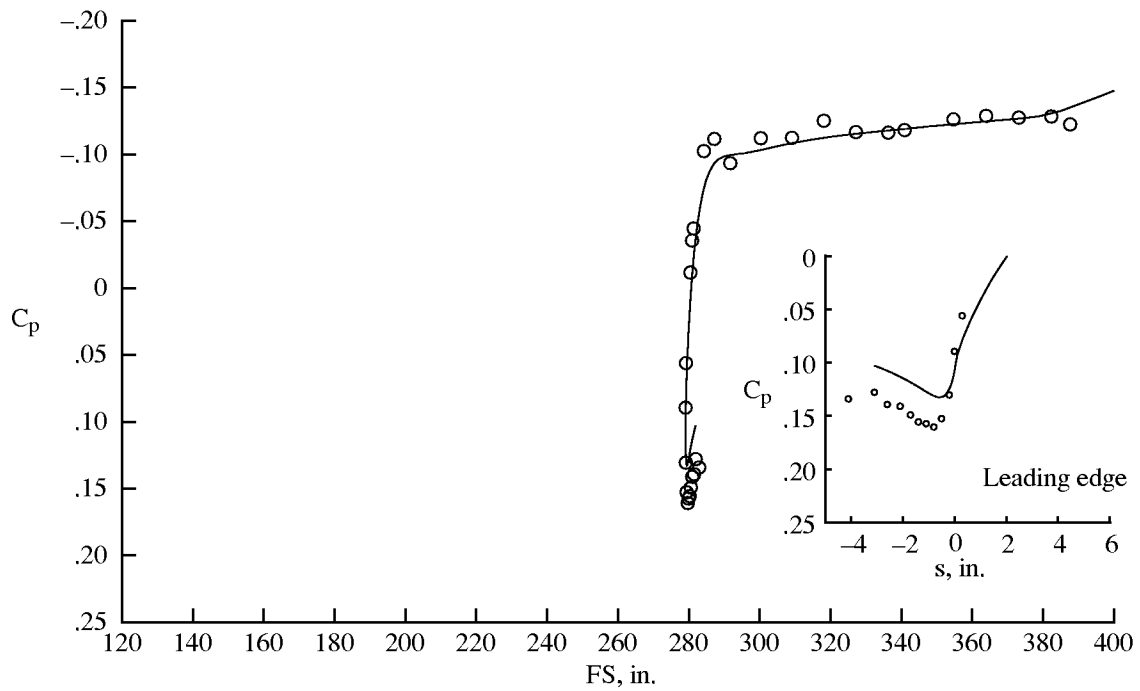


(d) BL 80.

Figure 83. Continued.



(e) BL 90.



(f) BL 100.

Figure 83. Concluded.

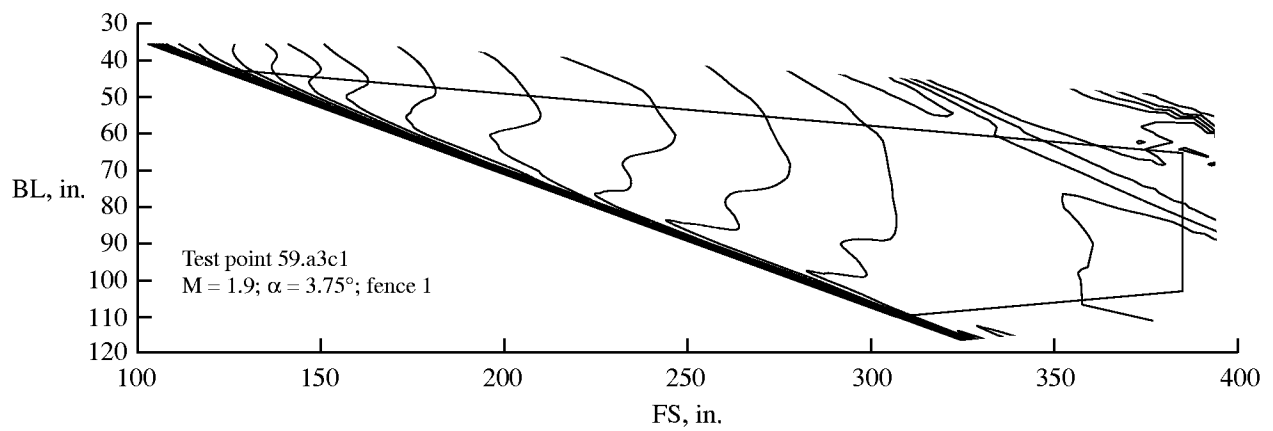
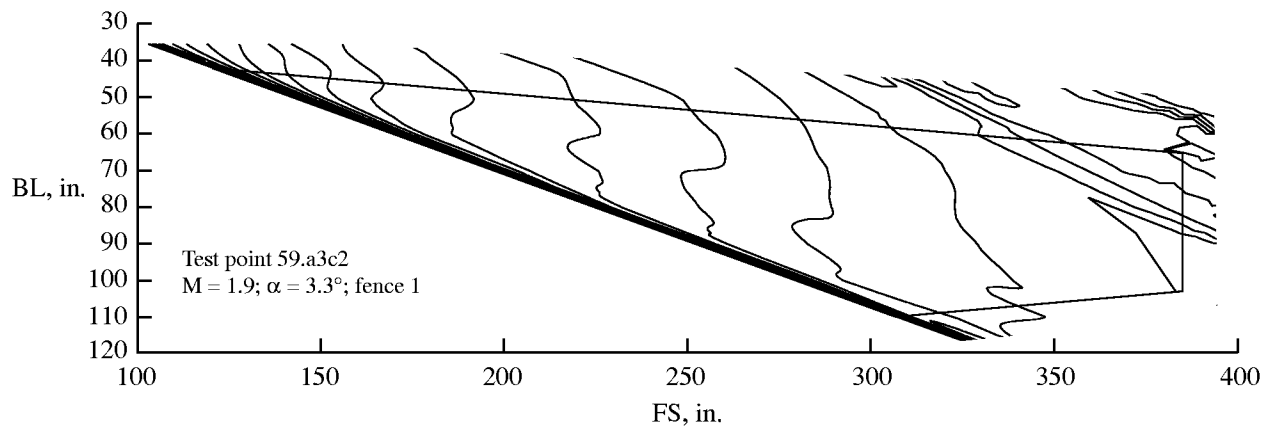
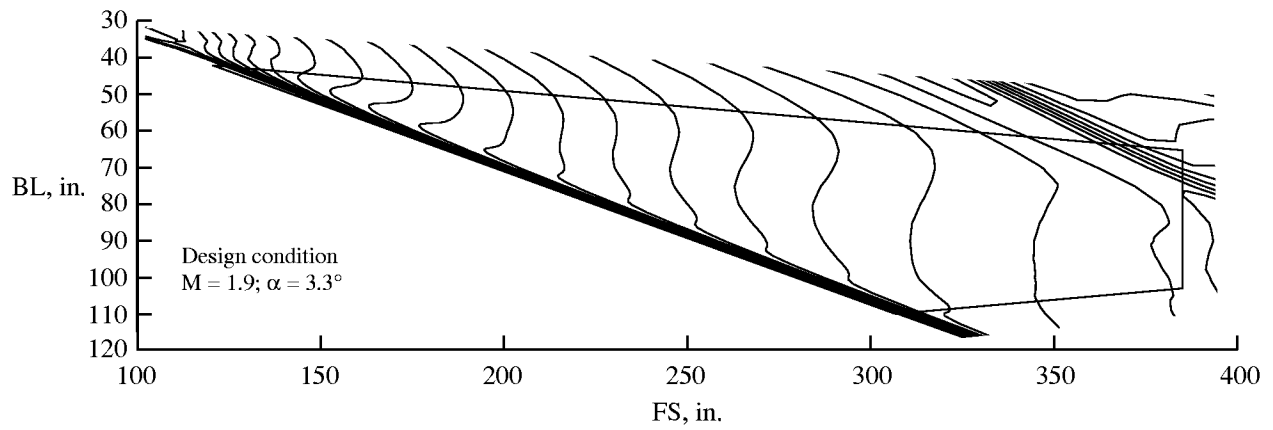
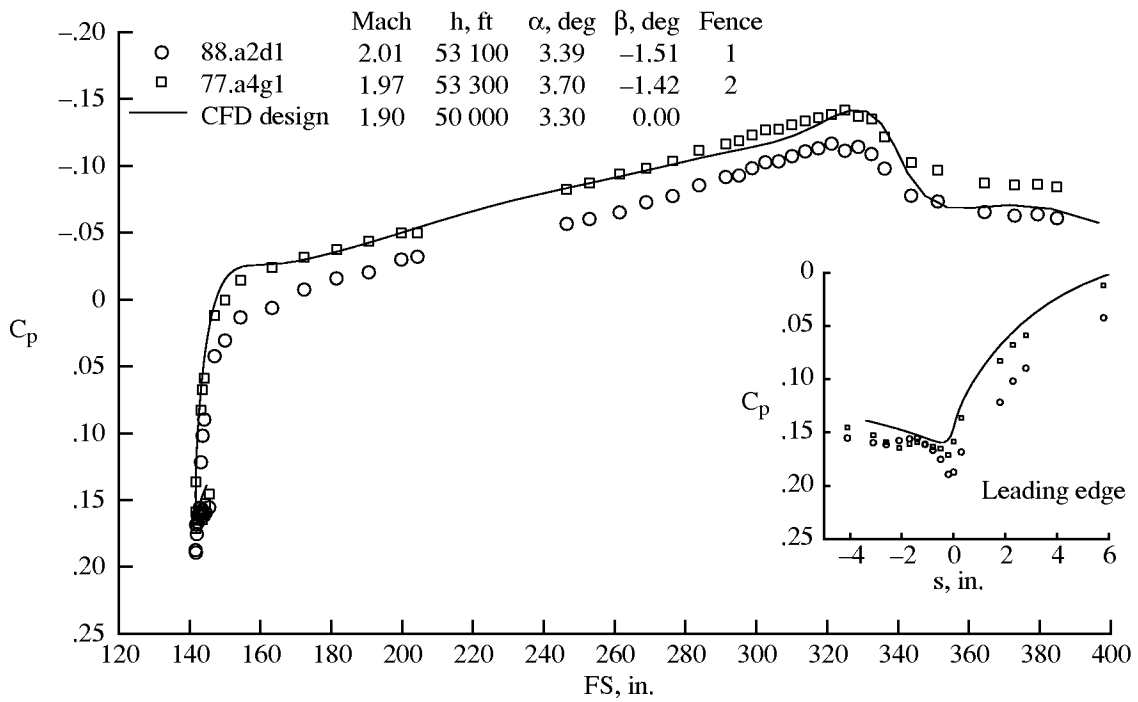
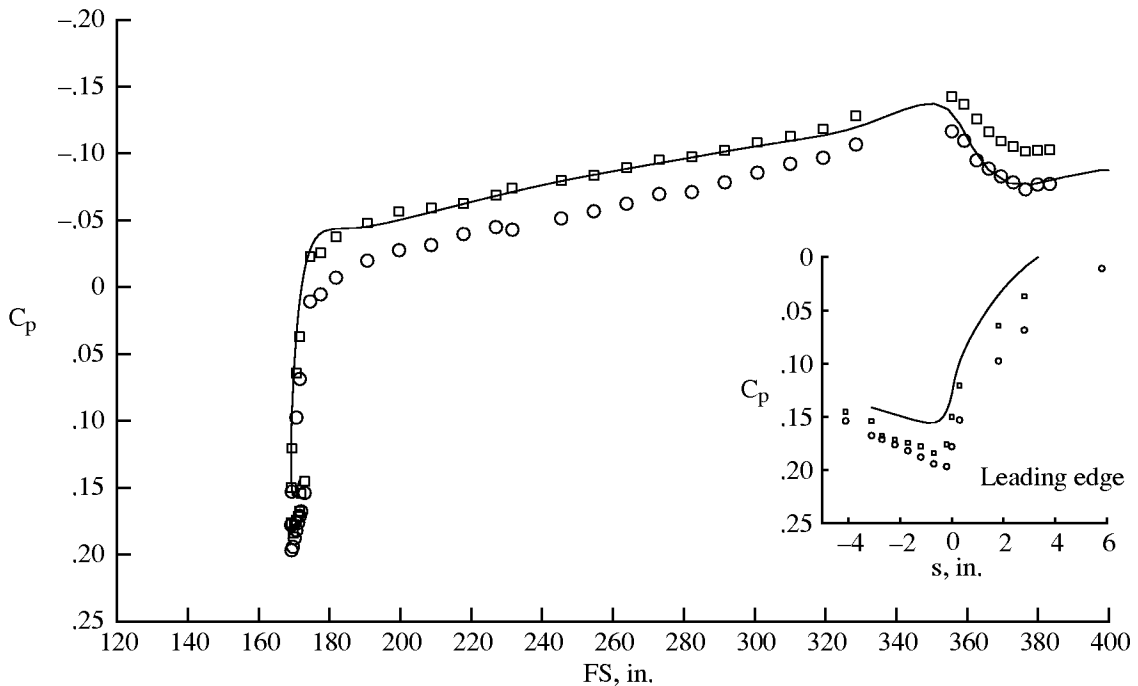


Figure 84. Comparison of experimental isobar patterns with CFD isobar pattern (CFD solution from BCAG). Isobar lines are spaced $0.01C_p$.

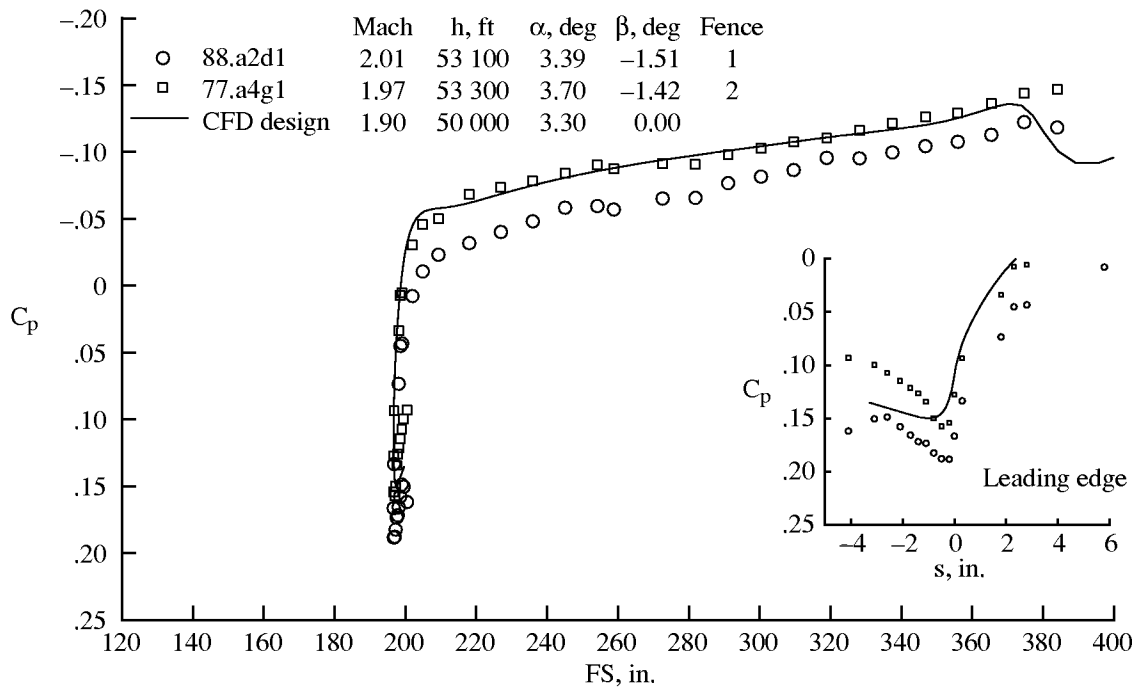


(a) BL 50.

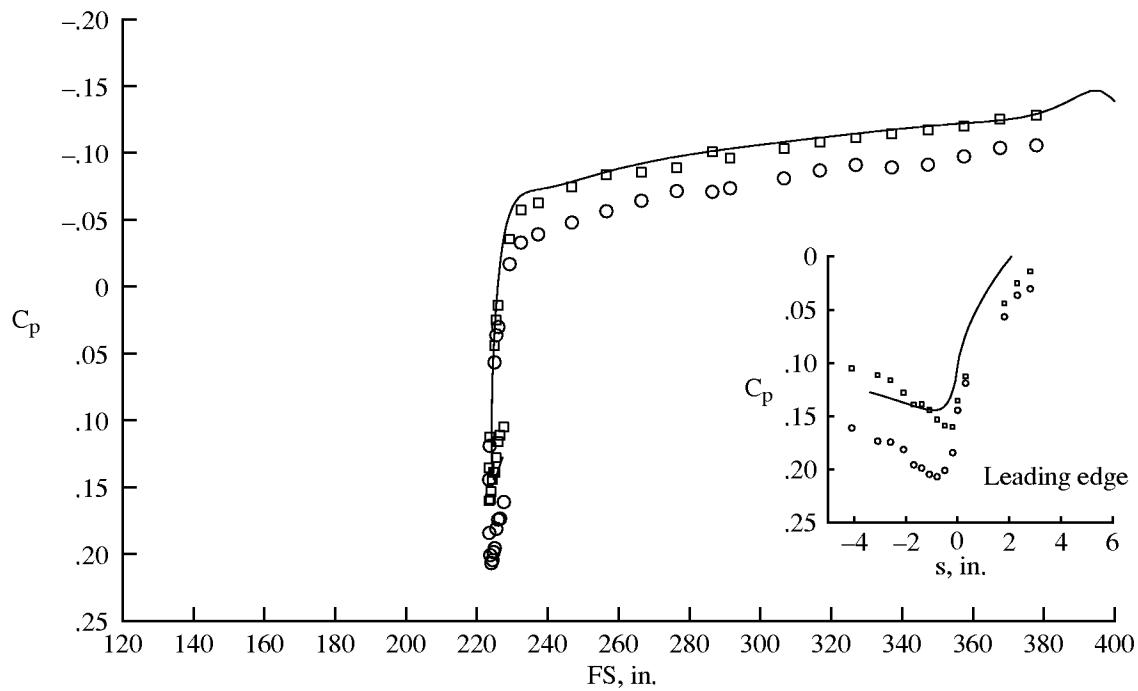


(b) BL 60.

Figure 85. CFD design comparison with experimental data at best laminar flow conditions for BL 50 and BL 60 (CFD solution from BCAG).

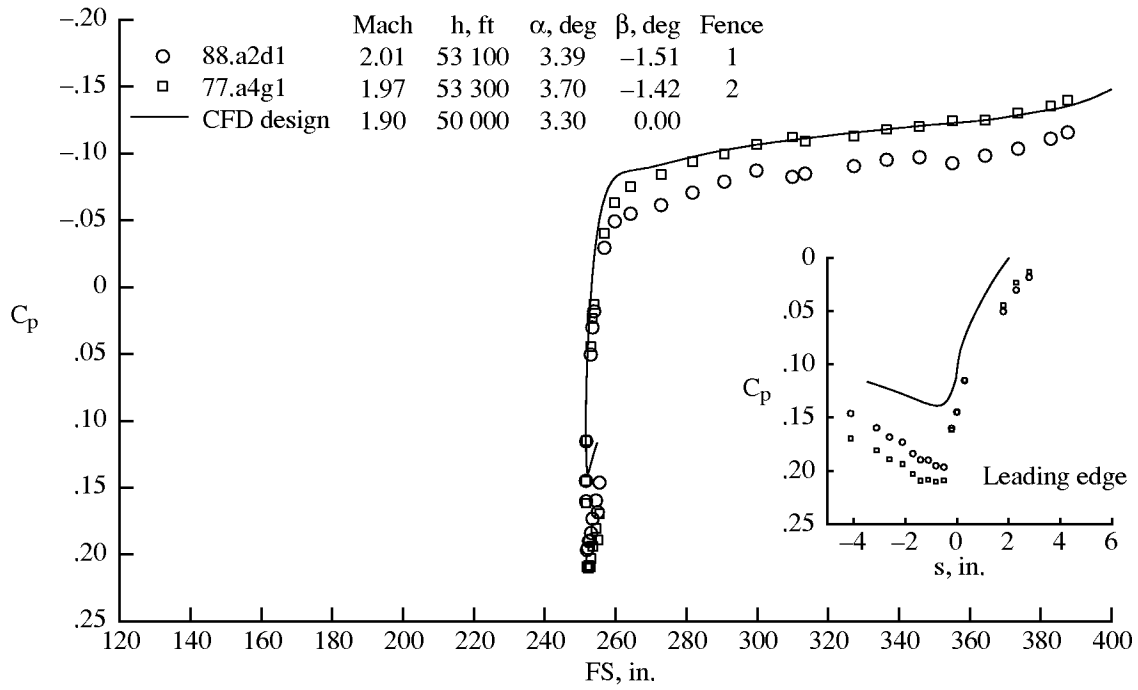


(c) BL 70.

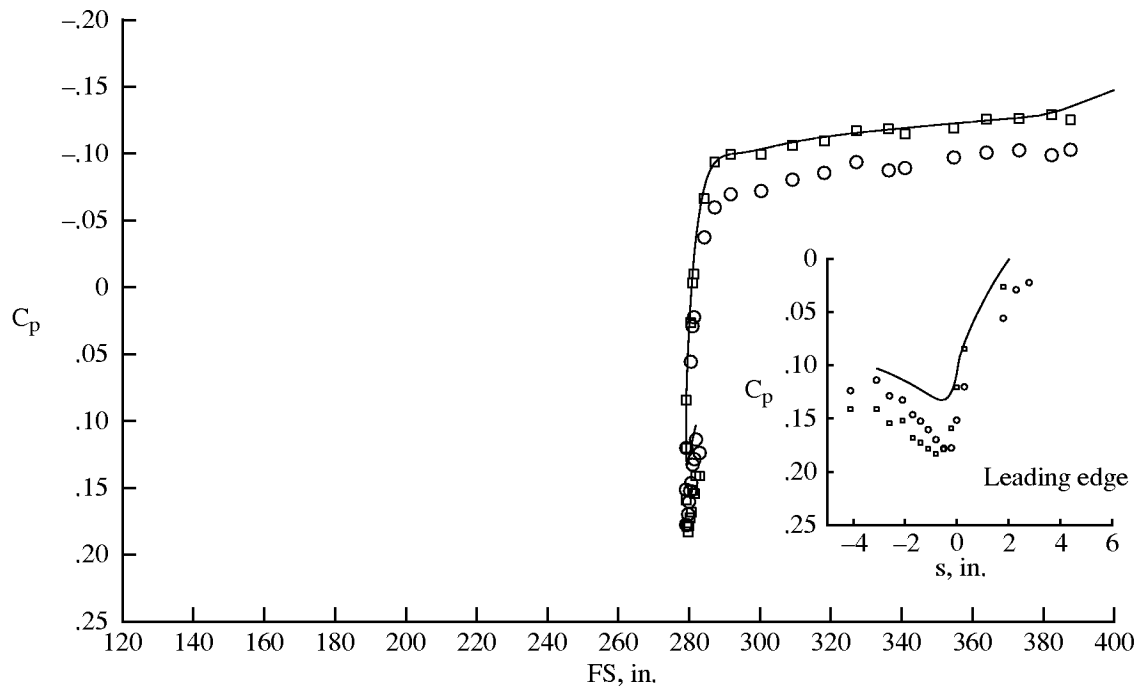


(d) BL 80.

Figure 85. Continued.



(e) BL 90.



(f) BL 100.

Figure 85. Concluded.

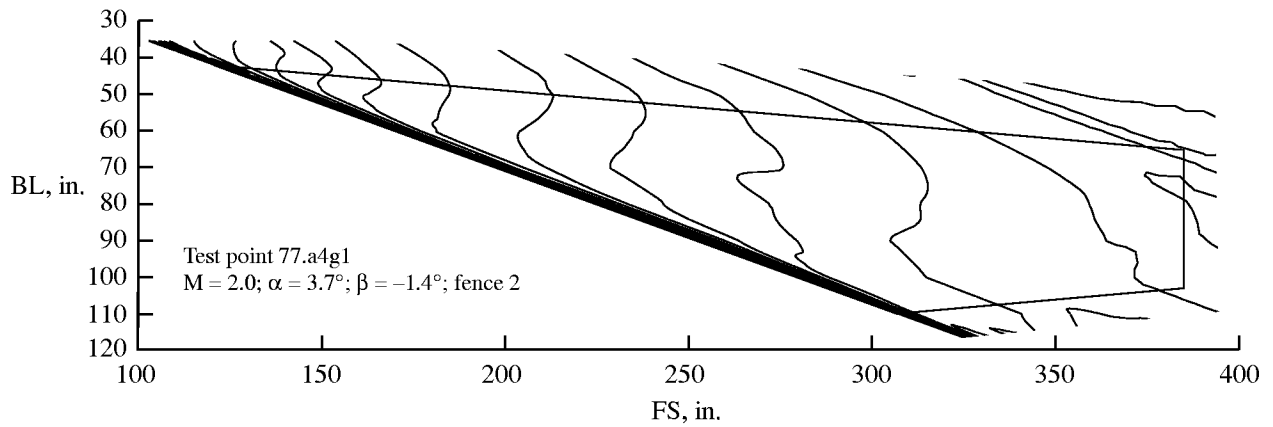
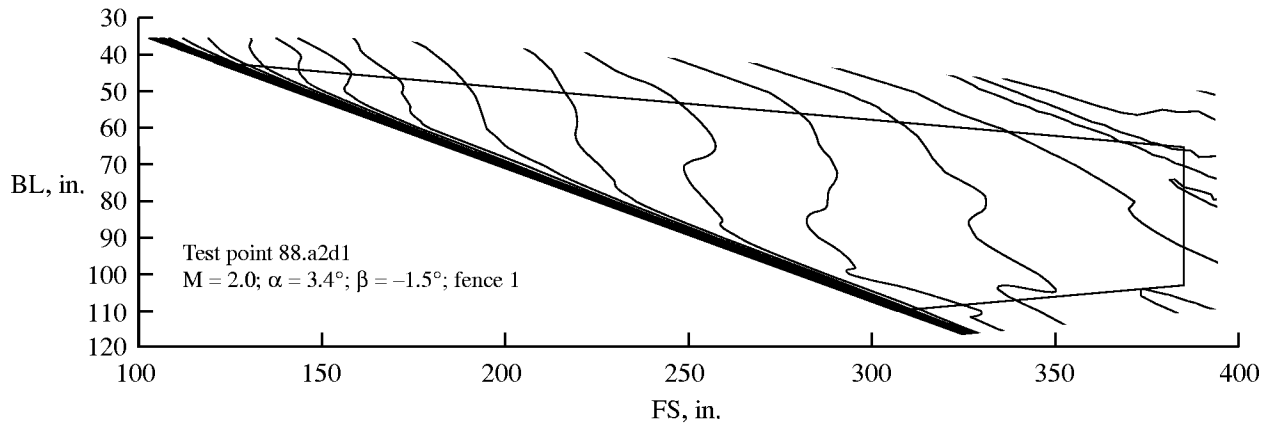
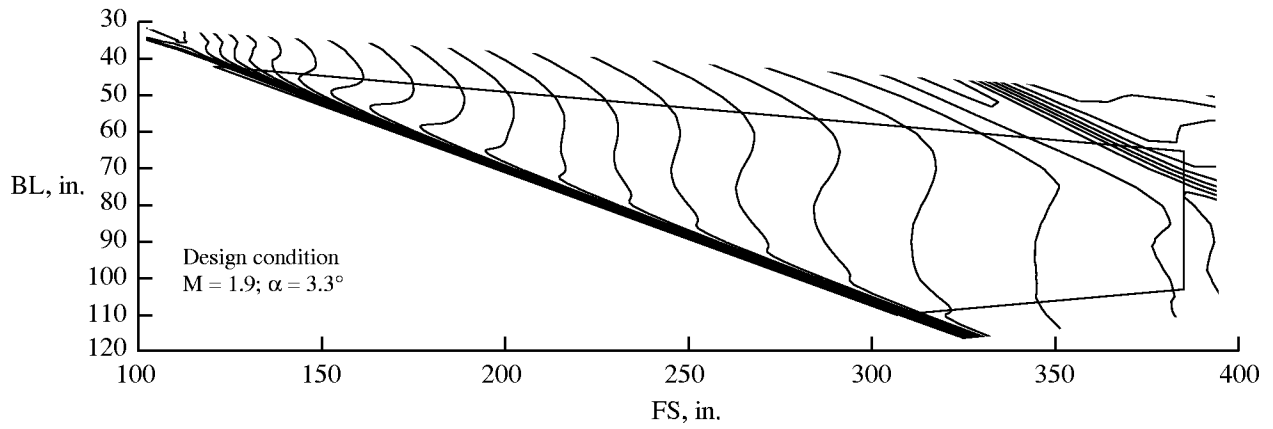


Figure 86. Comparison of experimental isobar patterns for extensive laminar flow with CFD isobar pattern (CFD solution from BCAG). Isobar lines are spaced $0.01C_p$.

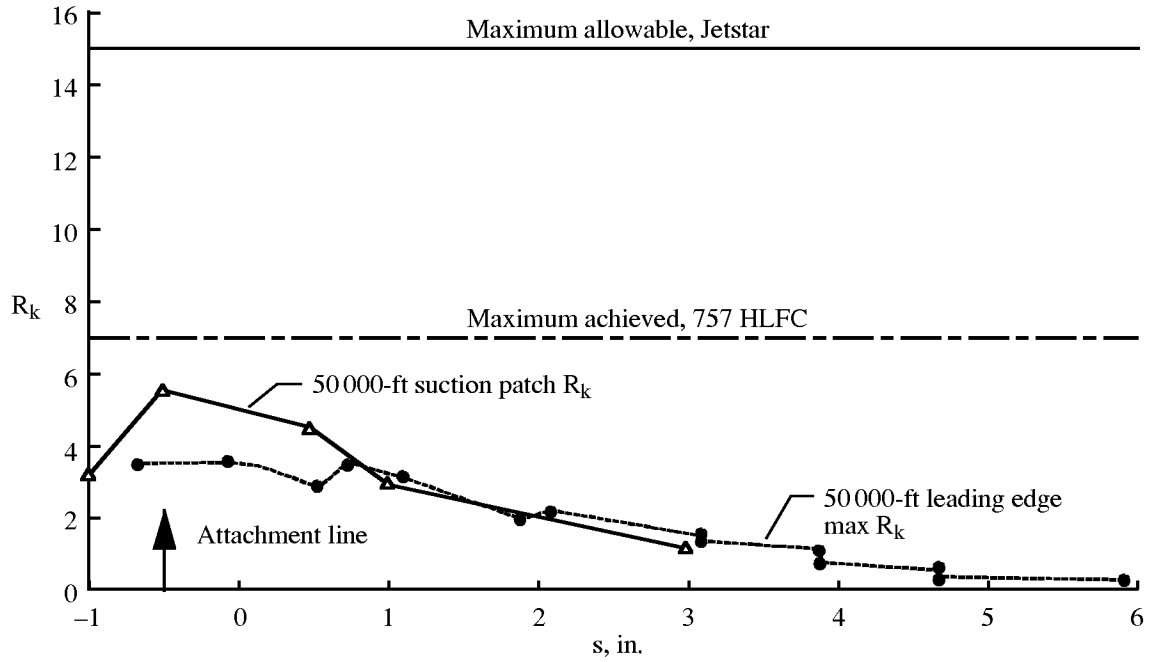


Figure 87. Maximum R_k levels used in design.

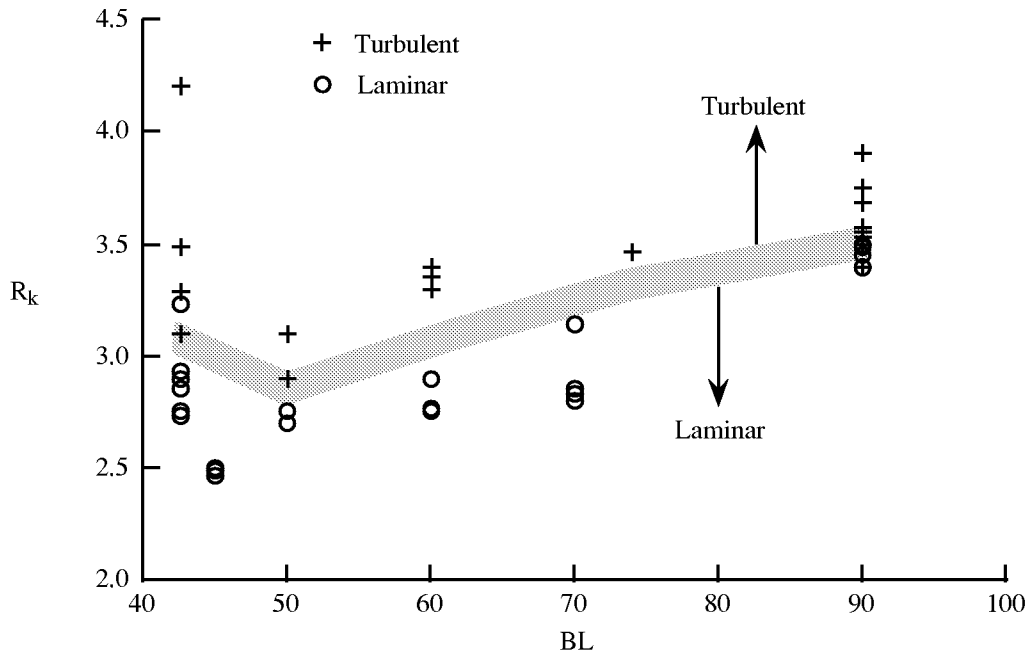


Figure 88. R_k limit behavior across span.

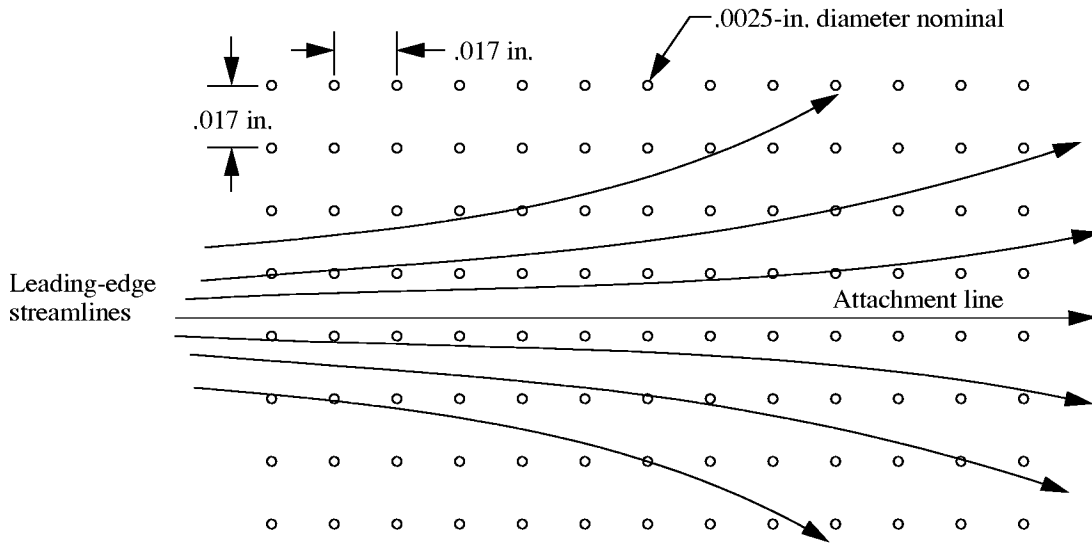


Figure 89. Perforation pattern in attachment-line region.

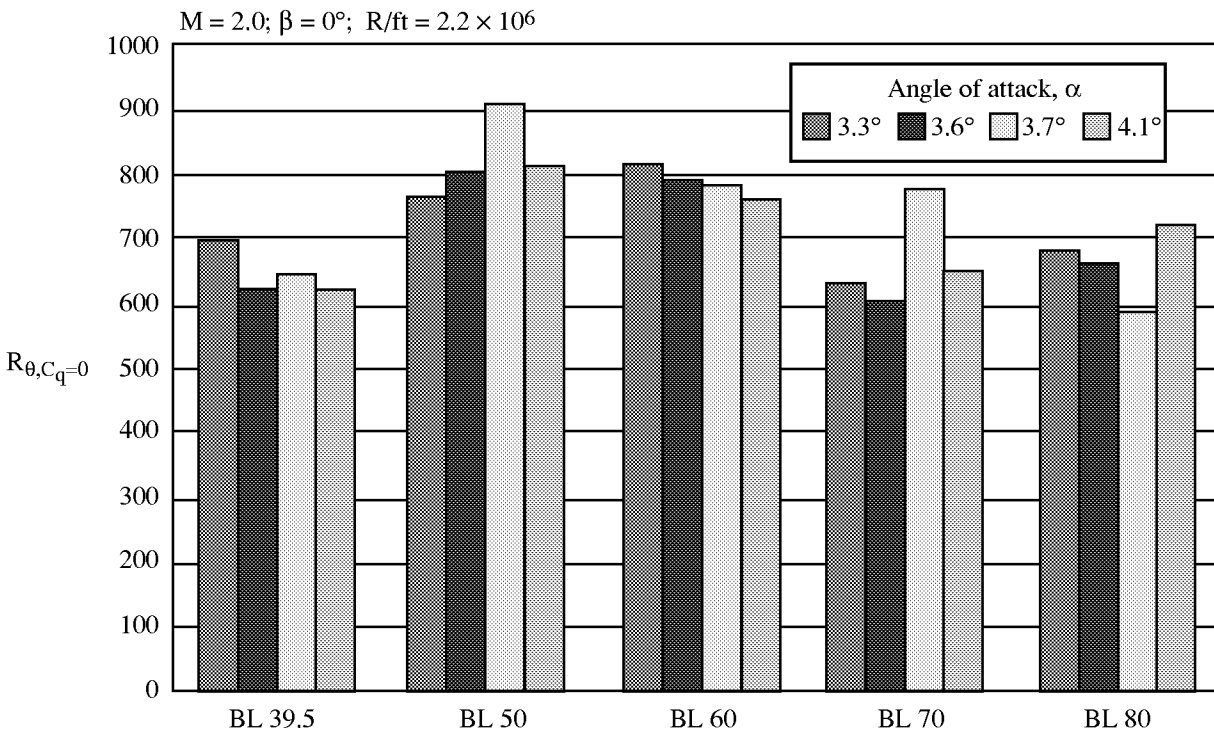


Figure 90. Attachment-line $R_{\theta, C_q=0}$ values calculated from flight data (generated by BCAG).

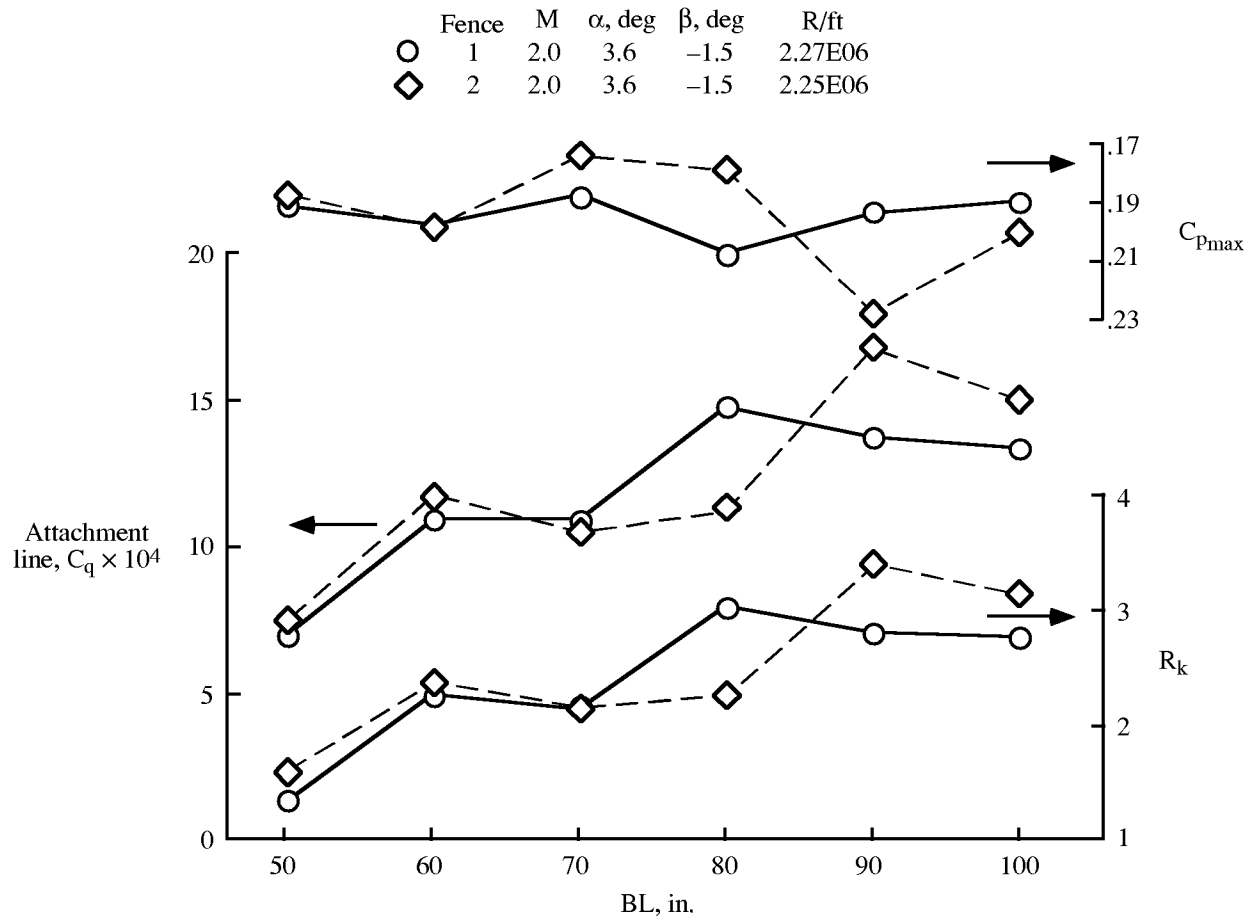


Figure 91. Attachment-line characteristics for fences 1 and 2.

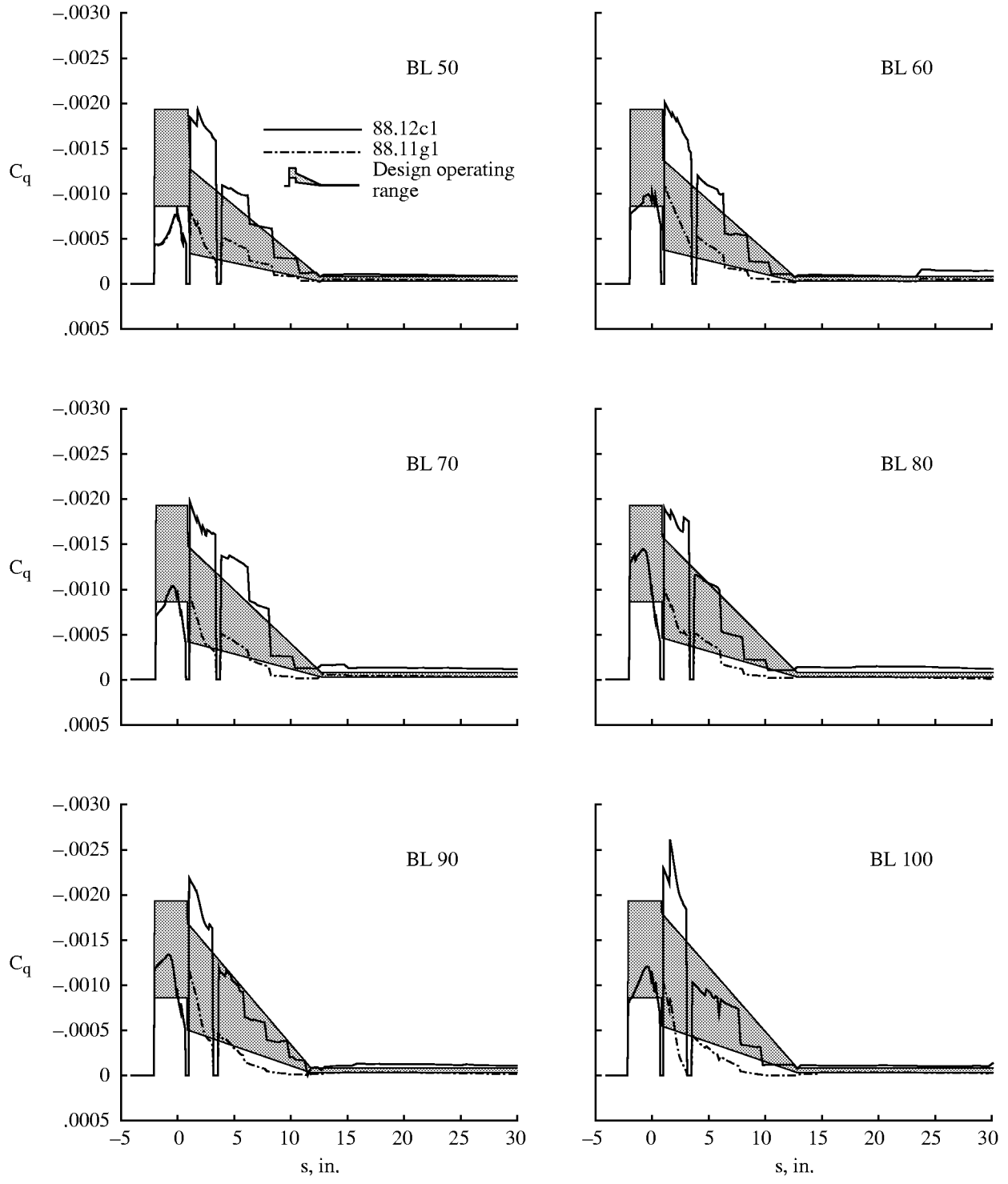


Figure 92. C_q profiles for test points 88.12c1 (C_q maximum except in flute 1) and 88.11g1 (C_q minimum except in flute 1) overlaid on design operating range envelope. Design conditions: $M = 1.9$; $\alpha = 3.3^\circ$; test conditions: $M = 2$; $\alpha \approx 3.4^\circ$. Flute 1 C_q set at same level for both test points to ensure a laminar attachment line.

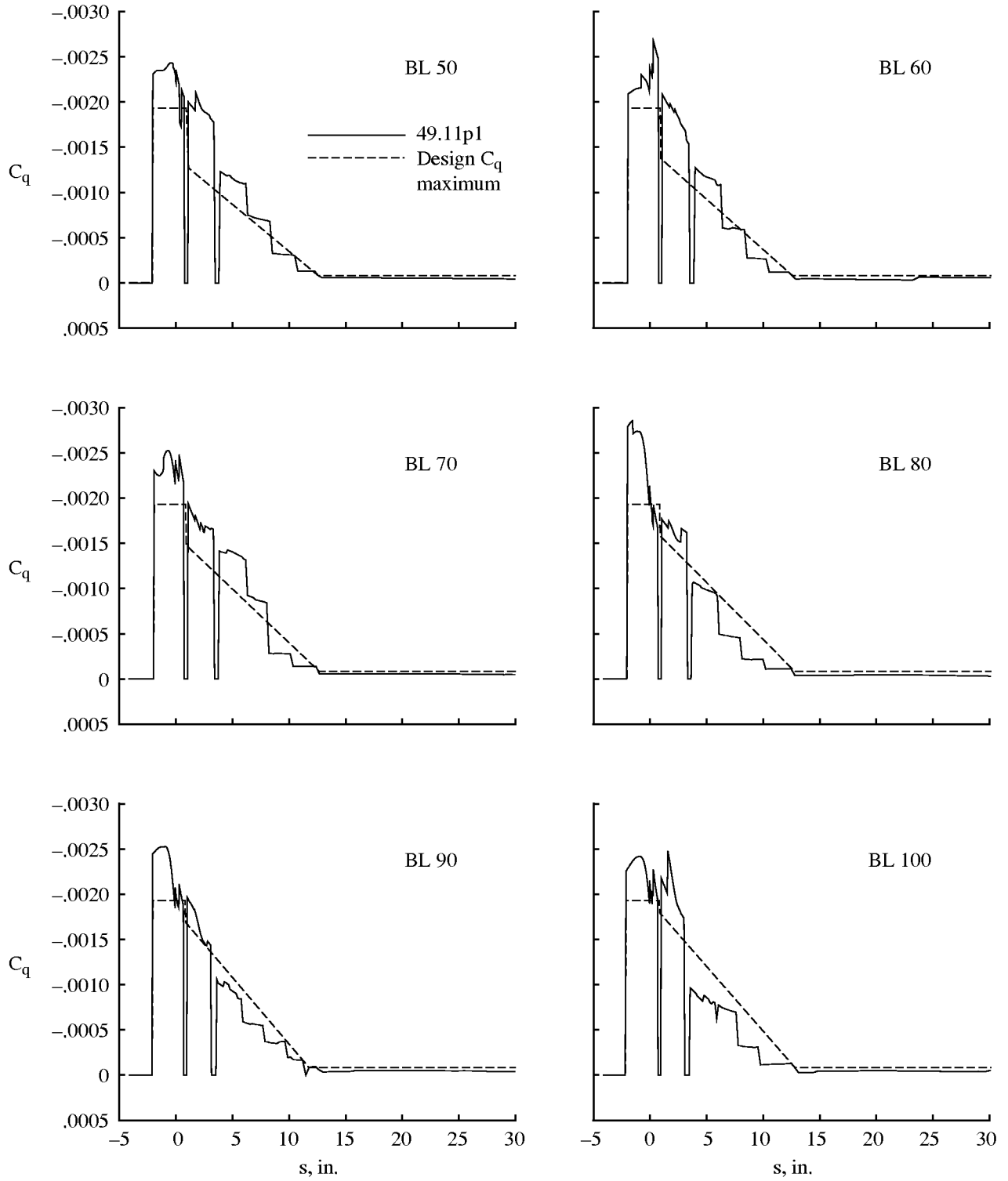


Figure 93. C_q profiles for test point 49.11p1 and upper limit of design C_q envelope. Design conditions: $M = 1.9$; $\alpha = 3.3^\circ$; test conditions: $M = 1.9$; $\alpha \approx 3.7^\circ$. Flutes 1, 2, and 3 set at full open position (maximum suction).

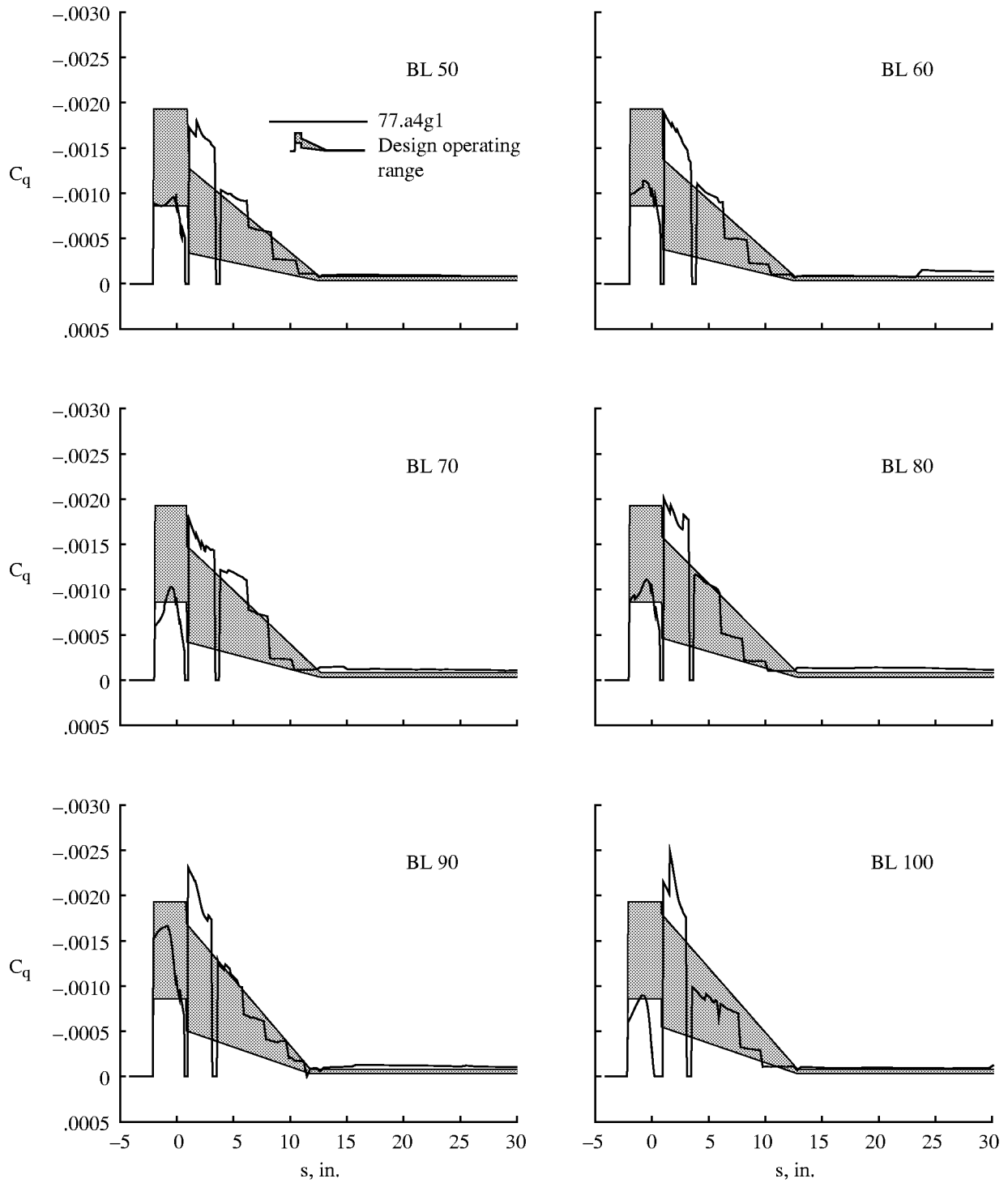


Figure 94. C_q profiles for test point 77.a4g1 (extended laminar flow achieved) and design operating range envelope. Design conditions: $M = 1.9$; $\alpha = 3.3^\circ$; test conditions: $M = 2$; $\alpha \approx 3.7^\circ$. Flute 1 set at suction level which supports laminar flow.

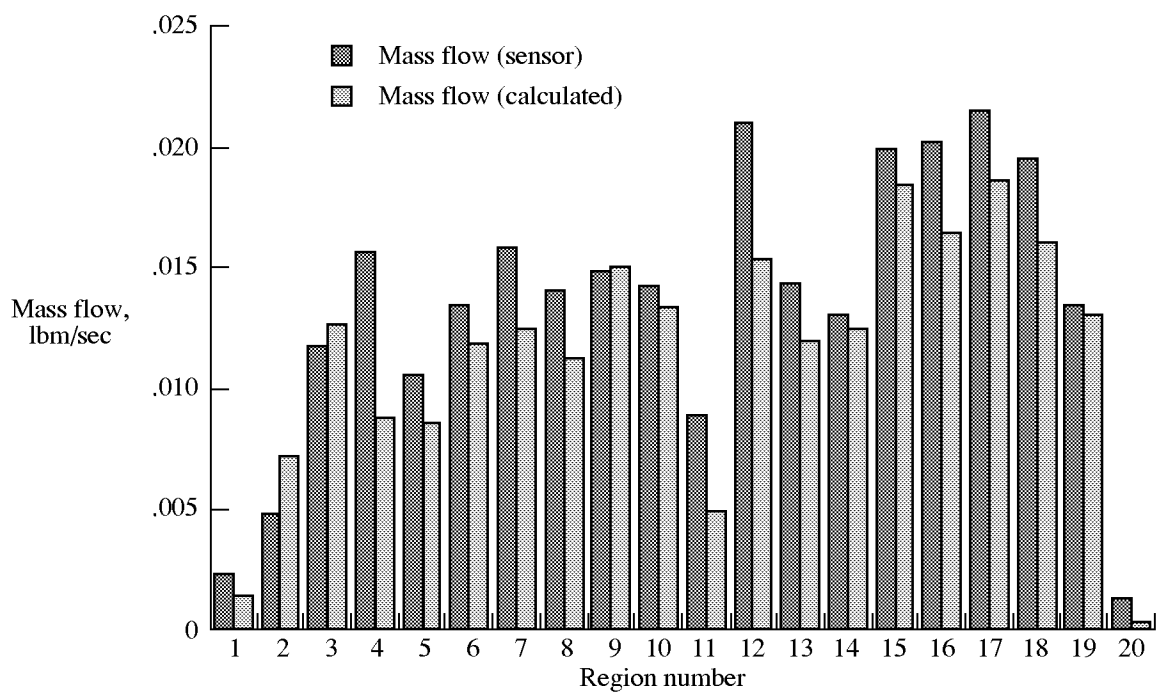


Figure 95. Comparison of calculated versus measured mass-flow rates. Test point 77.a4g1.

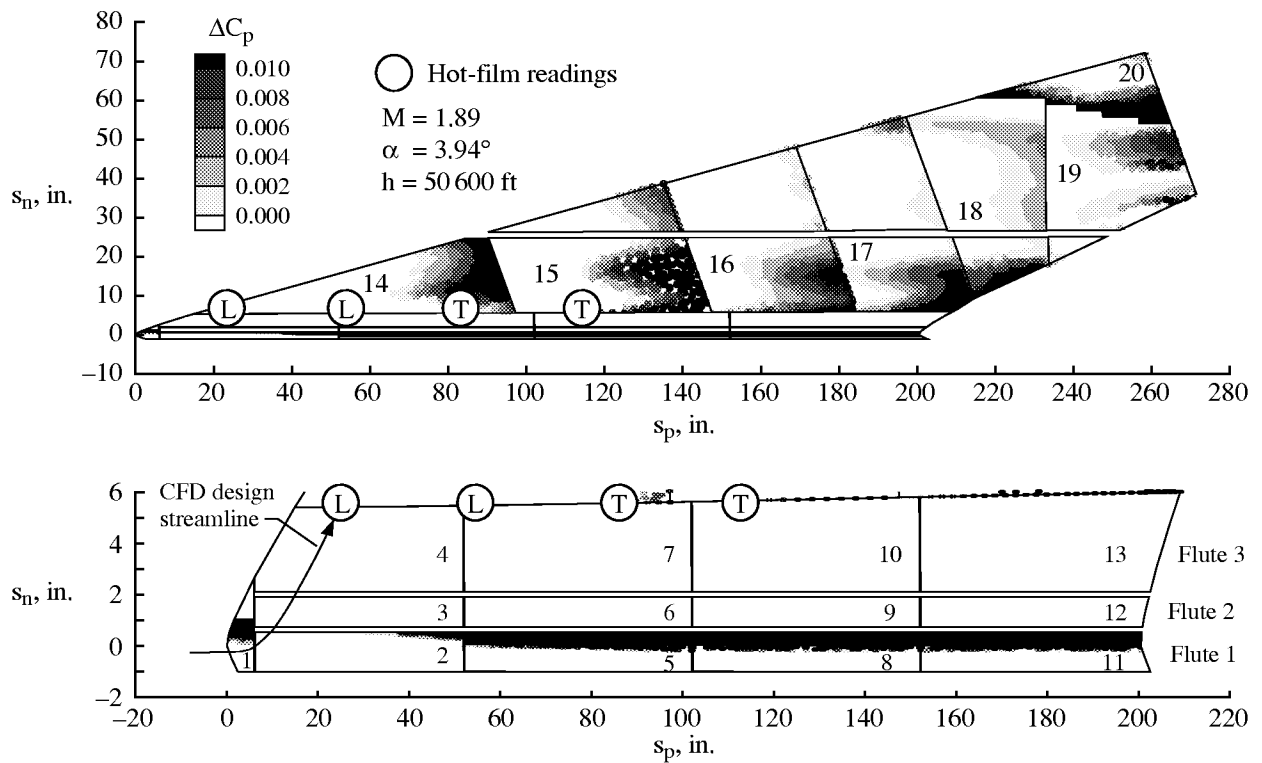


Figure 96. Outflow areas for test point 57.a3e5. Note: Valves closed for all regions except for those in flutes 2 and 3.

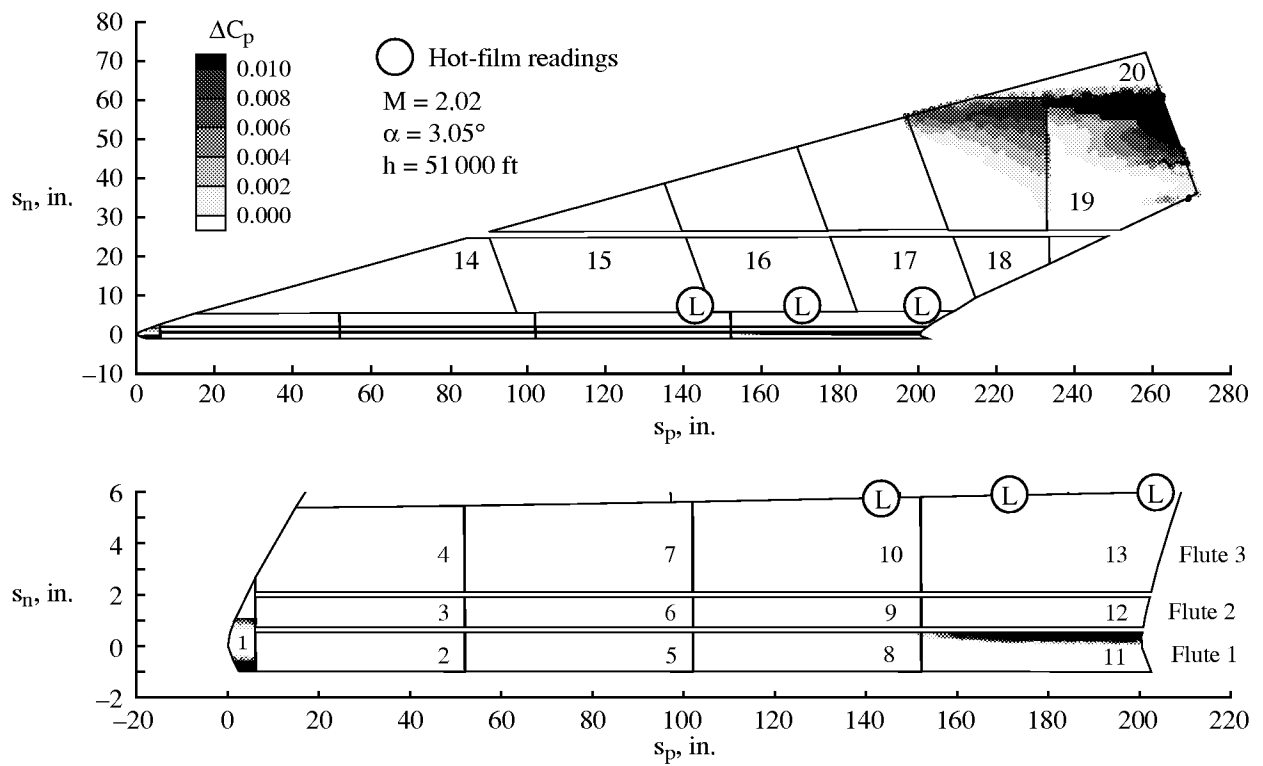


Figure 97. Outflow areas for test point 63.a15g.

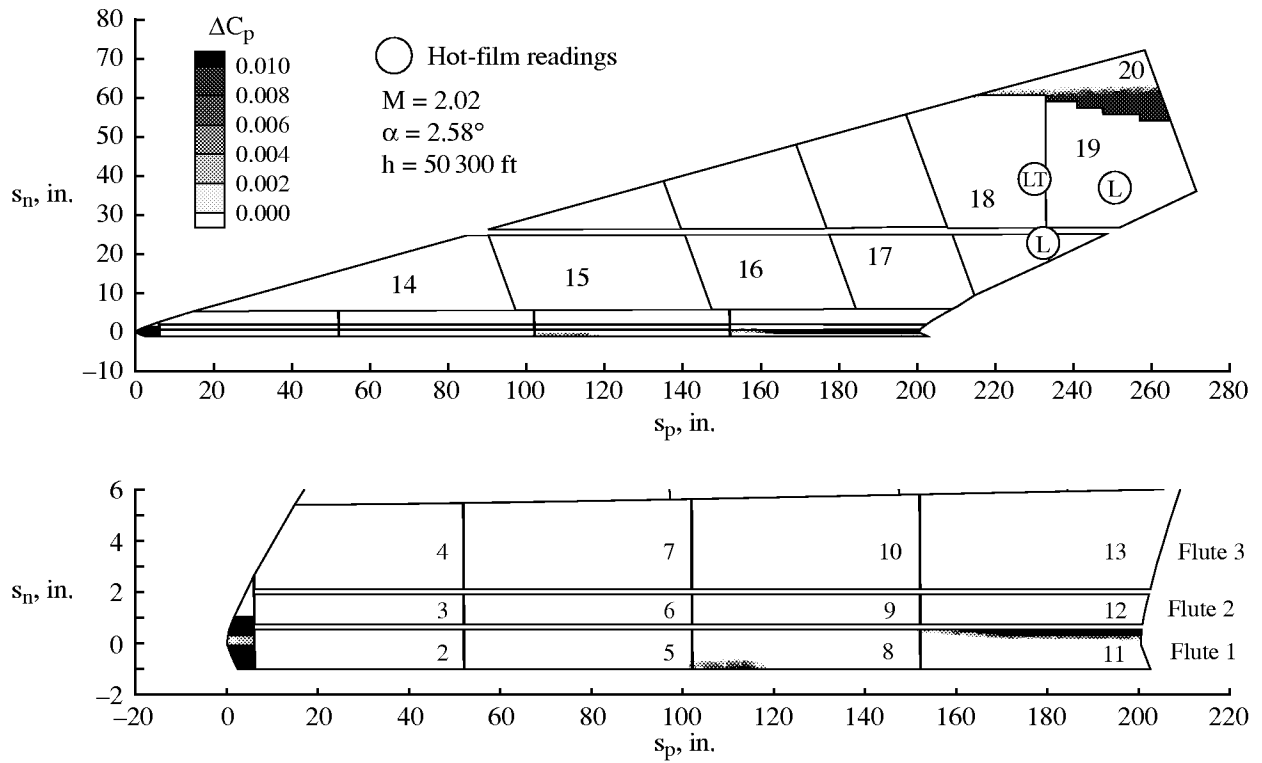


Figure 98. Outflow areas for test point 70.o4i1.

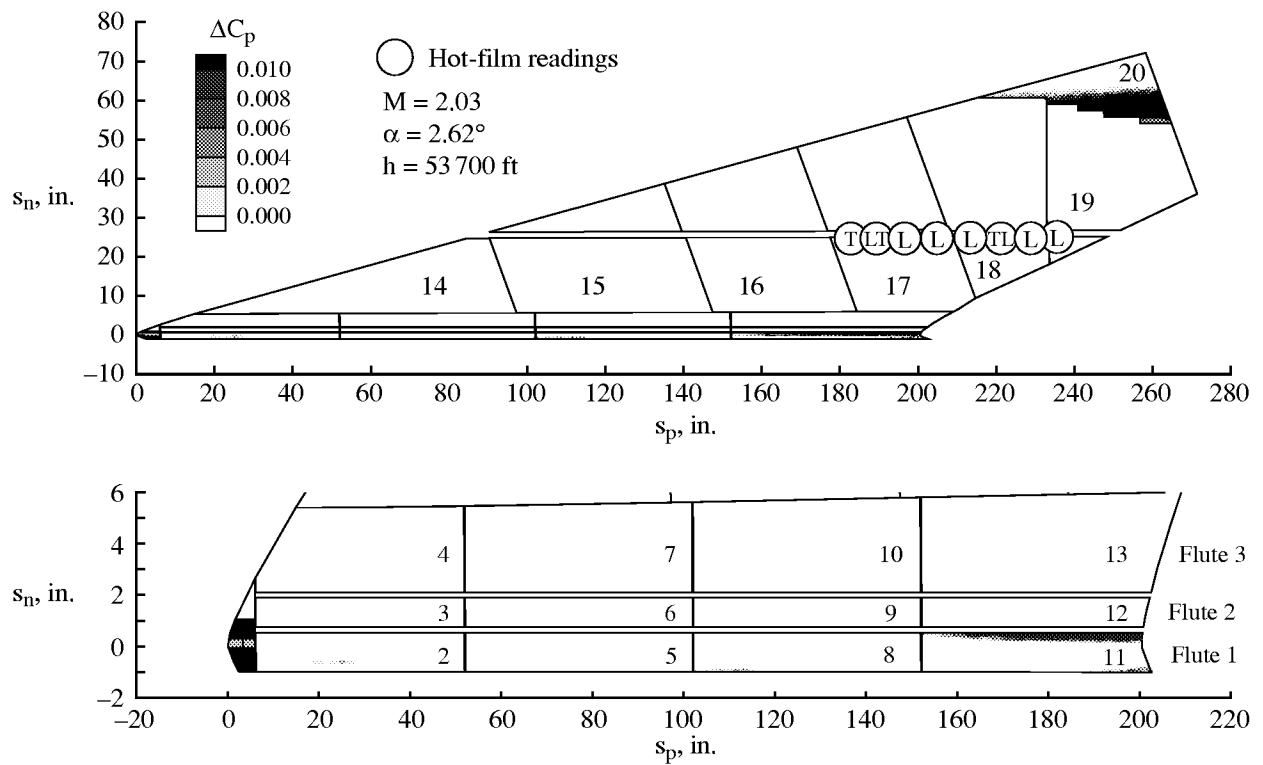


Figure 99. Outflow areas for test point 83.a2c1.

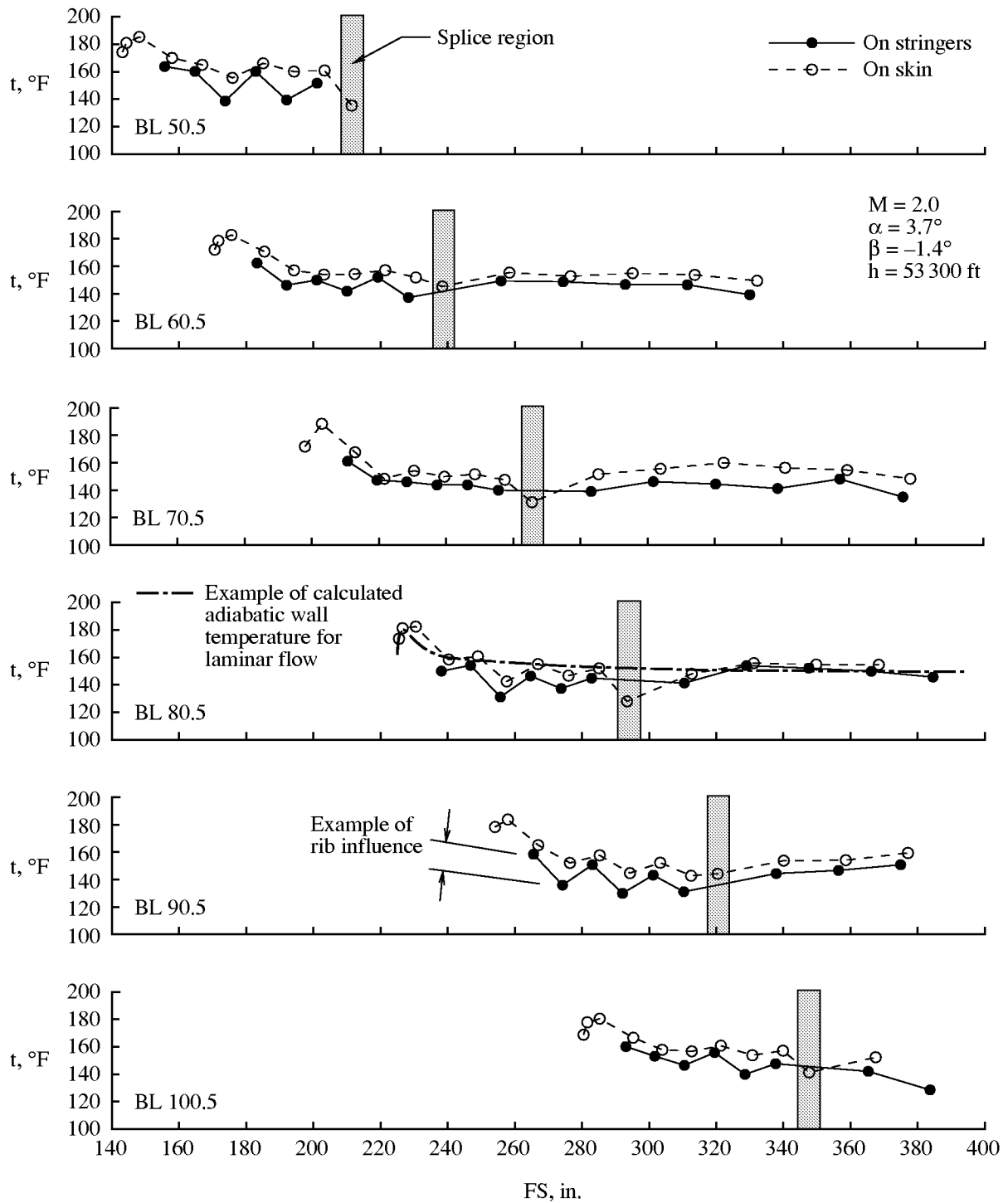


Figure 100. Temperature measurements on panel for test point 77.a4g1.

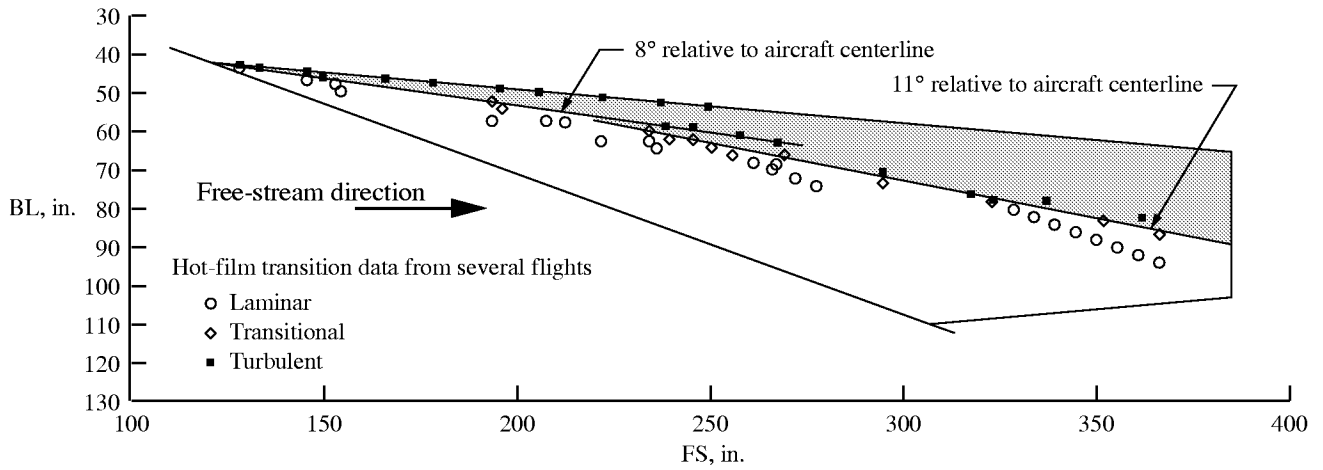


Figure 101. Hot-film results from selected test points showing definition of inboard turbulent region.

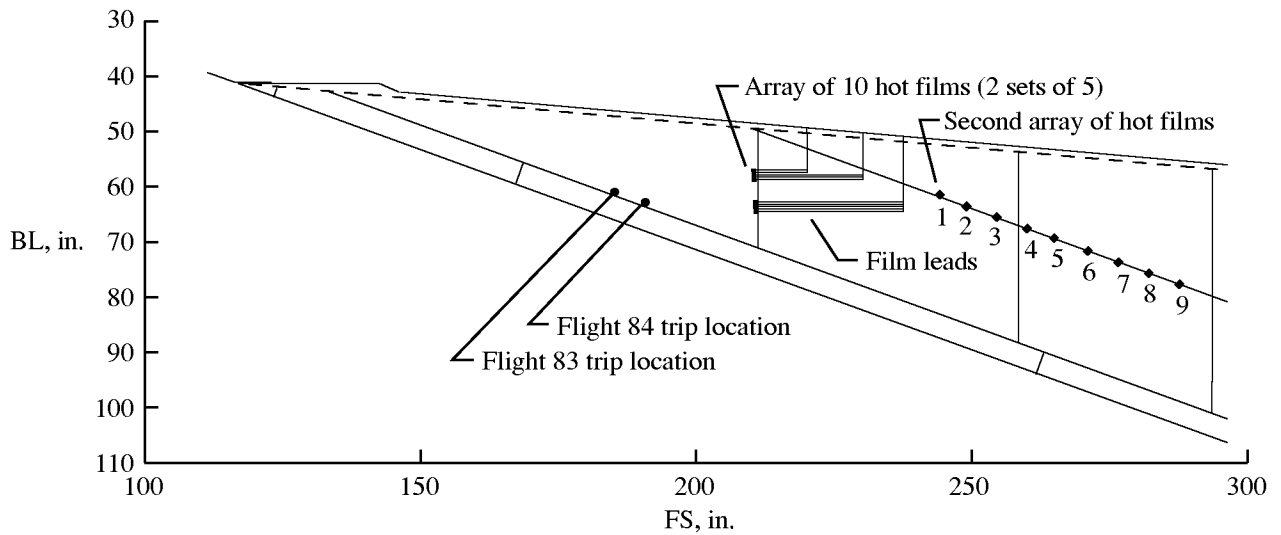


Figure 102. Hot-film and trip locations used in flights 83 and 84 to investigate turbulence spreading. Roughness element: 54 grit, 2 mm in diameter on 0.001-in-thick, 0.25-in-diameter patch of tape.

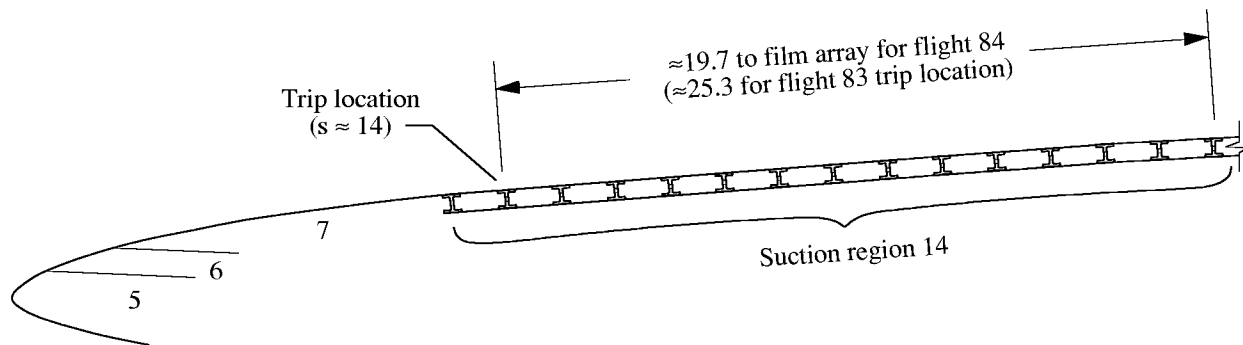


Figure 103. Wing cross section at spanwise station 62.9. Dimensions are in inches.

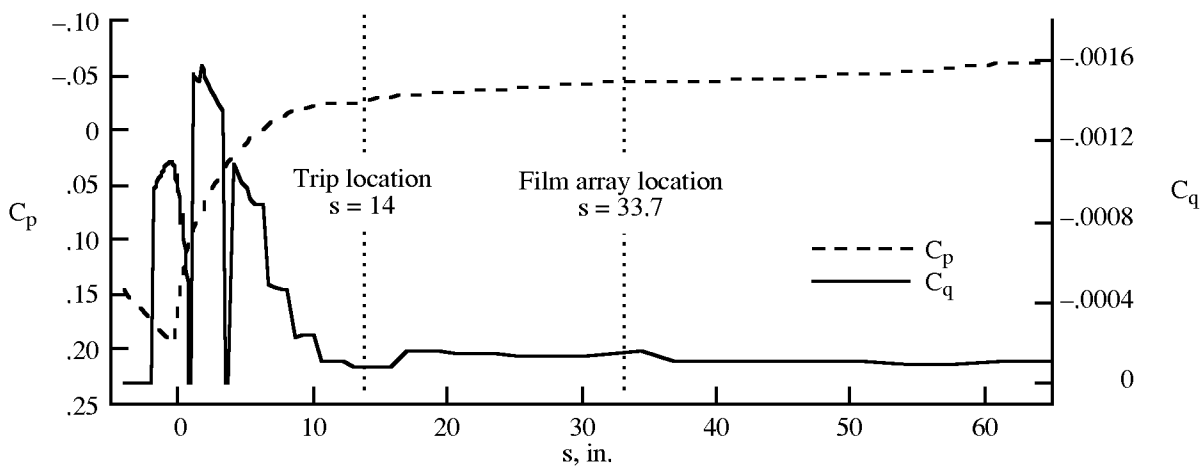


Figure 104. Pressure and suction coefficient at BL 62.5 for test point 84.10c1. Test conditions: $M = 2.02$; $\alpha = 3.70^\circ$; $\beta = -1.43^\circ$; $R/ft = 2.24 \times 10^6$; valve 14 at 75° . Dimensions are in inches.

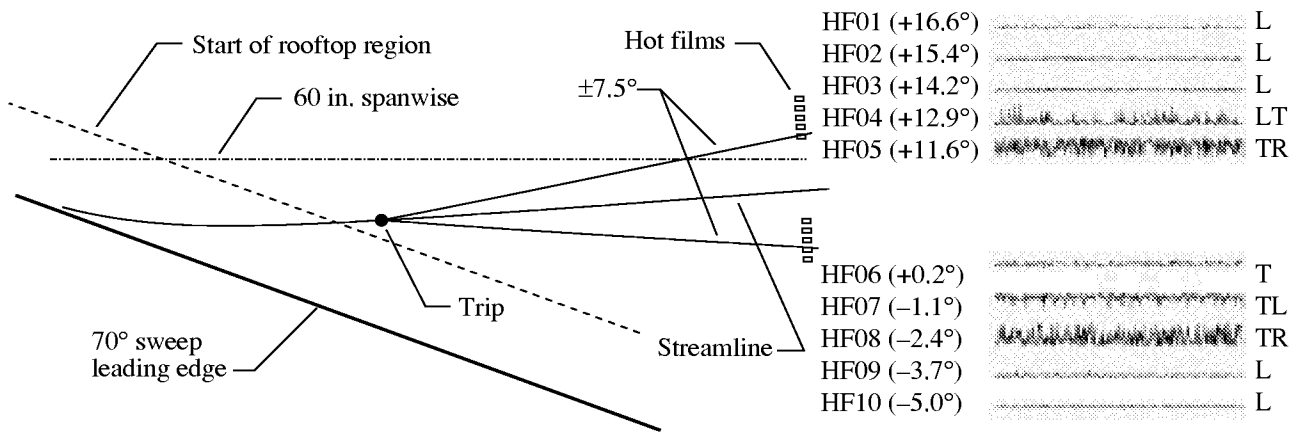


Figure 105. Typical turbulence spreading results from flight 84.10c1. Local streamline shown and $\pm 7.5^\circ$ spreading angles generated from experimental data using surface Euler code. Test conditions: $M = 2.02$; $\alpha = 3.70^\circ$; $\beta = -1.43^\circ$; $R/ft = 2.24 \times 10^6$; valve 14 at 75° .

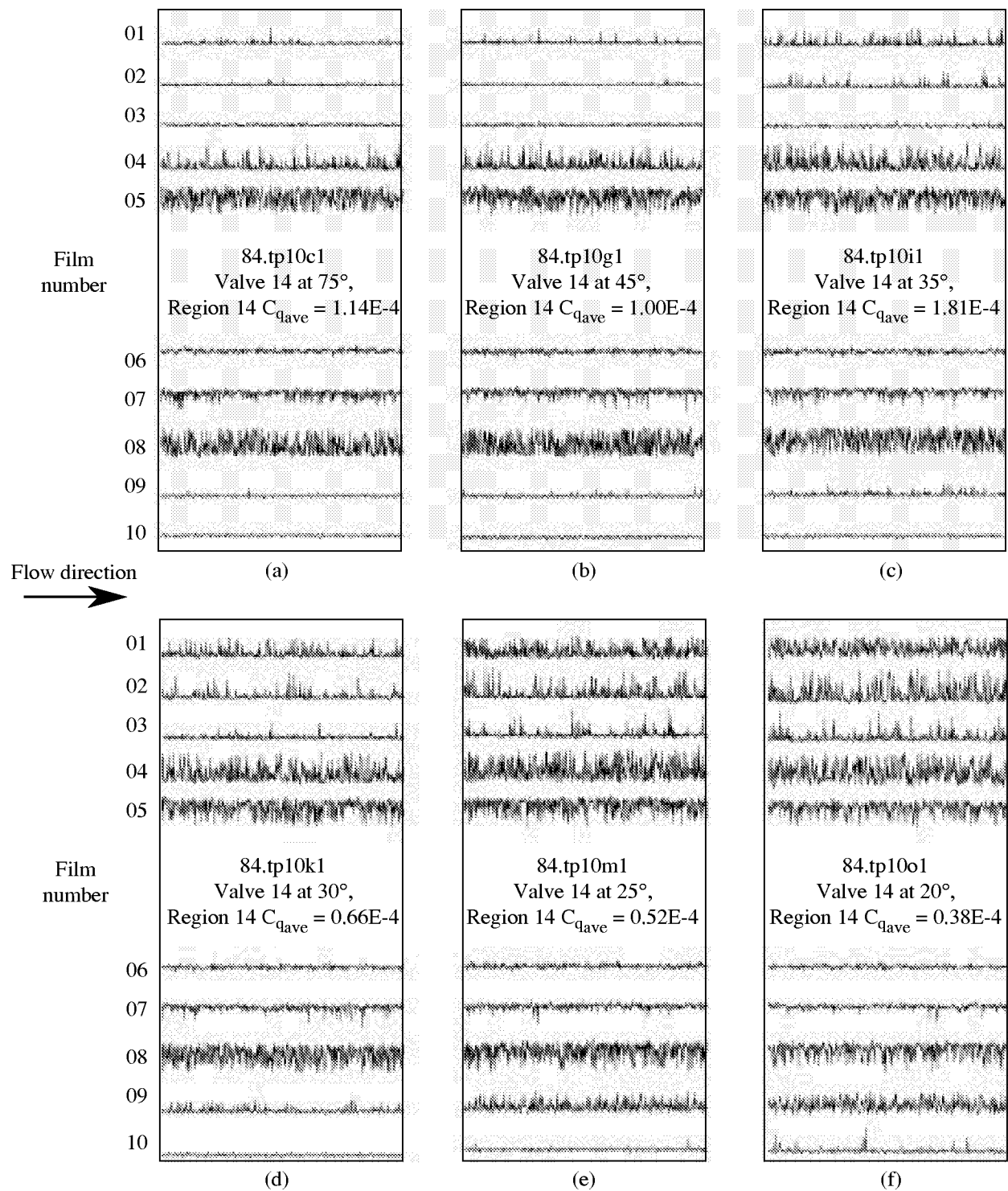


Figure 106. Effect of C_q reduction on lateral spreading of turbulence. Hot-film traces for 10-film array located aft of tripping element for test points taken during flight 84. Film 01 is most inboard film; film 10 is farthest outboard film.

Lateral spreading angle, deg	$C_q \times 10^4$	Source
5.5	0	Braslow (1959)
4.8-7.8	0	Fischer (1972)
7.0	1.14	F-16XL-2
7.8	0.38	F-16XL-2

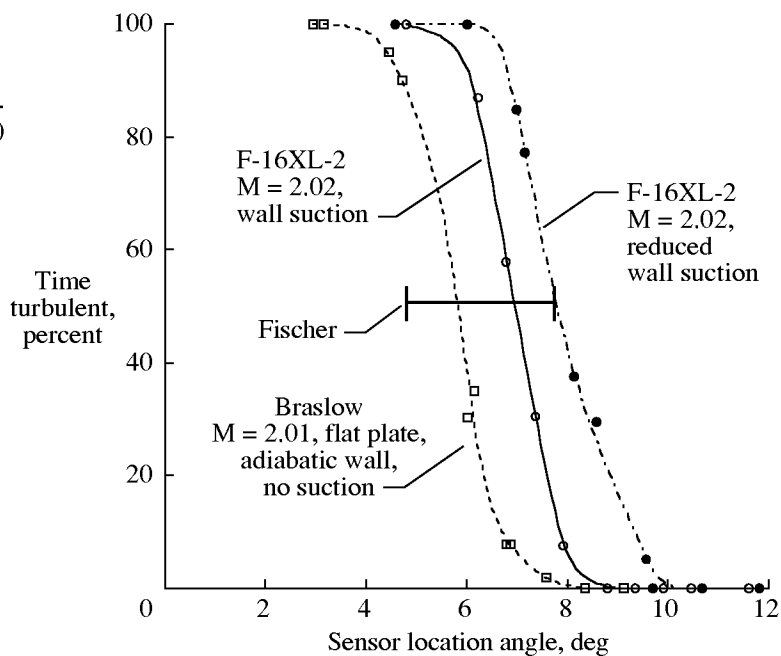


Figure 107. Comparison of F-16XL-2 lateral turbulence spreading with previously reported data. F-16XL-2 and Braslow values use angle calculated at 50-percent level.

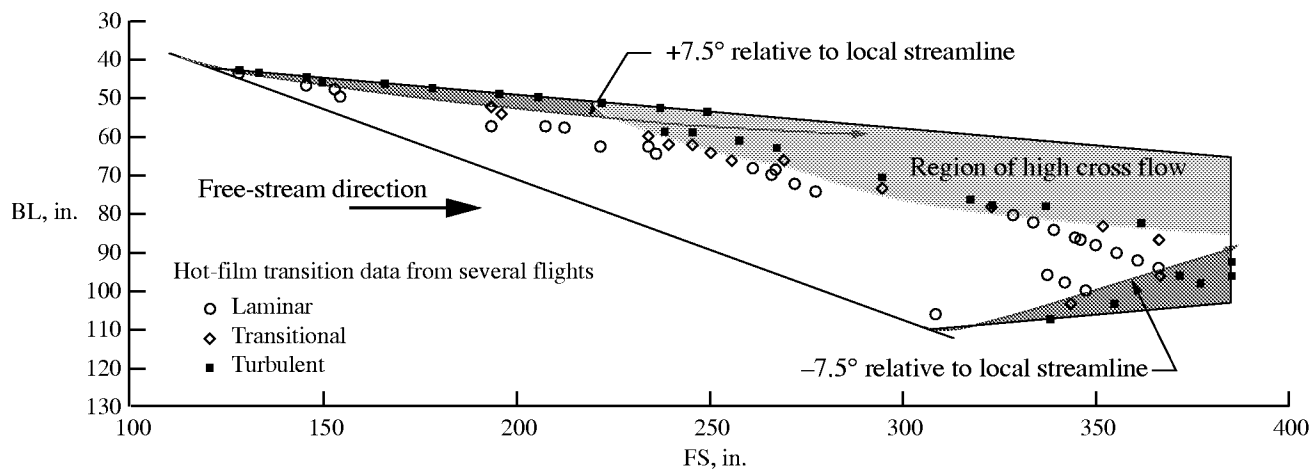
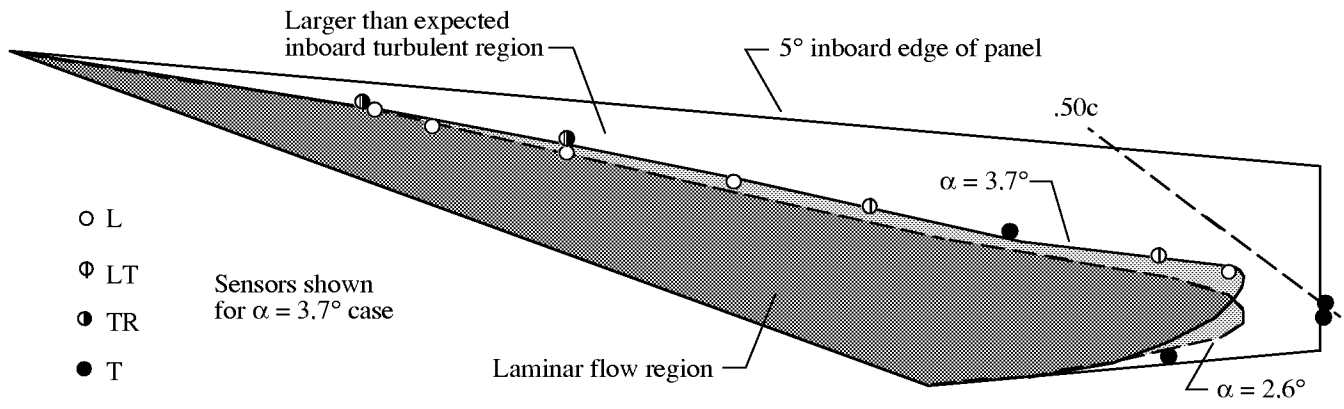
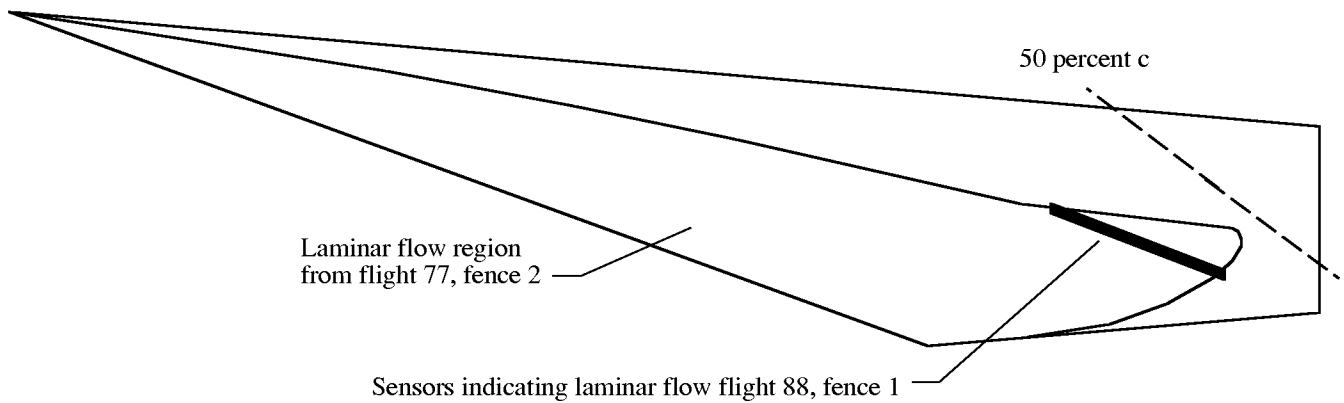


Figure 108. Disturbance path traces shown are for $M = 2.02$; $\alpha = 3.7^\circ$; $\beta = -1.4^\circ$; (84.10c1). Turbulence spreading is shown for $\pm 7.5^\circ$ relative to local streamline.



(a) Maximum extent of laminar flow achieved with fence 2.



(b) Comparison of laminar flow achieved with fences 1 and 2.

Figure 109. Maximum extent of laminar flow achieved. Maximum run of laminar flow = 10.5 ft (46 percent x/c); 70.04i1: $M = 2.0$; $h = 50\,000$ ft; $\alpha = 2.6^\circ$; $\beta = -.07^\circ$; 77a4g1: $M = 2.0$; $h = 53\,000$ ft; $\alpha = 3.7^\circ$; $\beta = -1.42^\circ$ (sensors shown). Fence 1: 88.a2d1: $M = 2.0$; $h = 53\,000$ ft; $\alpha = 3.4^\circ$; $\beta = -1.51^\circ$. Fence 2: 77.a4g1: $M = 2.0$; $h = 53\,000$ ft; $\alpha = 3.7^\circ$; $\beta = -1.42^\circ$;

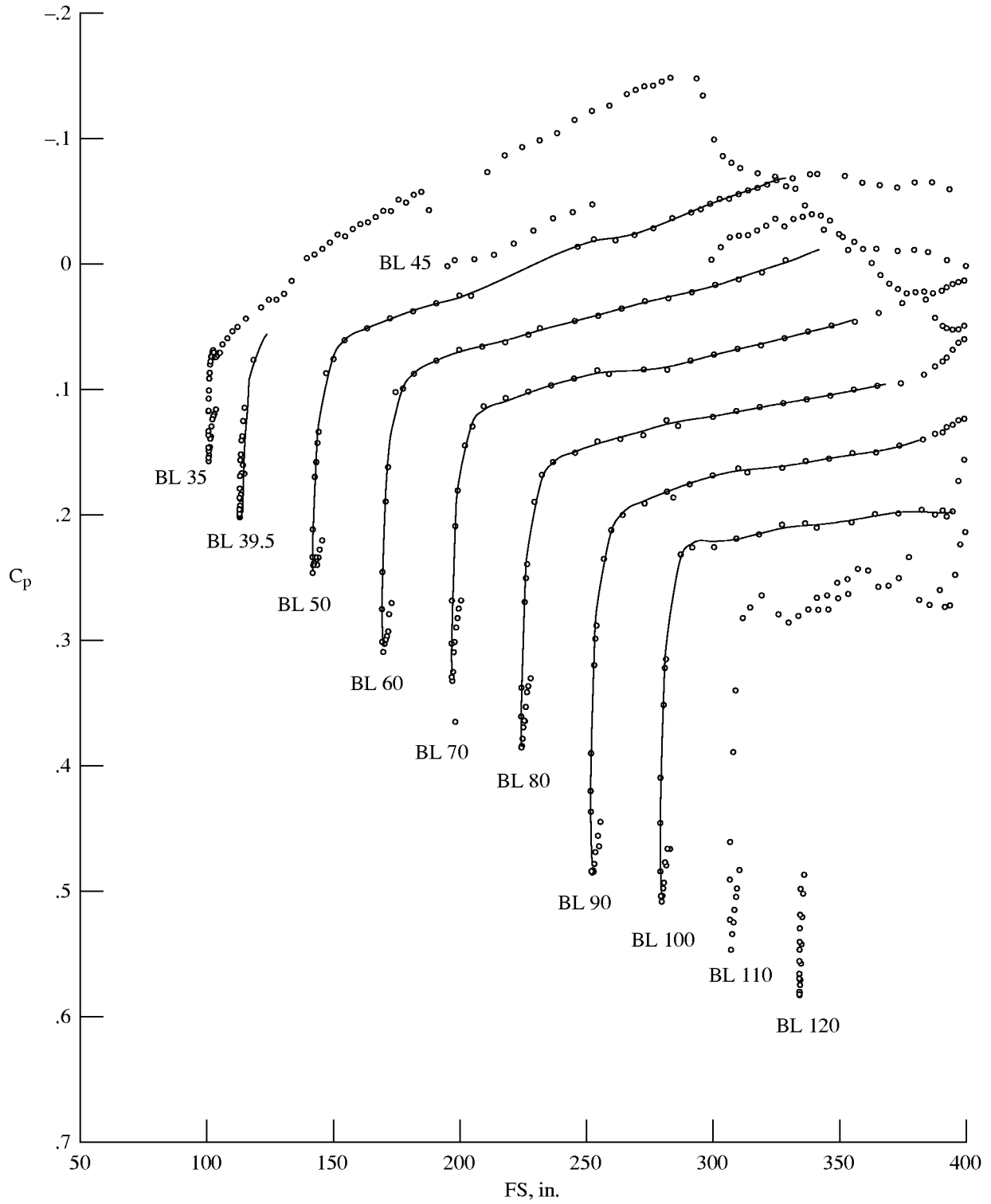


Figure 110. Fit of C_p data for test point 77.a4g1 (generated by HTC). $M = 1.97$; $\alpha = 3.7^\circ$; $\beta = -1.5^\circ$. C_p offset = 0.005 per 1-in. BL; y scale is for BL 35.

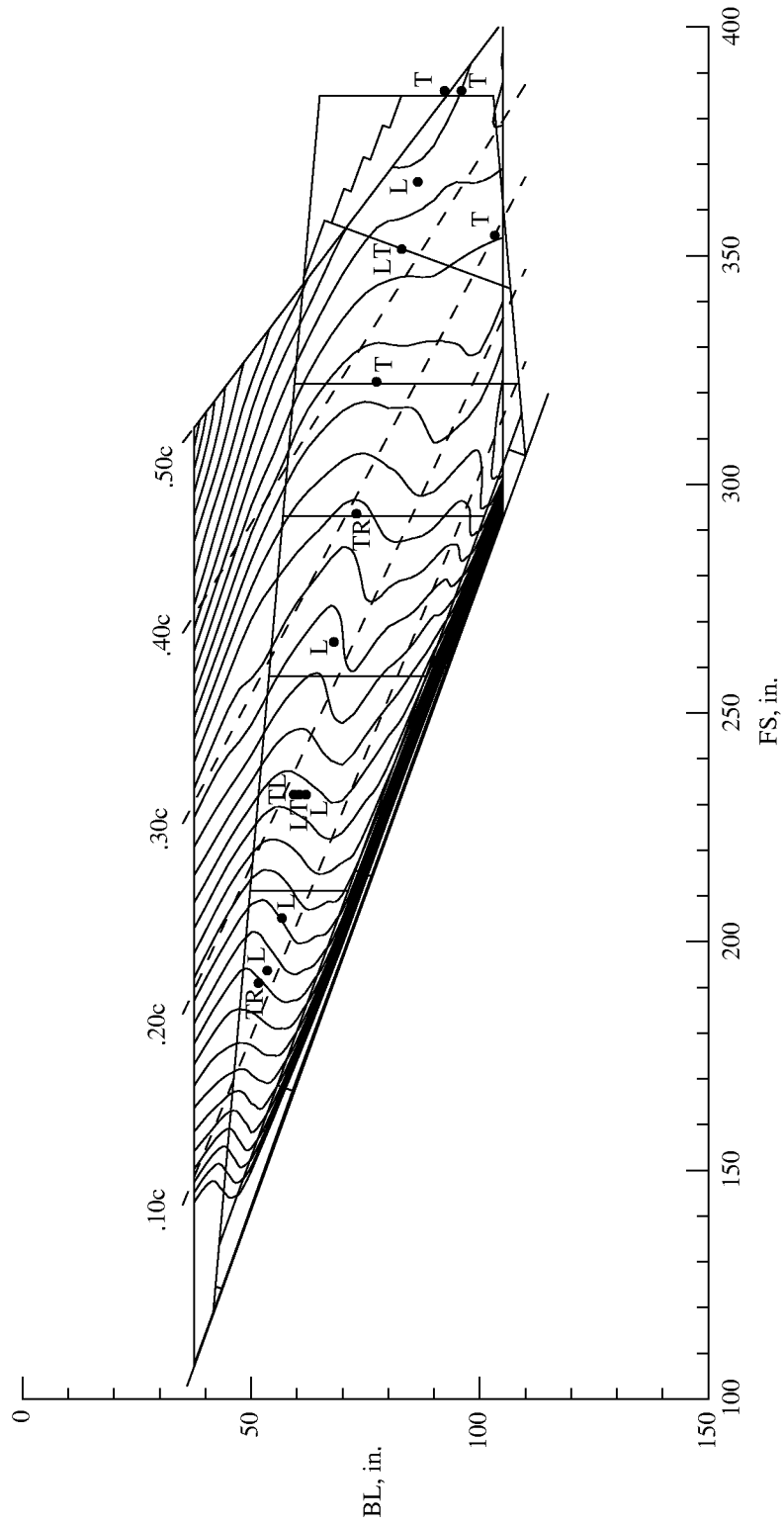


Figure 111. C_p contours for test point 77.a4g1 (generated by HTC). $M = 1.97$; $\alpha = 3.7^\circ$; $\beta = -1.5^\circ$.

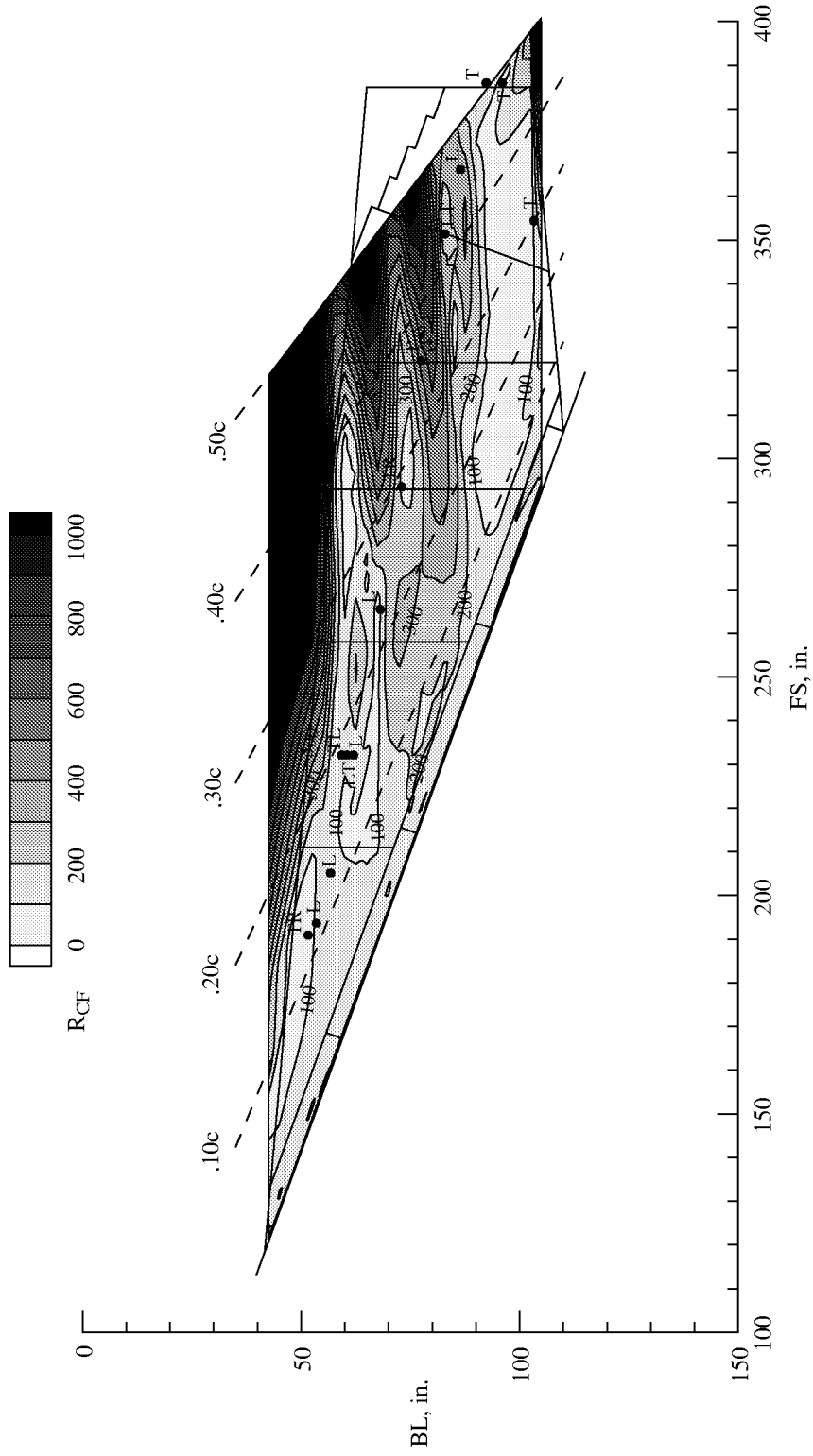


Figure 112. Cross-flow Reynolds number contours for test point 77.a4g1 (generated by HTC). $M = 1.97$; $\alpha = 3.7^\circ$; $\beta = -1.5^\circ$.

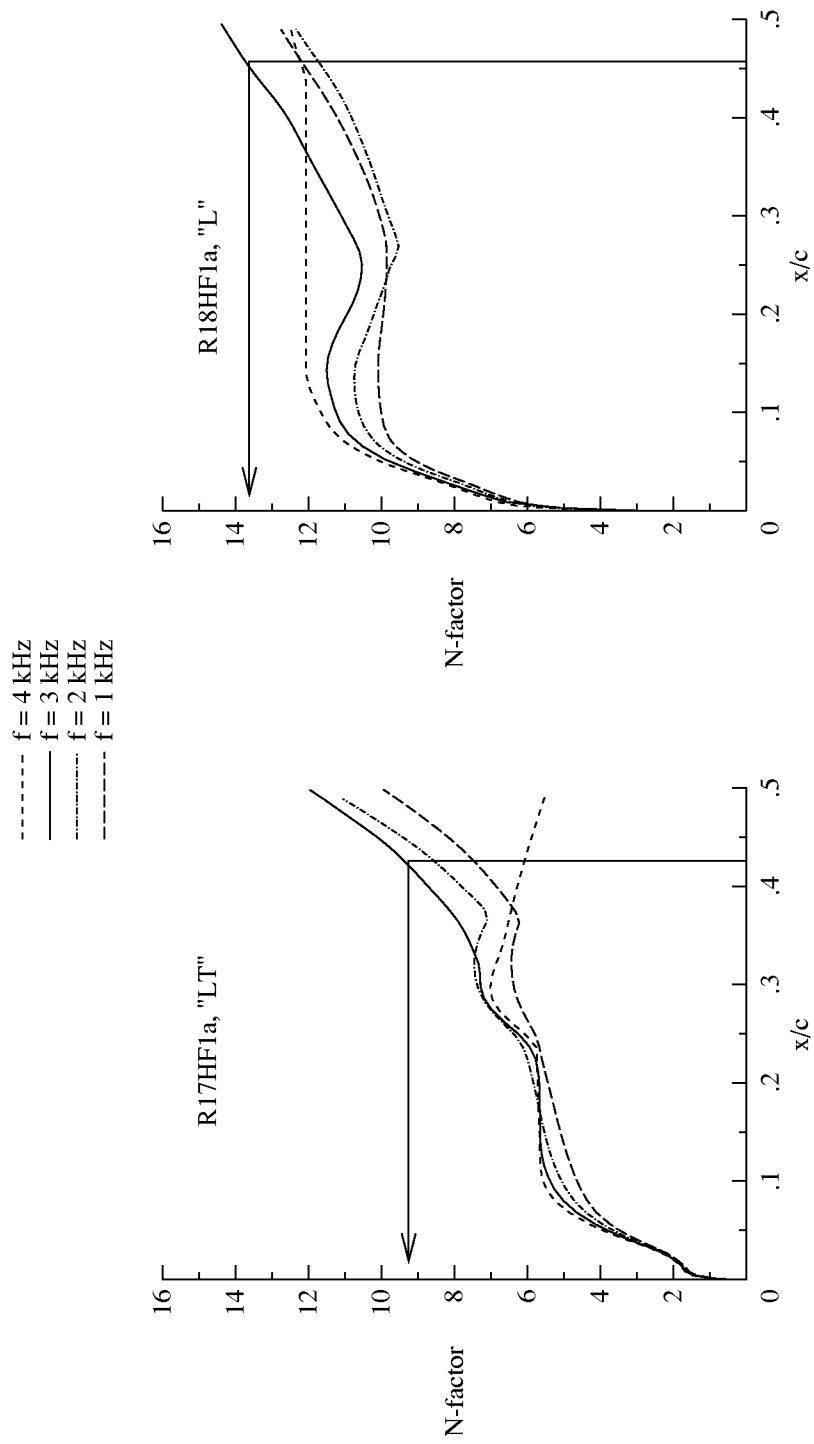


Figure 113. N-factor calculations for films R17HF1a and R18HF1a for test point 77.a4g1 (generated by HTC), $M = 1.97$; $\alpha = 3.7^\circ$; $\beta = -1.5^\circ$.

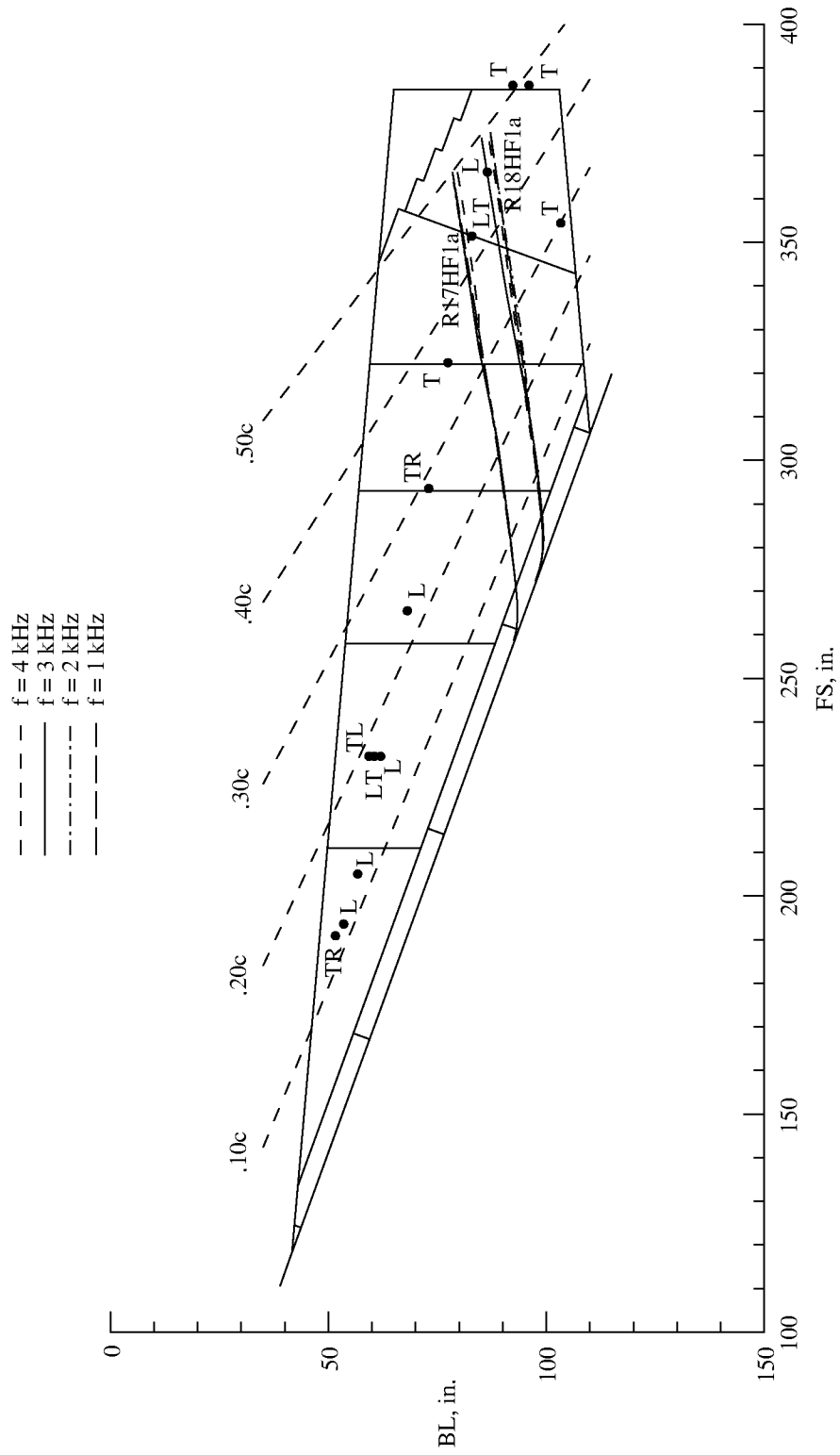


Figure 114. N -factor traces on glove for test point 77.a4g1 (generated by HTC). $M = 1.97$; $\alpha = 3.7^\circ$; $\beta = -1.5^\circ$.

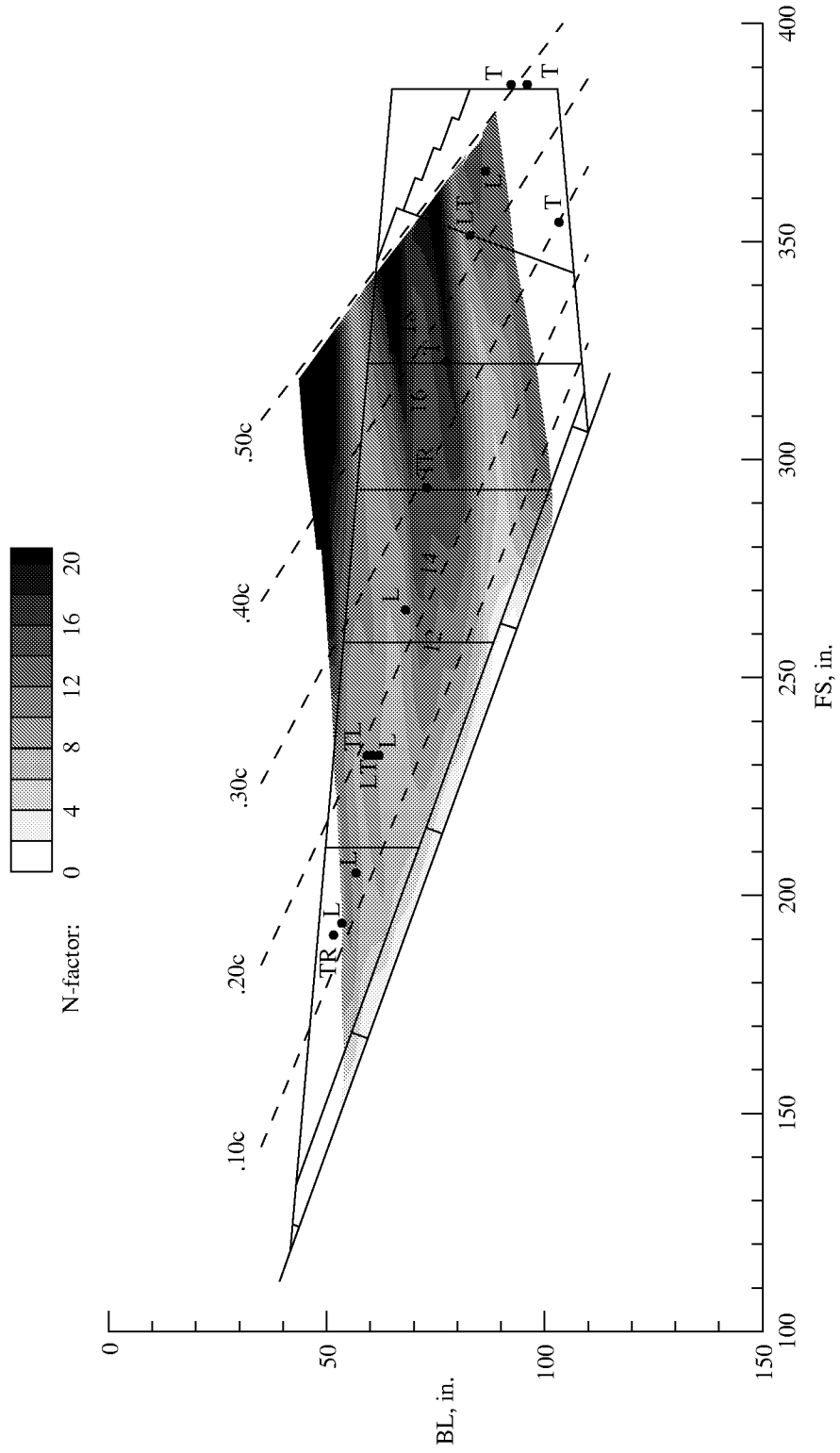


Figure 115. *N*-factor contours for test point 77.a4g1 (generated by HTC). $M = 1.97$; $\alpha = 3.7^\circ$; $\beta = -1.5^\circ$.

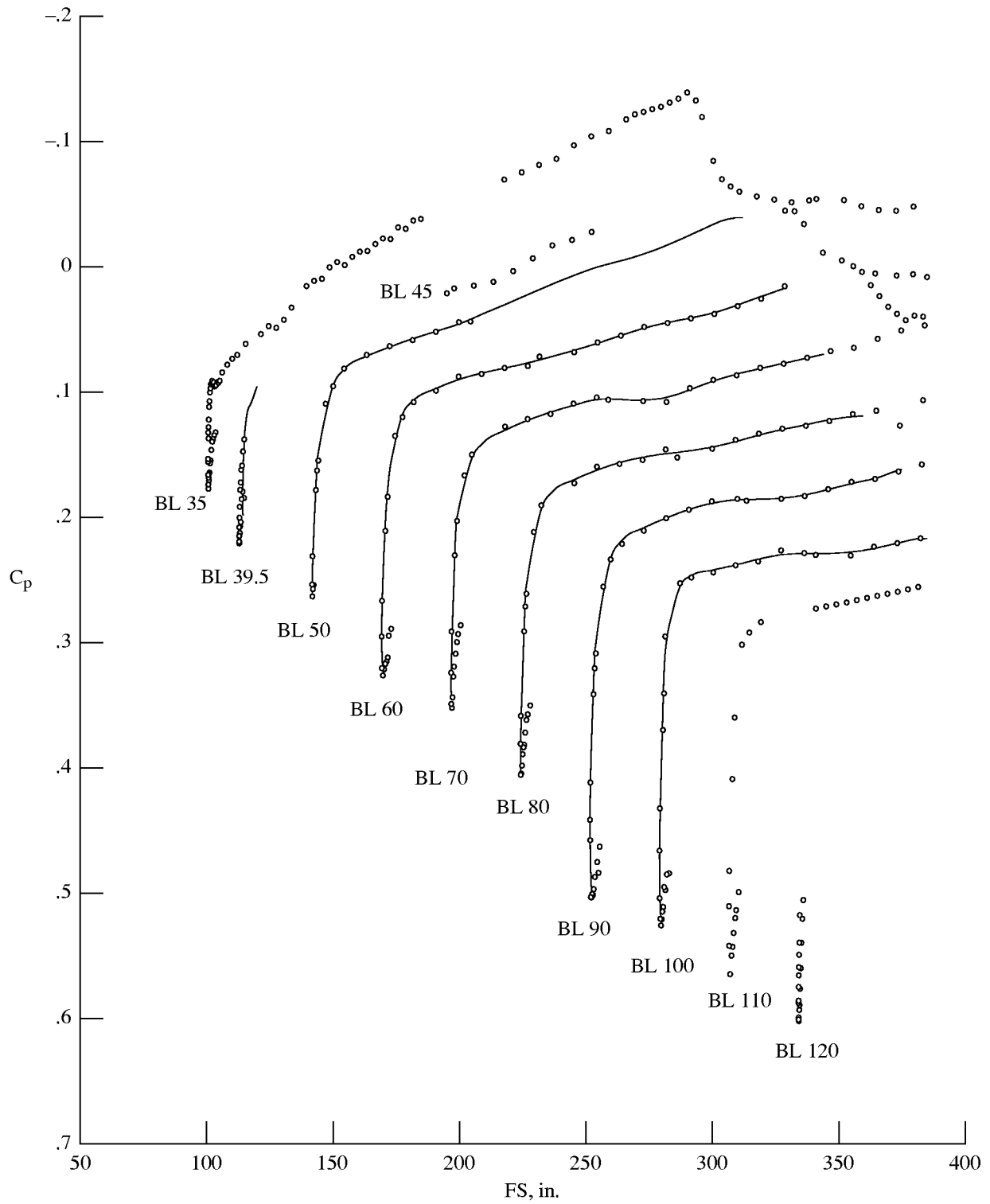


Figure 116. Fit of C_p data for test point 80.a3k1 (generated by HTC). $M = 2.02$; $\alpha = 3.7^\circ$; $\beta = -1.5^\circ$. C_p offset = 0.005 per 1-in. BL; y scale is for BL 35.

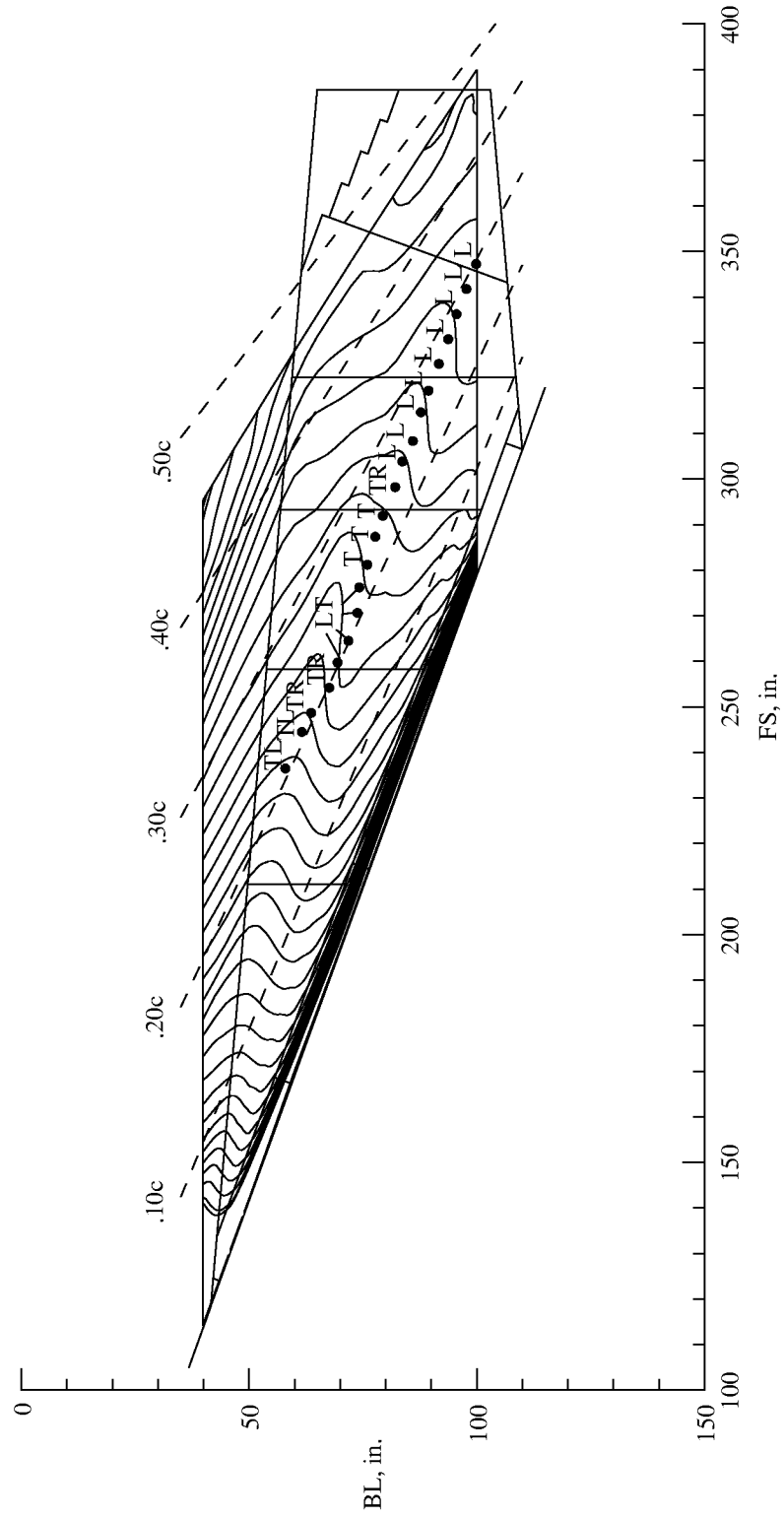


Figure 117. C_p contours for test point 80.a3k1 (generated by HTC). $M = 2.02$; $\alpha = 3.7^\circ$; $\beta = -1.5^\circ$.

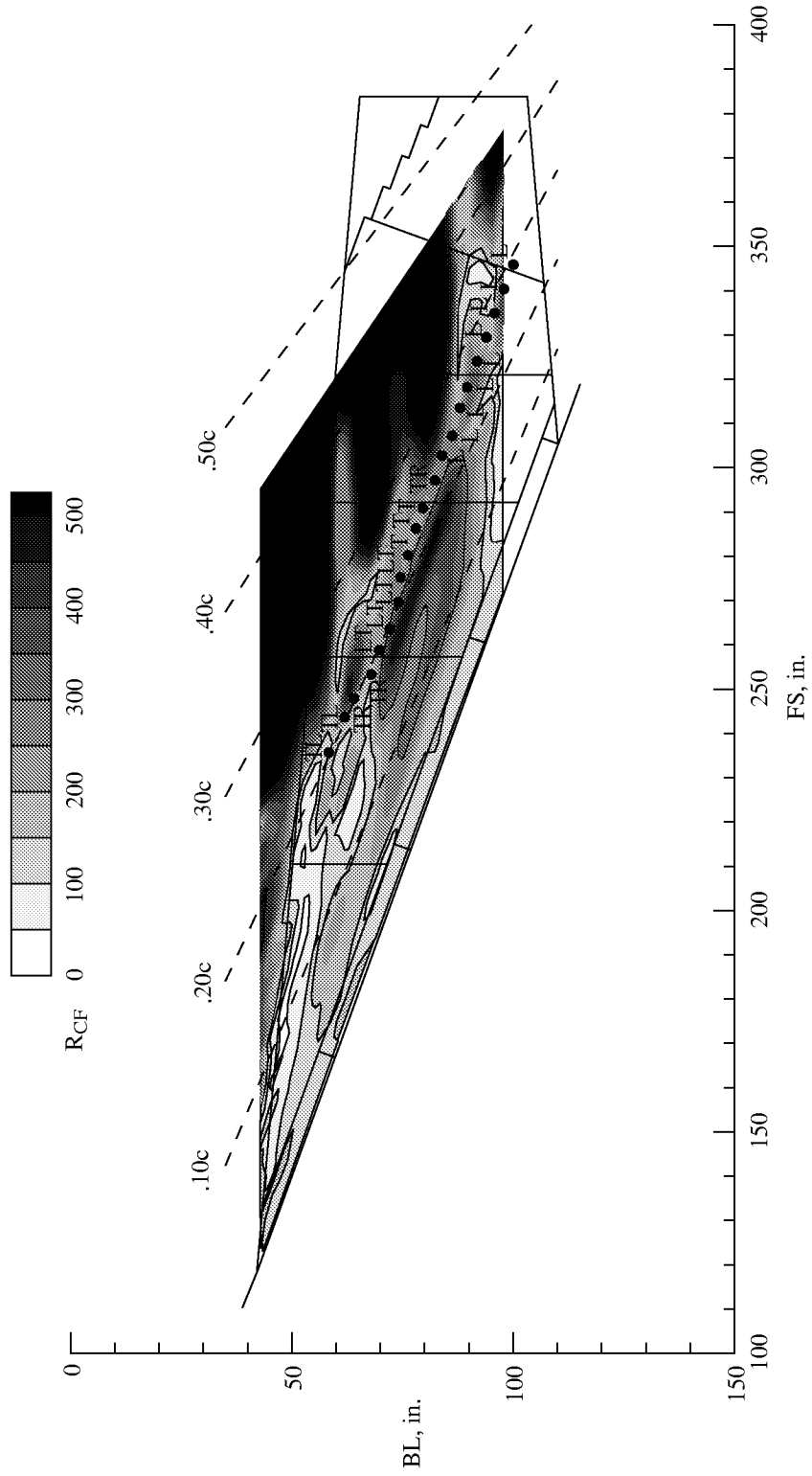
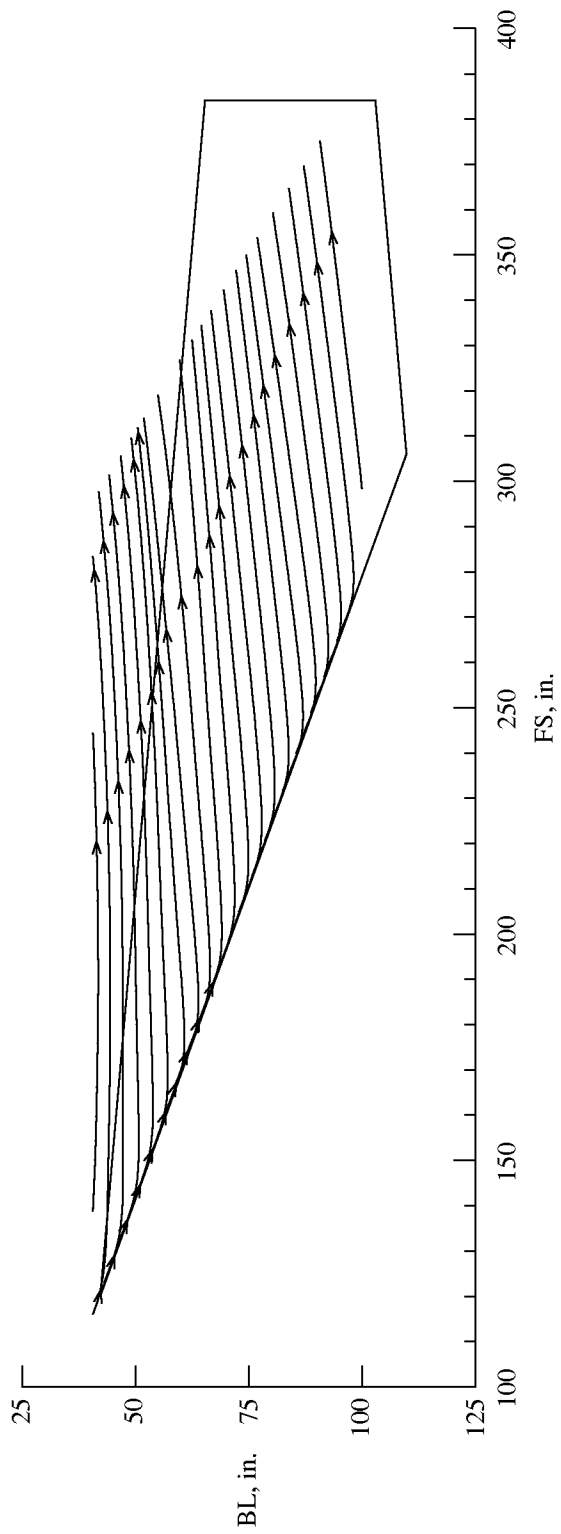
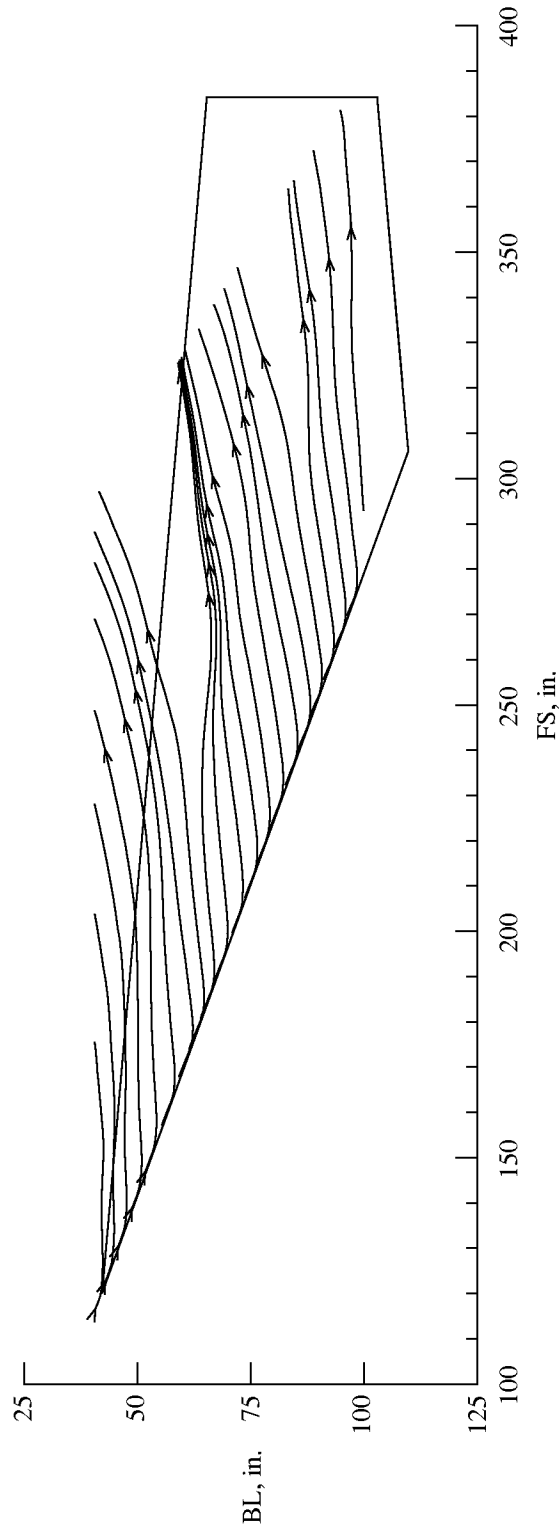


Figure 118. Cross-flow Reynolds number contours for test point 80.a3k1 (generated by HTC). $M = 2.02$; $\alpha = 3.7^\circ$; $\beta = -1.5^\circ$.



(a) Edge streamlines.



(b) Surface streamlines.

Figure 119. Edge and surface streamlines for test point 80.a3k1 (generated by HTC). $M = 2.02$; $\alpha = 3.7^\circ$; $\beta = -1.5^\circ$.

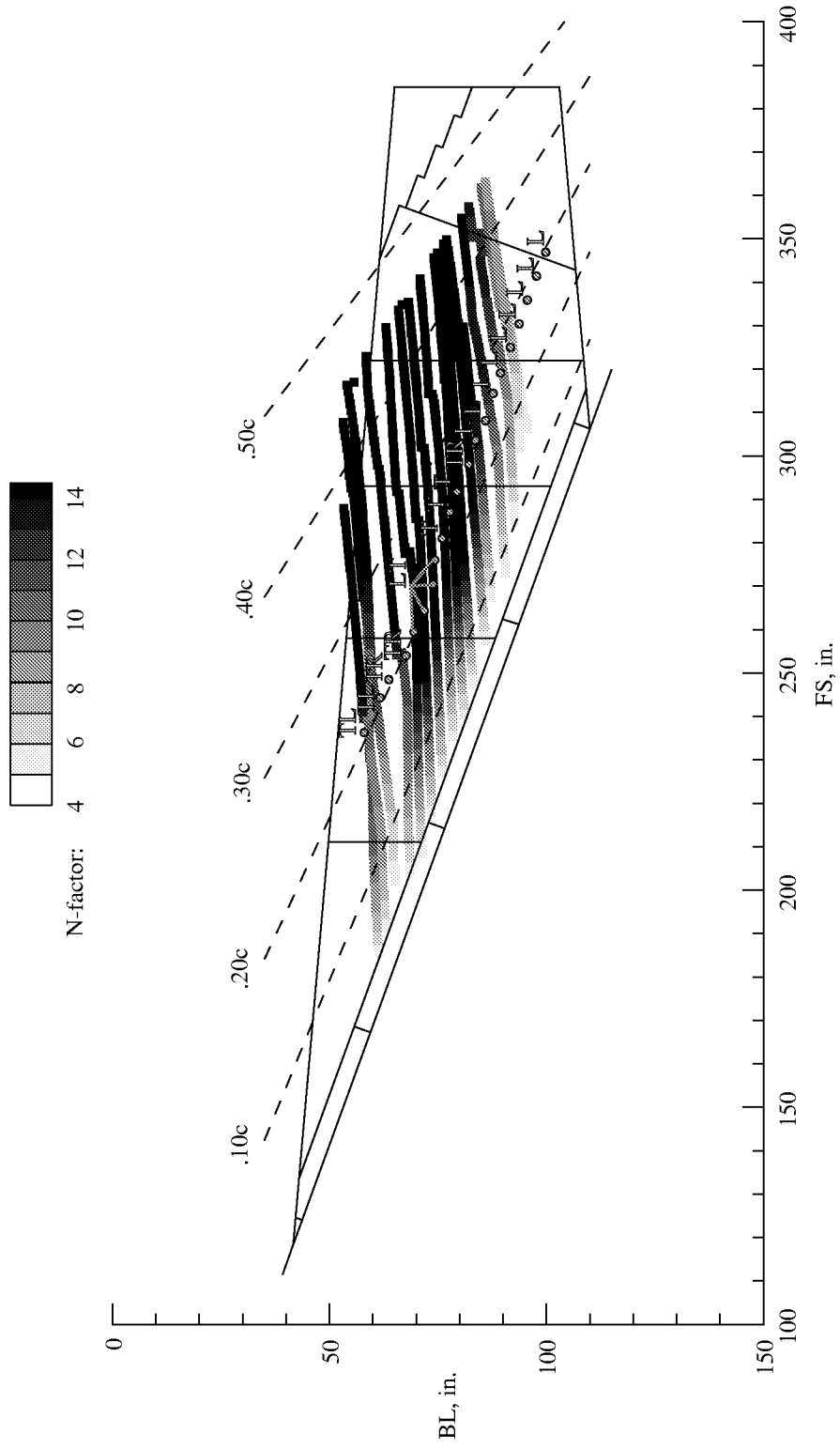


Figure 120. *N*-factor calculations for test point 80.a3k1 (generated by HTC). $M = 2.02$; $\alpha = 3.7^\circ$; $\beta = -1.5^\circ$.

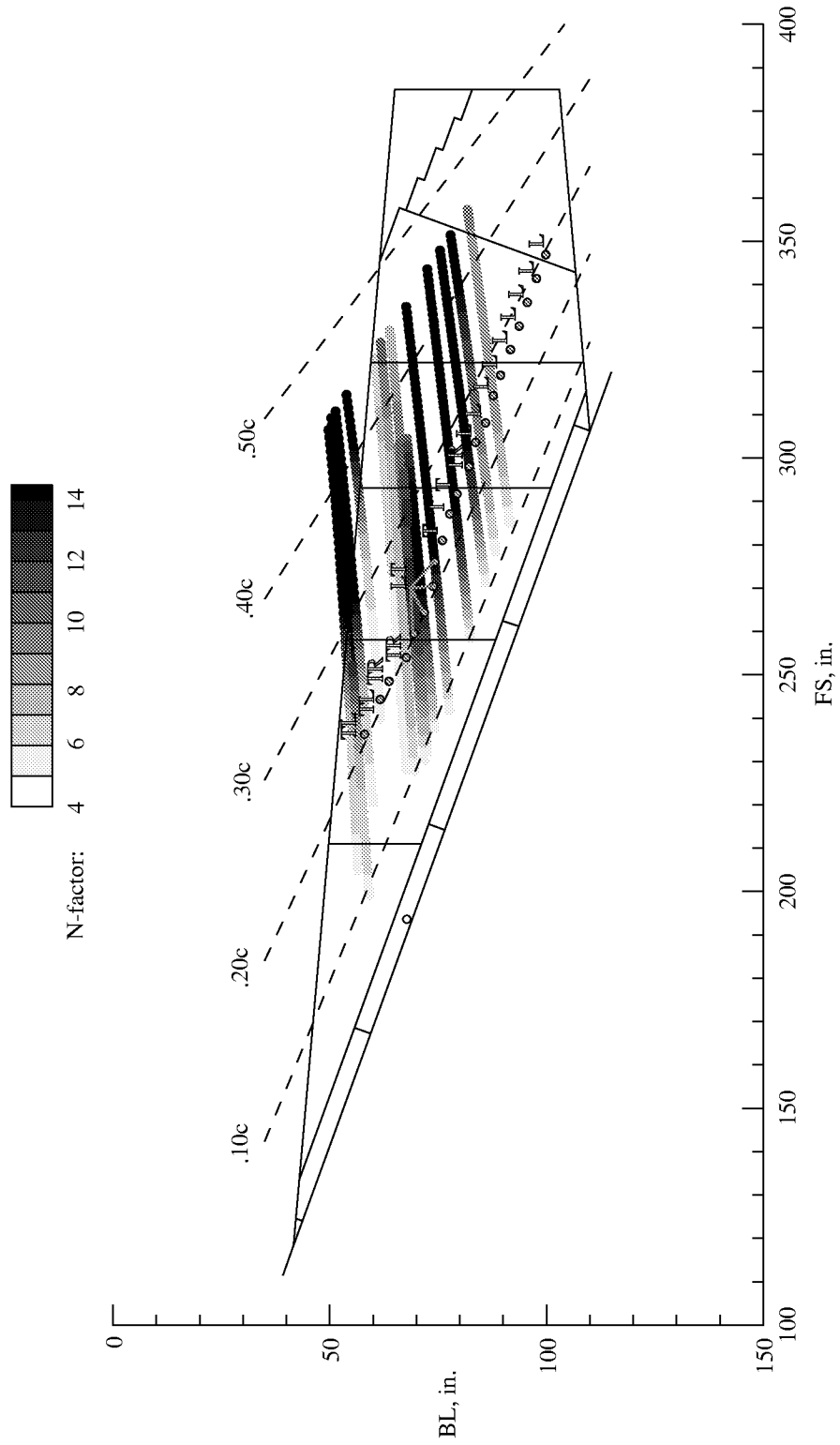


Figure 121. PSE results for test point 80.a3k1 (generated by HTC). $M = 2.02$; $\alpha = 3.7^\circ$; $\beta = -1.5^\circ$.

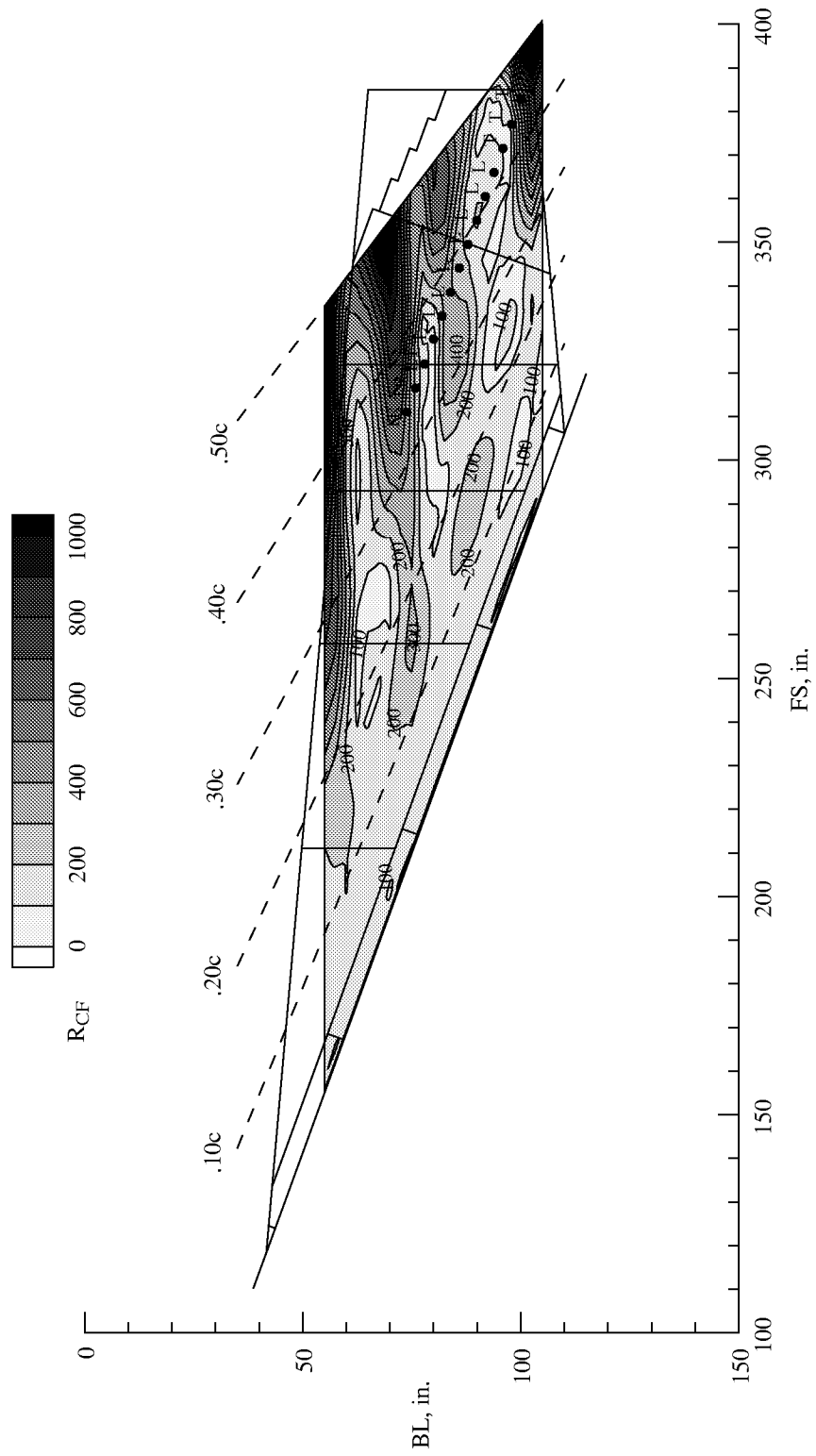


Figure 122. Cross-flow Reynolds number contours for test point 88.a2d1 (generated by HTC). $M = 2.01$; $\alpha = 3.39^\circ$; $\beta = -1.5^\circ$.

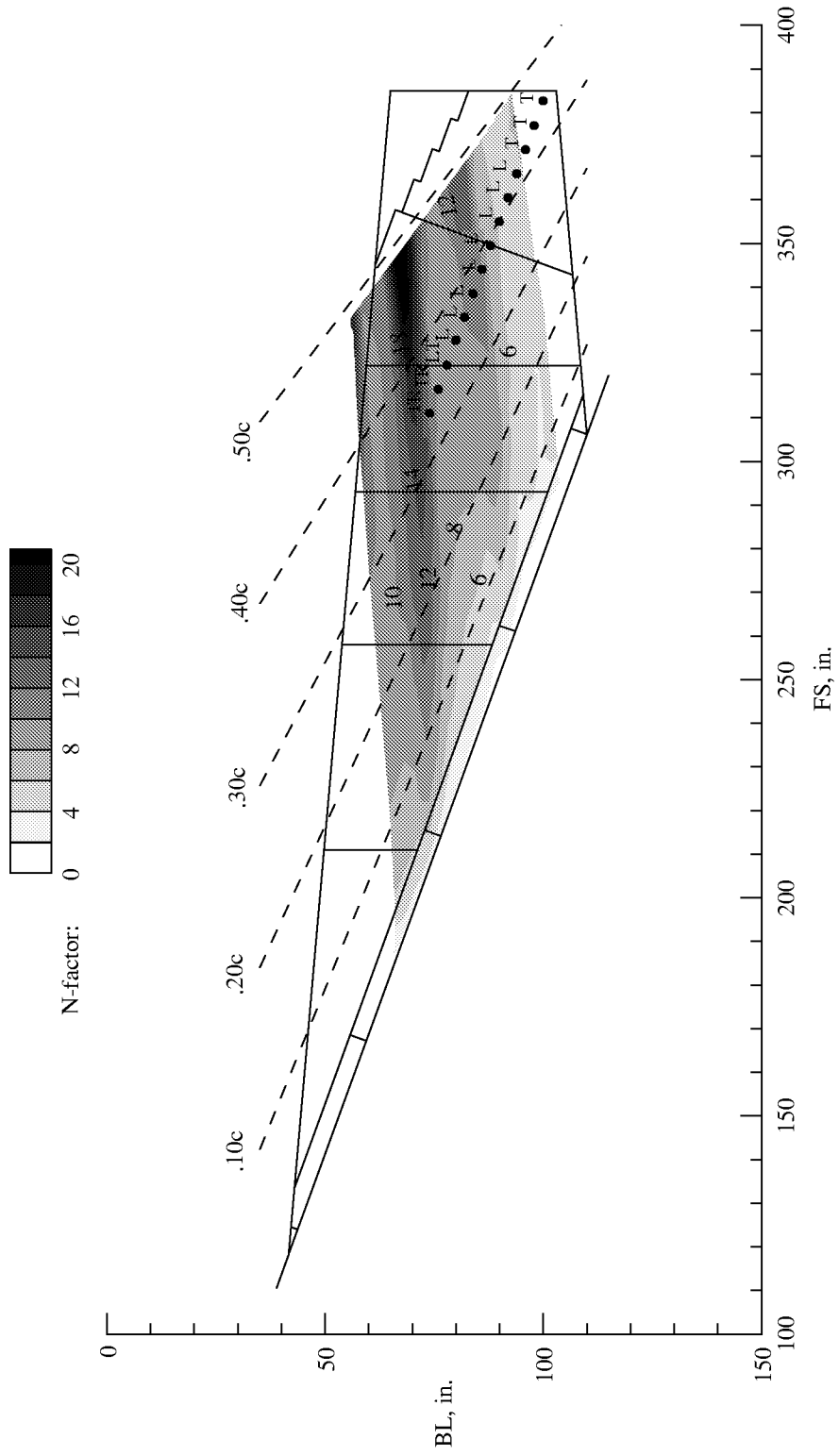


Figure 123. *N*-factor contours for test point 88.a2d1 (generated by HTC). $M = 2.01$; $\alpha = 3.39^\circ$; $\beta = -1.5^\circ$.

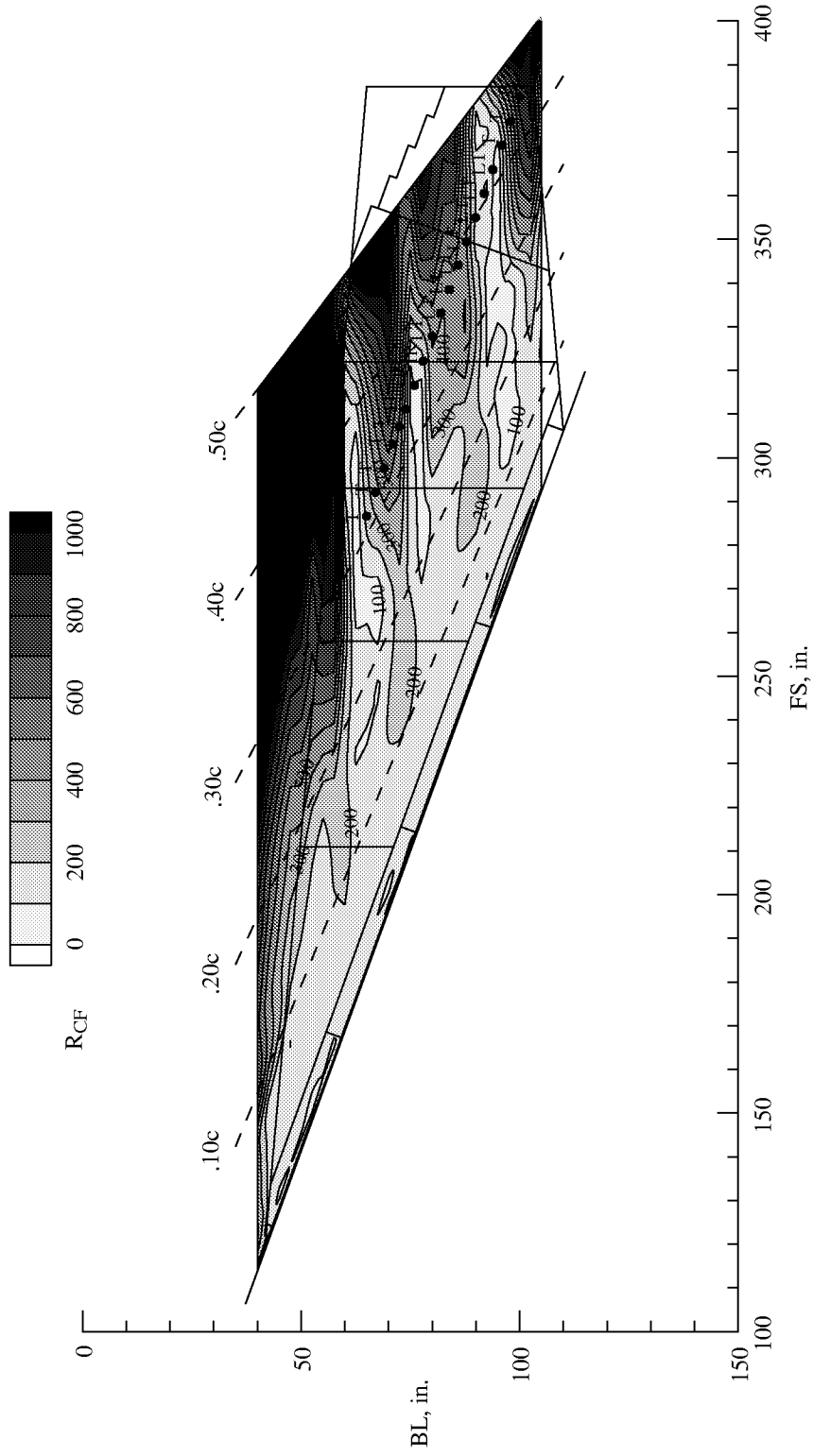


Figure 124. Cross-flow Reynolds number contours for test point 88.a4i1 (generated by HTC). $M = 1.99$; $\alpha = 3.38^\circ$; $\beta = -1.46^\circ$.

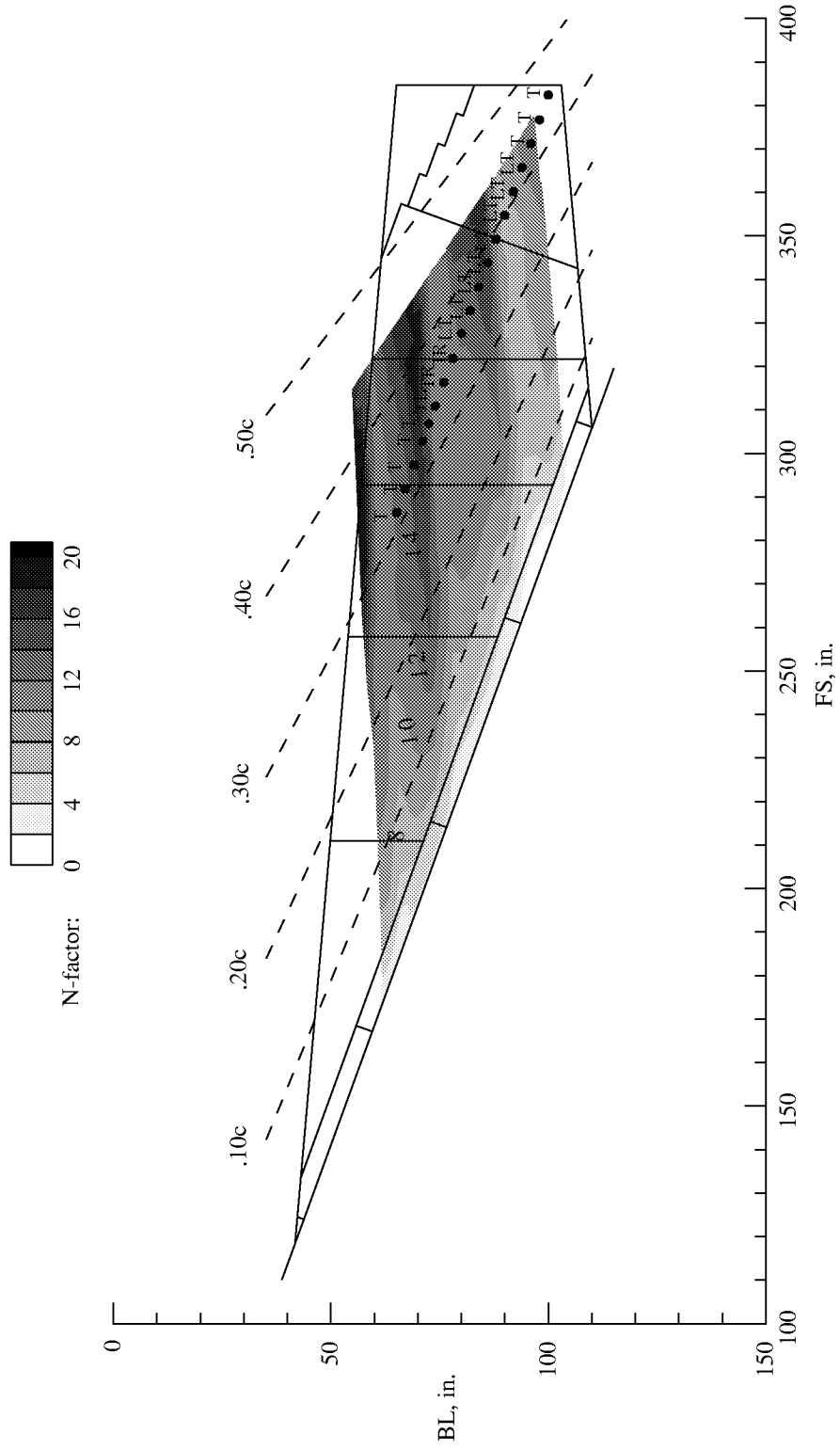


Figure 125. *N*-factor contours for test point 88.a4i1 (generated by HTC). $M = 1.99$; $\alpha = 3.38^\circ$; $\beta = -1.46^\circ$.

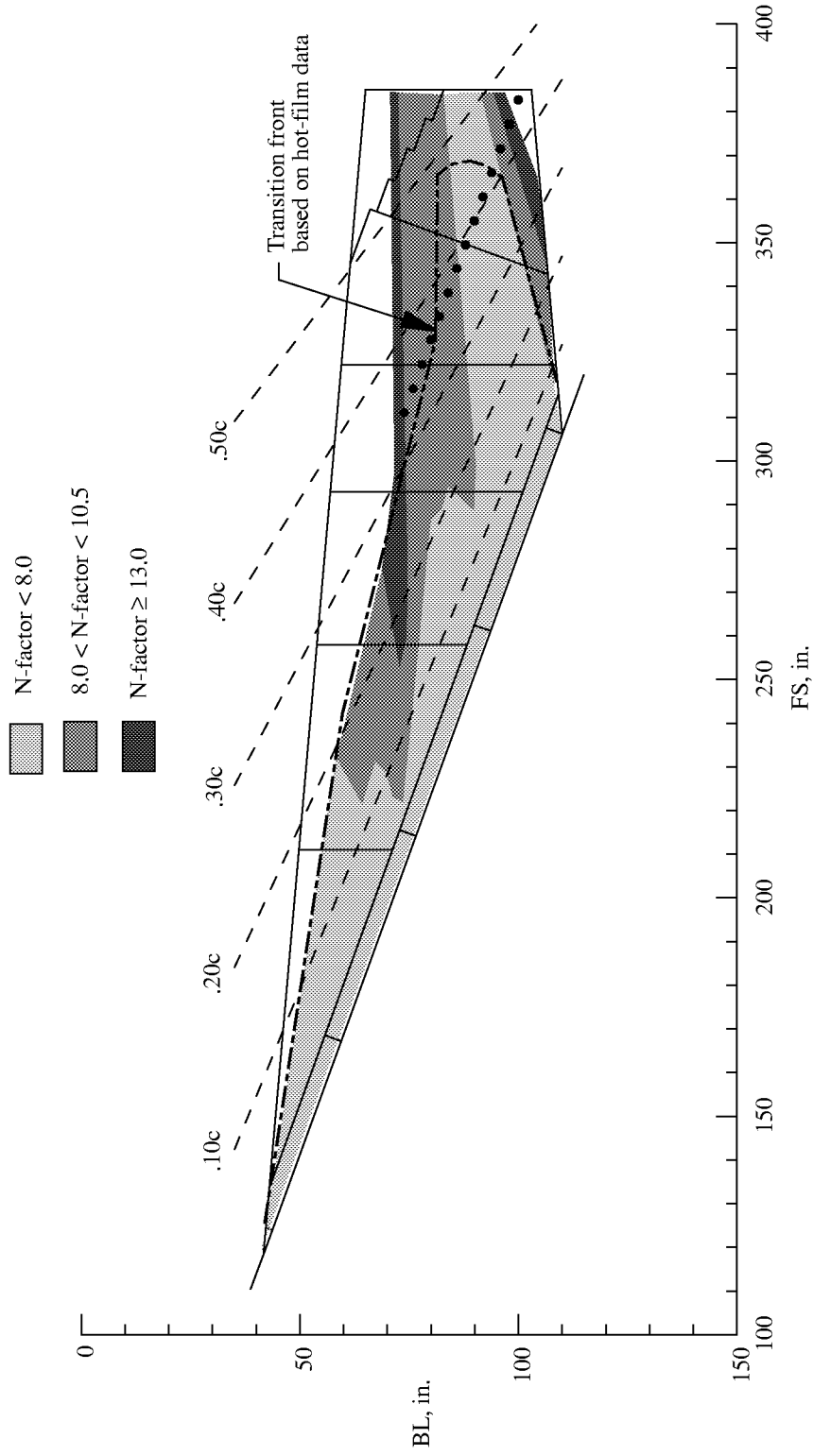


Figure 126. Estimate of maximum laminar flow on F-16XL-2 glove based on N -factor calculations (generated by HTC).

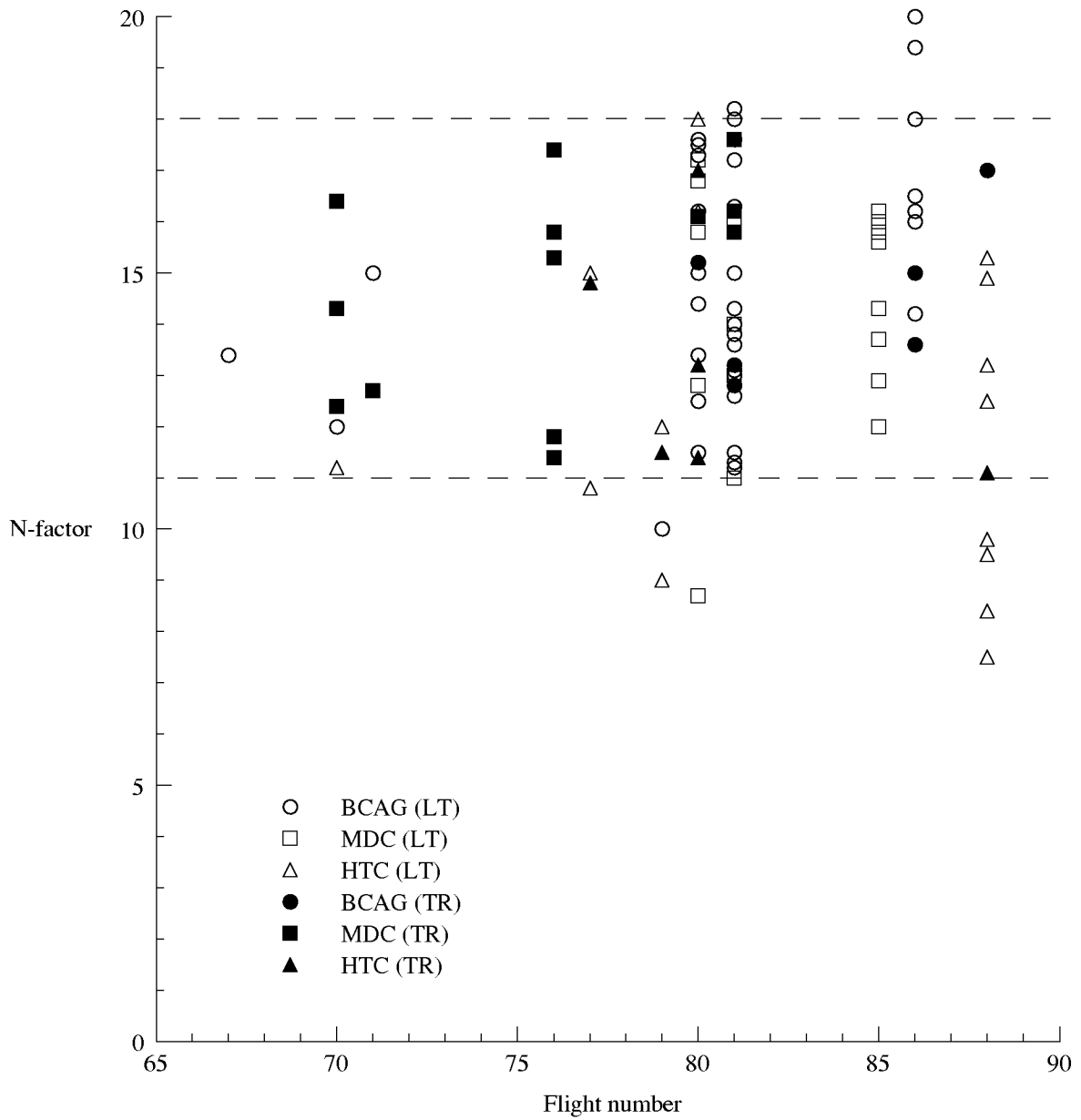


Figure 127. Summary of code calibration results for each flight.

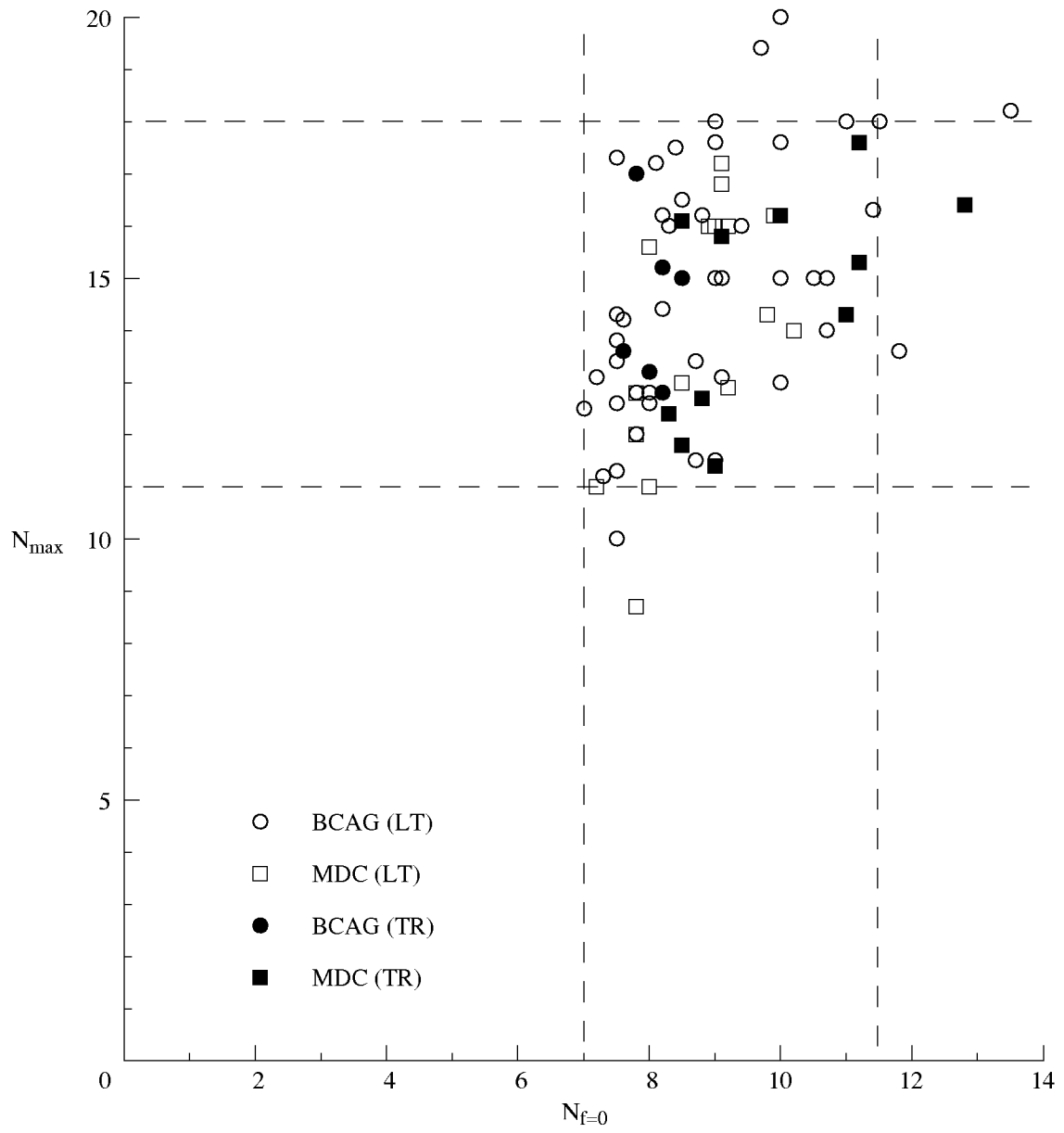


Figure 128. Code calibration results from MDC and BCAG.

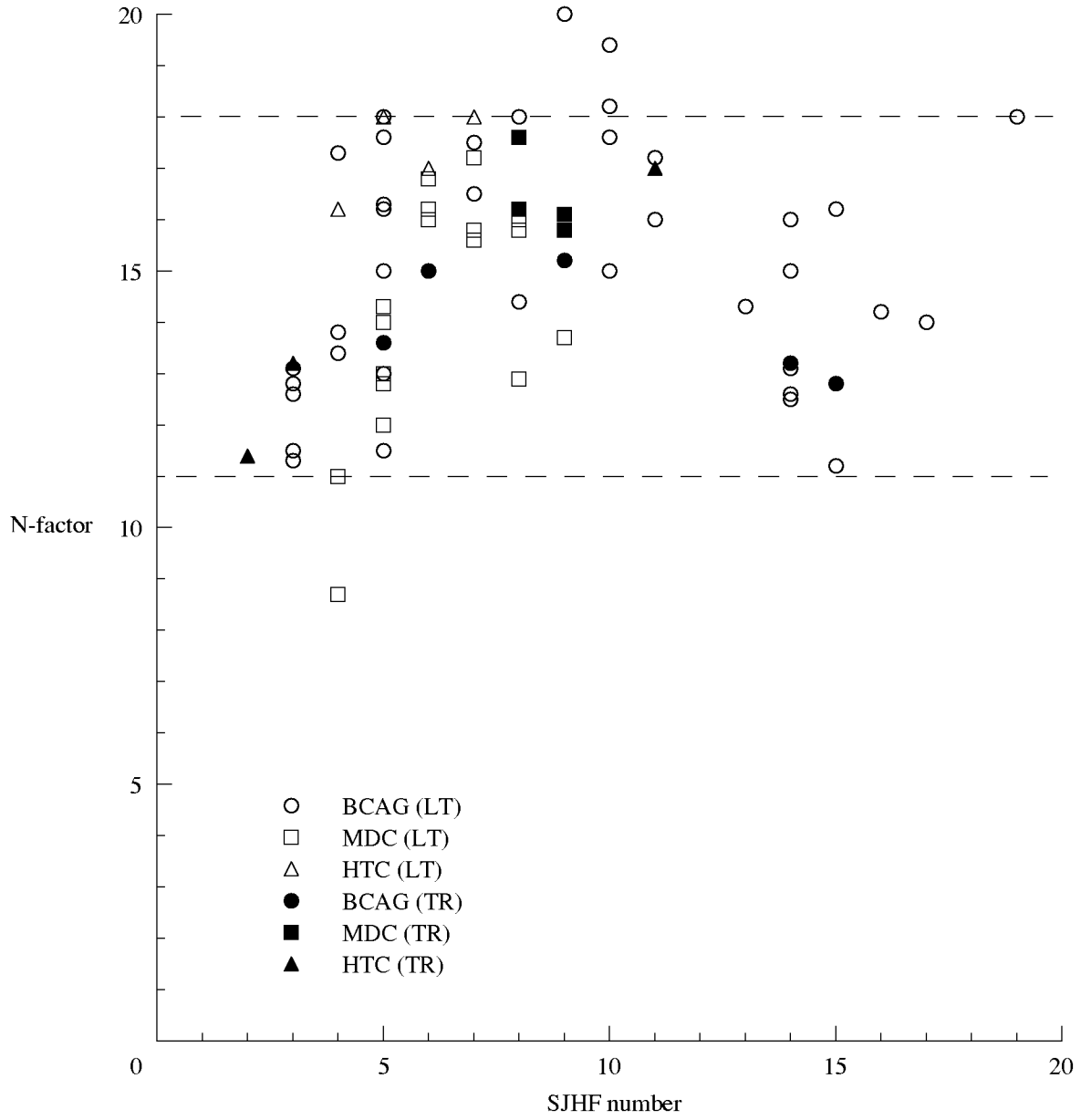


Figure 129. Maximum N -factors found for Splice Joint Hot Films (SJHF).

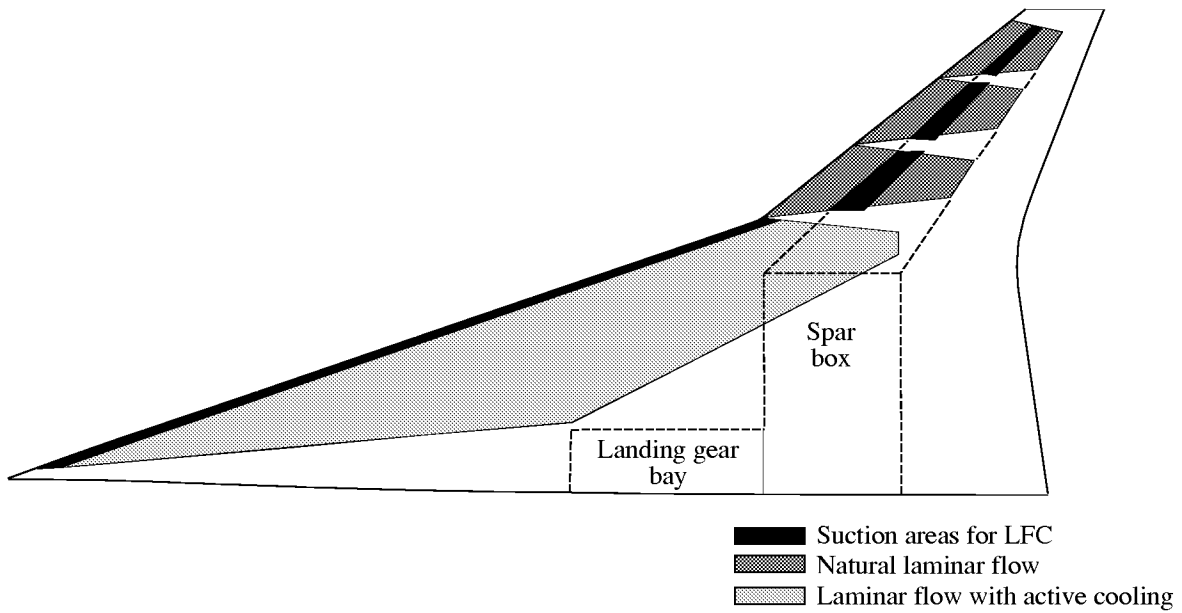


Figure 130. Laminarized area for SLFC benefits study.

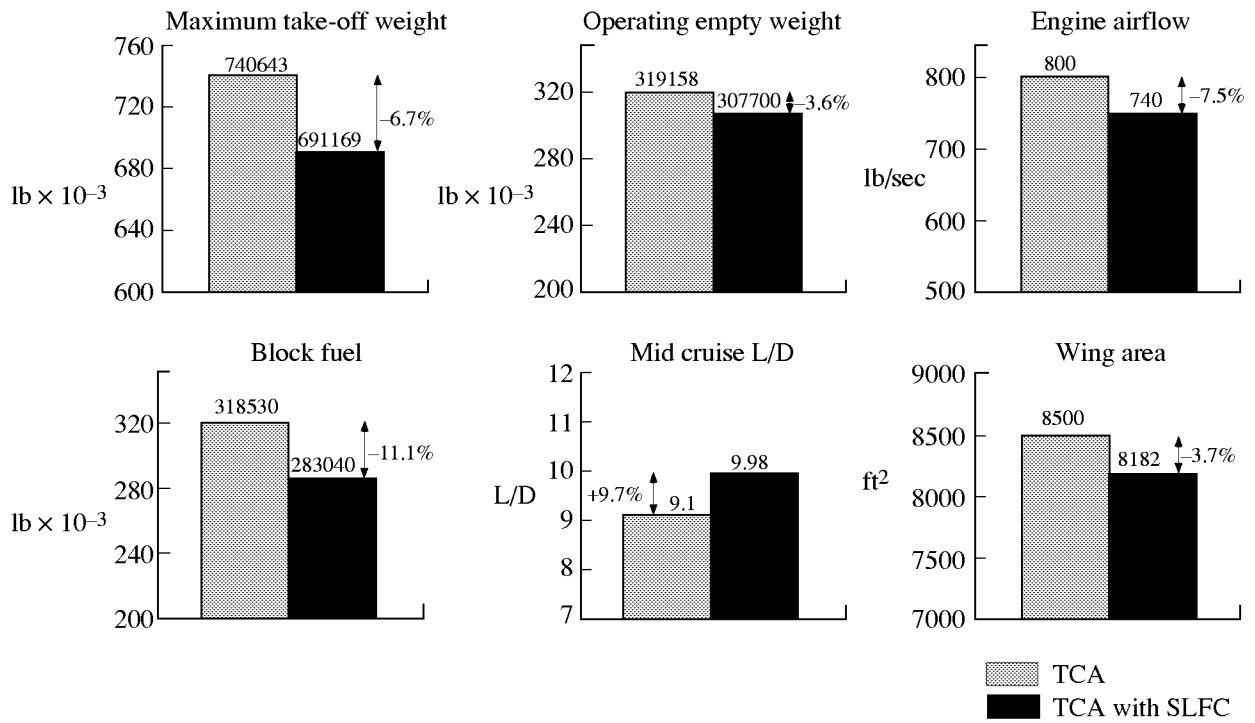


Figure 131. Results of SLFC benefits study.

